NASA/CP-1999-209692/VOL2

1998 NASA High-Speed Research Program Aerodynamic Performance Workshop

Volume II—High Lift

Edited by
S. Naomi McMillin
Langley Research Center, Hampton, Virginia

December 1999

The NASA STI Program Office . . . in Profile

Since its founding, NASA has been dedicated to the advancement of aeronautics and space science. The NASA Scientific and Technical Information (STI) Program Office plays a key part in helping NASA maintain this important role.

The NASA STI Program Office is operated by Langley Research Center, the lead center for NASA's scientific and technical information. The NASA STI Program Office provides access to the NASA STI Database, the largest collection of aeronautical and space science STI in the world. The Program Office is also NASA's institutional mechanism for disseminating the results of its research and development activities. These results are published by NASA in the NASA STI Report Series, which includes the following report types:

- TECHNICAL PUBLICATION. Reports of completed research or a major significant phase of research that present the results of NASA programs and include extensive data or theoretical analysis. Includes compilations of significant scientific and technical data and information deemed to be of continuing reference value. NASA counterpart of peer-reviewed formal professional papers, but having less stringent limitations on manuscript length and extent of graphic presentations.

- TECHNICAL MEMORANDUM. Scientific and technical findings that are preliminary or of specialized interest, e.g., quick release reports, working papers, and bibliographies that contain minimal annotation. Does not contain extensive analysis.

- CONTRACTOR REPORT. Scientific and technical findings by NASA-sponsored contractors and grantees.

- CONFERENCE PUBLICATION. Collected papers from scientific and technical conferences, symposia, seminars, or other meetings sponsored or co-sponsored by NASA.

- SPECIAL PUBLICATION. Scientific, technical, or historical information from NASA programs, projects, and missions, often concerned with subjects having substantial public interest.

- TECHNICAL TRANSLATION. English-language translations of foreign scientific and technical material pertinent to NASA's mission.

Specialized services that complement the STI Program Office's diverse offerings include creating custom thesauri, building customized databases, organizing and publishing research results . . . even providing videos.

For more information about the NASA STI Program Office, see the following:

- Access the NASA STI Program Home Page at ***http://www.sti.nasa.gov***

- Email your question via the Internet to help@sti.nasa.gov

- Fax your question to the NASA STI Help Desk at (301) 621-0134

- Telephone the NASA STI Help Desk at (301) 621-0390

- Write to:
  NASA STI Help Desk
  NASA Center for AeroSpace Information
  7121 Standard Drive
  Hanover, MD 21076-1320

NASA/CP-1999-209692/VOL2

1998 NASA High-Speed Research Program Aerodynamic Performance Workshop

Volume II—High Lift

Edited by
S. Naomi McMillin
Langley Research Center, Hampton, Virginia

Proceedings of a workshop sponsored by the
National Aeronautics and Space Administration,
Washington, D.C., and held in
Los Angeles, California
February 9–13, 1998

National Aeronautics and
Space Administration

Langley Research Center
Hampton, Virginia 23681-2199

December 1999

Available from:

NASA Center for AeroSpace Information (CASI)
7121 Standard Drive
Hanover, MD 21076-1320
(301) 621-0390

National Technical Information Service (NTIS)
5285 Port Royal Road
Springfield, VA 22161-2171
(703) 605-6000

PREFACE

The High-Speed Research Program sponsored the NASA High-Speed Research Program Aerodynamic Performance Review on February 9-13, 1998 in Los Angeles, California. The review was designed to bring together NASA and industry High-Speed Civil Transport (HSCT) Aerodynamic Performance technology development participants in areas of: Configuration Aerodynamics (transonic and supersonic cruise drag prediction and minimization), High-Lift, and Flight Controls. The review objectives were to: (1) report the progress and status of HSCT aerodynamic performance technology development; (2) disseminate this technology within the appropriate technical communities; and (3) promote synergy among the scientist and engineers working HSCT aerodynamics. In particular, single- and multi-point optimized HSCT configurations, HSCT high-lift system performance predictions, and HSCT Motion Simulator results were presented along with executive summaries for all the Aerodynamic Performance technology areas. The HSR AP Technical Review was held simultaneously with the annual review of the following airframe technology areas: Materials and Structures, Environmental Impact, Flight Deck, and Technology Integration. Thus, a fourth objective of the Review was to promote synergy between the Aerodynamic Performance technology area and the other technology areas within the airframe element of the HSR Program.

The workshop was organized in three sections as follows:

Section I	Independent Sessions
Section II	Plenary Session
Section III	Executive Summaries

The work performed in the Configuration Aerodynamics element of the High-Speed Research Program during 1997 was presented in the following sessions:

Analysis Methods and CFD Validation
Viscous Drag Predictions and Testing Methods
Aerodynamic Design Optimization Capability
Nacelle/Diverter Design and Airplane Integration
Configuration Assessments and Fundamental Studies
Technology Integration (TI) Studies related to Configuration Aerodynamics
(CA / TI Joint Session)

The work performed in the High Lift (HL) element of the High-Speed Research Program during 1997 was presented in the following sessions:

Concept Development
Test Programs and Techniques
Analytical Methods

The proceedings for the Aerodynamic Performance Annual Review are published in two volumes:

Volume I, Parts 1 and 2	Configuration Aerodynamics
Volume II	High Lift

AP Review Chairperson: Naomi McMillin
NASA Langley Research Center

CONTENTS

Nacelle/Diverter Design and Airplane Integration

Configuration Assessments and Fundamental Studies

Technology Integration (TI) Studies related to Configuration Aerodynamics (CA / TI Joint Session)

Volume 2 -- High Lift

Concept Development

Test Programs and Techniques

Analytical Methods

High Lift Aerodynamics Technology Development

High Lift Aerodynamics ITD Team
presented by Paul Meredith

Airframe Annual Review
February 12, 1998

High Lift Technology Development (Task 33)

Increase L/D, Develop Analysis/Design Methodology

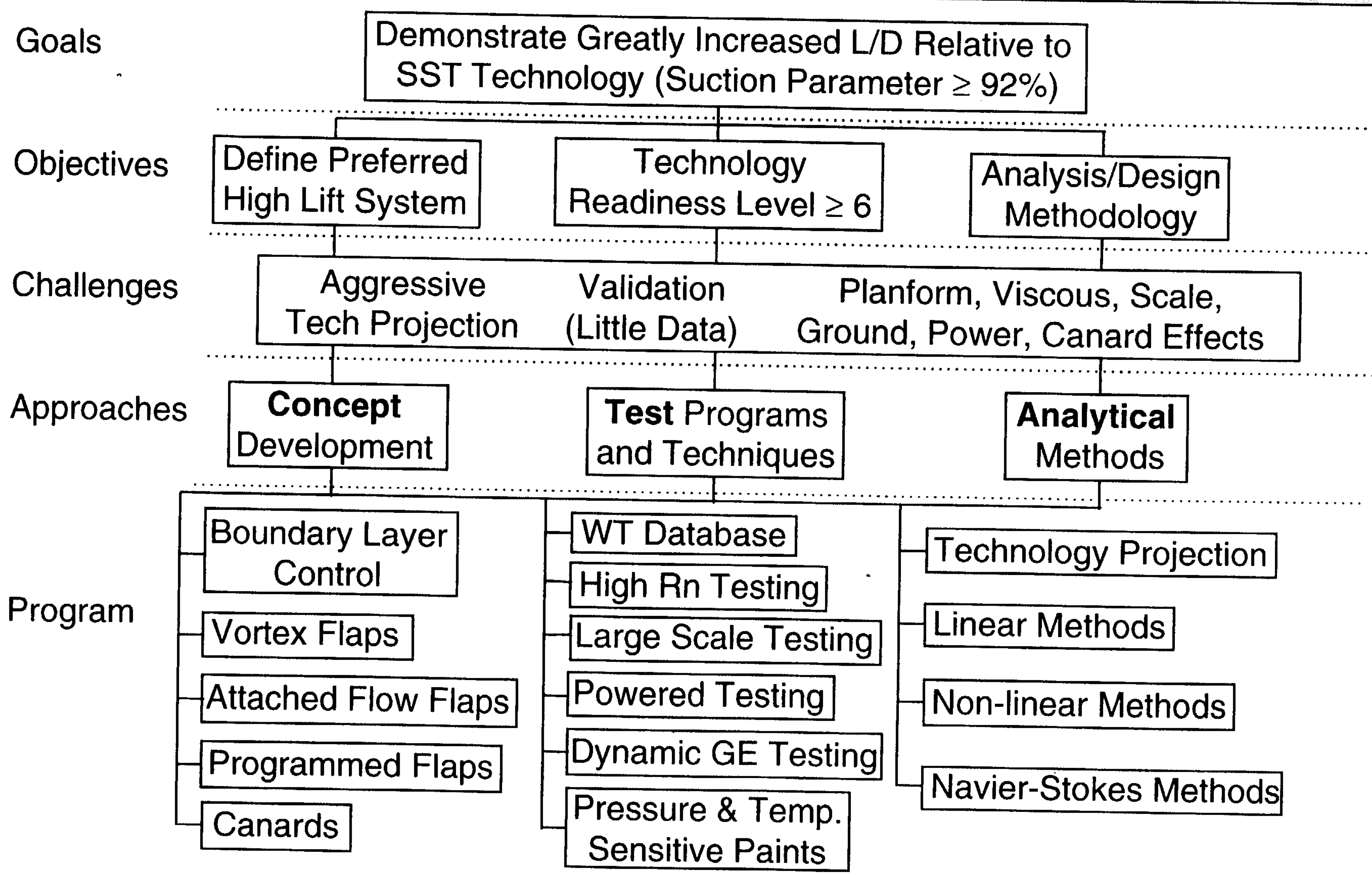

ITD Team Membership

Name	Organization	Phone	e-mail
Linda S. Bangert (Team Leader)	NASA LaRC	(757) 864-3022	l.s.bangert@larc.nasa.gov
Roger W. Clark	Boeing - Long Beach	(562) 982-5334	roger.w.clark@boeing.com
Peter G. Coen (TI Representative)	NASA LaRC	(757) 864-5991	p.g.coen@larc.nasa.gov
Michael B. Elzey (S&C Representative)	Boeing - Seattle	(425) 965-2767	michael.b.elzey@boeing.com
Paul T. Meredith	Boeing - Seattle	(425) 965-3468	paul.t.meredith@boeing.com
Brian E. Smith	NASA ARC	(650) 604-6669	besmith@mail.arc.nasa.gov

Overall Goals and Objectives

Increase L/D, Validate Analysis/Design Methodology

Greatly increase L/D relative to SST Technology (Suction Parameter ≥ 92%)

Establish & Validate Analysis/Design Methodology

Define Preferred High Lift System

Technology Readiness Level ≥ 6

PTC Sensitivity to Climbout L/D
Sized to Stage III -5 dB

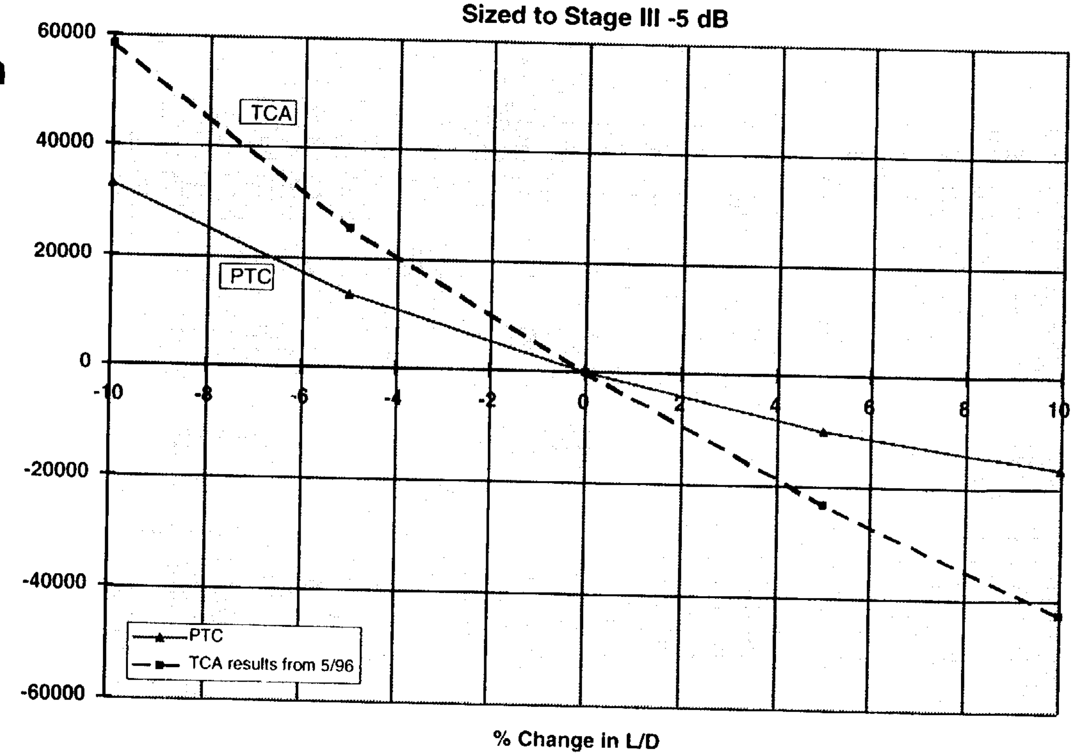

Technical Challenges

Aggressive Technology Projection

Aggressive Technology Projection

$S \geq 92\%$, no thrust, no canard, $S \geq 93\%$, no thrust, w/canard

Assumes turbulent boundary layer with fully attached flow

Unknown if it can be met with practical high lift system

Obtain Necessary Parametric and Validation Data

Planform Effects	Canard Effects	Viscous Effects
Scale (Rn) Effects	Ground Effects	Power Effects

Technical Approach

Three Major Thrusts

High Lift System Concept Development

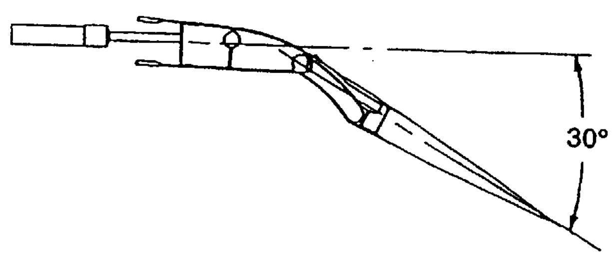

Analytical Methods

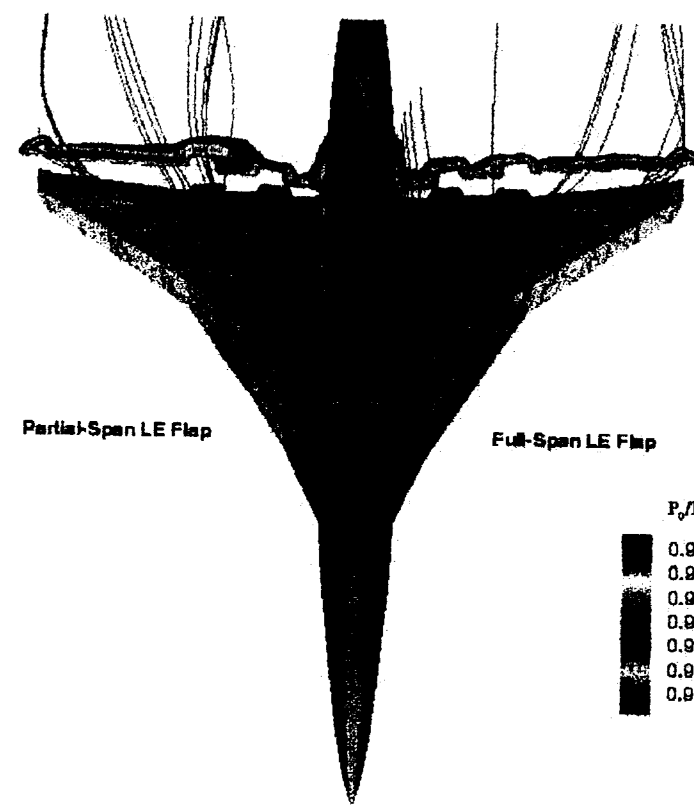

Test Programs and Techniques

PCD II Milestone Schedule

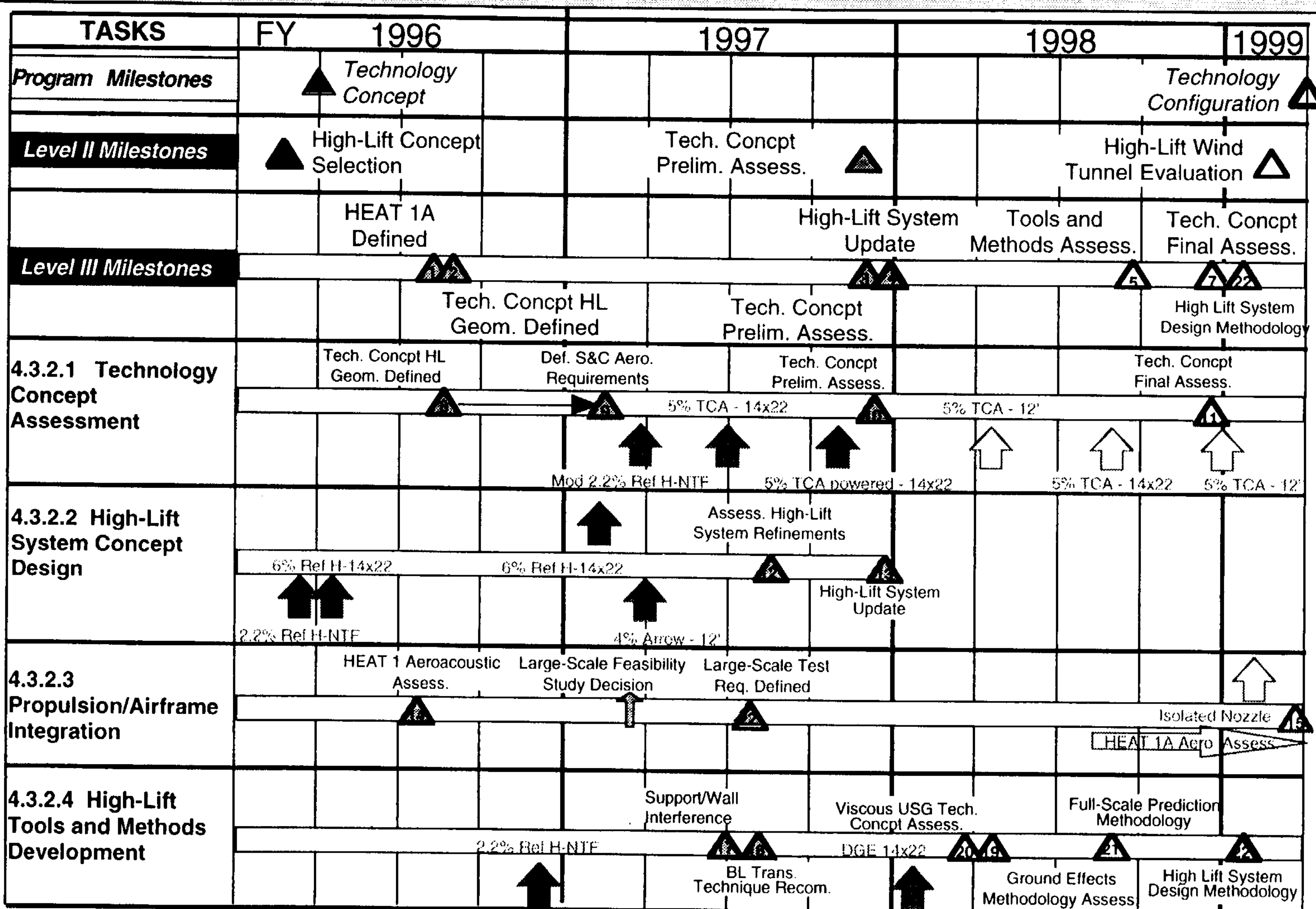

Shaded items are completed

Summary of FY97 Accomplishments

Good Progress, but High Lift PD Method Found to be Unreliable

Concept Development

- TCA preliminary assessment - poorer L/D than PD prediction
  - modified Ref. H in the LaRC NTF
  - TCA-1 test in the LaRC 14'x22'
    - LE flap span, outboard sealed slat studies
- Supported PTC development, 3-surface technology projection

Test Programs and Techniques

- Upflow & support interference (U&I) test in the LaRC 14'x22'
- First Ames 12' test - Arrow Wing model
- TCA-2, powered test in the LaRC 14'x22'
  - plume/tail interaction - no show stoppers
- First dynamic ground effect test in the LaRC 14'x22'
- HEAT 1A parts 60% complete, on schedule, on budget

Analytical Methods

- Routine use of Navier-Stokes for high lift configurations
- Assessing unstructured grid (USG) Navier-Stokes
- Time accurate linear and Euler dynamic ground effect analyses
- PD method (AERO2S based) not reliable - TCA not well predicted

Concept Development - 5% Scale TCA Model

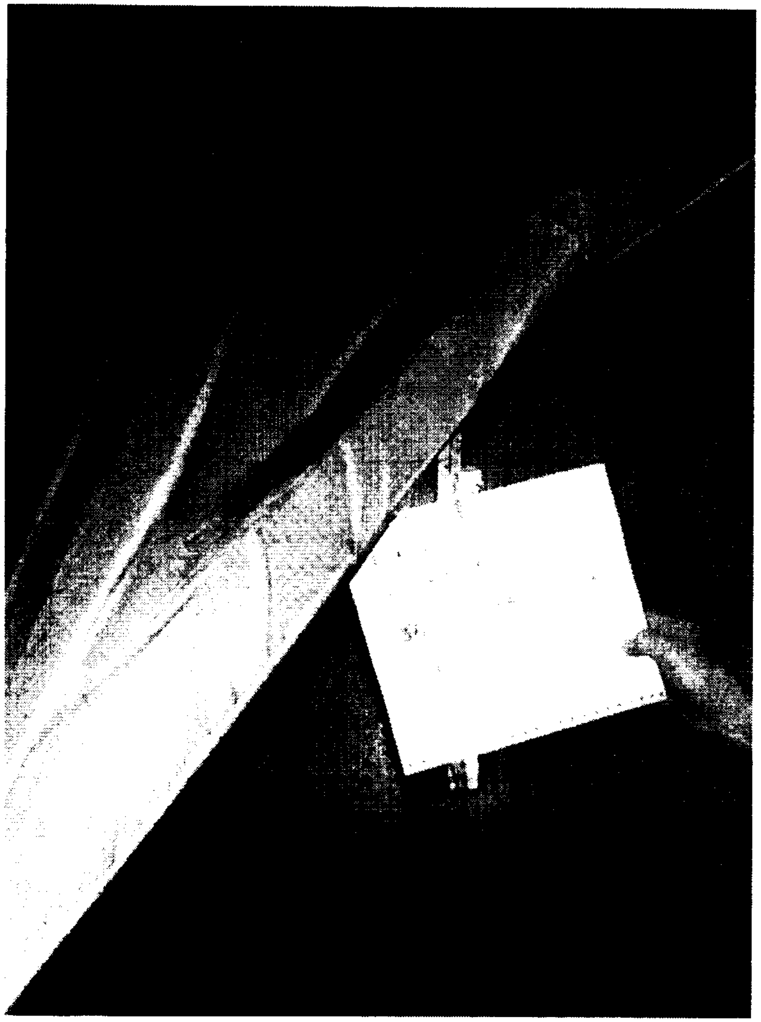

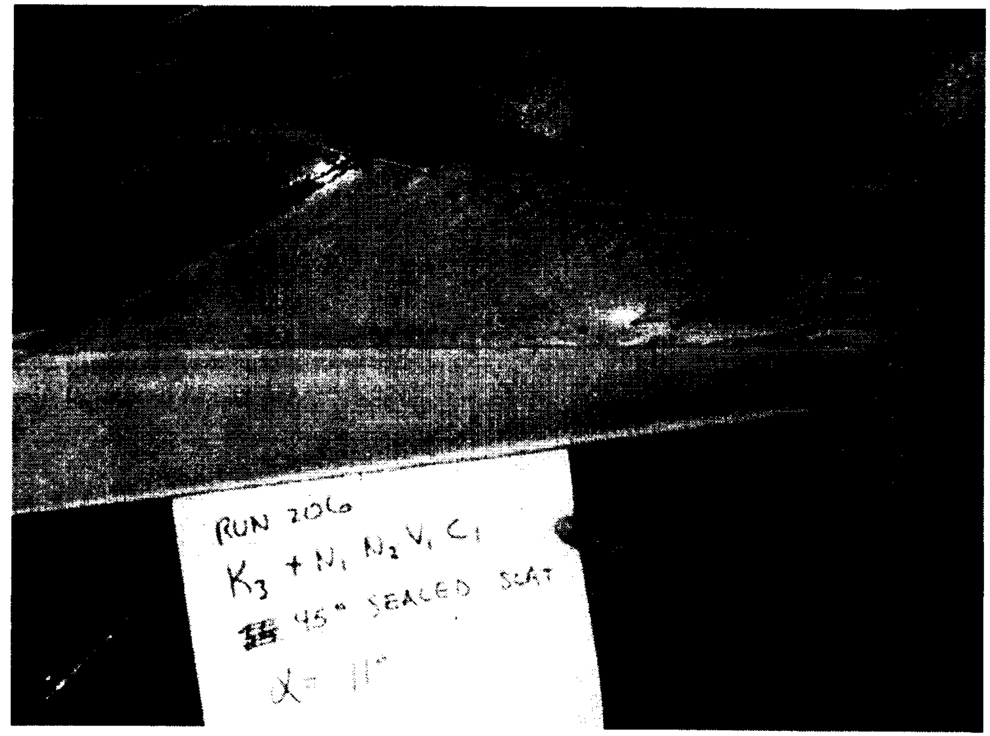

TCA 5% Model - Jack of all Trades
unpowered & powered (blowing nacelles)
stressed for Ames 12' (6 atmospheres)
removable LE, TE, and outboard wing

Concept Development - Ref. H, TCA, PTC L/D

Span is our Friend!

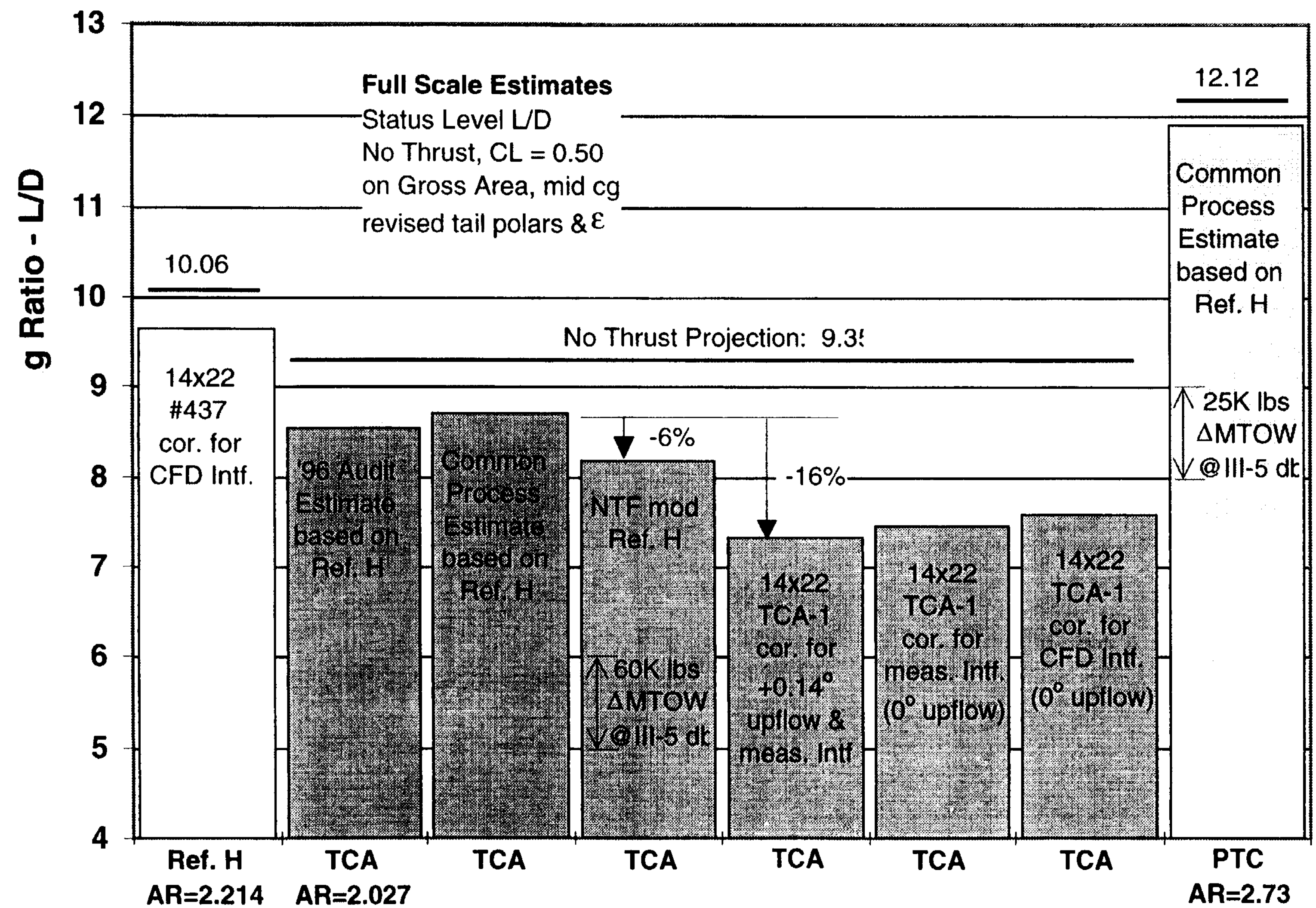

Concept Development - L.E. Flap Span

Minimize Leading Edge Flap Span

12° Angle of Attack

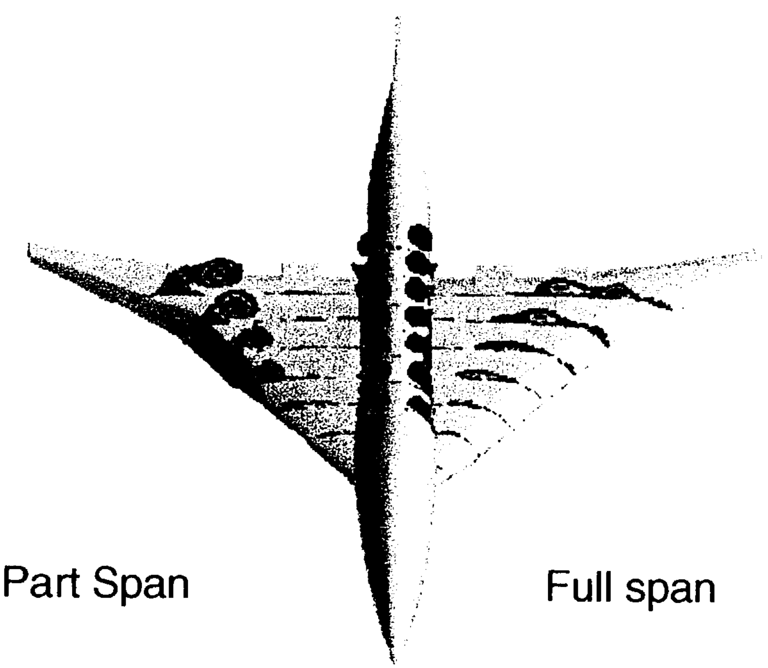

CFD Solution for TCA wing/body with full- and part-span l.e. flaps

L/D Ratio Variation with Lift

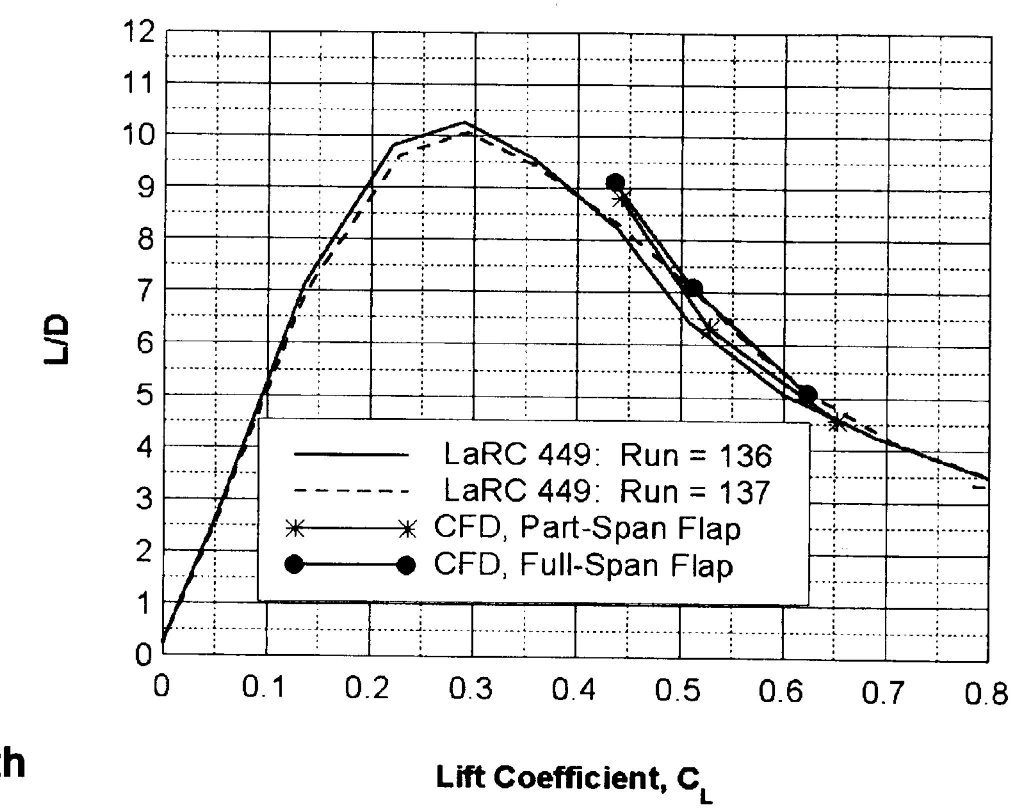

Concept Development - Outboard Sealed Slat

LE Flap Hingeline Curvature is Very Important

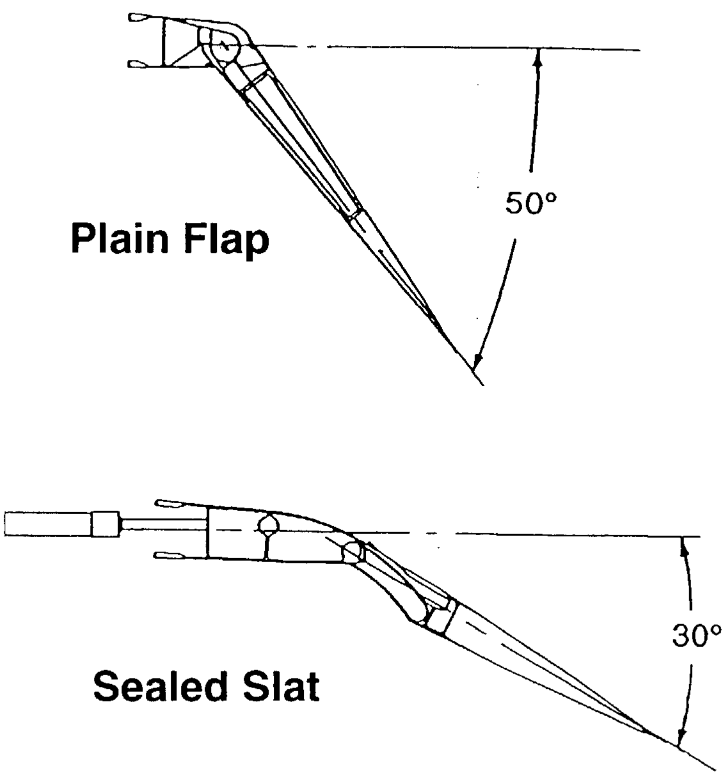

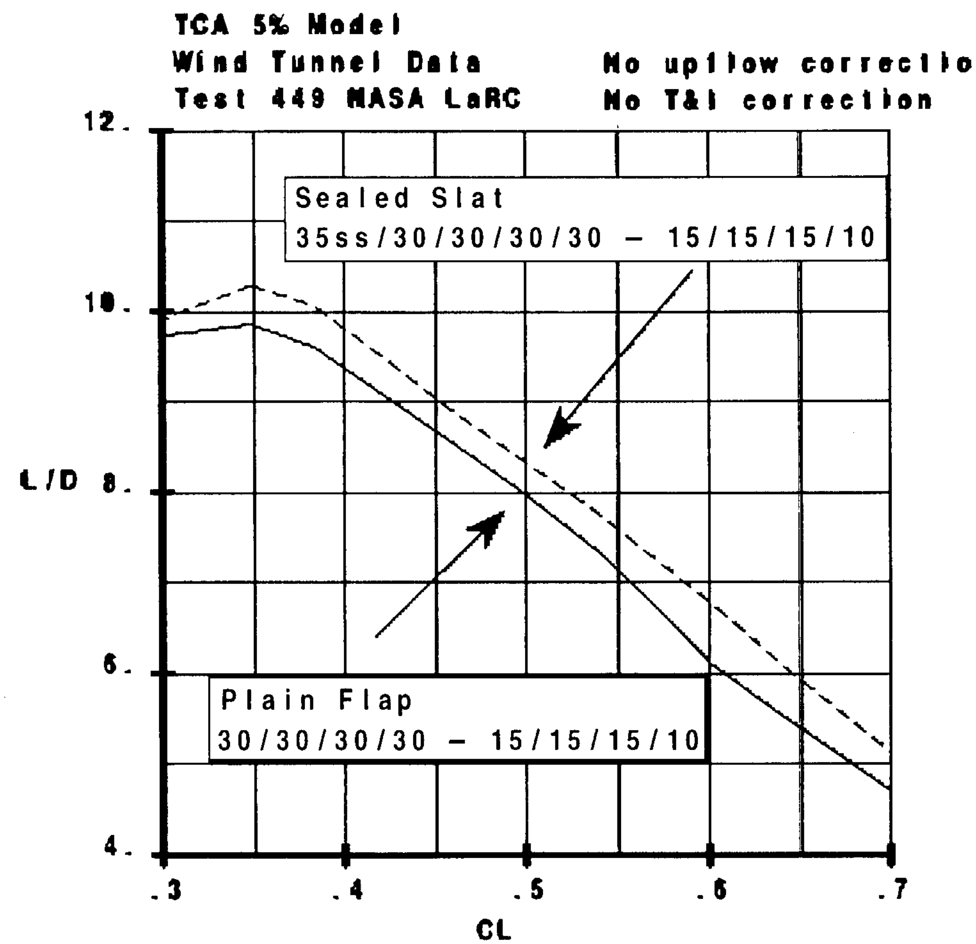

L/D increased by nearly 4% for both TCA & REF. H

Test Program - First HSR Test in ARC 12'

4% Scale Arrow Wing Model

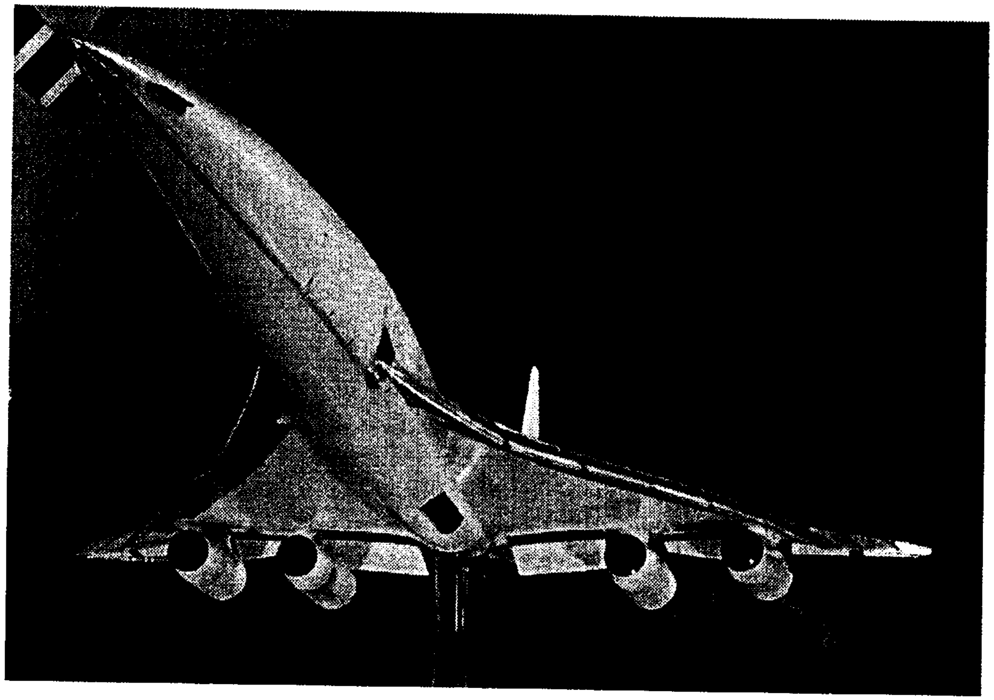

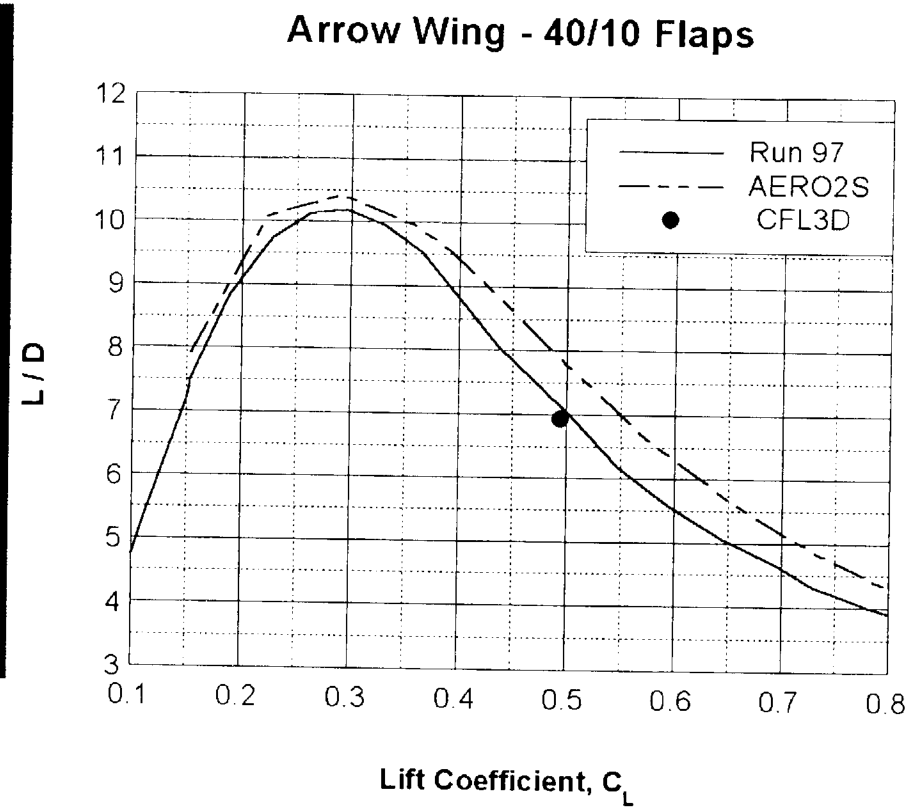

- Linear PD Method underpredicts vortex separation
- Navier-Stokes provides good agreement

Test Program - Powered TCA in Ground Effect

Plume/Tail Interaction - Not a Show Stopper

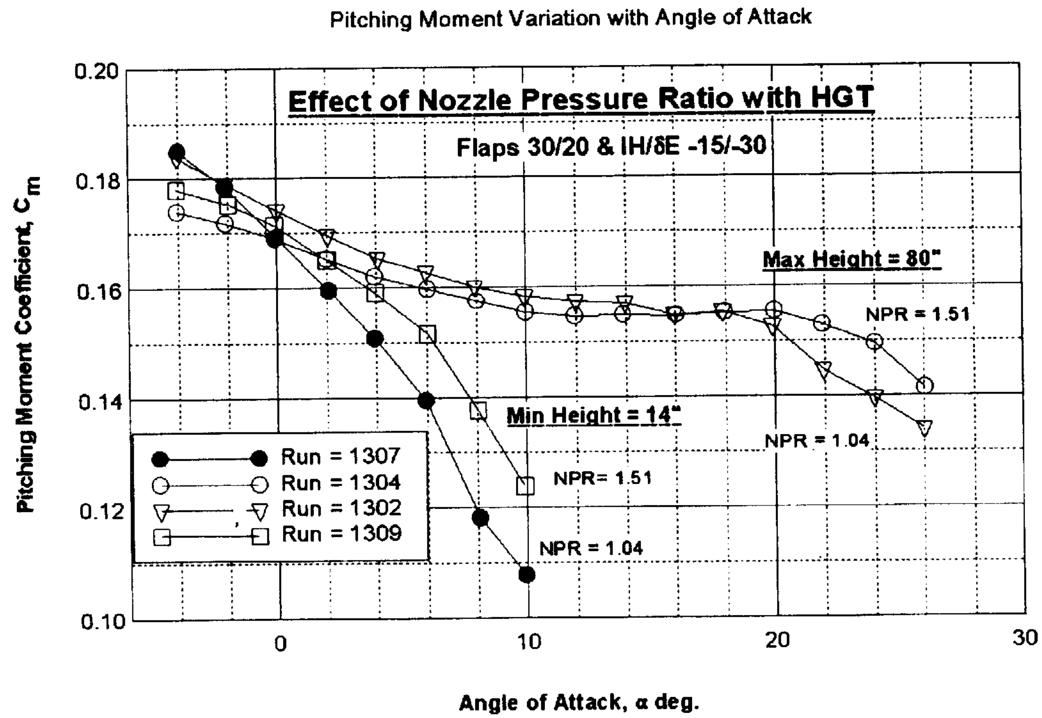

- 5% TCA Model with powered ejector nozzles
- Aft fuselage balance to directly measure tail loads
- No main model balance
- Power induced effects within acceptable limits

Test Program - Dynamic Ground Effect

New Capability in the LaRC 14'x22' Tunnel

Sketch of Plunging Rig for LaRC 14'x22' Tunnel

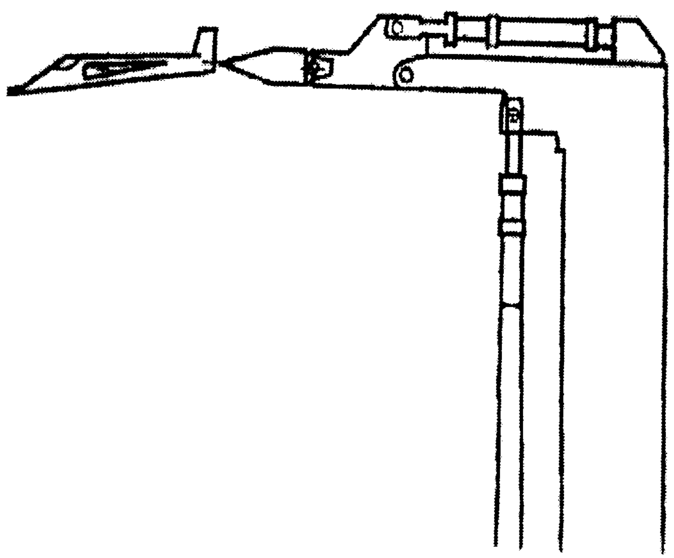

Tu-144 Lift Increase in Ground Effect
Nominal Descent Angle = 0.25 deg.

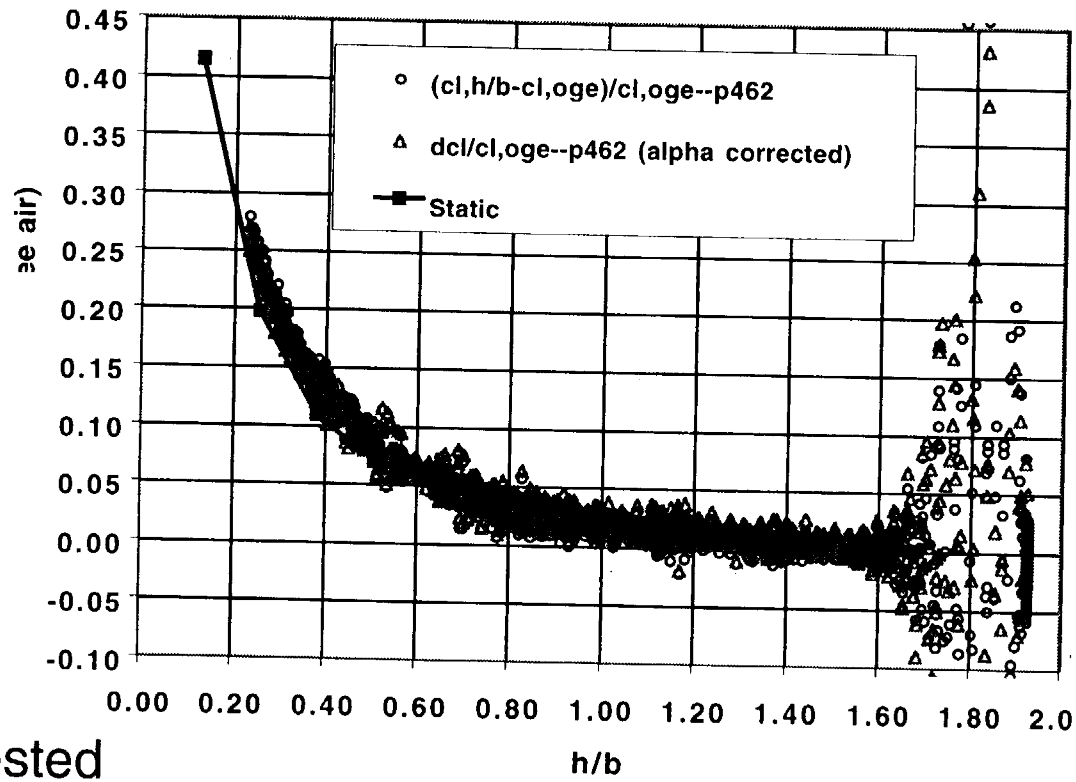

- Tu-144 & TCA planforms tested
- No significant dynamic effects observed

Analytical Methods - Navier-Stokes Studies

Routine use of Structured Grid Codes

Start with a Clean Grid (no flaps)

- Specify Flap Schedule (LEI, LEO, TEI, TEM, TEO)
- Run Flap Deflection Procedures
- Obtain Modified Volume Grid

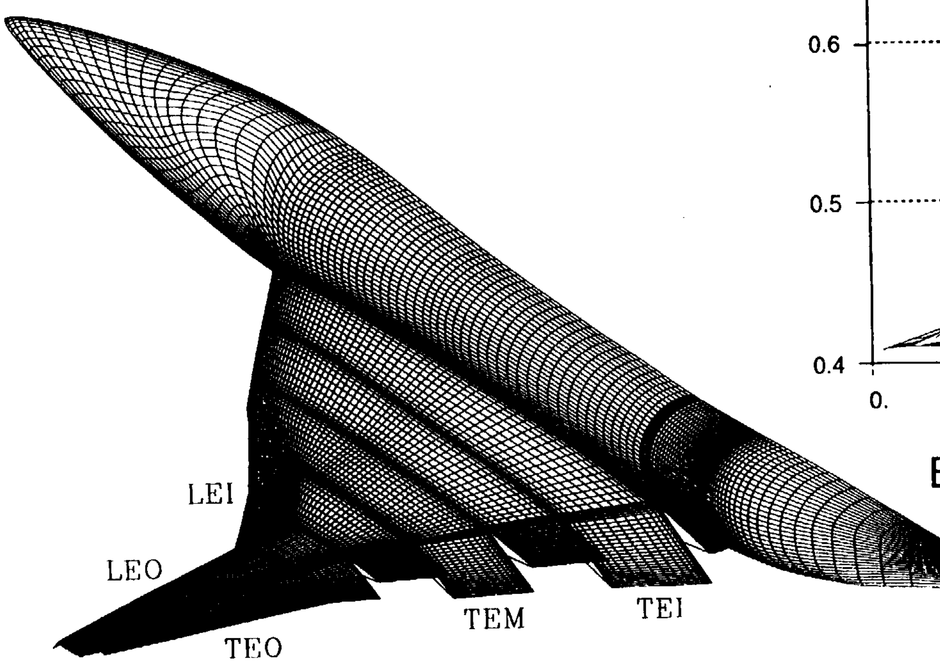

Analysis of TCA2.8-28 using CFL3D

M = 0.3, Rn = 8 Million, 25/10 Flaps

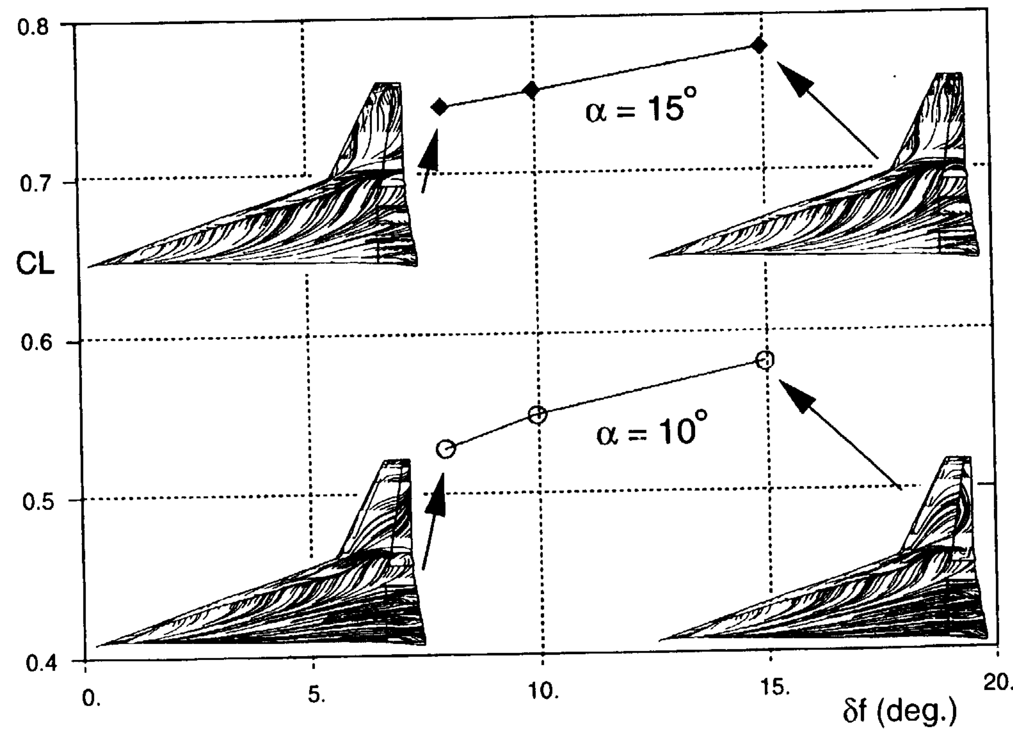

Effect of O/B Trailing-Edge Flap Deflection

Analytical Methods - Dynamic Ground Effect

Time Accurate Linear CFD Shows No Adverse Dynamic Effect

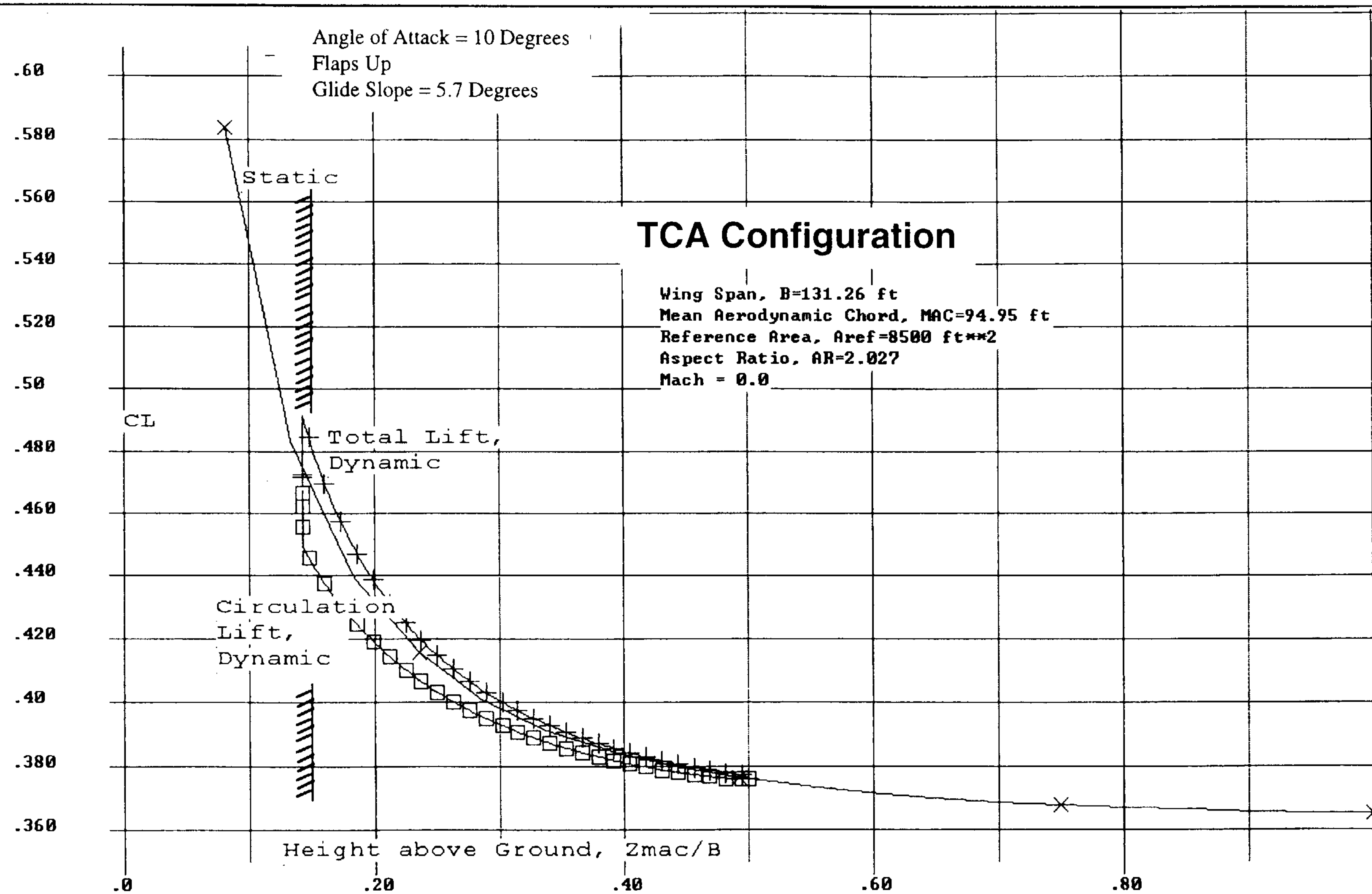

Analytical Methods - Dynamic Ground Effect

Time Accurate Euler CFD Shows No Adverse Dynamic Effect

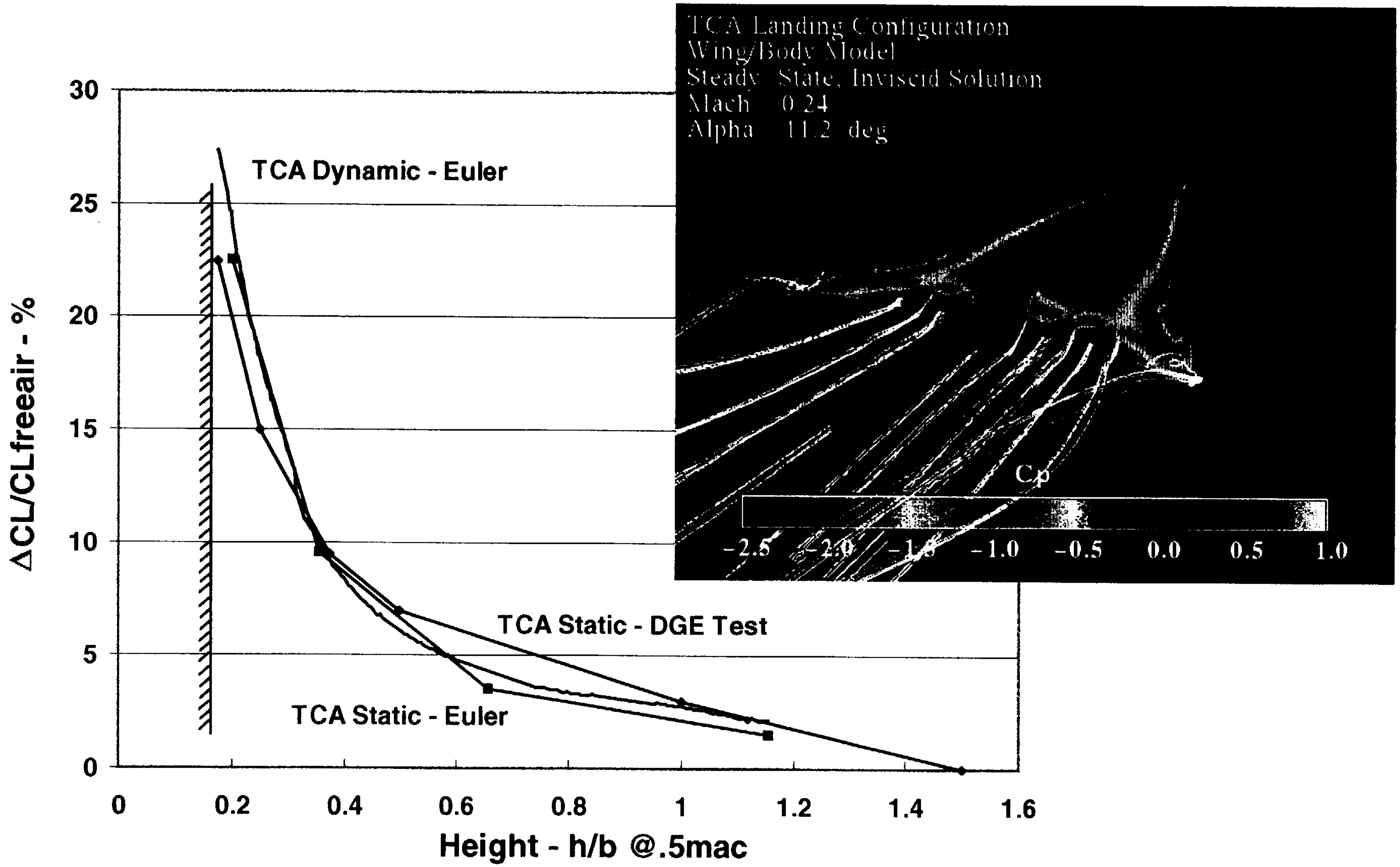

Metric AP-3 - Leading Edge Suction Parameter

Technology Projection is Aggressive

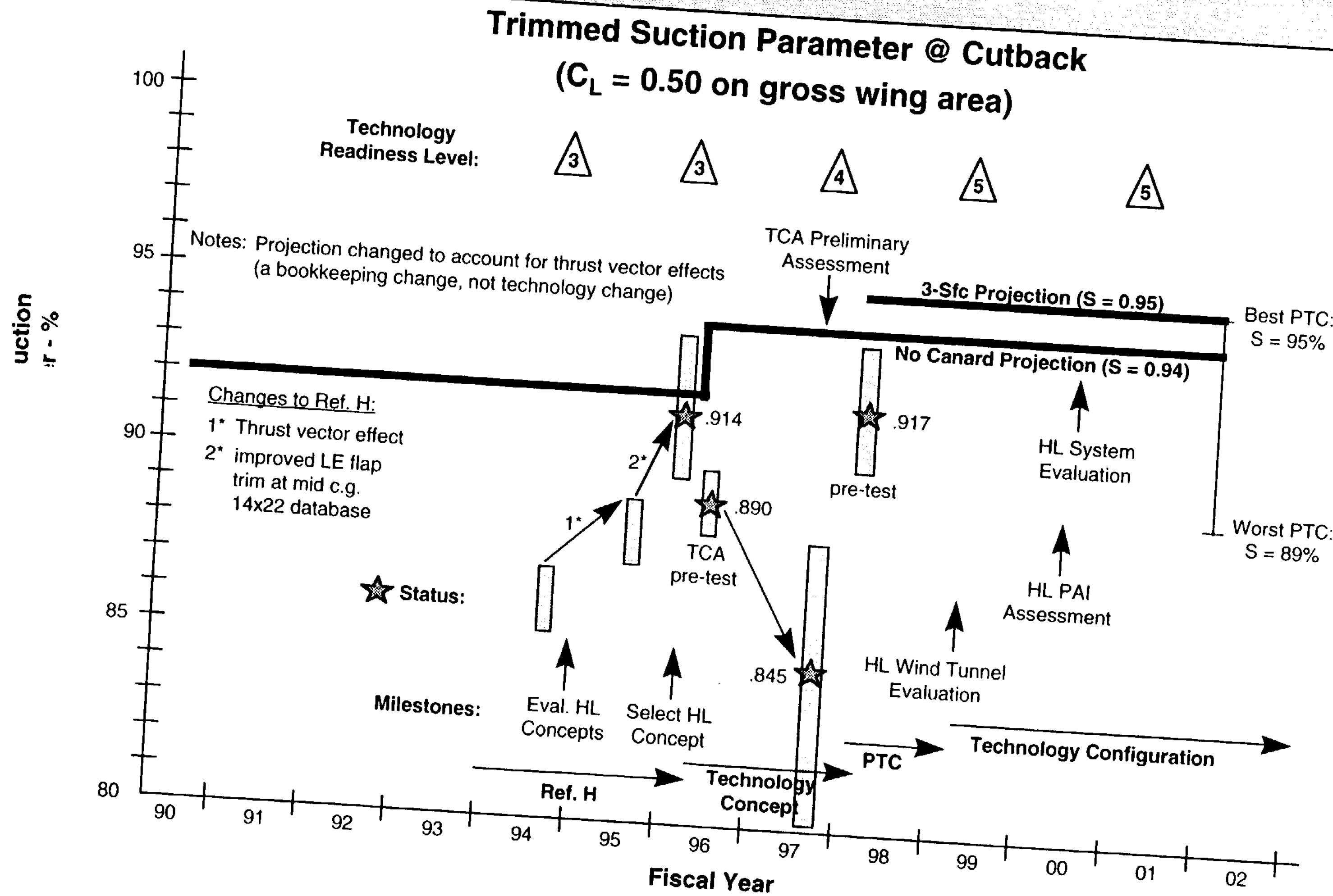

Metric AP-4 - Climb Out Lift/Drag Ratio

Span is our Friend!

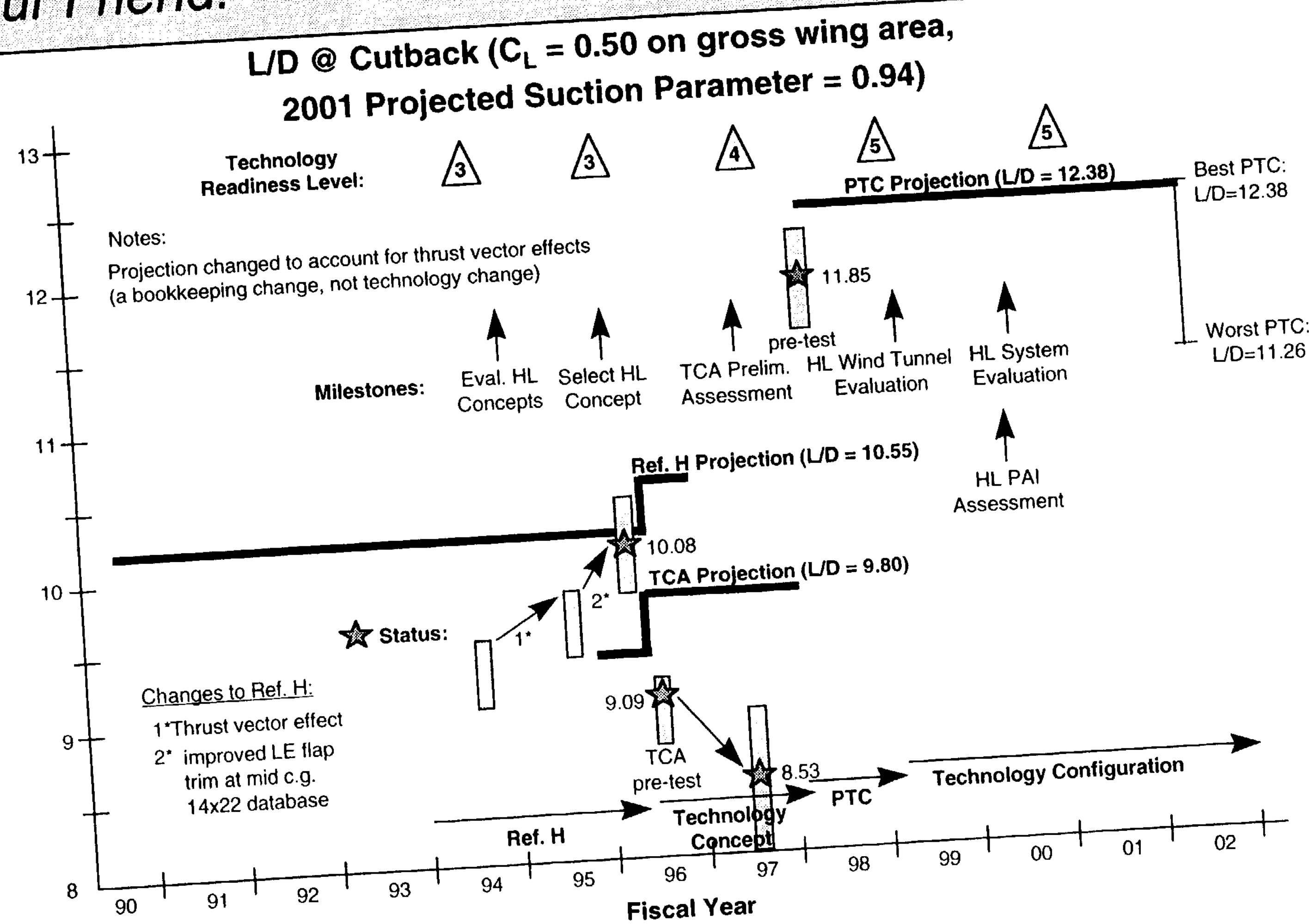

CY98 Plans and Technical Approach

Broaden Scope - *Planforms, Canards, Parametrics*

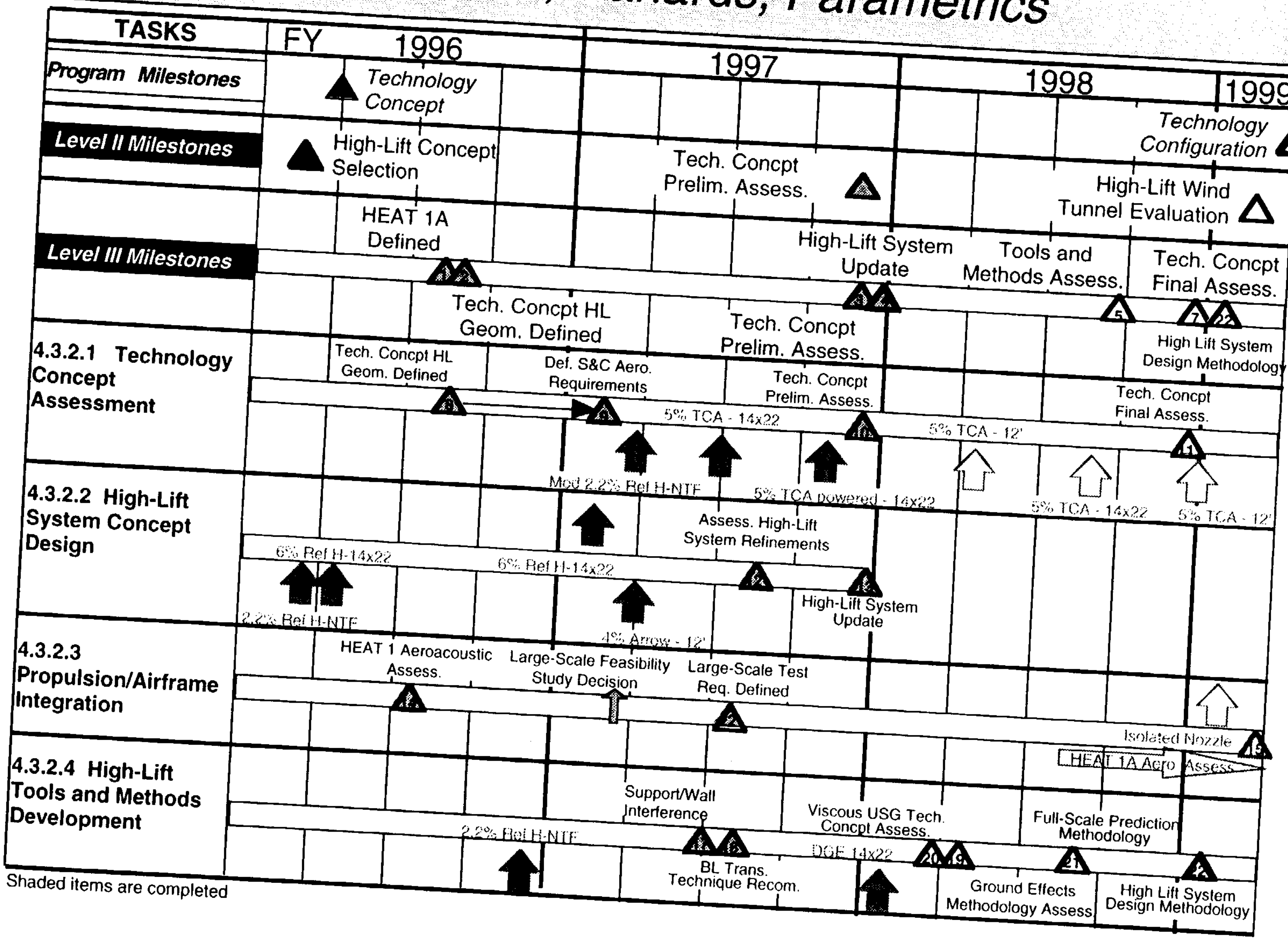

Shaded items are completed

Conclusions

(1) **Technology Projection is aggressive**
LE flap hingeline curvature is a key parameter
May require LE devices more complex than plain flaps

(2) **TCA climb-out L/D significantly less than predicted**
Also happened with Arrow Wing predictions
Need more parametric data to better calibrate PD process

(3) **Plume/Tail interaction not a show stopper**

(4) **Have not seen adverse dynamic ground effect in WT test or CFD data**
Flight test data in the literature shows substantial adverse effects for higher sweep delta wings

(5) **Demonstrated routine use of Navier-Stokes for high lift configurations**
Results very useful - but can be sensitive to numerical modeling
Grid generation tools being improved - flap/canard procedures
Computing times and solution turn around time still too long

(6) **High Lift program proceeding as planned (except for HEAT 1A slide)**

Issues

Much work remains to achieve Technology Projection & TRL of 6

TCA and Arrow Wing L/D Poorly Predicted by PD Process
- Need to improve PD tools - directly impacts validity of TI trade studies
- Need more parametric data to better calibrate PD process

Achieving the Technology Projection
- May require more complex, heavier leading edge device

Canard Effect on Performance and S&C Characteristics
- Need a lot more data & analytical work - PCD III

PAI - Potentially Favorable, Need HEAT 1A to Confirm
- HEAT 1A ARC 40'x80' test slid into PCD III

Full Cost Accounting Impact on PCD III Plans
- Wind tunnels
- NAS time

This page is intentionally left blank.

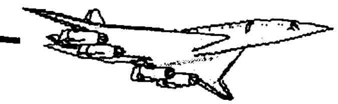

TCA High Lift Preliminary Assessment

G. H. Wyatt *D. T. Yeh*
R. C. Polito *M. E. Elzey*
J. T. Tran

Presented by Paul T. Meredith

Airframe Annual Review
February 9, 1998

The Boeing Company
NASA HSR II Contract No. NAS1-20220

4.3.2.1 deliverable

This page is intentionally left blank.

High Lift Technology Development (Task 33)

Increase L/D, Develop Analysis/Design Methodology

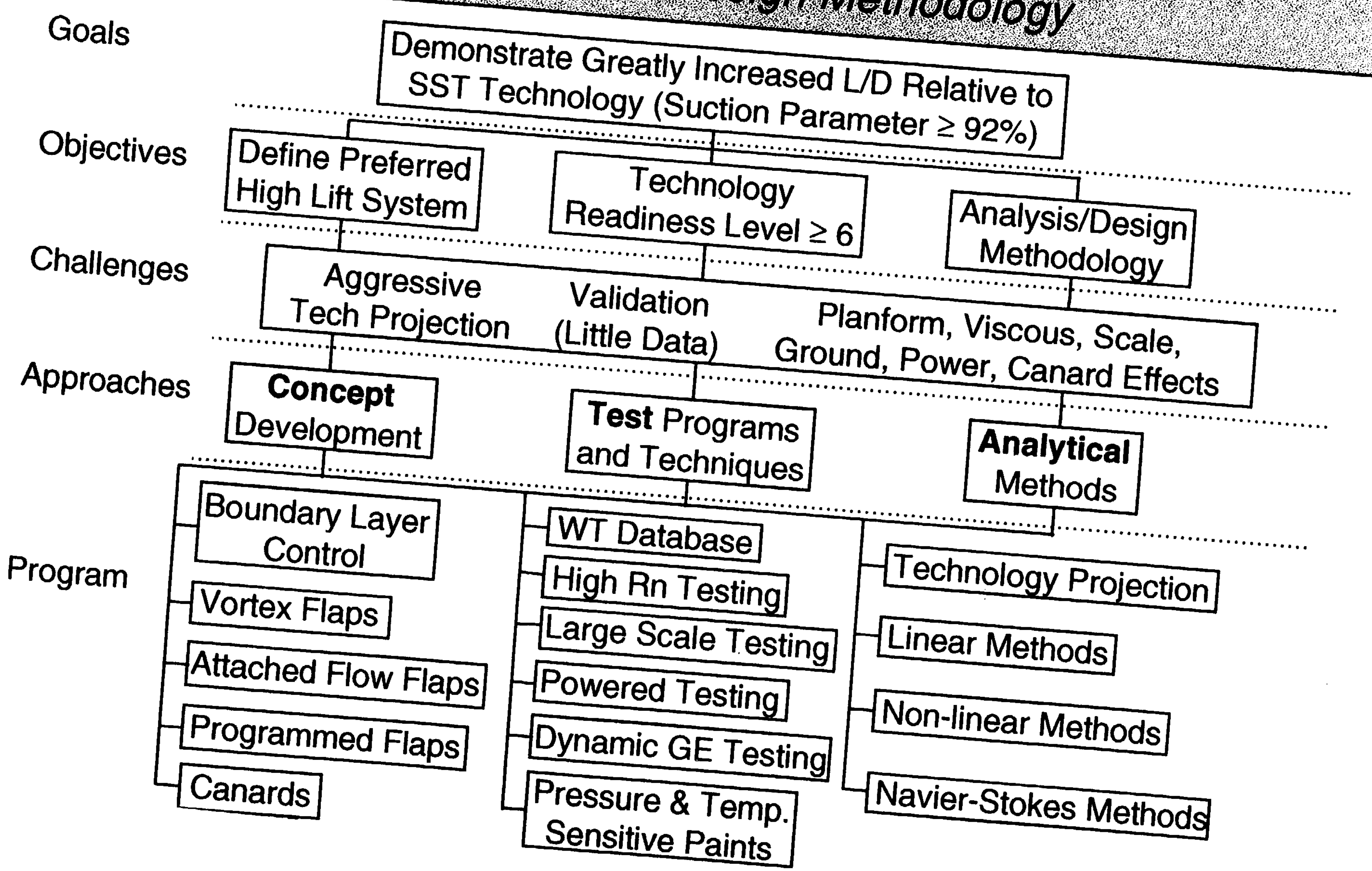

4.3.2.1 deliverable

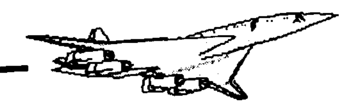

INTRODUCTION

This page intentionally blank.

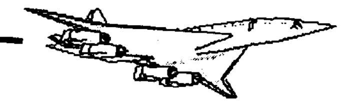

INTRODUCTION

- TCA 5% Model Characteristics
- TCA-1 Test (LaRC 14'x22' #449) Data Uncertainty
- Overview of TCA-1 Data
- Comparison of 14'x22' and NTF Results
- Full Scale Build-ups
- Conclusions

4.3.2.1 deliverable

Model Description

This page describes the 5% TCA model geometry

Model Description

Scale:	5%
Sref:	21.250 sqft
Cbar:	56.972 inches
Span:	78.757 inches
Aspect Ratio:	2.027
Model length:	195.6 inches

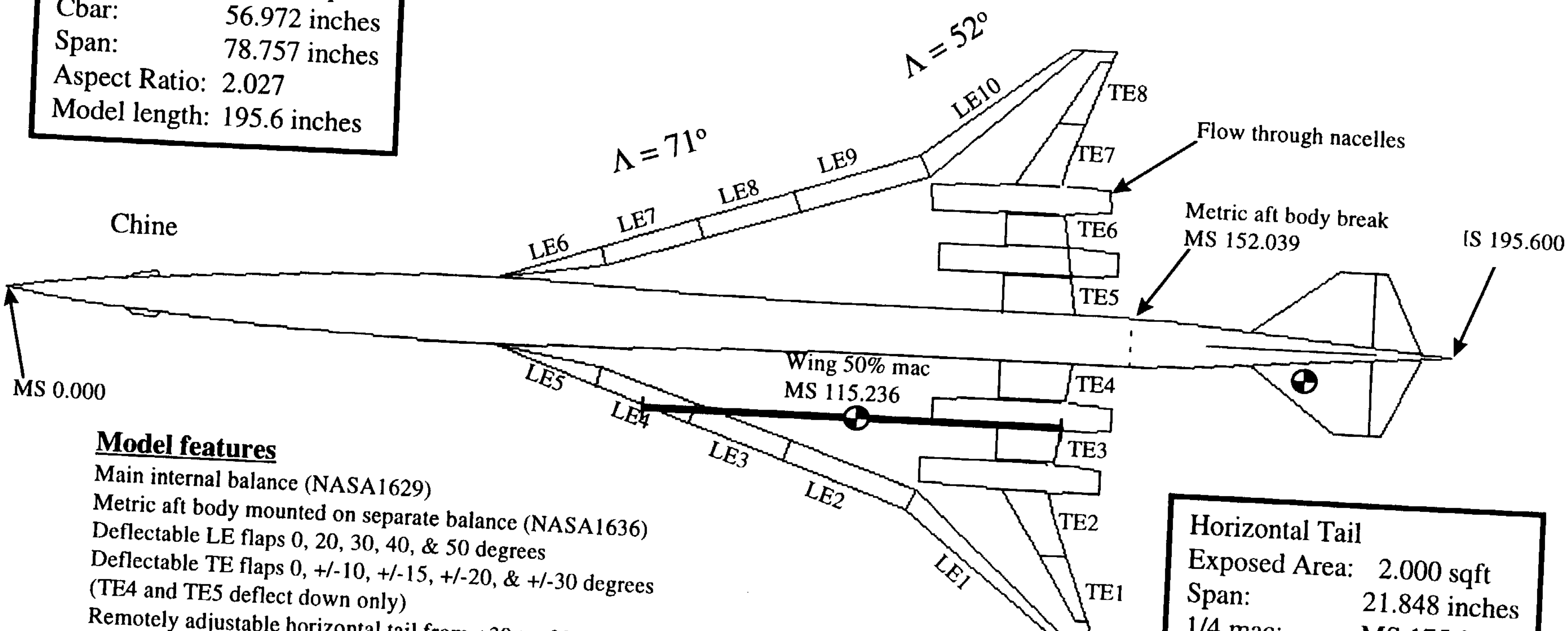

Model features

Main internal balance (NASA1629)
Metric aft body mounted on separate balance (NASA1636)
Deflectable LE flaps 0, 20, 30, 40, & 50 degrees
Deflectable TE flaps 0, +/-10, +/-15, +/-20, & +/-30 degrees
(TE4 and TE5 deflect down only)
Remotely adjustable horizontal tail from +30 to -30
Deflectable horizontal tail elevators 0, +/-10, +/-20, +/-25, +/-30
Fixed vertical tail with deflectable rudder 0, +10, +20, +25, & +30
Flow through nacelles
Landing gear
384 surface static pressures
Model weight approximately 725 lbs

Horizontal Tail	
Exposed Area:	2.000 sqft
Span:	21.848 inches
1/4 mac:	MS 175.386
Elevator HL	MS 184.471
Model length:	195.6 inches

4.3.2.1 deliverable

Model Mounting

These pictures show the 5% TCA model mounted in the NASA LaRC 14x22 tunnel. The model was post mounted on model cart # 2 in the forward bay of the 14x22 test section. Forces and moments were measured with the NASA 1629 internal strain gage balance. The post mount moves vertically on the cart to provide different ground heights. Angle of attack variations are provided by a sliding pitch arm mounted aft of the post. Yaw variations are provided by rotating the cart turntable.

Test conditions:	
Dynamic pressure	85 psf
Angle of attack	-5 to 30 degrees
Yaw angles	-20 to +20 degrees
Model height	14 to 80 inches (87 is tunnel centerline)

Model Mounting

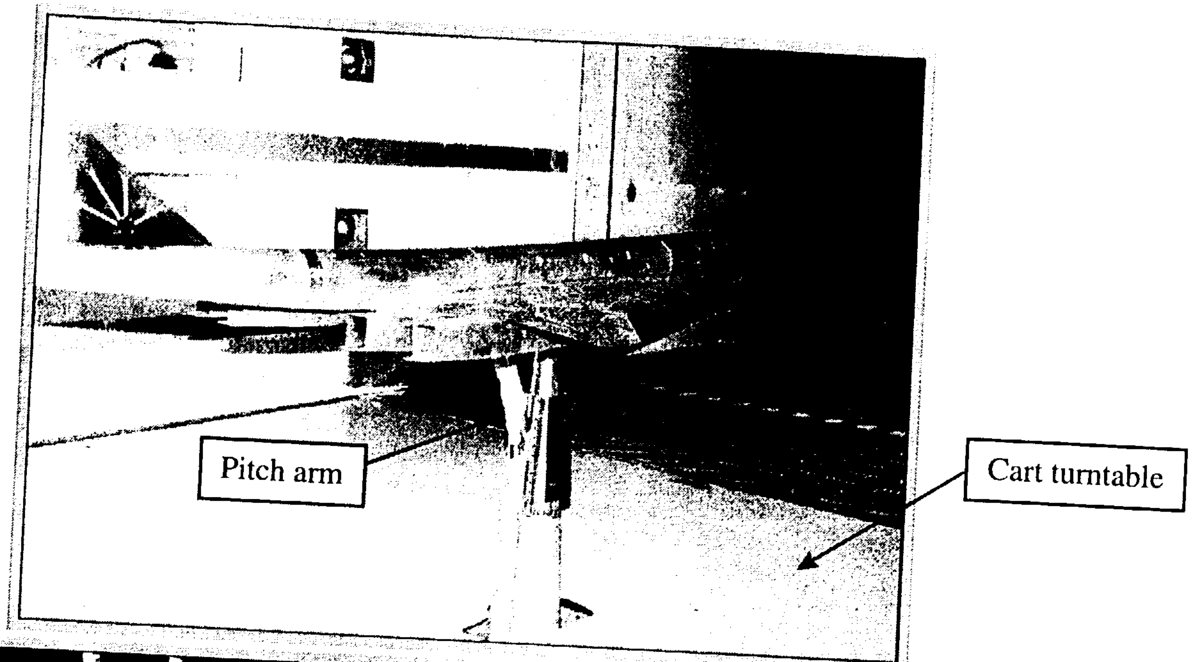

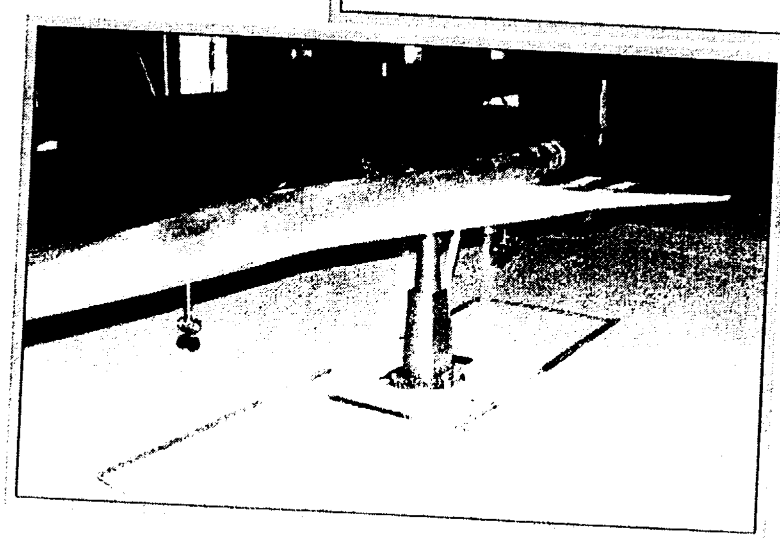

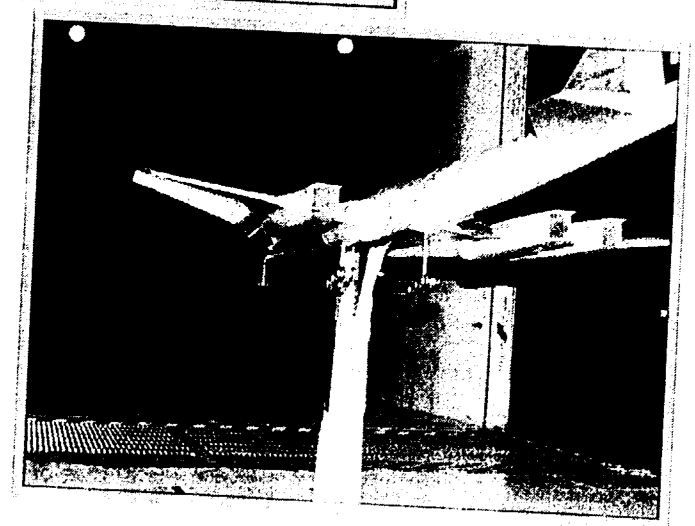

4.3.2.1 deliverable

Data Repeatability (Drag)

Estimates of data repeatability considering balance and angle of attack accuracy for this system are considered below:

Balance accuracy from the 1629 calibration report		
NF	.08% of full scale reading	+/- 2.4 lbs
AF	.09% of full scale reading	+/- .45 lbs
Angle of attack accuracy		+/- .01 degrees

These variations in measurements yield an uncertainty of:

Component	Uncertainty
C_L	+/- .0014
C_D	+/- .0006

Although these uncertainty values do not reflect other factors such as the uncertainty of the electrical system measuring and recording the data, past experience has shown these other factors to be of less magnitude.

Previous experience in the 14x22 facility has been mixed, with some tests approaching the above level of uncertainty with repeat runs. Other tests have faired much worse. This test is one of the latter. Balance normal force drift was a constant battle during this test. The drift seemed to be associated with thermal effects.

This chart shows drag repeatability. During this test repeatability was worse than expected, requiring more repeat runs to periodically check the integrity of the data. There were 17 repeat runs of the LE=30/30/30/30/30 TE=15/15/15/10 configuration. Drag repeatability at C_L=0.50 is +/- 11 counts.

Data Repeatability (Drag)

95% Prediction and 95% confidence interval

Repeat runs for climbout flaps
30/30/30/30/30 15/15/15/10
175 181 182 183 184 198 199
227 228 251 462 463 465 466
476 477 598

- **Drag repeatability is not good**

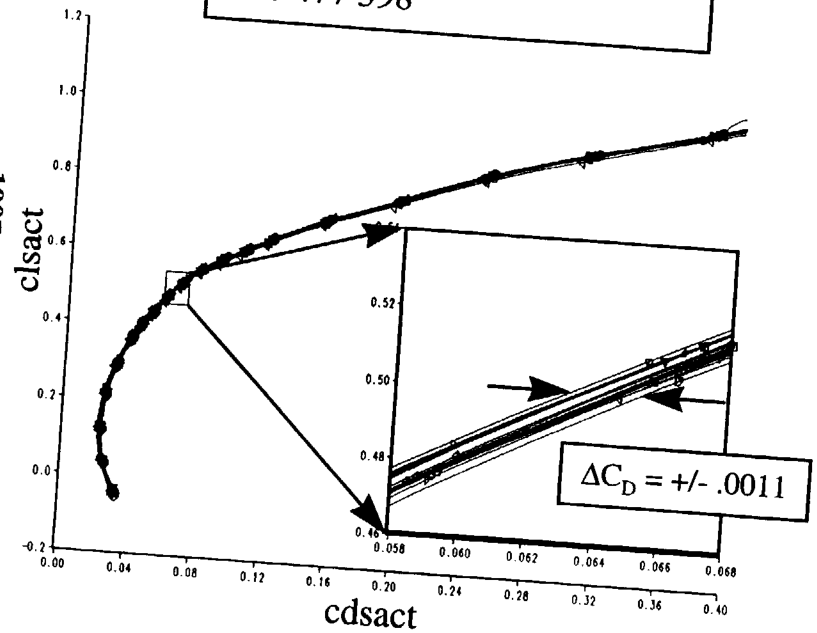

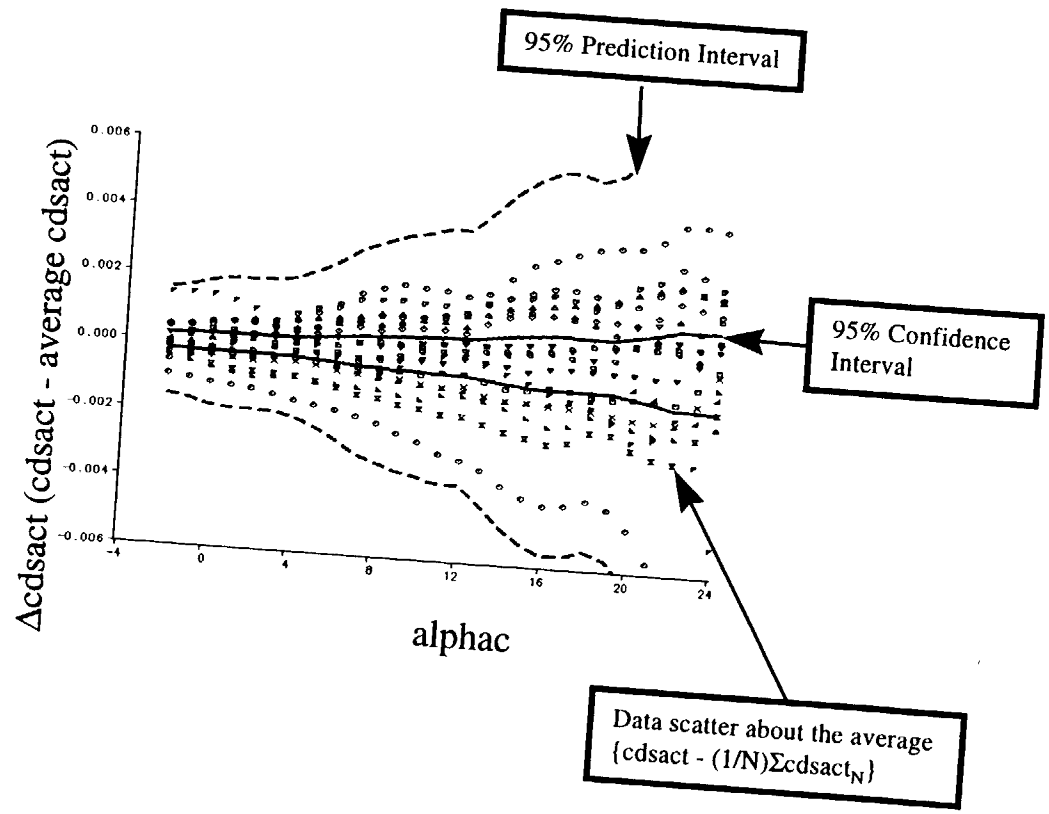

Note: this is not final data - don't use for drag level

4.3.2.1 deliverable

Effect of Inboard L.E. Flap Span

The part span inboard leading edge flap does not work as well as the full span flap, unlike the Ref. H. This correlates with the findings from the 2.2% modified Ref H test in the NTF. The full span inboard leading edge flap provides the highest trimmed L/D and more gentle pitching moment characteristics. Even though the trimmed L/D is only slightly better at C_L=0.5 it is more significant at higher C_L's such as required during approach.

It is believed that fairly small changes to the inboard leading edge geometry such as increased camber, increased leading edge radius, and decreased sweep, would make the part span flap equivalent to the full span flap in terms of L/D at the climb-out CL.

Effect of Inboard L.E. Flap Span

Inboard Leading Edge Flap Span Coverage
Trimmed Drag - 5% TCA model data from test 449. Data trimmed with Ref H tail drag polar

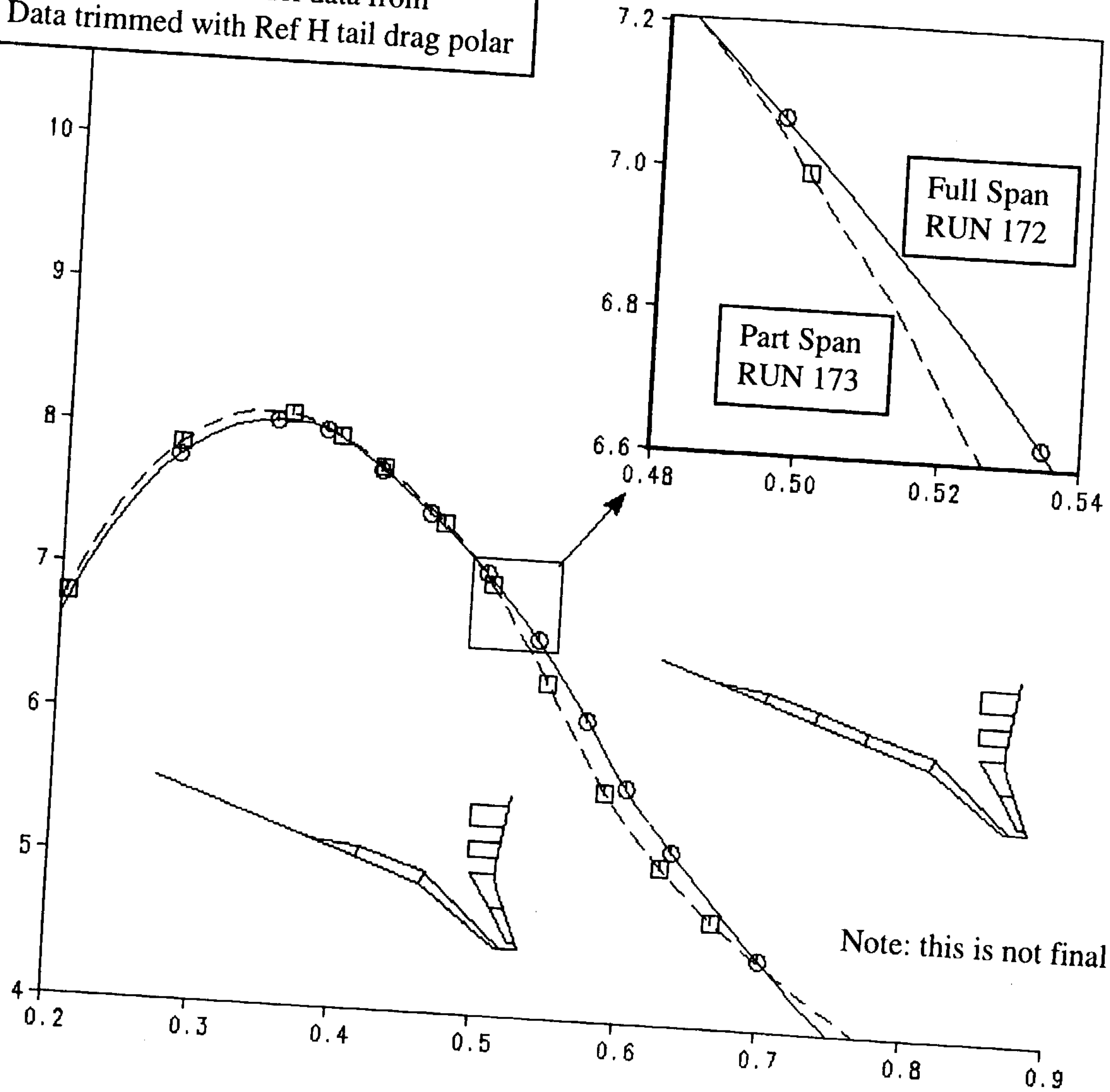

Note: this is not final data - don't use for drag level

4.3.2.1 deliverable

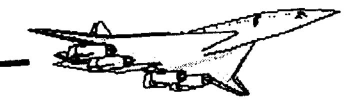

Effect of Inboard L.E. Flap Span

As can be seen by this chart the full span leading edge flap provides more desirable pitching moment characteristics. There is a slight C_{M_o} shift and pitchup is delayed and reduced at higher C_L's.

Effect of Inboard L.E. Flap Span

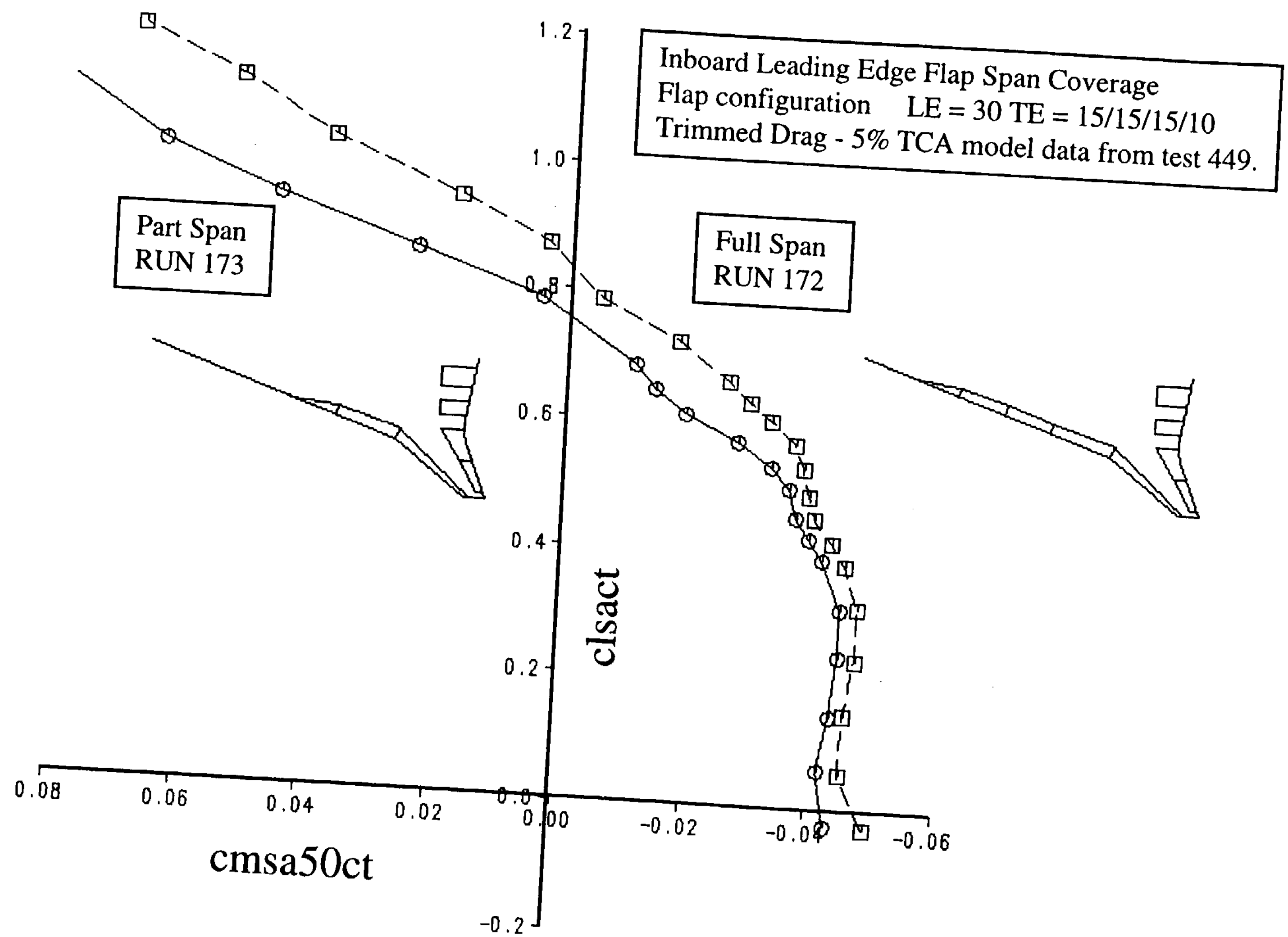

4.3.2.1 deliverable

Comparison of 14'x22' TCA-1 With NTF Modified Ref. H

This chart shows a comparison of the 5% TCA data to the 2.2% modified Ref H data from NTF test 089. The correlation is remarkable considering the different models, tunnels, and mount systems.

Comparison of 14'x22' TCA-1 With NTF Modified Ref. H

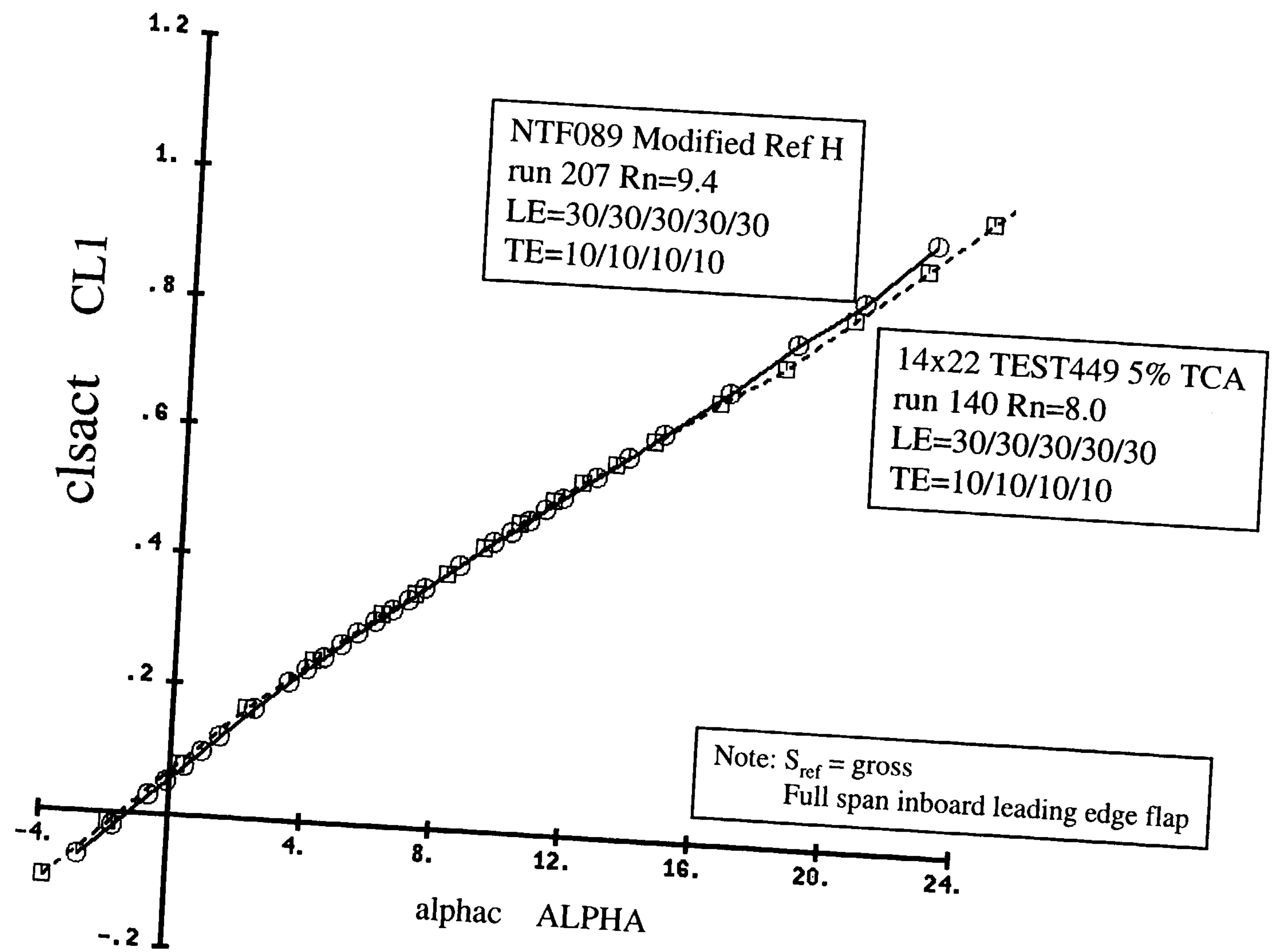

4.3.2.1 deliverable

Comparison of 14'x22' TCA-1 With NTF Modified Ref. H

This chart shows a comparison of the 5% TCA-1 data to the 2.2% modified Ref. H data from NTF test 089. The NTF drag was adjusted by 12 drag counts to account for the missing aft body and vertical tail. The TCA-1 data on the curve was inadvertently over corrected for upflow (0.25° instead of 0.14°). The star indicates the L/D for a 0° upflow correction. At CL=0.5, L/D is down about 1.2 units relative to the modified Ref. H NTF results. This is surprising since the lift curves were in good agreement.

Comparison of 14'x22' TCA-1 With NTF Modified Ref. H

- NTF mod Ref. H & 14'x22' TCA L/Ds do not agree

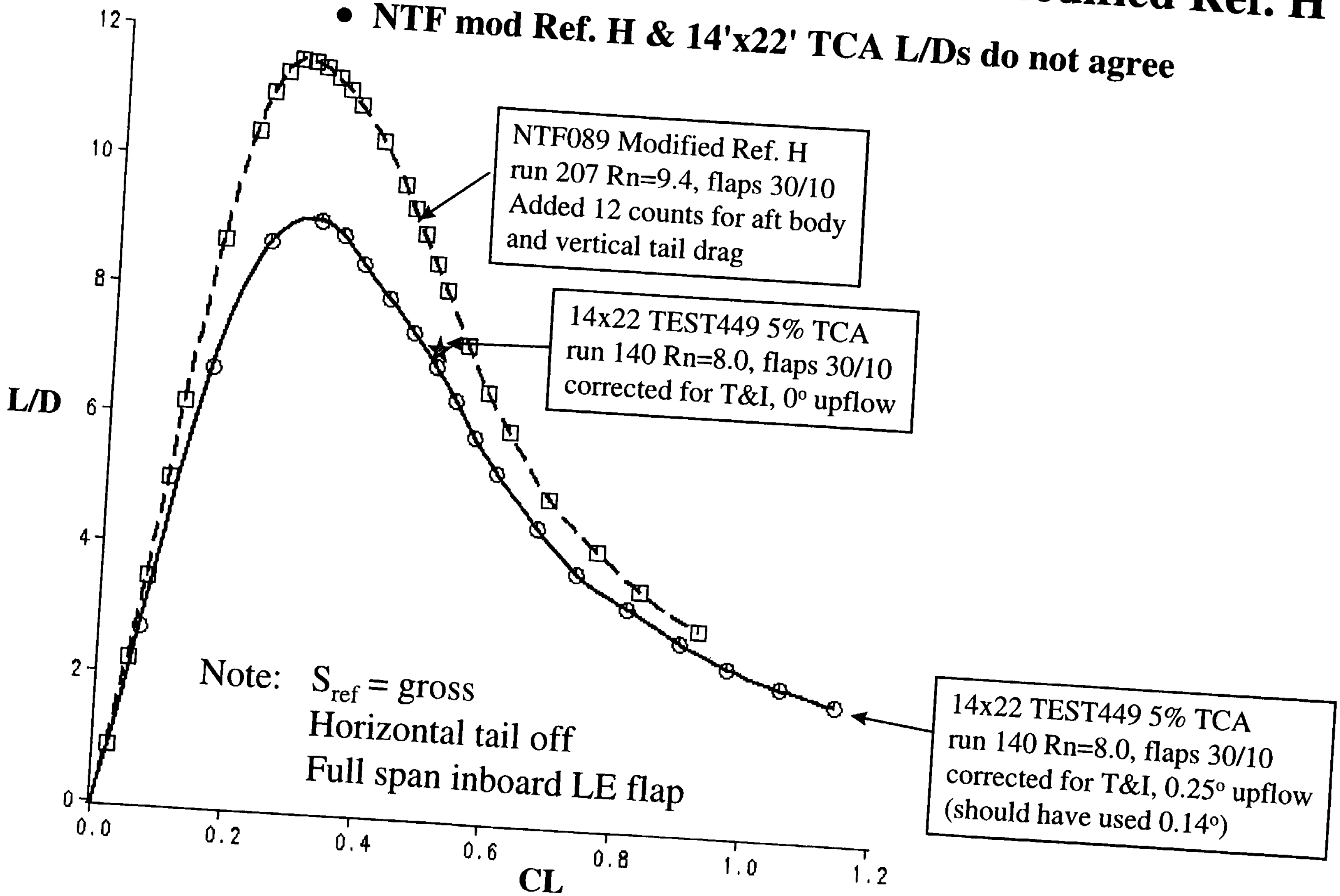

4.3.2.1 deliverable

Comparison of 14'x22' TCA-1 With NTF Modified Ref. H

This chart shows a comparison of the 5% TCA data to the 2.2% modified Ref H data from NTF test 089. The pitching moment correlation shown here is very good, with only a slight C_{M_O} mismatch. The two curves have the same shape up through the higher C_L's.

Comparison of 14'x22' TCA-1 With NTF Modified Ref. H

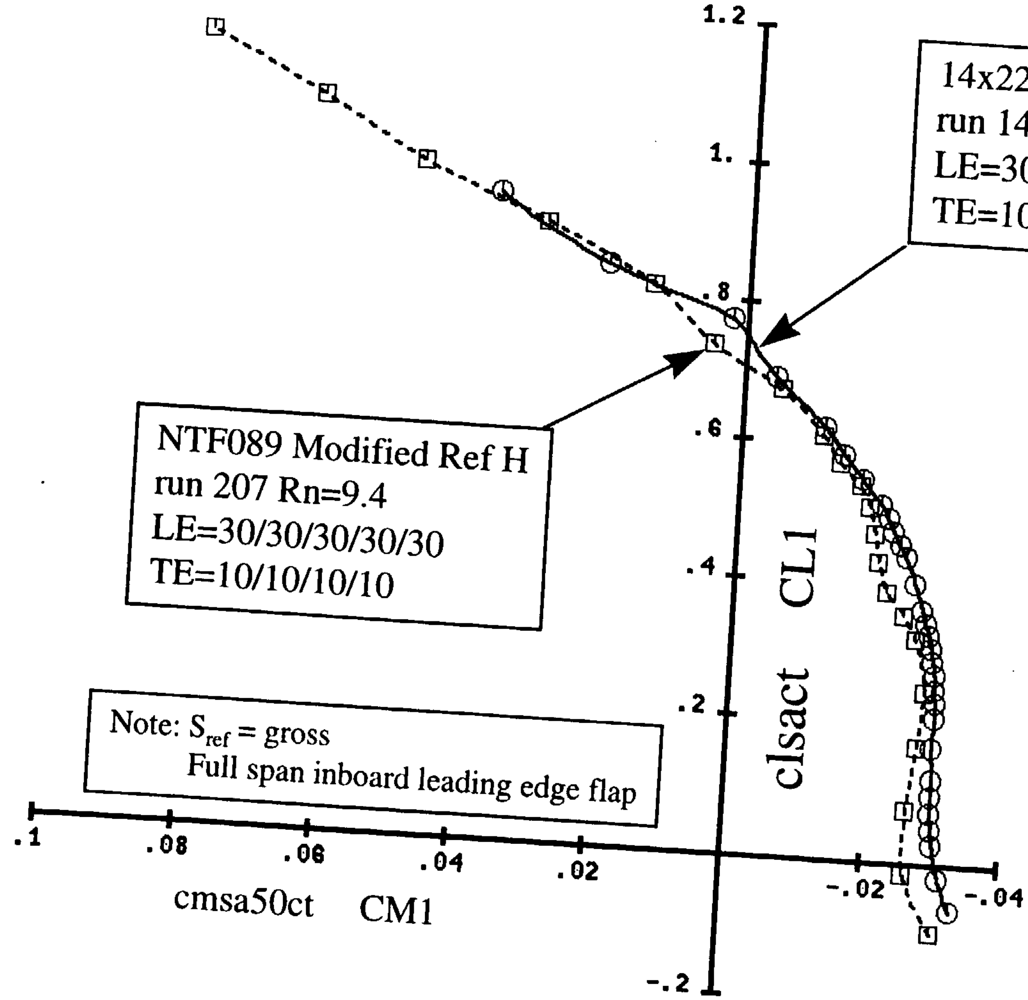

4.3.2.1 deliverable

Comparison of 14'x22' and NTF Ref. H Results

This chart shows a comparison of full scale lift curve estimates based on 6% Ref. H 14'x22' and 2.2% Ref. H NTF data for 30/10 flaps. The agreement is good.

Tail polars and downwash used for trimming were based on 14'x22' data with suitable adjustments for Reynolds number.

Comparison of 14'x22' and NTF Ref. H Results

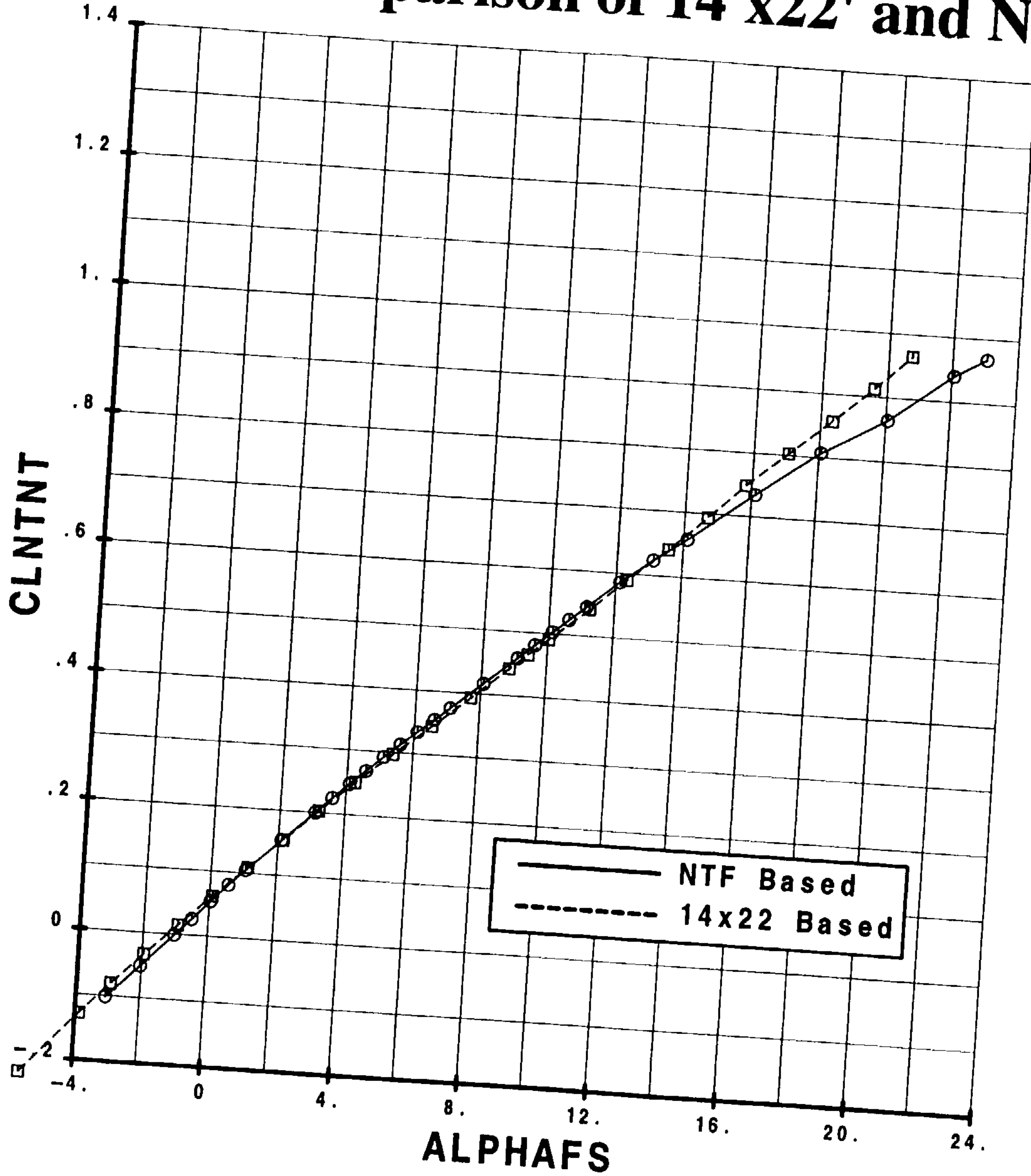

S_{ref} = gross (8500 sqft)
30/10 Flaps
Full span inboard leading edge flap
Full scale predictions, no thrust

Notes: 14'x22' data assumes no upflow, uses CFD support interference correction

4.3.2.1 deliverable

Comparison of 14'x22' and NTF Ref. H Results

This chart shows a comparison of full scale status L/D estimates based on 6% Ref. H 14'x22' and 2.2% Ref. H NTF data for 30/10 flaps. The agreement is good at operational lift coefficients (roughly 0.5 to 0.6).

Tail polars and downwash used for trimming were based on 14'x22' data with suitable adjustments for Reynolds number. These tail polars are optimistic so both build-ups, while consistent, are about 20 counts optimistic at CL=0.50.

The NTF drag was adjusted by 12 drag counts to account for the missing aft body and vertical tail.

Comparison of 14'x22' and NTF Ref. H Results

- NTF Ref. H & 14'x22' Ref. H L/Ds in good agreement

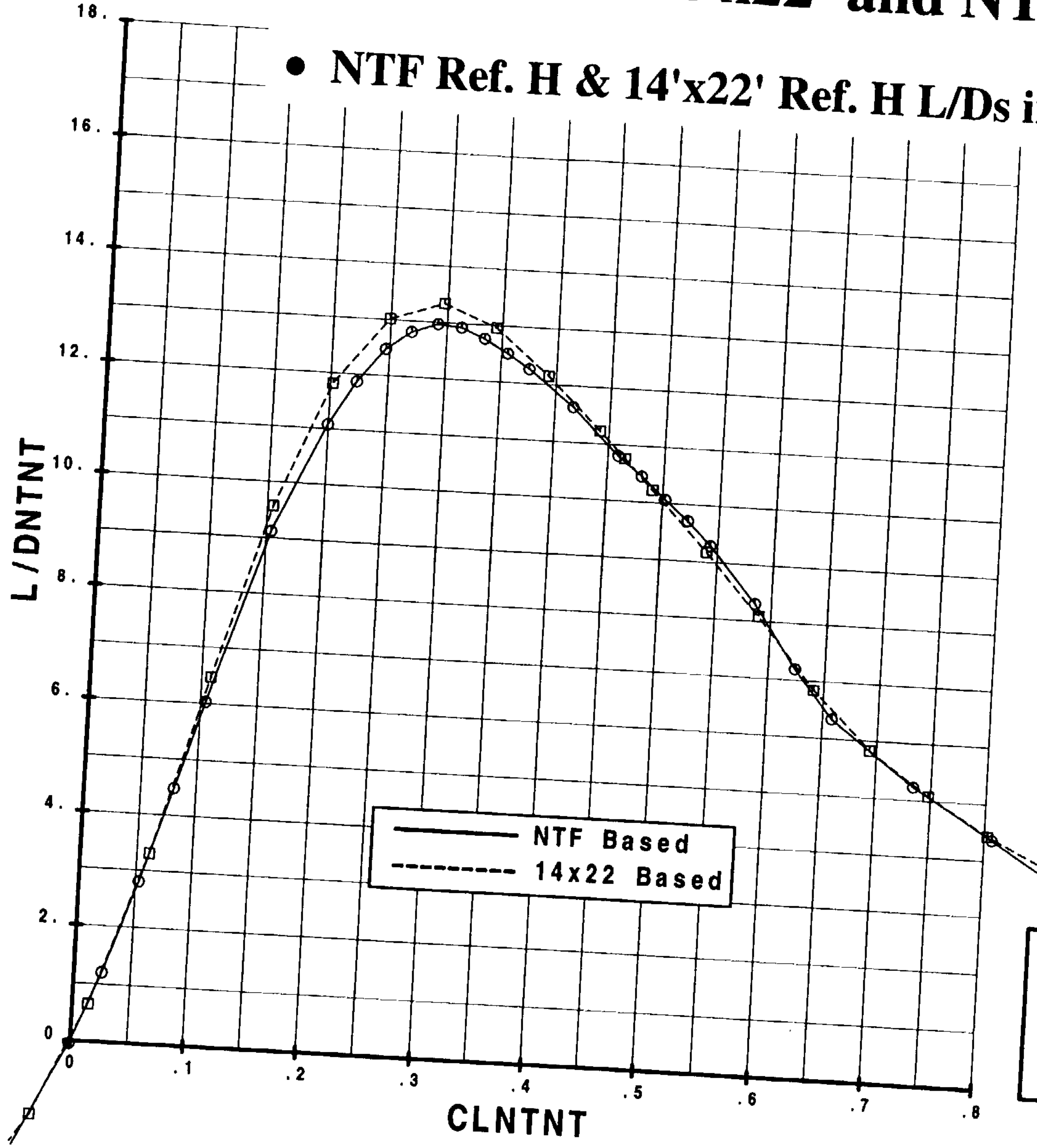

S_{ref} = gross (8500 sqft)
30/10 Flaps
Full span inboard leading edge flap
Full scale predictions, no thrust status level L/D (about 20 counts optimistic due tail polar used)

4.3.2.1 deliverable

Effect of Outboard Sealed Slat on TCA

This chart shows the L/D benefit available from a sealed slat on the outboard leading edge. The L/D gain at C_L =0.5 is 0.22 units, or 18 drag counts, relative to the baseline simply hinged plain flap.

Effect of Outboard Sealed Slat on TCA

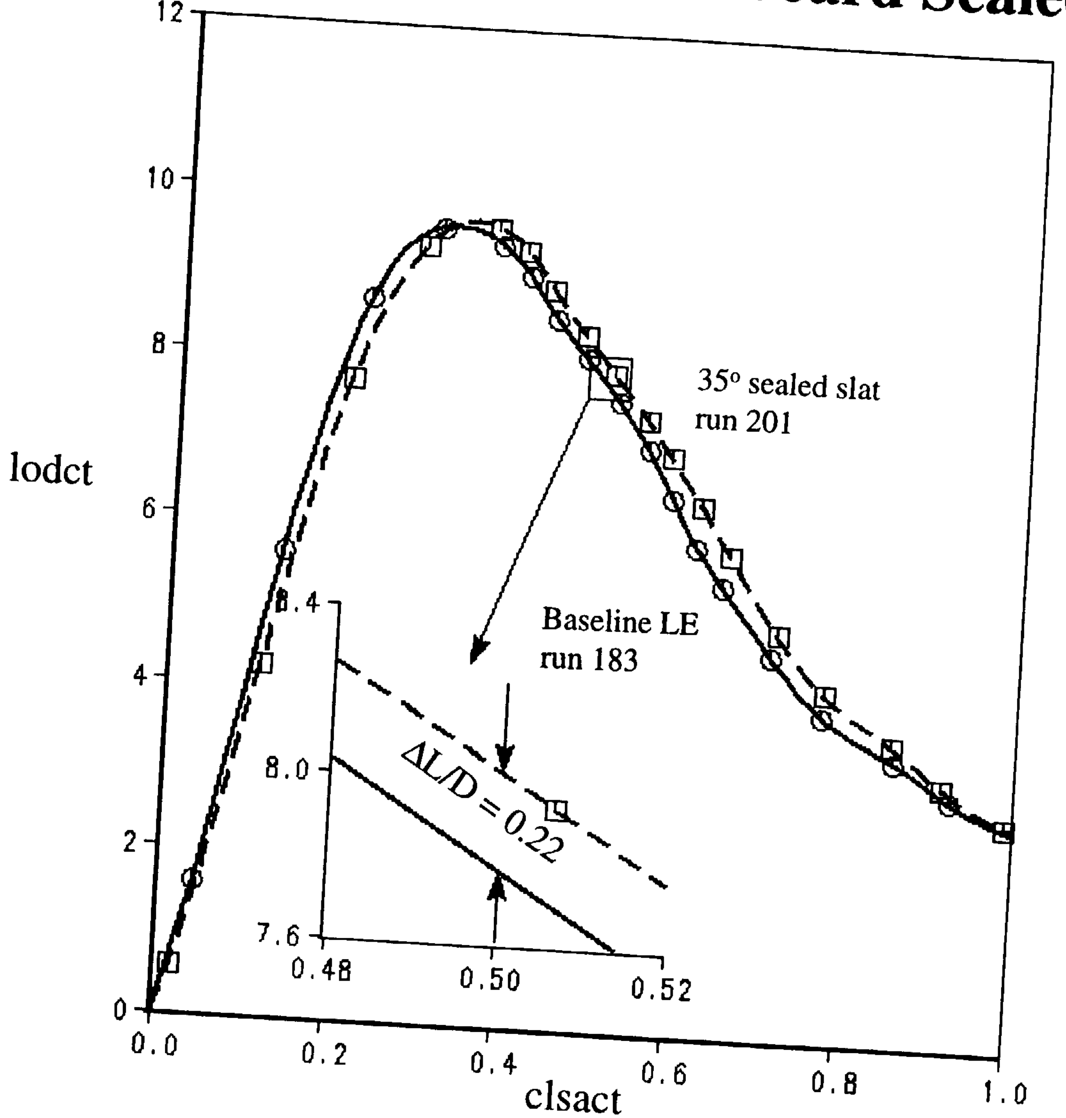

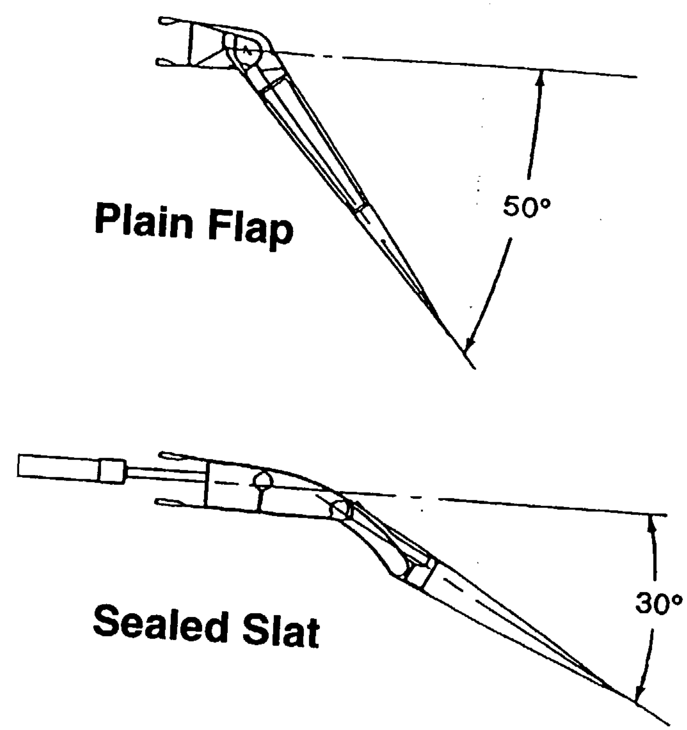

- **The outboard sealed slat improves L/D @ C_L =0.50 by 0.22 units, (18 drag counts).**

Note: this is not final data - don't use for drag level

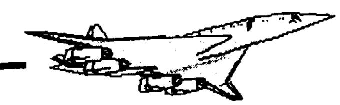

TCA Full Scale Build-ups

This slide shows the two methods used to predict full scale aerodynamic characteristics.

When wind tunnel data for the study configuration is unavailable, an incremental method is used (common PD process). In this method, AERO2S is used to estimate CL, CD, and Cm differences between the study and reference configurations. These increments are then applied to a wind tunnel database for the reference configuration. Skin friction and excrescence drag adjustments are then applied and the configuration is trimmed. The final step to achieve the status build-up is to determine the flap deflections which optimize L/D at each CL (programmed flaps).

When wind tunnel data is available for the study configuration, a bottom up build-up process is used. Essentially, the reference database + AERO2S increments are replaced by the wind tunnel database for the study configuration.

If the tool used to estimate the increments
(AERO2S in this case) is perfect, the two build-ups will be identical.

TCA Full Scale Build-ups

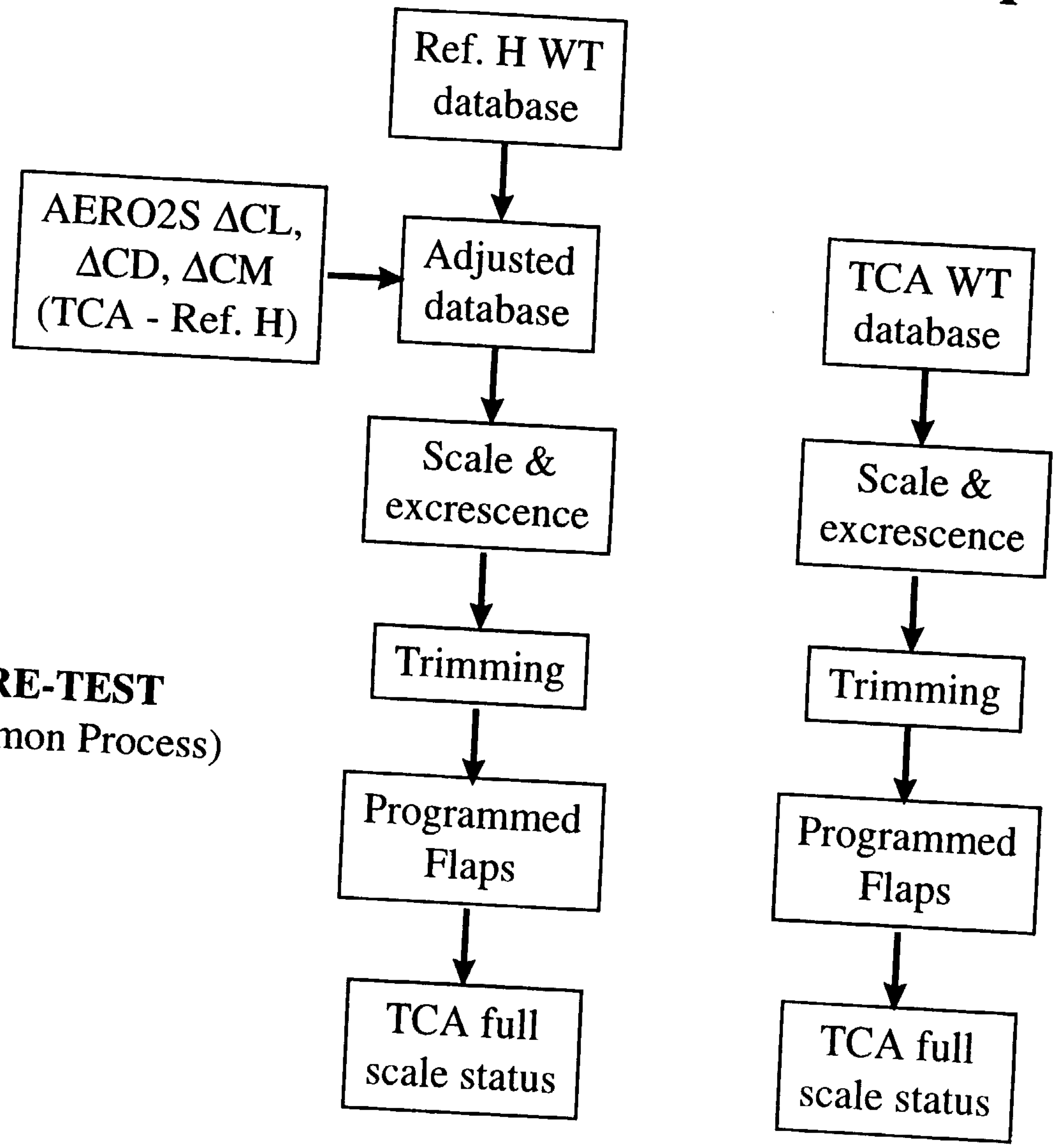

PRE-TEST
(Common Process)

POST-TEST
(Bottom Up)

4.3.2.1 deliverable

Full Scale L/D Comparisons

This slide compares predicted full scale, no thrust, status L/D for the Ref. H, TCA, and PTC. The lines above the bars show the projected L/D values corresponding to suction parameters (no thrust) of 92% for the Ref. H and TCA and 93% for the PTC (due to its canard).

The Ref. H status L/D is based on 14'x22' Ref. H data and is within about 5% of the projected L/D. The PTC status L/D is from the common process based on 14'x22' Ref. H data and is within about 2% of the projected L/D

The left two TCA bars are PD build-ups based on Ref. H 14'x22' data. The common process results in a status L/D about 6% less than the projection. The next bar shows the bottom up result using NTF modified Ref. H data. The L/D is 6% less than the common process prediction. The next bar shows the bottom up result using 14'x22' TCA data with measured upflow and support interference corrections; the status L/D is 10% worse than for the NTF based build-up. 10% poorer L/D is equivalent to 60,000 lbs of MTOW for the TCA sized to cutback noise of stage III-5 db. Assuming no upflow and using a slightly more favorable CFD based support interference, The TCA based on 14'x22' data is still about 7% poorer than the modified Ref. H result, 13% poorer than the common process prediction, and nearly 20% below the projected L/D.

The TCA results call into question the PTC prediction and the results of TI trade studies for which the climb-out L/D is an important parameter.

Full Scale L/D Comparisons

- High Lift PD Tools Not Yet Reliable
- Impacts Validity of TI Trade Studies

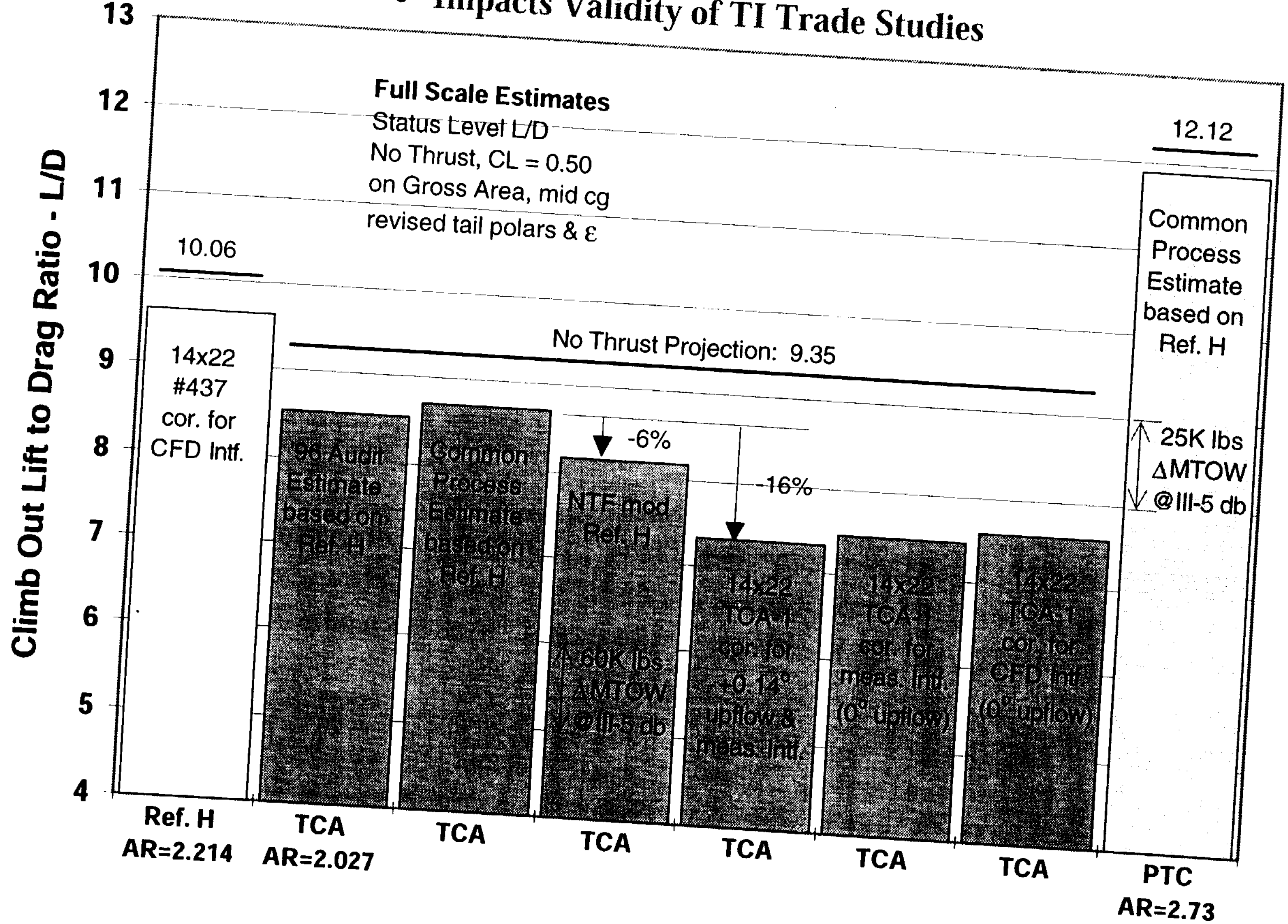

4.3.2.1 deliverable

TCA Full Scale Touchdown Lift Curves

This slide shows the free air and in ground effect lift curves for the TCA with 00/30 flaps. For an approach speed of 155kt and assuming a 3% speed bleed off during the flare, a touchdown CL of about 0.70 is required. This results in a touchdown attitude (alpha) of about 7.3°. The maximum permissible touchdown attitude is about 6.3° for a margin to aft body or nozzle contact of 3°.

The TCA, with the flaps set to maximize lift (00/30), cannot simultaneously meet the approach speed and contact margin requirement.

TCA Full Scale Touchdown Lift Curves

- **The TCA cannot meet 155kt Vappr with a 3° contact margin**

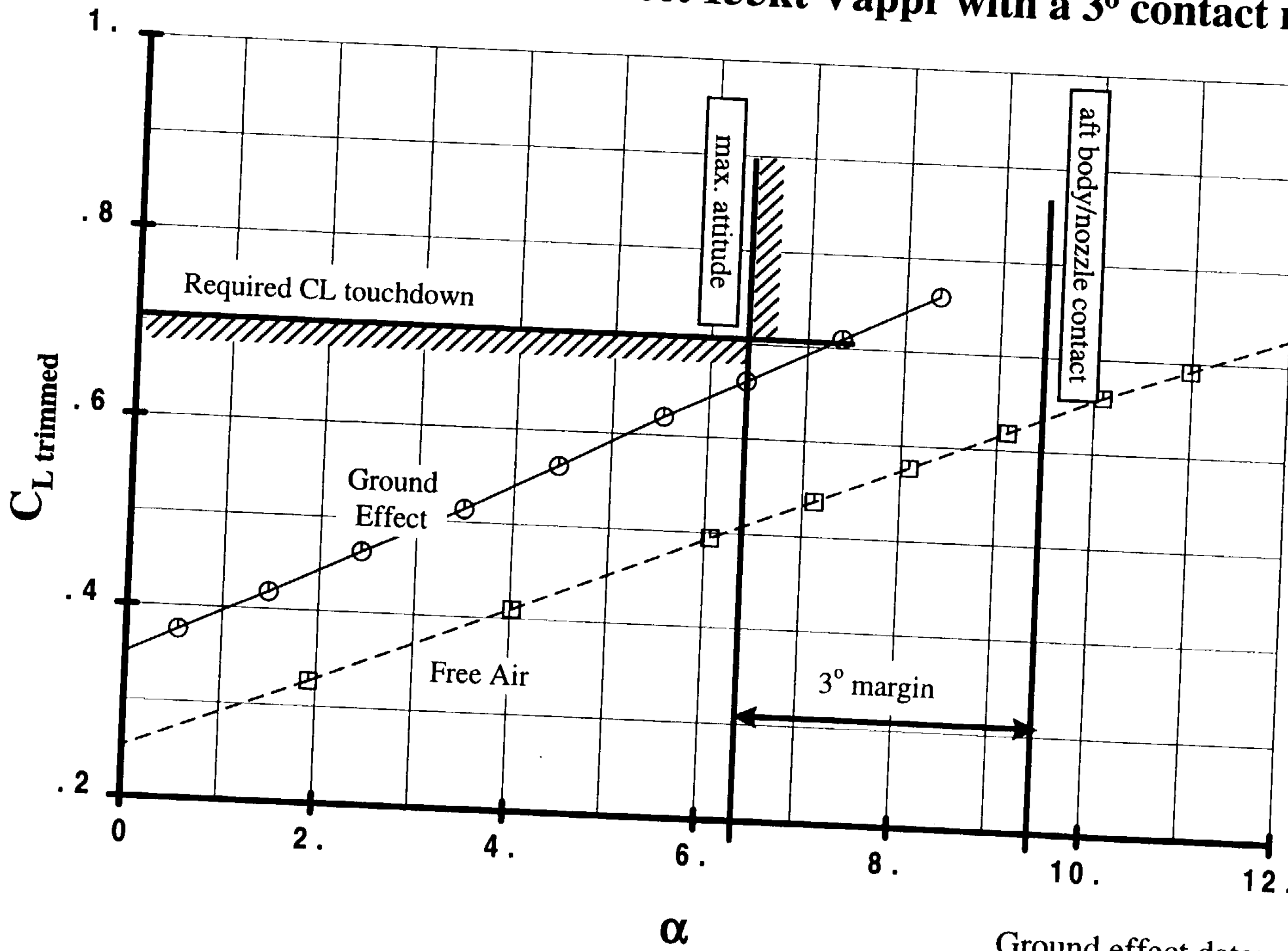

TCA-1 14x22 Test Data
0 deg. upflow
Flaps 00/30
Sref=8500 sq. ft.

Approach:
MLW=470,000 lbs.
Vappr=155 kts.

Ground effect data: no T&I correction
Free air data: T&I corrected

4.3.2.1 deliverable

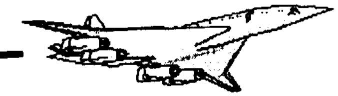

Conclusions

This page intentionally blank.

Conclusions

(1) Current PD tools underpredict the effect of planform changes on L/D.

Impacts the validity of TI trade studies, especially planform selection.

(2) There are large differences in drag between 14'x22' TCA and NTF modified Ref. H.

14'x22' U&I uncertainties do not explain the differences.

The modified Ref. H, while not identical to the TCA, is a close approximation.

(3) Full span leading edge flaps are beneficial to the TCA as tested but should not be considered a requirement for future technology baselines.

(4) Outboard leading edge sealed slats provide about the same benefit to the TCA L/D as they did for the Ref. H.

TI trade study will determine if the drag improvement offsets the increased complexity and weight relative to a plain outboard leading edge flap.

This page is intentionally left blank.

TCA Planform and Leading–Edge Study at High Lift Conditions

David T. Yeh and Roger W. Clark
Boeing, Long Beach

HSR Airframe Technical Review
High Lift Aerodynamics
at
Los Angeles, CA
February 9–13, 1998

BOEING

This page is intentionally left blank.

High Lift Technology Development (Task 33)

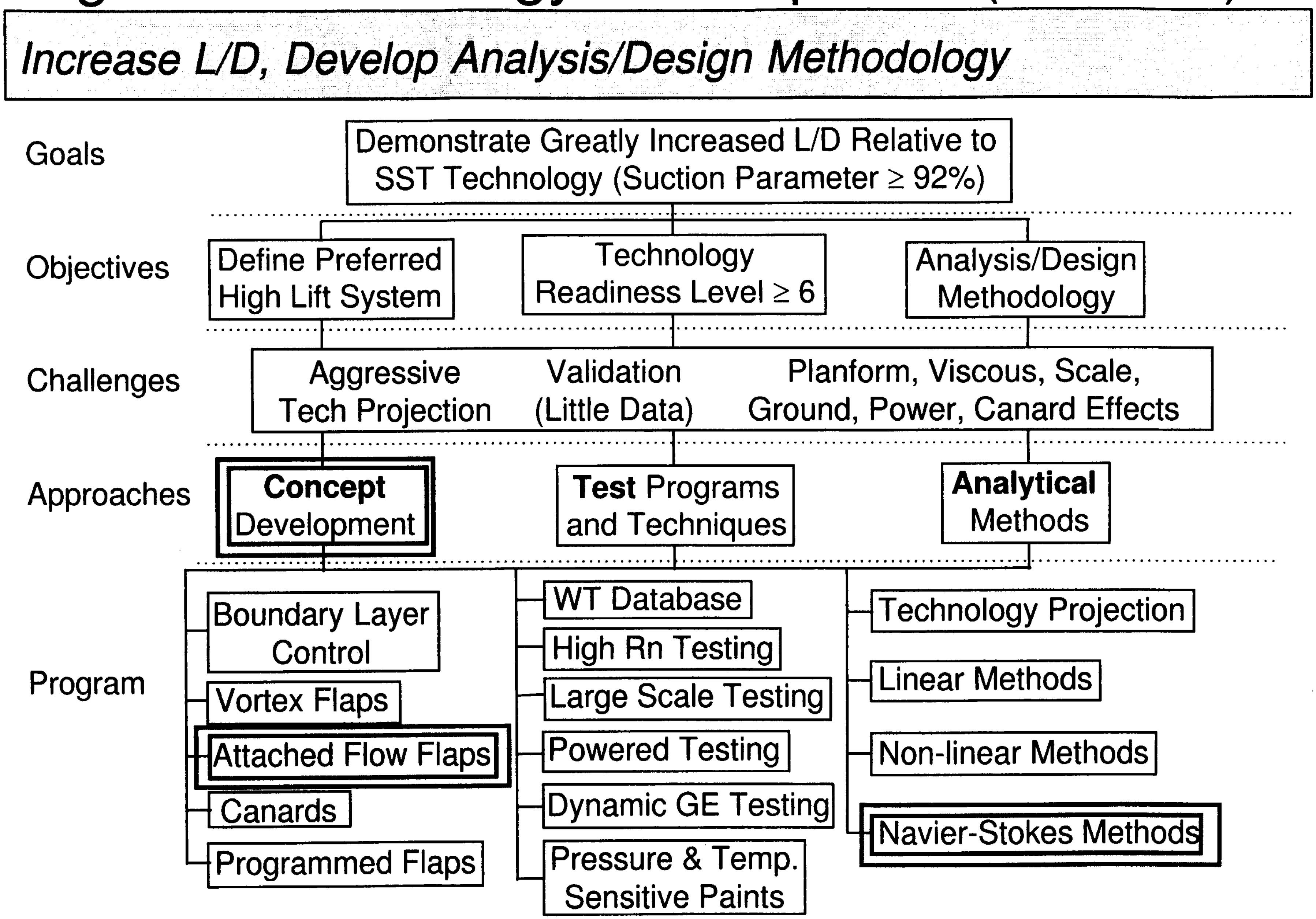

Outline

This report starts with the description of the objectives for the HSCT high-lift aerodynamics, followed by the numerical approach. Numerical results will be presented and comparison will be made with available test data or another CFD code. The basic flow characteristics for the TCA configuration will be first described, followed by the discussions of the effects of spanwise extent of the leading-edge flaps, inboard leading-edge camber increase and the planform variation of the TCA2.8-28 from the baseline TCA configuration. This report concludes with a summary and future plans.

OUTLINE

HSCT Aerodynamics, Long Beach

- Objectives
- Approach
- Numerical Results and Validation
    * TCA Basic Flow Characteristics
    * Spanwise Extent of LE Flaps
    * Inboard LE Camber Increase
    * Planform Variation (TCA2.8–28)
- Summary and Future Plans

BOEING

Objective - HSCT High Lift Aerodynamics

The over all objective for the HSCT high lift aerodynamics is to increase the high lift performance in order to minimize the noise, runway length etc. The aerodynamic performance is typically measured by the lift-to-drag ratio. To optimize the performance, the high lift devices, such as the leading- and trailing-edge flaps, are utilized. The leading-edge flaps are used to promote attached flow or to suppress the leading-edge vortex, while the trailing-edge flaps are deployed to optimize the span loading and increase lift at a given angle of attack.

To design and analyze the high lift devices, it is necessary to apply and validate the numerical methods in order to support the wind tunnel tests and to provide a better physical understanding of the flow phenomena as the configuration evolves. The numerical simulations will also be used to complement the wind-tunnel results in deriving optimum high lift systems through parametric studies.

OBJECTIVE – HSCT High Lift Aerodynamics

HSCT Aerodynamics, Long Beach

Increase Performance (Maximize L/D)
- LE Flaps : Promote Attached Flow
- TE Flaps : Optimize Span Loading

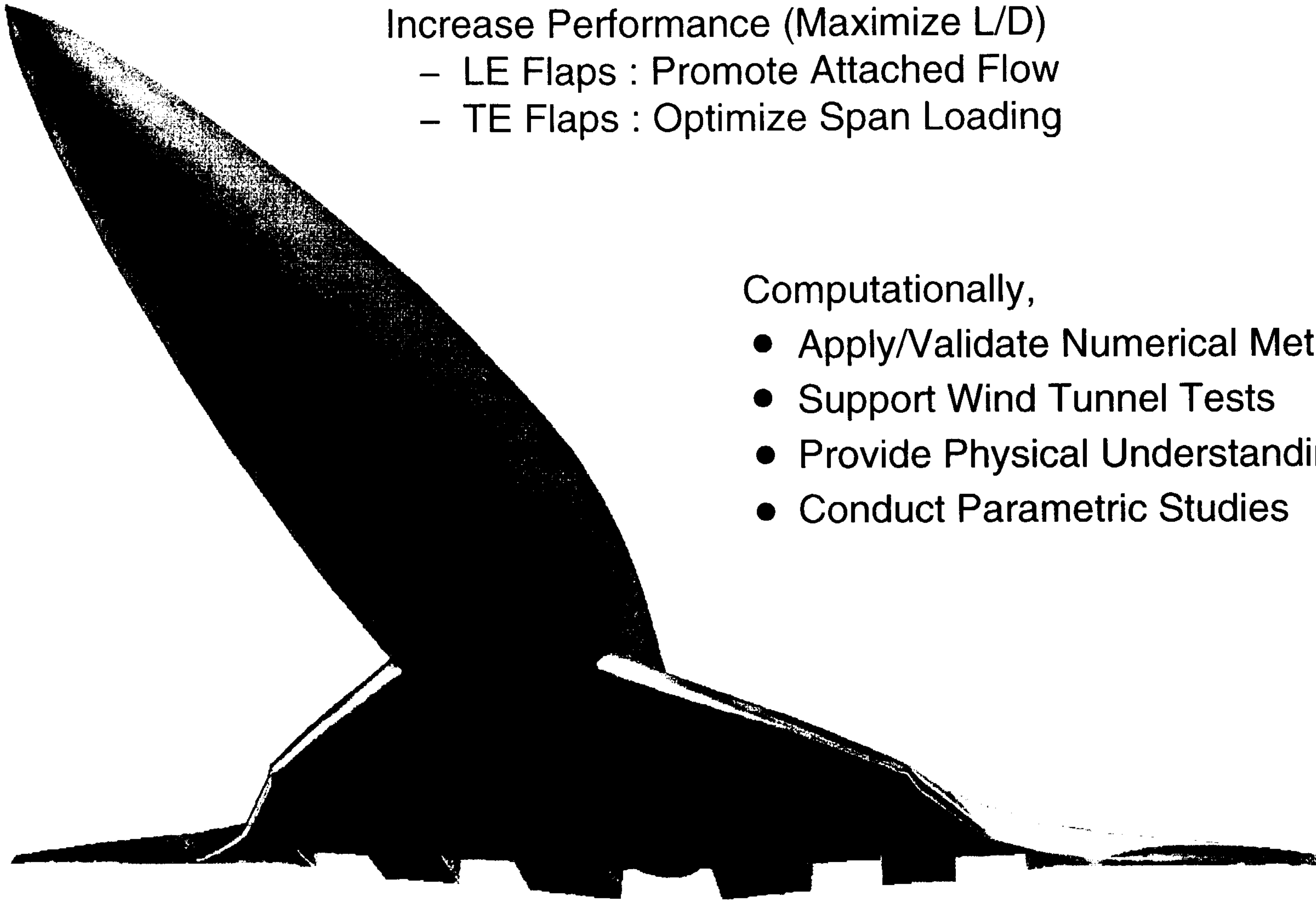

Computationally,
- Apply/Validate Numerical Methods
- Support Wind Tunnel Tests
- Provide Physical Understanding
- Conduct Parametric Studies

Current Study Focus

The current study is focused on the geometric variation of the TCA configuration and its effects on the high lift performance. Specifically, the emphasis will be focused in the following 3 areas:

1. Spanwise extent of the leading-edge flaps:

TCA configurations with part span and full span LE flaps will be analyzed with flap deflection of (LE/TE) 30/10. The comparison between the numerical solutions and test results based on TCA-1 test will be presented.

2. Inboard leading-edge camber increase:

The effect of inboard leading-edge camber on the part span leading edge flap configuration is evaluated and compared with the baseline TCA at the same flap setting. Two modified inboard camber are studied including the drooped and cambered configurations that are currently being tested (TCA-3 test) in the 12-ft tunnel at NASA Ames.

3. Planform Variation

Pre-test analysis of TCA2.8-28 configuration has been conducted to assess the effect of planform variation on the high lift performance and to support the upcoming TCA-4 test. The geometric difference between the TCA2.8-28 and the baseline TCA occurs in the outboard wing panel with a lower leading edge sweep and a higher aspect ratio.

Current Study Focus

HSCT Aerodynamics, Long Beach

1. Spanwise Extent of LE Flaps (Validate TCA–1 Test)

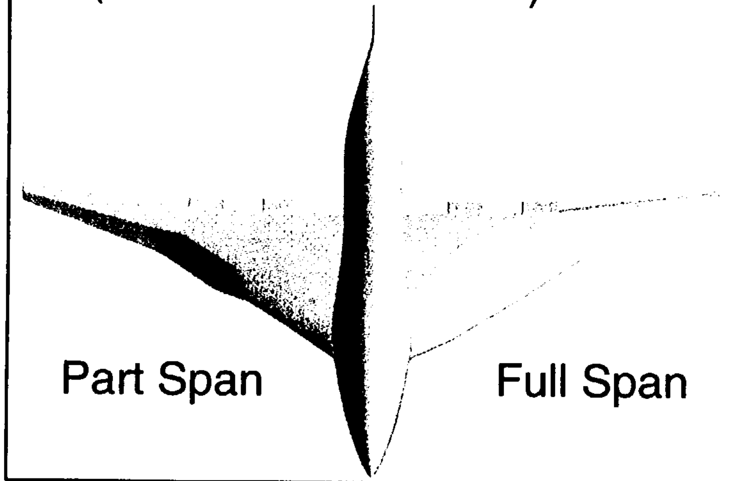

2. Inboard LE Camber Increase (Support Ongoing TCA–3 Test)

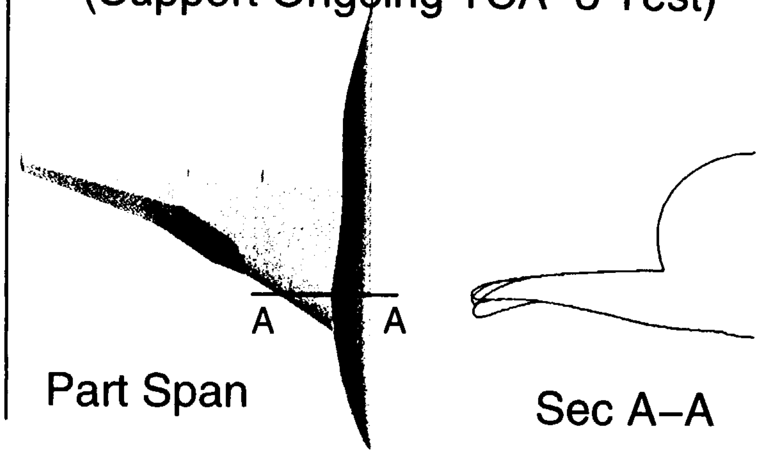

3. Planform Variation (TCA2.8–28) (Support Upcoming TCA–4 Test)

- O/B LE sweep
- Aspect ratio

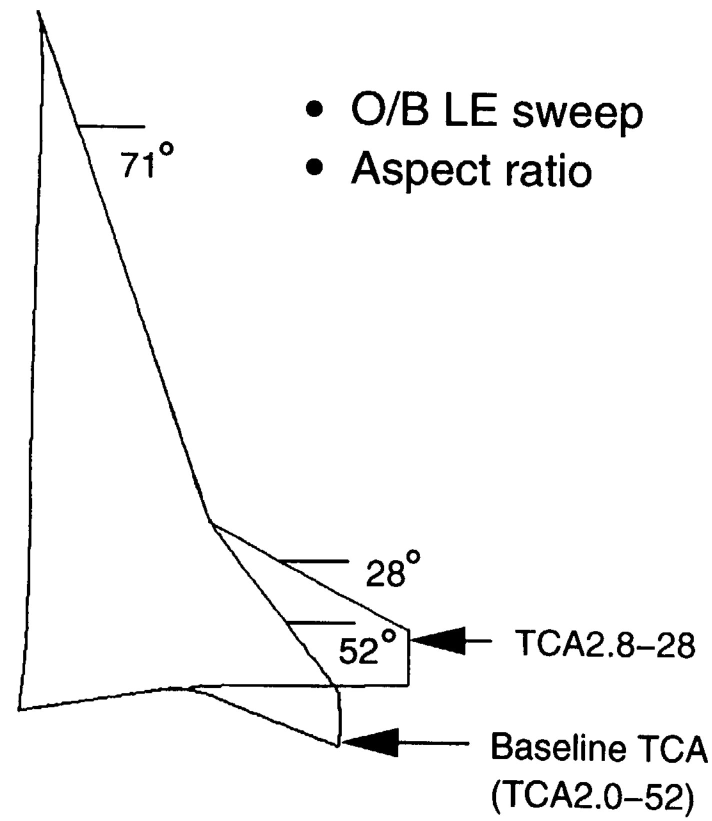

BOEING

Approach

The approach is to utilize the recent development of the automated flap deflection procedures and the CFL3D code developed at NASA LaRC for high-lift flow simulations. The numerical results are compared with available test data for code validation as well as load estimation for test support and wind-tunnel model design. The effects of planform and leading-edge variation on the flow are analyzed through detailed graphical illustration and the associated impact on the high lift performance will be evaluated.

APPROACH

HSCT Aerodynamics, Long Beach

- Automated flap deflection procedures

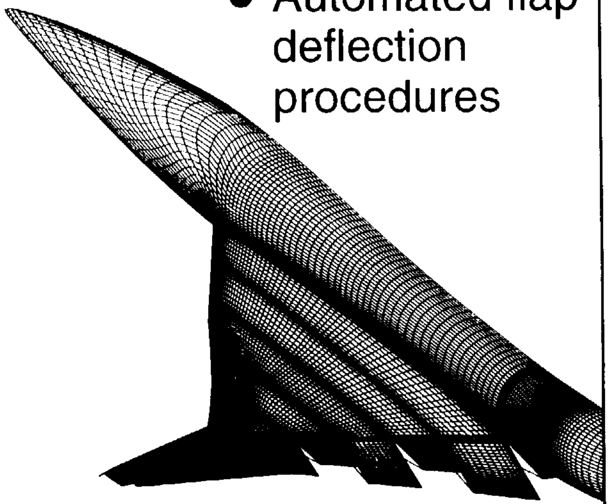

- Numerical wind tunnel

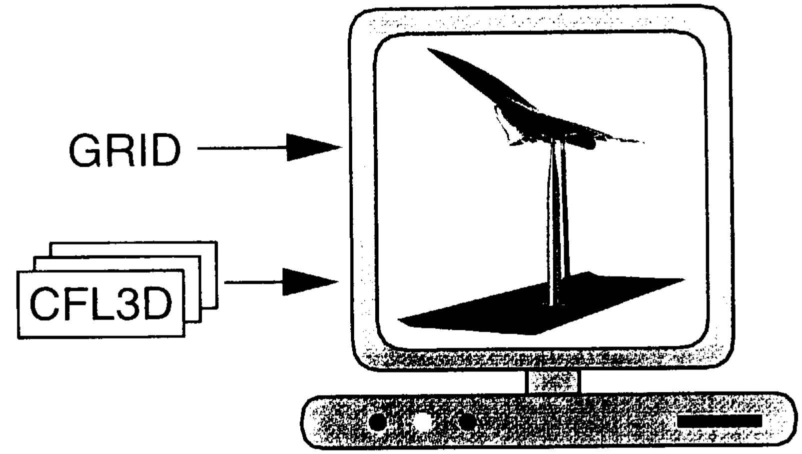

- Flow visualization
- Performance assessment

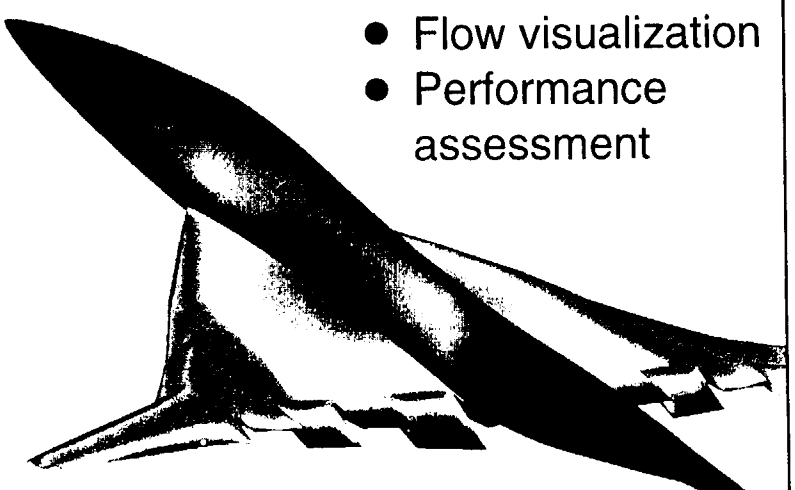

- Code validation & test support

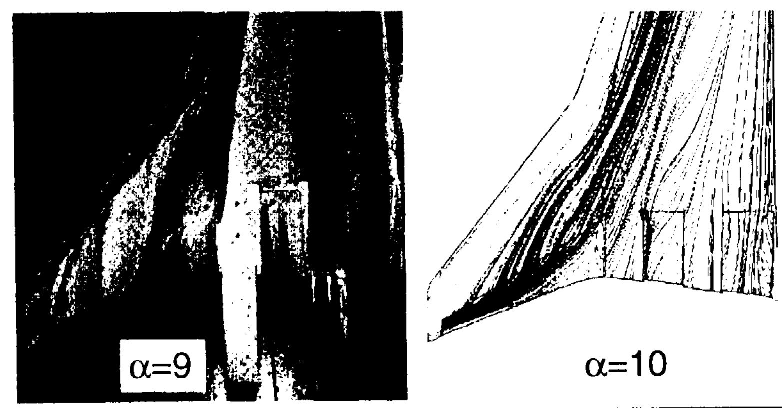

BOEING

Effects of Flaps on TCA Flow Field

Some of the basic flow features for the TCA configurations are illustrated in this chart which includes the clean (flaps up) and a 30/10 (LE/TE) configurations. For the clean configuration, the leading edge vortex is formed along the leading edge which induces a low pressure region on the wing. A separate vortex originated from the wing break is also visible. The flow condition is at $M=0.3$, $\alpha=10$ degrees with the Reynolds number of 8 million based on the mean aerodynamic chord (MAC). The upper surface limiting streamlines are plotted on the right of the configuration where separation (converging) and attachment (diverging) streamlines are both visible as a result of leading edge separation and the resulting vortices.

For the 30/10 part span leading edge flap configuration at the same high lift condition, only a weak vortex is formed just inboard of the leading edge flap. Low pressure regions are also visible along the LE and the hinge lines. This comparison illustrates the suppression of the leading edge vortex through flap deflection.

Effects of Flaps on TCA Flow Field

HSCT Aerodynamics, Long Beach

M=0.3, α=10 deg, Re=8 million (MAC)

Pressure (left) / Limiting Streamlines (right)

Clean (Flaps Up) $\qquad$ δ(LE/TE)=30/10 (Part span LE flaps)

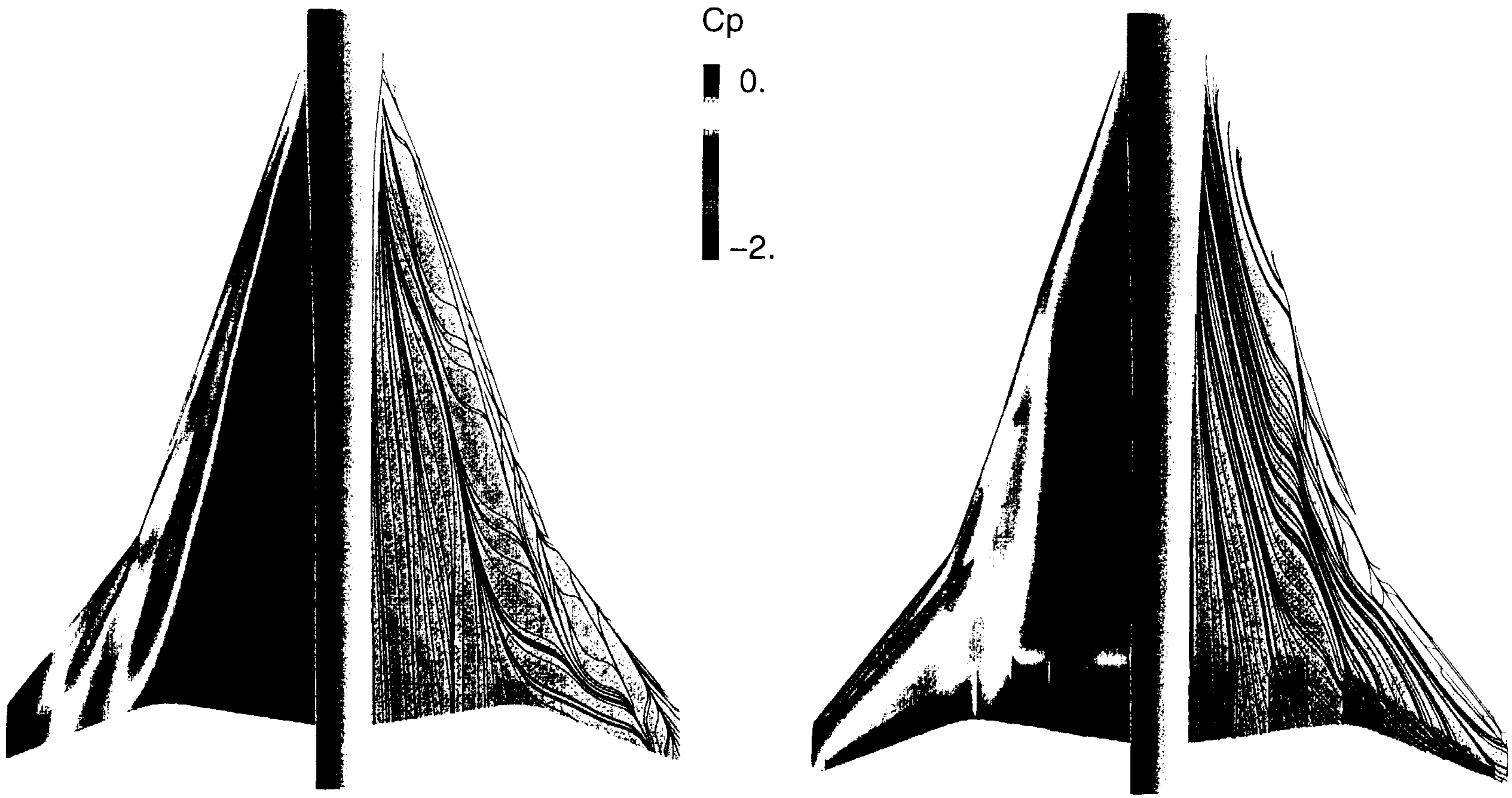

Lower Surface Limiting Streamlines for TCA Configuration

Another flow feature of a highly swept TCA configuration is the formation of an attachment line rather than a stagnation point due to the 3-dimensionality of the flow. The computational solutions show the inboard attachment lines for both flap-up and flap-down cases are both located on the lower surface where the leading edge is rounded. In the outboard region, the attachment line is located close the leading edge where the geometry is typically sharp.

Lower Surface Limiting Streamlines for TCA Configurations

HSCT Aerodynamics, Long Beach

M=0.3, α=10 deg, Re=8 million (MAC)

- Inboard Attachment Lines are located on the lower surface

Clean (Flaps Up)

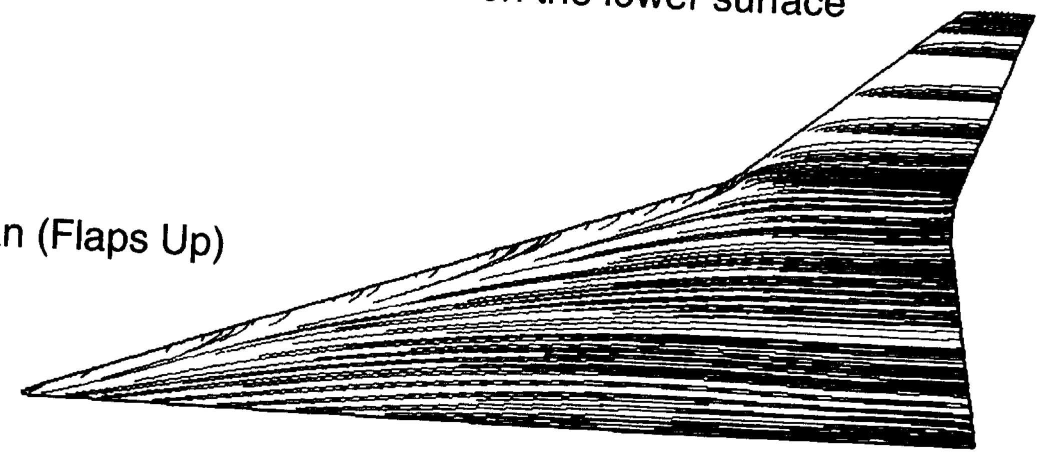

δ(LE/TE)=30/10 deg

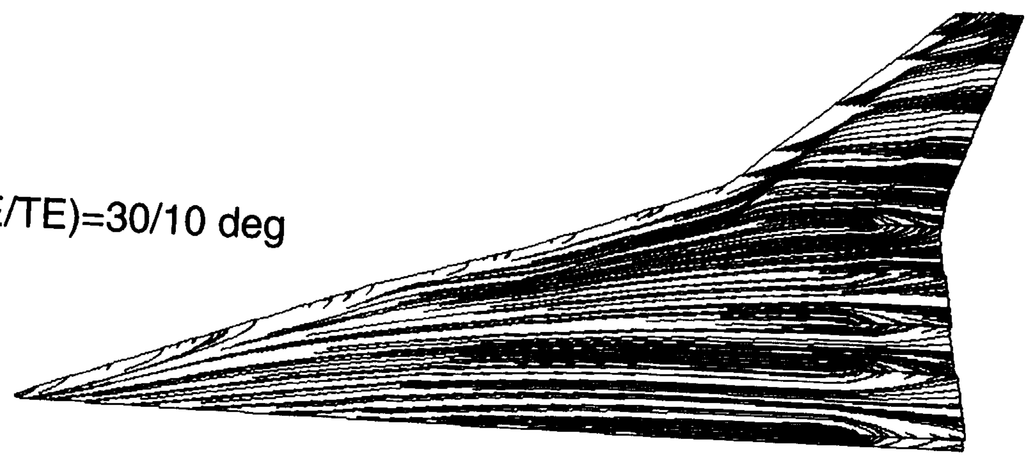

BOEING

Pressure Tap Locations for the TCA Configuration

Surface pressure comparison between the CFD solution and the TCA-1 test data has been made at 6 buttlines and 8 fuselage stations for code validation. This chart shows the planform locations for the buttline and fuselage stations. All the dimensions have been converted from the 5% model size to the full scale.

Pressure Tap Locations for the TCA Configuration

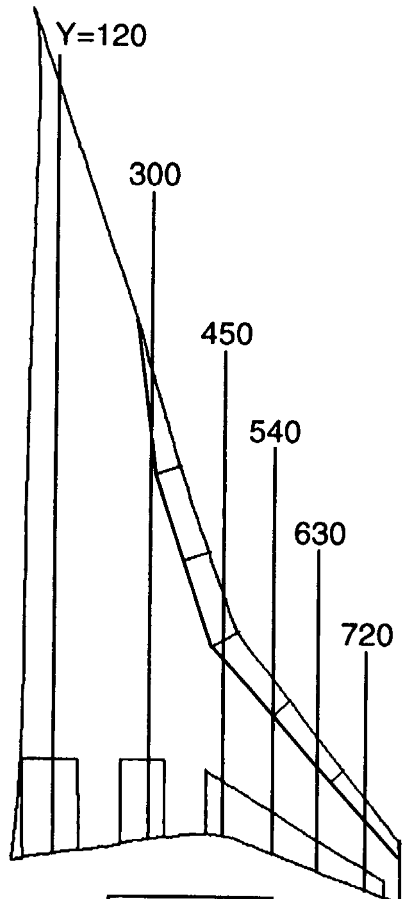

Buttline

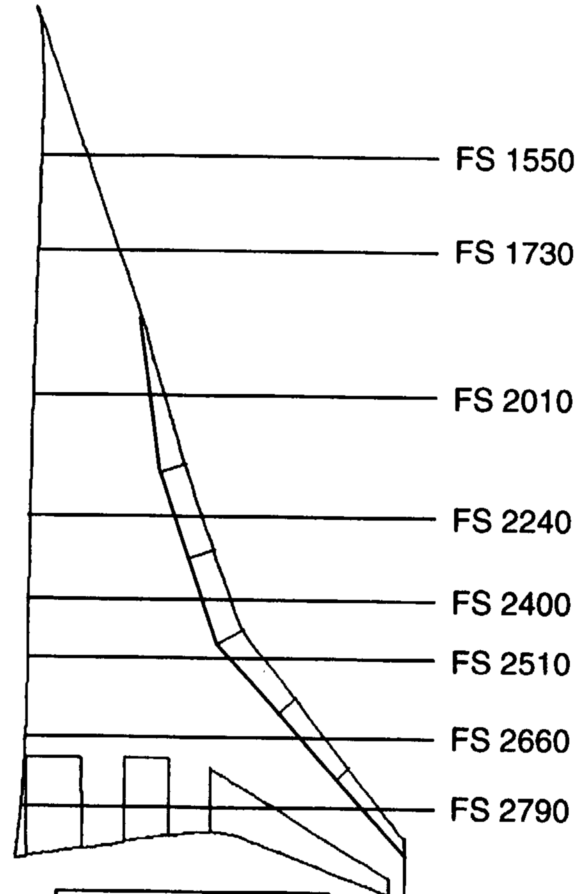

Fuselage Station

Chordwise Pressure Comparison for TCA 30/10 (Part Span)

This chart shows the chordwise pressure comparison for the 6 buttlines at $M=0.3$, $\alpha=10$ degrees, Reynolds number of 8 million with the part span LE flap deflection of 30 degrees and TE flap deflection of 10 degrees. The comparison shows a good agreement between the CFL3D solution and the measured test data. It is also interesting to note the discrepancy on the lower surface at Y=120" may be caused by the flow acceleration around the post that supports the model resulting a lower pressure on the model lower surface. As a consequence, the numerical predicted lift could be higher than the test data.

Since the leading edge flaps have a strong influence on the wing flow field, it would be desirable to put additional pressure ports on the leading edge flap region in order to verify the numerical solution in the region.

Chordwise Pressure Comparison for TCA 30/10 (Part Span)

HSCT Aerodynamics, Long Beach

M=0.3, AoA=10 deg, Re=8 Million (MAC)

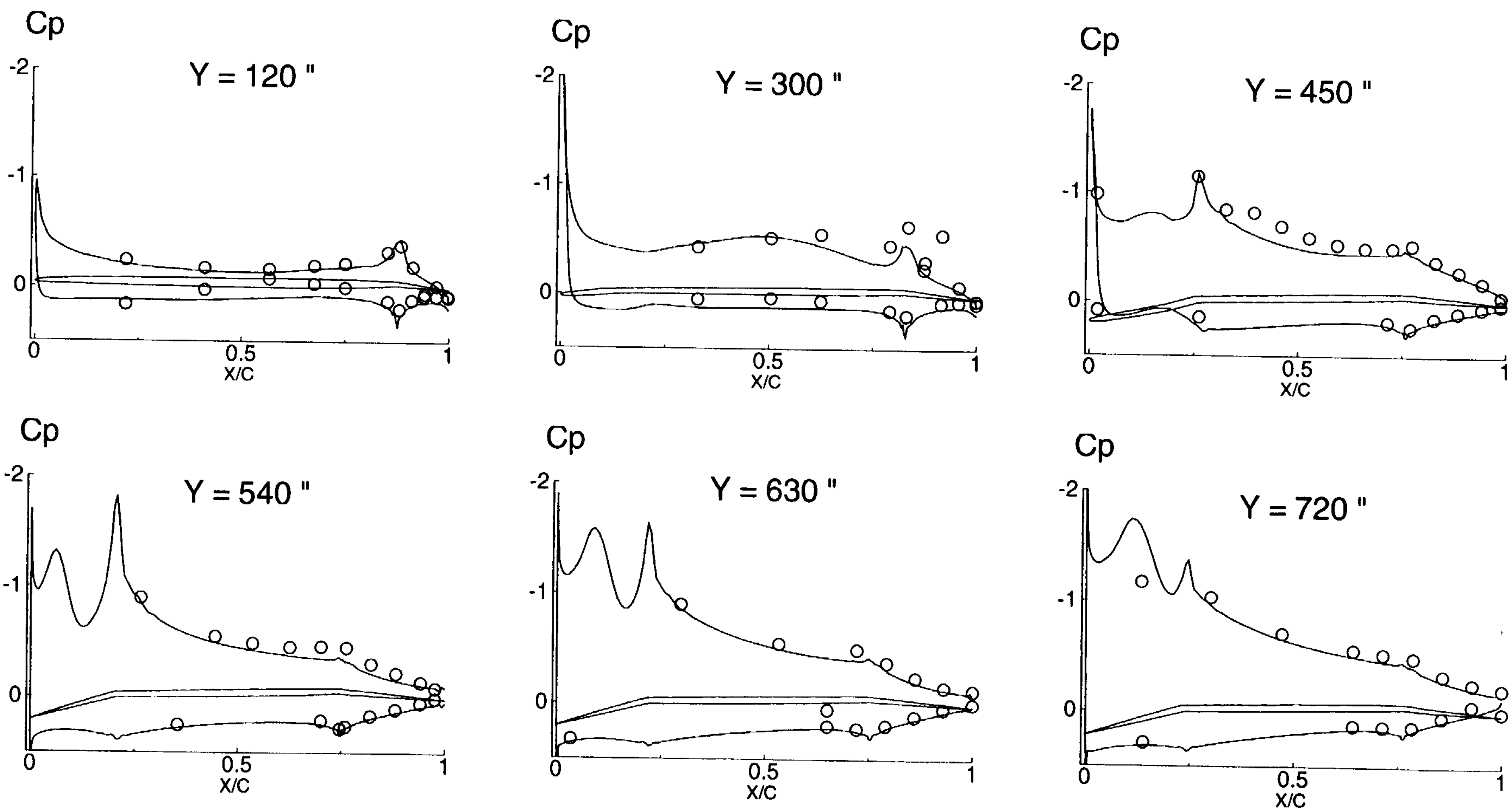

Spanwise Pressure Comparison for TCA 30/10 (Part Span)

This chart shows the spanwise pressure comparison for the 8 fuselage stations at the same flow conditions. A favorable comparison is observed between the numerical prediction and the test data. The vortex induced suction peaks downstream of x=2010 show good agreement both in the location and magnitude which indicates an accurate prediction of the vortex location and strength.

Spanwise Pressure Comparison for TCA 30/10 (Part Span)

HSCT Aerodynamics, Long Beach

M=0.3, AoA=10 deg, Re=8 Million (MAC)

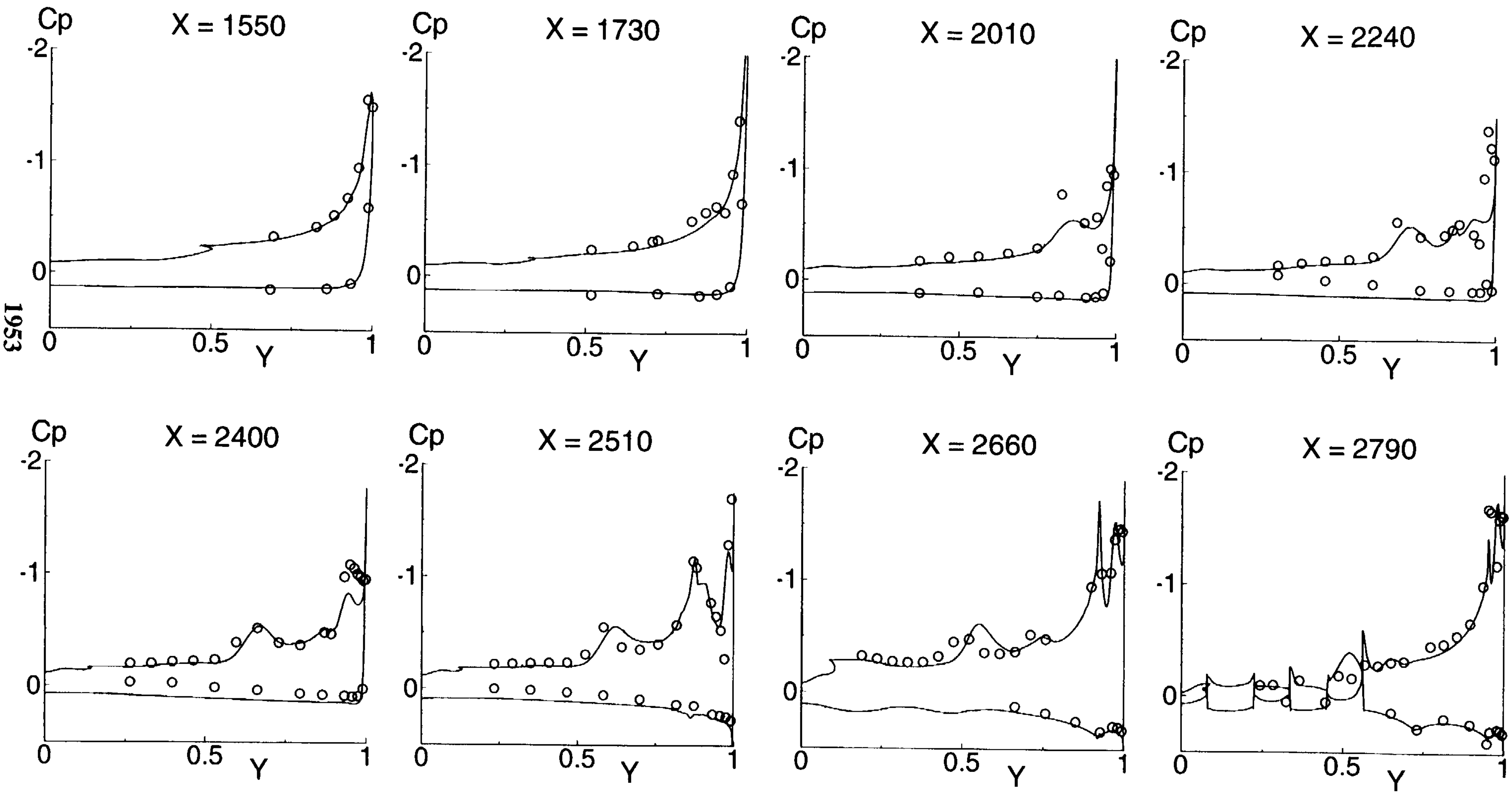

Effect of LE Flap Angle on Surface Pressure

The effect of the leading edge flap angle on the surface pressure is illustrated in this chart where 2 LE flap deflections (30 and 35) are plotted against each other. A higher leading edge flap deflection reduces the leading edge suction peak which would create a more favorable attached flow environment. However, higher leading edge flap deflection increases the curvature around the hinge line resulting a higher suction which increases the probability of hinge line separation.

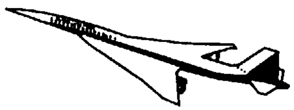

Effect of LE Flap Angle on Surface Pressure

HSCT Aerodynamics, Long Beach

M=0.3, AoA=10 deg, Re=8 million (MAC)

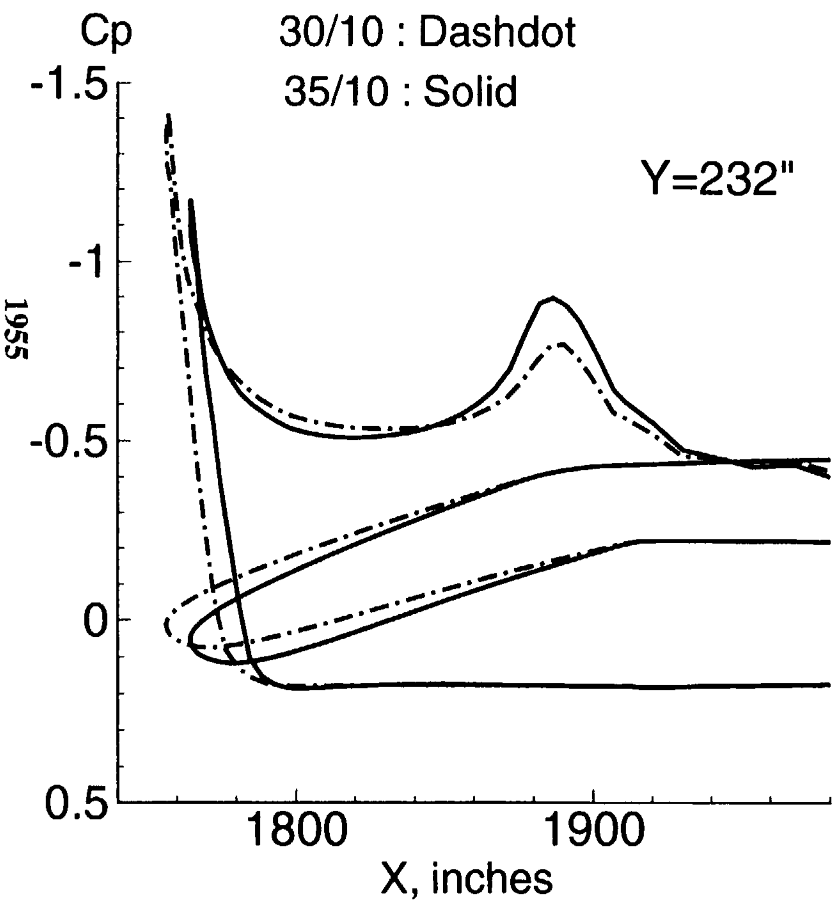

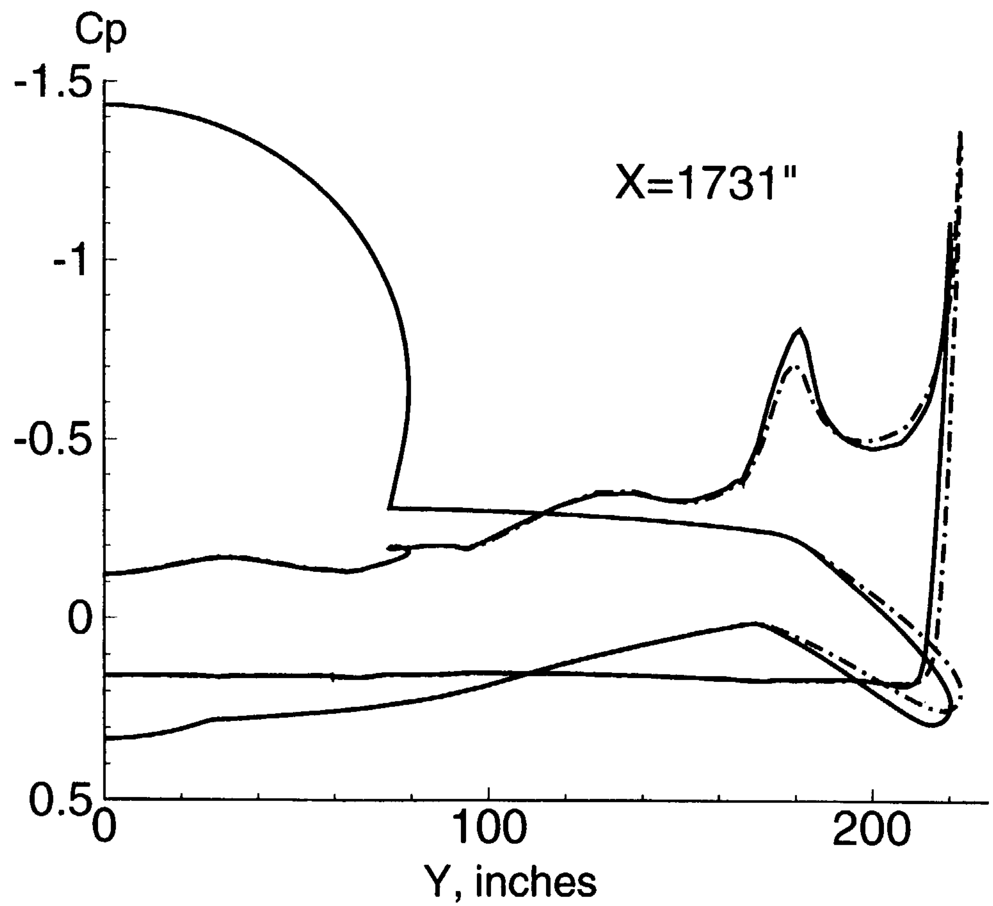

BOEING

Spanwise Extent of the LE Flaps for TCA Configurations

The effect of the spanwise extent of the leading edge flaps on the flow field has been studied. Computational models of a part span leading edge flap and a full span have been generated for the TCA configuration at the flap deflection of (LE/TE) 30/10 degrees.

Spanwise Extent of the LE Flaps for TCA Configurations

HSCT Aerodynamics, Long Beach

$\delta(LE/TE) = 30/10$

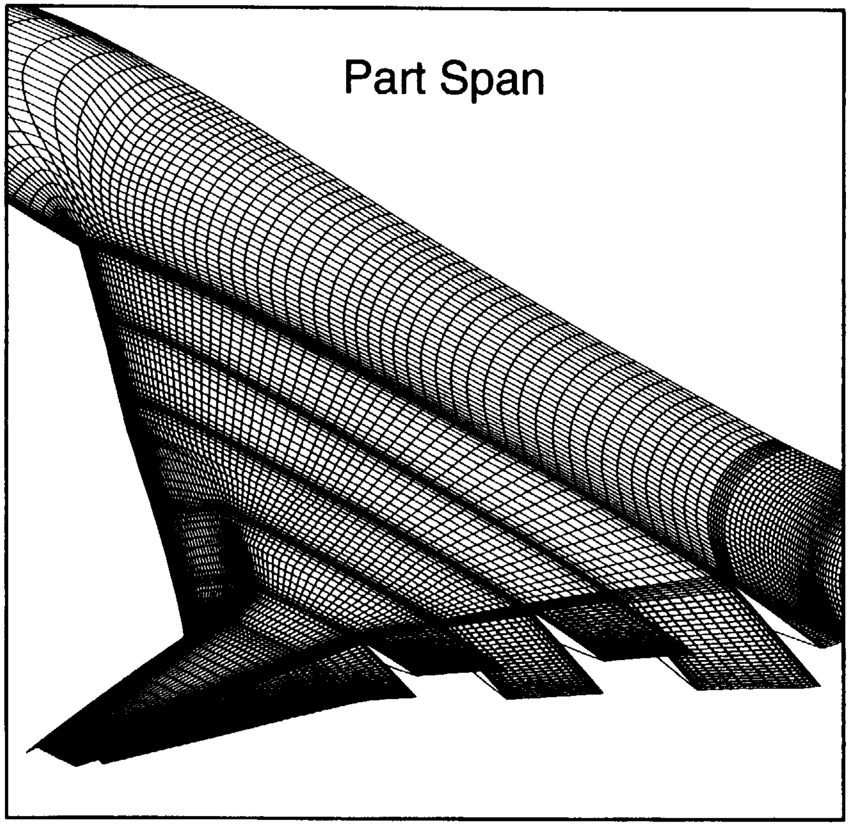

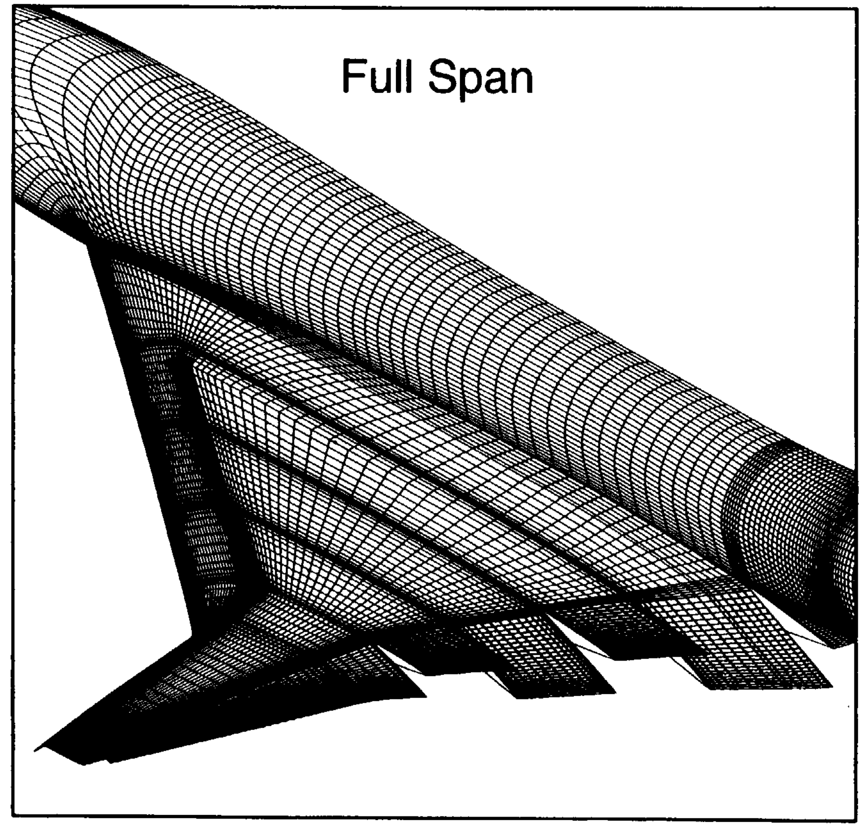

BOEING

Effects of the LE Flap Extent on the Vortical Flow

This chart shows the normalized total pressure contours for the part span and full span leading edge flaps. The total pressure is used for tracking the vortical flow because there is a total pressure loss across the boundary layer and the shear layers in the subsonic flows.

It clearly shows that the part span flap leads to a stronger leading edge vortex due to a premature leading edge separation just inboard of the part span leading edge flap.

Effects of the LE Flap Extent on the Vortical Flow

HSCT Aerodynamics, Long Beach

TCA 30/10 Configurations

Total Pressure

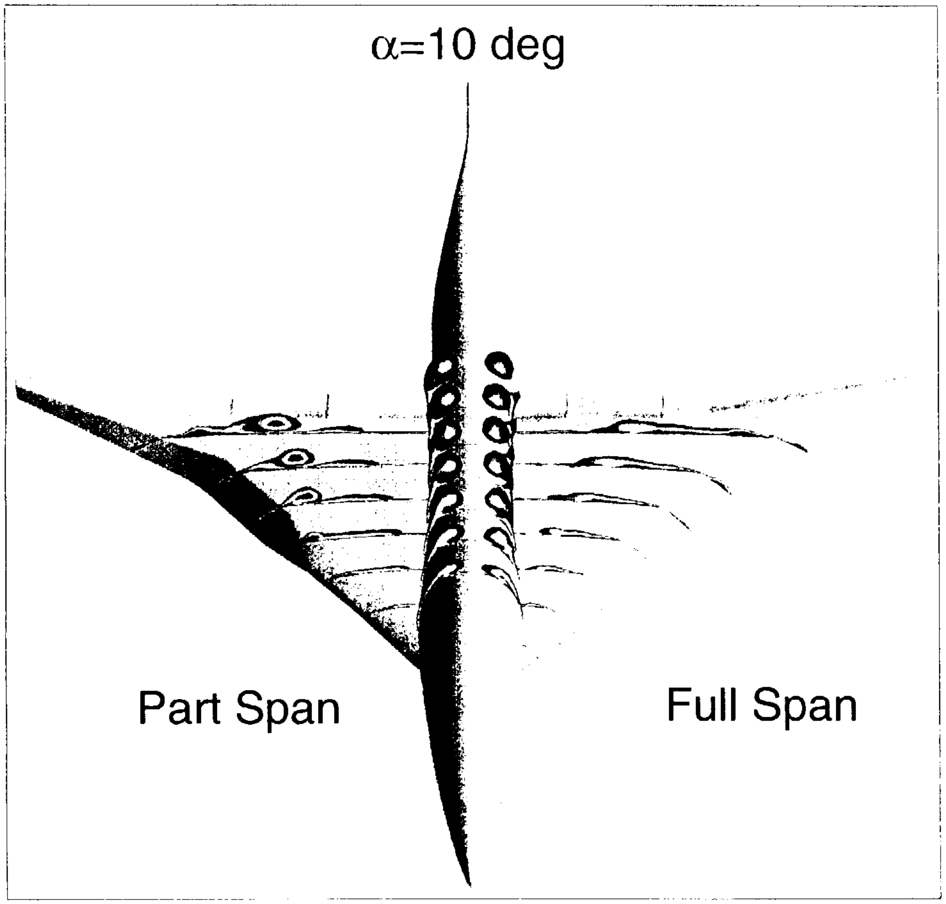

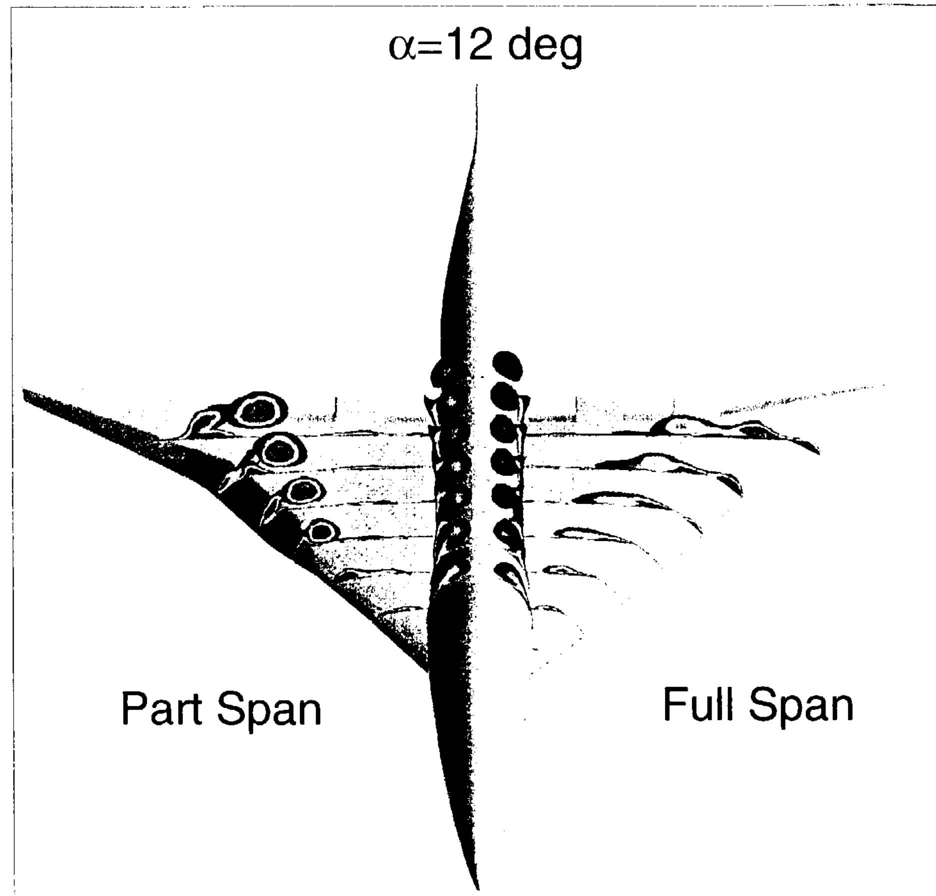

BOEING

Effect of Inboard LE Flaps on the Flow Characteristics

The effect of inboard leading edge flaps on the flow separation is illustrated through the releasing of the limiting streamlines from the leading edge. At 10 degrees angle of attack, the separation starts just inboard of the part span flap, whereas as an attached flow is attained on the deflected inboard leading edge flaps. As a result, the full span flap promotes attached flow inboard and delays a premature leading edge separation.

Effect of Inboard LE Flaps on the Flow Characteristics

HSCT Aerodynamics, Long Beach

TCA 30/10 Configuration at M=0.3, $\alpha=10^{\circ}$, Re=8 Million

Limiting Streamlines

Part Span LE Flap

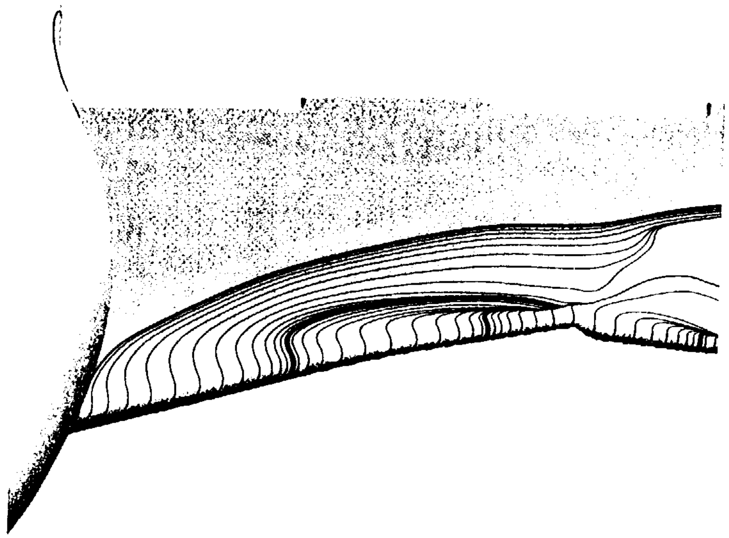

- Separation starts inboard of LE flaps

Full Span LE Flap

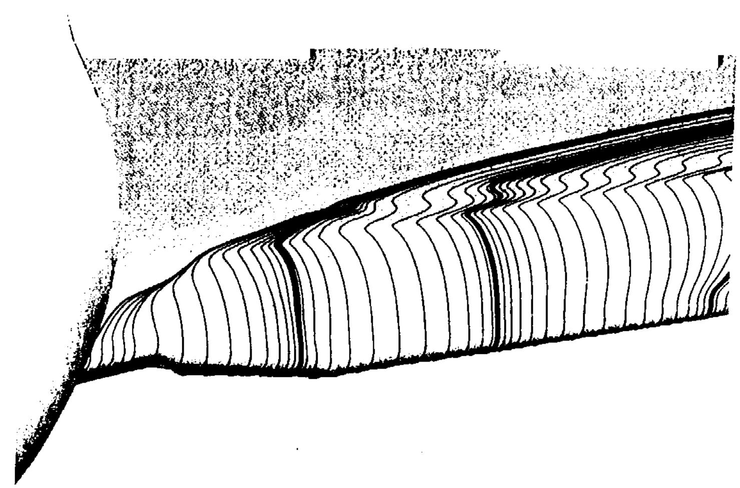

- Attached flow achieved on the deflected inboard LE flaps

Effect of Spanwise Extent of LE Flaps on Force and Moment

The force and moment comparison with Run 137 and 138 from the TCA-1 test (Test 449) are illustrated in the figure. Although the magnitudes are slightly different, the over all trend of the part span vs. full span leading flaps is clearly captured.

The results for the part span leading edge flap show higher lift than the full span flap configuration which indicates the presence of premature leading edge separation resulting a stronger leading edge vortex. As a result, a significantly more nose-up pitching moment is generated for the part span than the full span flap configuration.

Effect of Spanwise Extent of LE Flaps on Force and Moment

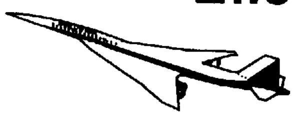

HSCT Aerodynamics, Long Beach

TCA 30/10 (LE/TE) Configurations at M=.3, Re=8 million

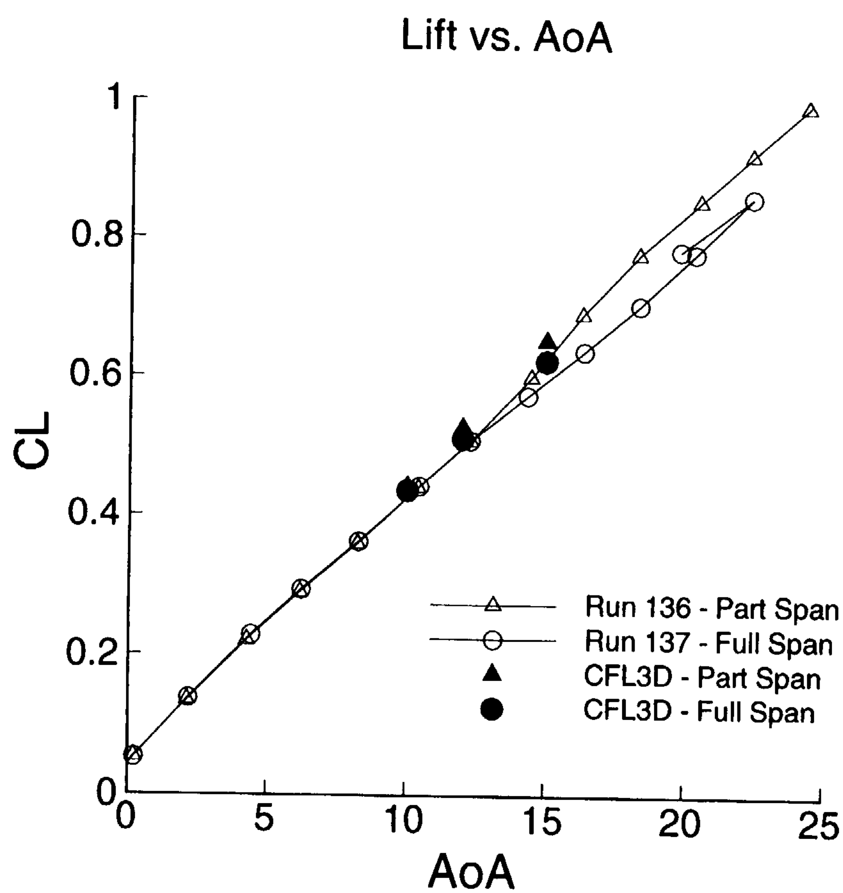

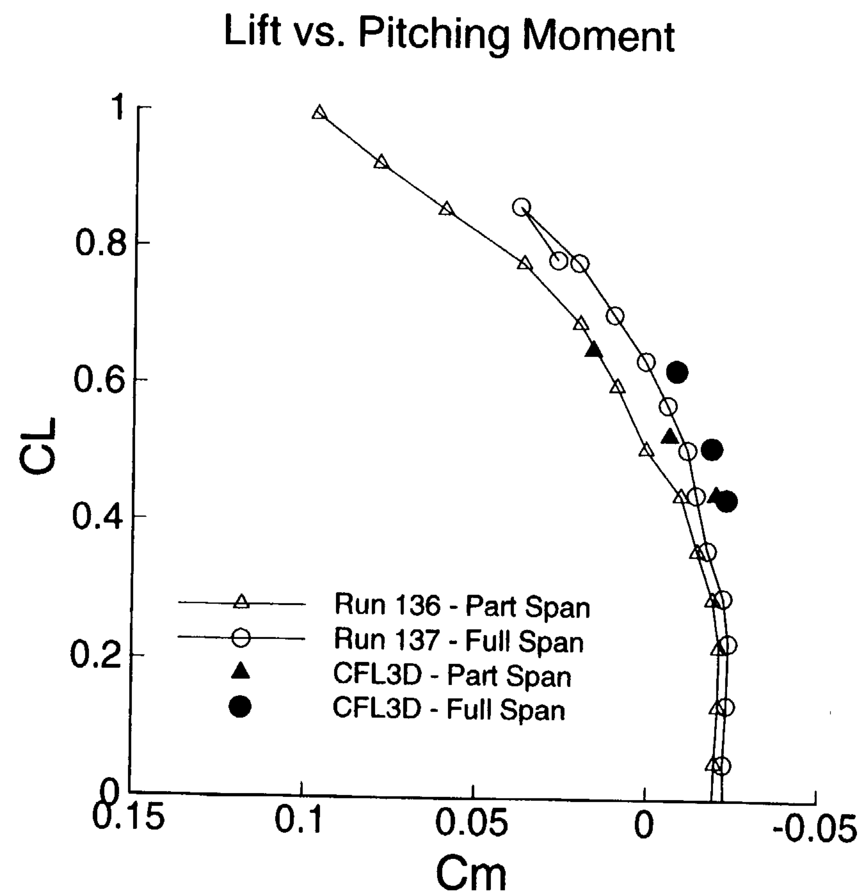

BOEING

Effect of Spanwise Extent of LE Flaps on Drag and Performance

This figure shows the comparison of drag and lift-to-drag ratio between CFL3D solutions and TCA-1 test results for part- and full-span leading-edge configurations. Since the part span flap configuration generates a stronger leading edge vortex as compared with the full span flap configuration, the part span flap results show a higher drag and lower lift-to-drag ratio.

Effect of Spanwise Extent of LE Flaps on Drag and Performance

TCA 30/10 (LE/TE) Configurations, M=0.3, Re=8 million

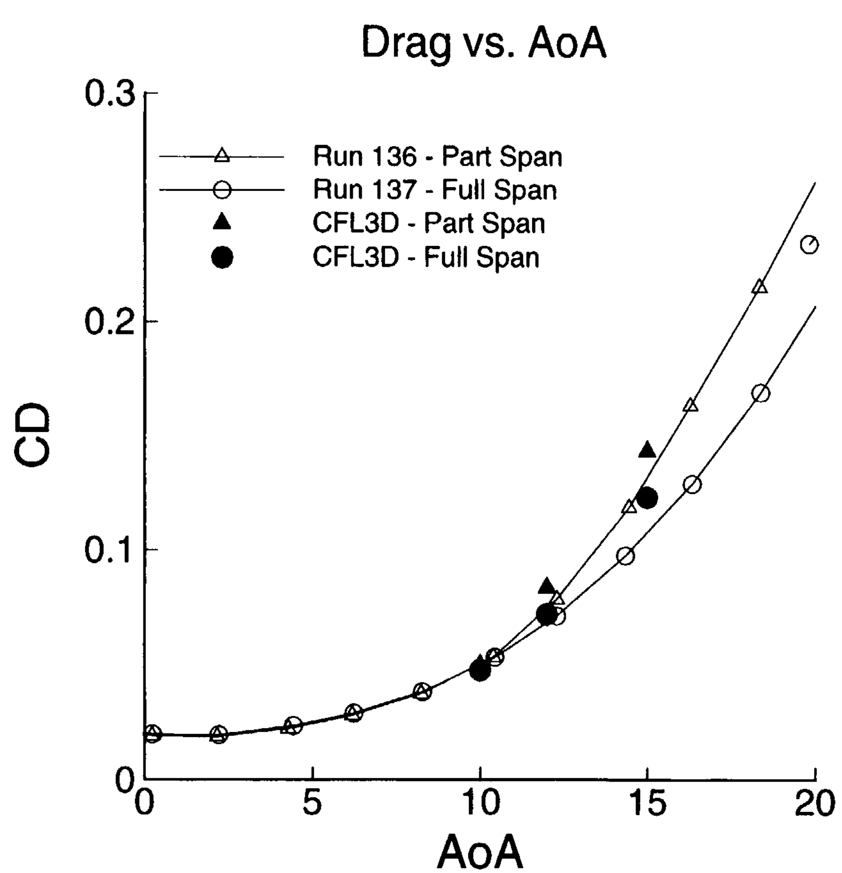

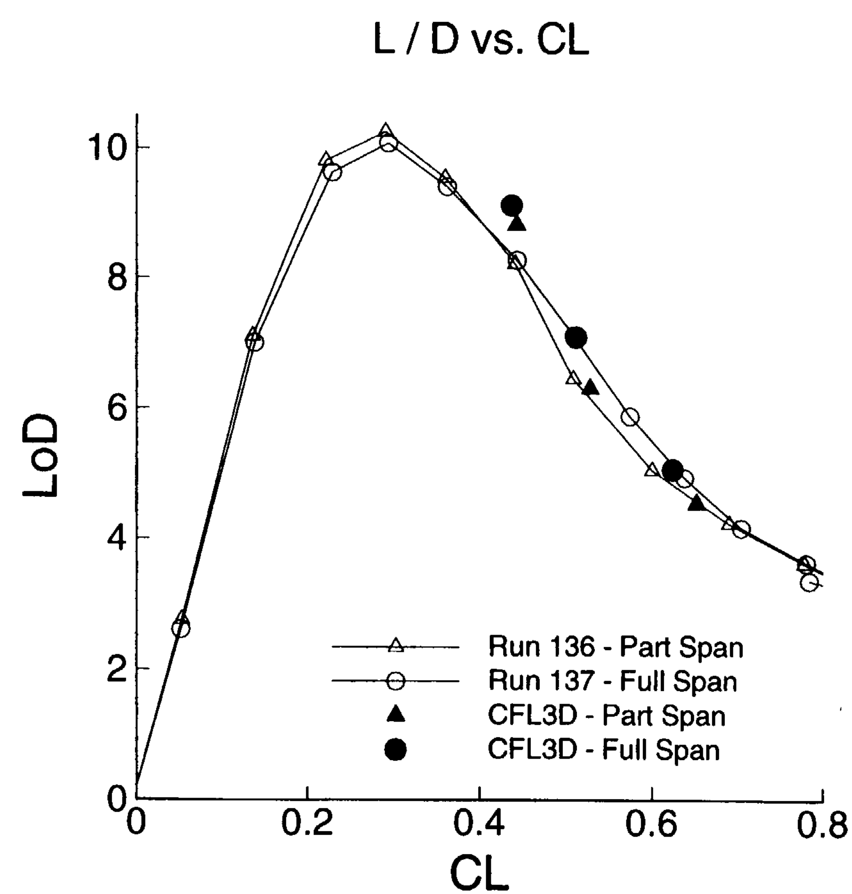

Inboard LE Droop/Camber Variation for Performance Study

The objective of inboard camber study is to understand the flow physics around the inboard leading edge and the effect of geometry variations on the flow. Two inboard camber variations have been analyzed, including the geometries for droop and camber. These configurations are currently being tested at Ames 12-ft tunnel under TCA-3 test. The numerical findings will be verified with test data once they become available.

Inboard LE Droop/Camber Variation for Performance Study

HSCT Aerodynamics, Long Beach

Fuselage Station Cuts in the Wing Inboard Region

TCA Configurations

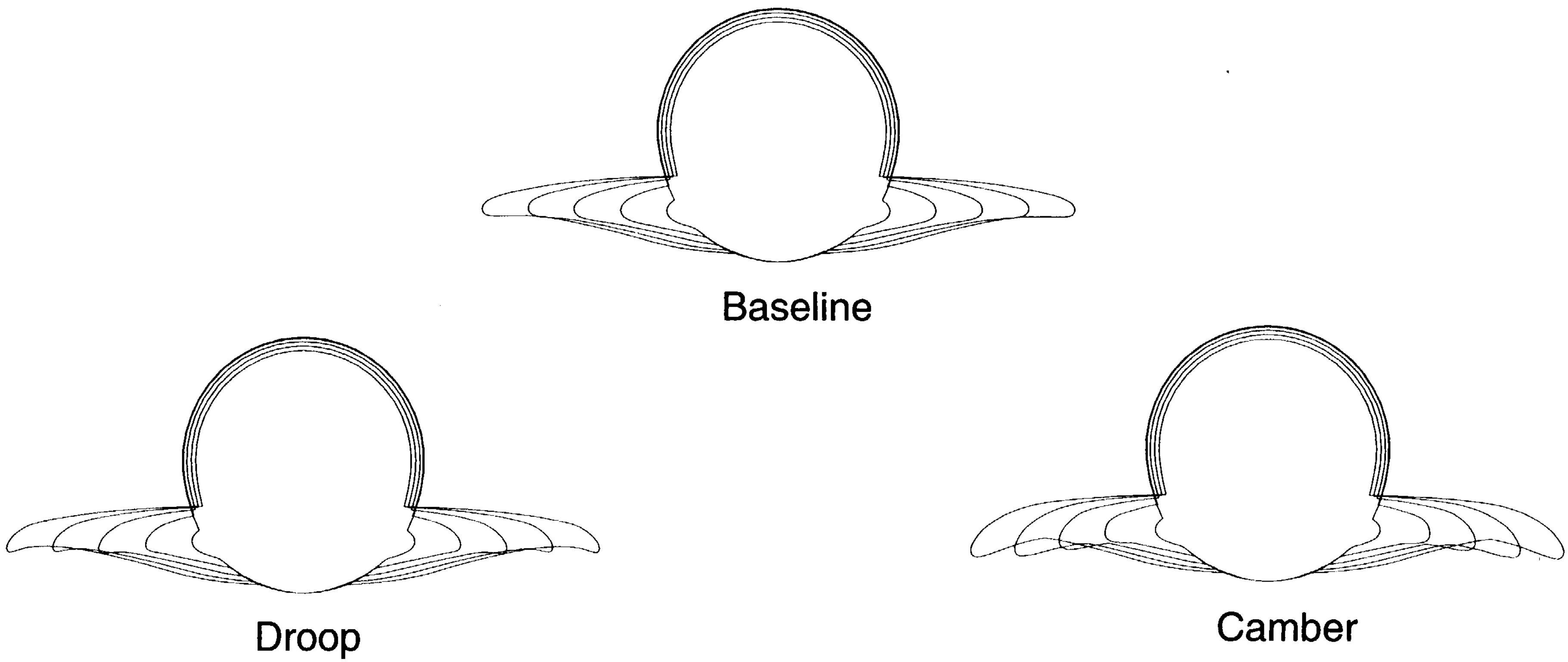

TCA Inboard LE Modifications

This chart shows the TCA inboard leading edge modification process.

For the cambered configuration, the inboard leading edge is modified based on the inboard flap deflection at a specified angle. A 20-degree deflection was specified for the cambered configuration. The upper surface was then fitted with a cubic splined surface to ensure a smooth transition of slopes on the upper surface. The modification was made approximately normal to the leading edge for the inboard 3 flap elements. In order to fit the modified model parts into the original TCA wing/flap definition, the inboard and outboard flap elements are modeled as transition pieces where the deflection angle and the fitted surfaces are gradually relaxed to match with the original geometry.

For the drooped configuration, the modification was performed in the streamwise direction. The leading edge point was sheared downward to provide the desirable camber, while the upper and lower surfaces were blended into the original wing through quadratic curves. Linear interpolation was performed for the transition pieces to match with the original definition.

It is noted that the chordwise extent of the modified region for the cambered configuration is significantly larger than that of the dropped configuration. Therefore, this study will also provide some insight for the future study on the effect of the chordwise extent of the leading edge flaps on the flow.

TCA Inboard LE Modifications

HSCT Aerodynamics, Long Beach

- Cambered

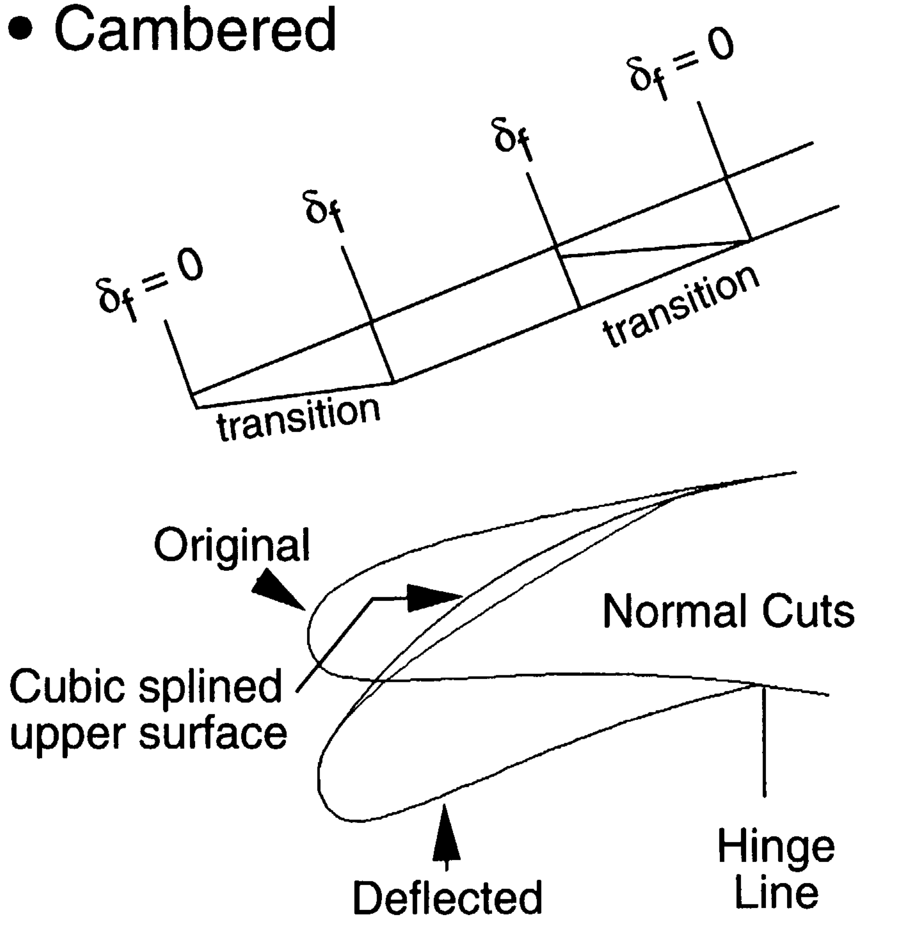

- Drooped

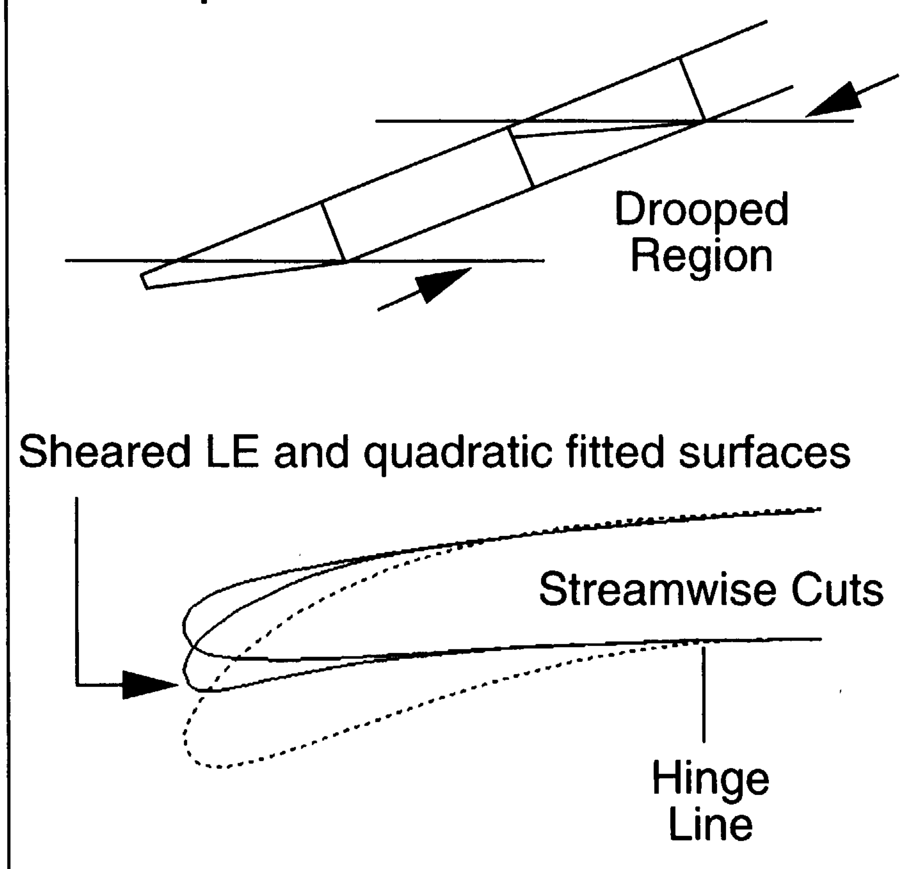

BOEING

Effects of Inboard Droop/Camber on Flow Separation

The effect of inboard droop/camber on the flow separation is illustrated through the releasing the limiting streamlines along the leading edge. The flow condition was chosen to be at α=12 degrees, so that the flow separation and associated vortex flow will be clearly visible just inboard of part span leading edge flap. The inboard drooped geometry shows some improvement on the leading edge flow separation but limited to the small region that has been modified. The cambered geometry shows a greater extent of the attached flow region as compared to the drooped configuration.

Effects of Inboard Droop/Camber on Flow Separation

HSCT Aerodynamics, Long Beach

TCA 30/10 Configurations

M=0.3, α=12 deg, Re=8 million (MAC)

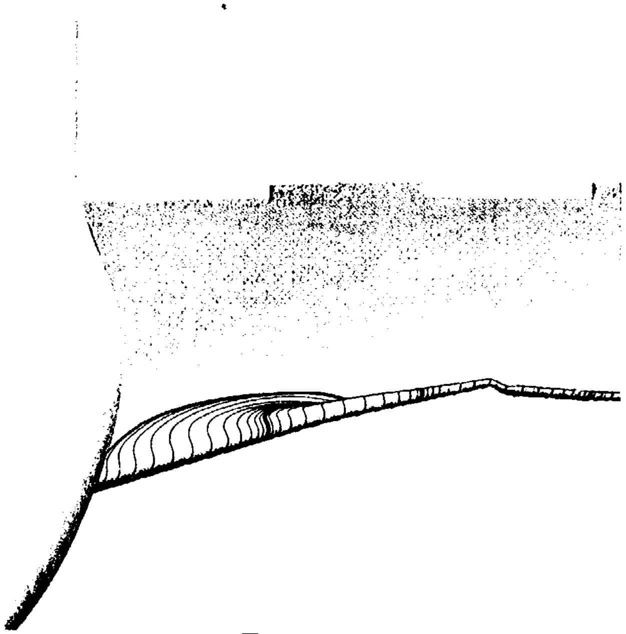

Baseline

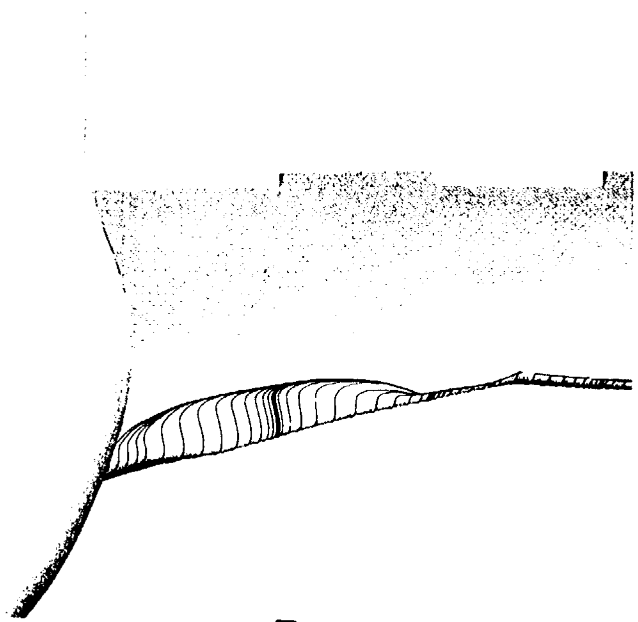

Droop

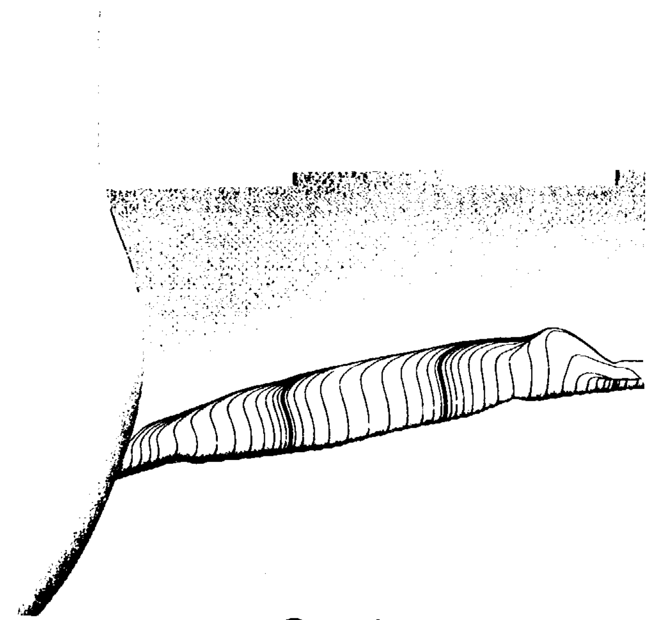

Camber

Effects of Inboard Droop Camber on TCA Flow Solutions

This chart shows the total pressure contours at a few fuselage stations accompanied by the particle traces released along the leading edge. The formation of the leading edge vortex just inboard of the part span leading edge flap is clearly visible for the baseline configuration.

A similar LE vortex formation is observed for the drooped case except the vortex is formed further inboard behind the drooped region and interact with the apex vortex. Since the drooped region is confined in the LE region, the attraction of the upstream vortex closer to the leading edge may create unfavorable upwash outboard.

The formation of the apex vortex is also visible for the cambered case. Because the modified region spans a greater chordwise extent, the inboard vortex remains inboard. Moving the leading edge vortex further inboard and delays the leading edge separation would reduce the unfavorable upwash at the outboard leading edge which would translate into higher aerodynamic performance.

Effects of Inboard Droop/Camber on TCA Flow Solutions

HSCT Aerodynamics, Long Beach

M=0.3, α=12°, Re=8 million

δ(LE/TE)=30°/10°

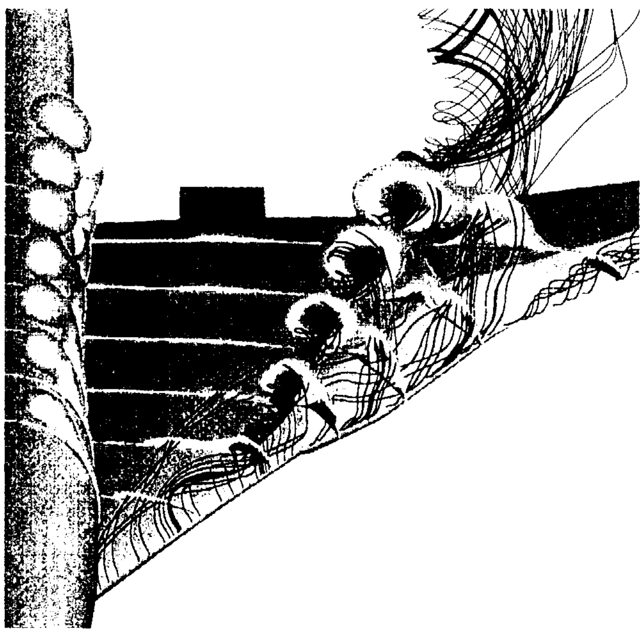

Baseline

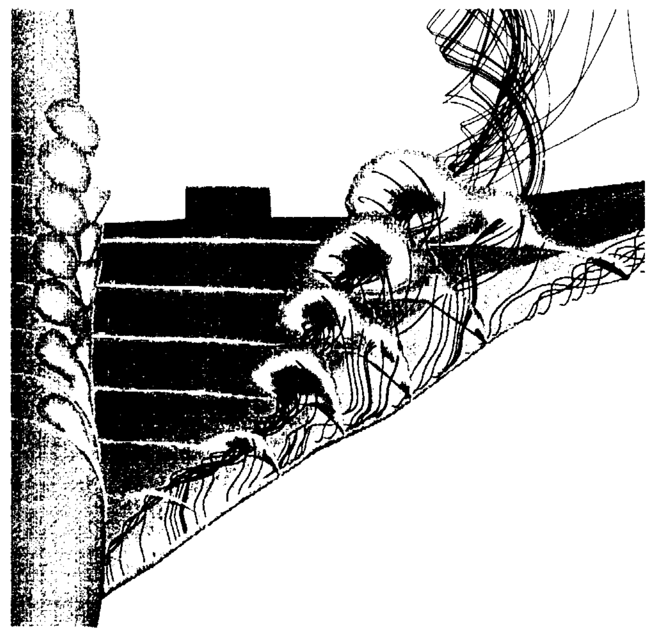

Droop

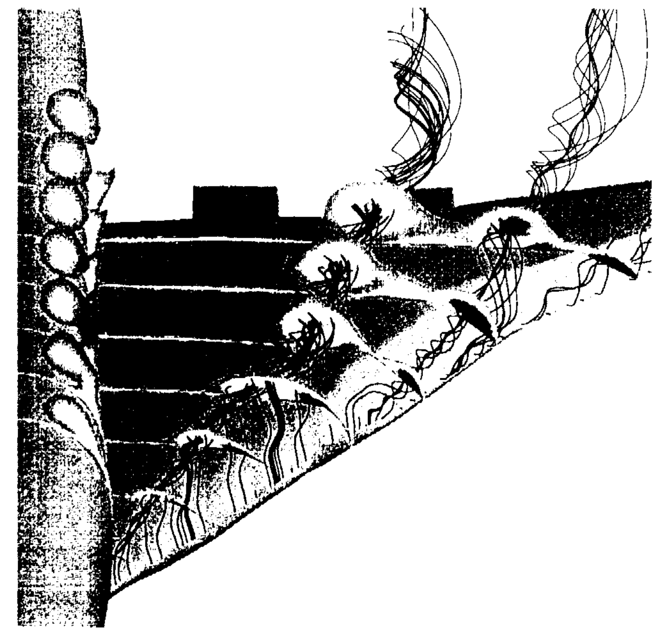

Camber

Chordwise Pressure Variation due to Inboard Droop/Camber

This chart shows the effect of inboard geometries on the chordwise pressures. The drooped geometry reduces the the leading suction peak due to the downward camber but has a similar vortex induced suction near the leading edge as compared to the baseline.

For the cambered case, the leading edge suction is further reduced due to a slightly higher downward deflection and a larger LE radius as compared to the drooped case. A smooth upper surface curvature is seen to reduce the pressure gradient and the suction on the hinge line. The LE vortex induced suction is further downstream and its magnitude is lower as compared to the baseline and the drooped cases.

Chordwise Pressure Variation due to Inboard Droop/Camber

HSCT Aerodynamics, Long Beach

M=0.3, α=10 deg, Re=8 million

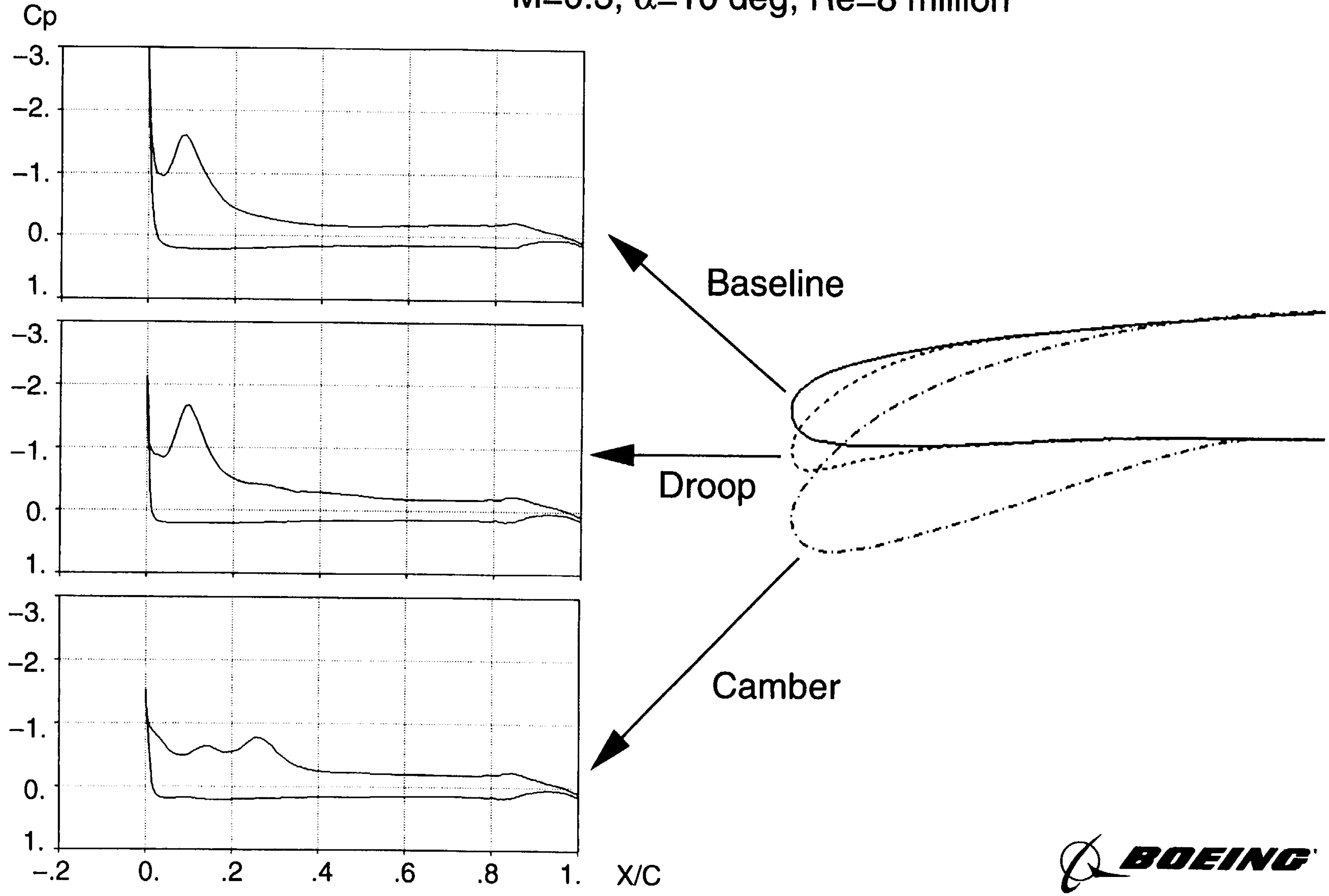

TCA2.8-28 Flow Analysis

Numerical study of the effect of planform change has been conducted. One of the benefits of increasing the wing AR is to achieve a higher lift at a lower angle of attack. However, lower stall angle and flow unsteadiness associated a lower LE sweep angle and higher AR may have an adverse impact on the aerodynamic performance and control quality.

The objective of this study is to utility CFD analysis to provide a better understanding of the flow characteristics for the TCA2.8-28 configuration. The effect of the lower leading edge sweep and a higher aspect ratio on the outboard trailing edge flap effectiveness is also evaluated.

TCA2.8–28 Flow Analysis

HSCT Aerodynamics, Long Beach

Numerically assess:

- Basic flow physics due to planform change (Λ, AR)
- TE O/B flap effectiveness

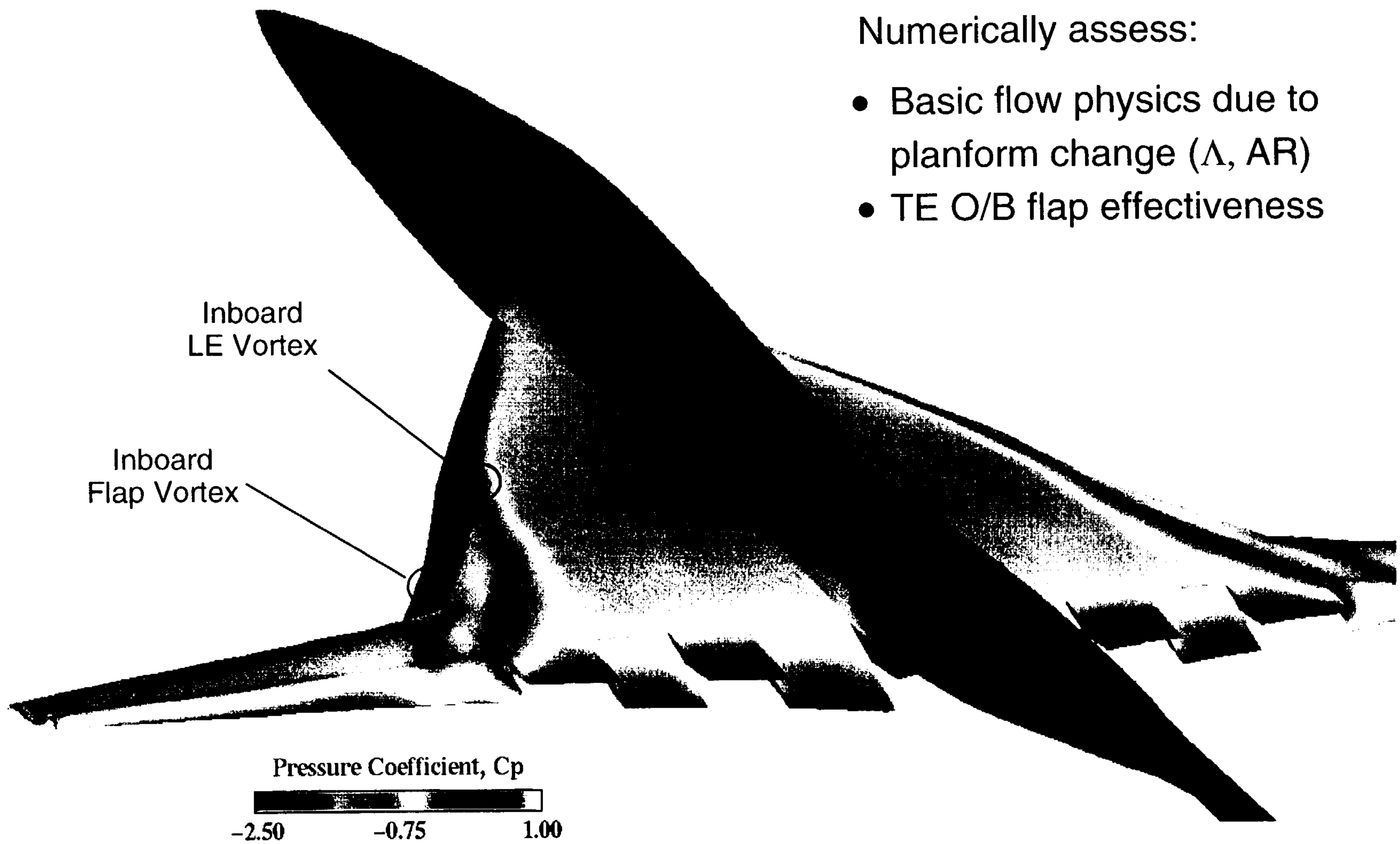

BOEING

Planform Comparison for the TCA Configurations

This figure shows the planform comparison for the baseline and TCA2.8-28 configurations.

The planform change occurs only in the outboard wing panel with a lower LE sweep (28 degrees) and a higher aspect ratio (AR=2.8). The inboard geometry (inboard of the wing leading edge break) was kept the same for both configurations.

Planform Comparison for the TCA Configurations

HSCT Aerodynamics, Long Beach

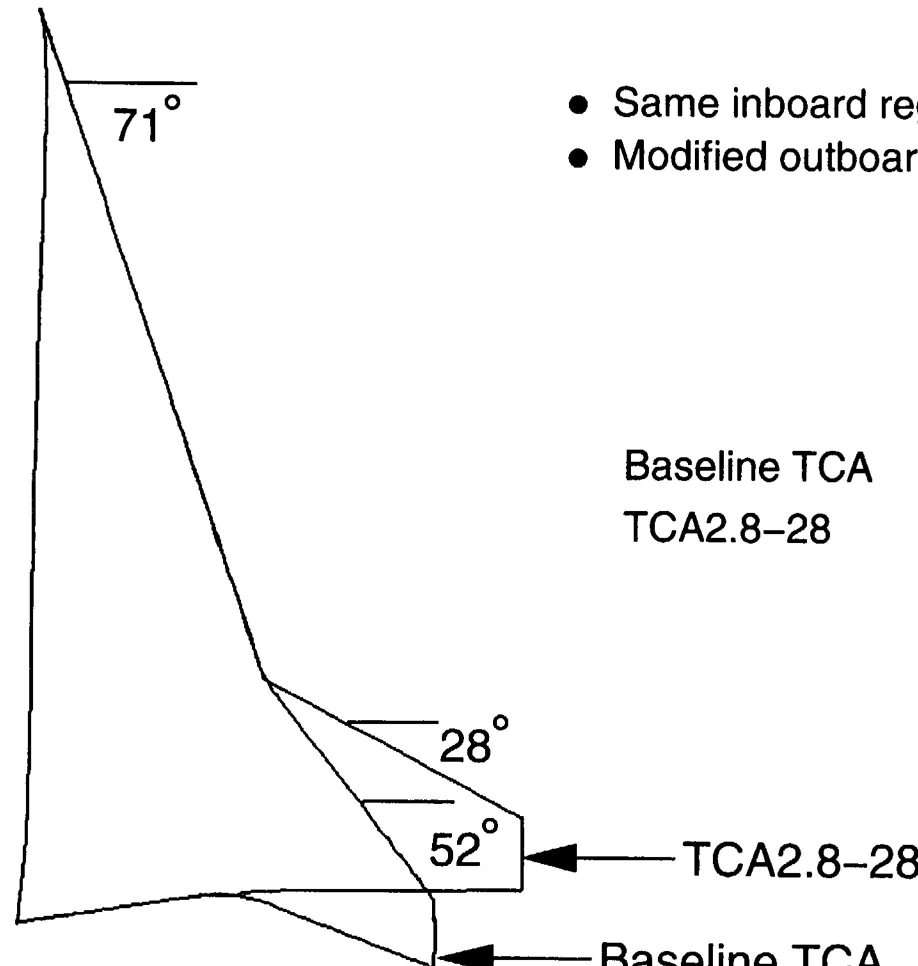

- Same inboard region
- Modified outboard region

	O/B Λ	AR
Baseline TCA	52°	2.0
TCA2.8–28	28°	2.8

AERO2S Flap Optimization Results for TCA2.8-28

To simulate the TCA2.8-28 at a typical high lift condition, the AERO2S linear code was used to determine the optimum flap setting. The optimum LE flap setting of 25 degrees was determined based on the maximum leading edge suction level in the region of CL=.5 corresponding to the design condition. Therefore, the flap setting of (LE/TE) 25/10 degrees has been used in the current study to represent a typical TCA2.8-28 high lift configuration.

It is noted that the hingewise deflection required to achieve the optimum performance is less for the wing with a lower leading edge sweep. As a result, the optimum leading edge flap deflection for the TCA2.8-28 (25 deg) is less than that of the baseline (30 deg) due to the lower outboard leading edge sweep.

AERO2S Flap Optimization Results for TCA2.8–28

- Optimum Flap Setting (LE/TE) = 25/10 degrees (at CL=0.5)

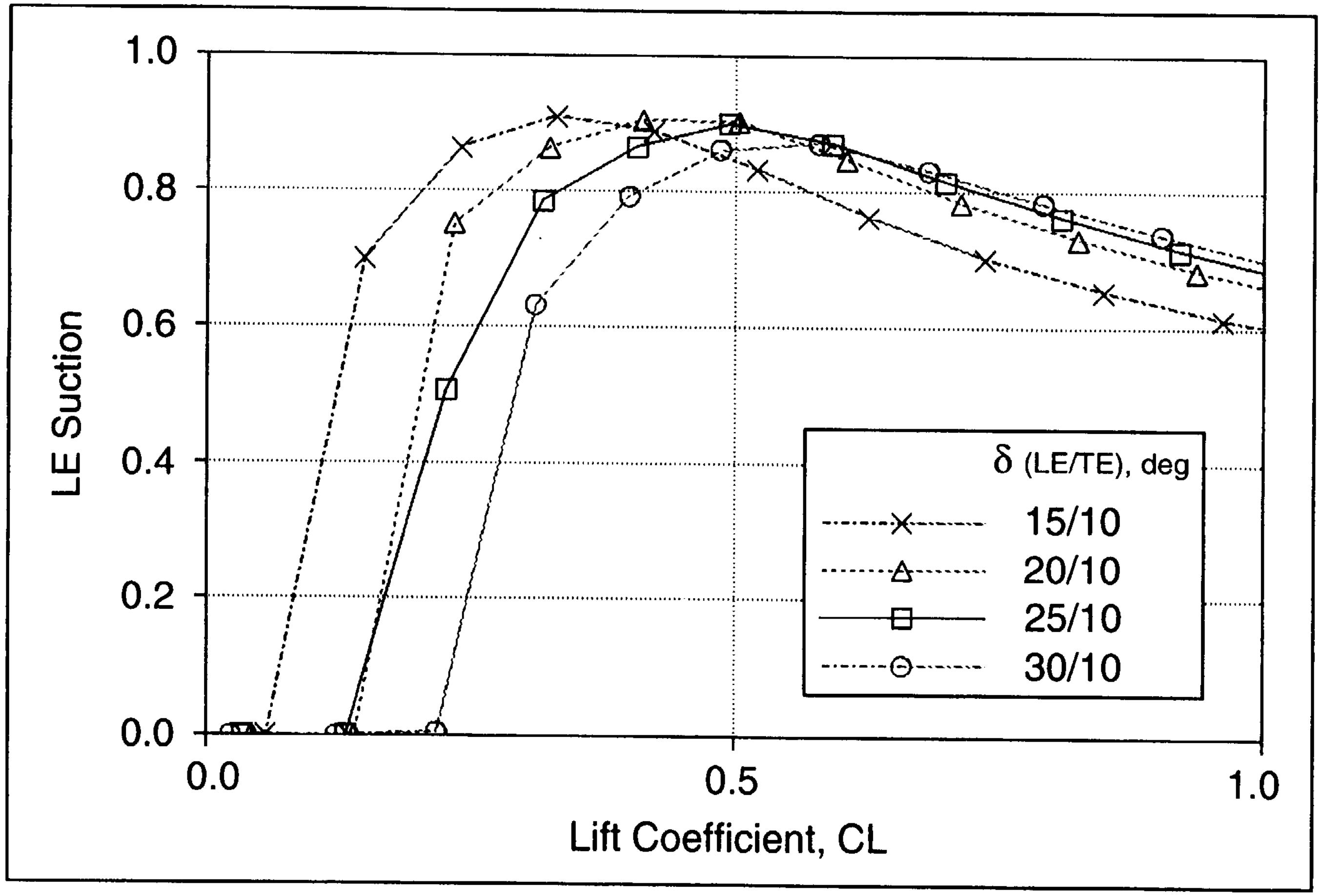

Computational Surface Grid for the TCA2.8-28 25/10 Configuration

This figure shows the surface grid of the TCA2.8-28 25/10 wing/body configuration with a part span leading edge flap. The computational model started with a clean (no flaps) configuration. The flaps are then modeled using the available automated flap deflection procedures. Due to the lack of the hingeline definition in the outboard region, the hingelines are modeled on the lower surface for both leading- and trailing-edge flaps.

The flap effectiveness of the outboard trailing edge flap is also evaluated by perturbing the deflection angle from 8 degrees to 15 degrees while keeping the leading edge flap deflection at 25 degrees and the inboard and middle trailing edge flaps at 10 degrees.

Computational Surface Grid for the TCA2.8–28 25/10 configuration

HSCT Aerodynamics, Long Beach

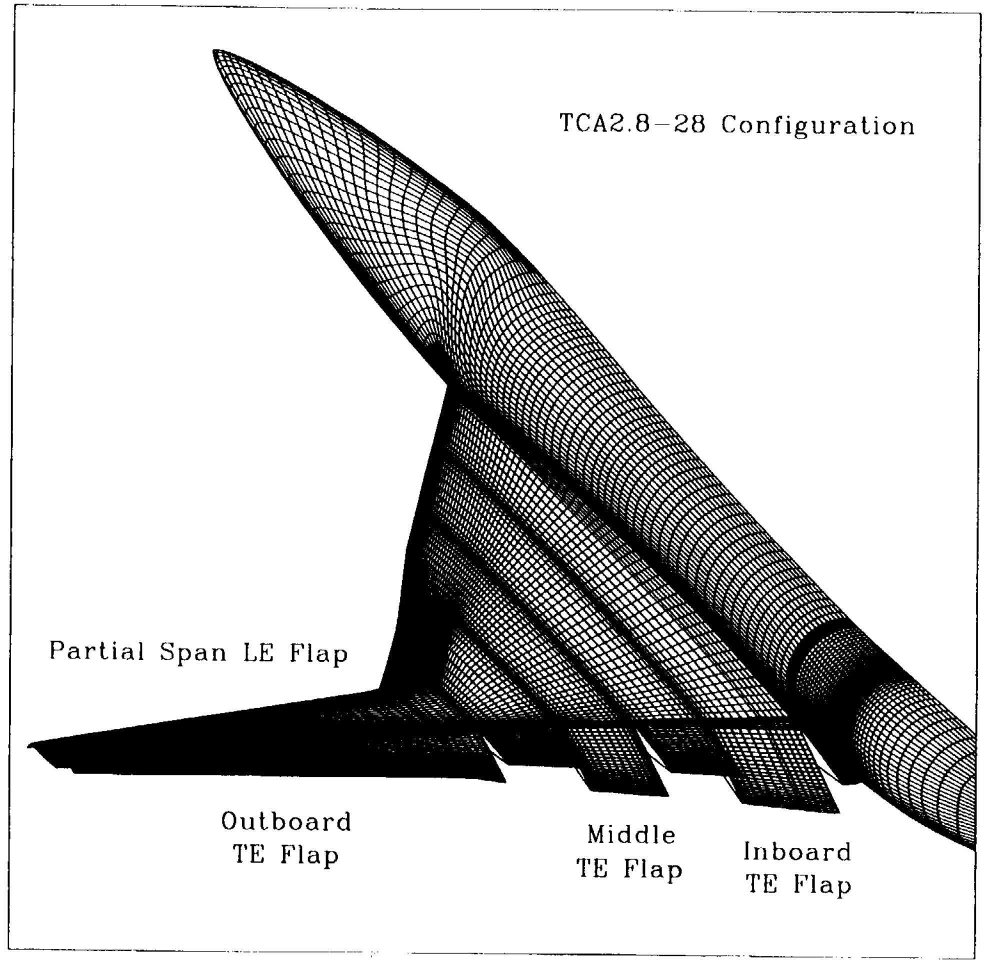

- For Flap Effective Study : $\delta_{o/b\ TE}$ = 8, 10, 15 degrees

Flow Solution for the TCA2.8-28 25/00 Configuration

The flow solution for the TCA2.8-28 25/00 configuration at α=10 degrees is illustrated in this figure which shows the surface pressure and some particle traces released along the LE and the wing tip. Flow acceleration around the inboard rounded LE and the outboard hinge line is clearly visible as indicated by the low pressure regions (colored by blue and green). The formation of the leading edge vortex just inboard of the part span flap as well as the wing tip vortex are visible through the releasing of particle traces.

Flow Solution for the TCA2.8–28 25/00 Configuration

HSCT Aerodynamics, Long Beach

M=0.3, α=8 deg, Re=8 million (MAC)

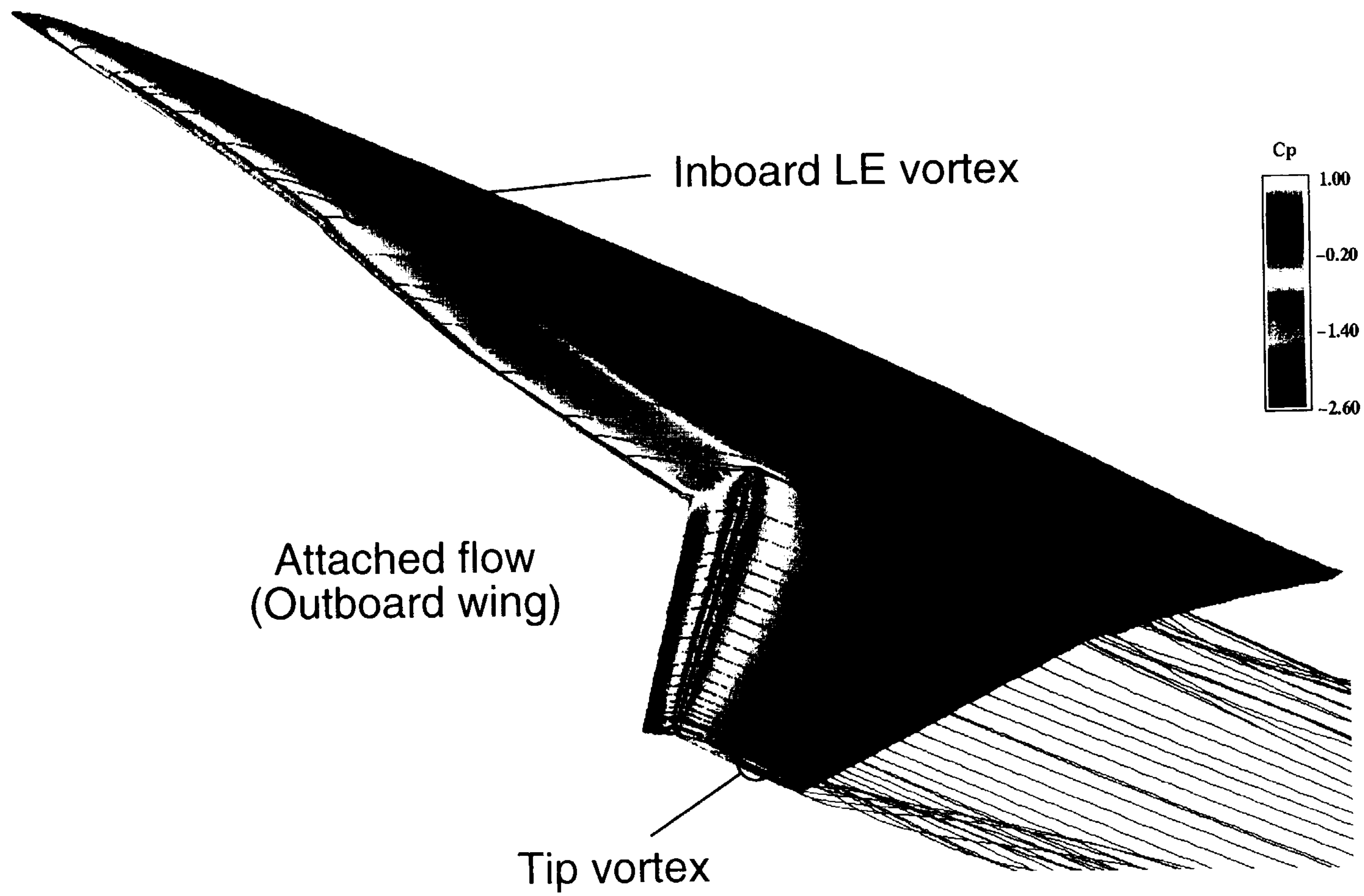

BOEING

TCA2.8-28 25/10 Flow Solutions at α-sweep

This figure shows the plan view of the surface pressure and the limiting streamlines for the TCA2.8-28 25/10 configuration at alpha-sweep. The footprint of the inboard leading edge vortex is clearly visible as indicated by the vortex induced low pressure region and the associated spanwise flow. The inboard leading edge vortex is seen to move upstream toward the apex as the angle of attack increases. In the outboard region, the flow remains somewhat attached up to α=10 degrees. At higher angles of attack, a typical stall flow pattern appears where the flow starts to separate along the outboard leading edge.

TCA2.8–28 25/10 Flow Solutions at α–sweep

HSCT Aerodynamics, Long Beach

M=0.3, Re=8 million (MAC)

- Upper Surface Pressure

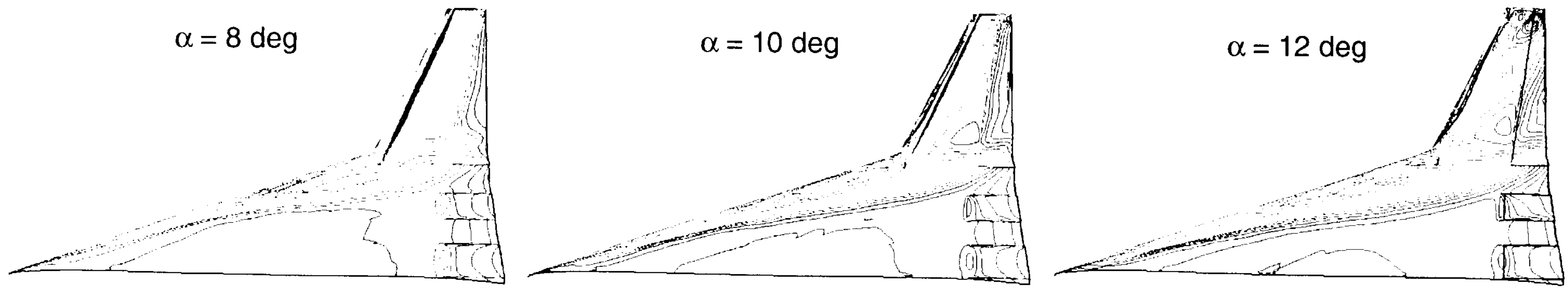

- Upper Surface Limiting Streamlines

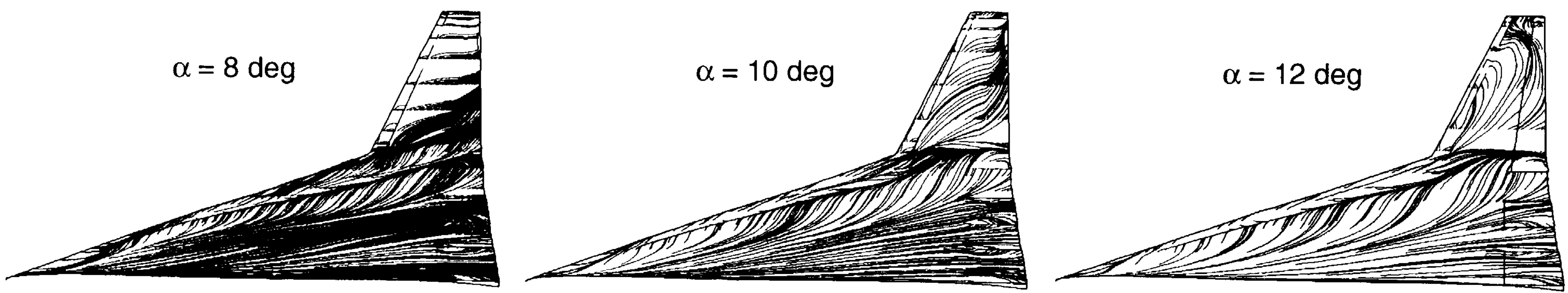

BOEING

Lift & Drag Comparison for TCA2.8-28

Since there is no test data available for the TCA2.8-28 configuration, the CFL3D solutions are compared with the linear AERO2S results.

This figure shows the lift variation as a function of angle of attack. The comparison for the 25/00 case at alpha=8 deg. shows a good agreement. This is to be expected since the flow is primarily attached under this condition. On the other hand, the linear code probably over predicts the lift when the trailing edge flaps are modeled since the viscous effect of boundary layer becomes important when the trailing edge flaps are modeled. In addition, the outboard stall phenomena predicted by the CFL3D code at high angle of attack further drives the linear and nonlinear solutions apart.

The drag variation as a function of angle of attack is also illustrated in the figure. A skin friction drag of 93 counts has been added to the linear AERO2S results to approximately account for the viscous effects at low to moderate angles of attack. As a result, the numerical results agree quite well for the alpha=8 degrees cases with and without the TE flaps. However, the deviation of the solutions arises as the outboard wing panel becomes separated, and the discrepancy magnifies at higher angles of attack.

Lift & Drag Comparison for TCA2.8-28

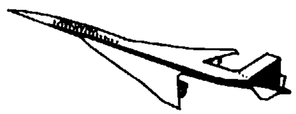

HSCT Aerodynamics, Long Beach

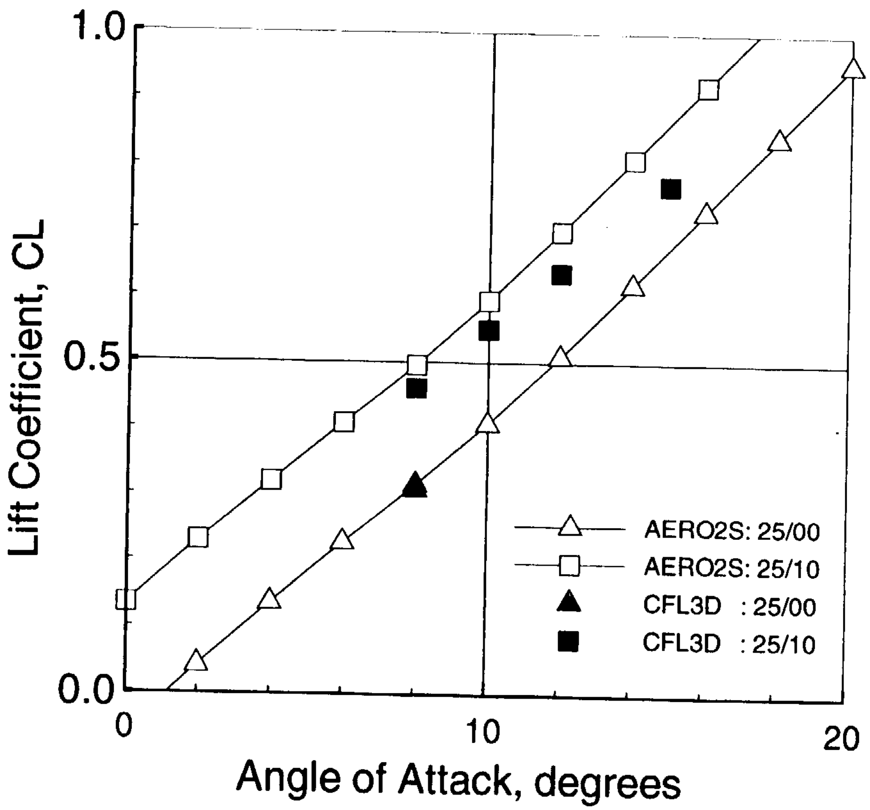

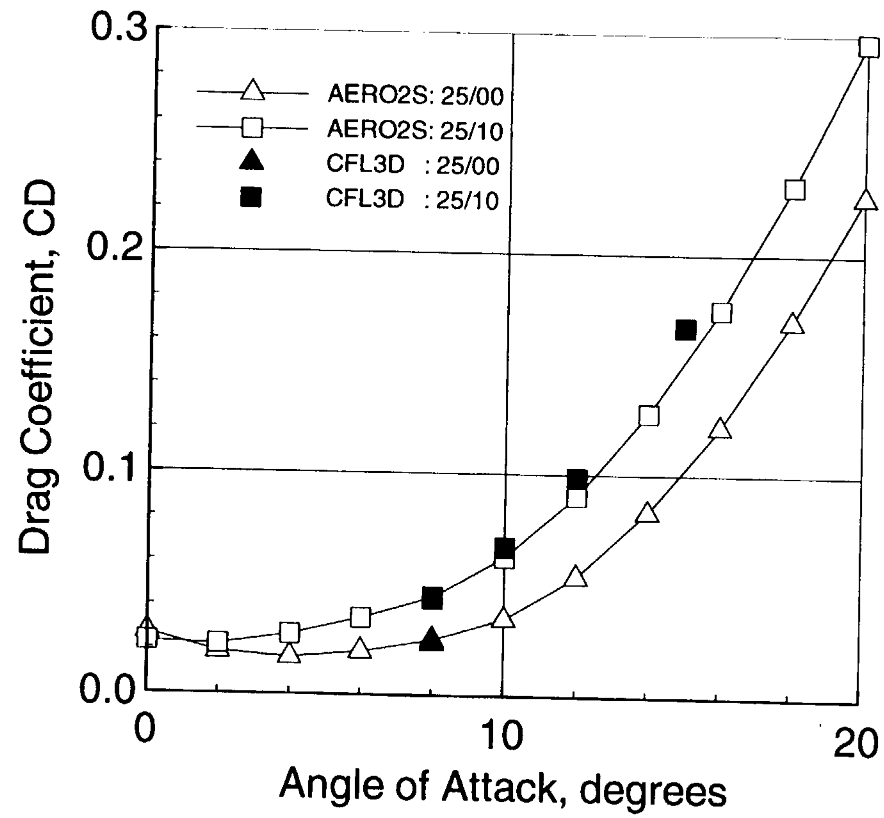

** Add CD0=93 counts to AERO2S

BOEING

Pitching Moment comparison for TCA2.8-28

This chart shows the pitching moment comparison. A good agreement is shown for the 25/00 case in the linear region. For the 25/10 cases, however, some discrepancies are observed between the linear and nonlinear solutions in both magnitude and slope. The difference in the solutions increases at higher angles of attack when the flow condition is in fact dominated by the viscous (nonlinear) phenomena. The rapid decrease in nose-down pitching moment at higher angles of attack is a result of the leading edge vortex that moves further upstream and the outboard flow separation. Clearly, the linear method does not capture the break in the pitching moment curve due to vortex separation.

Pitching Moment Comparison for TCA2.8-28

HSCT Aerodynamics, Long Beach

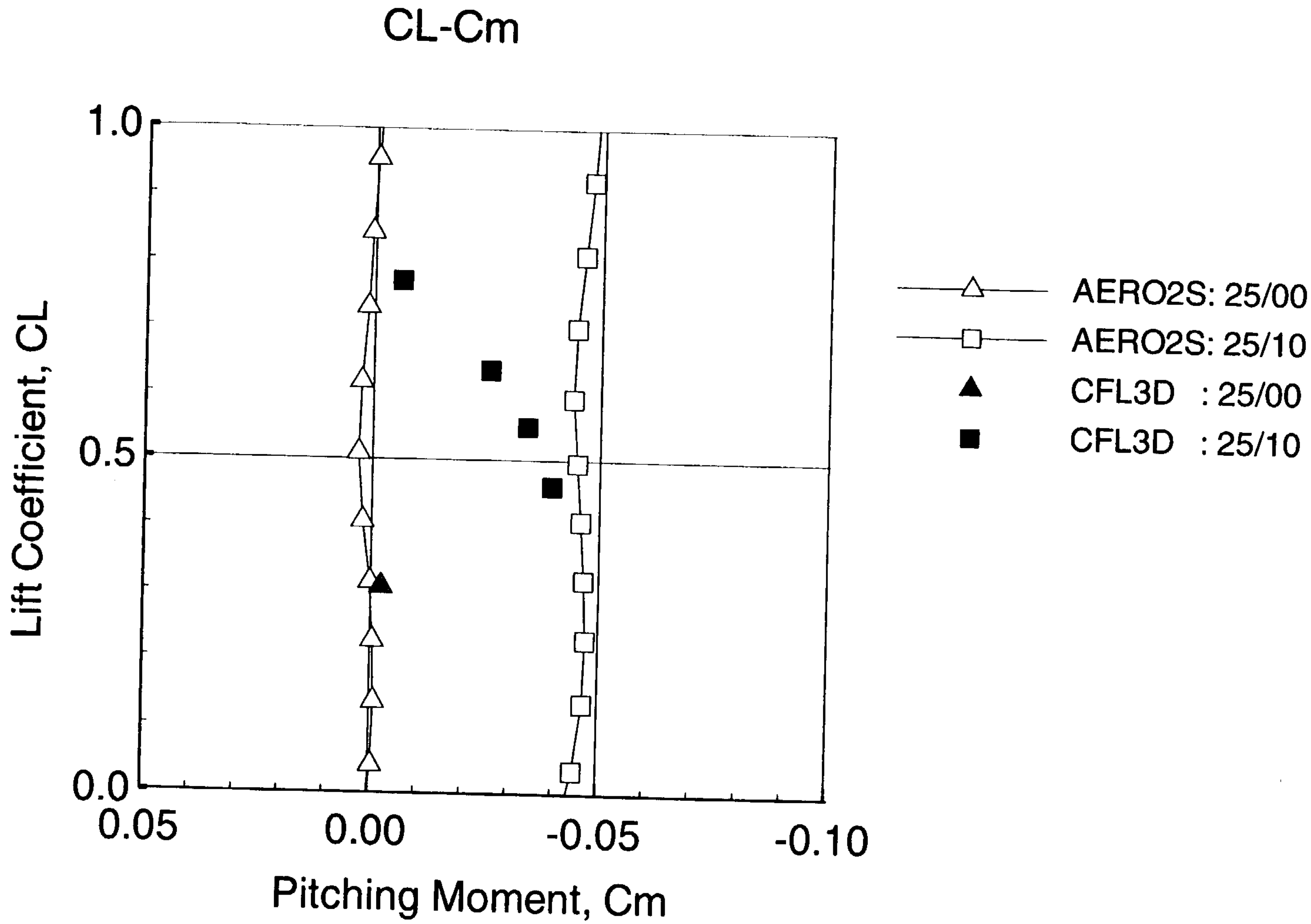

TCA2.8-28 Outboard TE Flap Characteristics

In an effort to better understand the control authority of the outboard trailing edge flap, numerical simulation of variable outboard trailing edge flap deflection has been conducted for the TCA2.8-28 configuration. The flow solutions have been obtained for flap (LE/TE) deflection of 25/10 degrees while varying the outboard trailing edge flap at 8, 10 and 15 degrees. The total lift variation as a function of the outboard trailing edge flap deflection for alpha=10 and 15 degrees are shown in the figure. The upper surface flow patterns corresponding to the upper and lower bound of the outboard trailing edge flap settings are inserted in the figure for illustration.

At α=10 degrees, the flow pattern on the outboard trailing edge flap is seen to be attached at δ=8 degrees and the flow becomes separated at δ=15 degrees. The control effectiveness of the flap upper surface decreases as the flow becomes separated on the flap surface. As a result, there is an drop in the lift slope at higher flap deflection angles.

At α=15 degrees, the flow is virtually separated along the leading edge. A similar flow pattern on the outboard trailing edge flap for the upper and lower bound of the flap deflections implies that the flap effectiveness due to the upper surface vanishes when the outboard wing is completely separated. The additional flap control power at a higher deflection angle is primarily attributed to the higher pressure acting on the flap lower surface and varies linearly with the deflection angle.

TCA2.8–28 Outboard TE Flap Characteristics

HSCT Aerodynamics, Long Beach

M=0.3, Re=8 million, δ(LE/TE)=25/10 deg

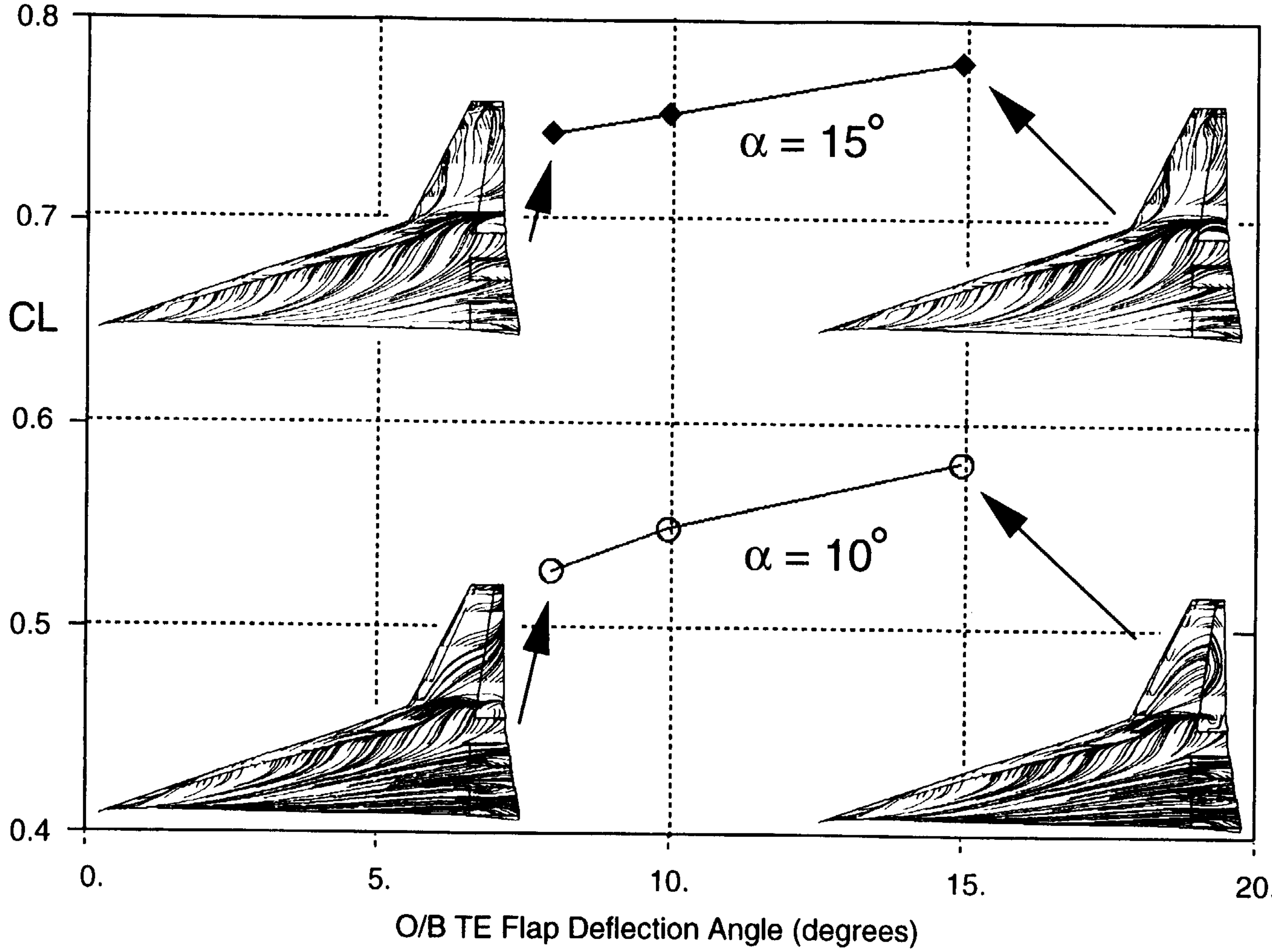

Baseline TCA Outboard TE Flap Characteristics

For comparison, this chart shows the lift variation as a function of the outboard trailing edge flap deflection for the baseline TCA 30/10 configuration. For both of the angle-of-attack cases, the lift is shown to increase linearly with the increase of the outboard trailing edge flap deflection. At α=10, the outboard trailing edge flap is dominated by a spanwise flow and the linear lift increase at a higher flap deflection is primarily attributed to the higher pressure acting on the lower surface. Similarly, the formation of the outboard leading edge vortex at α=15 degrees induces separated flow on the upper surface and the linear increase in lift is also due to the contribution from the lower surface.

Baseline TCA Outboard TE Flap Characteristics

HSCT Aerodynamics, Long Beach

M=0.3, Re=8 million, δ(LE/TE)=30/10 deg

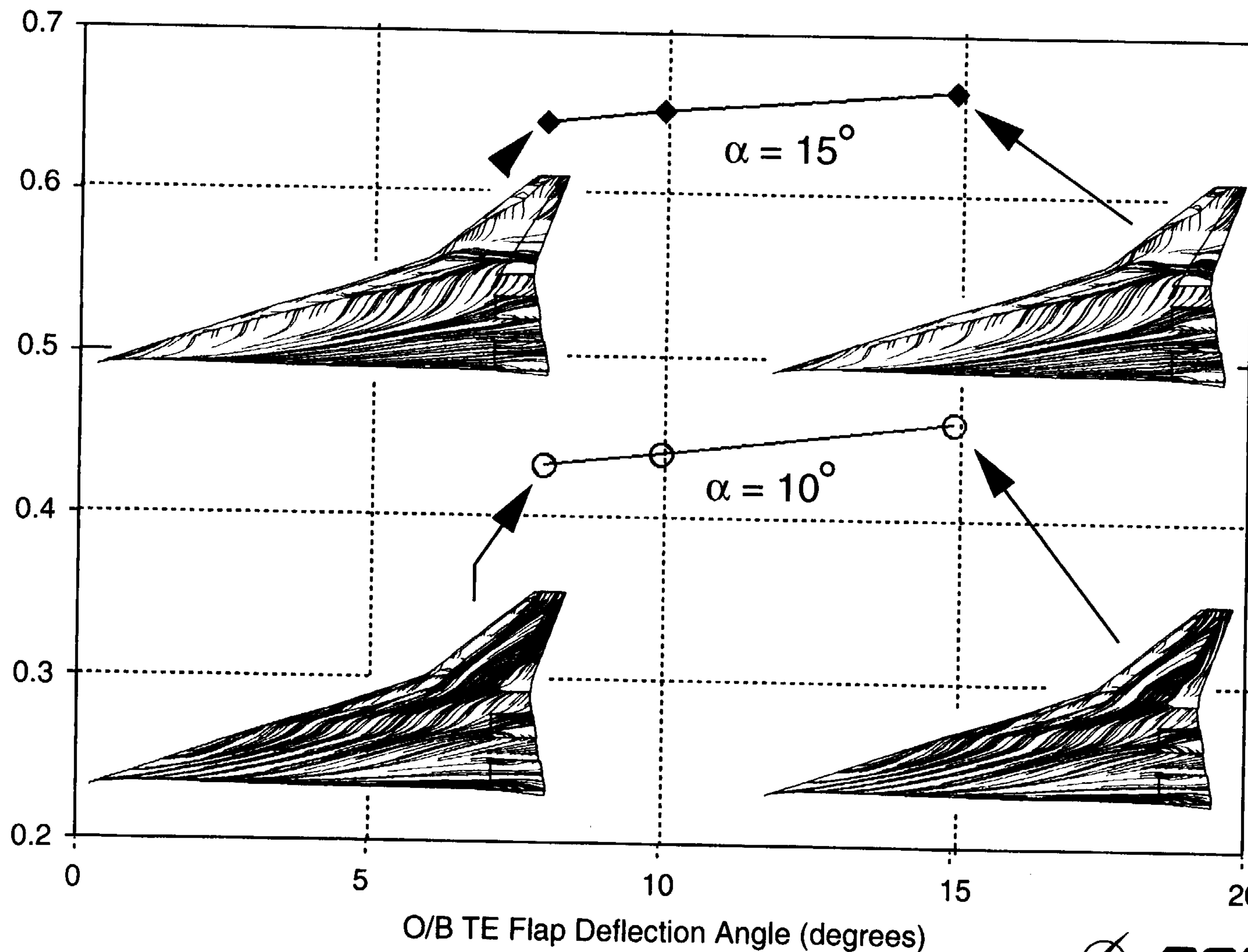

BOEING

Surface Flow Patterns at an Off-Design Condition

The effect of leading edge sweep on the surface flow pattern at a high angle of attack condition is presented in the figure. The solutions are obtained for TCA2.8-28 25/10 and TCA2.0-52 30/10 configuration, at the same free stream condition of M=0.3, α=15 degrees, with Reynolds number of 8 million. A similar vortex dominated flow pattern is observed for both configurations since the inboard geometries for the both configurations are the same. For the higher outboard leading edge sweep case (baseline TCA), the outboard is dominated with vortical flow that originates near the wing break. As the outboard leading edge sweep decreases, the flow pattern gradually becomes chordwise separation. The chordwise separation often creates potentially unsteady flows.

Surface Flow Patterns at an Off–Design Condition

HSCT Aerodynamics, Long Beach

M=0.3, AoA=15 deg, Re=8 million

I/B : Vortex dominated flow
O/B : Separated flow

Baseline TCA (2.0–52)

δ=30/10 deg

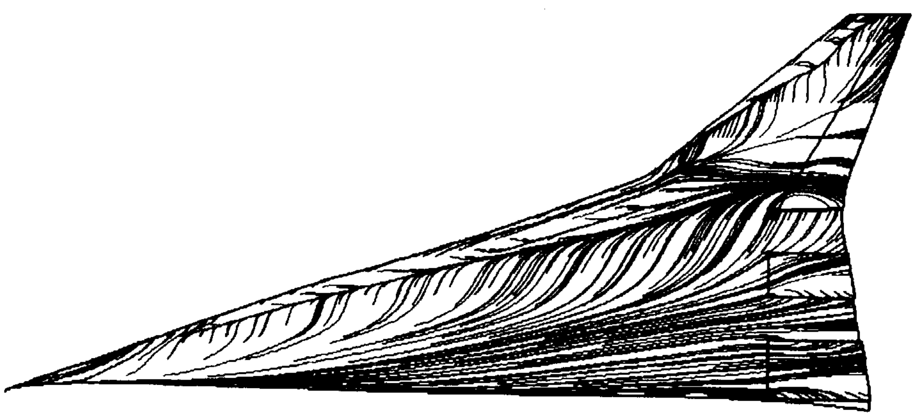

TCA2.8–28

δ=25/10 deg

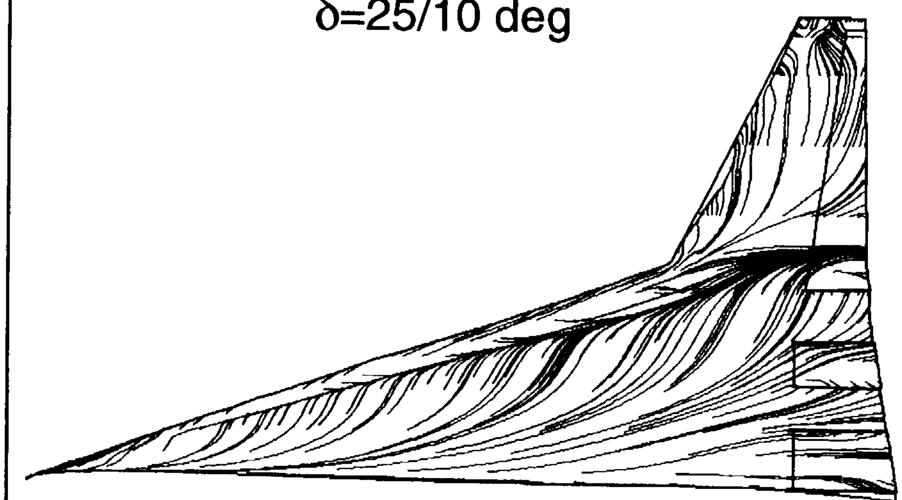

BOEING

Summary - 1

In summary, numerical study of the planform variation and leading edge geometries has been performed to better understand their impact on the high lift performance. The numerical solutions have shown to compare favorably with the available test data.

The numerical results have shown that the use of leading edge flaps under high lift conditions reduces the pressure peak near the leading edge which would promote a favorable attached flow environment. However, large leading edge flap deflection creates a higher suction around the hingeline which increases the probability of hingeline separation. Both computational and experimental results have shown that the full span leading edge flap surpass the part span in performance and in pitching characteristics. The inboard camber increase promotes attached flow, but its effectiveness would be a function of degree of camber, chordwise extent, upper surface curvature and the leading edge radius.

SUMMARY – 1

- Sensitivity studies of TCA planform and LE variation have been conducted to provide a better physical understanding of the flow

- CFL3D solutions, in general, have been shown to compare favorably with test data and associated flow physics

- Numerical studies of LE variation have shown:
  (1) LE flap deflection reduces the pressure peak near LE
  – promotes attached flow
  (2) Higher flap deflection creates higher hingeline suction
  – promotes hingeline separation
  (3) Full span LE flap surpasses part span performance
  – suppresses inboard LE separation
  (4) Inboard camber promote attached flow, effectiveness= f(degree of camber, chordwise extent, curvature, LE radius)

BOEING

Summary - 2

The numerical results obtained for the TCA2.8-28 configuration have shown that the increase in aspect ratio results in a higher lift at low angle of attack. The benefit is obtained primarily from the outboard wing panel where the flow is attached at the design condition. The CFD and AERO2S results have shown to compare favorably in the linear region where the flow is dominated with attached flow. However, discrepancy appears in the non-linear region when the viscous effects become important such as boundary layer growth for trailing edge flap modeling, and when the flow is massively separated.

The outboard trailing edge flap for the TCA2.8-28 should perform as well as or better than that of the baseline TCA, partially due to the outboard attached flow at a similar CL.

The outboard flow separation characteristics change from a normally stable vortex to somewhat chordwise separation at high angle-of-attack conditions as the leading edge sweep decreases. A chordwise separation typically produces potentially unsteady flows.

SUMMARY – 2

Numerical study of TCA2.8–28 (planform variation) has shown:

(1) AR increase results in a higher lift at lower AoA
  – benifit from O/B attached flow at lower α

(2) CFD solutions compare qualitatively well with AERO2S results except at higher TE flap deflection and higher AoA

(3) TCA2.8–28 O/B TE flap is more effective than TCA2.0–52 at the design condition (CL=.5)
  – Attached flow vs. spanwise flow

(4) O/B separation charateristics change as the O/B LE sweep decreases

BOEING

High Lift CFD Activities

The current CFD activities at Long Beach primarily involve in the pre-test analyses for the ongoing TCA-3 test and the upcoming TCA-4 test. The numerical studies are focused in the inboard leading edge camber increase, variable leading edge flap deflection, TCA planform variation as well as canard integration for high lift performance assessment. Post-test validation will be conducted once the test data becomes available. Additional parametric studies will be initiated to optimize the aerodynamic performance for various high lift systems.

High Lift CFD Activities

HSCT Aerodynamics, Long Beach

Current Activies:

* Conduct pre–test analysis for the ongoing TCA–3 test
  - Inboard LE camber increase
* Perform pre–test analysis for the upcoming TCA–4 test
  - Planform variation
  - Canard integration (present results on Wednesday)

Planned Activies:

* Continue wind–tunnel support for high lift configurations
* Perform code validation as test data becomes available
* Conduct parametric studies for performance optimization
  - Flap chord, LE radius, canard variation

This page is intentionally left blank.

Prediction of High Lift Characteristics of the PTC

Keith Ebner
Boeing Commercial Airplane Group

February 9, 1998

Topics

The topics included in this presentation are:

- A brief look at the differences between the TCA and the PTC that are important to high lift aerodynamics.
- An overview of the process that is used to evaluate the high lift characteristics. This process has evolved through discussions and agreements reached in the TI ADP work including representatives from NASA and industry.
- A brief discussion of the baseline data that is used in configuration assessments.
- A detailed look at the major steps included in the buildup from the baseline data to the PTC untrimmed data.
- A discussion of the method used to trim the PTC data using both the canard and the tail.
- A summary of the method used to generate programmed flap data
- A brief look at the technology projection application to the programmed flap data
- A discussion of the touchdown requirements and performance

Topics

- PTC vs. TCA configuration aspects
- Common process overview
- Baseline wind tunnel data
- Buildup to PTC
- 3-surface optimization
- Programmed flap
- Technology projection
- Touchdown performance

TCA vs. PTC

There were two changes that were made to the TCA in the layout of the PTC that significantly affect the high lift performance.

The outboard wing span was increased giving both a larger wing area and a higher aspect ratio. The higher aspect ratio will provide a high lift-to-drag ratio, thereby significantly contributing to improved noise performance at cut-back.

A canard has been added to the PTC. Canards offer the benefit of trimming with positive lift, thereby allowing the wing and tail to fly at lower lift-coefficients for the same total trimmed lift-coefficient as a 2-surface airplane. In addition to the small lift-to-drag ratio improvement, the canard offers an airplane attitude reduction at constant trimmed lift-coefficient.

TCA vs. PTC

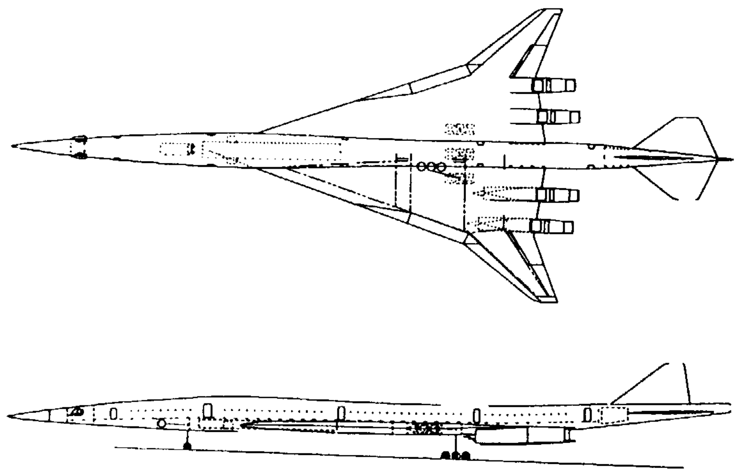

Model 2.0-52

Wing Area	8500 sq. ft.
Wing Span	131.3 sq. ft.
Aspect Ratio	2.0
MAC	1139.4 in.
Indb. Sweep	71 deg.
Outbd. Sweep	52 deg.
H-tail Area	800 sq. ft.
V-tail Area	407 sq. ft.

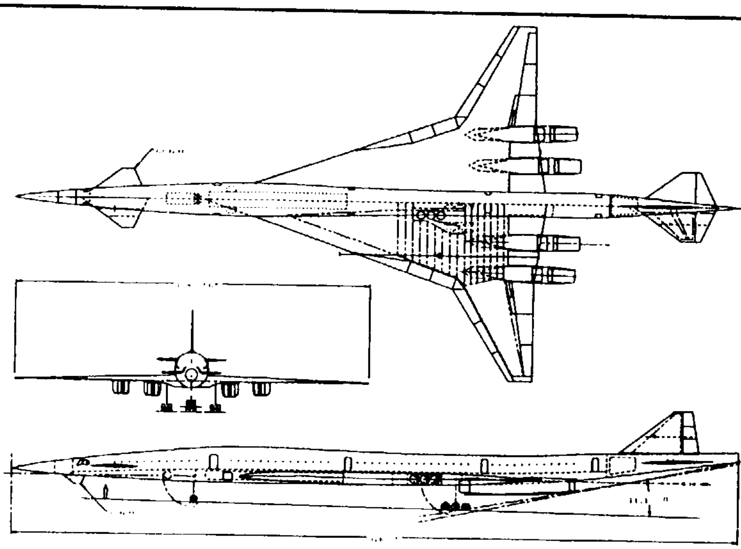

PTC Cycle 2

Wing Area	9200 sq. ft.
Wing Span	158.5 ft.
Aspect Ratio	2.73
MAC	1077.9 in.
Inbd. Sweep	71.0 deg.
Outbd. Sweep	32.0 deg.
H-tail Area	545 sq. ft.
V-tail Area	415 sq. ft.
Canard	220 sq. ft.
Chin fin	25 sq. ft.

Common Process

The high lift common process team has reached concensus on most of the major steps in the assessment of candidate configurations. The flow chart summarizes the steps used to build up from wind tunnel data the trimmed lift curves and drag polars of new configurations.

The steps to the left of the dashed line are not routinely performed. These steps are only required when a new wind tunnel database is obtained.

The steps to the right of the dashed line are performed for **each** flap setting with the exception of calculation of ΔC_{D_o} in A389.

Depending on what baseline data is available, AERO2s may be used to predict not only the effects of the planform changes from the baseline configuration to the new configuration, but also the effects of flap deflection changes.

In the case of the PTC buildup, the Ref H baseline data set only includes the LE/TE flap combinations of 00/00, 00/30, and 30/10. Any other flap settings for the PTC are predicted using AERO2s to increment from one of these available baseline settings.

In the case of the programmed flap, the process is used 169 times (13 leading edges and 13 trailing edges) to create 169 different polars that are interpolated to find the LE/TE combination giving the best L/D.

Common Process

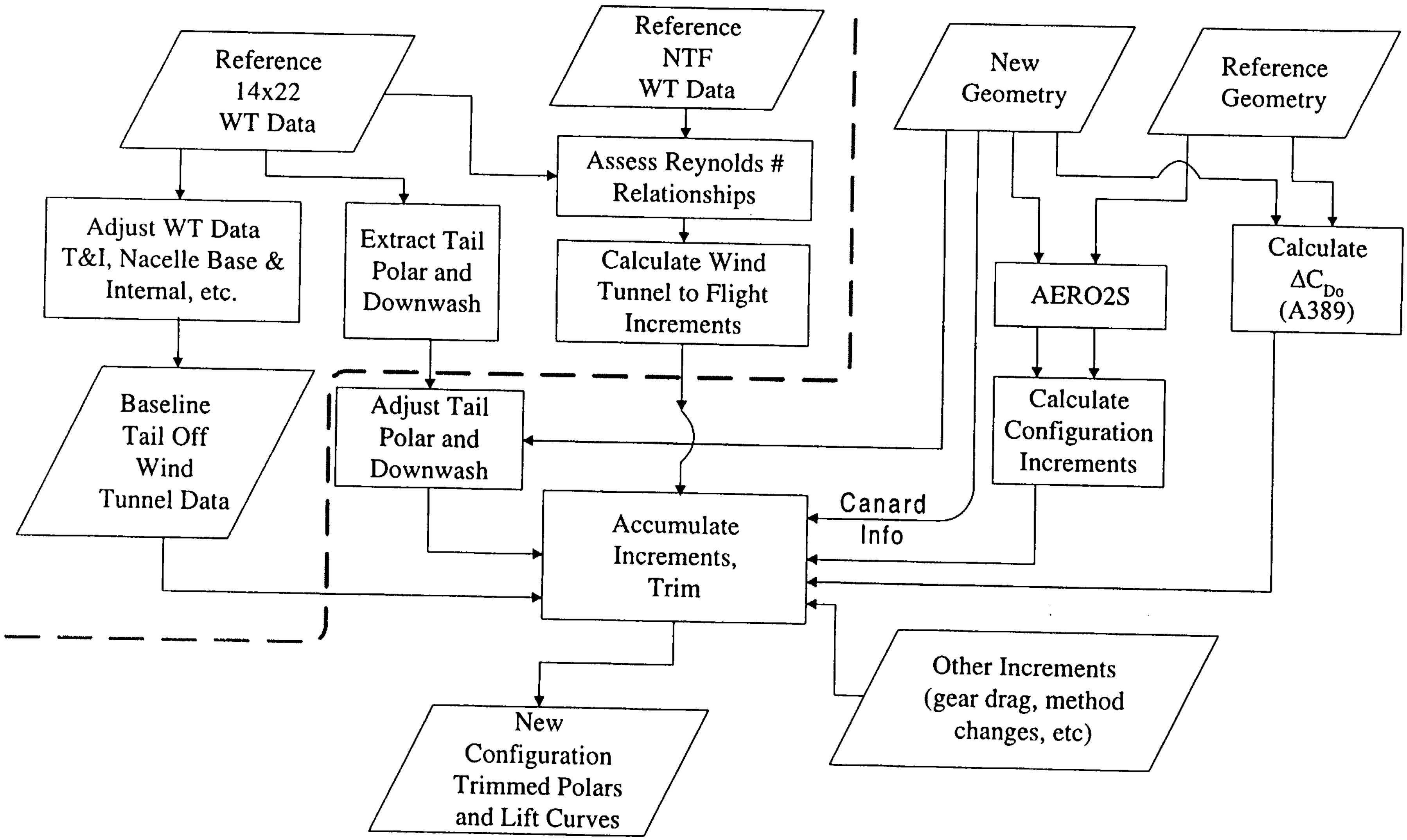

Ref H Data

The plots show the wind tunnel data used as the basis of the PTC buildup. The data were obtained in the 14x22 LaRC wind tunnel on the Ref H configuration. The appropriate wall corrections have been applied along with tare and interference corrections. Nacelle internal forces and nacelle base drag corrections have been made. All data is gear up.

The Ref H data shown is for LE/TE flap combinations: 00/00, 00/30, and 30/10.

Due to the remaining uncertainty about upflow in the 14x22, upflow corrections have not been applied to the wind tunnel data.

Ref H Data

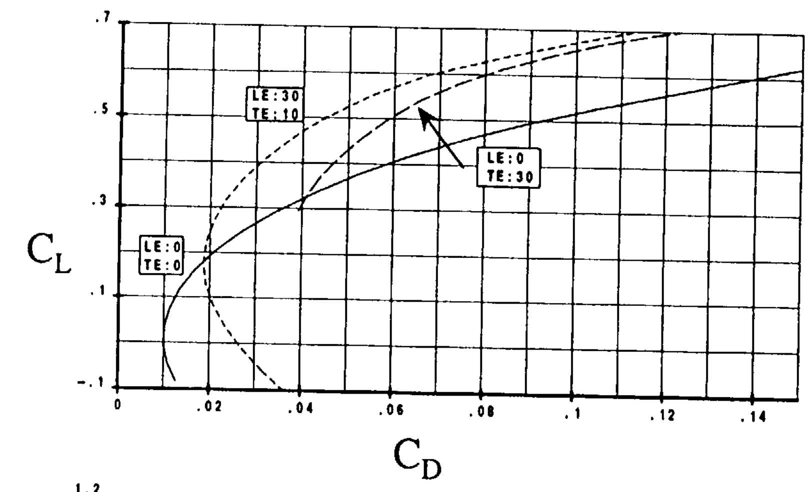

- •Ref H Configuration 14x22 Corrected Data
- •Adjusted for A502 T&I; no upflow corrections
- •Adjust for Nacelle Internal Forces and Nacelle Base Drag
- •Sref=Sgross=7590 ft^2
- •Gear up

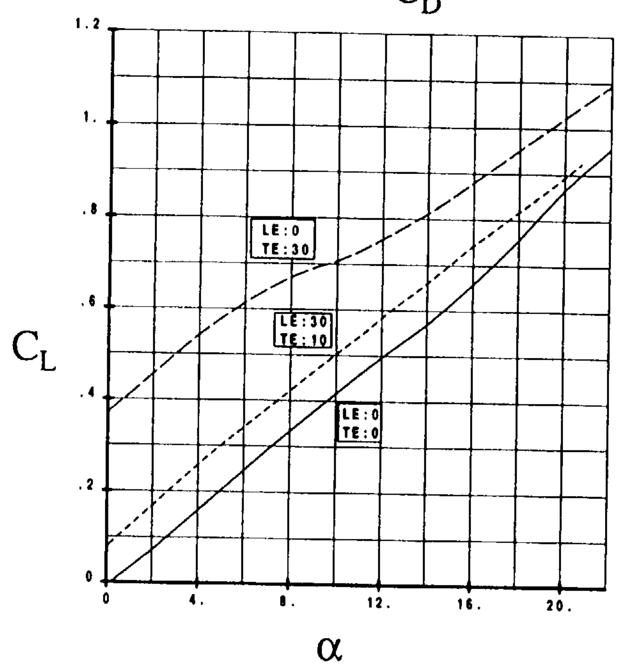

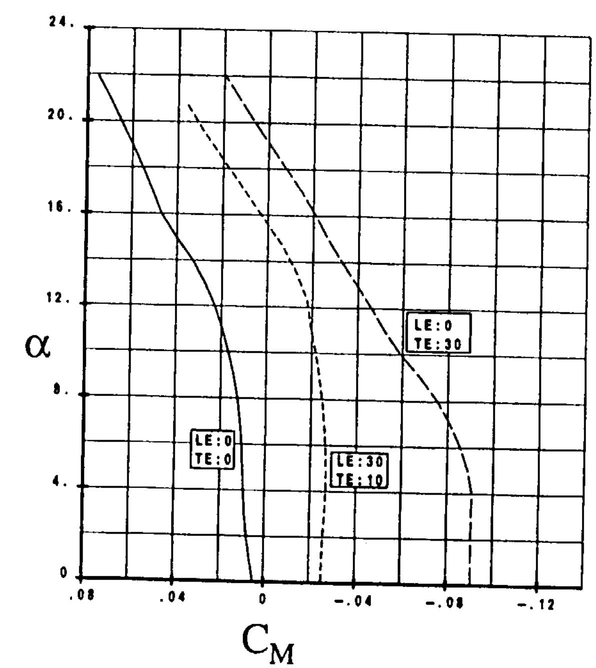

Wind Tunnel to Flight (Ref H)

The large difference in Reynolds number between the 14x22 model and the flight vehicle requires accounting for the skin friction changes. The table shows the buildup of the skin friction adjustment using NTF data to obtain a major portion of the adjustment. A389 is used for the adjustment from the maximum NTF Reynolds number to the flight Reynolds number.

Full scale vehicles typically have excrescences that do not exist at wind tunnel model scales. The excrescence portion of the build up is also shown in the table.

Wind Tunnel to Flight (Ref H)

- Skin Friction adjustments

  from Re = 8 million (wind tunnel)

  to Re = 200 million (flight)

NTF Reynolds number data (8E6 -> 90E6)	-17.4 counts
A389 aft body, tails (8E6 -> 90E6)	-3.7 counts
A389 full airplane (90E6 -> 200E6)	-7.7 counts
	ΔC_D = -28.8 counts

- Excrescence Drag ΔC_D = +5.2 counts

Skin Friction Adjustments

After the Ref H data is adjusted to the Flight level drag, an additional skin friction correction is made to account for the configuration differences between the Ref H and the PTC. The table shows how the increment is obtained.

Skin Friction Adjustments

- Skin Friction Drag adjustments
  - from Ref H (flight)
  - to PTC (flight)

PTC C_{D0} (A389)	70.9 counts
Ref H C_{D0} (A389)	- (72.1 counts)
	ΔC_D = -1.2 counts

Includes excrescence factor

AERO2s Lift Increments

AERO2s is used to calculate the effects planform and flap setting changes on lift, drag, and pitching moment between the reference configuration and the new configuration. The following three figures show these effects for the change from the Ref H configuration to the PTC.

AERO2s Lift Increments

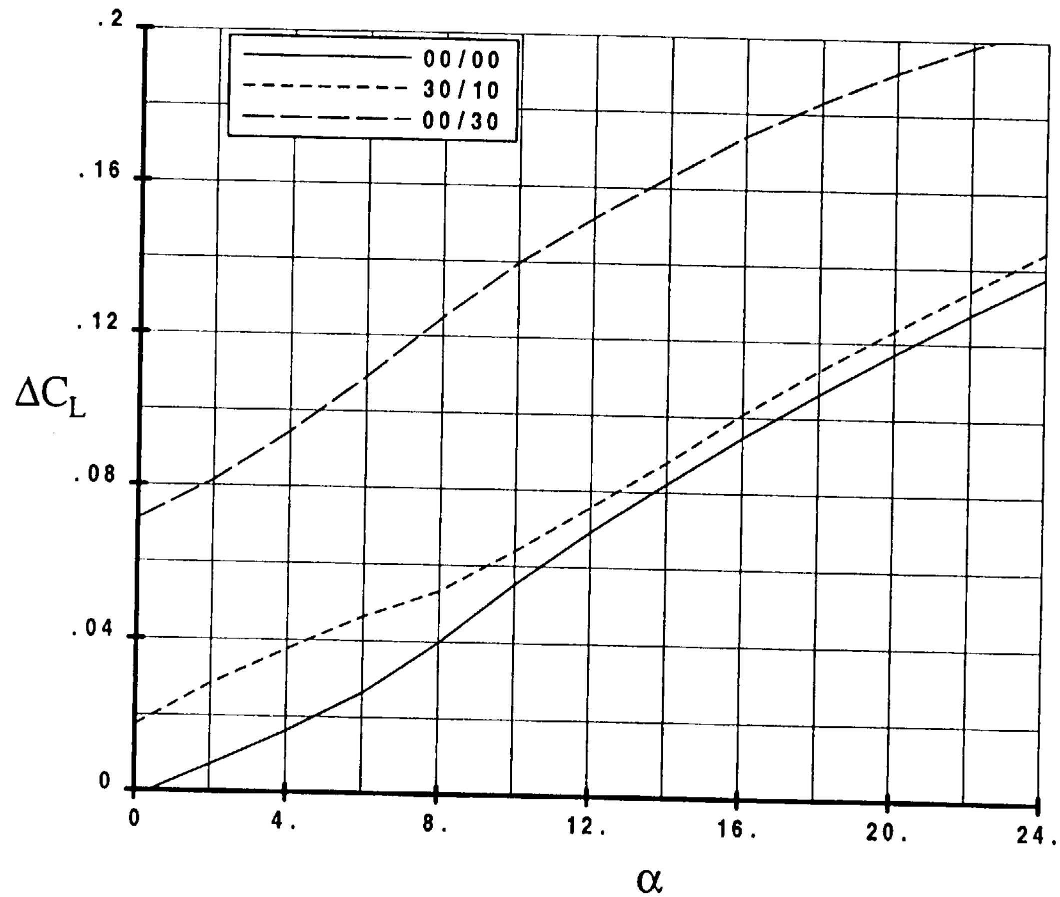

Lift increments calculated by AERO2s from Ref H to PTC

$$\Delta C_L = C_{L_{PTC}} - C_{L_{RefH}}$$

AERO2s Drag Increments

The AERO2s predicted drag increments are presented in the figure in two forms. The drag increment is shown (ΔC_D) and the non-ideal portion of this ΔC_D is also shown as $\Delta\left\{C_D - \frac{C_L^2}{\pi \cdot AR}\right\}$

AERO2s Drag Increments

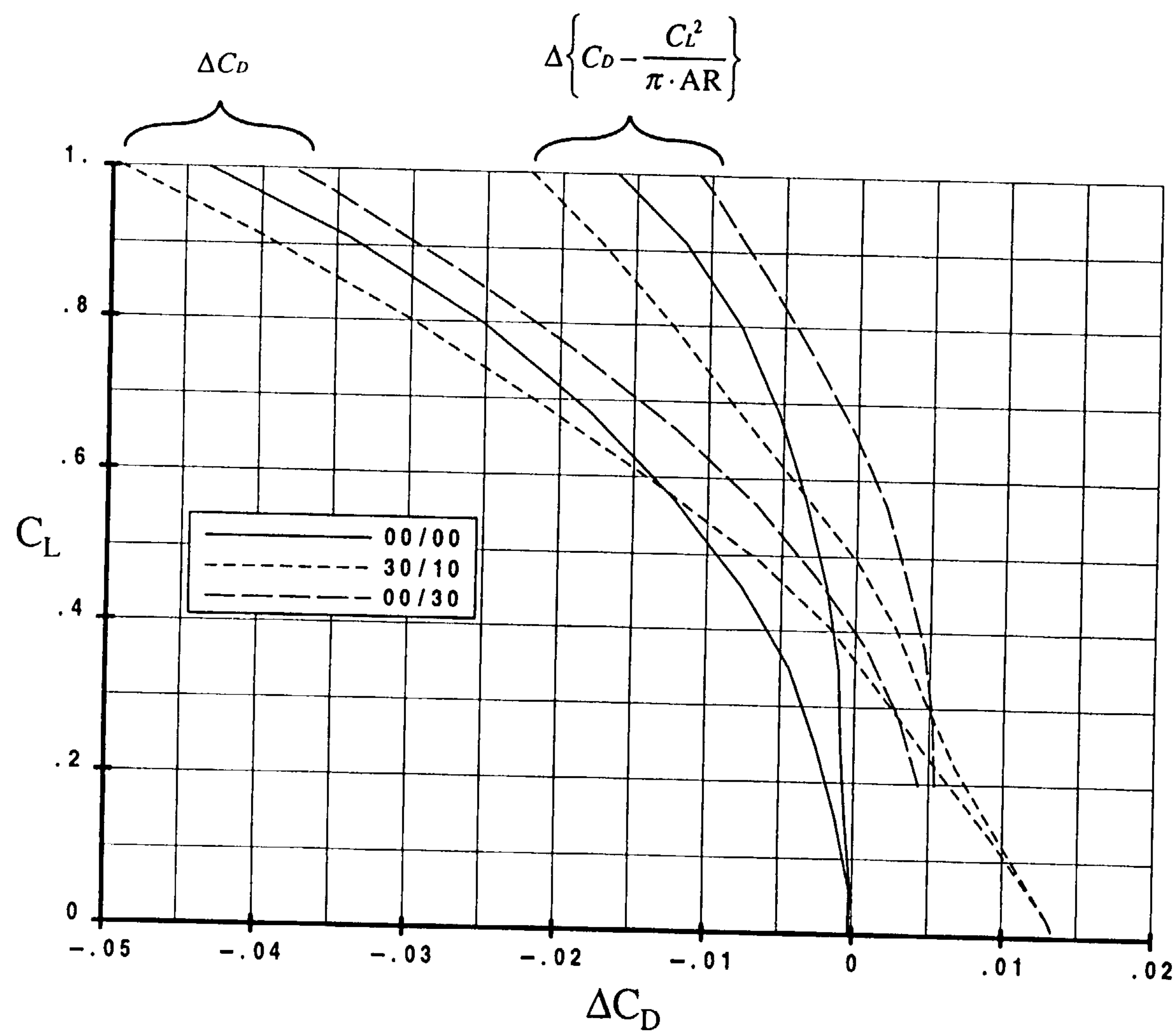

Drag increments calculated by AERO2s from Ref H to PTC

$$\Delta C_D = C_{D_{PTC}} - C_{D_{RefH}}$$

BOEING AERO2s Pitching Moment Incs.

HSCT High Lift Aerodynamics

Intentionally blank.

AERO2s Pitching Moment Incs.

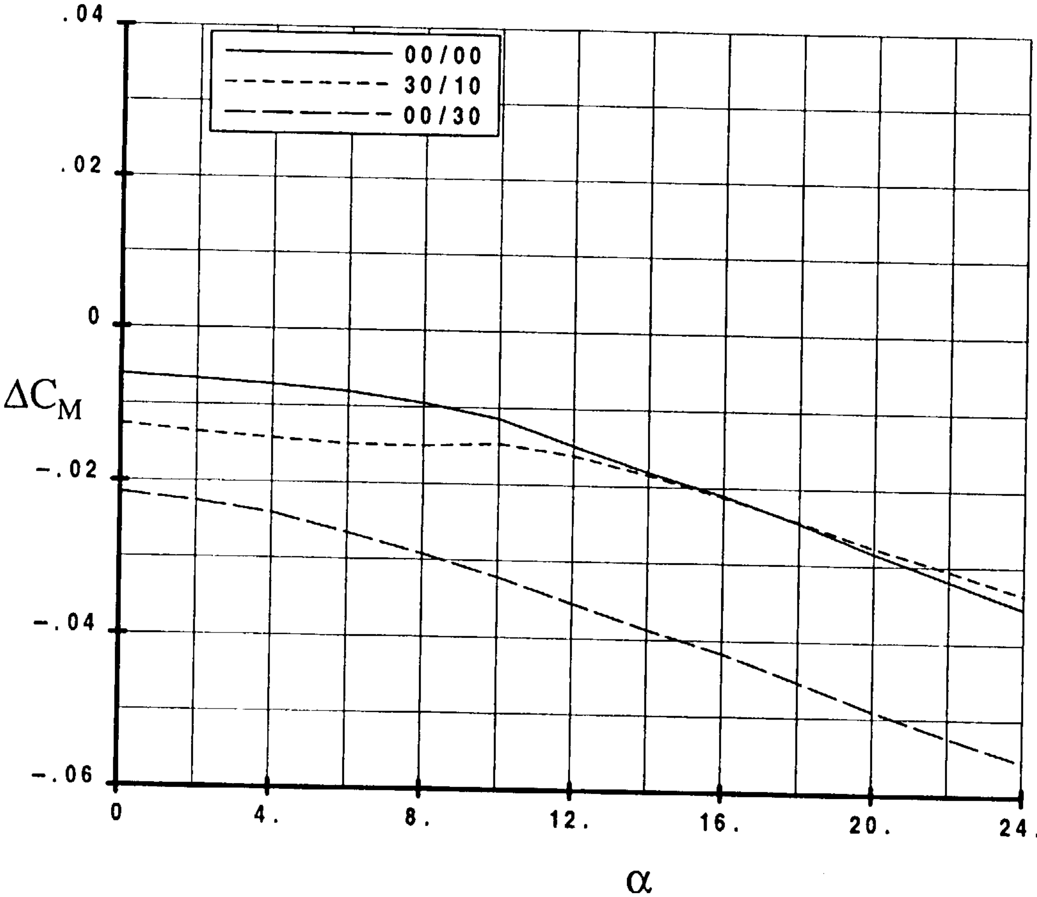

Pitching Moment increments calculated by AERO2s from Ref H to PTC

$$\Delta C_M = C_{M_{PTC}} - C_{M_{RefH}}$$

PTC Gear Effects

For the gear down configurations gear effects are added to the PTC gear up build up. The gear effects shown in the figure are wind tunnel based with a correction made for reference area differences.

The presence of the gear influences lift only slightly, while the drag impact is rather large.

PTC Gear Effects

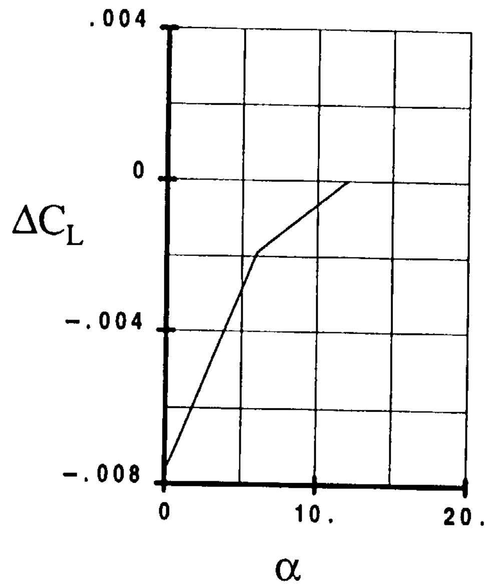

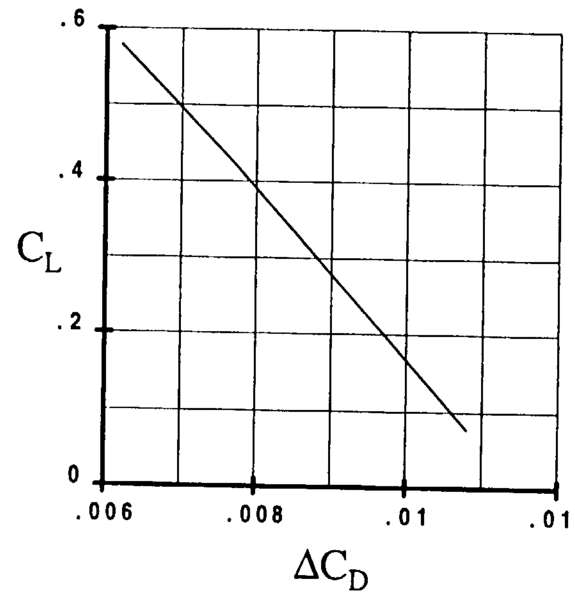

PTC Wing/Body Data

The effects of all of the increments discussed thus far are shown in the plots. The 00/30 data includes the gear effects.

PTC Wing/Body Data

BOEING

HSCT High Lift Aerodynamics

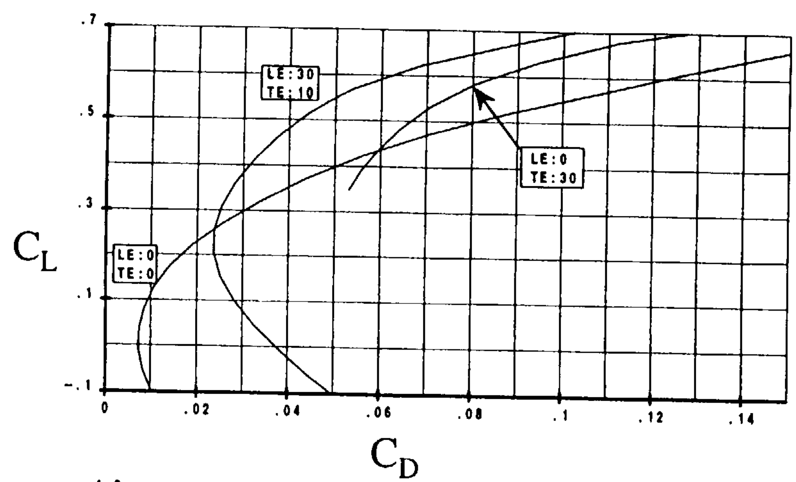

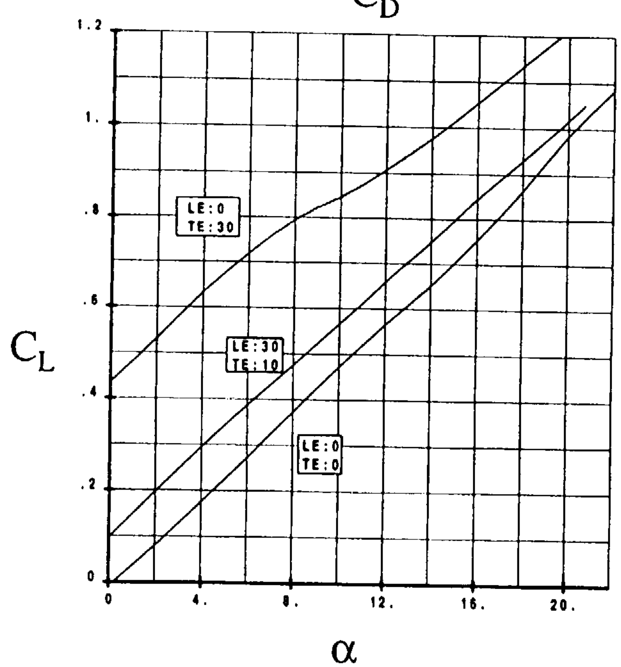

PTC Flight Data is Ref H 14x22 Data Adjusted for:

- Wall corrections, A502 T&I, no upflow corrections
- Nacelle Internal Forces and Nacelle Base Drag
- Reynolds Number Effects
- Excrescence
- Configuration Differences
  (skin friction, AERO2s)
- Gear Drag (where applicable)

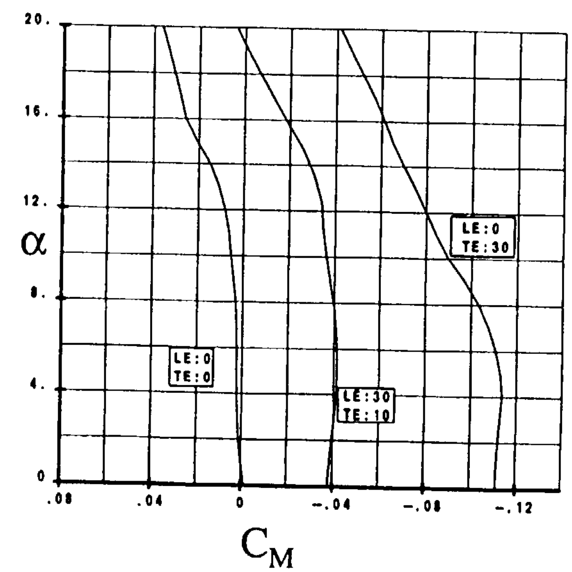

3-Surface Trimming

A method has been developed in the common process discussions that can be used to determine the optimum trim settings for the canard on a 3-surface airplane. The method achieves an optimum by expressing the additional drag created by trimming the wing/body pitching moment in terms of the individual drag contributions of the canard, wing, and tail. An equation representing this trim drag is then minimized and simplified to provide the best canard lift as a function of wing/body C_L and C_M.

Once the best canard lift is determined for a particular wing/body C_L and C_M, the effects of the canard (lift, drag, and pitching moment) on the airplane are added to the wing/body alone data. This wing/body/canard data is then trimmed with the tail.

The table of data above the flow chart lists the values used for the PTC 3-surface method of determining the optimum canard lift.

3-Surface Trimming

PTC

	AR	e
wing	2.73,	.9
tail	1.257,	.7
canard	2.071,	.7

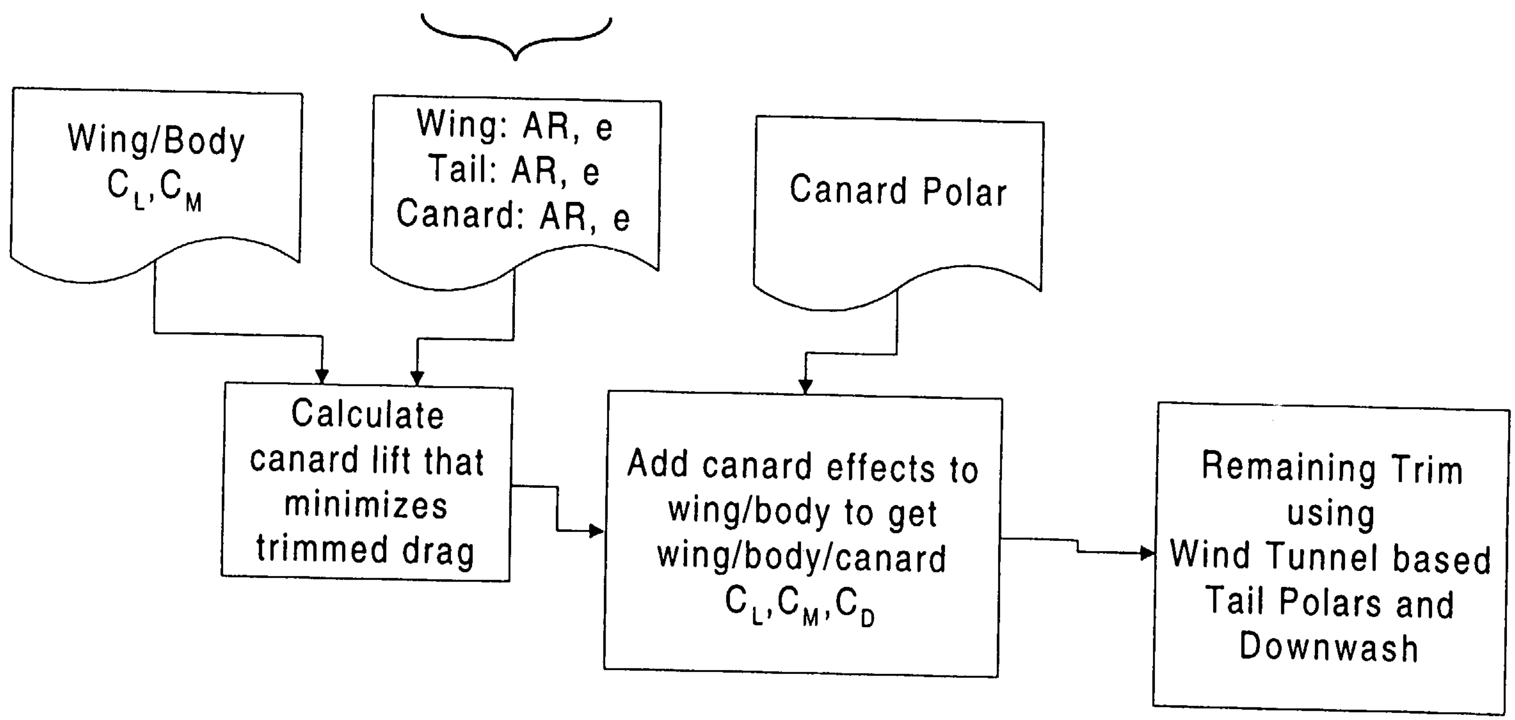

3-Surface Trimming

The plots show the optimum canard lift-coefficient as a function of wing/body C_L and C_M for the PTC.

The method has an option to limit the canard lift-coefficient. The effects of this option can be seen on the 00/30 data where the max canard lift-coefficient was set to be 1.0.

3-Surface Trimming

PTC

Optimum canard lift

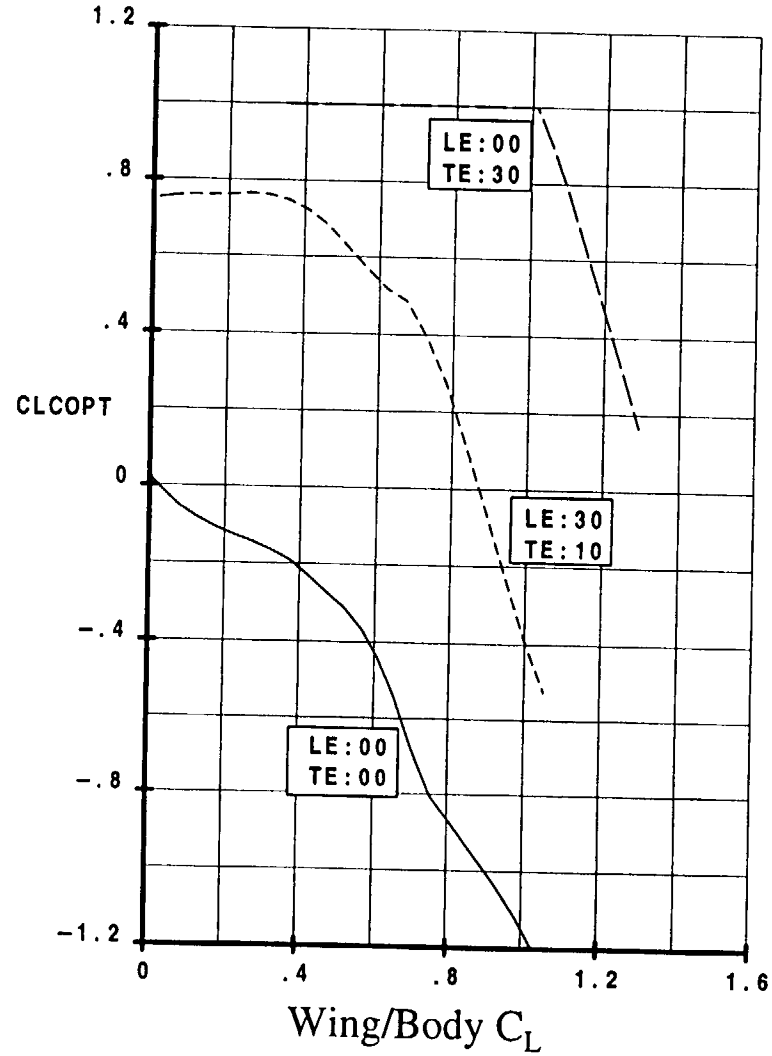

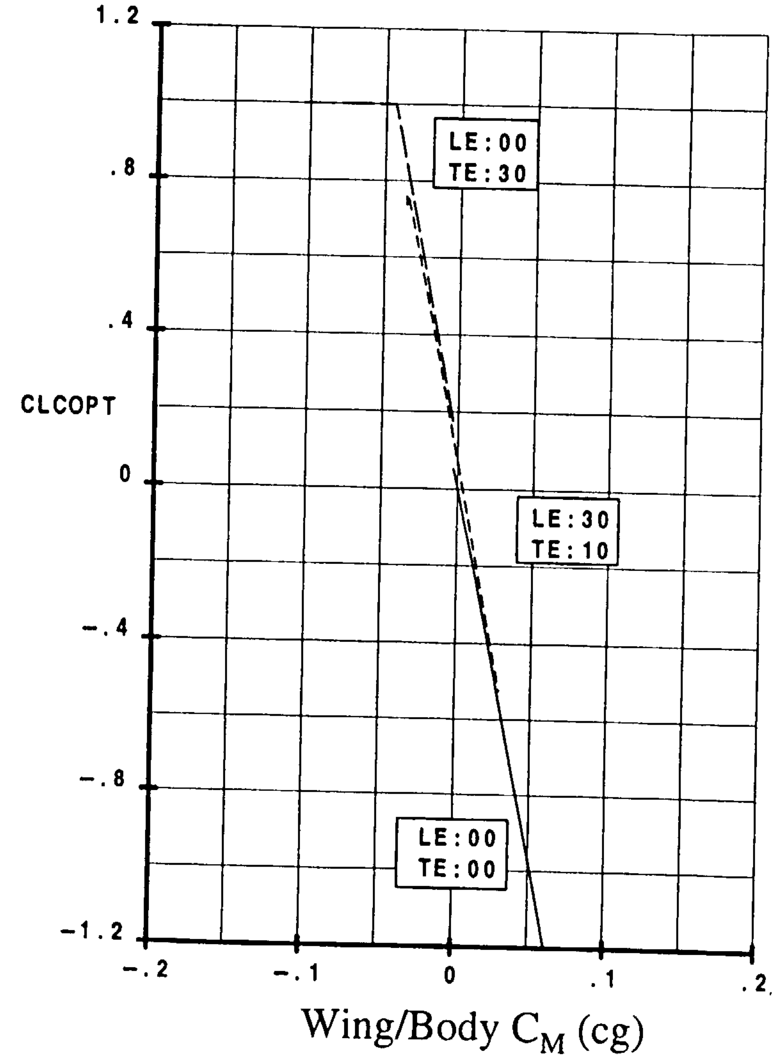

Trim Effects on Lift

The results of the 3-surface trimming for the 30/10 flap setting are shown in the plots. The wing/body data is plotted with the short-dashed line. After the optimum canard lift-coefficient is calculated, the canard effect is added to the lift curve - solid line. The best canard setting, however, is not one that completely trims the airplane. The tail is used to trim the remaining wing/body/canard pitching moment resulting in a slight lift reduction from the wing/body/canard lift level- long dashes.

The plot to the right magnifies the area of interest.

Trim Effects on Lift

PTC Flaps 30/10

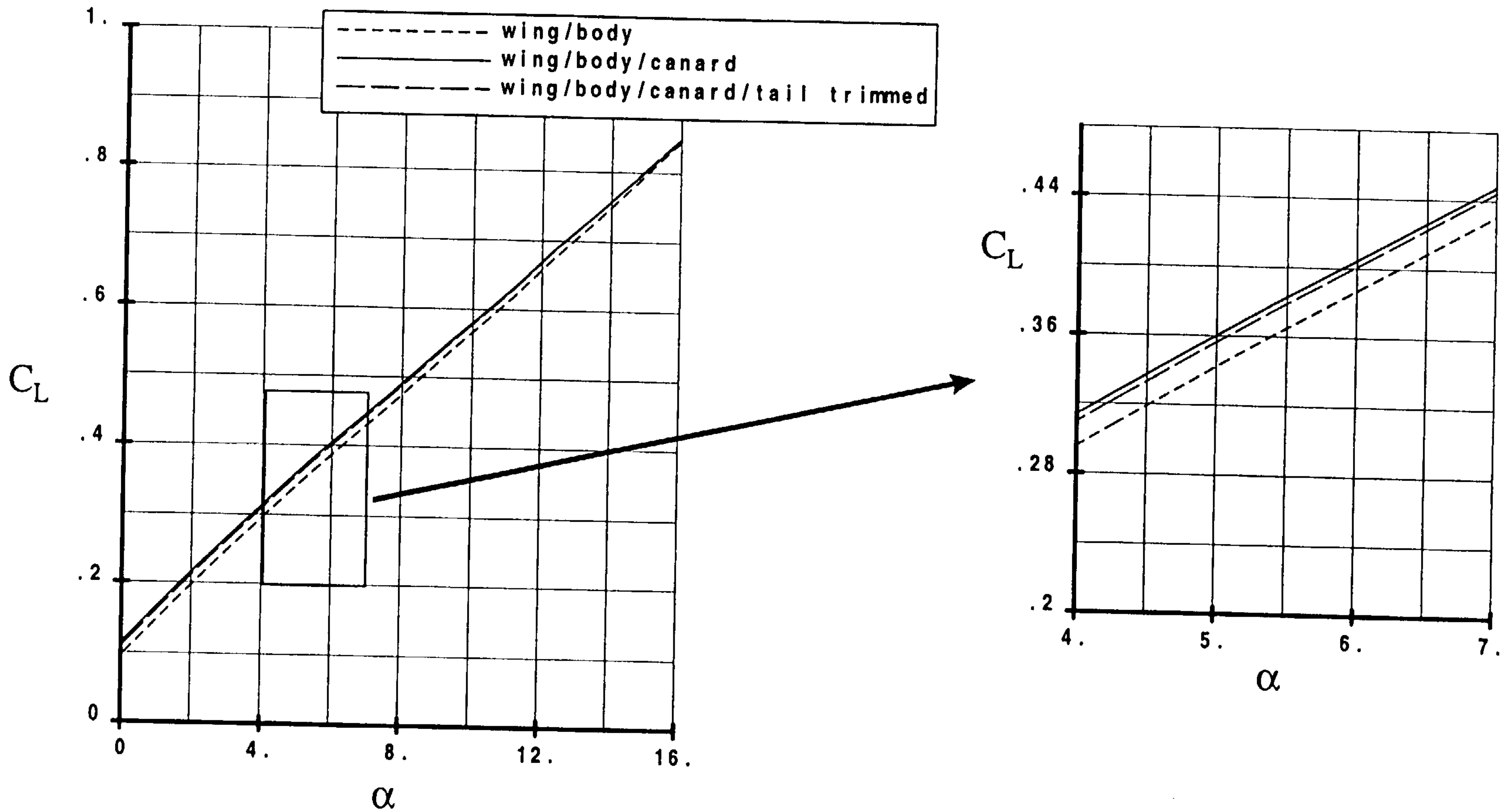

Trim Effects on Drag

The results of the 3-surface trimming for the 30/10 flap setting are shown in the plots. The wing/body data is plotted with the short-dashed line. After the optimum canard lift-coefficient is calculated, the canard effect is added to the lift curve - solid line. For clarity only the non-elliptic portion of drag is shown in the plots.

The canard does not completely trim the airplane. The remainder of the trimming is done with the tail, which also adds drag.

The dot-dash line represents the trimmed polar if there were no canard. This data, however, is somewhat pessimistic because the tail size on the PTC would not be large enough without the canard. A larger tail would improve the trim drag characteristics of the tail-only airplane.

Trim Effects on Drag

BOEING

HSCT High Lift Aerodynamics

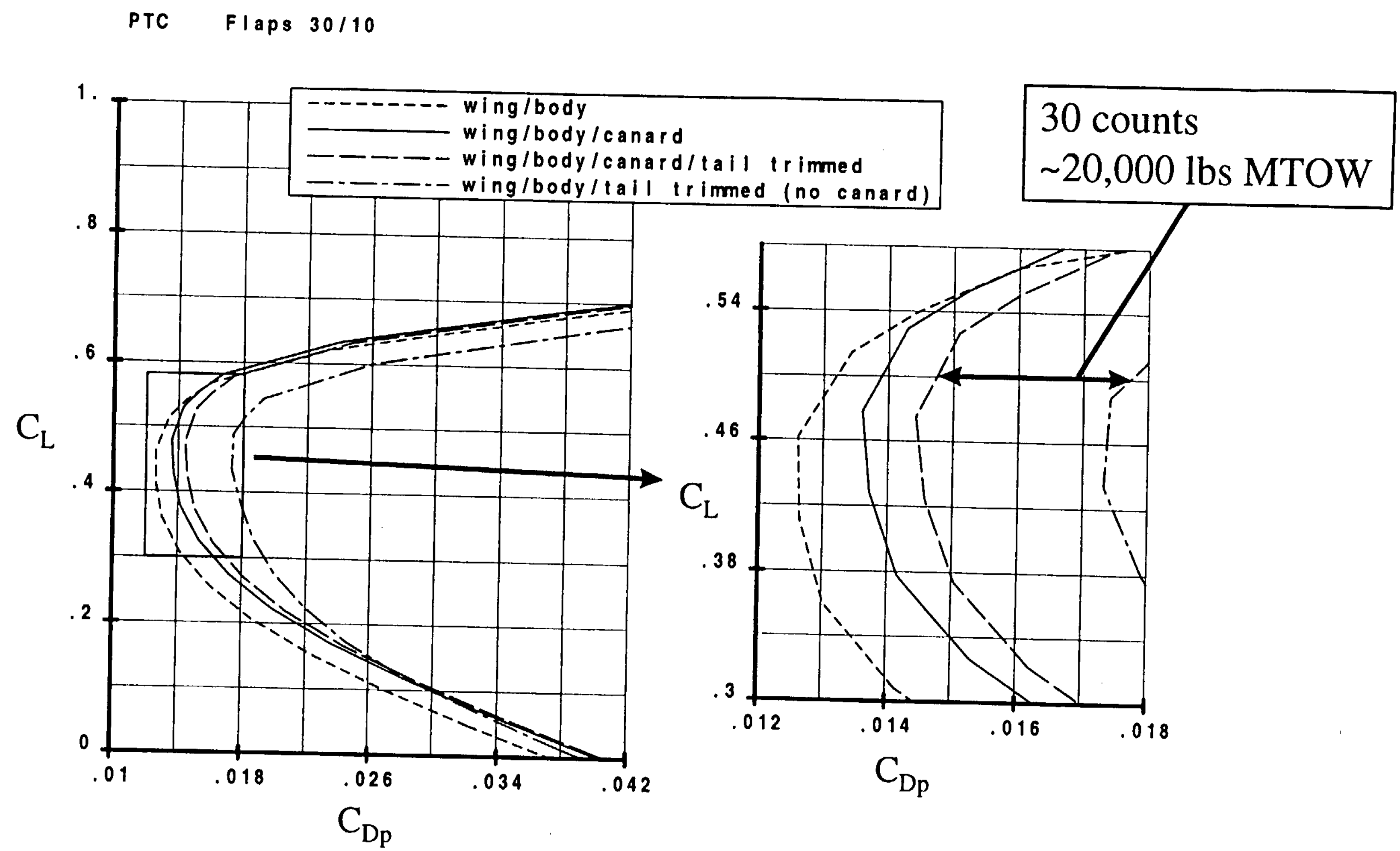

Programmed Flap

For the climbout segment of flight, the programmed flap system adjusts the leading edge and trailing edge flap settings to obtain the best L/D for the current airplane lift-coefficient. This maximizes climb gradient for a given thrust setting, which provides the highest cut-back altitude to minimize community noise.

To predict the programmed flap lift curve and drag polar for a particular configuration the process illustrated in the figure is followed. A matrix of 169 separate polars is created representing the high lift characteristics of various leading edge and traling edge combinations. These polars (using the current common process) all originate from the Ref H 30/10 wind tunnel data. To this wind tunnel data the process adds increments determined by AERO2s to account for both the configuration change and the flap setting changes. Each of these 169 polars are created separately by running through the buildup process mentioned previously. Each of these polars is then interpolated at a series of lift-coefficients to determine which flap combination offers the best L/D at each lift-coefficient. The resulting polar is termed the "status" programmed flap polar.

At each of the lift-coefficients the angle-of-attack for the best flap combination is also determined.

Programmed Flap

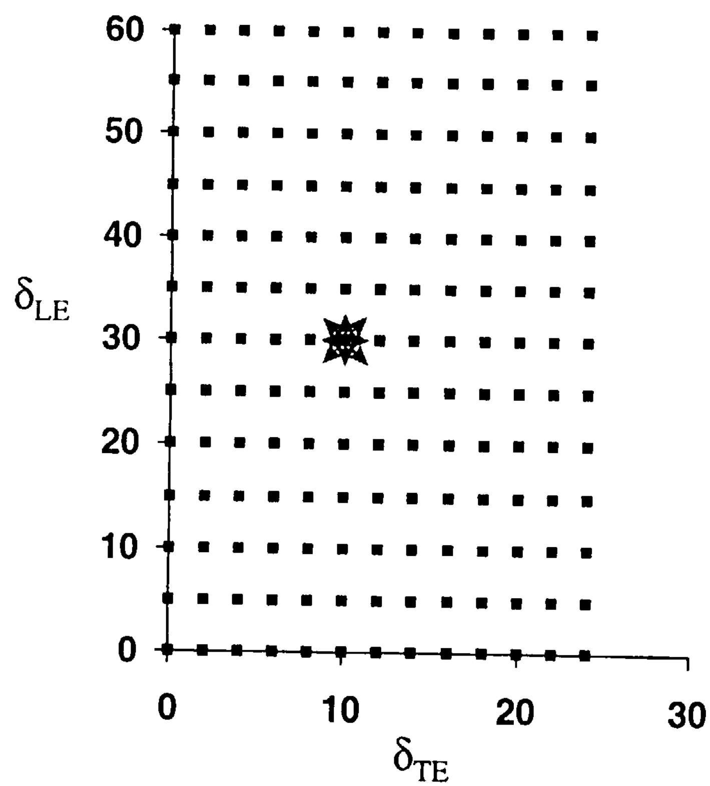

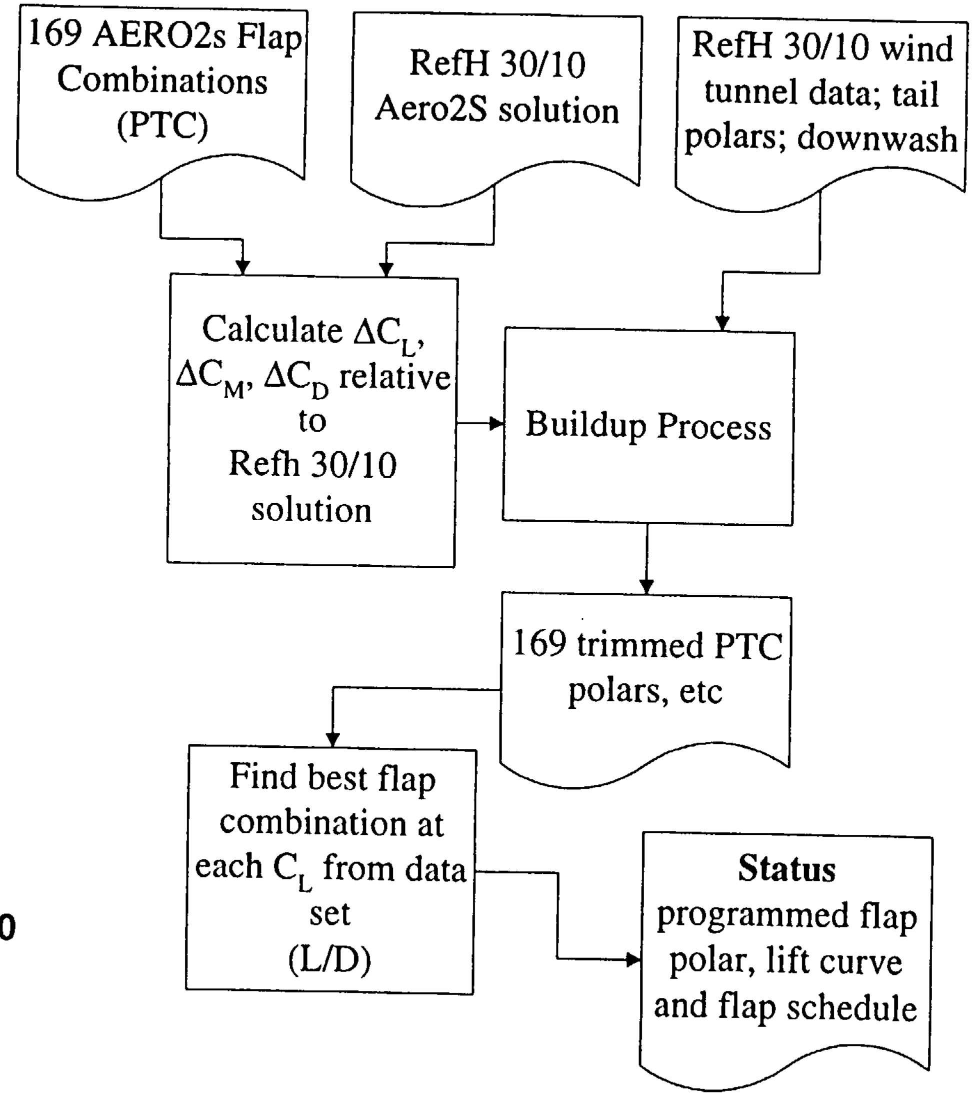

Programmed Flap (Status)

The plots show the resulting status programmed flap lift cuve and flap schedule for the PTC. Each plot contains two sets of data. The dashed line data represents the programmed flap setting and lift curve that result from selecting from only the 169 polars of the matrix. The solid line data represents the programmed flap setting and lift curve that result from interpolating through the large matrix giving a smoothly varying flap setting throughout the polar and lift curve.

Programmed Flap (Status)

Gear Up   No Thrust Effects

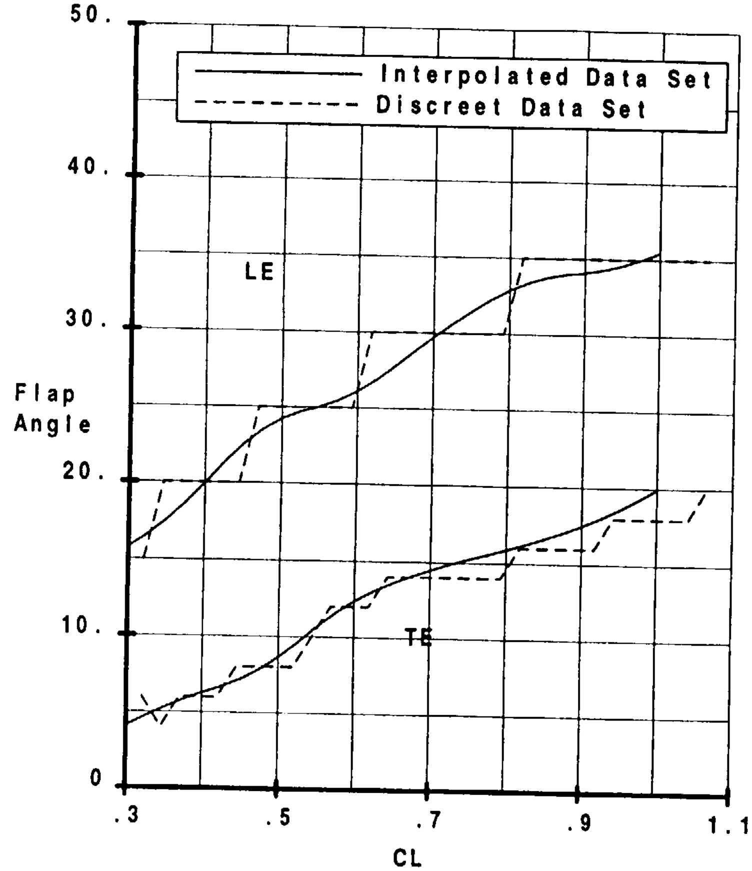

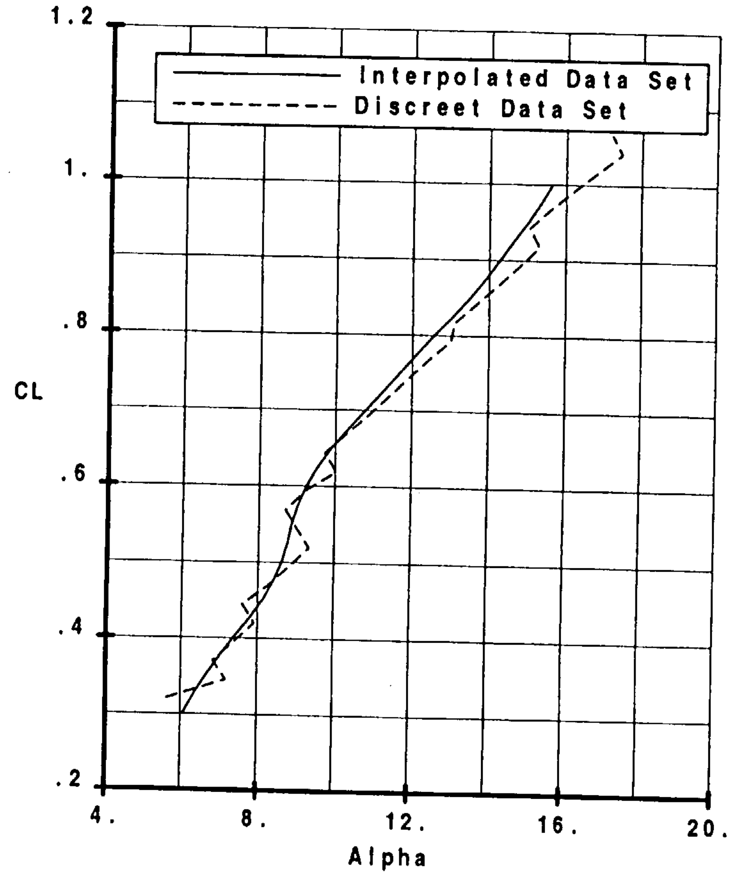

Programmed Flap (Status)

The plots show the status programmed flap L/D and suction parameter. The 3-surface target (projected technology) suction level of 93% is also indicated.

BOEING

Programmed Flap (Status)

HSCT High Lift Aerodynamics

Gear Up   No Thrust Effects

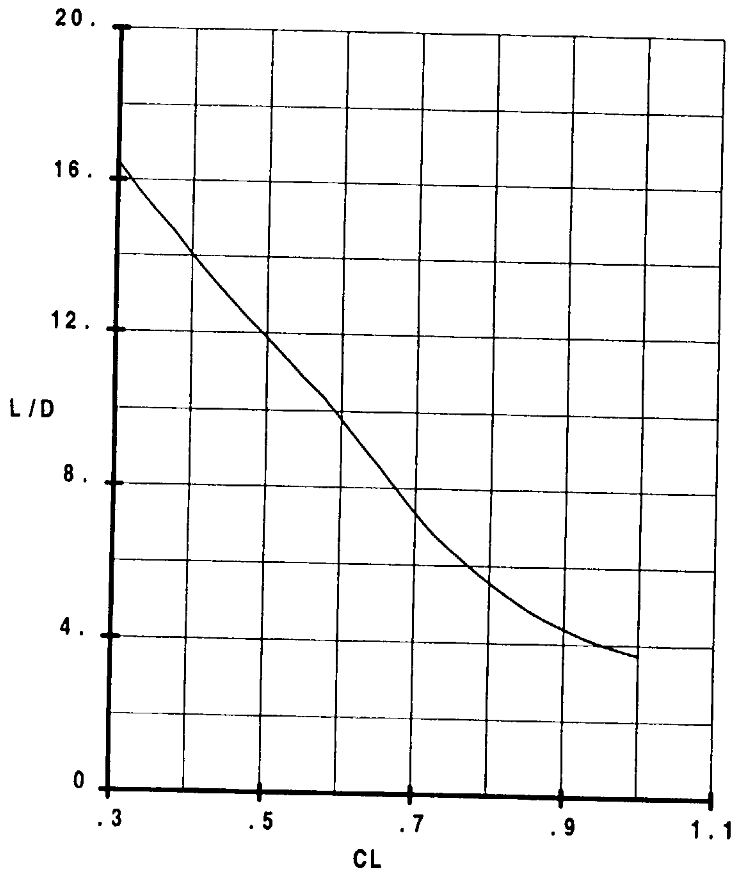

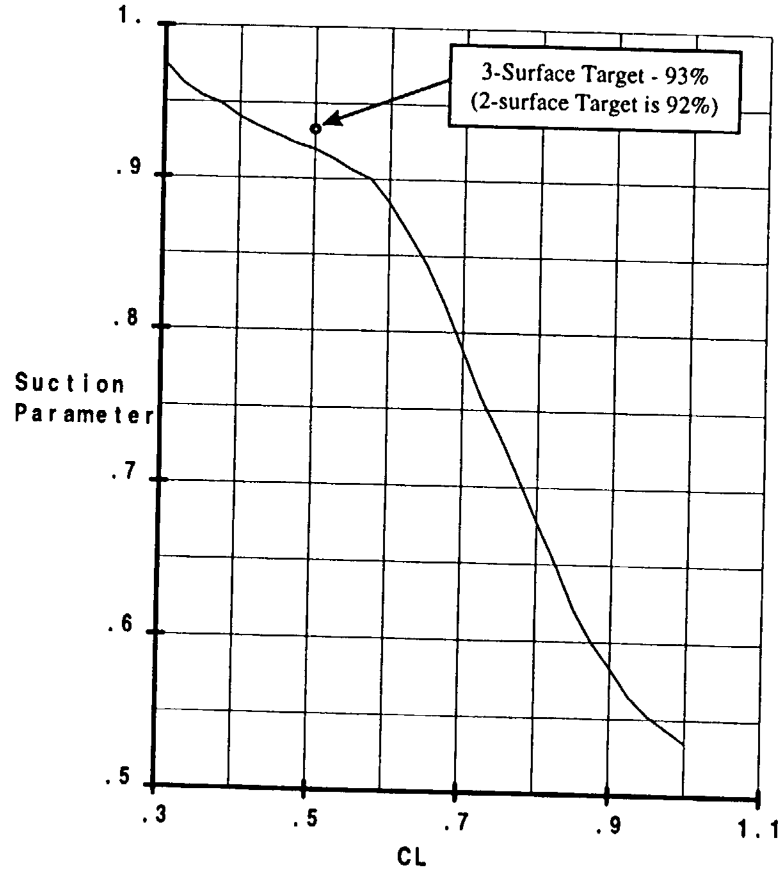

Technology Projection

To obtain the targetted suction level of 93% at C_L=.5 a drag reducing increment must be applied to the status level data. The plot on the right shows the required drag increment to increase the suction level to 93% from the status level. At C_L=.5 the drag reduction is about 7.5 counts or about 2% of total drag.

The drag increment applied is washed out to zero at low and high C_L values.

Technology Projection

How much less drag do we need?

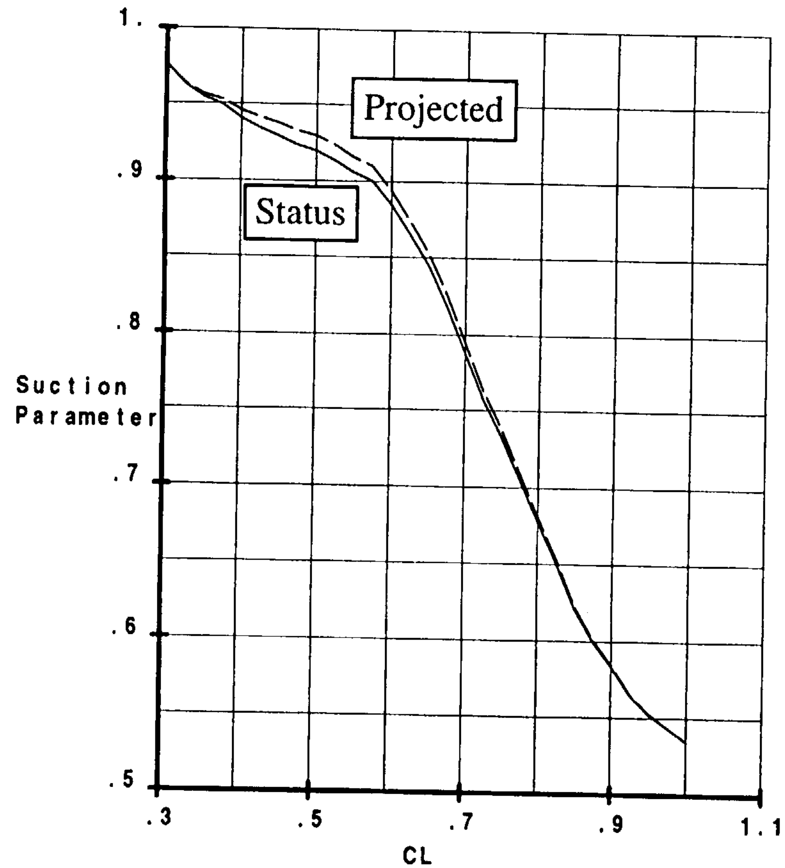

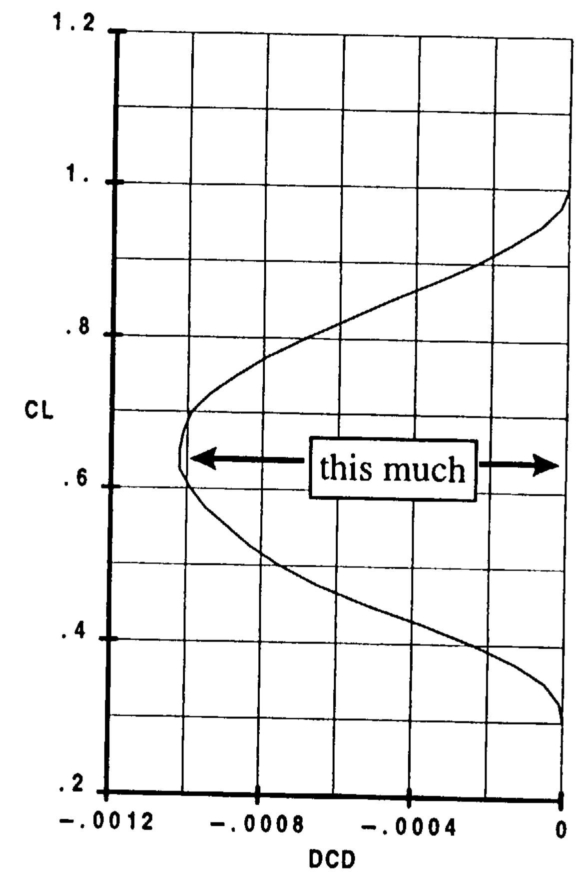

PTC vs TCA

The plots summarize programmed flap status and projected levels relative to the TCA configuration.

The PTC status level is much closer to its projected suction level of 93% than the TCA is to its projected level of 92%.

PTC vs TCA

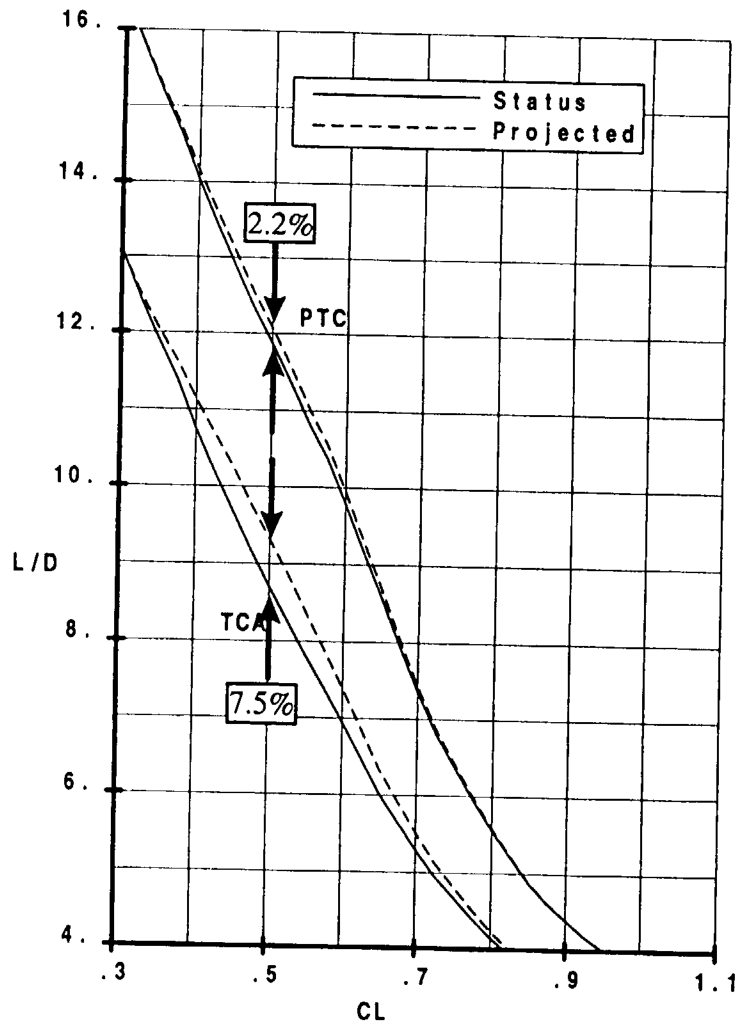
16.
14.
12.
10.
8.
6.
4.
L/D
.3
.5
.7
.9
1.1
CL
Status
Projected
2.2%
PTC
TCA
7.5%

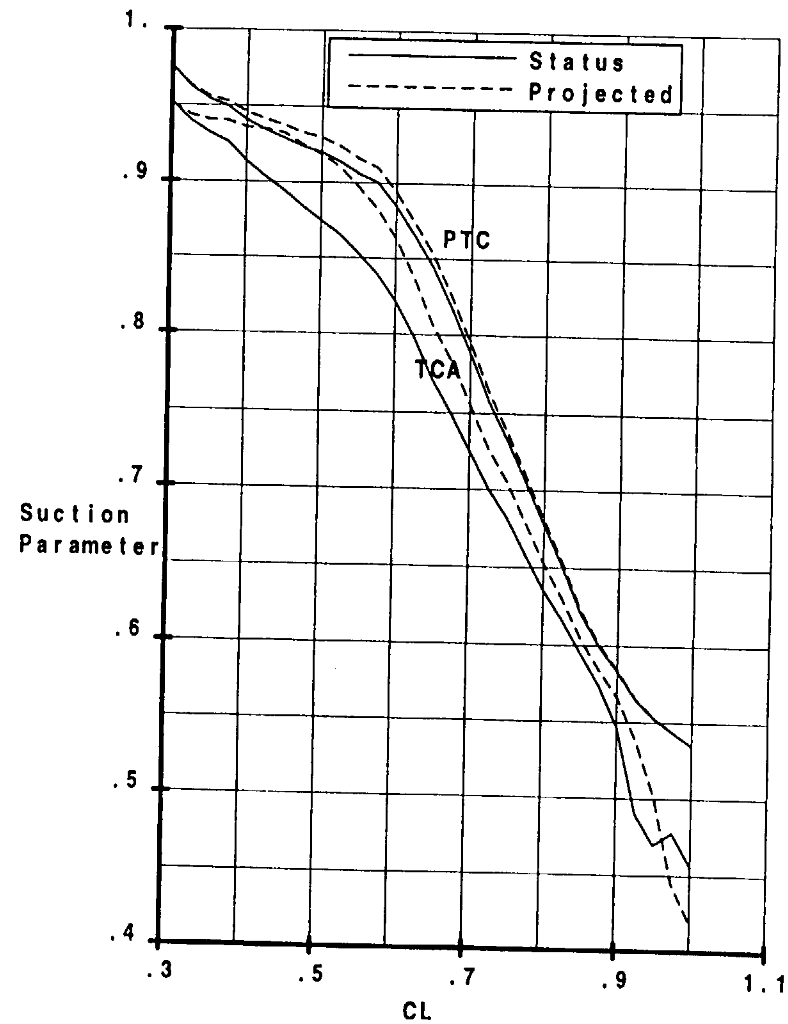
1.
.9
.8
.7
.6
.5
.4
Suction Parameter
.3
.5
.7
.9
1.1
CL
Status
Projected
PTC
TCA

Landing Performance

The method of selecting the required touchdown flap setting is illustrated in the figure.

Given a Maximum Landing Weight and a maximum approach speed the touchdown C_L can be determined - assuming a 3% speed bleed during flare and touchdown.

Also given the airplane geometry and the required margin to tail strike upon touchdown the maximum allowable touchdown attitude can be determined.

A family of lift curves in ground effect are shown on the plot. The selected flap setting must provide at least the required touchdown C_L at the maximum attitude line. Such a flap setting would be approximately 00/16.

The PTC, as opposed to the TCA (not shown), has adequate flap deflection available to acheive the required 3 degree margin at the minimum touchdown speed.

Landing Performance

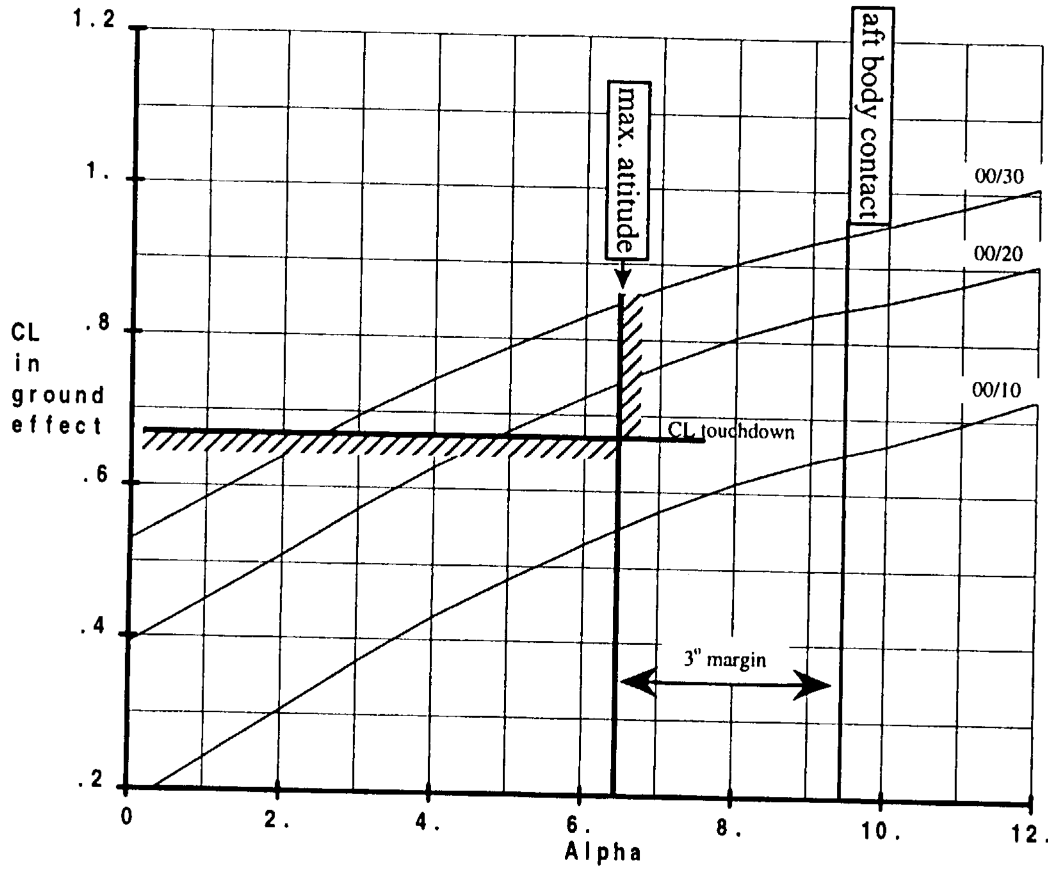

Touchdown Requirements:

- Vappr=155 kts with 3% speed bleed during flare
  => $C_{L_{TD}}$=.672 for MLW=473000 lbs.
- 3 degree contact margin

Landing Performance

The previous slide detailed the method used to determine the required minimum flap setting to meet the touchdown requirements. What is not shown is that there is a family of leading edge and trailing edge flap combinations that will meet the requirements. If the leading edge flap is set to 25 degrees, the trailing edge flap only needs to increase to 18 degrees.

The plot shows the penalty if the approach were flown at the 25/18 touchdown flap setting rather than the programmed flap setting. The penalty is about 4% in L/D.

Landing Performance

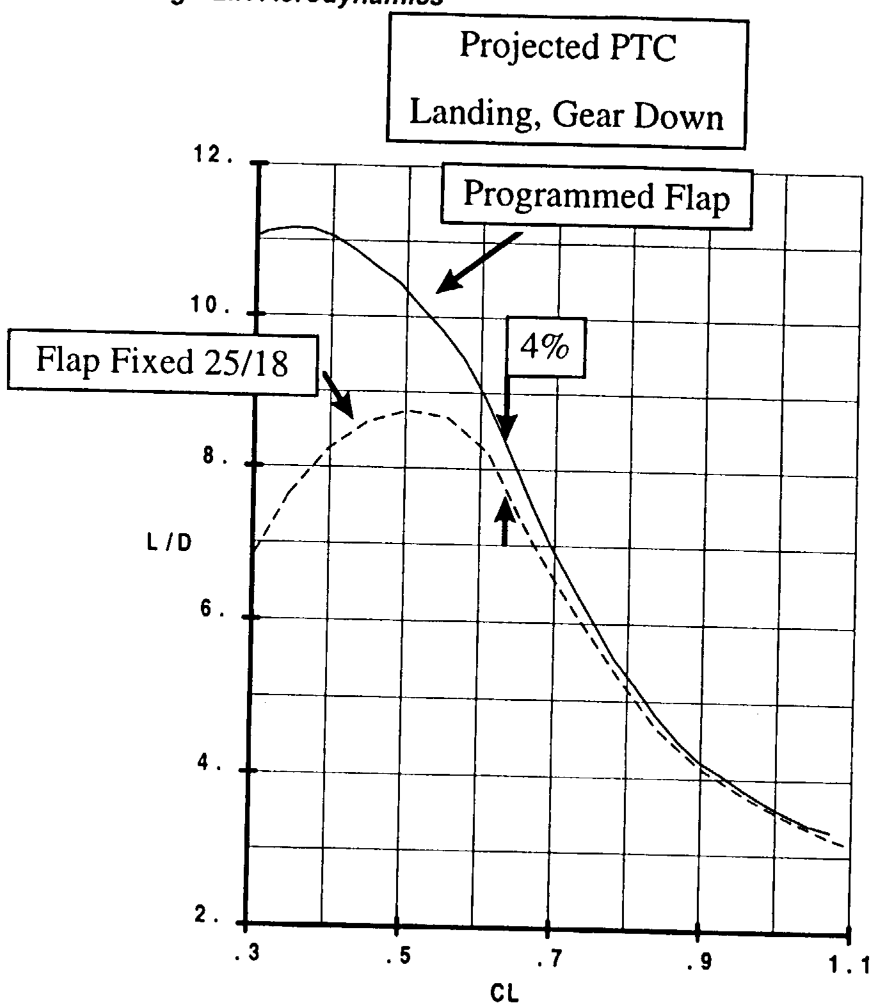

Do we need programmed flap on landing?

Maybe not...

- 25/18 works for touchdown as well as 00/16
- Use 25/18 for approach rather than programmed flap => 4% penalty in L/D

Conclusions

Intentionally blank.

Conclusions

Conclusions:

- The common process work is essentially complete and can support current build up requirements
- The PTC made significant advances toward the technology projected L/D
- The PTC has more than adequate landing attitude capability

But ...

Issues

Intentionally blank.

Issues

Issues:

- Upflow uncertainty in wind tunnel data
- AERO2s being used to predict effects of large flap deflection changes. Programmed flap extrapolating from one wind tunnel run (Ref H 30/10)
- Lack of canard "polars"
- AERO2s prediction of TCA relative to Ref H was very optimistic ... What about the PTC relative to Ref H?

This page is intentionally left blank.

Correlation Of CFD Calculations And Wind Tunnel Measurements For The M2.4–7A Arrow Wing Configuration

by

Chung–Jin Woan
Boeing Information, Space & Defense System
Phantom Works – Technology & Define Process
Seal Beach, California

HSR Airframe Technical Review
Aerodynamics Performance TMT
High Lift ITD

Westin Hotel, Los Angels Airport
February 9–13, 1998

This page is intentionally left blank.

HIGH LIFT TECHNOLOGY DEVELOPMENT (TASK 33)

This study falls under the subject areas:

1) Concept development,

2) Attached flow flaps, and

3) Navier–Stokes methods

OUTLINE

The presentation of this paper is divided into five sections:

1) objectives,
2) accomplishments in 1997,
3) results, including both the CFD calculated results and the wind tunnel measured data,
4) concluding remarks, and
5) current plans

BOEING

OUTLINE

- Objectives
- Accomplishments in 1997
- Results
- Concluding remarks
- Current plans

BOEING

OBJECTIVES

The objectives of this study are:

1) to develop an integrated wind–tunnel/free–air CFD process to speed up CFD turnaround time in HSCT high–lift configuration development,

2) to study the effects of wind–tunnel wall and supports on the model aerodynamic characteristics, and

3) to validate/evaluate the CFD results by comparison with experimental data.

BOEING

OBJECTIVES

- Develop an integrated wind–tunnel/free–air CFD process to speed up CFD turnaround time in HSCT high–lift configuration development
- Investigate the effects of wind tunnel wall and model supports on the model aerodynamic characteristics
- Validate/evaluate the CFD resluts by comparison with experimental data

ACCOMPLISHMENTS IN1997

During FY 1997, a working CFD procedure has been developed and tested for wind tunnel flow simulation starting from a given free-air airplane grid and the surface definitions of wind tunnel wall and model supports to the final engineering force and moment integrations. The procedure will be discussed in the next two view graphs.

A Navier-Stokes CFD solution has been obtained for the 4%-scale M2.4-7A Arrow Wing inside the NASA/Ames 12-ft wind tunnel with model supporting posts.

A report, Boeing NA-97-1289, has been written to document the works performed in 1996-1997. Most of the materials presented in this paper are extracted directly from this report.

BOEING

ACCOMPLISHMENTS IN 1997

- Developed a CFD process for wind tunnel CFD flow simulation
- Obtained a Navier–Stokes CFD solution for the 4%–scale M2.4–7A Arrow Wing inside the NASA/Ames 12–ft wind tunnel with model supporting posts
- Documented CFD process, results, and comparison with wind tunnel test data as a Boeing report, NA–97–1289

BOEING

PROCEDURE FOR CFD SIMULATION OF WIND TUNNEL FLOW

This is a self-contained working CFD procedure for wind tunnel flow simulations. Programs are provided at every stage in the process to perform various tasks.

The procedure has effectively coupled the widely used NASA/LaRC's CFL3D/MAGGIE package with the NASA/Ames' FOMOCO package for overset grid flow simulations and force and moment integrations. As shown in the flow chart, the linkage between the two software packages is established by two utilities MKIB and MERGEGIB. MKIB reads the MAGGIE's interpolation data file and produces an iblank data file containing the grid connectivity information. MERGEGIB combines the connectivity information produced by MKIB into the PLOT3D/FAST grid file produced by CFL3D to recreate a PLOT3D/FAST grid file suitable for FOMOCO code. This recreated PLOT3D/FAST grid file and the CFL3D produced PLOT3D/FAST Q file can then be fed into FOMOCO for force and moment integrations with consideration of grid overlapping.

Also used are the NASA/Ames' FAST and XYPLOT. BROWSF is a PLOT3D/FAST grid and Q data based postprocessor. It's capabilities include listing and outputting various flow properties at user-specified grid points and/or at intersection between grids and any user-specified space plane. In addition, coordinate scaling and various coordinate transformations may be performed. It is of particular useful in processing CFD results to compare for models of varying scales.

The coupling of CFL3D with FOMOCO has elevated CFL3D to a new level of CFD production applications to complex geometries using overset grid technique.

BOEING

PROCEDURE FOR CFD SIMULATION OF WIND TUNNEL FLOW

- A very "concrete" CFD procedure
- Elevate CFL3D to a new level of production applications

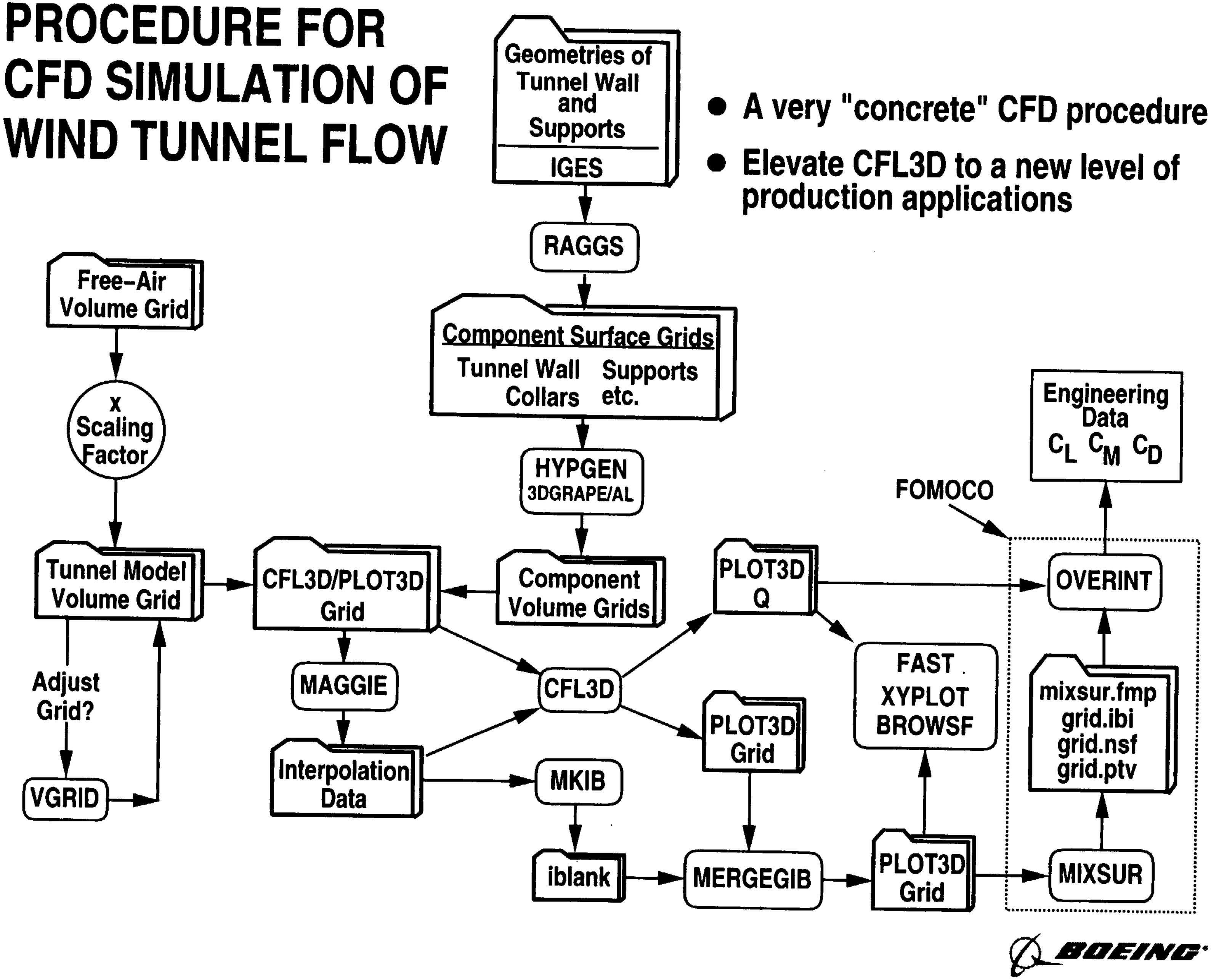

FOMOCO ZIPPER GRIDS

The top figure shows two overlapping surface grid regions. To account for grid overlapping, FOMOCO constructs a hybrid surface grid with zipper grids filling in each of the overlapping regions as shown in the lower figure. Force and moment integrations are performed on the non–overlapping hybrid grid.

FOMOCO ZIPPER GRIDS

USED FOR FORCE AND MOMENT INTEGRATIONS

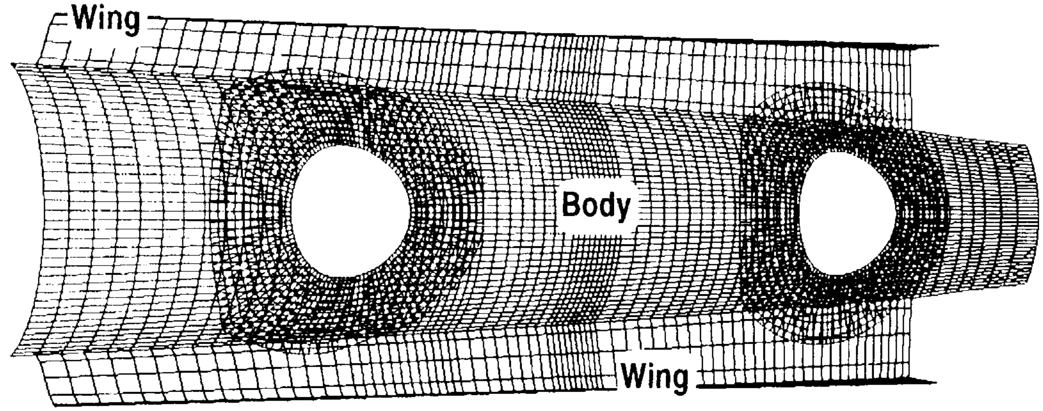

Overset Surface Grids

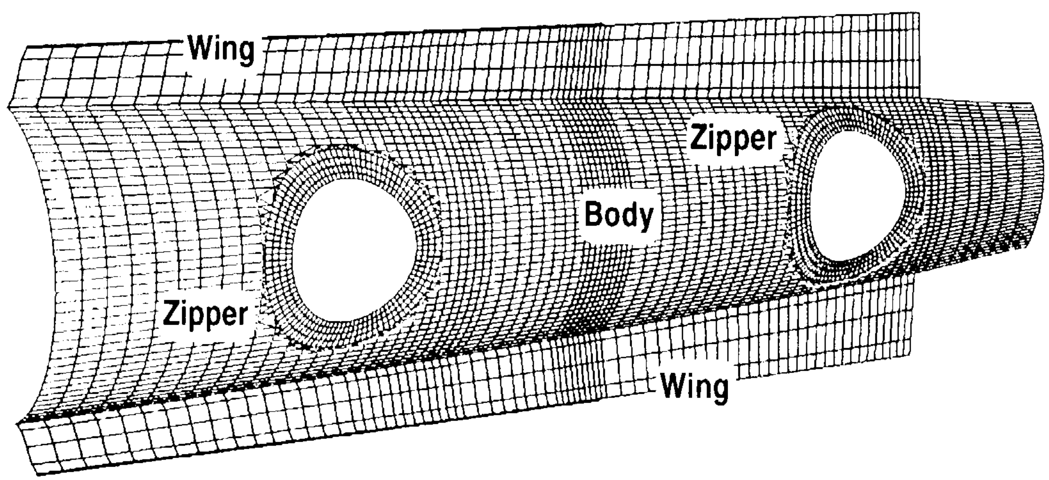

Hybrid Composite Surface Grid with Zipper Grids of Triangles

BOEING

HSCT ARROW WING M2.4–7A

The three CFD solutions to be presented are:

1) the full–scale free–air case,

2) the 4%–scale model/tunnel case, and

3) the 4%–scale model/tunnel/posts case.

The full–scale free–air solution was provided by Dr. Yeh of Boeing. The solution of the 4%–scale model/tunnel case was completed in 1996 while the solution of the 4%–scale model/tunnel/posts was completed in 1997. The CFD wind tunnel wall geometry is the NASA/Ames 12–ft wind tunnel cross section.

All the flows were calculated at Mach = 0.3, α = 10 degrees, and Re = 8 million.

The airplane has a 40–degree deflected LE flap and three 10–degree deflected TE flaps. A wing cross section is shown in the figure.

BOEING

HSCT ARROW WING M2.4–7A

1. M2.4–7A Free–Air CFD

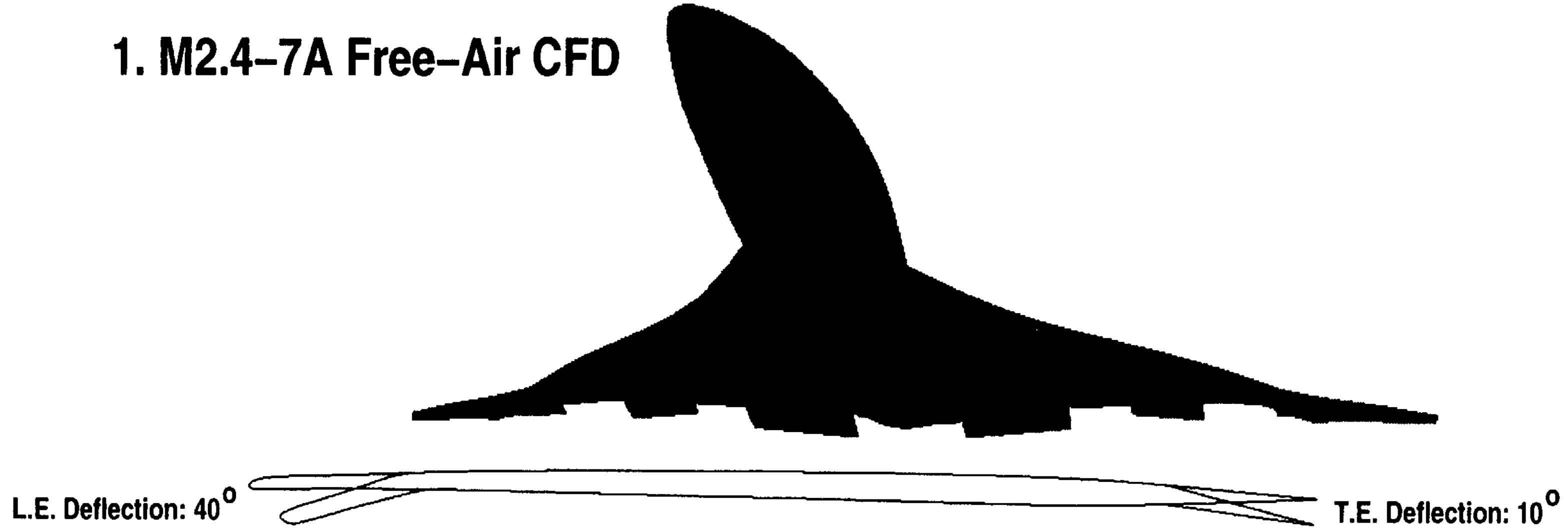

2. 4%–Scale M2.4–7A/Tunnel CFD

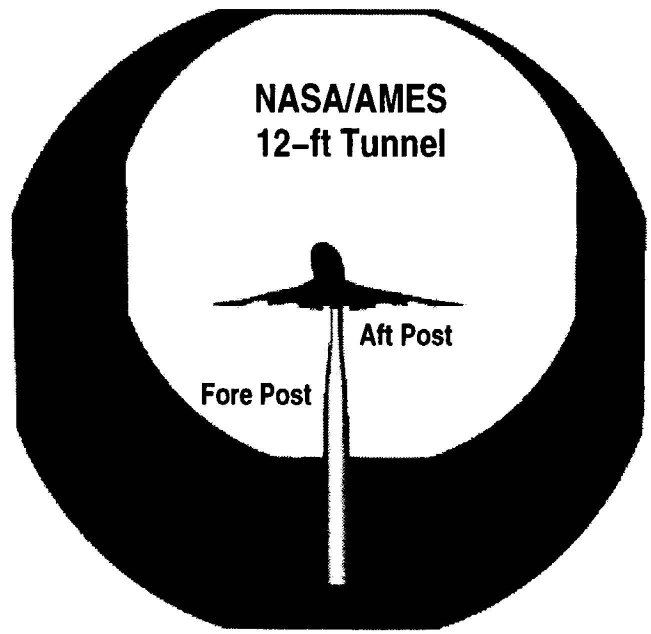

3. 4%–Scale M2.4–7A/Tunnel/Posts CFD

BOEING

OVERSET GRID

The key to speeding up CFD turnaround time is to employ overset grid technique, where a computational grid may be constructed from a series of simple, independently generated component grids.

This is a 3–D view of the 4%–scale M2.4–7A model situated inside the NASA/Ames 12–ft wind tunnel. Also shown is the overset grid in the plane of symmetry. The CFD grid consists of 9 blocks with a total of 6,214,873 grid points.

BOEING

OVERSET GRID

FOR THE 4%–SCALE HSCT ARROW WING M2.4–7A

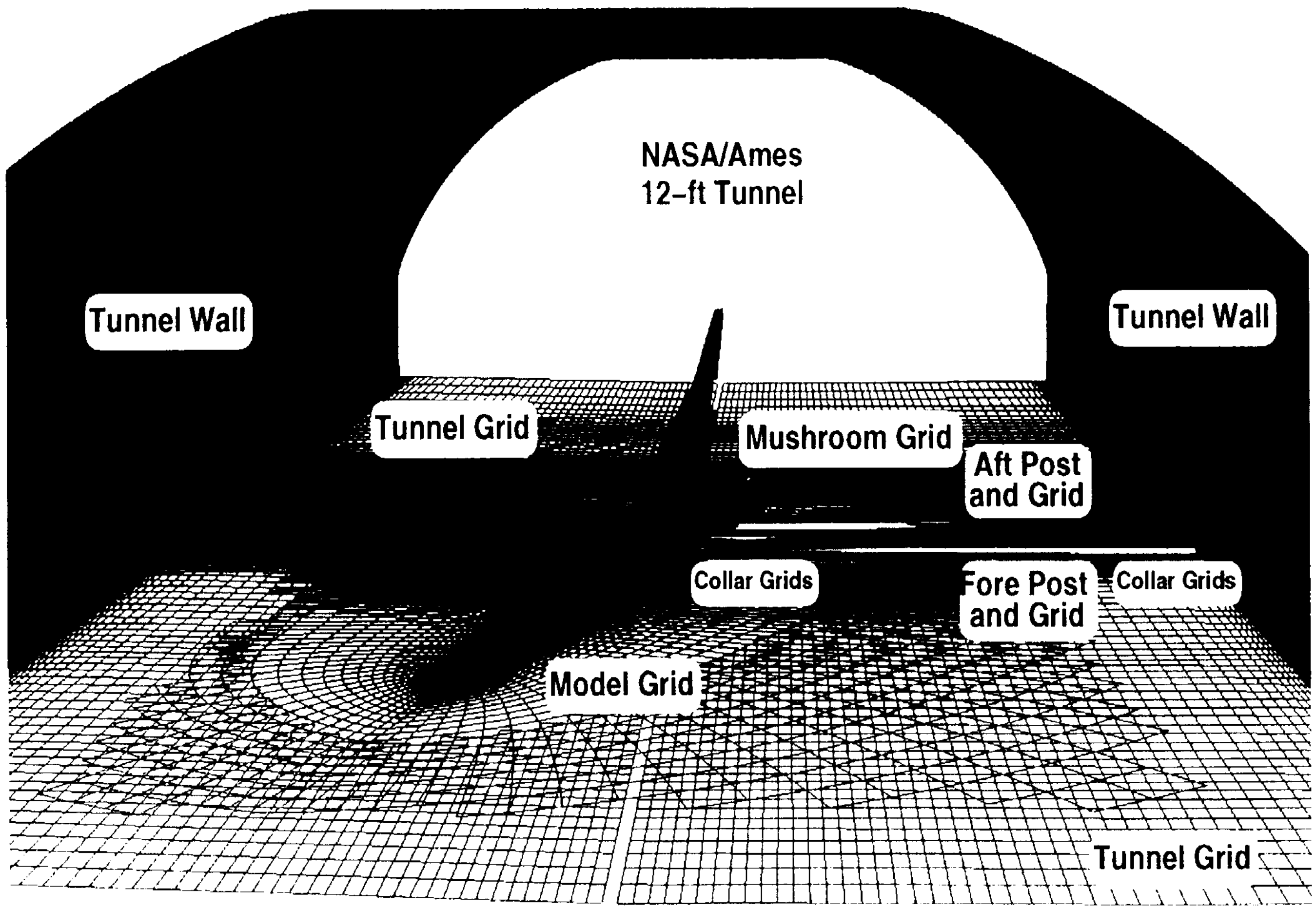

BOEING

MAGGIE CALCULATED OVERSET GRID

This figure shows the overlappings of the 9–block grid in the plane of symmetry.

MAGGIE CALCULATED OVERSET GRID
FOR THE 4%–SCALE HSCT ARROW WING M2.4–7A

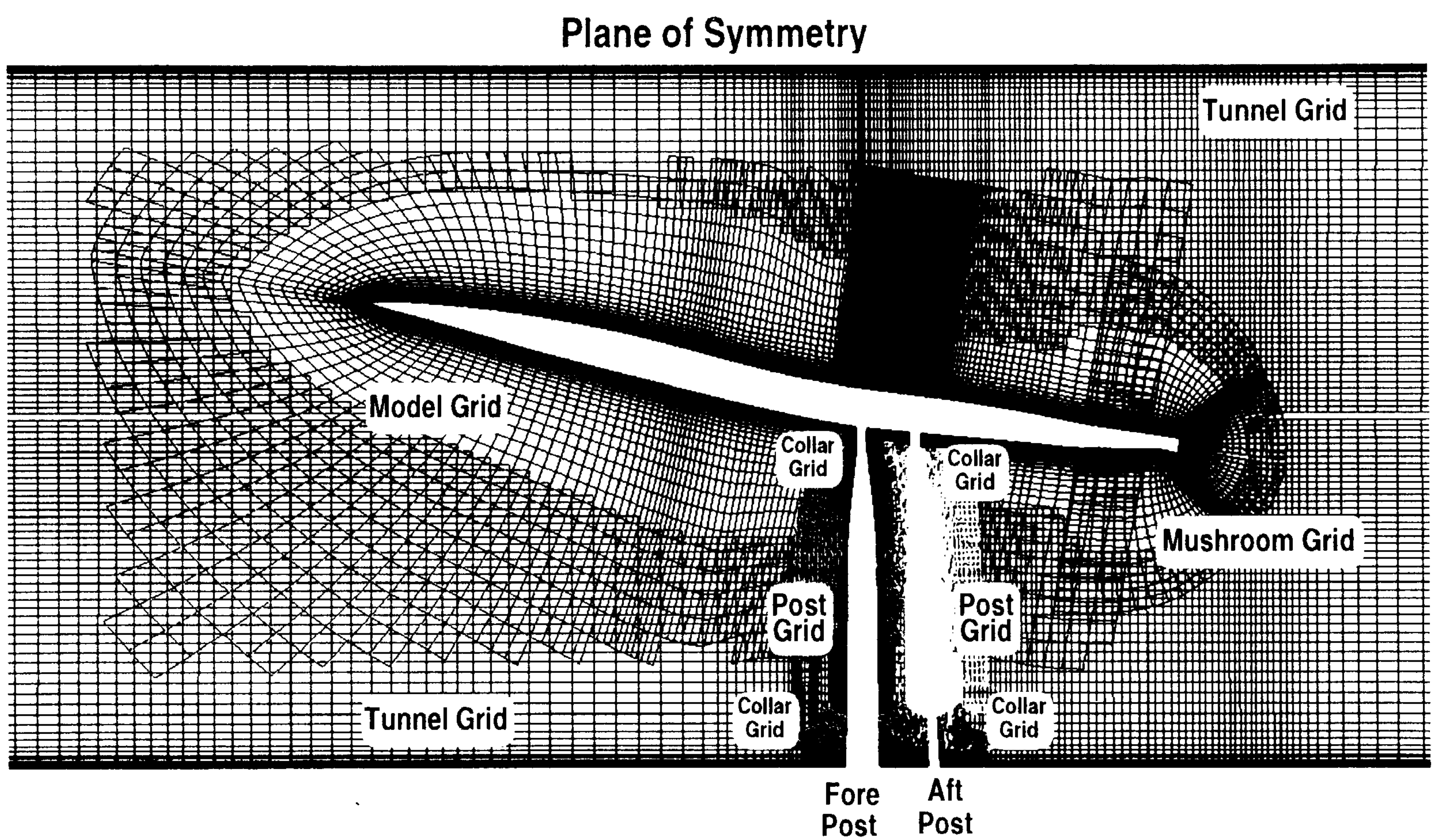

BOEING

CFD PARTICLE TRACES

Comparison of the lower left picture with the other two shows clearly that the model supporting posts have altered the over–wing vortex flow. In fact, the over–wing vortex flow has been suppressed and the flow became attached.

Wind–tunnel wall alone does not alter the over–wing vortex flow structure as shown in the upper and the lower left figures.

BOEING

CFD PARTICLE TRACES
M2.4–7A ARROW WING

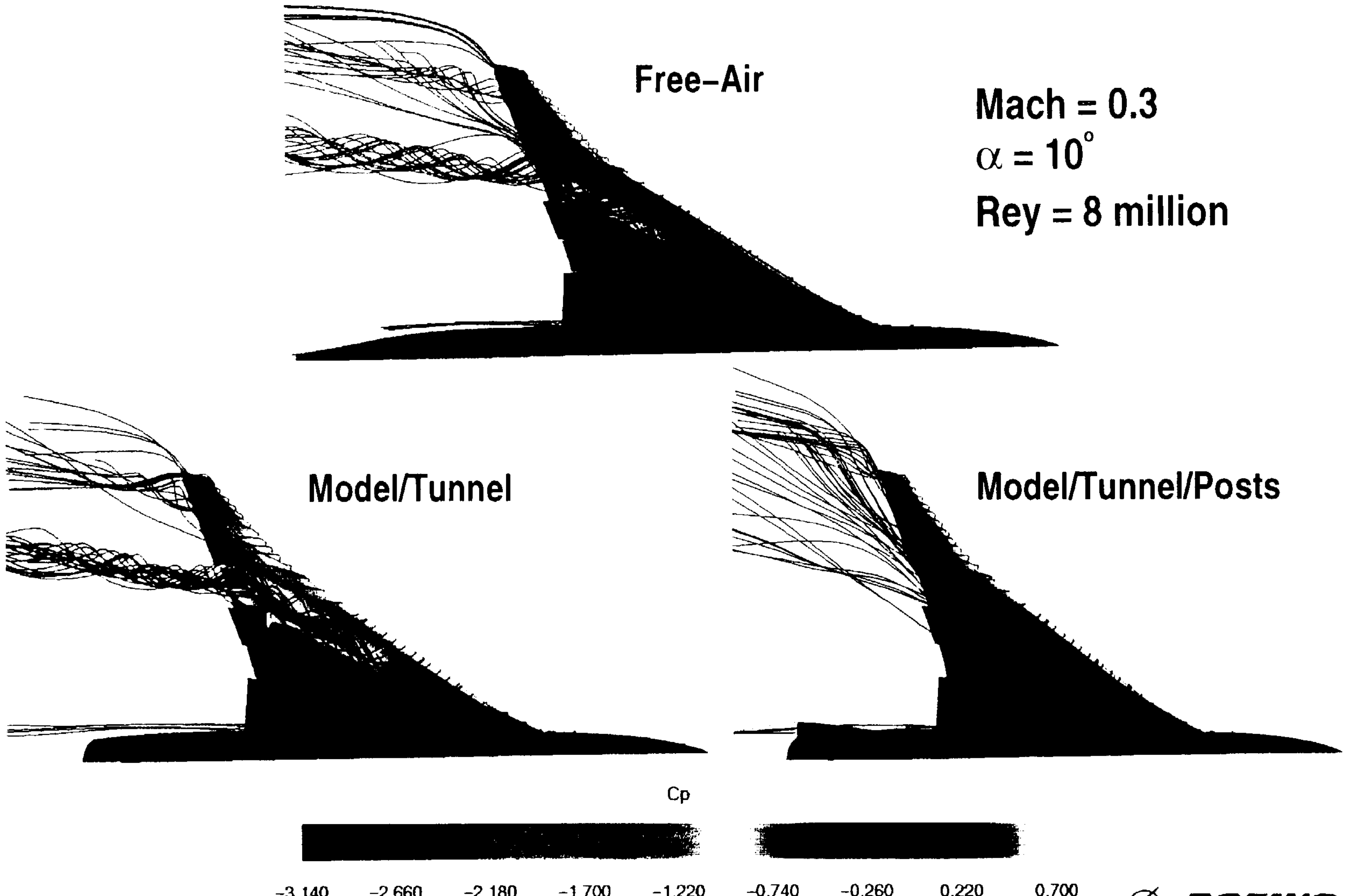

SURFACE PRESSURE CONTOURS

This figure further demonstrates the effect of model supporting posts on the flow structure.

There is a low pressure pocket on the wing upper surface in the free–air and mode/tunnel cases as shown in the upper two pictures. This low pressure pocket is due to the over–wing vortex flow as shown in the previous figure.

The patterns of the surface pressures for the free–air and model/tunnel cases are very similar as shown in the two upper pictures. However, the pattern of the surface pressure contours for the model/tunnel/posts case is very much different from those for the free–air and model/tunnel cases as shown in the figure.

BOEING

SURFACE PRESSURE CONTOURS
ON THE UPPER SURFACE OF ARROW WING M2.4–7A

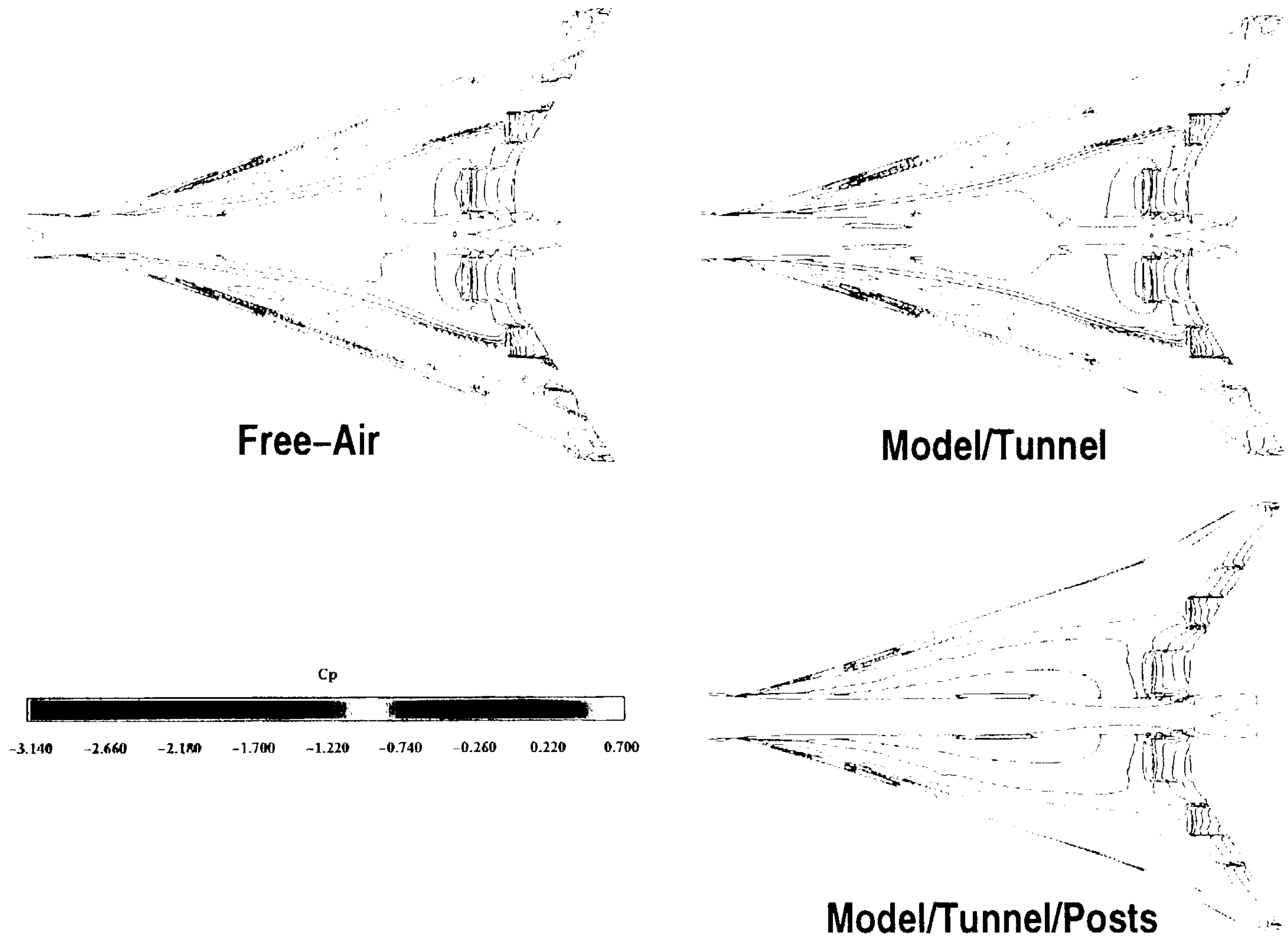

BOEING

SURFACE PRESSURE CONTOURS ON POSTS AND CROSS SECTIONS

The flow is unsteady due to the shedding of vortices from the two supporting posts as shown in the figure.

The current CFD grid was not intended to accurately capture the details of the unsteady flow phenomenon.

BOEING

SURFACE PRESSURE CONTOURS
ON POSTS AND CROSS SECTIONS

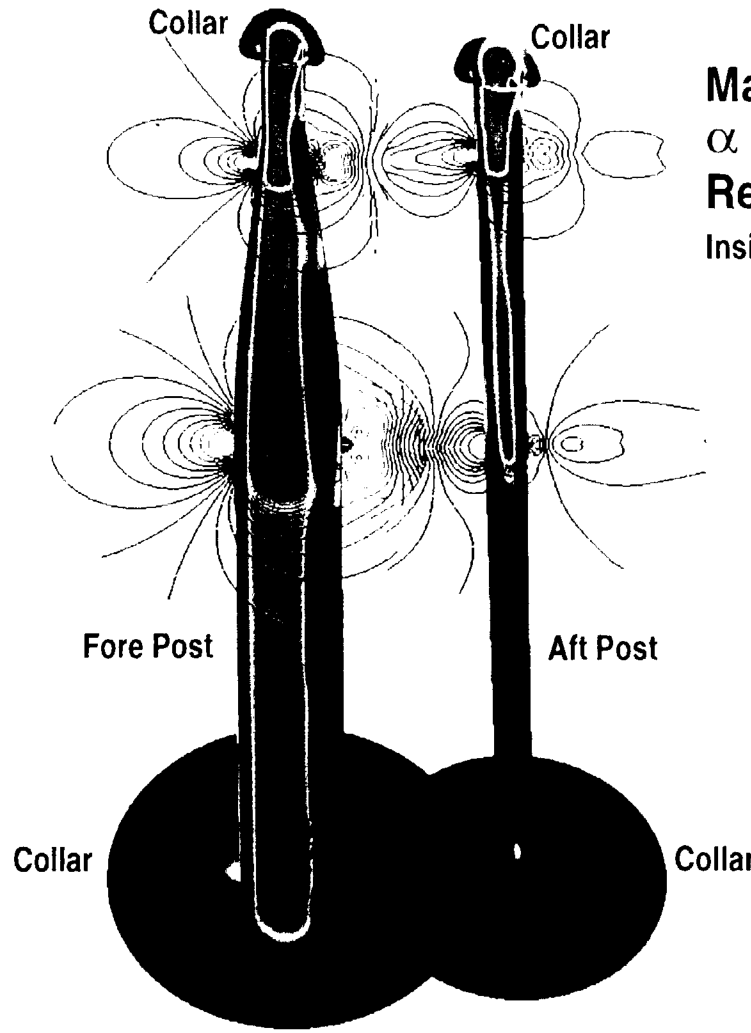

Mach = 0.3
$\alpha = 10^{\circ}$
Re = 8 Million
Inside NASA/Ames 12-ft Tunnel

BOEING

SURFACE PRESSURE CONTOURS ON MODEL/TUNNEL WALL/POSTS

This figure shows two 3–D views of the CFD calculated surface pressure contours for the model/tunnel/posts case.

BOEING

SURFACE PRESSURE CONTOURS

ON TUNNEL WALL/POSTS/4%-SCALE M2.4–7A MODEL

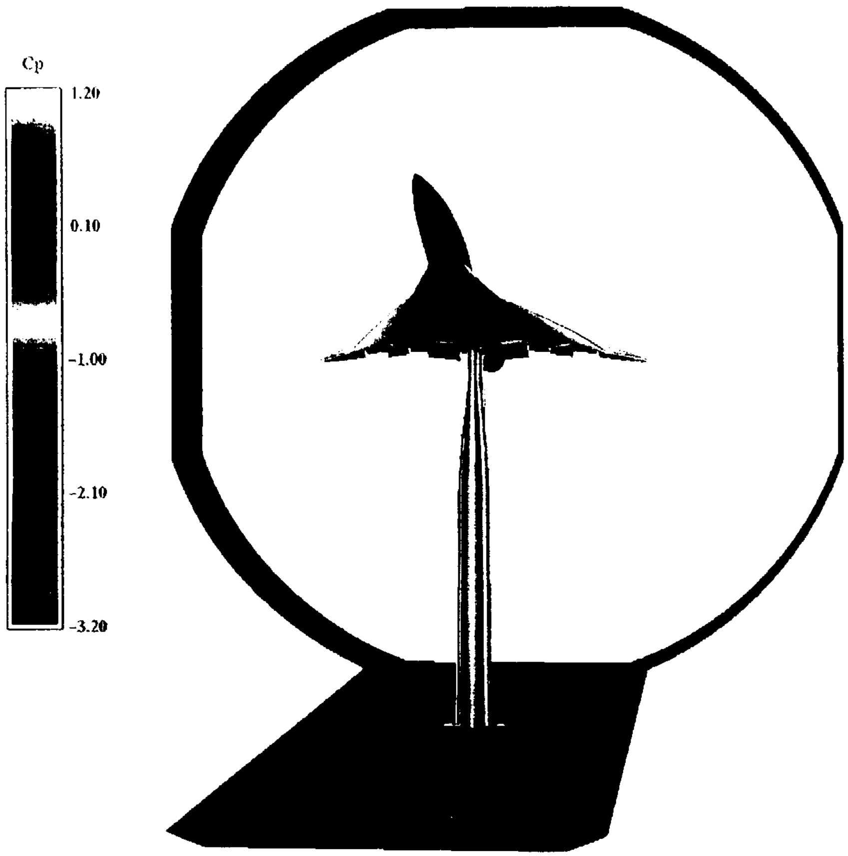

Mach = 0.3
$\alpha = 10^{\circ}$
Re = 8 Million
Inside NASA/Ames 12-ft Tunnel

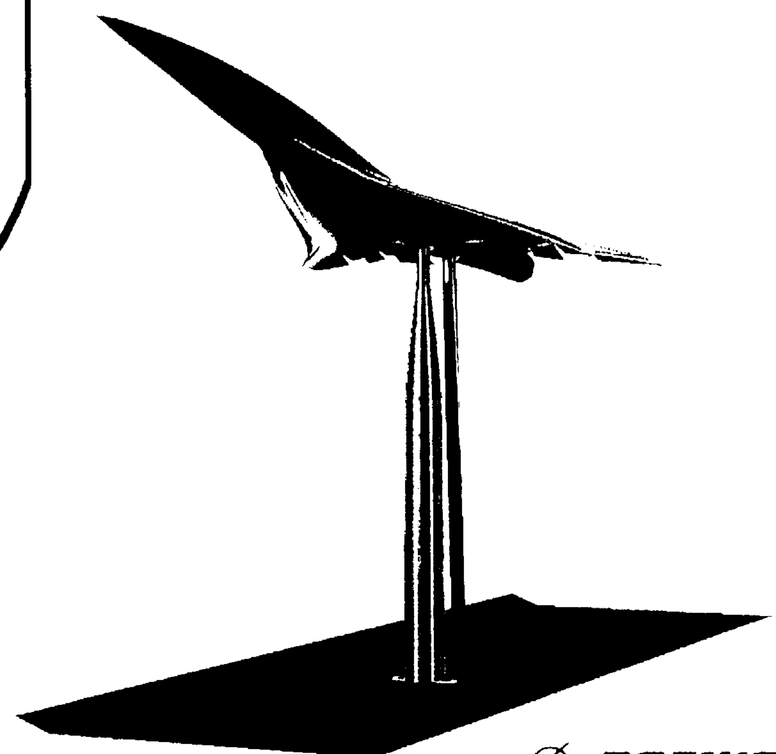

BOEING

LOCATION OF THE MOMENT AXIS

The location of the center of the moment axis is shown in this figure for $\alpha = 10$ degrees configuration. Also shown is the CFD coordinate system which has it's origin located at the pivot point and the x, y, and z axes pointing downstream, vertical, and spanwise directions, respectively.

BOEING

LOCATION OF THE MOMENT AXIS
INSIDE NASA/AMES 12-FT TUNNEL

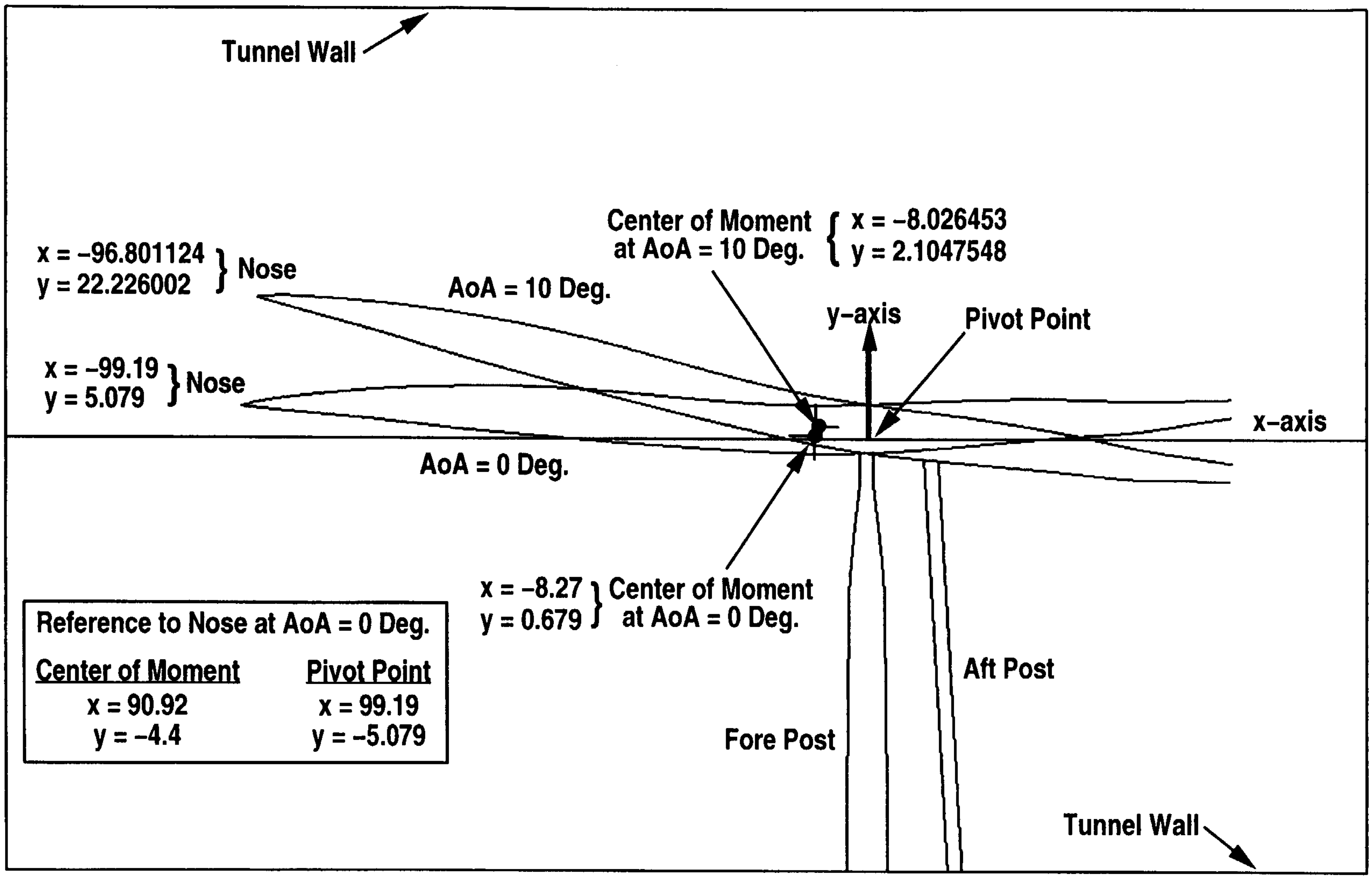

BOEING

COMPARISONS OF FORCES AND MOMENT

Here, the CFD calculated and wind tunnel measured C_L, C_D, and C_M are compared. The test data are from the NASA/Ames 12–ft wind tunnel test run 125. The test data are given at $\alpha = 9.894$ degrees and 10.916 degrees and have been corrected with the effects of tunnel wall, posts, and angle of attack.

As shown in the table, the effect of the wind tunnel wall alone is to give larger values in C_L, C_D, and C_M as compared with the free–air case. The effect of the model supporting posts is to lower the values of C_L, C_D, and C_M as compared with the model/tunnel case. Both CFD wind tunnel cases predict pitch up while pitch down was calculated by the free–air case and measured by the wind tunnel test.

Except C_M, the calculated free–air C_L, and C_D are correlated very well with the test data. Since the test data are in corrected form, a quantitative comparison can not be made between the test data and the two CFD wind tunnel cases.

BOEING

COMPARISONS OF FORCES AND MOMENT

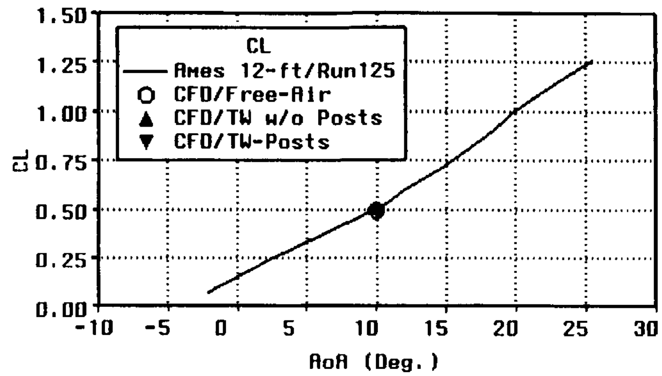

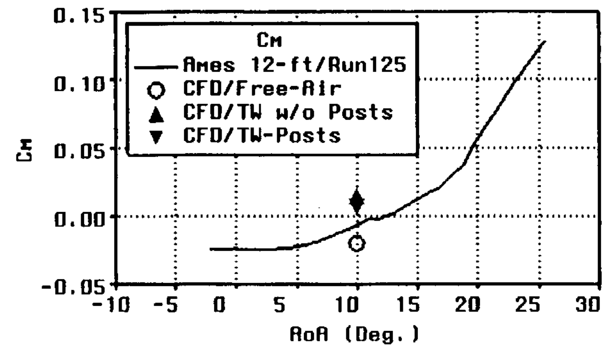

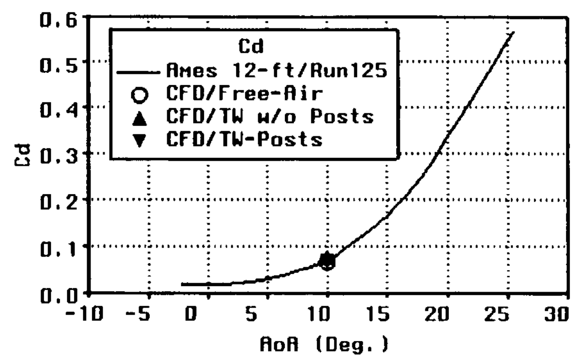

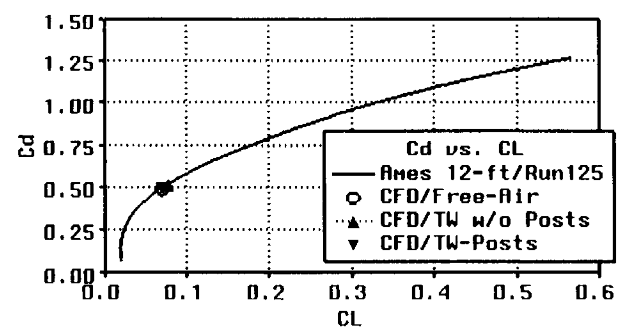

	α	C_L	C_D	C_M	L/D
Free-Air	10^{o}	0.49458	0.071459	−0.018853	6.92117
Model/Tunnel	10^{o}	0.51624	0.078614	0.015483	6.56676
Model/Tunnel/Posts	10^{o}	0.49807	0.072398	0.008716	6.87960
NASA/Ames 12-ft Tunnel	9.894^{o}	0.49954	0.071460	−0.006410	6.99048
NASA/Ames 12-ft Tunnel	10.916^{o}	0.54161	0.087206	−0.001690	6.21069

BOEING

THE SPAN STATIONS

It is regrettable that at the time this paper was written, the measured surface pressure data from the NASA/Ames 12-ft wind tunnel tests were not available for correlation with CFD results. Therefore, in the following, the pressure comparisons of the CFD results will be made with the measured pressure data from NASA/LaRC 14'x22' wind tunnel test run 152 at $\alpha = 9.92$ degrees.

This figure shows the five span stations where the measured pressure data are available. They are, in the full-scale dimensions: 115.25" (model, 4.61"), 119.75" (model, 7.67"), 372.25" (model, 14.89"), 602.25" (model, 24.09") and 715.00" (model 28.60").

THE SPAN STATIONS

WHERE CFD RESULTS ARE COMPARED WITH TEST DATA

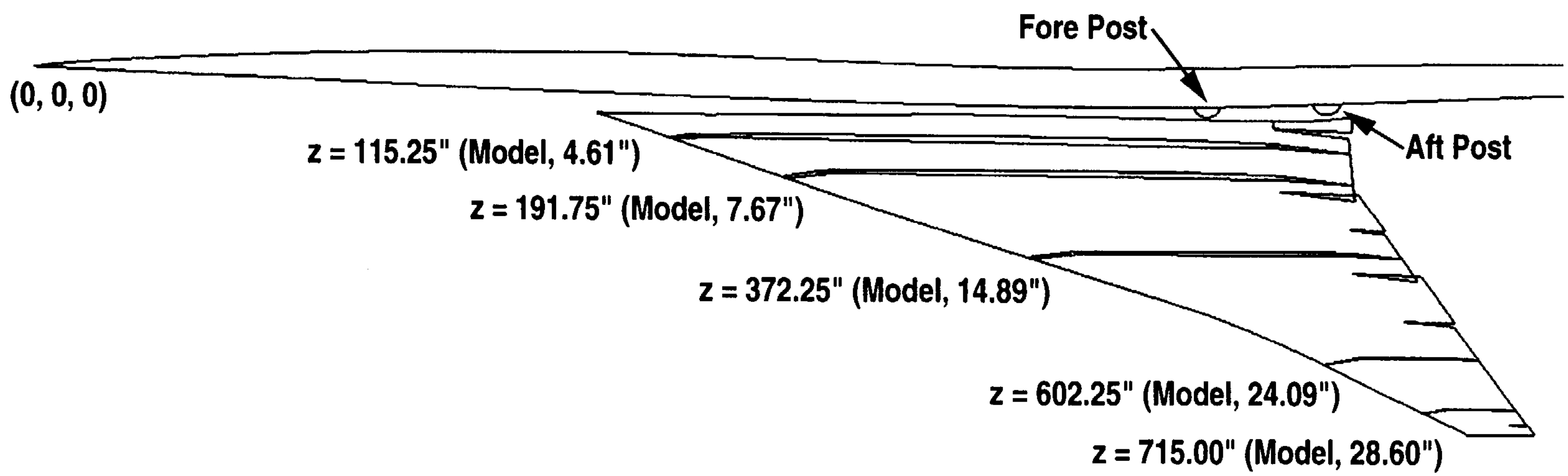

BOEING

COMPARISON OF CHORDWISE C_p

The pressure distributions of the free–air and model/tunnel cases are very similar. In most of the comparisons that follow the model/tunnel case will not be presented.

This figure shows the chordwise pressure comparisons for the two inboard wing sections. The solid lines represent the CFD calculated pressures for the model/tunnel/posts case, the chaindot for the free–air case, and the symbols for the test data from the NASA/LaRC 14'x22' wind tunnel test run 152.

In general, the characteristics of the pressure distributions are very similar for all the cases. The lower pressures on the lower surface for the model/tunnel/posts case as compared with the free–air case are due to the accelerated air flow due to the model supporting posts.

BOEING

COMPARISON OF CHORDWISE Cp

BETWEEN CFD CALCULATED AND WIND TUNNEL TESTED RESULTS

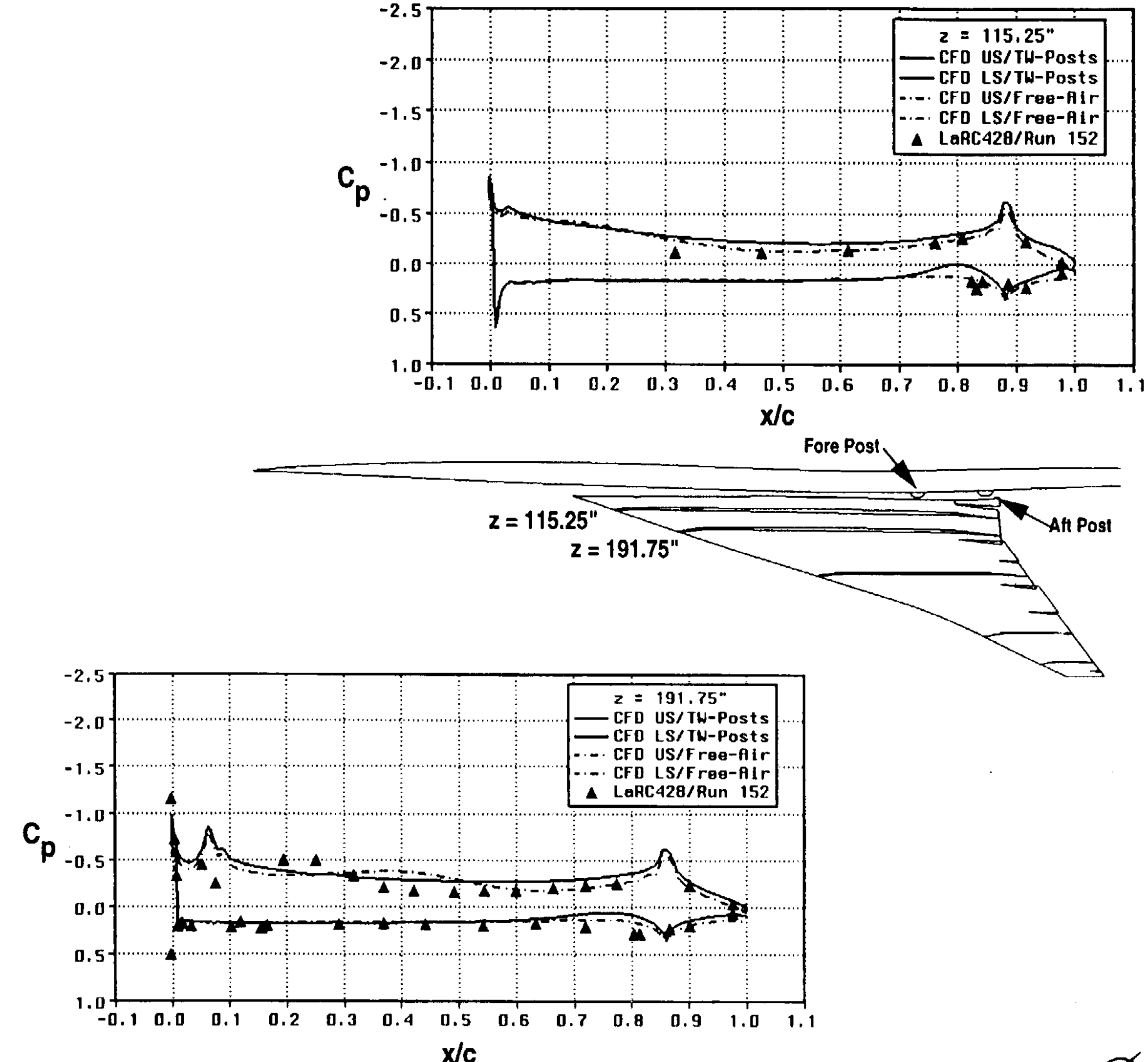

BOEING

COMPARISON OF CHORDWISE C_p (Continued)

Again, the low pressure pocket in $0.4 < x/c < 0.8$ for the free–air and model/tunnel cases is due the the over–wing vortex flow.

The test data seems to confirm the CFD calculated effect of the model supporting posts on the over–wing flow when the solid line is compared with the symbols.

COMPARISON OF CHORDWISE Cp

BETWEEN CFD CALCULATED AND WIND TUNNEL TESTED RESULTS

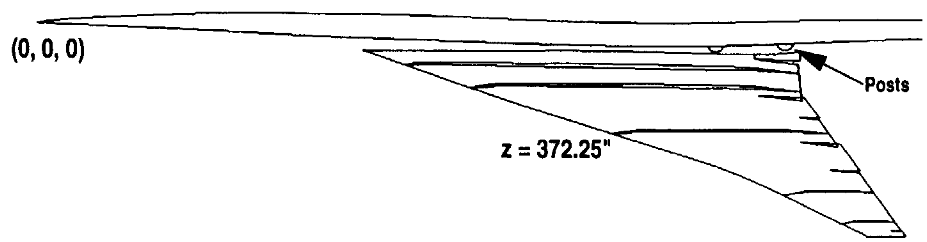

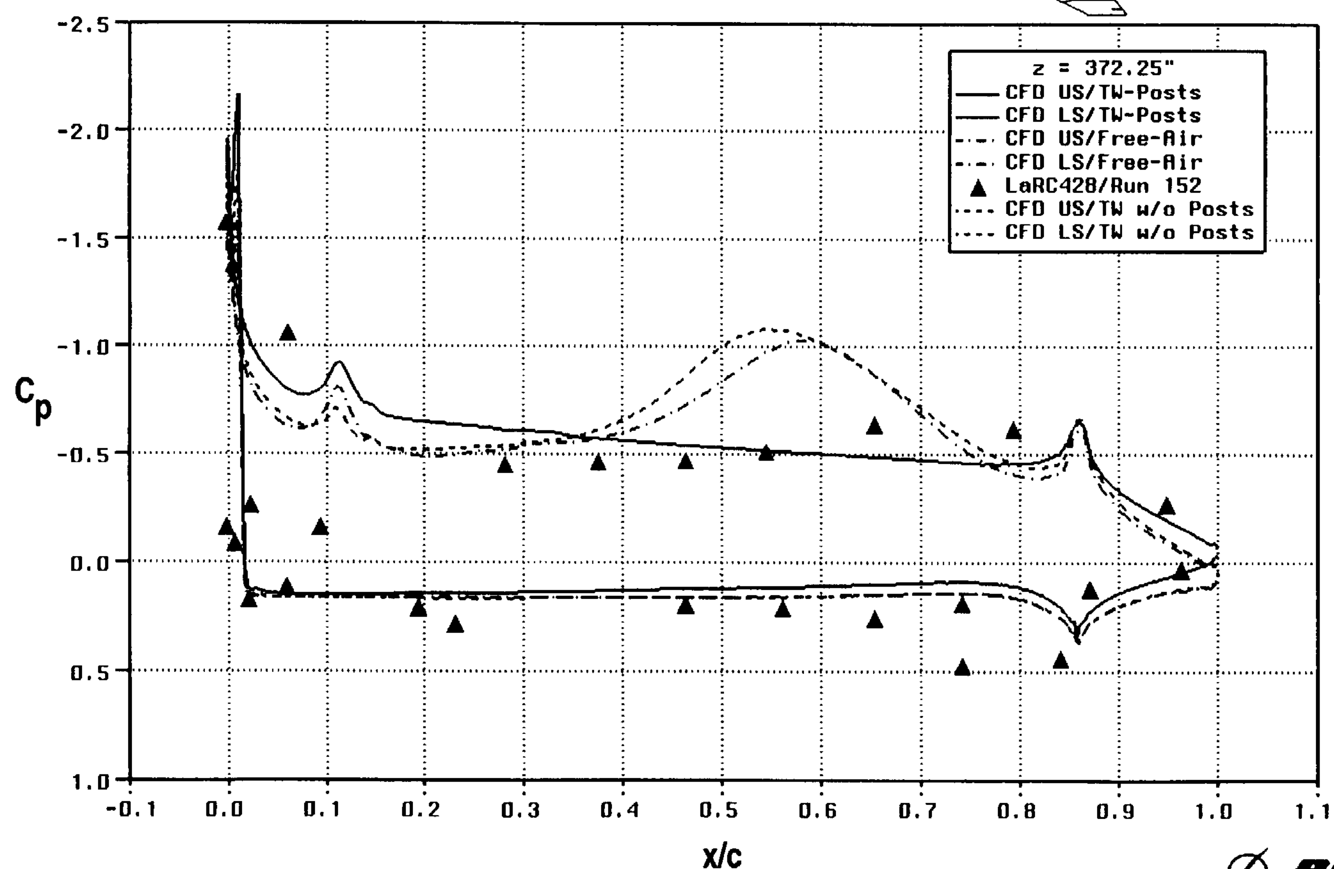

BOEING

COMPARISON OF CHORDWISE C_p (Concluded)

The chordwise pressures for the two outboard sections are shown in this figure. The lower surface pressures are correlated well for all the cases. The test data on the upper surface are somewhat scattered.

BOEING

COMPARISON OF CHORDWISE Cp

BETWEEN CFD CALCULATED AND WIND TUNNEL TESTED RESULTS

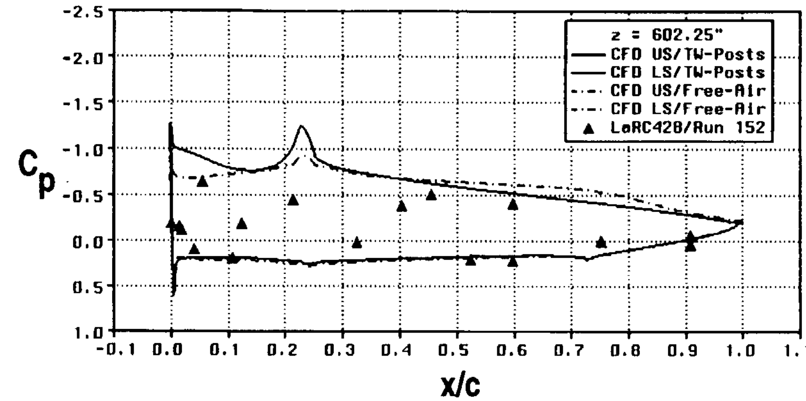

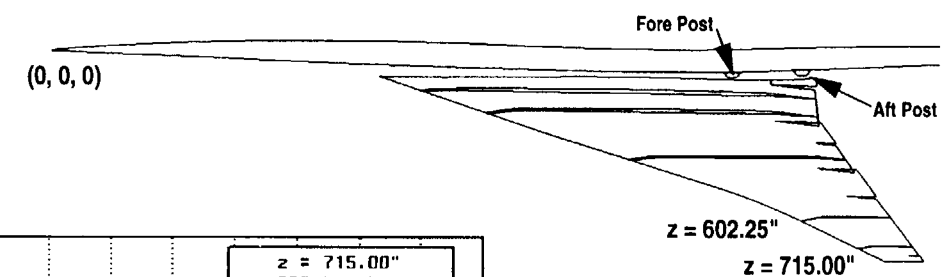

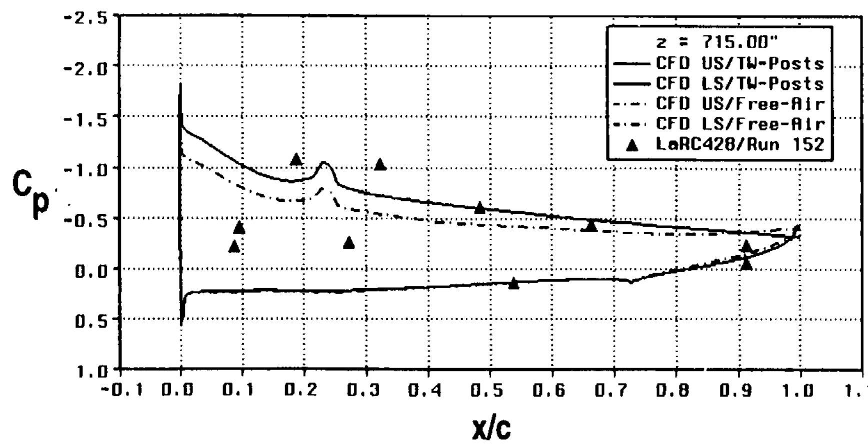

BOEING

THE AXIAL STATIONS

This figure shows the seven axial stations where the measured pressure data are available. They are, in the full-scale dimensions: 1546.40" (model, 61.85"), 1792.48" (model, 71.69"), 2009.75" (model, 80.39"), 2227.78" (model, 81.11"), 2445.80" (model, 97.83"), 2671.35" (model, 106.85"), and 2879.00" (model, 115.16").

BOEING

THE AXIAL STATIONS

WHERE CFD RESULTS ARE COMPARED WITH TEST DATA

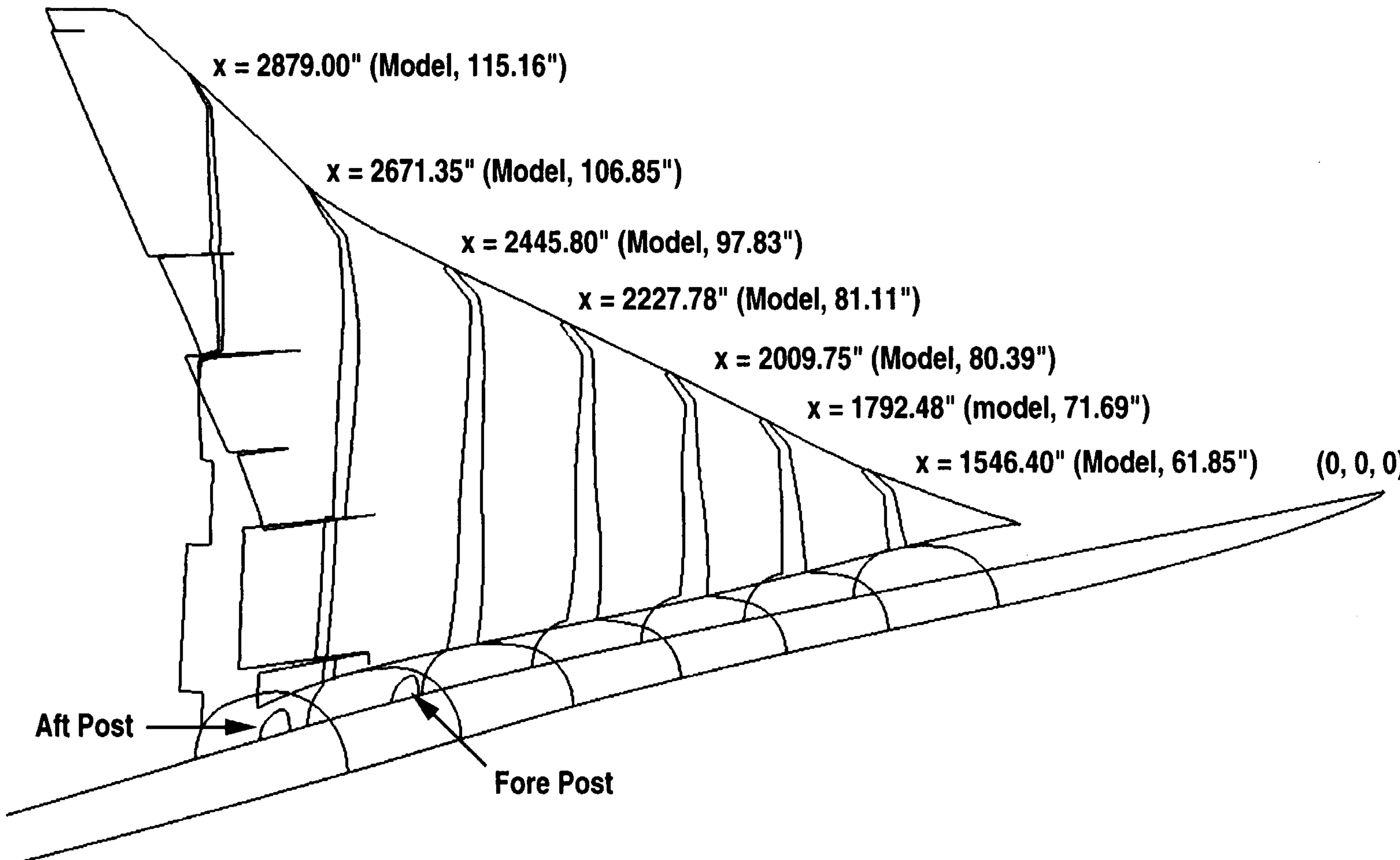

BOEING

COMPARISON OF SPANWISE C_p

The discrepancies between the two CFD results are due mainly to the over–wing vortex flow existing in the free–air case.

BOEING

COMPARISON OF SPANWISE Cp
BETWEEN CFD CALCULATED AND WIND TUNNEL TESTED RESULTS

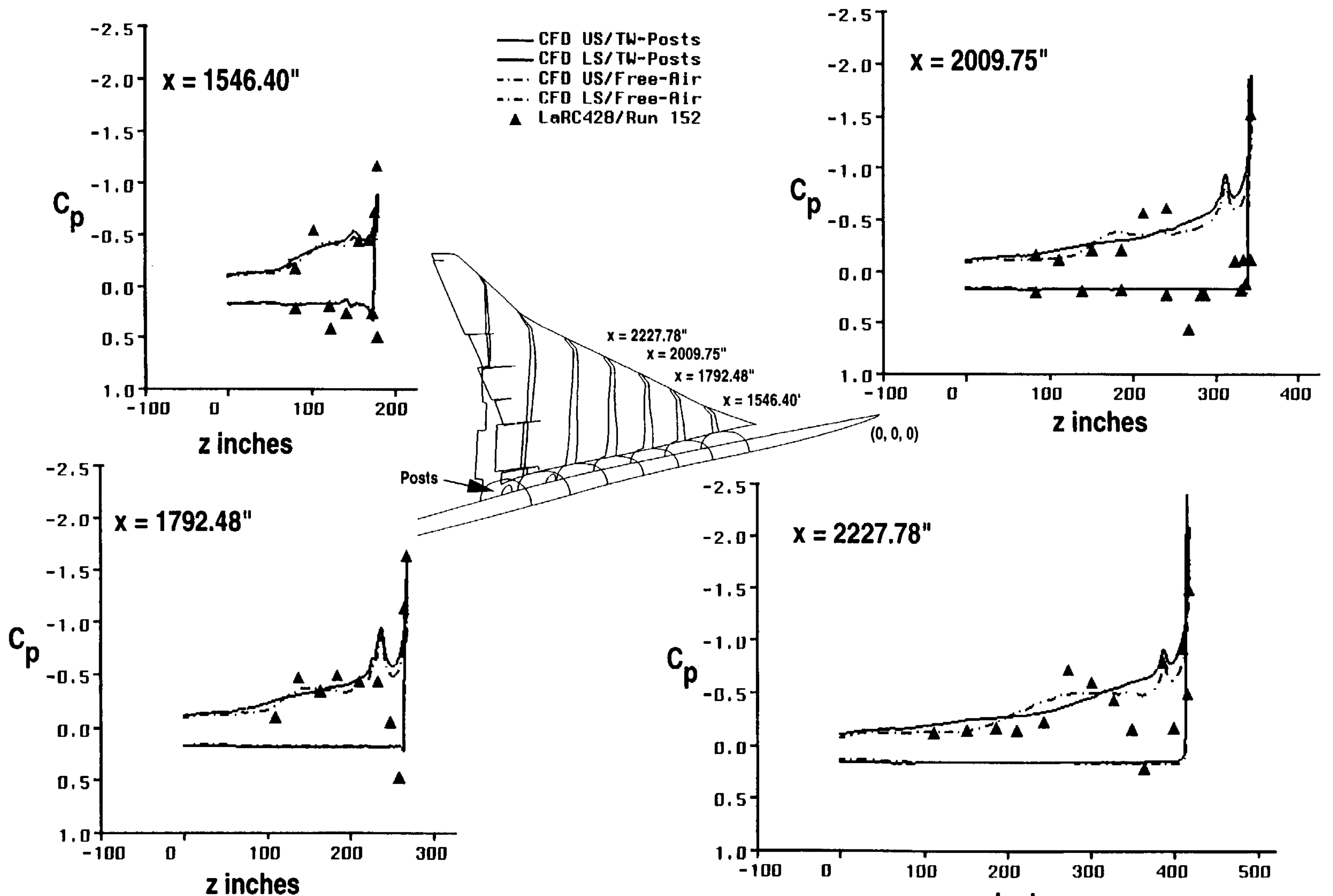

BOEING

COMPARISON OF SPANWISE C_p (Concluded)

Again, the discrepancies between the two CFD results are due mainly to the over–wing vortex flow existing in the free–air case.

BOEING

COMPARISON OF SPANWISE Cp

BETWEEN CFD CALCULATED AND WIND TUNNEL TESTED RESULTS

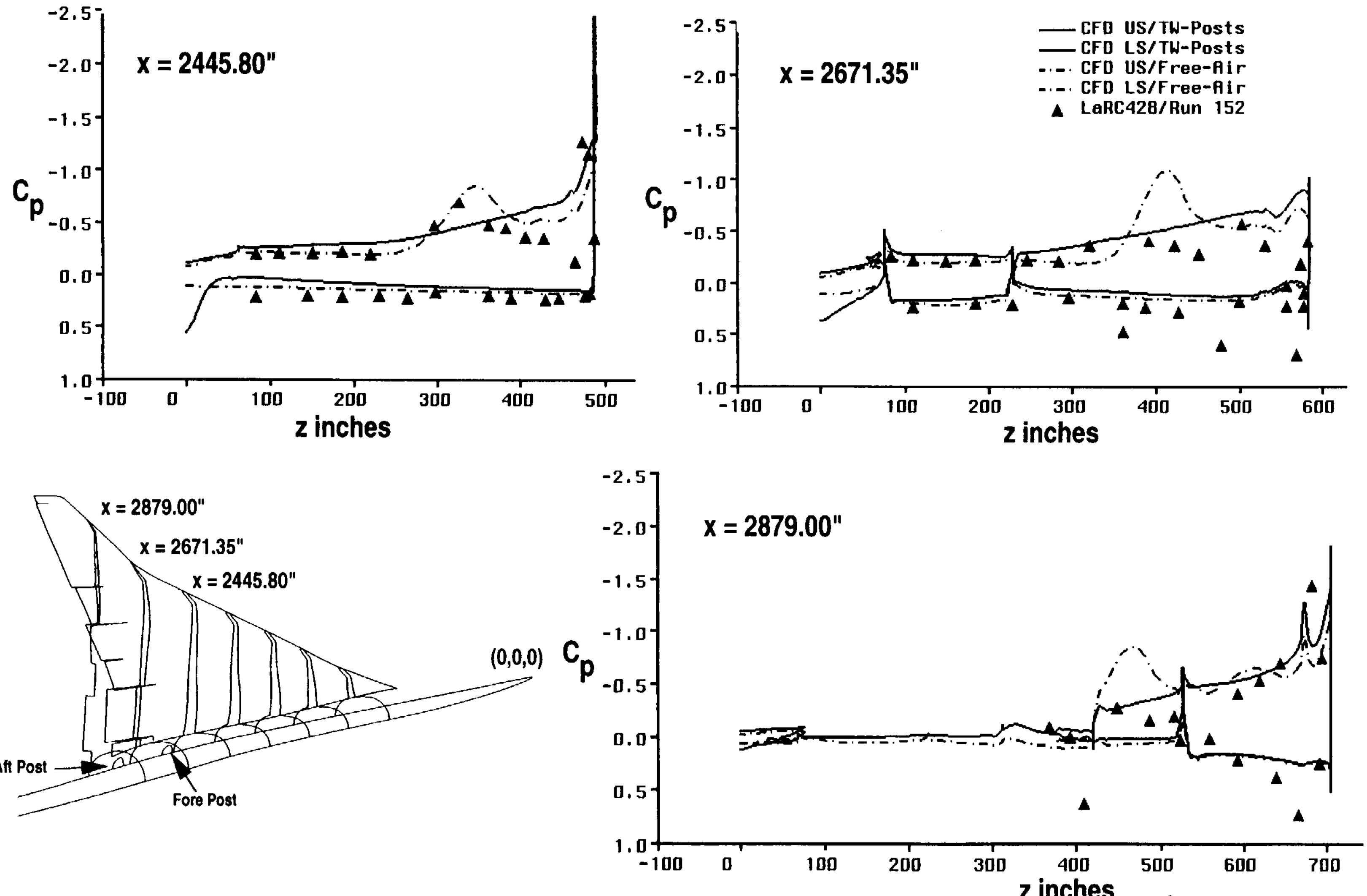

BOEING

COMPUTER USAGE

The computer usage is summarized in this figure. All the computations were performed on the NASA/NAS Cray C90.

BOEING

COMPUTER USAGE

	Number of Grid Points	MAGGIE CPU Time (Hrs. on C90)	CFL3D CPU Time (Hrs. on C90)	CFL3D Time Steps	CFL3D Memory (MWords)
Model/Tunnel	3,689,755	0.93196	21.33	2412	153.9883
Model/Tunnel/Posts	6,214,873	1.92277	66.42	3752	259.1563

BOEING

CONCLUDING REMARKS

A self-contained working CFD procedure has been presented for wind tunnel flow simulations.

The procedure has been applied to obtain two Navier-Stokes solutions for the 4%-scale M2.4-7A model inside the NASA/Ames 12-ft wind tunnel with and without posts.

The effect of the tunnel wall alone was found to give larger values in forces and moment as compared with the free-air case. However, tunnel wall alone did not change the over-wing vortex flow structure existing in the free-air case.

The effect of the model supporting posts has been found to eliminate the over-wing vortex flow existing in the free-air case. The test data from NASA/LaRC 14'x22' wind tunnel tests seemed to support this observation.

Good quality test data are in need to further validate CFD solutions.

In order to provide adequate and valuable data for CFD validation, it is recommended to use CFD to identify locations of pressure ports for wind tunnel data measurement.

CONCLUDING REMARKS

- A self-contained working CFD procedure has been presented for wind tunnel flow simulations and applied to the 4%-scale M2.4-7A Arrow Wing inside the NASA/Ames 12-ft wind tunnel with and without model supporting posts
- The effect of the tunnel wall alone was found to give larger values in forces and moment as compared with the free-air case. However tunnel wall alone did not change the over-wing vortex flow structure existing in the free-air case
- The effect of the model supporting posts has been found to eliminate the over-wing vortex flow existing in the free-air case. The test data from the NASA/LaRC 14'x22' wind tunnel tests seemed to support this observation
- Good quality test data are in need to further validate CFD solutions
- It is recommended to use CFD to identify locations of pressure ports for wind tunnel data measurements

BOEING

CURRENT PLANS

The current plans consist of the following three tasks:

1) Compare the existing CFD solution for the M2.4–7A Arrow Wing in NASA/Ames 12–ft wind tunnel with experimental data.

2) Evaluate the the agreement with the test data and refine the computational model if necessary.

3) Apply the established computational model to the Technology Concept Aircraft (TCA) model in the NASA/Ames 12–ft wind tunnel and compare the CFD results with the experimental data to be obtained.

CURRENT PLANS

- Compare the existing CFD solutions for the M2.4–7A Arrow Wing in the NASA/Ames 12–ft wind tunnel with experimental data
- Evaluate the agreement with the test data and refine the computational model if necessary
- Apply the established computational model to the Technology Concept Aircraft (TCA) model in the NASA/Ames 12–ft wind tunnel and compare the CFD results with the experimental data to be obtained

BOEING

This page is intentionally left blank.

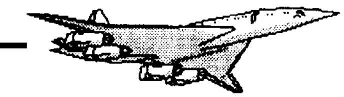

4% Arrow Wing Model Test in NASA Ames 12ft. Pressure Tunnel

Robin Edwards, Ryan Polito, and
Roger Clark

Boeing, Long Beach

HSR Airframe Technical Review

Los Angeles, California February 9-13, 1998

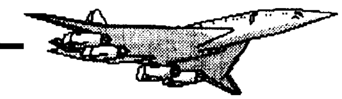

This figure shows the overview of the high lift program

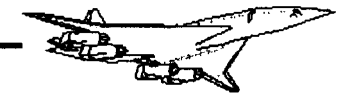

Increase L/D, Develop Analysis/Design Methodology

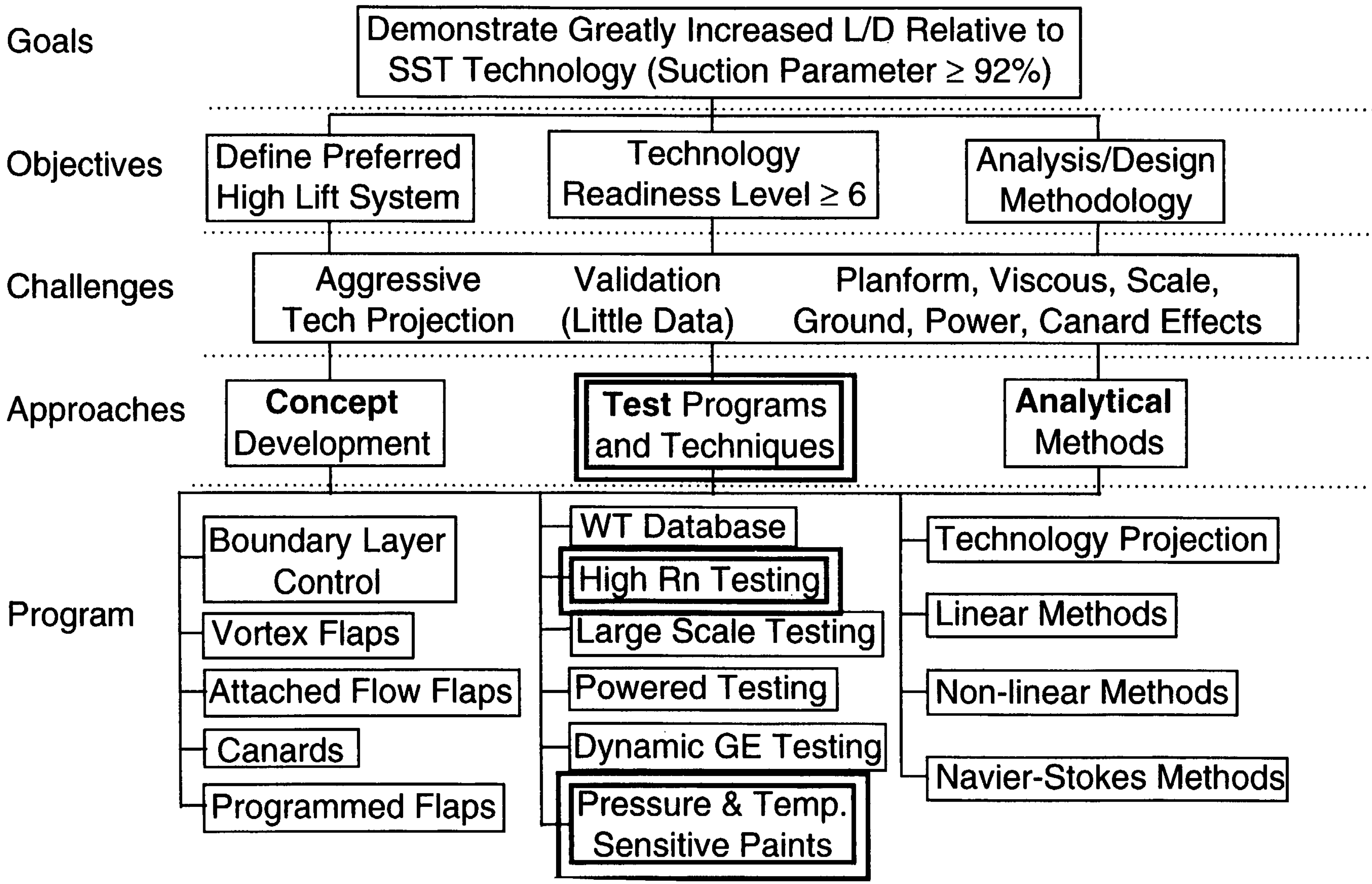

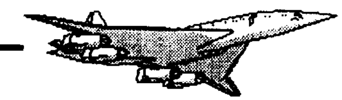

This figure shows an outline of the presentation

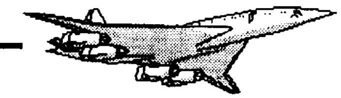

Outline

- Test objectives
- Test & Model Details
- Tunnel to tunnel comparison
- Effect of leading-edge radius increase
- Flap optimization
- Reynolds number effects
- Model deformation
- Flow visualization
- Summary

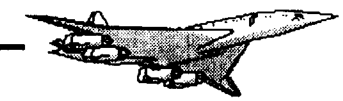

This figure shows the test objectives for the test of the M2.4-7A Arrow Wing Model in the Ames 12' Pressure Tunnel

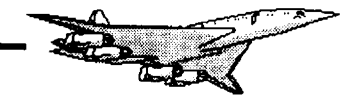

Test Objectives

- Compare results with previous test in Langley 14'x22' tunnel
- Investigate effect of increased le radius
- Investigate Re no effects on an alternate planform
- Optimize le/te flap deflection for climb
- Gather wing deformation data (LaRC)
- Gather flow visualization data
  - mini-tufts (Boeing)
  - pressure sensitive paint (ARC)

This figure shows the main details of the test of the M2.4-7A Arrow Wing Model in the Ames 12' Pressure Tunnel

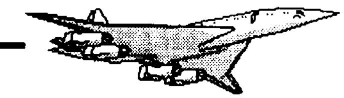

TEST DETAILS

- Tested 3 Feb.- 8 Mar 1997
- 363 Runs in 240 hr. (1.51 Runs/hr)
- Mach no range 0.225- 0.575
- Re no range
  - 1.88-8.51 Million/ft
  - 7.06-31.96 Million/MAC
- Pressure range 1- 6 atmospheres.
- Supported by - MDC, BCAG, LMAS, ARC, LaRC.

This figure shows the main details of the 4% M2.4-7A Arrow Wing Model

4% M2.4-7A Arrow Wing Model

Reference Quantities	
Sref	14.32 sq. ft.
CMAC	45.10"
LE Sweep	71°/61.5°
TE Sweep	0°/31.2°
AR	1.84

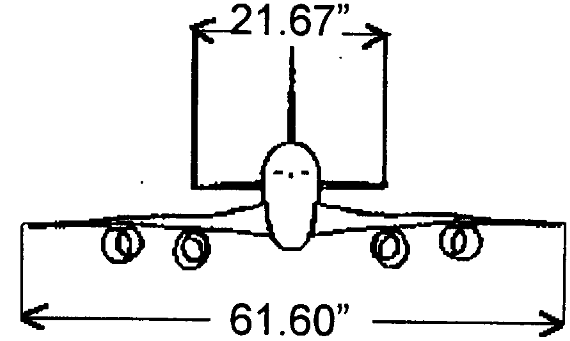

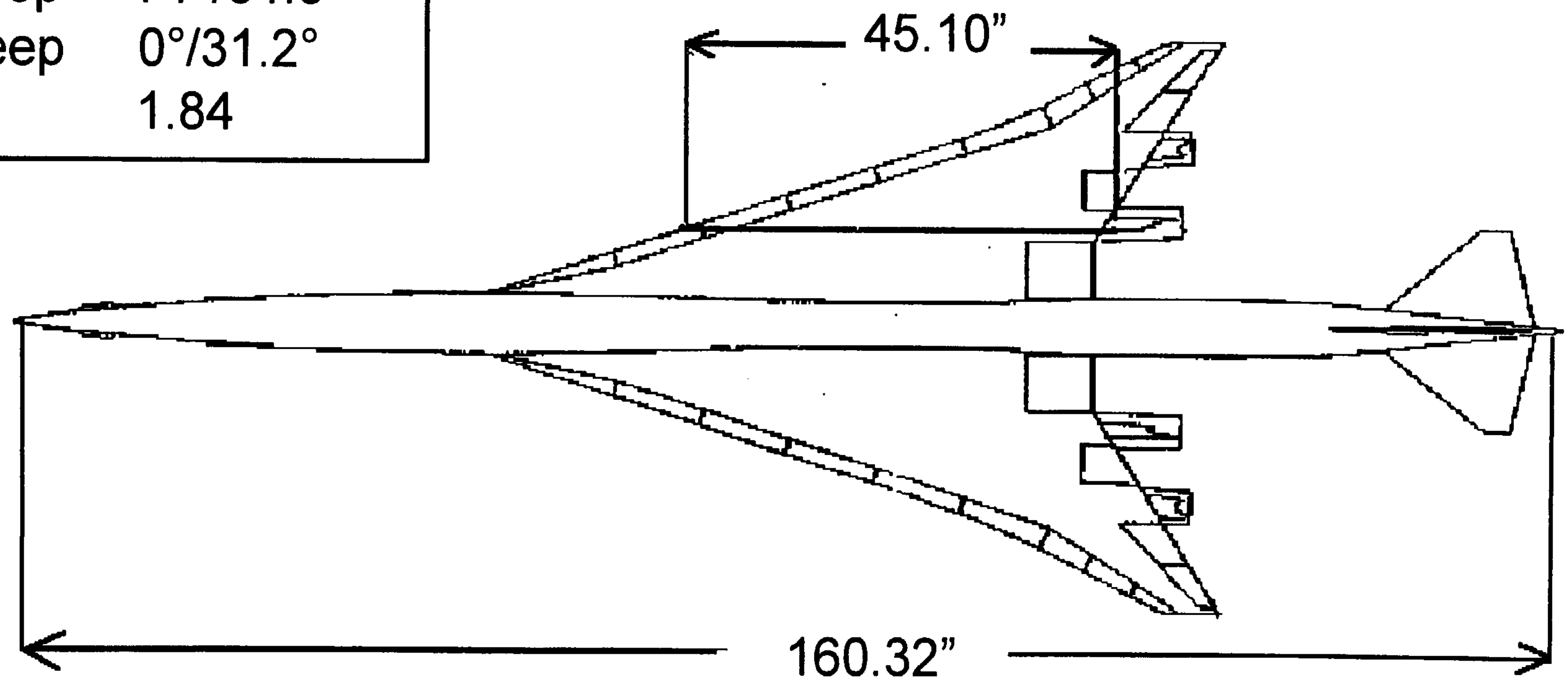

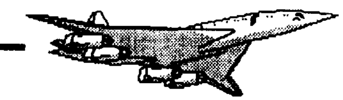

This page is intentionally blank

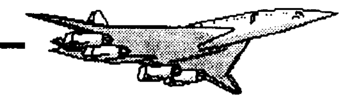

Comparison with LaRC 14'x22' Test

This figure shows a test to test comparison of the data obtained in the ARC 12' tunnel with that obtained in the LaRC 14'x22' low speed wind tunnel. This figure shows the lift and pitching moment curves. The lift agrees reasonable well with the 14'x22' data, while there is a bigger difference observed in the pitching moment. This difference is believed to be mainly due to the post interference. The 14'x22' test used a blade mount which will cause less interference (at zero side slip angle) than the bipod mount used in the 12' test. The bipod post mount is similar in diameter to the post mount used for the Ref H Upflow and Interference (U & I) test in the 14'x22' tunnel, and the U & I test did indicate that the post support will have a significant effect on the pitching moment.

HSR Airframe Technical Review Feb. '98

HSCT High Lift Aerodynamics

Comparison with LaRC 14x22 Data

Tail off, 40°/10° Flaps

Lift Curve

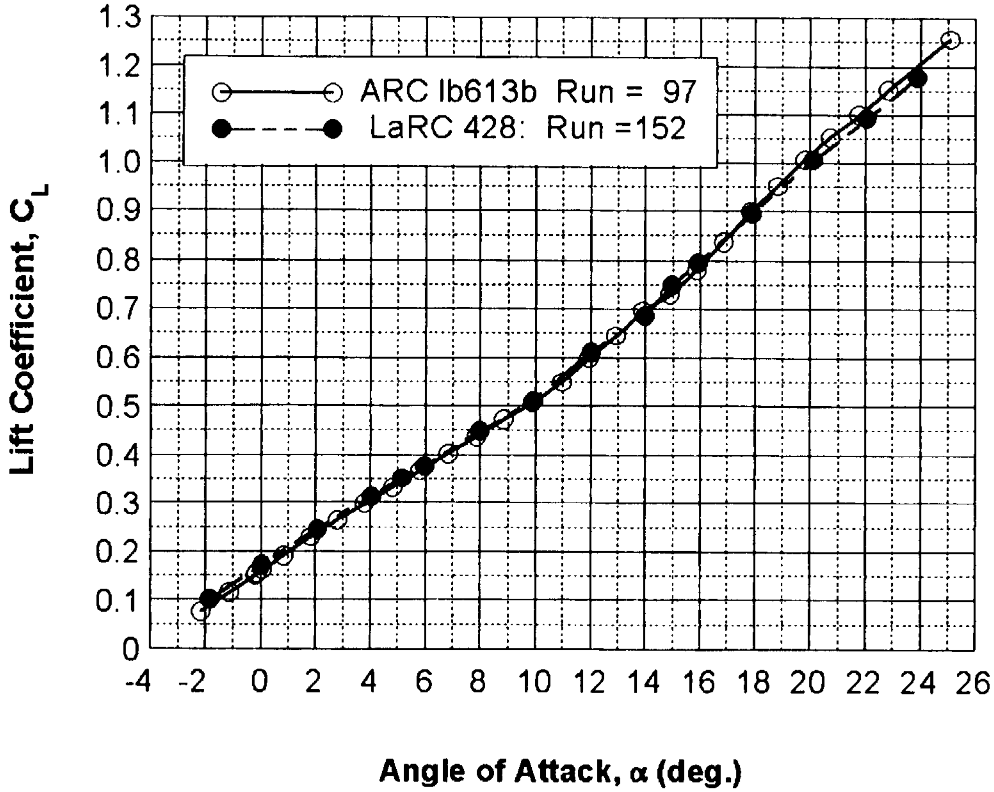

Lift Variation with Pitching Moment

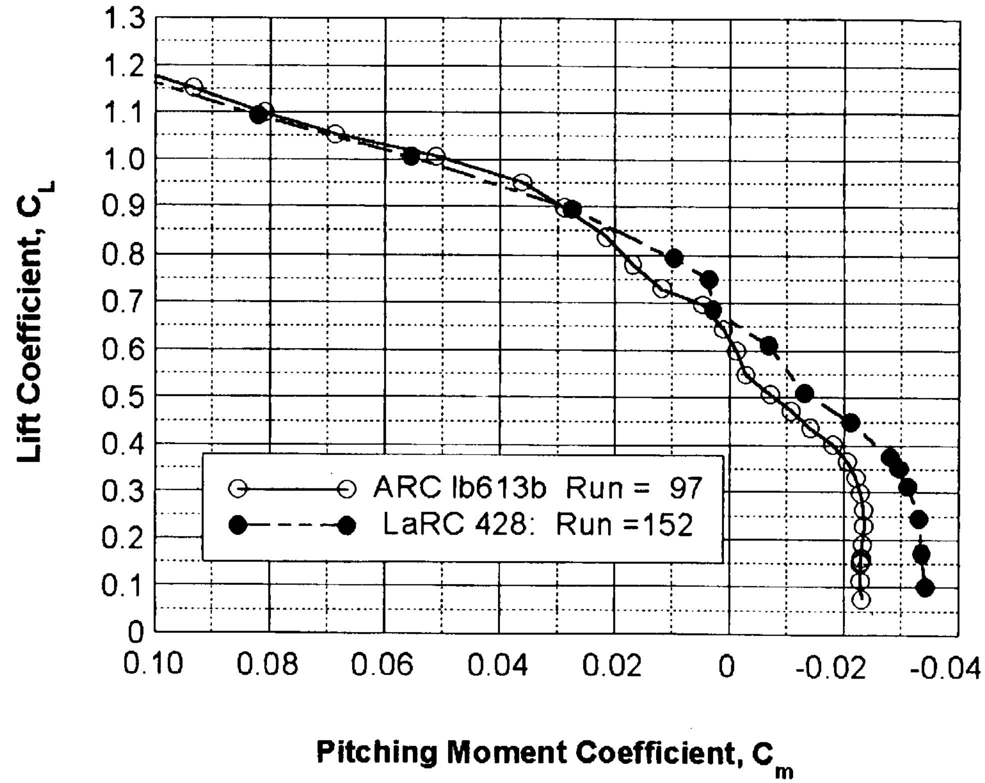

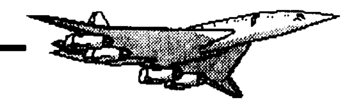

This figure shows a test to test comparison of the data obtained in the ARC 12' tunnel with that obtained in the LaRC 14'x22' low speed wind tunnel. This figure shows the drag polar comparison. In the expanded plot shown on the right, it can be seen that there is a shift in measured minimum drag with the 12' data indicating slightly higher drag. At higher lift conditions, the 12' data indicates a lower drag. However, between zero CL and CL = 0.5, the variation in drag between the two tests is only 10 counts.

Comparison with LaRC 14x22 Data
Tail off, 40°/10° Flaps - Variation of Lift with Drag

Drag Polar

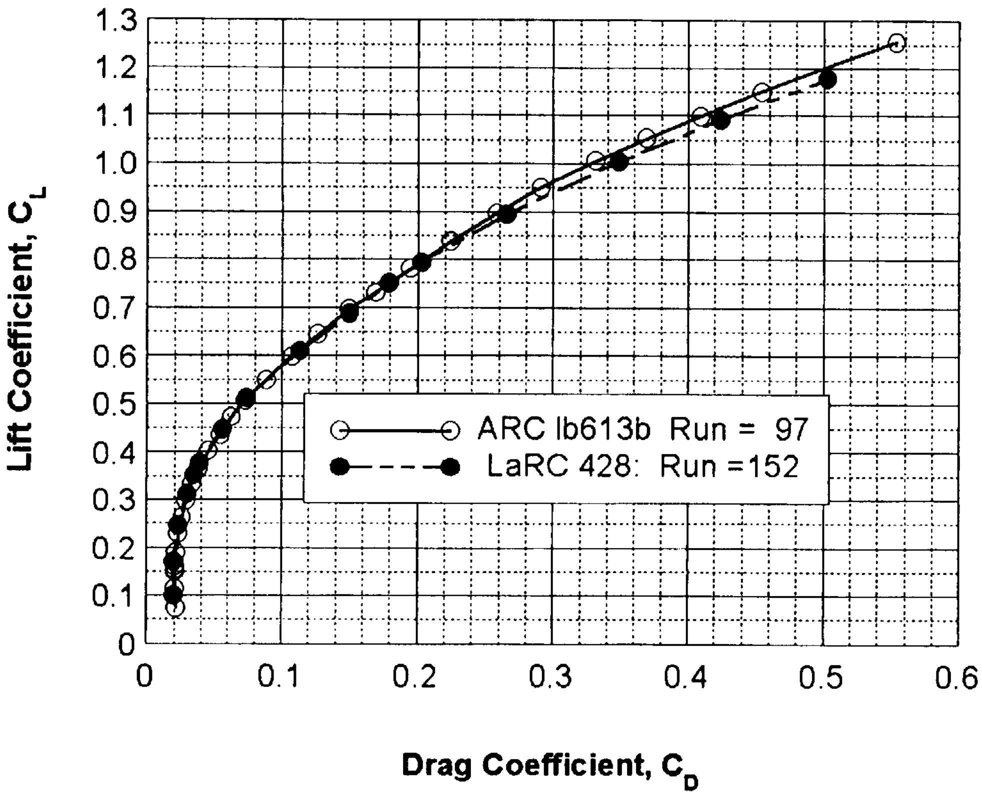

Drag Polar

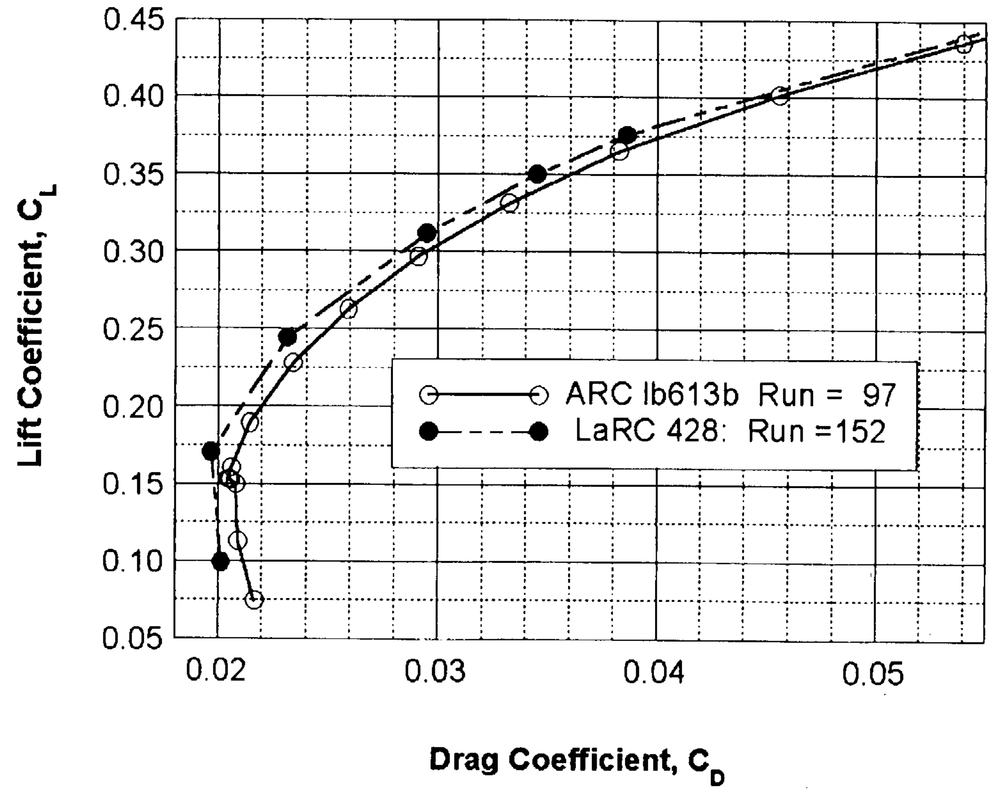

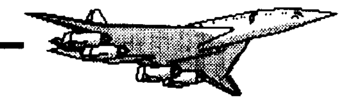

This page is intentionally blank

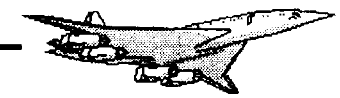

Leading-Edge Radius Modification

A modified leading edge flap was built for this test in an attempt to reduce the premature separation which was observed in the 14'x22' test of this configuration. As can be seen in this figure, the original geometry had a fairly sharp region on the lower surface at the leading edge. Since at high-lift conditions, the leading-edge attachment line occurs on the lower surface, a modified leading-edge was designed to smooth out this region.

Leading-Edge Radius Modification

- Modified to increase l.e. radius
- CFD analysis of 0/0 flaps configuration used in design

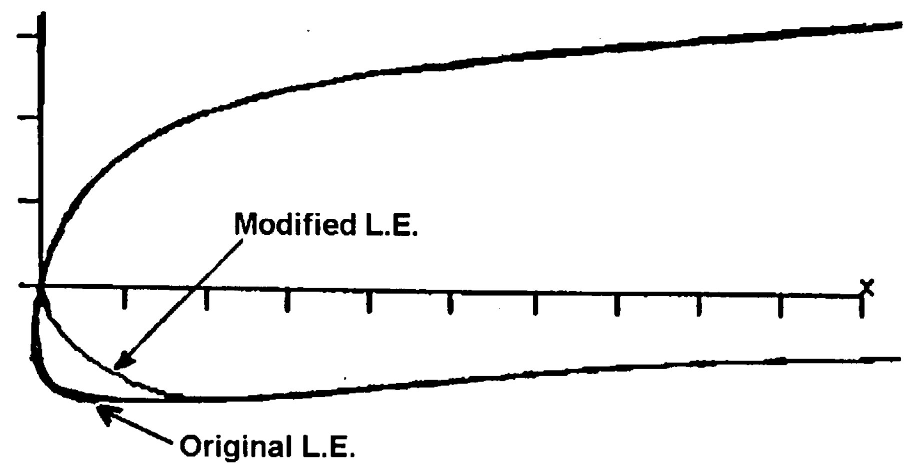

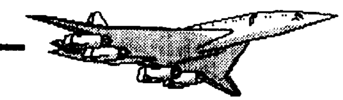

The leading-edge modification was developed with the aid of CFD. At the time this work was undertaken, the grid generation capability did not permit an extensive computational evaluation of the high-lift configuration, and so the geometry modifications were evaluated at lower lift conditions with the leading-edge flap undeflected. The lift/drag ratio shown here verifies that a small increase in L/D was achieved up to about 6° angle of attack. At higher angles, the leading-edge separation is well established, and small changes in leading-edge radius will have little effect on the nature of the flow.

Effect of Leading-Edge Radius - 0/0 Flaps, Rn = 7.06 Million

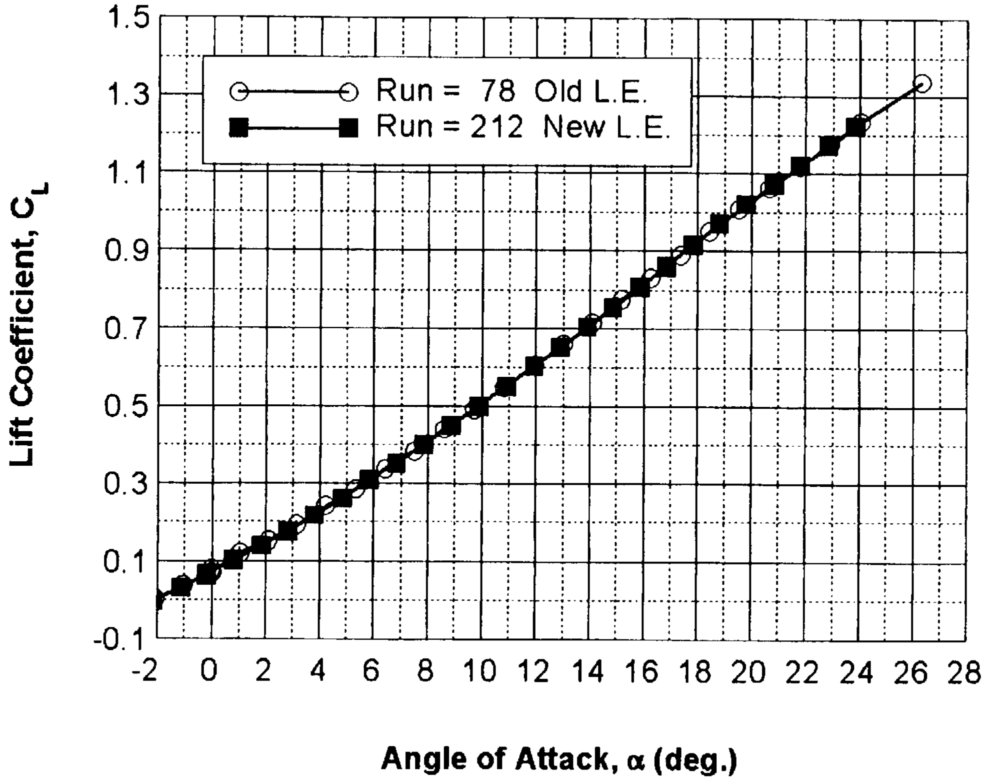

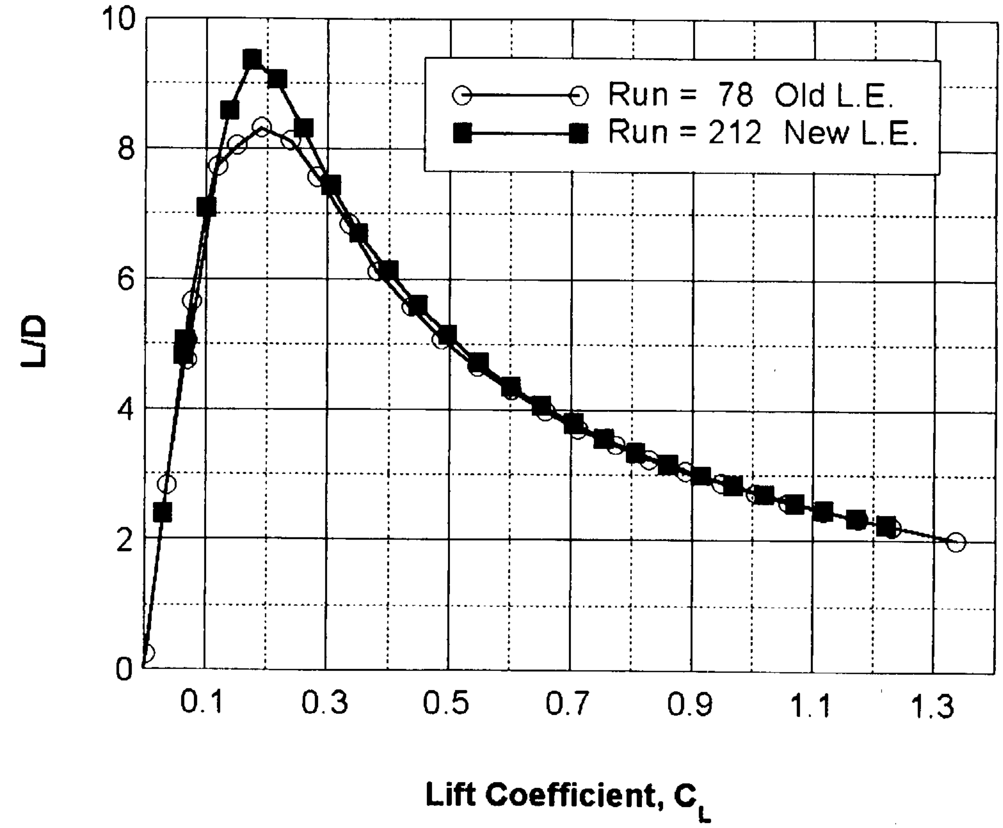

However, for the high-lift configuration, the changes to the leading-edge radius did not achieve any significant improvement in L / D. This result emphasizes the need to perform leading-edge design work with the aid of computational analysis on the full high-lift configuration.

Effect of Leading-Edge Radius
40°/10° Flaps, Rn = 7.06 Million

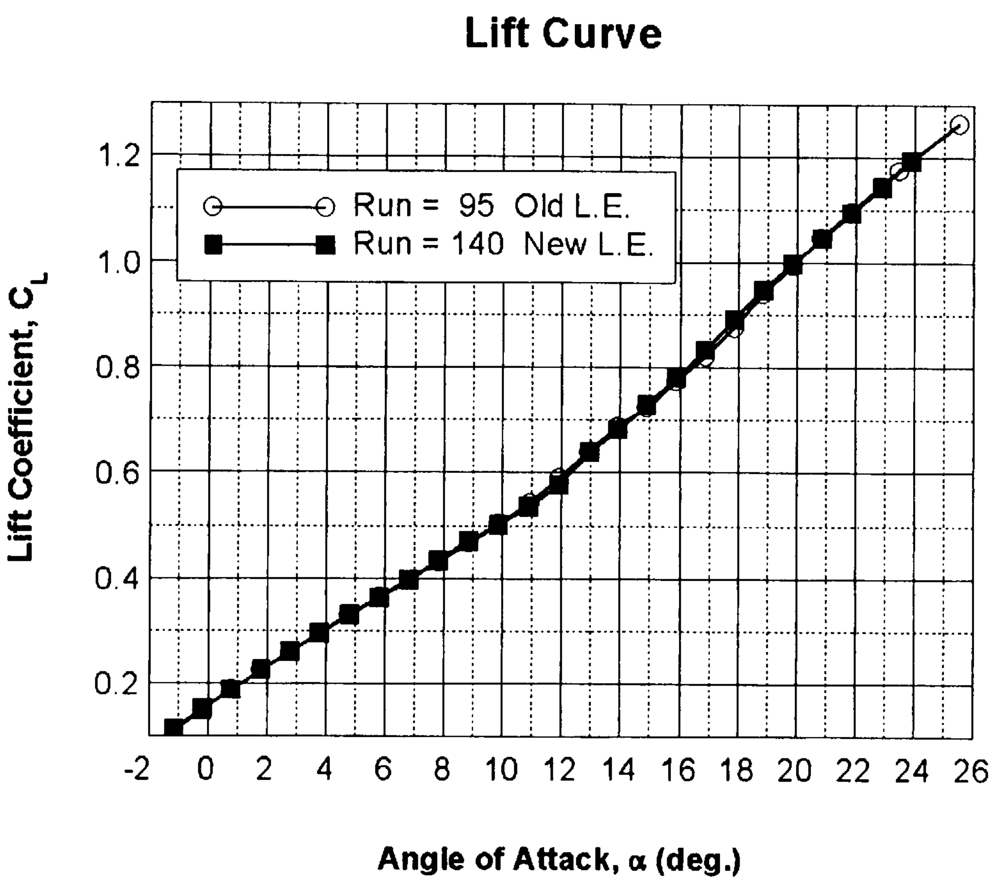

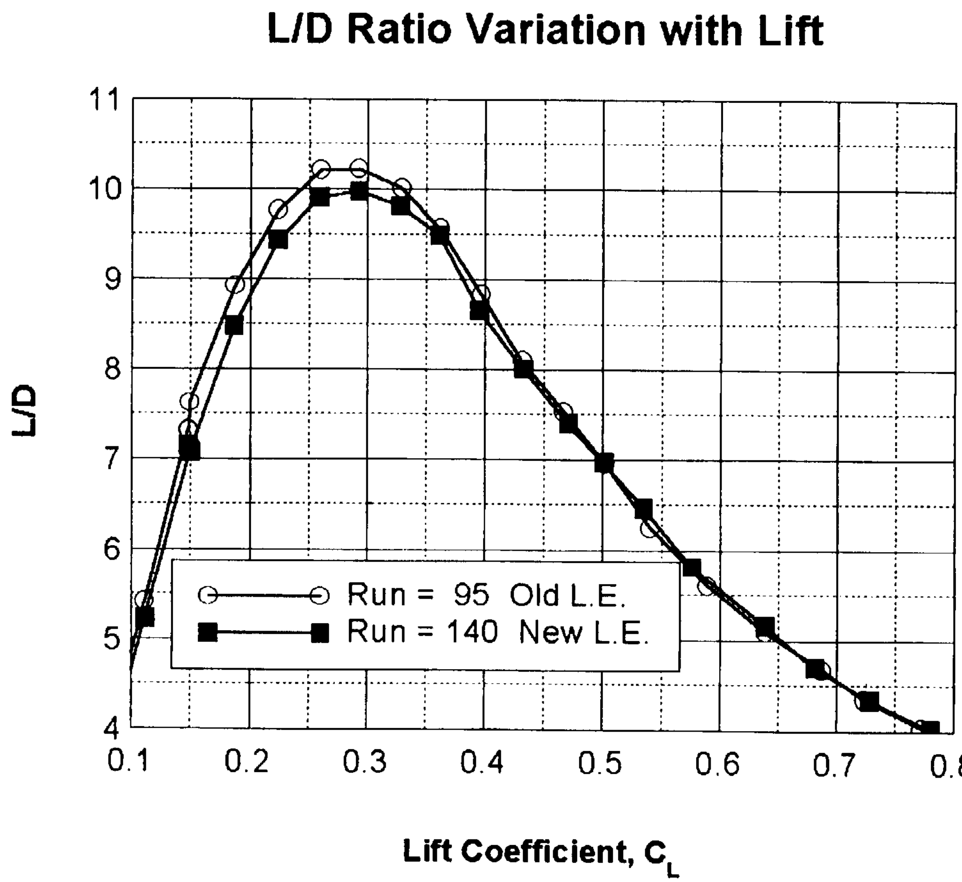

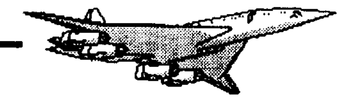

This page is intentionally blank

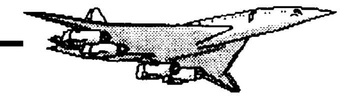

Leading- and Trailing-Edge Flap Optimization

This figure shows the effect of the leading- and trailing-edge flap deflection on the measured L / D. The leading-edge flap variation is shown on the left for the tail-off configuration, while on the right, the trimmed L / D is plotted for various trailing-edge flap deflections.

The optimum flap configuration identified is 35° leading edge deflection, and 15° for the three inboard trailing-edge flaps, and 10° for the outboard flap. It is interesting to note that this optimum trailing-edge flap setting resulted in a lower deflection for the outboard flap, rather than the increased deflection which would be expected to provide an improved span load distribution. The reasons for this are not clearly understood.

Optimized Flap Settings - New L.E.

Effect of L.E. -Tail off

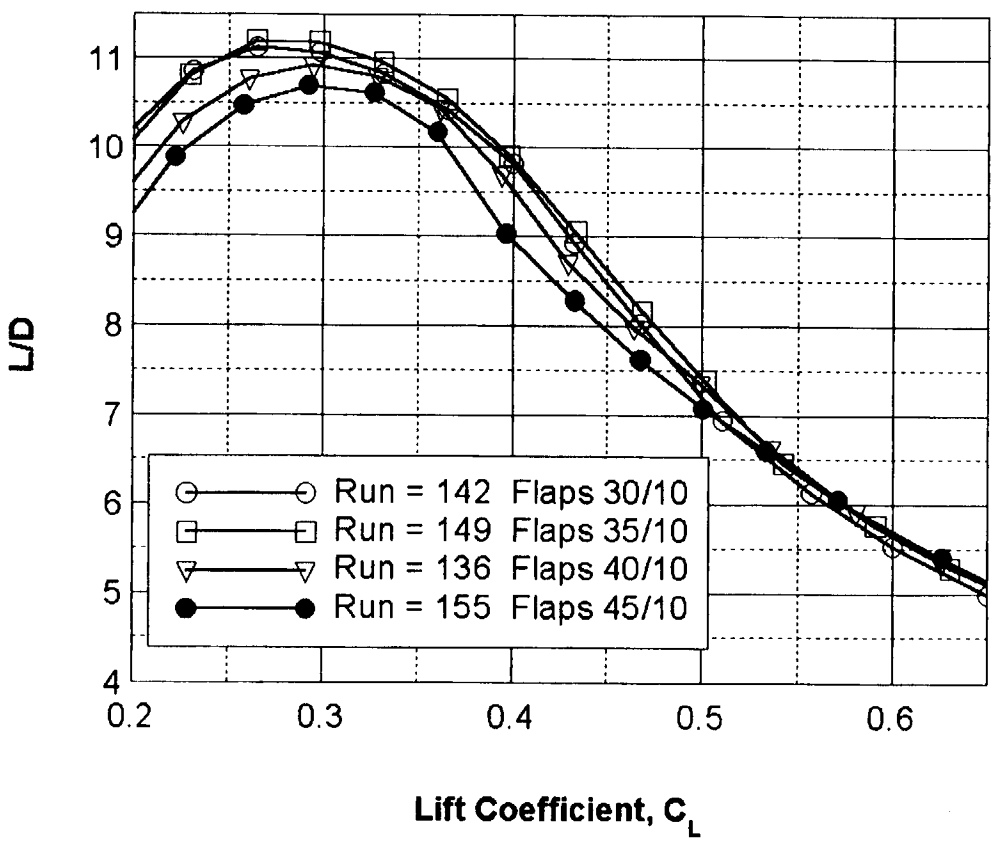

Effect of T.E. - Trimmed

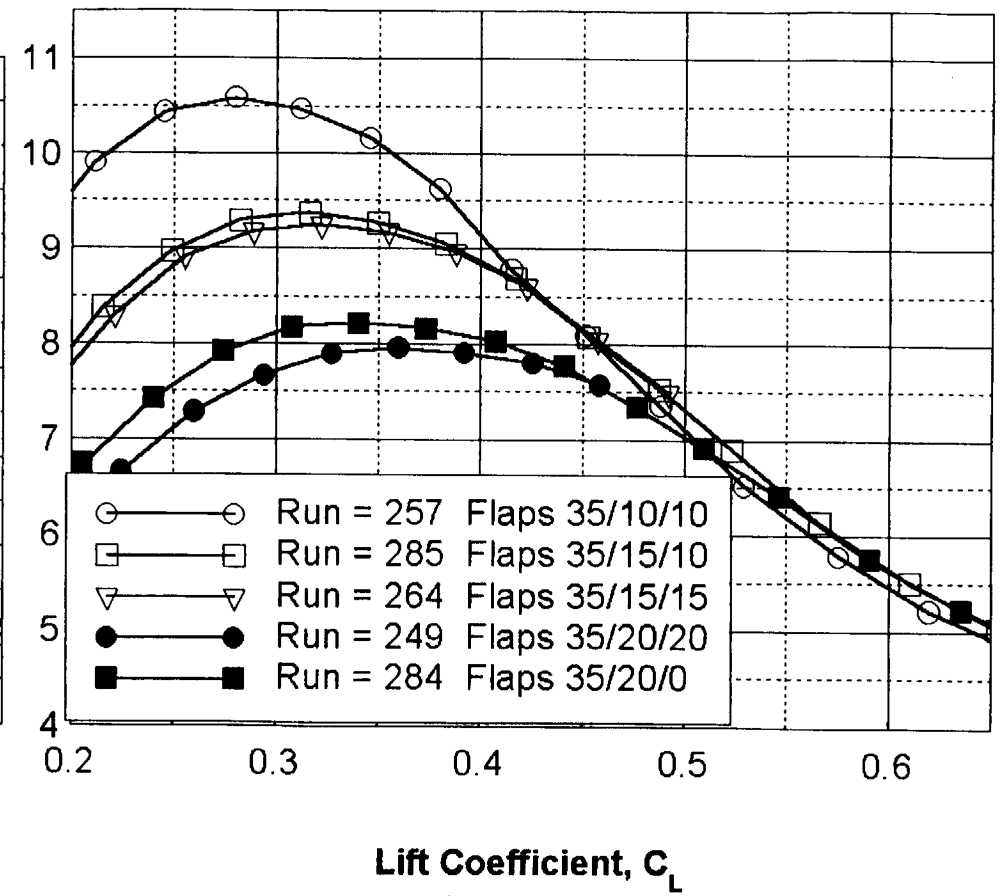

The following figures show the effect of the Reynolds number on the lift and pitching moment of the clean wing/body and the optimum high-lift configurations. The 12' Pressure tunnel provides a Reynolds number range from 7.06 Million (based on the Reference chord) at atmospheric pressure, up to 31.96 Million at six atmospheres.

Based on the results obtained from the NTF tunnel for the 2.2% Ref H model, there are some transitional effects observed for Reynolds numbers up to about 30-40 Million, after which the flow appears to be fully turbulent. It is therefore believed that the Reynolds number range which can be achieved in the 12' Pressure tunnel should provide useful data.

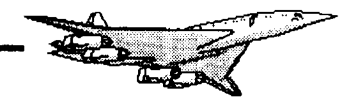

Effects of Reynolds Number

This figure shows the effect of the Reynolds number on the lift and pitching moment of the clean wing/body configuration.
The lift curve indicates that the lift decreases at the higher Reynolds number. While this would be consistent with a reduction in leading-edge vortex separation at the higher Reynolds number, that would not be expected to result in a change in the lift curve slope at the higher angles of attack when the leading-edge vortex will be fully established regardless of the Reynolds number. It is believed that the change in lift seen here is due to model deformation at the higher dynamic pressure.
There is a significant shift in the pitching moment between the two Reynolds number results. This could be caused be caused in part by a lessening of the interference between the support post viscous wake and the horizontal tail. It could also be an aeroelastic effect caused by twist induced at the wing tips.

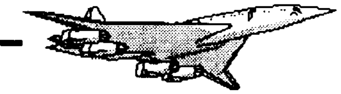

Rn Effects - 0/0 Flaps

Tail on, (ih=0°)

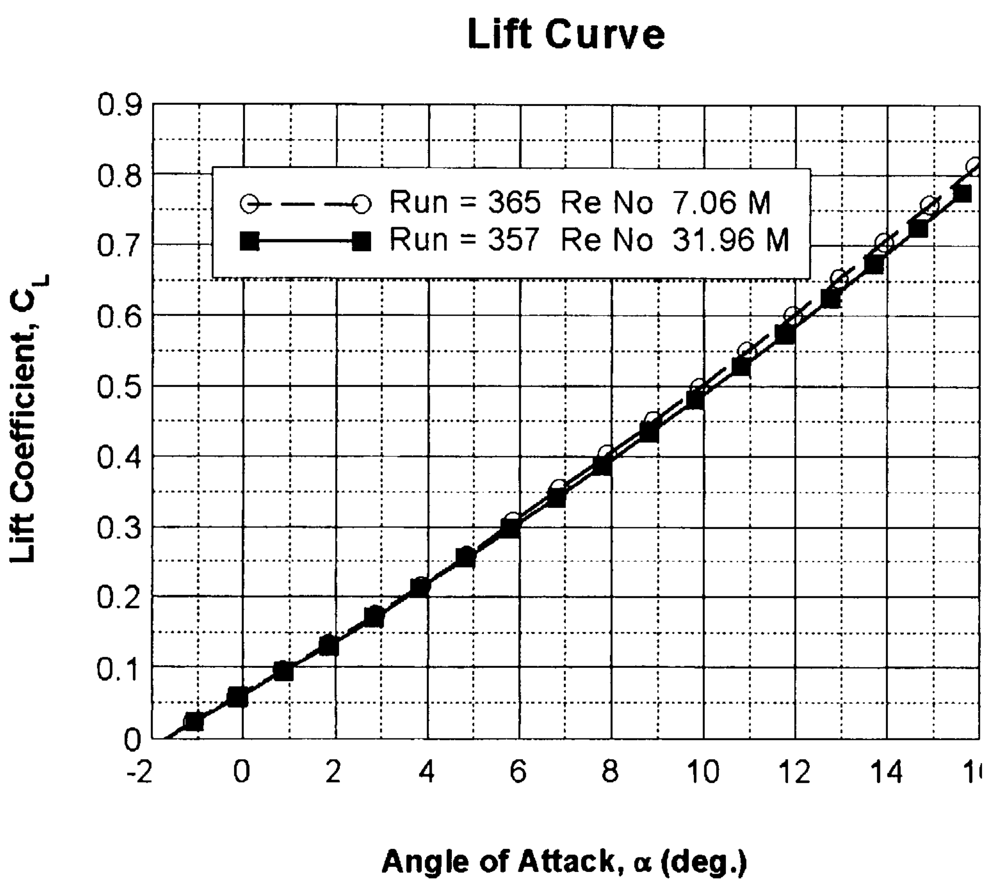

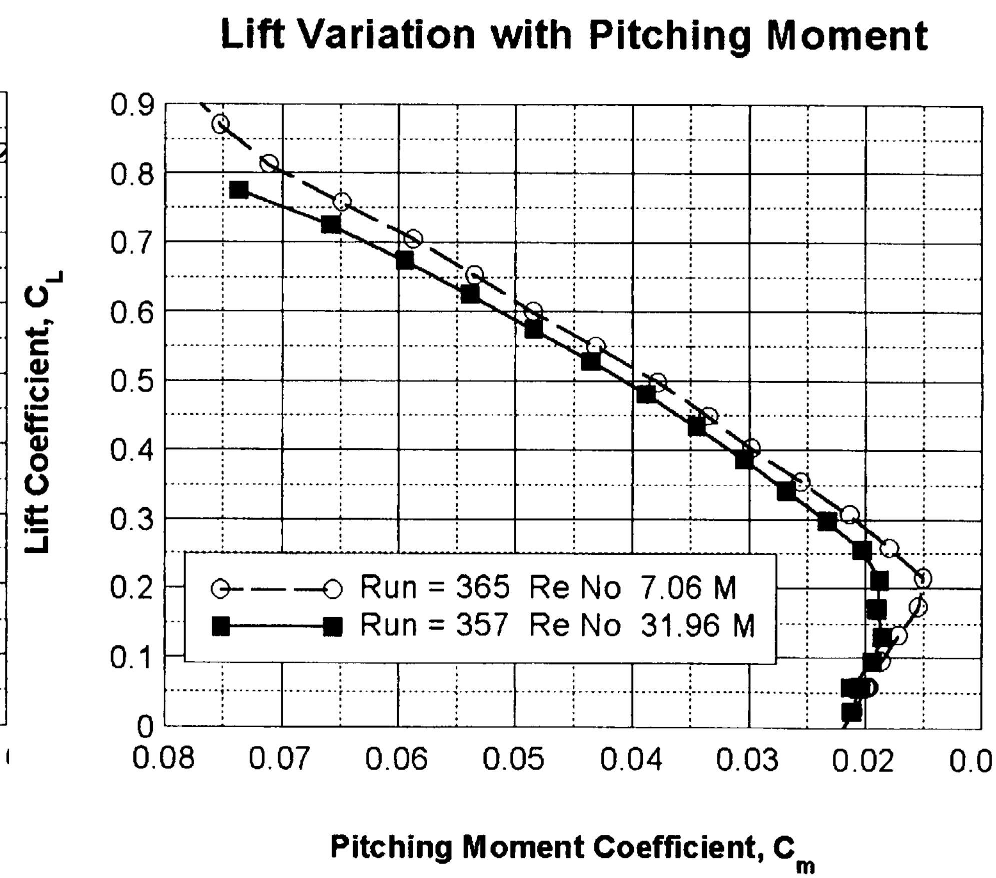

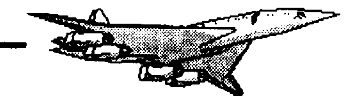

This figure shows the effect of the Reynolds number on the drag polar and induced drag of the clean wing/body configuration.

At low lift conditions, the left hand figure shows that there is a reduction of about 10 drag counts as the Reynolds number is increased which is consistent with the reduction to be expected from the reduced skin friction.

The figure on the right plots the induced drag versus lift coefficient. It can be seen that there is very little Reynolds number evident in the induced drag, which indicates that, for this configuration which has a relatively sharp leading-edge, there is little Reynolds number effect.

Again, this indicates that the change in the lift curve seen in the previous figure is due to model deformation rather than differences in the leading-edge vortex behavior.

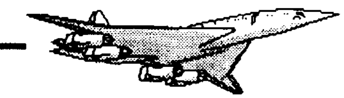

Rn Effects - 0/0 Flaps

Tail on, (ih=0°)

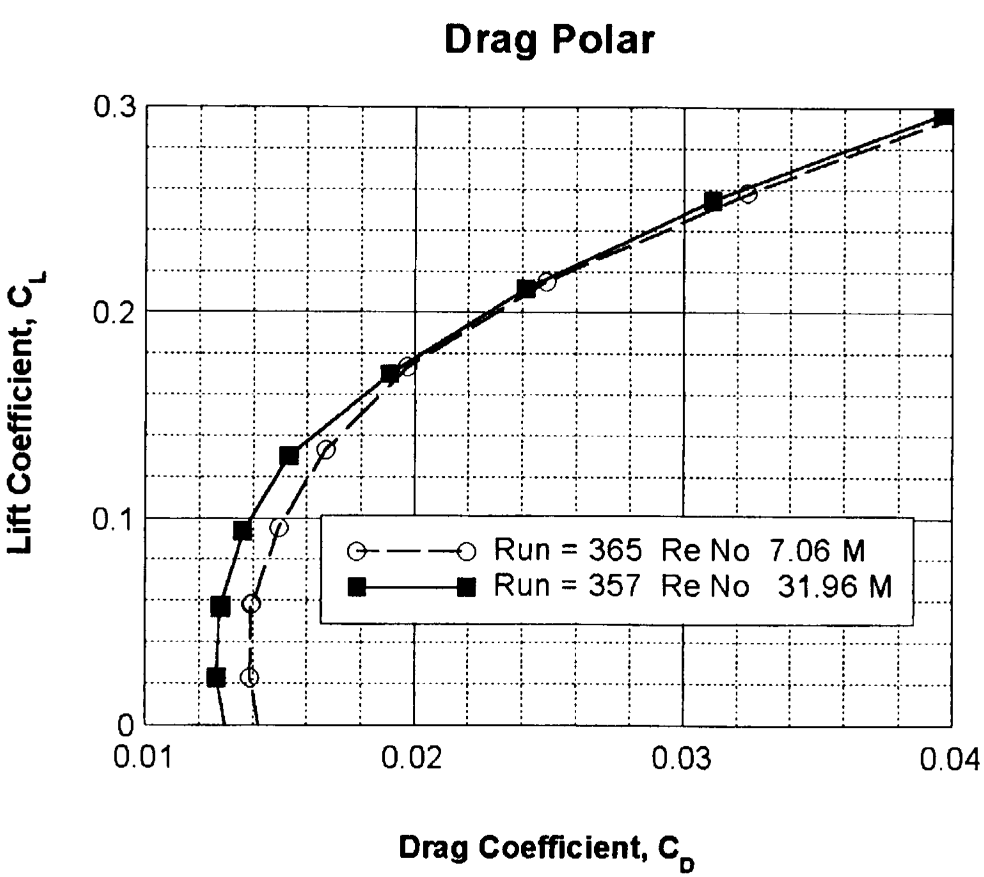

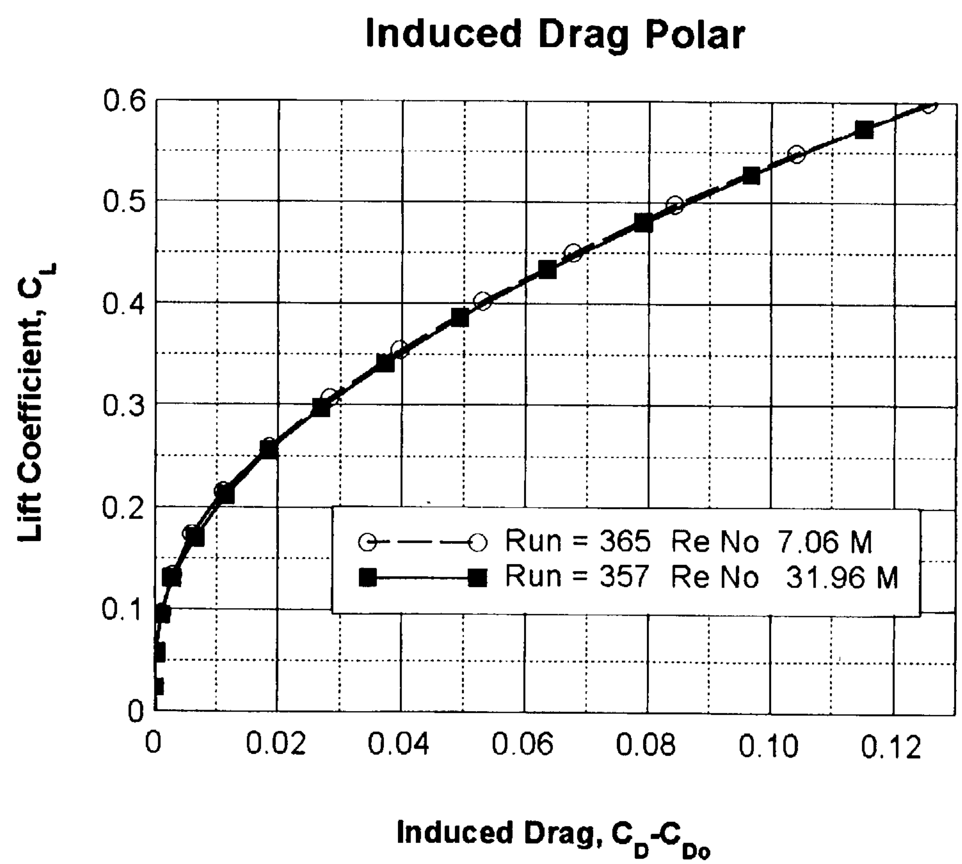

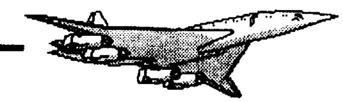

This figure shows the effect of the Reynolds number on the lift curve and pitching moment for the optimum high-lift configuration.

It can be seen that there is very little change in lift.

There is a shift in the pitching moment which as discussed above is believed to be due to the interaction of the support post wake with the horizontal tail and/or model deformation effects.

Rn Effects - 35°/15°/10° Flaps

Tail on (ih=0°)

Lift Curve

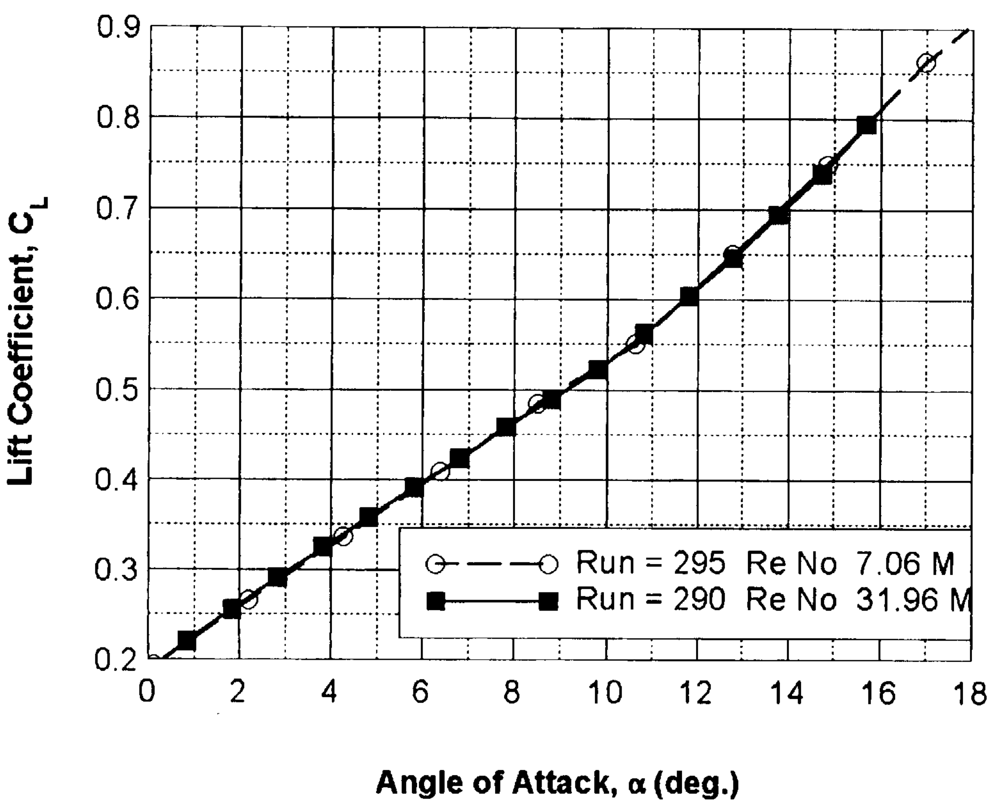

Lift Variation with Pitching Moment

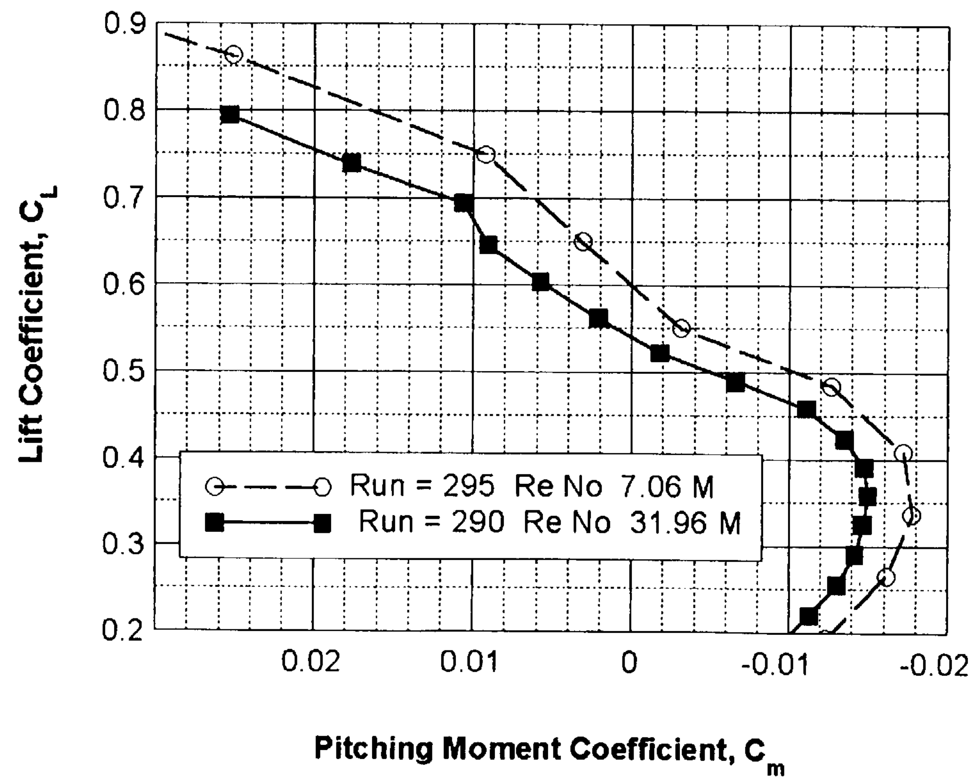

This figure shows the effect of the Reynolds number on the drag polar and the L / D for the optimum high-lift configuration.
At lower lift conditions, there is again a reduction of about 10 drag counts as the Reynolds number is increased which is consistent with the reduction to be expected from the reduced skin friction. Again, this difference reduces at higher lift conditions, although the 31.96 Million Reynolds number results still show slightly less drag than the lower Reynolds number data.

Rn Effects - 35/15/10 Flaps

Tail on (ih=0°)

Drag Polar

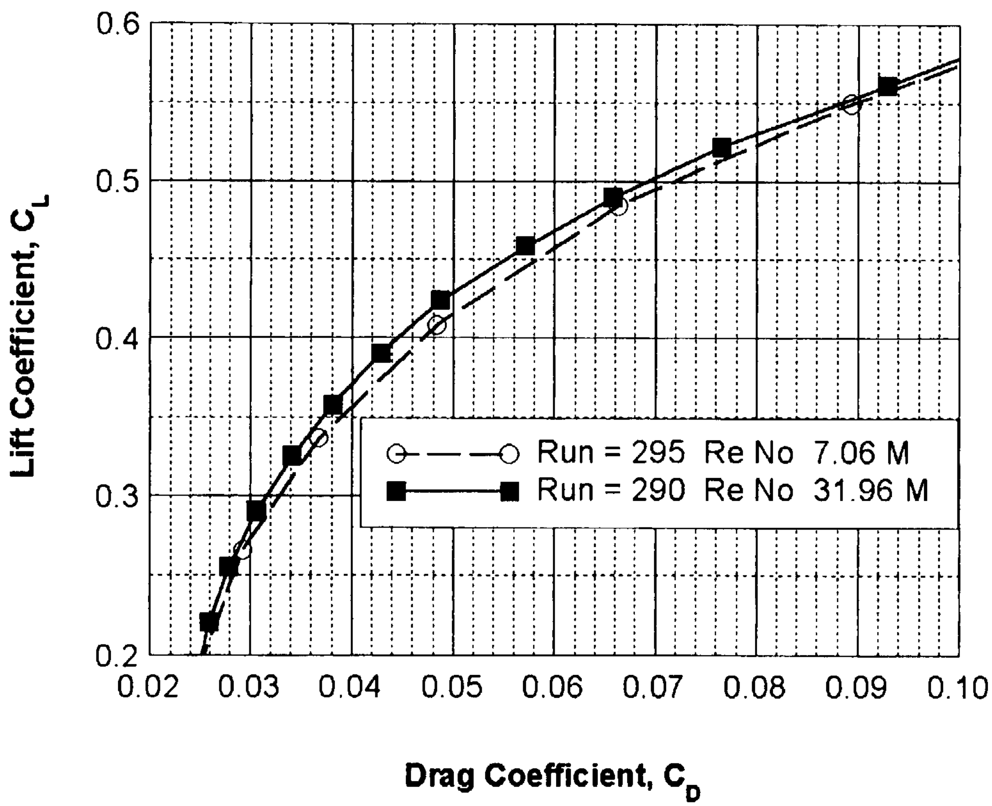

L/D Ratio Variation with Lift

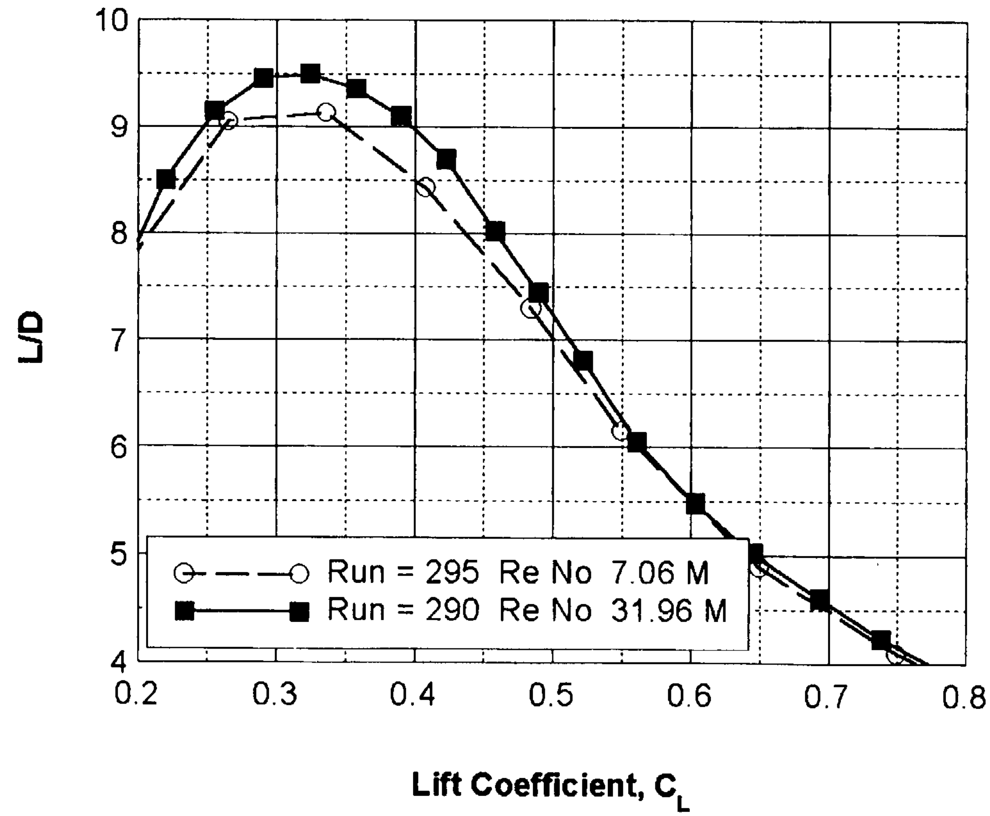

As discussed in the previous figures, the increased Reynolds number data is obtained by increasing the tunnel pressure. This increase in dynamic pressure results in increased loading on the model which will result in substantially greater model deformation under highly loaded conditions. During the test entry, optical model deformation data was obtained for a limited number of configurations. This data has been used to perform a numerical evaluation of the predicted aerodynamic effects which would be caused by this model deformation for the high-lift configuration with 40° leading-edge and 10° trailing-edge flap deflection. The following figures present these results.

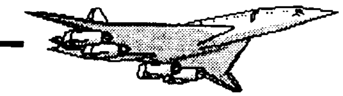

Model Deformation Effects

The optical data obtained consists of wing twist and displacement between the wind-off and wind-on model, and data was obtained for a range of angles of attack. The results presented here look at the effects of the measured deformation which occurred at 10° angle of attack.

This figure shows the measured model deformation for the 40°/10° high-lift configuration. The deformation data consists of wing twist and displacement.

It can be seen that the displacement at the wing tip is close to 1", with about 2° nose down twist.

Measured Model Deformation
10° angle of attack, 40°/10° Flaps, Tail off

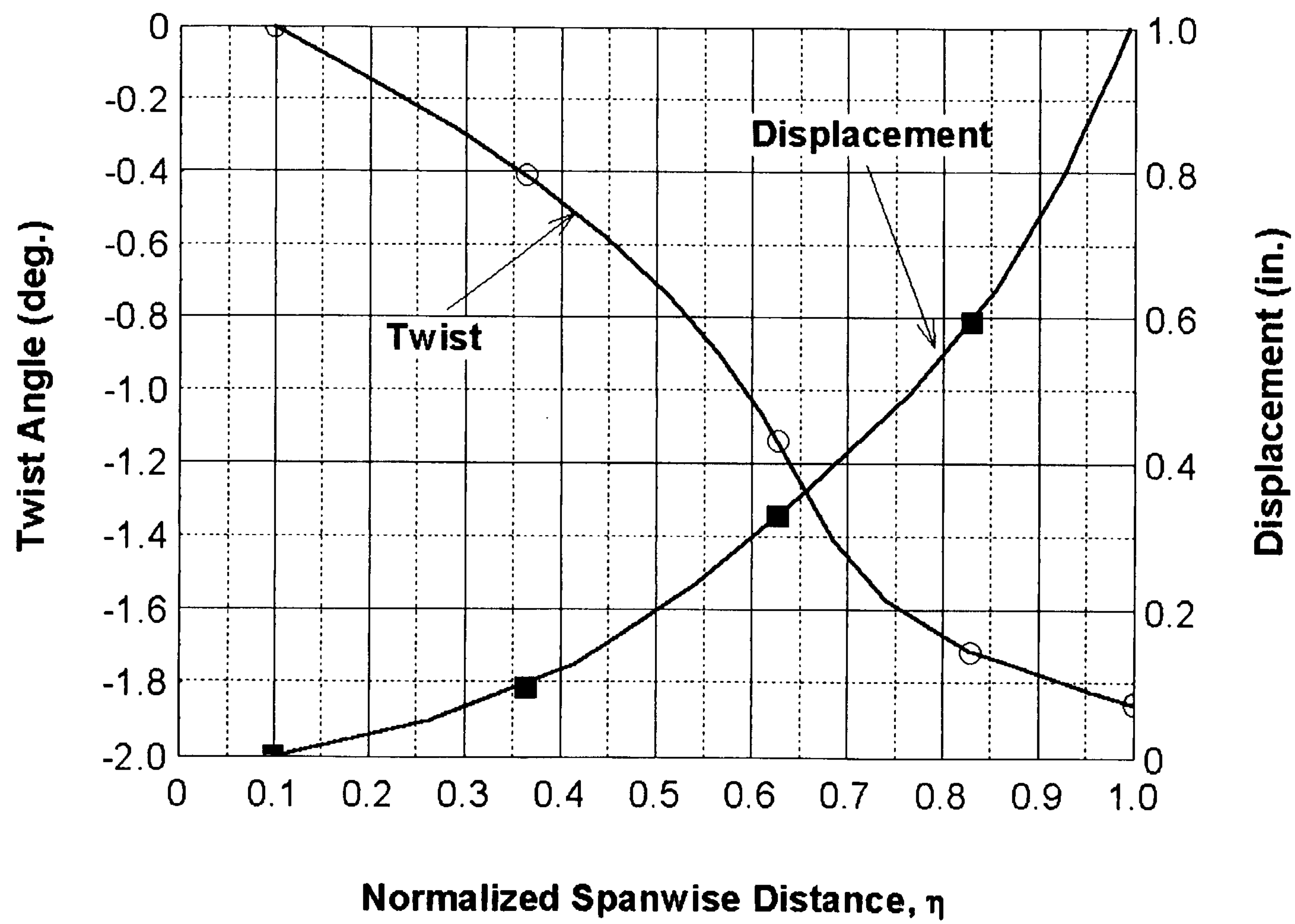

This figure compares the grid for the deformed configuration with the baseline grid. The wing displacement at the tip can be clearly seen.

Model Deformation Effects

CFD Grid for Deformed Geometry

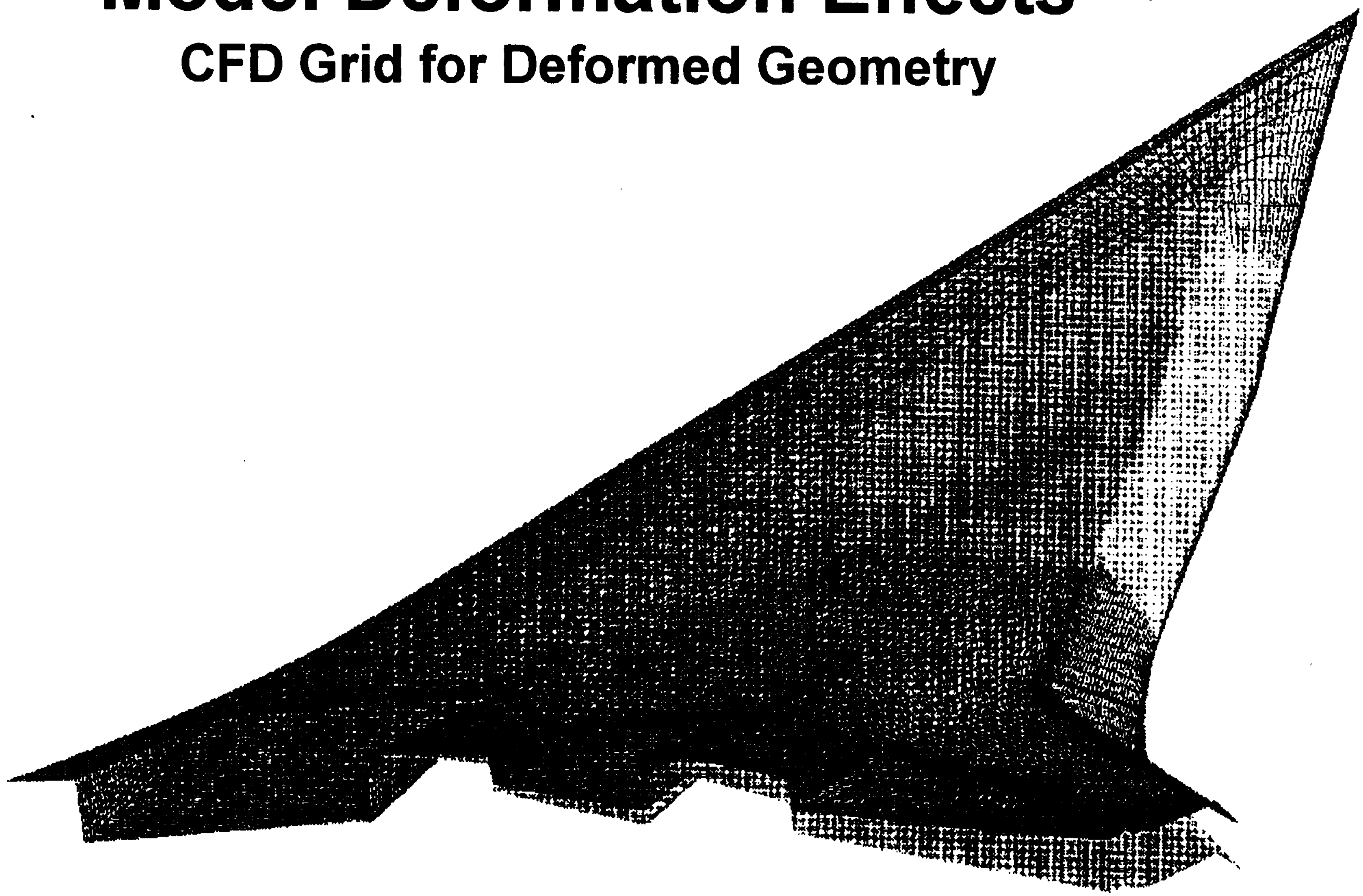

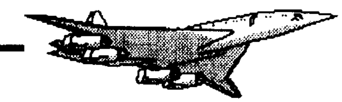

This figure shows the effect of Reynolds number for the 40°/10° high-lift configuration compared with the computed effects due to the model deformation.

The experimental data shows that there is only a small change in the lift curve as the Reynolds number is increased. The lower Reynolds number data shows a higher lift between about 10° and 14° angle of attack, which is consistent with the earlier onset of the leading-edge vortex separation.

However, the computed effects of the wing deformation, obtained with the Navier-Stokes code, CFL3D, indicate that there should be about a 4% reduction in lift at the higher dynamic pressure.

However, there does not appear to be any comparable reduction in lift observed experimentally at 10° angle of attack. The reason for this discrepancy is unclear.

It can be seen from the experimental pitching moment curves that the shift in pitching moment with increasing Reynolds number seen in the tail-on data presented earlier is not seen here with the tail off.

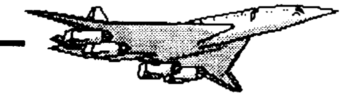

Computed Effect of Model Deformation - 40°/10° Flaps, Tail off

Lift Curve

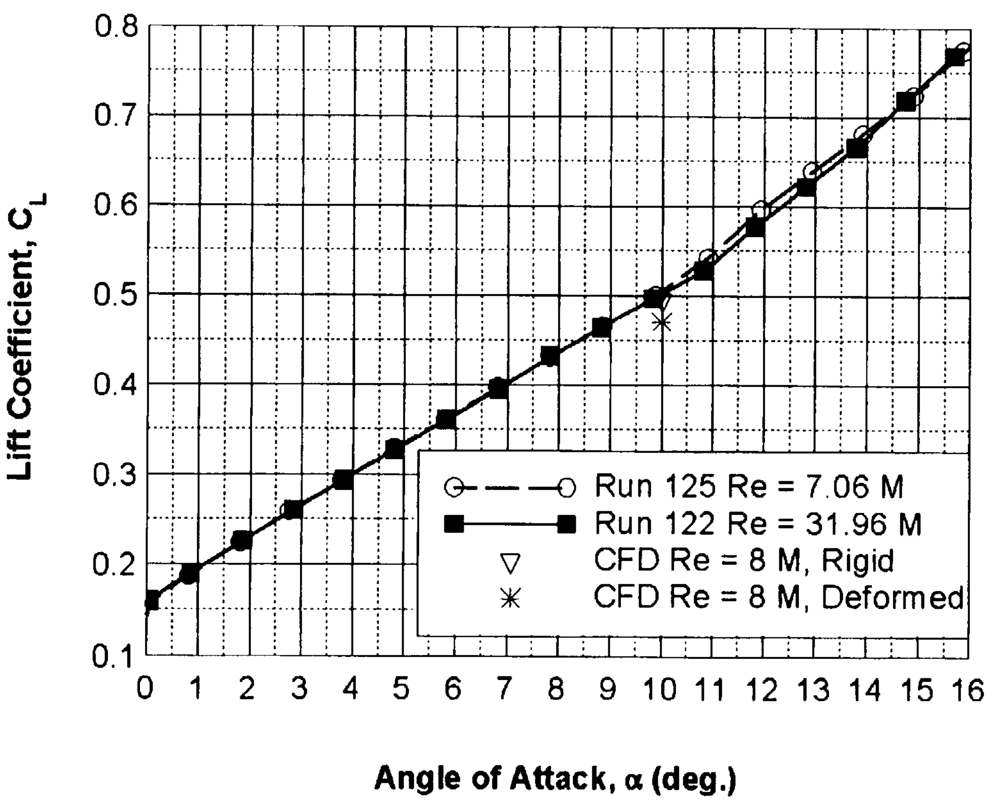

Lift Variation with Pitching Moment

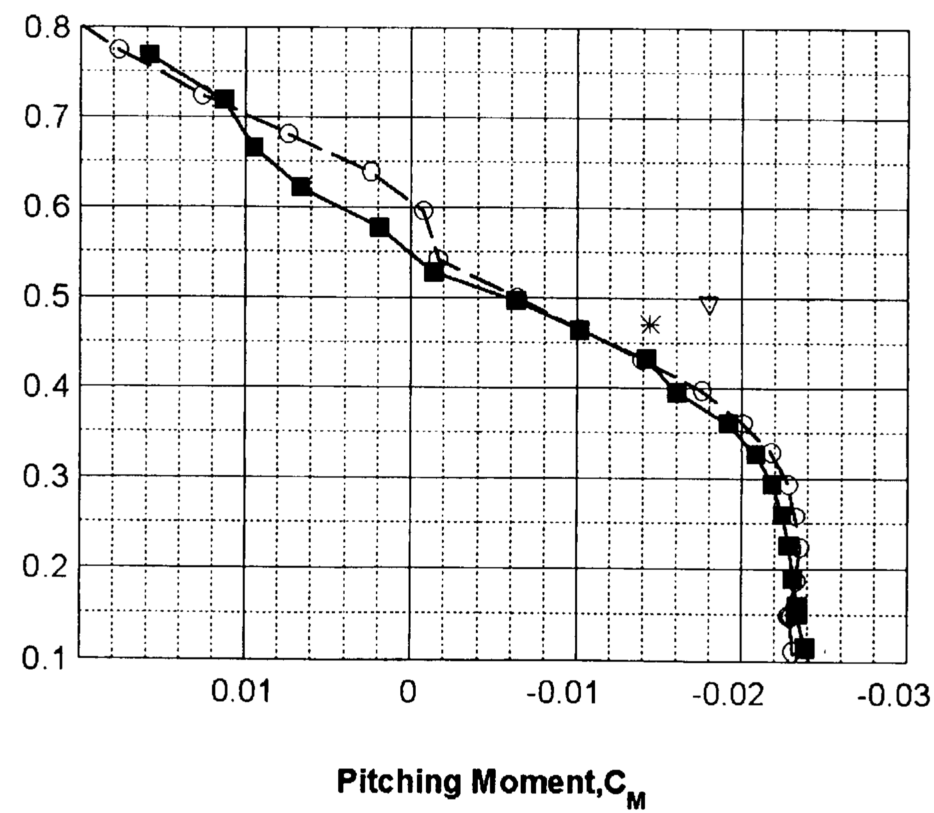

This figure shows the effect of Reynolds number for the 40°/10° high-lift configuration compared with the computed effects due to the model deformation.

The experimental drag polar indicates that there is a decrease in drag as the Reynolds number (and dynamic pressure) is increased. However, the computational results indicate that the model deformation should lead to an increase in drag of approximately 30 counts at a constant lift coefficient. This change is similar in magnitude, although of opposite sign, to the measured Reynolds number variation. It is therefore clear that the effects of the aeroelastic model deformation should be fully accounted for in evaluating the Reynolds number effects.

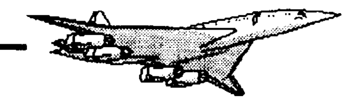

Computed Effect of Model Deformation - 40°/10° Flaps, Tail off
Drag Polar

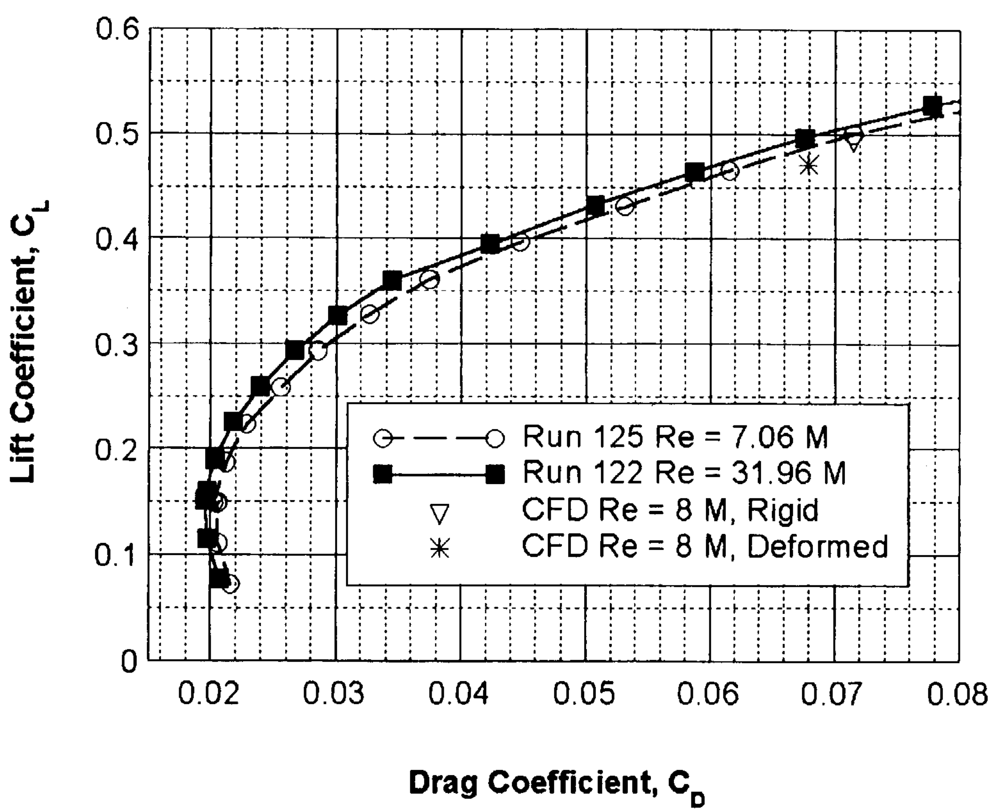

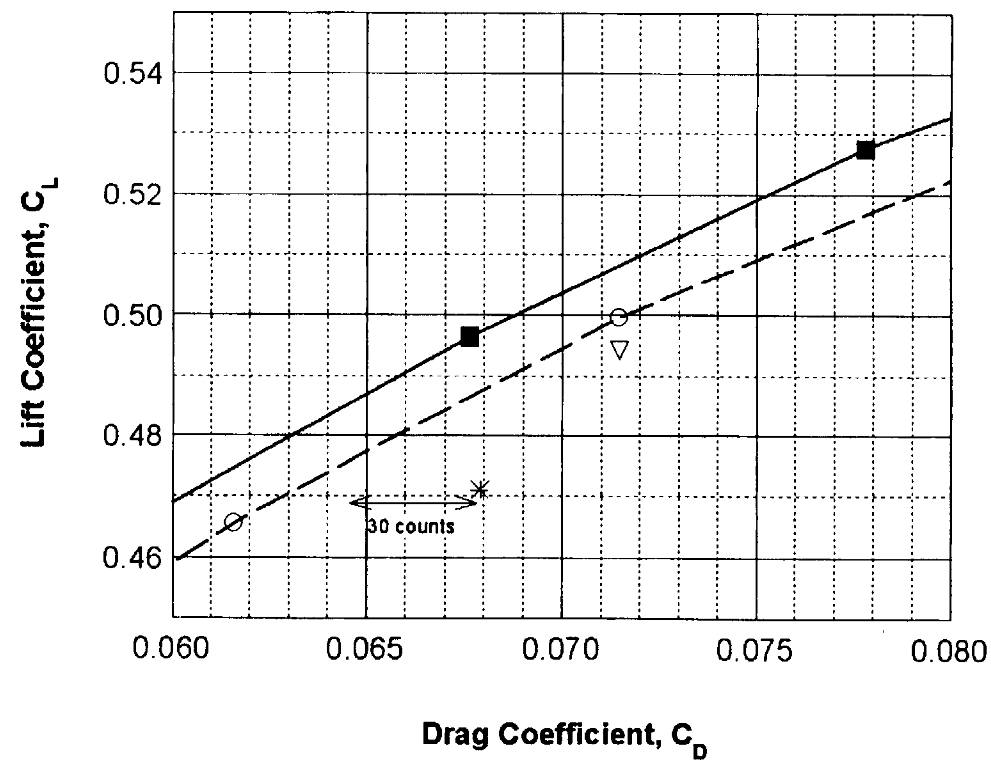

This figure compares the computational pressure distribution, obtained with the Navier-Stokes code, CFL3D, and the measured pressure distribution obtained using Pressure Sensitive Paint (PSP). It can be seen that the basic flow features are very well predicted by the CFD result. The leading-edge vortex originating close to the apex of the wing is present in both the computational and the measured data, as is a second vortex emanating from the leading edge planform break station.

Surface Pressure Comparison

PSP Image

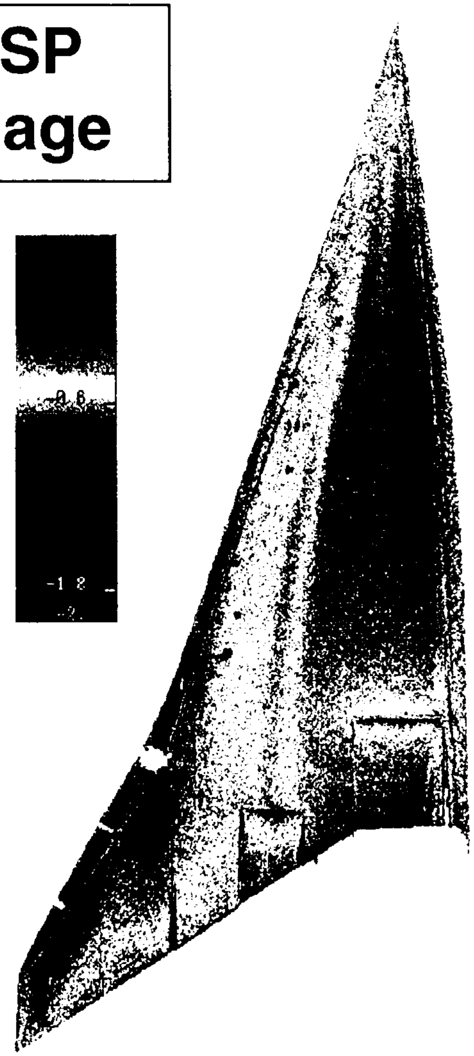

CFD Solution

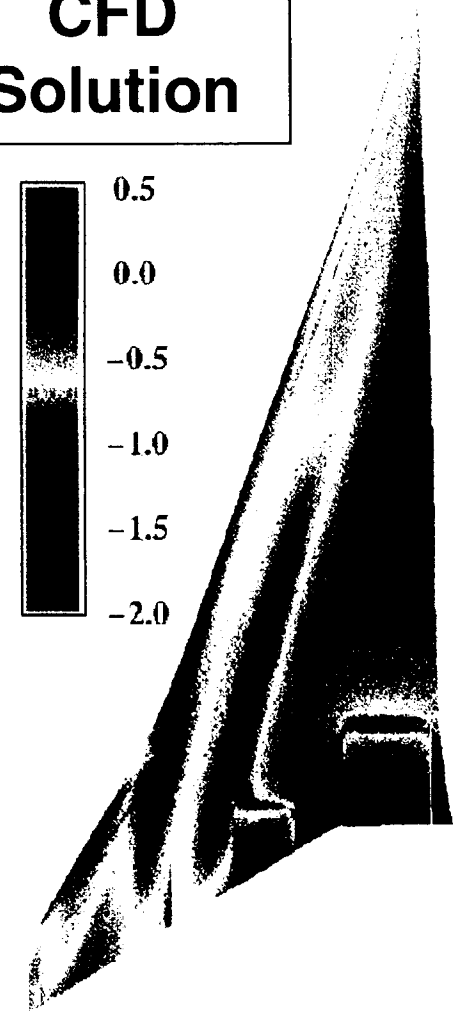

This figure lists the main conclusions drawn from this test.

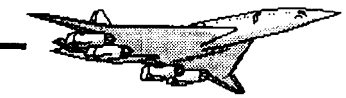

Summary

- Test provided good tunnel to tunnel comparison
- Little benefit due to increased l.e. radius
- Flap optimization requires intermediate flap deflections
- Reynolds number effects are small
- Computed effect due to model deformation at high Reynolds number (higher dynamic pressure) is comparable to the observed Reynolds number effects
- Surface pressure distribution is very well predicted by CFL3D Navier-Stokes method

This page is intentionally left blank.

Power Effects on High Lift, Stability & Control Characteristics of the TCA Model Tested in the LaRC 14' X 22' Wind Tunnel

February 9, 1998

Paul T. Glessner
(562) 982-6054
paul.t.glessner@boeing.com

High Lift Research
Contract NAS1-20220 Task 33

High Lift Technology Development (Task 33)

Increase L/D, Develop Analysis/Design Methodology

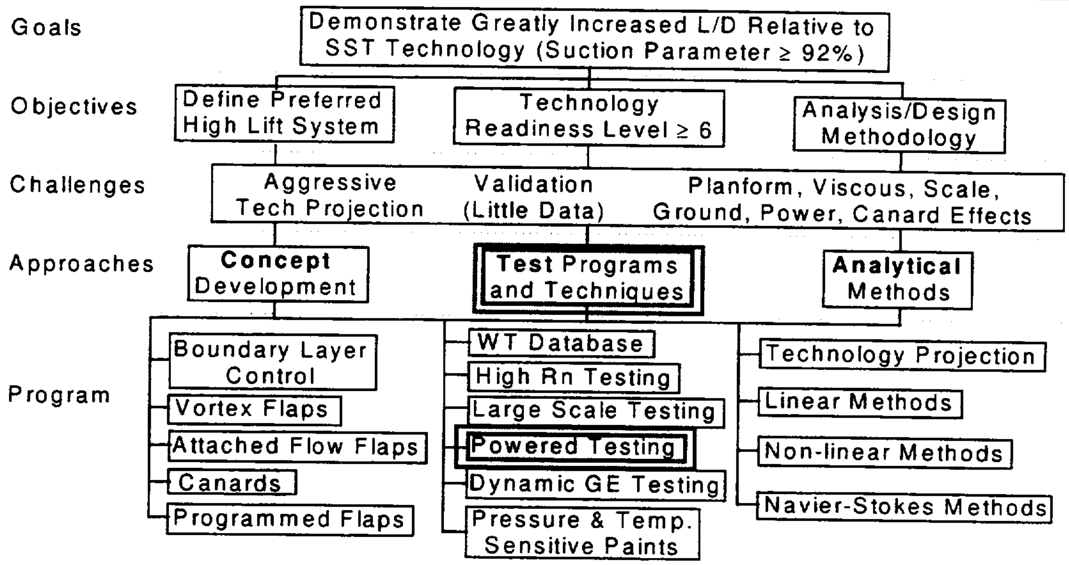

The powered TCA-2 test performed at Langley's 14' x 22' resides under the Test Programs and Techniques Approach within Task 33, High Lift Technology Development.

Outline

- Introduction - LaRC 455 in the TCA WTT Plan
- Test Objectives
- Test Configuration Matrix
- 5% TCA Model Description
- Results
- Conclusions
- Lessons Learned
- Recommendations

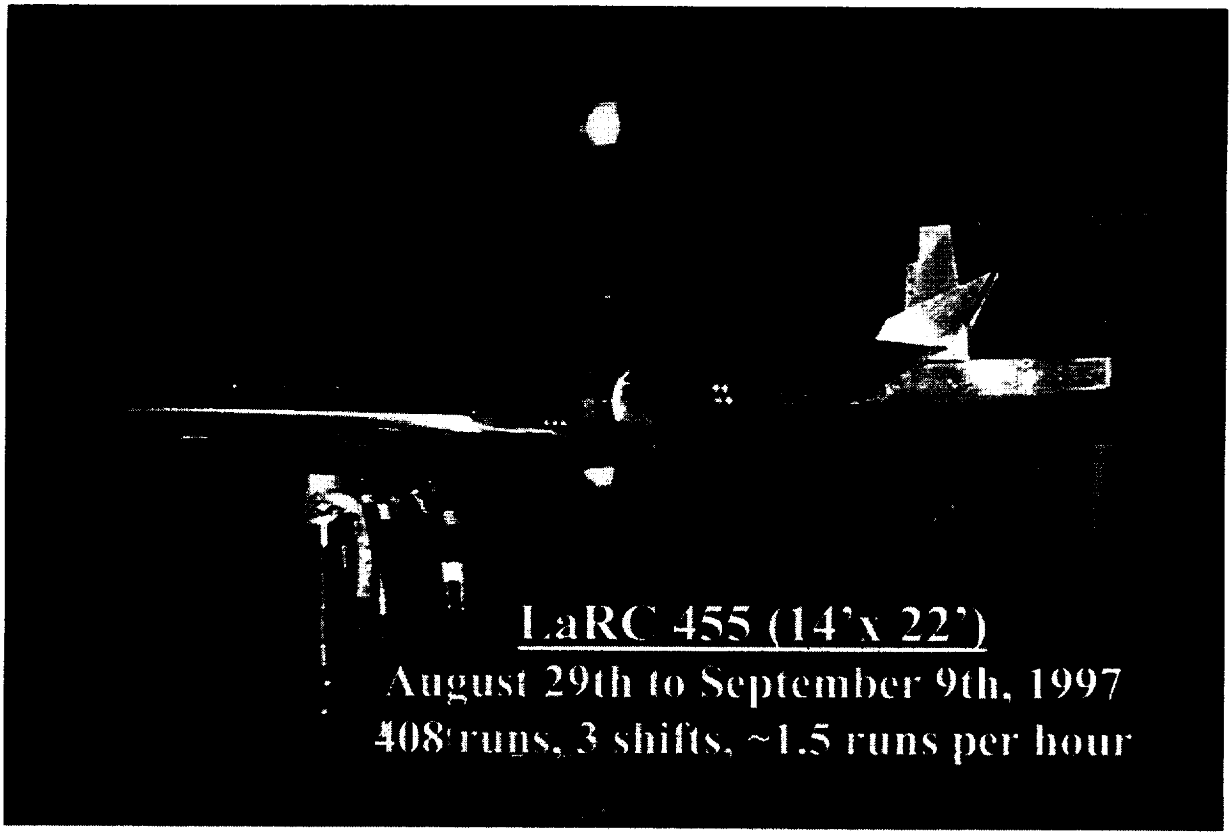

The test was performed from August 29th to the 9th of September, 1997. The average run rate, including model installation was 1.5 runs per hour. The picture above depicts the aft end of the powered 5% HSCT TCA model. The model will be discussed in more detail later in the presentation. The above picture will be referred to at that time.

WIND-TUNNEL TEST SCHEDULE FOR 5% TCA MODEL

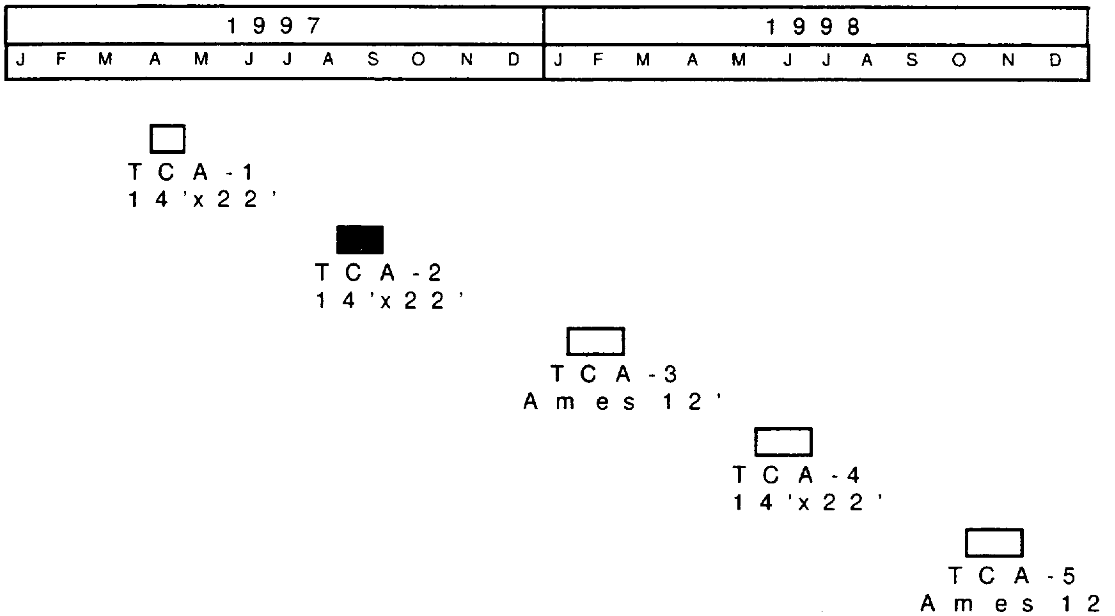

The TCA-2 wind-tunnel test was the second in a series of planned tests utilizing the 5% Technology Concept Airplane (TCA) model. Each of the tests was planned to utilize the unique capabilities of the NASA Langley 14'x22' and the NASA Ames 12' test facilities, in order to assess specific aspects of the high lift and stability and control characteristics of the TCA configuration. However, shortly after the completion of the TCA-1 test, an early projection of the Technology Configuration (TC) identified the need for several significant changes to the baseline TCA configuration. These changes were necessary in order to meet more stringent noise certification levels, as well as, to provide a means to control dynamic structural modes. The projected changes included a change to the outboard wing (increased aspect ratio and lower sweep) and a reconfiguration of the longitudinal control surfaces to include a medium size canard and a reduced horizontal tail. The impact of these proposed changes did not affect the TCA-2 test, because it was specifically planned to address power effects on the empennage and a smaller horizontal tail was in the plan to be tested. However, the focus of future tests was reevaluated and the emphasis was shifted away from assessment of TCA specific configurations to a more general assessment of configurations that encompass the projected design space for the TC.

Test Objectives of LaRC 455

1. **Determine Exhaust effects on the Empennage in Free-air (F-A) and in Ground-Effect (G.E.)**
   - Baseline (800 ft.^{2}) & Half (400 ft.^{2}) Stabilizers
   - Takeoff vs Flow-thru Eng. Exhaust Nozzles
   - Interference Effects

     a. High Pressure Air Supply Lines

     b. Domed Nacelles

The test's main objective was to quantify the effects of simulated engine plumes on the empennage at several thrust levels with emphasis on the thrust level that most closely represents take-off conditions. Additional objectives included investigating: 1) the plumes' effects on the half-sized (400 ft.^{2}) baseline tail, 2) difference in nozzle positions to acquire the desired exhaust effects, and 3) the interference effects of the high pressure air supply lines and domed nacelles.

Test Configuration Matrix

Five configurations that were tested:

1. Takeoff flaps (LE/TE = 30/20), 3 Power settings
   - Baseline stabilizer
   - Half-size stabilizer
2. Undeflected flaps (0/0), 3 Power settings, baseline stabilizer
3. Takeoff flaps, flow-thru nacelles
   - with high pressure air lines installed
   - with high pressure air lines removed

The test configuration matrix was structured to ensure the test's main objective would be met and the remaining objectives were prioritized. This matrix was designed into the plan of test (POT) which can be obtained from the 'ADAPT" web page. The High Lift and Stability & Controls objectives for best trimmed lift, L/D, simulation and control power assessment of the exhaust's effects on the tail were combined and prioritized.

The test was centered around the terminal area takeoff and climbout conditions. Most of the test was conducted with the wing in the takeoff flap configuration - leading edge flaps at 30 degrees and trailing edge flaps at 20 degrees (LE/TE 30/20). The clean wing configuration (0/0) was also studied. The undeflected flap configuration was tested for baseline simulation data and additional confirmation about downwash at the empennage. The data obtained from this test will be additive to the unpowered TCA-1 test data to culminate in a powered, ground effect and free-air TCA database.

The test included runs to determine interference effects that must be accounted for because of the air supply lines and domed inlets. At the start of the test, the need to test the 'flow-thru' nozzles was eliminated by the ability to obtain flow-thru NPRs with the takeoff nozzles.

The baseline TCA horizontal tail (H1) was primarily used to determine the thrust effects on the empennage. H1 was tested with both 0 degree and -30 degree elevators. A horizontal tail with half the area of H1 (H2) was also tested. H2 did not have provisions for elevator deflections.

Tunnel Test Conditions

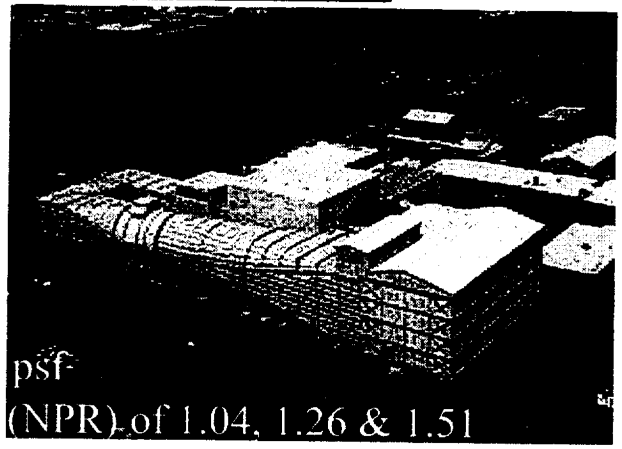

- $Re_c = 7.54 \times 10^6$
- Mach Number of 0.245
- Dynamic Pressure of 85 psf
- Nozzle Pressure Ratios (NPR) of 1.04, 1.26 & 1.51
- h/b (height*) of 0.18 (14"), 0.21, 0.30, 0.49, & 1.0 (77")
  * height (HGT) is W.L. of l.e. 50% cbar to tunnel floor.

The TCA-2 test was performed at the LaRC 14' x 22' atmospheric wind tunnel. The TCA-1 was previously tested in the same tunnel with a balance located in both the body and the tail section.

Three NPRs were tested and the model's height was varied as indicated above.

5% TCA Model Description

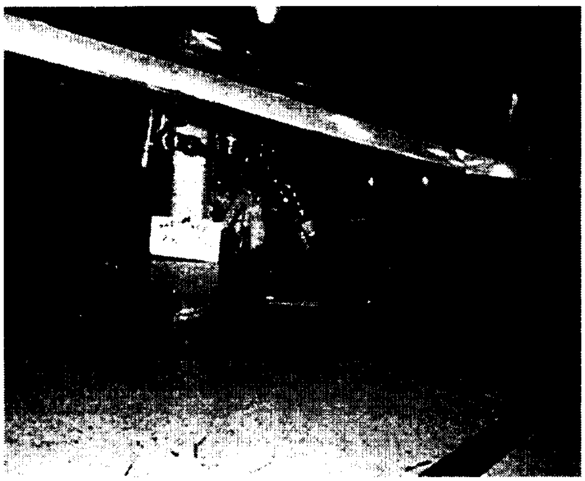

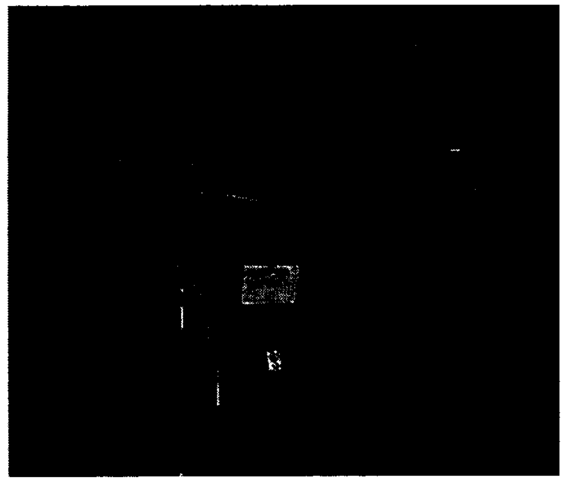

- Cover Plate and Floor Tufts
- Hose Slot
- Domed Inlets
- Non-Metric/Metric Bal. Split
- HP Hoses
- Takeoff Nozzles

The model's configuration is based on the TCA 1080-1450 outer mold line (OML) definition released in March of 1996. The model has been designed to be tested in the NASA Langley's 14' by 22' tunnel both powered and unpowered and also in NASA Ames' 12' pressure tunnel, unpowered, for Reynolds number effects. The model was constructed to determine the TCA configuration's low speed aerodynamic performance, provide a database for subsequent analysis and simulation, and examine the simulated nozzles' propulsion effects on the TCA configuration's performance, stability and control in ground effect.

The model's wing was originally designed to accommodate high pressure air plumbing necessary for powered testing. All four nacelles were supplied with separately controlled high pressure air, regulated by two choke plates in each nacelle, in order to acquire desired Nozzle Pressure Ratios (NPR). The above figures depict the provisions made for the high pressure air supply lines; their stiffness introduced concerns about tare and routing. The six-component internal balance was located between the mid-body and empennage. This facilitated the measurement of the aft-body's control surfaces' aerodynamic forces without requiring a complex tare reduction mechanism or mathematical tare removal. High pressure air supply hoses required special routing through a sliding slot in the floor aft of the support post. A diagram of the nacelle's called a 'Jet Flow Simulator' follows in a few pages.

Two sets of nozzles were built for the nacelles. One set was intended for use at the takeoff NPR settings, while the other was for the "flow-through" setting. Early studies showed that swapping the nacelles during the test was unnecessary and the "flow-through" NPR setting could be run with the takeoff nozzles. Slide #4 can be viewed for additional detail.

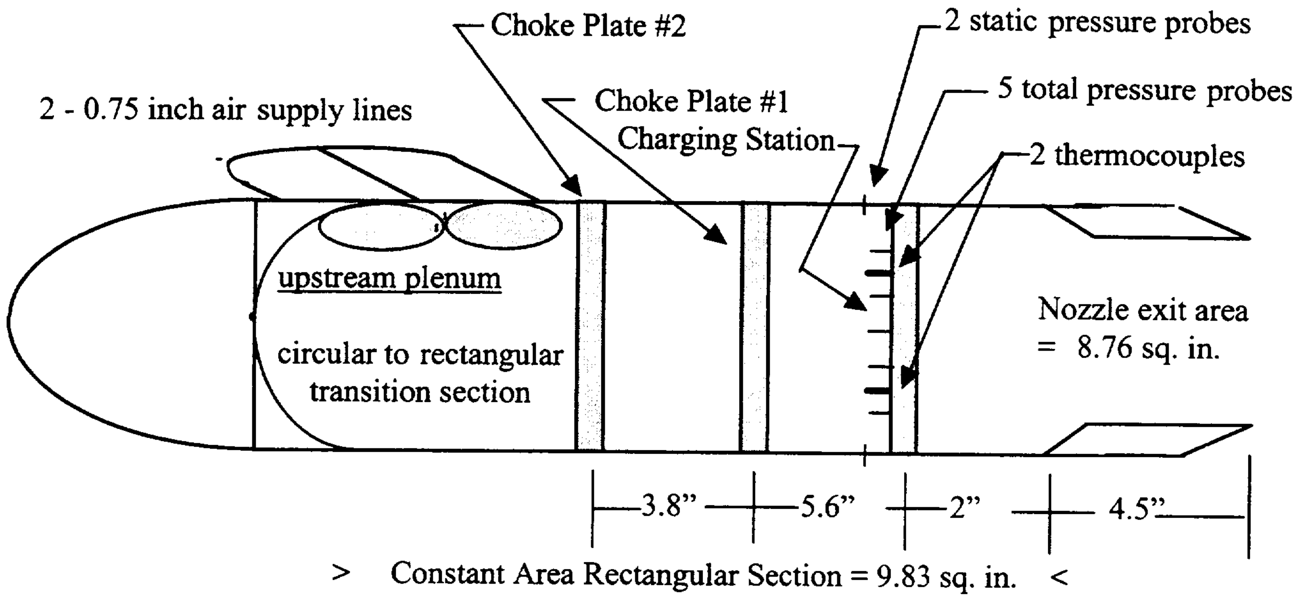

Jet Flow Simulator

The Jet Flow Simulator diagram depicts its functional construction. The high pressure supply lines injected air at approximately 340 psi to the nacelle's plenum. The pressurized air was moved along the circular to rectangular transition and choked through the two choke plates #1 and #2 to achieve the desired internal flow conditions. The Nozzle Pressure Ratio was determined by dividing the total pressure at the charging station over the ambient static pressure. This enabled an exhaust plume that most closely represented the full-scale plume.

Mass flow rate was determined by pressures and temperatures obtained from the total and static pressure probes and the thermocouples. Total pressure probe placement was important. Erroneous total pressure readings could have been obtained if the estimated internal flow profile was not known prior to start of the test. The probes were placed in a cosine distribution to best capture the conventional channel flow profile.

The takeoff and flow-thru nozzles were separate pieces attached to the aft end of the nacelles. The designed nozzle deflections were similar. Since the flow-thru NPR was attainable, the time spent to change between the two nozzles was saved by deleting the flow-thru nozzle from the test matrix.

Results

$$\Delta C_{m\ \mathrm{Exhaust\_gefa}} = (C_{m\ \mathrm{full\ thrust}} - C_{m\ \mathrm{flow\text{-}thru}})_{\mathrm{ground\ effect}} - (C_{m\ \mathrm{full\ thrust}} - C_{m\ \mathrm{flow\text{-}thru}})_{\mathrm{free\ air}}$$

"If $\Delta C_{m\ \mathrm{Exhaust\_gefa}} > 0.015$, test entire matrix."

1. **Ground Effects** achieved by varying the model **HGT** from 77"$\longrightarrow$ 14".
2. **Exhaust Effects** via varying **NPR**: 1.04 & 1.51.

The following data are presented as plots of pitching moment coefficient both absolute and incremental. Pitching moment was selected as the parameter to be used as a metric because small changes in the tail's local flow field are easily observed. Although the results are shown and discussed as incremental changes in pitching moment, the results are also quantified in terms of the change in the local angle of attack at the tail resulting from a change in either stabilizer incidence, downwash, or airplane angle of attack. The change in local angle of attack at the tail was determined by dividing the measured incremental pitching moment by the stabilizer effectiveness (typically -0.0045/deg.). Although the above equation sums up the additive effects of both ground effect and power, the following plots predominantly separate these effects for clarity. The plots and related text predominantly address the 10 degree angle of attack region. This was chosen as a reasonable alpha for takeoff and initial climbout regimes.

A delta of 0.015 in pitching moment coefficient was agreed on by team researchers prior to the start of the test in order to determine how much of the test matrix would have to be tested. If the delta obtained was greater than 0.015, the test was to progress through the entire test matrix of heights and power settings. The delta obtained early on in the test was greater than the 0.015; therefore the test proceeded accordingly.

Testing in ground effect was performed by moving the model from the tunnel centerline of 77" to 14" above the tunnel floor. An NPR of 1.26 was also obtained but used mainly for trends and not presented here.

The test centered around the takeoff flap setting of LE/TE = 30/20 with the stabilizer/elevator deflected to -15/-30. This stabilizer/elevator deflection provides the most airplane nose-up pitching moment simulating the nosewheel lift-off maneuver. Although the data was obtained on the aft balance, all pitching and yawing moments are referenced to the 50% cbar of the wing. Tail-off and nominal stabilizer settings of -15/0 were also tested to determine stabilizer effectiveness and downwash at the horizontal tail.

Pitching Moment Variation with Angle of Attack

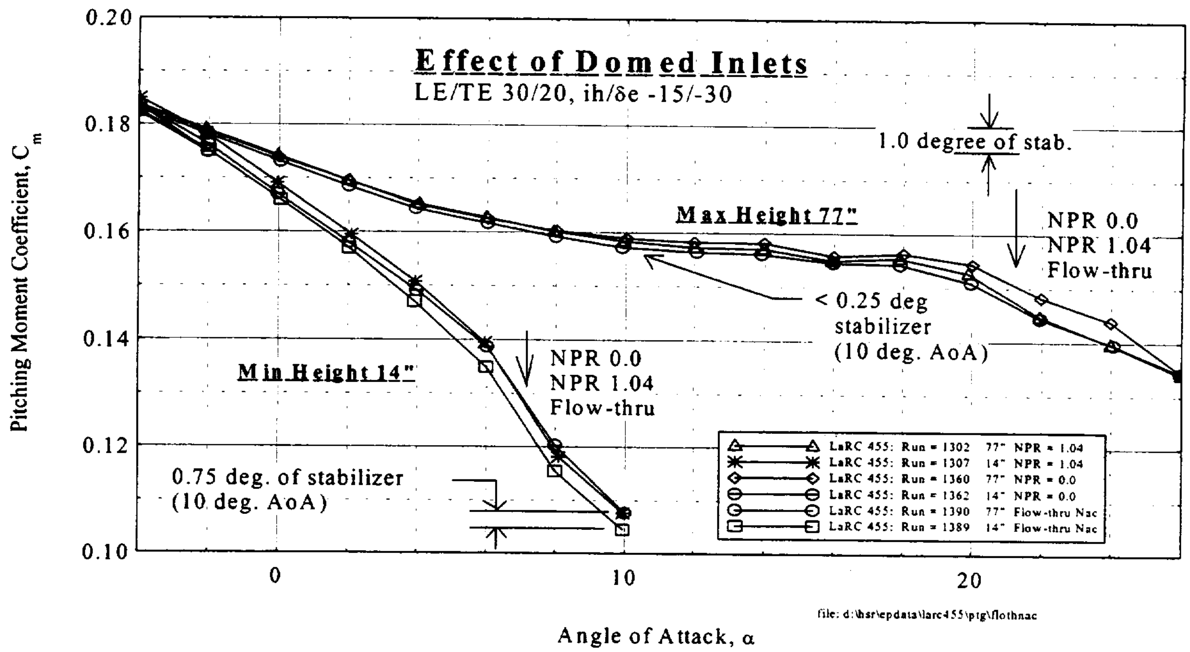

The above plot shows the impact of domed inlets at both 77 inches and 14 inches ground heights. A positive increment in pitching moment due to the presence of the domes is seen at both heights. While the impact of the domes is relatively small at the maximum height, equivalent to a 1/4 degree change in tail angle of attack, the impact at the minimum height is significantly more, about 3/4 degree change in tail angle of attack.

Pitching Moment Variation with Angle of Attack

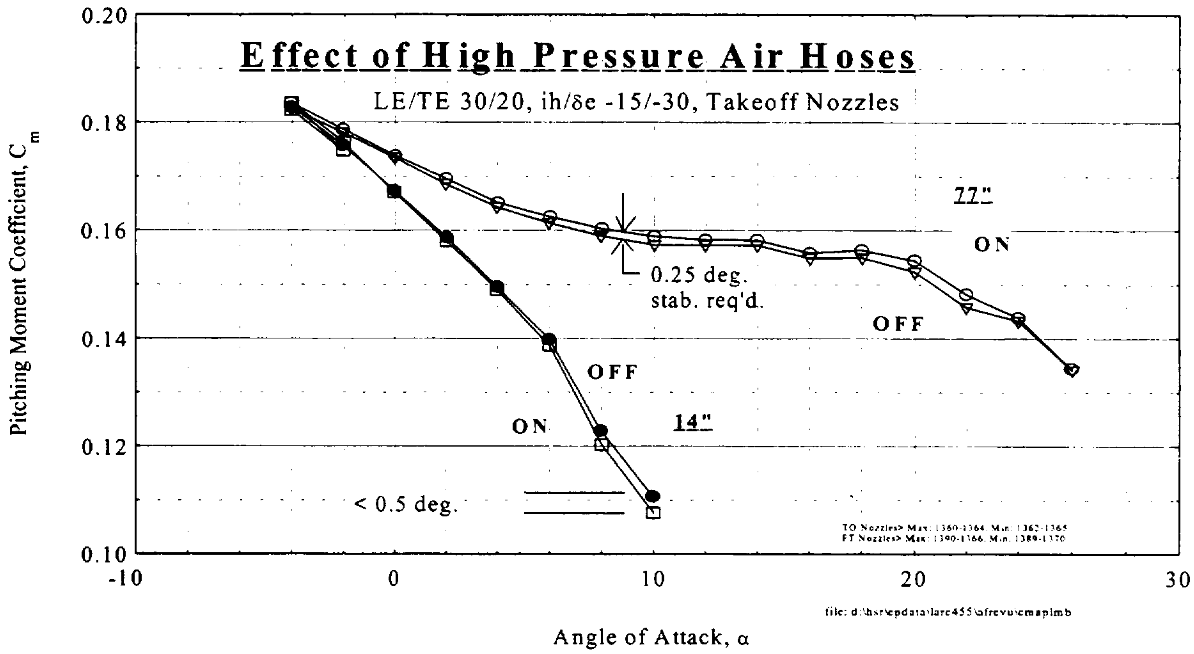

The above chart shows the impact of the air supply lines on the measured pitching moment coefficients. A positive increment in pitching moment is seen due to the presence of the air supply lines in free-air, while a negative increment is seen in ground effect. The magnitude of the increments at 10 degrees angle of attack appear to be the same at both heights and are equivalent to a 1/4 degree change in tail angle of attack.

Pitching Moment Variation with Angle of Attack

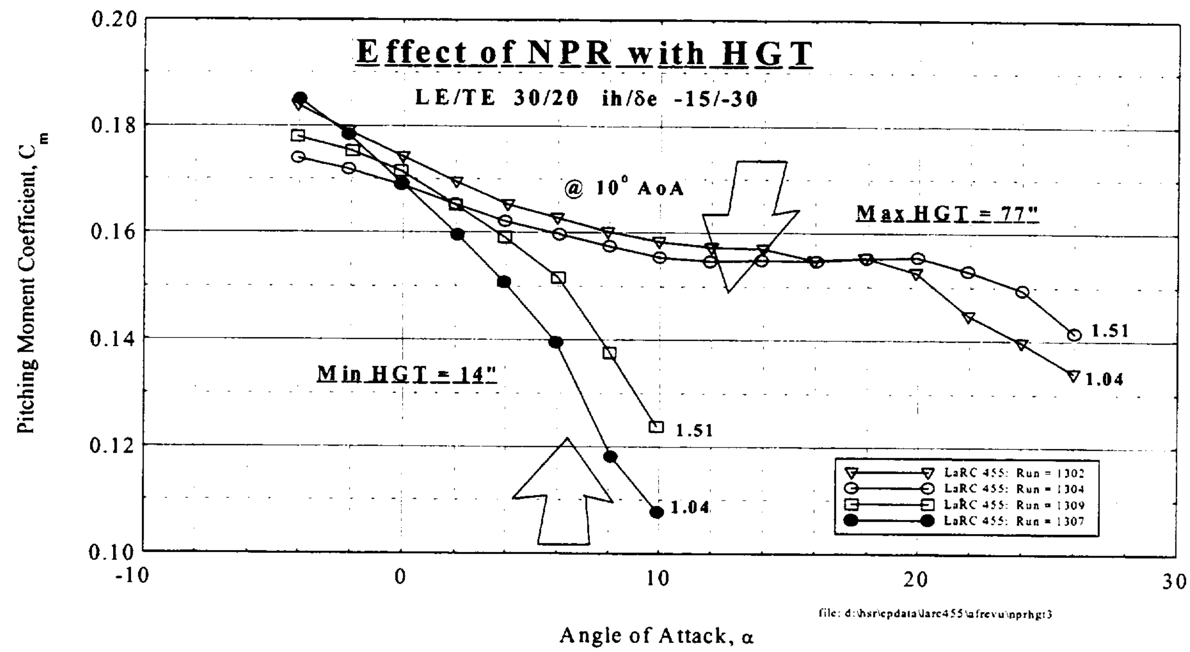

The above chart shows the impact of NPR on pitching moment in both free-air and ground effect for the takeoff flaps and the stabilizer/elevator deflection of -15/-30 configuration. As NPR is increased from 1.04 to 1.51, a significant increase in pitching moment is observed at the minimum height, approximately equivalent to a 3.5 degree change in stabilizer incidence. However, at the maximum height, the effect of NPR is greatly diminished and results in a decrease in pitching moment, approximately equivalent to a 3/4 degree change in stabilizer incidence.

The overall nose-down tendency in free-air is most likely due to the entrainment of the wing's downwash with the exhaust plume thus reducing the local angle of attack of the horizontal tail. The crossover in free-air at 16 to 18 degrees angle of attack indicates that increasing NPR has little impact on pitching moment because the tail is in the wing's wake.

The ground effect set of curves show a significant amount of nose-up due to a dynamic pressure or venturi effect acting on the lower surfaces of the horizontal tail. The slide on page 19 shows oil flow visualization highlighting this phenomenon.

The next slide summarizes the impact of the interference effects on the above measured data.

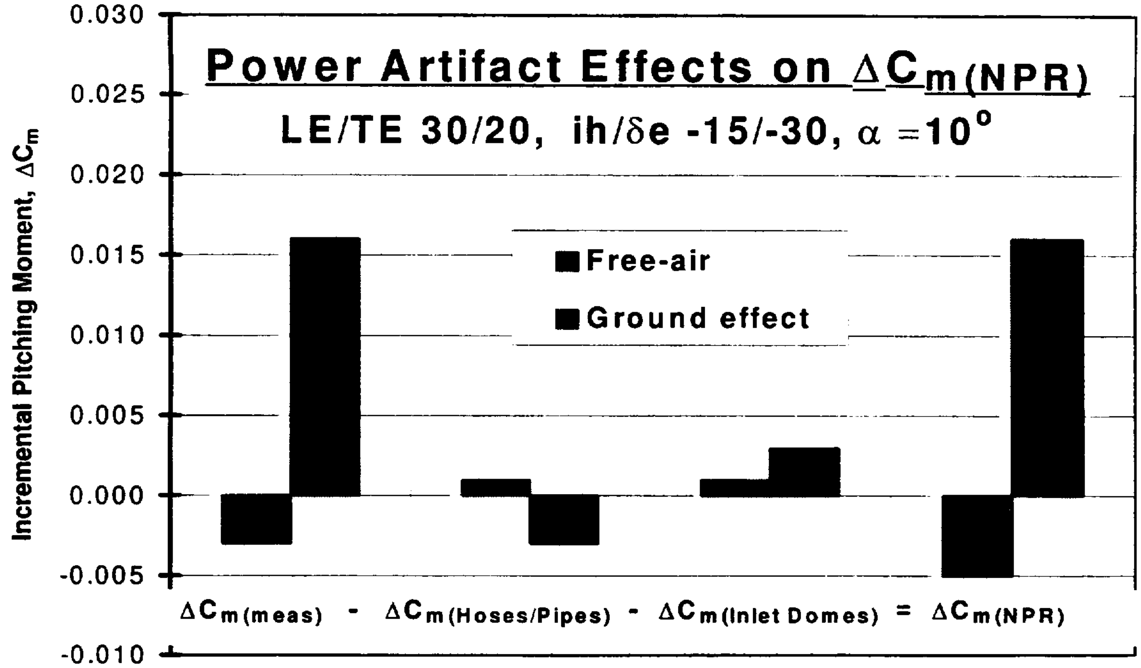

The above chart shows the combined effects of domed inlets and air supply lines on the measured incremental pitching moment coefficients. The final increment data (not including wind tunnel data reduction schemes) will be obtained by removing the cumulative power artifact effects (interference of domed inlets and air supply lines) from the measured data. The final power effect increments in both free-air and ground effect can be applied to the simulation database.

Note that in ground effect the artifact effects negate each other while in free-air they are additive and thus increase the measured pitching moment increments. Final incremental data for the above case shows the free-air pitching moment increment decreasing to just over one degree of tail angle of attack while the ground effect increment remains the same.

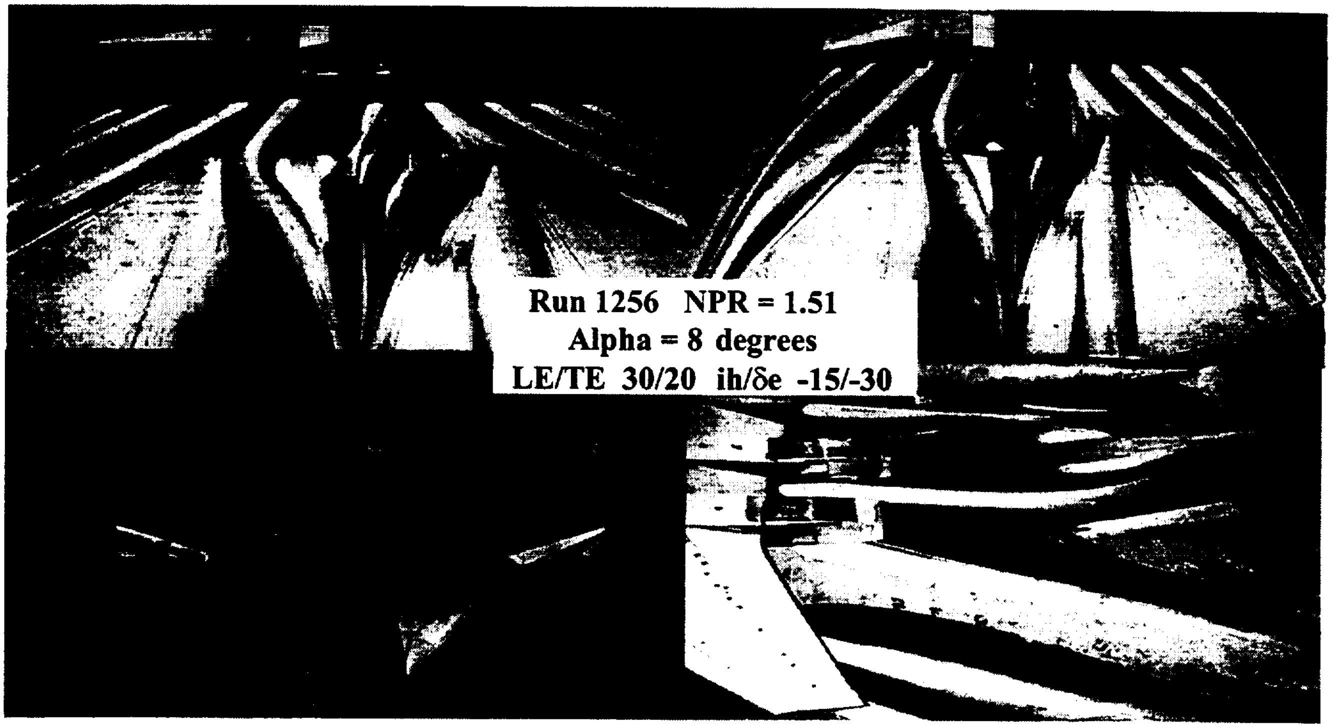

<u>Pictures: Top 1 -> 2, Bottom 3 -> 4.</u>

The above pictures illustrate some of the oil flow visualization performed during the test. These pictures are of the same run from different perspectives. Note that the oil pattern in picture 2 looks very symmetrical but when viewed from a different angle, such as picture 1, the flow lines are somewhat distorted and seem 'braided.' Although it was thought that the air lines were going to cause significant interference, they did not by virtue of the results shown on the previous chart. Pictures 1-3 depict the wing's cross-flow and vortices even at this relatively small angle of attack of 8 degrees. It should be evident from the above pictures that the air is sped up under the tail consistent with a venturi effect which creates lower pressures and thus results in the increased airplane nose-up pitching moment increment. Picture 4 is just a side view; the tail's upper surface can be seen.

Pitching Moment Variation with Angle of Attack

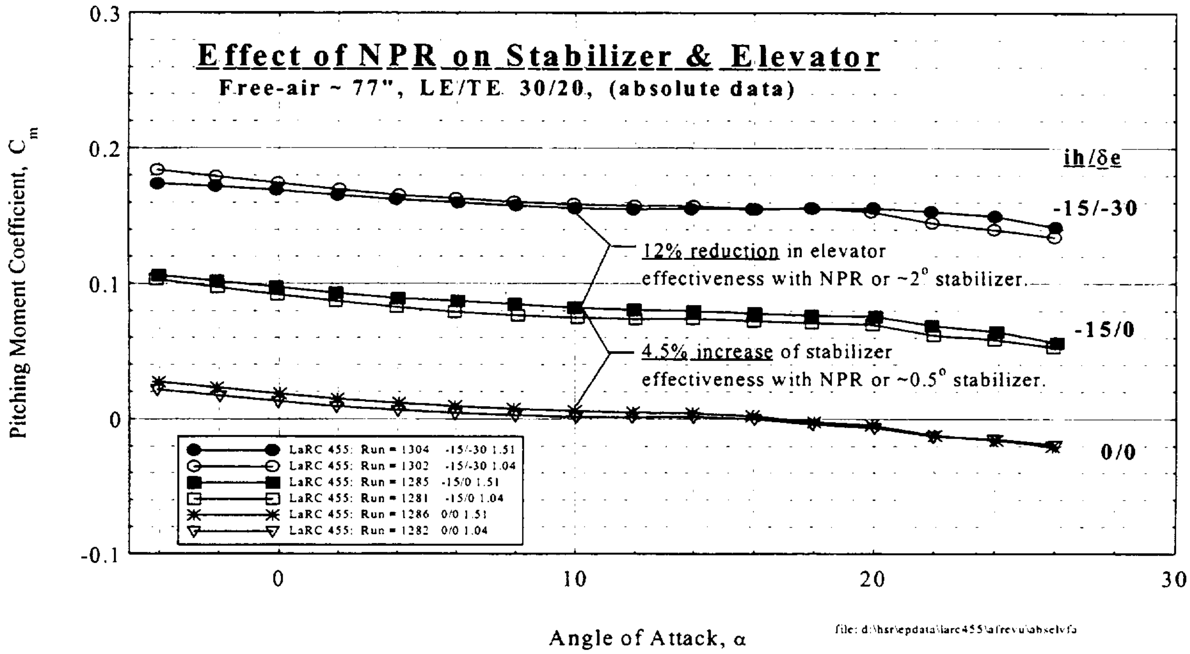

The next four slides show the effect of NPR on both elevator and stabilizer effectiveness for stabilizer/elevator deflections of -15/0 and -15/-30 with takeoff flaps LE/TE 30/20. The data are presented in free-air and in ground effect separately. The data are presented at the two heights as both absolute and incremental.

The above chart shows the absolute pitching moment data in free-air. As NPR is increased, the elevator's effectiveness is shown to reduce by 12% while the stabilizer's effectiveness is increased by 4.5%. This reduction of elevator effectiveness is puzzling and is better illustrated in the next slide.

Incremental Pitching Moment Variation with Angle of Attack

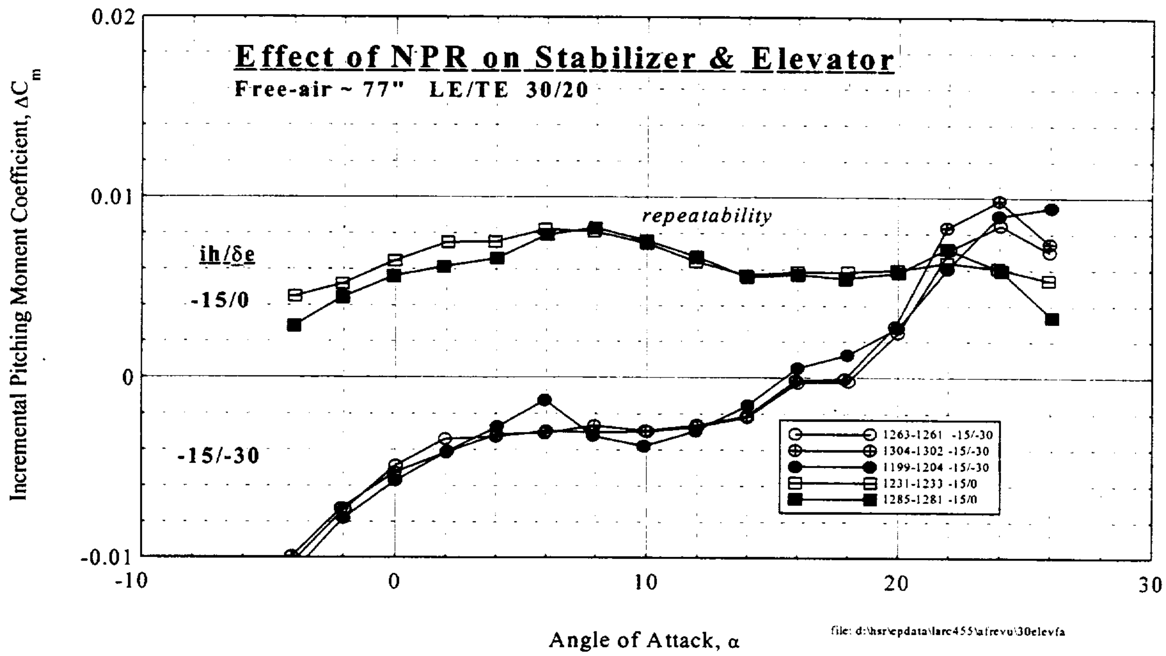

The above chart shows the incremental pitching moment effect of increasing NPR in free-air on the two specific stabilizer/elevator combinations. The increment is calculated by subtracting the absolute data at NPR = 1.04 from the absolute data at 1.51 for each stabilizer/elevator configuration shown. The incremental pitching moment effect of NPR on the -15/0 stabilizer deflection is positive over the entire angle of attack range. The positive increment equates to approximately a -2 degree stabilizer incidence change.

Note, as NPR is increased with the stabilizer/elevator deflection of -15/-30, the pitching moment increment is negative for the terminal area alpha range. This reduction in elevator effectiveness equates to approximately a 3/4 degree change in stabilizer incidence.

Repeat runs are also shown in this plot. Repeatability is shown to be reasonable, particularly at 10 degrees alpha. Consistent NPR settings would obviate much of the variance in the data and will be discussed later.

Pitching Moment Variation with Angle of Attack

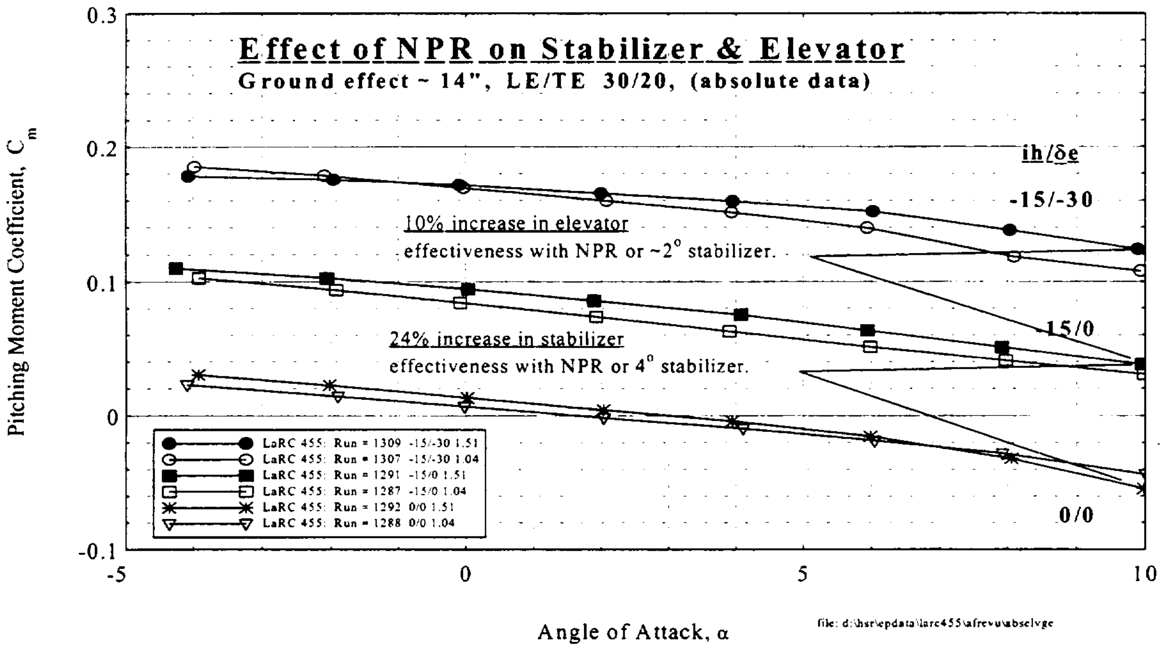

The above chart shows the absolute pitching moment data in ground effect. This chart shows that increasing NPR in ground effect has a beneficial effect on both stabilizer and elevator effectiveness. This significant increase in stabilizer effectiveness equates to approximately a -4 degrees change in additional stabilizer incidence. The increase in elevator effectiveness is similar to a -2 degree change in stabilizer incidence. The following slide better illustrates the benefits.

Incremental Pitching Moment Variation with Angle of Attack

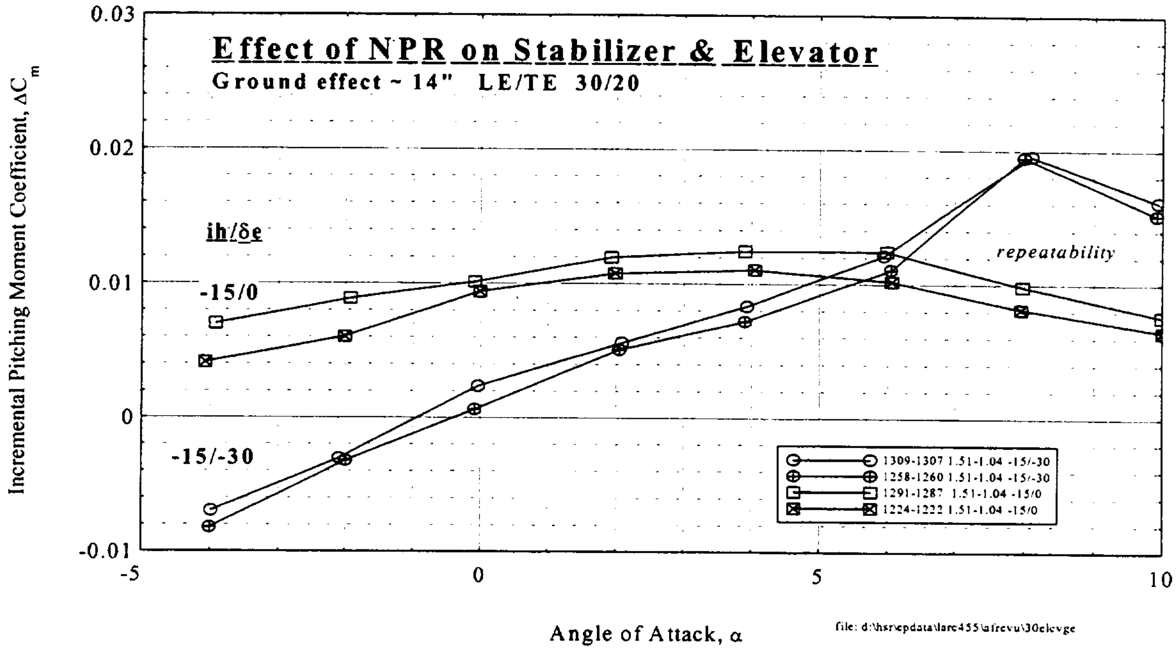

The above chart shows that increased NPR increases both the stabilizer and elevator effectiveness in ground effect for all positive angles of attack. The increments are calculated by subtracting the absolute data at NPR = 1.04 from the absolute data at 1.51 for each stabilizer/elevator configuration shown.

Repeat runs are also shown in this plot. Repeatability of the data is worse in ground effect than in free-air but is sill acceptable, particularly for the -15/-30 stabilizer/elevator configuration. Overall, repeatability could have been improved by maintaining more consistent NPRs. The tail balance showed no significant anomalies during the test that would have resulted in unsatisfactory repeatability.

Incremental Pitching Moment Variation with Angle of Attack

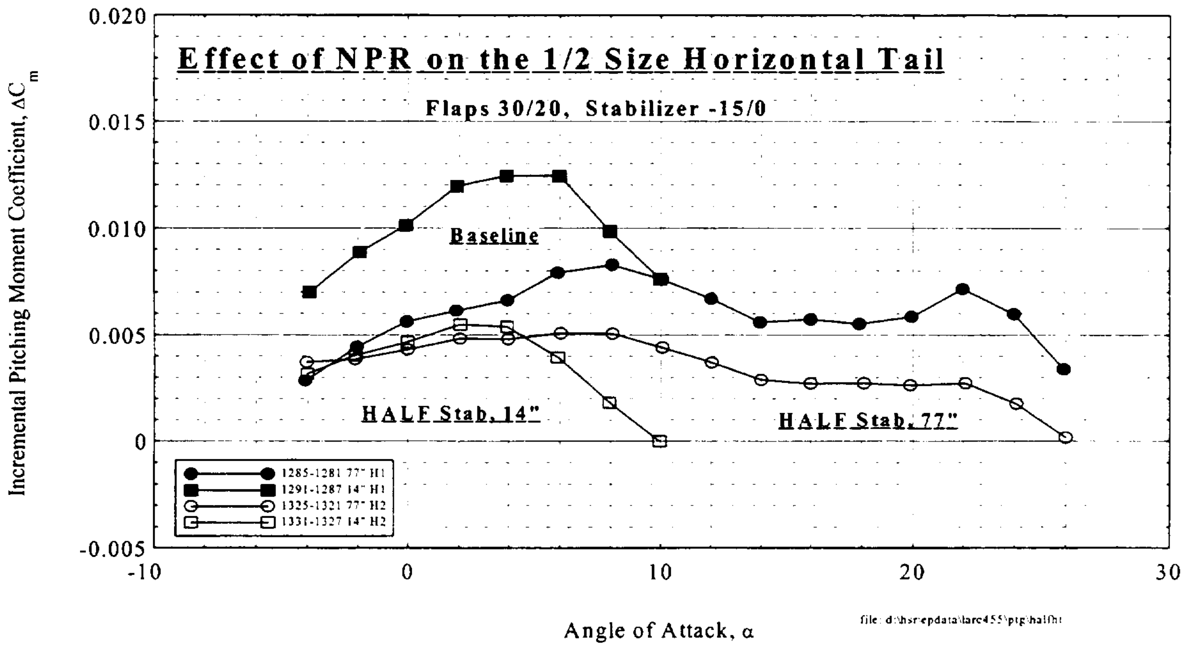

The above chart shows the incremental effect of NPR on the half-sized (H2) horizontal tail (400 sq. ft.) both in free-air and ground effect. The incremental effect of NPR on the baseline (H1, 800 sq. ft.) is also shown for comparison. Both H1 and H2 are at a stabilizer/elevator deflection of -15/0 in the above incremental data plot.

In general, the incremental effect of NPR on the H2 tail in free-air is more than half the increment observed on the H1 tail at low to moderate angles of attack. This incremental effect is approximately half at higher angles of attack until 20 degrees is reached where the effect reduces to no observable effect at 26 degrees alpha.

However, in ground effect the incremental effect of NPR on the H2 tail is approximately half that observed for the H1 tail up to about 4 degrees angle of attack. Beyond 4 degrees alpha, the incremental effect on the H2 tail begins to rapidly diminish with no effect evident at 10 degrees alpha.

Incremental Pitching Moment Variation with Angle of Attack

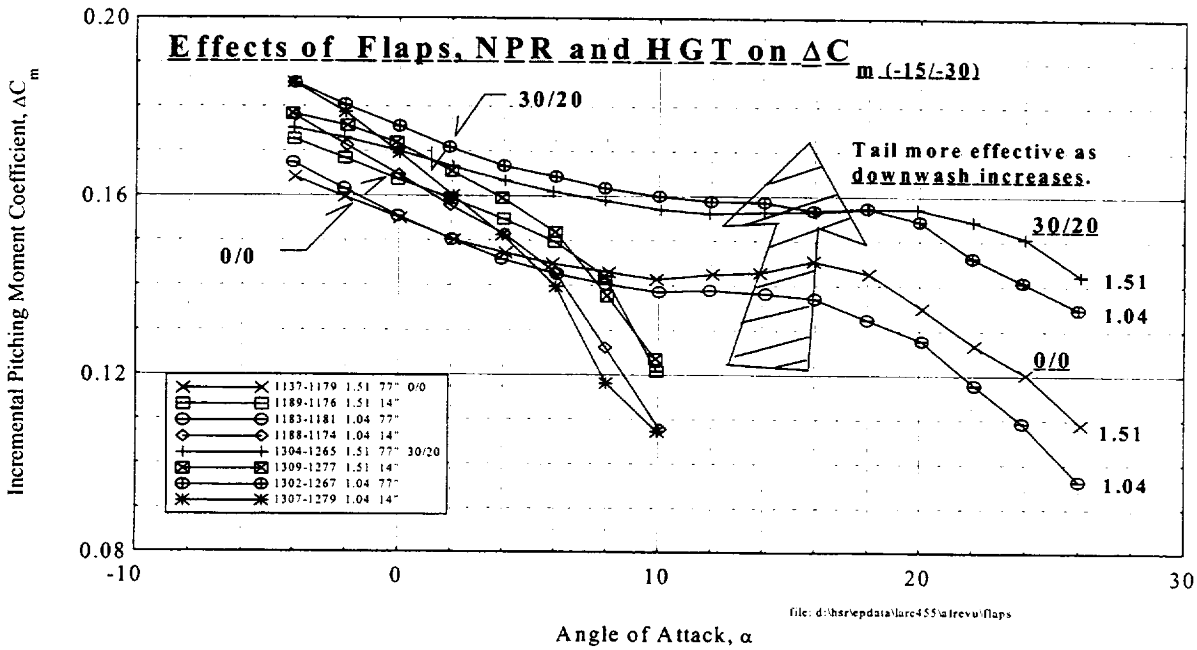

The above plot shows the effect of NPR on the 0/0 and 30/20 flap configurations at both free-air and ground effect heights for the incremental pitching moment of the stabilizer/elevator deflected -15/-30. The 0/0 flap deflection was tested in conjunction with the 30/20 flap deflection in order to provide an increment for the simulation database. The reduced level of pitching moment for the 0/0 flap when compared to the 30/20 flap configuration is the result of reduced downwash and thus reduced local alpha at the tail.

The trends in pitching moment increment due to NPR and height changes are similar for the 0/0 flaps when compared to the 30/20 flaps. One exception is when NPR is increased in free-air for the 30/20 flap deflection; -4 to 16 degrees alpha shows an airplane nose-down pitching increment while the 0/0 flaps shows the opposite increment. The ground effect curves of the two different flaps settings show comparable, positive increments.

Yawing Moment Variation with Angle of Sideslip

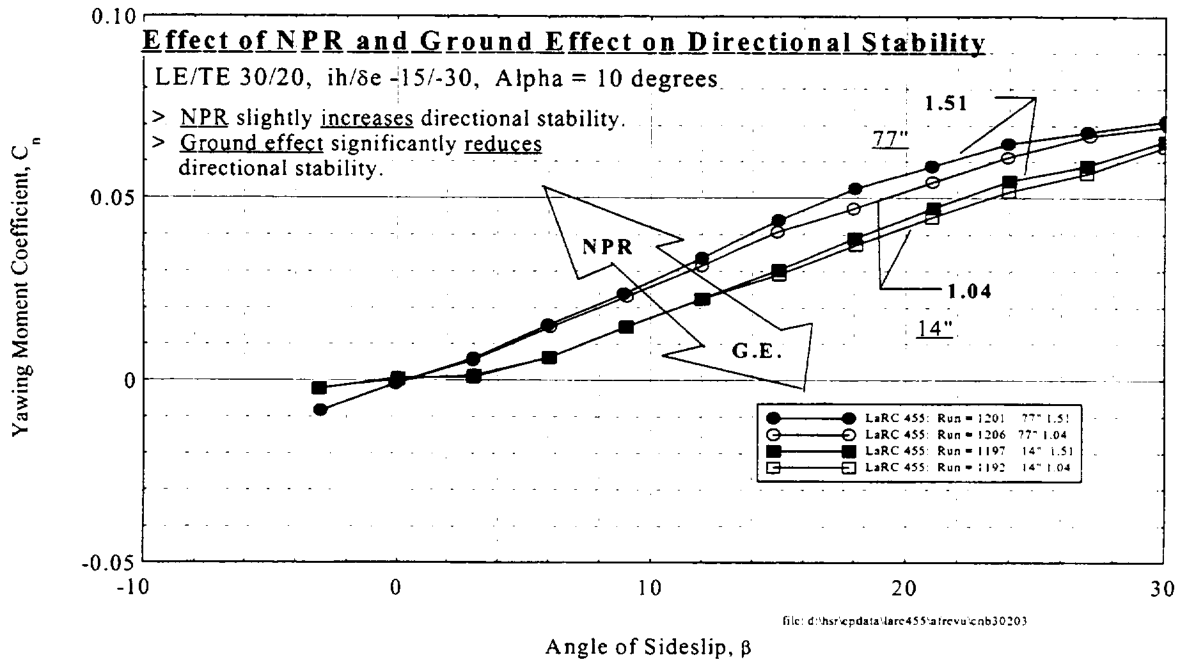

The above plot shows the effect of NPR on directional stability for alpha = 10 degrees. Both in free-air and in ground effect, the data show that increasing NPR increases directional stability. While the effect of NPR is of primary interest, ground effect is shown to significantly reduce directional stability particularly at small sideslip angles. At all angles of sideslip, the yawing moment due to sideslip is greater in free-air than in ground effect.

Conclusions

- Impact of exhaust on tail is a 'non-issue' as the stabilizer is far from stalled.
- ΔCm_NPR (30/20 Flaps): negative in free-air due to reduced downwash from plume entrainment and positive in ground effect due to a dynamic pressure increase on tail near the ground.
- Elevator effectiveness lessens in free-air and increases in ground effect while stabilizer effectiveness increases at both heights.
- Half-sized horizontal tail effectiveness due to NPR was greater than half of the baseline tail's in free-air and less than half in ground effect.
- Increased Cn_{β} due to NPR.

The main conclusion drawn from the data thus far indicates that the exhaust plume simulating takeoff power shows no detrimental effects to longitudinal control power.

An additional nose-up pitching moment increment due to NPR was obtained in ground effect for the -15/-30 stabilizer/elevator deflection for both flap configurations tested. However, the flaps 30/20 free-air case showed a slight airplane nose-down increment with the application of power.

Stabilizer effectiveness was shown to increase in both free-air and ground effect for the baseline horizontal tail with the application of power. Elevator effectiveness on the baseline tail was reduced in free-air while in ground effect it was shown to increase. The half-sized horizontal tail effectiveness increase due to NPR was shown to be greater than half of the baseline tail's. This effect due to NPR was reduced in ground effect. Both increases in stabilizer and elevator effectiveness benefit the nosewheel lift-off maneuver at takeoff.

Power increased directional stability.

Lessons Learned

- High pressure flex-hoses don't have to be stowed.
- Repeatability from precise control of NPR a must.
  - *a. NPR control of 0.05 desired while 0.1 was the norm.*
  - *b. NPR settings would drift as run was on-going.*
  - *c. No acceptable repeatability by human intervention.*
- Leak rate less than 0.005 lbs/sec difficult to meet.
- Precise, consistent stabilizer drive needed.
- Good mass flow calculation is f(Probe placement within the nacelle).
- Prominently mark pertinent model pieces.
- Probes fail.

Prior to the start of the test, the air supply lines were anticipated to have a significant effect thus reducing the quality of the data. This turned out not to be the case as shown previously.

Data repeatability could be improved by maintaining more consistent NPR settings. NPR settings varied during runs and were not easily maintained even with the assistance of human intervention. Better control of NPR would reduce any potential repeatability problems.

Maintaining a leak rate below the target of 0.005 lbs/sec was difficult. The model was very susceptible to leaking if touched by the mechanics.

The stabilizer was susceptible to drift. Maintaining constant stabilizer incidence would improve repeatability.

The placement of total pressure probes affect the mass flow calculations. The flow profile must be known apriori in order to place total pressure and temperature probes in a logical set of locations for good mass flow calculations.

A portion of the test was performed with the wrong outboard flaps, which cost valuable research time. Model parts need to be prominently marked for easy identification.

Pressure and temperature probes failed. This led researchers to substitute readings from one probe to that of another location. This leads to errors in specific flow quantities and can provide misleading results when data are reduced for mass flow calculations.

Recommendations

- Perform an isolated check out of powered nacelle(s).
- Design larger powered models to further reduce any high pressure air-line routing impact if the testing facilities are capable.
- Ensure tail drive mechanism has no hysteresis in its inherent design by increasing estimated loads.
- Revamp the controllability of sustaining NPR.
- Acquire ability to seed plume.
- Heated plumes recreate buoyancy (ejectors/bypass).
- Know that 'leaks' are not a 'good' thing.

The following recommendations are given for future powered tests. It seems logical to ensure that the workings of the jet flow simulators (JFS) are fully functional before the actual test start date. Perhaps an isolated test of the JFSs is necessary. Leak rates could have been reduced earlier which would have allowed the actual data taking to have started earlier.

Data repeatability can always be improved by reducing the mast wake turbulence, increasing the controllability of NPR and eliminating the drift in tail incidence. A fairing around the air supply lines could have reduced further any interference from these artifacts. Controllers used to monitor NPR need to be analyzed. As mentioned before, NPR settings varied greatly during a test run.

Hysteresis in any control surface drive mechanism needs to be determined by calibrating with substantially more loads than anticipated in the test.

There is a definite need to view the exhaust plume in three-dimensions. Oil flow does not give height nor breadth. This would have been more insightful and should be provided where flow visualization is needed or requested.

Heated plumes create buoyancy which better simulate the real exhaust plume. The effect of ejector and bypass door turbulence was not investigated in this test. These are added complications but factors that lead to a closer approximation of the exhaust plumes. Some of these items were looked at in the HEAT 1 test.

In closing, when performing a powered test, know that leaks in pressurized nacelles do not assist in gathering good data.

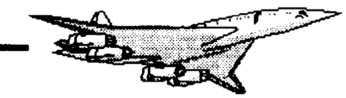

Assessment of Boundary-Layer Transition Detection and Fixing Techniques

Marvine Hamner and Roger Clark
Boeing, Long Beach

HSR Airframe Technical Review
Los Angeles, California February 9-13, 1998

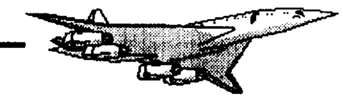

This page intentionally left blank

Increase L/D, Develop Analysis/Design Methodology

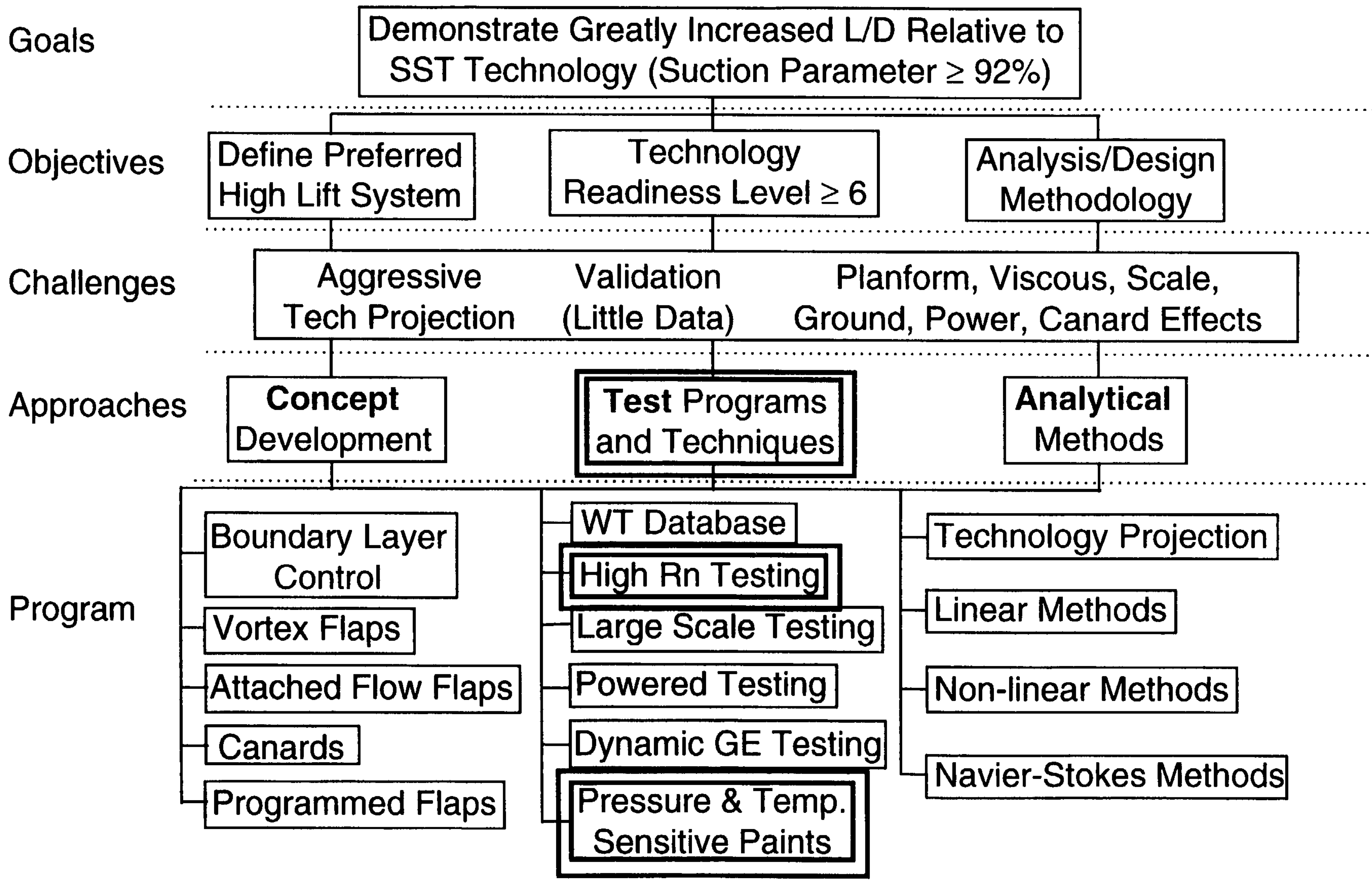

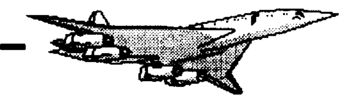

This page intentionally left blank

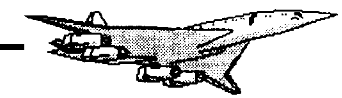

Outline

- Introduction
- Transition Detection Techniques
- TSP System Detail
- TSP Results
- Summary

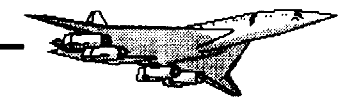

This page intentionally left blank

Introduction

- Effect of boundary layer transition
  - all low speed testing performed with free transition
  - results must be extrapolated to full scale Reynolds number
  - typical wind tunnel Reynolds number ~ 8 Million (based on MAC)
  - Flight Reynolds number ~ 200 Million
- What is the extent of laminar flow at low Reynolds number

Of the many techniques available for transition detection and boundary-layer analysis, four candidate techniques were selected for evaluation. These are the four techniques listed in the chart below.

Development of IR imaging in cryogenic environments had been largely carried out by Dr. Ehud Gartenberg of Old Dominion University. His results are documented in "Boundary-Layer Transition Detection with Infrared Imaging Emphasizing Cryogenic Applications," circa 1992.

Development of TSP imaging has been carried out by a number of sources. The specific application of TSP to transition detection had been primarily carried out at Purdue University by a number of investigators under the tutelage of Dr. John Sullivan. Papers on the subject include: "A Preliminary Investigation of the Effect of Acoustics and Leading-Edge Heating on Boundary-Layer Transition," Marvine Hamner and Joseph B. McGuire; and "Temperature Sensitive Fluorescent Paints for Aerodynamics Applications," Bryan Campbell.

Dynamic acoustic detection is a technique that has been discussed for some time now but has not yet been extensively developed. "Dynamic Acoustic Detection of Boundary Layer Transition," by Jonathan (J.r) Grohs and Guy Kemmerly discusses this technique.

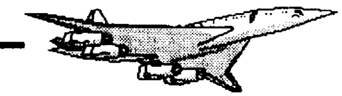

Transition Detection Techniques Evaluation and Selection

4 Candidate Techniques Identified

- IR Imaging
- TSP Imaging
- Dynamic Acoustic Detection
- Hot Films

A significant effort had already been expended in developing a technique for boundary-layer analysis in LaRC's NTF. The previous focus had been on IR imaging. Many complications exist in applying this technique to metal models in a cryogenic environment and in acquiring the increasingly long wavelength signals emitted as the test temperature is decreased. As discussed in Gartenberg's paper, extending the wave band of a given IR imaging system to cover the entire HSR NTF temperature range would not be a trivial effort in terms of either manpower or dollars.

A significant effort had already been expended in development of TSP in an academic environment. TSP had been found to be a relatively easy to use and robust wind tunnel test technique. Early efforts required that a model be heated in order to create a temperature difference between the model surface and the atmospheric wind tunnel total temperature present during testing. Rather than heating the model, in facilities such as the 0.3m and the NTF the tunnel total temperature could be varied to create the same overall system.

TSP alone has sufficient resolution to acquire steady-state data for boundary-layer analysis. However, as with all other types of instrumentation, the sensor (in this case TSP) is only one component of a system in which many sources of noise exist. Current TSP system's signal-to-noise ratio is insufficient to permit acquisition of steady-state boundary-layer data directly. Hence a temperature step is used to perturb the system and acquire the desired data.

Advantages/Disadvantages of Candidate Techniques

- IR Imaging
  - A significant amount of development work had already been completed for this technique in the 0.3m Cryogenic Wind Tunnel at LaRC.
  - The technique was found to have a limited operating range and would not operate over the entire HSR NTF temperature range. Hence, the Reynolds number range using this technique would be limited.
- TSP Imaging
  - A significant amount of development work had already been completed for this technique in academia.
  - The technique had not been tested in a production facility.

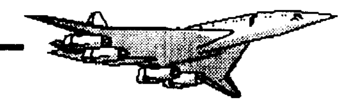

Although dynamic acoustic detection appeared to be a plausible alternative for HSR, many unanswered questions existed regarding this technique. The technique would use existing pressure ports so that no model modification was required to acquire the data for the upper surface. The lower surface contains only a sparse number of pressure ports. In addition, several dynamic EPS modules would be required to acquire data from the many ports necessary to characterize the boundary-layer state over the entire wing. There wasn't enough space available in the model for these modules.

Advantages/Disadvantages of Candidate Techniques (continued)

- Dynamic Acoustic Detection
  - Very little development work had been done on this technique.
  - This technique would require the use of dynamic EPS modules in the model which were not currently available in a size that would fit in the available model space. In addition, the length of pressure tubing had been found to affect the data acquired. A substantial effort would be required to determine if this effect could be overcome

Hot films are a traditional method of transition detection. Typically the rms signal from the hot film is analyzed to determine the change from a laminar boundary-layer to a transitional boundary-layer and finally to a fully turbulent boundary-layer. The hot film itself will trip the boundary-layer; and, a turbulent wedge is seen aft of the device. This requires the careful placement of the hot films to obtain meaningful data and hence some prior knowledge of the boundary-layer state from experiment, CFD, or boundary-layer stability analysis.

Advantages/Disadvantages of Candidate Techniques (continued)

- Hot Films
  - Traditional method of measuring boundary-layer transition.
  - However, the use of hot films over the entire HSR NTF temperature range had not been demonstrated. In addition, because hot films make discrete measurements, placement of these devices on highly swept wings that would ensure successful data acquisition had to be developed. This development would require knowledge of the boundary-layer state that was the focus of the original effort.

This page intentionally left blank

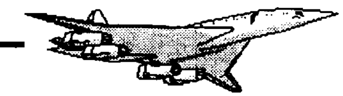

TSP System Detail

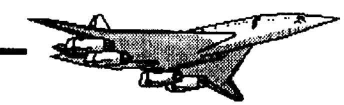

Temperature sensitive paint (TSP) is composed of two parts: the binder, currently a polymer matrix; and the probe molecule which luminesces upon excitation.

A paint's luminescence, or light emission, depends on a variety of parameters: the probe molecules quantum yield, the thickness of the paint layer and any undercoat present, and the excitation light. The paint can be excited by either continuous or flash lighting.

A thermal pathway to de-excitation exists for temperature sensitive paints; whereas pressure sensitive paints exhibit a sensitivity to molecular oxygen. This means that with variations in temperature a temperature sensitive paint will emit more or less photons.

TSP's currently used in the NTF are based on a variety of ruthenium complexes. The University of Florida developed one, Ru(tdp), specifically to extend the temperature operating range of TSP. Unfortunately, in extending the operating range enough sensitivity was lost that this paint does not yield consistent results with the current TSP system's signal-to-noise ratio

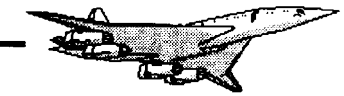

Temperature Sensitive Paint (TSP)

- Contains two parts:
  - The paint binder, currently a polymer matrix
  - The probe molecule, currently a variety of ruthenium complexes which display temperature sensitivity
- Paint luminescence:
  - Depends on the excitation light, currently about 400 nm
  - Varies with changes in local temperature
- Operating range and sensitivity:
  - Temperature sensitive paints have been developed with increased operating range at the expense of sensitivity. With the current TSP system in the NTF, paints with a sensitivity of ~1% change in luminescence per °F yielded good results. Paints with a sensitivity of ~0.85% change in luminescence per °F did not yield consistent results.

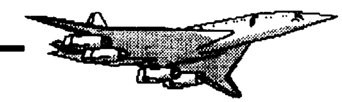

TSP System architecture is almost identical to PSP System architecture. Differences occur in the paint applied and hence the wavelength of the excitation lighting. Other differences occur in the types of noise reduction and image processing applied.

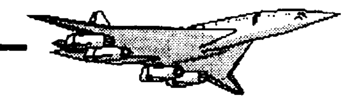

TSP Systems

- TSP System development strongly parallels pressure sensitive apint (PSP) system development. A schematic of a typical paint system, in this case a PSP system , is shown below

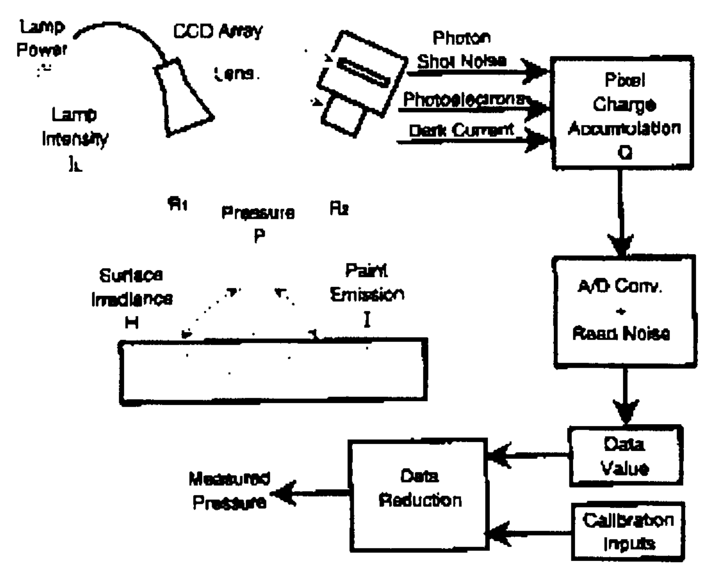

Figure 7 - Pressure Sensitive Paint Transduction Mechanism Details

Taken from "Measurement Techniques" by Roger C. Crites, VKI LS 1993-05

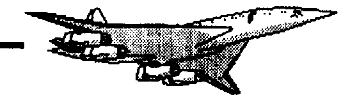

This slide describes components of the current NTF TSP System. This is a prototype system; it will likely change.

Flash lighting was used in NTF084 and NTF080. About 65% of the light's capacity provided sufficient illumination after filtering. The filters used only passed approximately 20 percent of the light. The filters were centered at 400 nm.

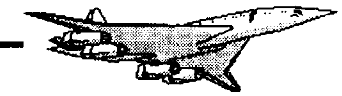

TSP Systems (continued)

- Current NTF TSP System Configuration:
  - Excitation lighting consists of one or more 4000 Watt-Second flash lamps.
  - A filter is applied to the flash lamps that is centered at 400 nm.
  - Three cameras are currently available:
    - 14-bit Photometrics CH250
    - 12-bit Photometrics SenSys
    - 12-bit Silicon Mountain Design (not currently used)
- Redundant image processing systems exist:
  - PC based system for ratioing images
  - SGI based system for complete image processing

This page intentiionally left blank

TSP Results

This slide illustrates a comparison between previous sublimating chemical results and NTF084 TSP results. Two sets of data are available for this comparison. The results shown for the Mach = 0.9 case compare well. Notice the absence of sublimating chemical at the leading-edge as well as the similar darker region in the TSP results indicative of the thin laminar boundary-layer present in that area. Because the laminar boundary-layer is so thin in this area, the mass or heat transfer rate, respectively, is the same as or greater than that of the turbulent boundary-layer. Unfortunately, the sublimating chemical picture available for the Mach = 0.3 case includes the presence of a significant amount of chemical residue on the inboard panel which is suspected to be the result of an overly thick application of the chemical prior to running. Hence the Mach = 0.3 case does not compare well.

Comparison of Sublimating Chemical and TSP Results

Mach = 0.9
Chord Reynolds Number = 10.2 Million
Alpha = +4 Degrees
Lower Surface

TSP Results

Sublimating Chemical Results

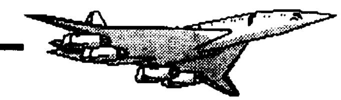

This slide illustrates the TSP results for the high-lift configuration. No evidence of laminar flow was found on this configuration except possibly at +4 degrees angle-of-attack and a chord Reynolds number of 5.5 million. This configuration was tested over an angle-of-attack range from 8° to 14°, and +/- 4°. The Reynolds number range tested was from 5.5 Million to 21.6 Million based on the reference chord.

Untripped High-Lift Configuration

Chord Reynolds Number = 8.5 Million
Mach = 0.3
Alpha = +10 Degrees
Upper Surface

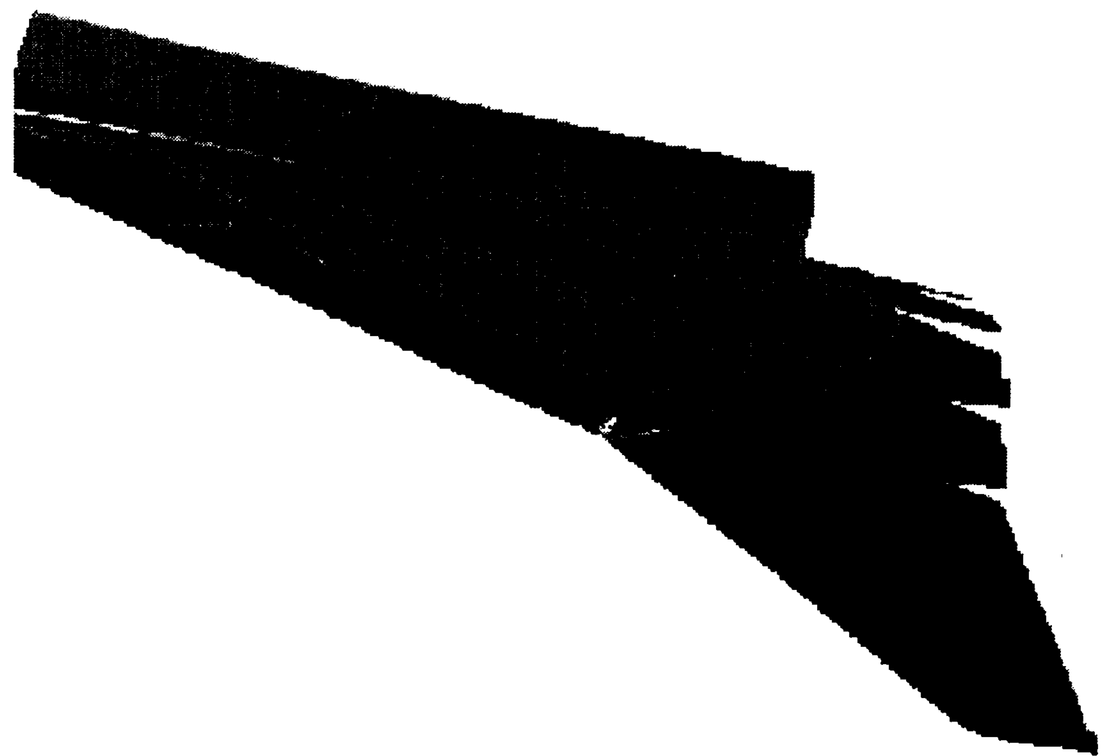

No evidence of lamina
at high-lift design poin

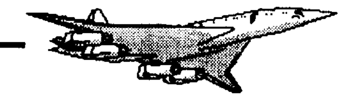

This slide illustrates the TSP results for the transonic configuration. As can be seen the boundary-layer is tripped at the leading-edge flap hingeline.

Untripped Transonic Configuration

Chord Reynolds Number = 10.3 Million
Mach = 0.9
Alpha = +1 Degrees
Upper Surface

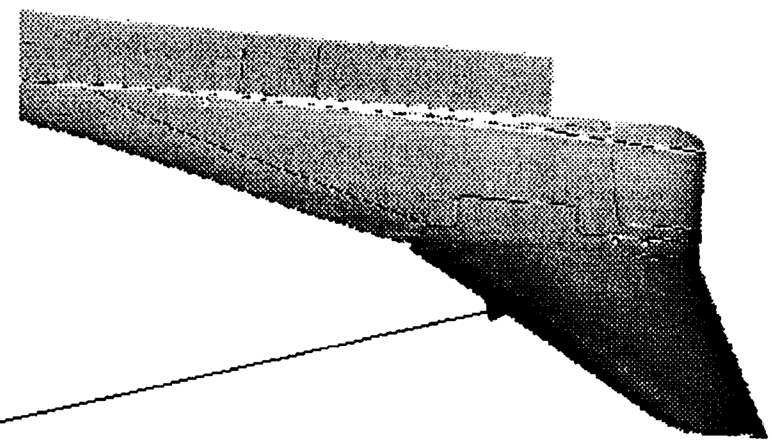

Boundary-Layer is tripped at the leading-edge hinge line

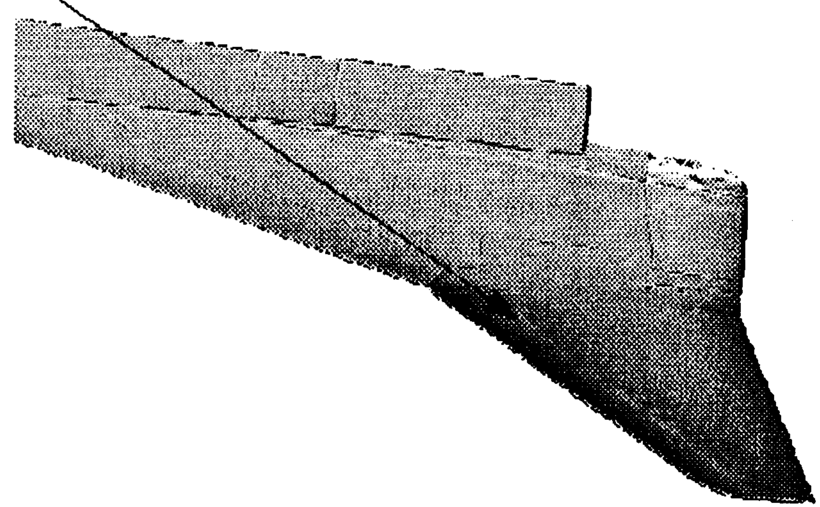

Chord Reynolds Number = 10.3 Million
Mach = 0.9
Alpha = +3 Degrees
Upper Surface

The variation in laminar boundary-layer extent with Reynolds number is clearly evident in this chart.

This chart shows a comparison of TSP results, wind tunnel drag data, and analytical skin-friction predictions at Mach = 0.3. The wind tunnel data point at chord Reynolds number = 40 million has been determined to be a bad data point. The analytical skin-friction curves in this chart were anchored using chord Reynolds number = 90 million drag data.

TSP results are plotted as percent laminar, or laminar fraction, versus chord Reynolds number. The technique for extrapolating from low Reynolds number data to full scale flight conditions will involve acquiring drag data at low Reynolds number and spotting the corresponding laminar fraction point at that drag level. This would shift the analytical skin-friction curves up or down to allow extrapolation without having to acquire high Reynolds data.

This chart also illustrates the larger than expected laminar surface area present.

Reynolds Number Effects on Boundary Layer Transition - Mach = 0.3

Rn=8.5 M

Rn=14.4 M

Rn=21.6 M

Rn=34.0 M

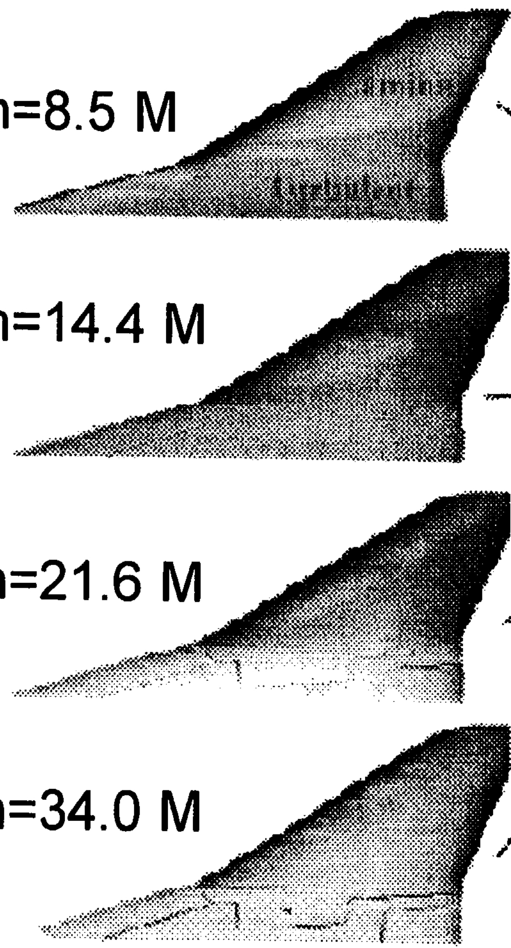

Transition detection using TSP

Analytical skin friction drag predictions and wind tunnel force data

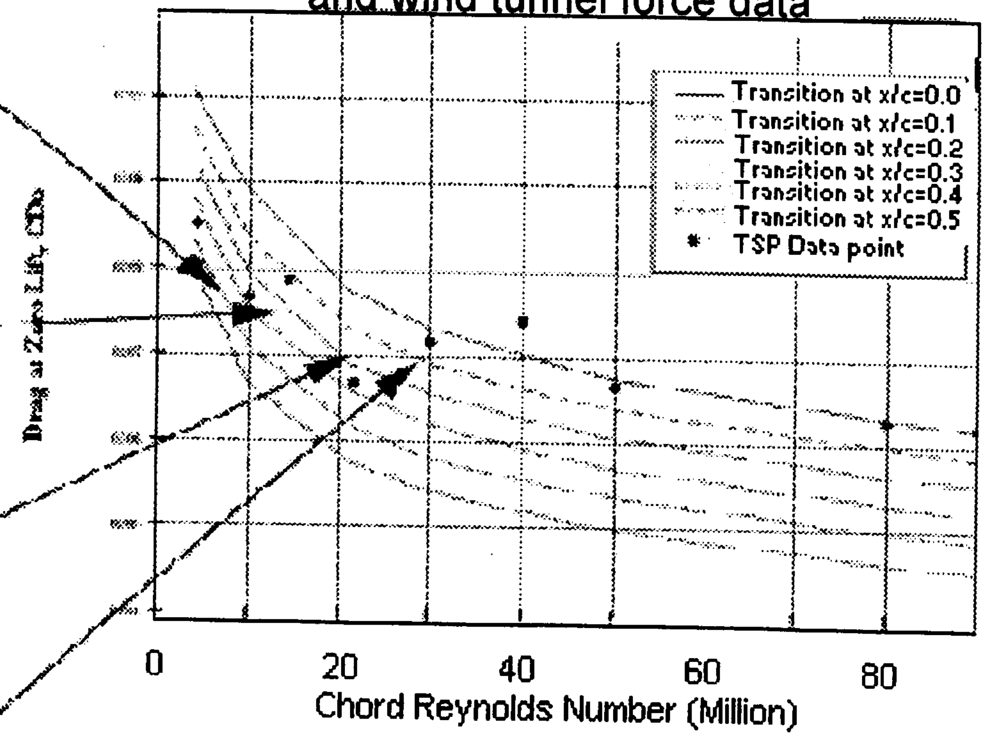

All experimental data represents free transition

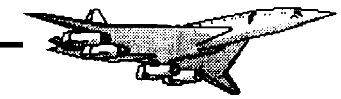

The variation in laminar boundary-layer extent with Reynolds number is also clearly evident in this chart.

This chart shows a comparison of TSP results, wind tunnel drag data, and analytical skin-friction predictions at Mach = 0.9.

Notice again the larger than expected laminar surface area.

Reynolds Number Effects on Boundary Layer Transition - Mach = 0.9

Analytical skin friction drag predictions and wind tunnel force data

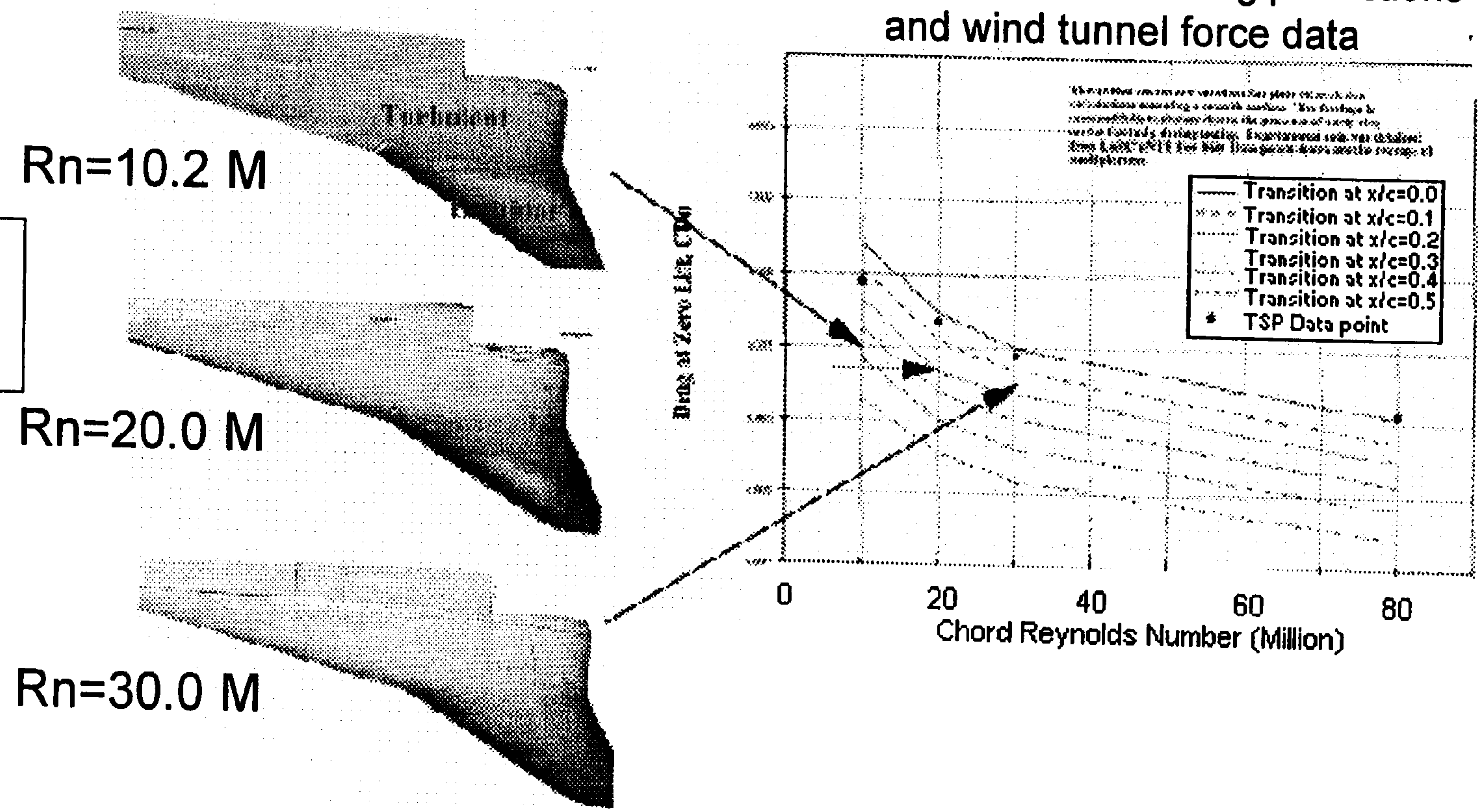

Transition detection using TSP

All experimental data represents free transition

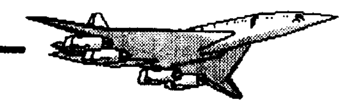

This slide illustrates the baseline trip's effectiveness. It was found in general that the conventionally defined trip was only effective over a limited angle-of-attack range. This is presumably due to changes in location of the attachment line as the angle of attack is varied. The trips were defined using Braslow criteria for grit size and location, assuming the attachment line to be at the leading-edge of the wing.

Trip Effectiveness

Mach = 0.9, Re = 10.3M, α = +1°, Flaps up, Lower Surface

NTF084
Run 52
TP 934

- **Untripped**

NTF084
Run 125
TP 1935

- **Conventional trip Grit #150**

NTF084
Run 142
TP 2144

- **Conventional trip Grit #120 / Grit #100**

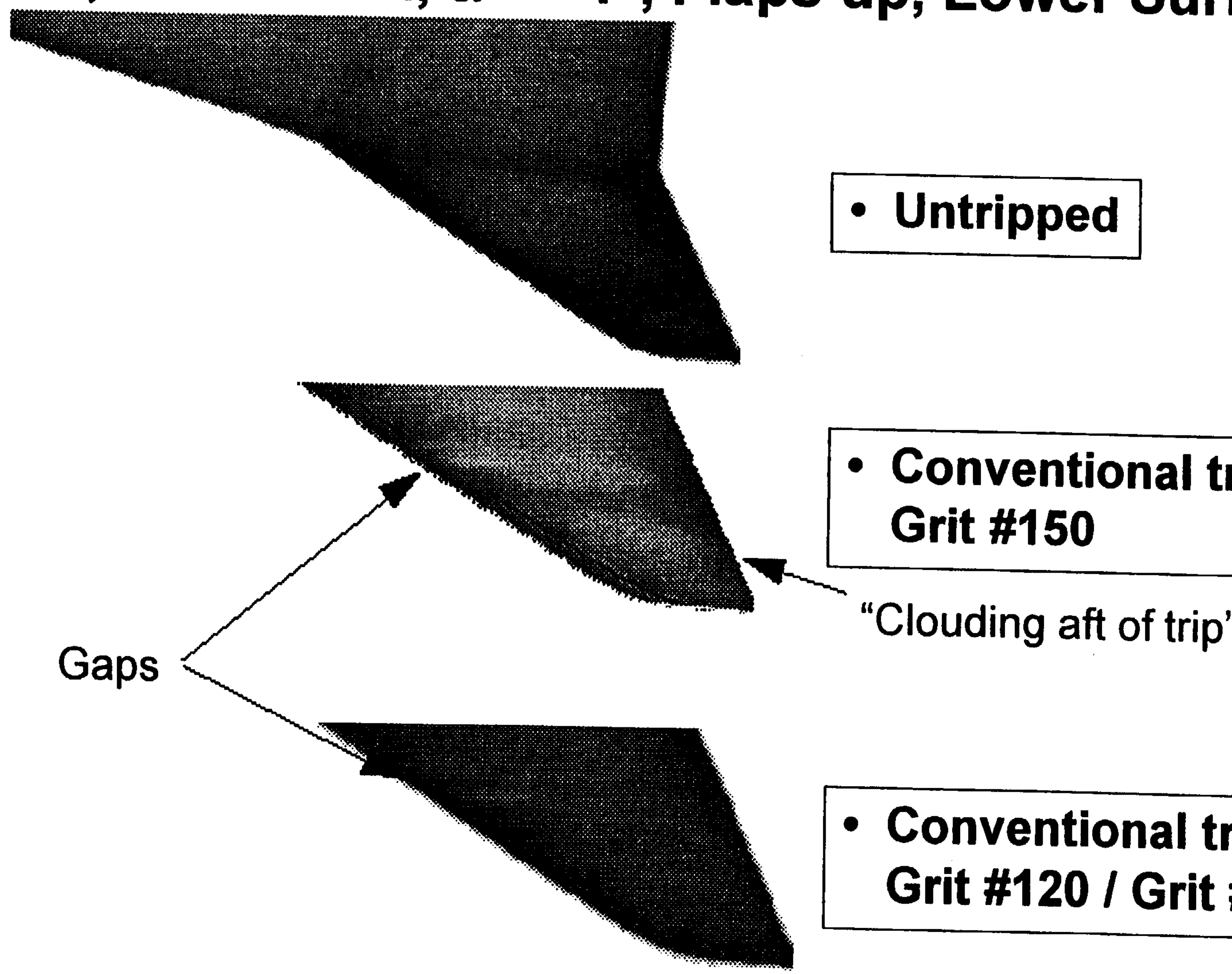

Results of free transition testing on the baseline, undeflected flaps configuration indicate significantly more laminar flow than analytical methods predict. Figures in the TSP Results section of this report which illustrate Reynolds number effects at Mach 0.3 and 0.9, clearly show this result. The surface area covered by regions of laminar flow has been determined from the mapped images shown in these figures. This area has been divided by the gross wing area to determine a laminar fraction. Conventional trips were defined using Braslow criteria for grit size and location, and assuming the attachment line to be at the leading-edge. Clouding aft of the "baseline" trip indicates that it was probably undersized for some test conditions. When the grit size was increased on the outboard panel and the test condition was repeated no clouding was seen in the TSP image.

Summary of Results

- Baseline (undeflected flaps) configuration:
  - A laminar region exists on the baseline, undeflected flaps configuration for both Mach = 0.3 and 0.9 for Chord Reynolds numbers below 40 Million, particularly on the outboard panel of the wing. The extent of this laminar region is greater than predicted by analytical methods.
  - Clouding of the TSP images was observed aft of the baseline, conventional trip indicating that the transition strip was undersized for some of the conditions tested. A trip with increased grit size was tested which eliminated this clouding.

No evidence of laminar flow was found on the high-lift configuration at the high-lift design point. A small region of laminar flow is suspected on the leading-edge flap at 4° angle-of-attack and a chord Reynolds number of 5.5 Million.

As shown in the Figure in the TSP Results section of this paper, the boundary-layer is tripped at the leading-edge flap hingeline on the transonic cruise configuration.

Results of free transition show that the greatest extent of natural laminar flow on the baseline, undeflected flaps configuration occurs at +1° angle-of-attack. This is very close to the angle-of-attack corresponding to CDmin. It is also the tested angle-of-attack where the outboard panel is most closely aligned with the flow when the outboard twist of -1.5° is taken into account.

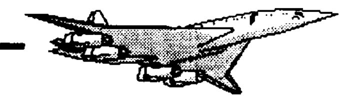

Summary of Results (continued)

- High-Lift configuration:
  - At the high-lift design point no laminar flow was detected on the high-lift configuration at all Reynolds numbers.
- Transonic configuration:
  - For Chord Reynolds numbers below 30 Million laminar flow was observed on the leading edge of the transonic configuration. The boundary-layer is tripped at the leading-edge flap hingeline.

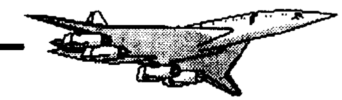

As angle-of-attack deviates in either direction from +1° the extent of natural laminar flow is reduced. This illustrates the changes in importance of the various mechanisms affecting boundary-layer transition, for example cross-flow instabilities, with changes in angle-of-attack.

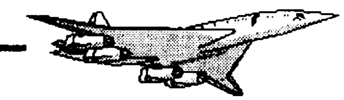

Summary of Results (continued)

- Additional observations:
  - The baseline, undeflected flaps configuration displayed the greatest extent of laminar flow at about +1° angle-of-attack. This is very close to the angle of attack where the outboard panel is aligned with the flow direction and also to CDmin.
  - As the angle of attack deviates from +1°, flow phenomena, other than the existing pressure gradient, play a larger role in boundary-layer transition and the extent of laminar flow is reduced.

This figure shows the recommendations to emerge from this work.

Recommendations

- At the take-off and climb out conditions for the high-lift configuration no boundary-layer tripping is required.
- For accurate measurement of drag levels at low lift conditions for the undeflected flap configuration, boundary-layer tripping may be required, particularly at transonic flow conditions.
- TSP is a useful tool for boundary-layer analysis. Improvement over the current system and development of advanced analysis tools could yield additional information such as detecting the presence of vortices and separated flows.

Title Chart - No Facing Page Description

HSCT High Lift Aerodynamics

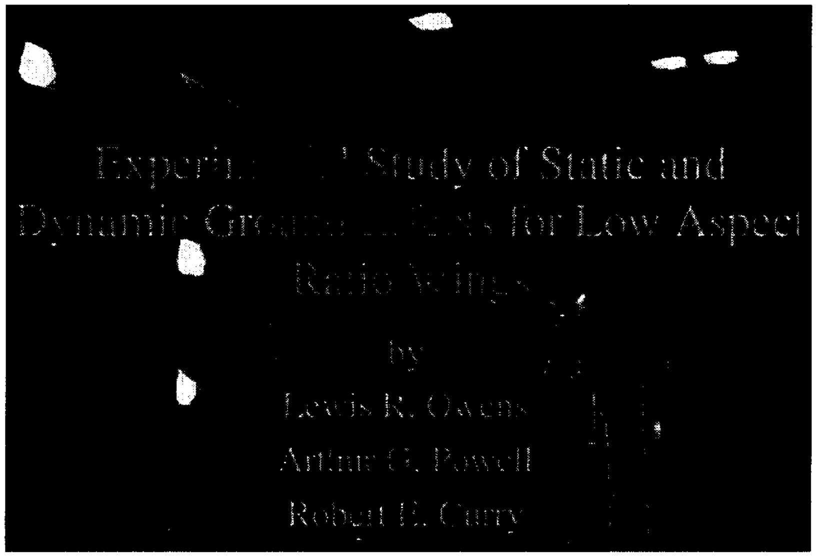

This presentation includes a summary of a recent experimental study of the static and dynamic ground effects for low aspect ratio wings. The authors would like to thank the many members of the Dynamic Ground Effects (DGE) Team whose contributions were invaluable in this effort.

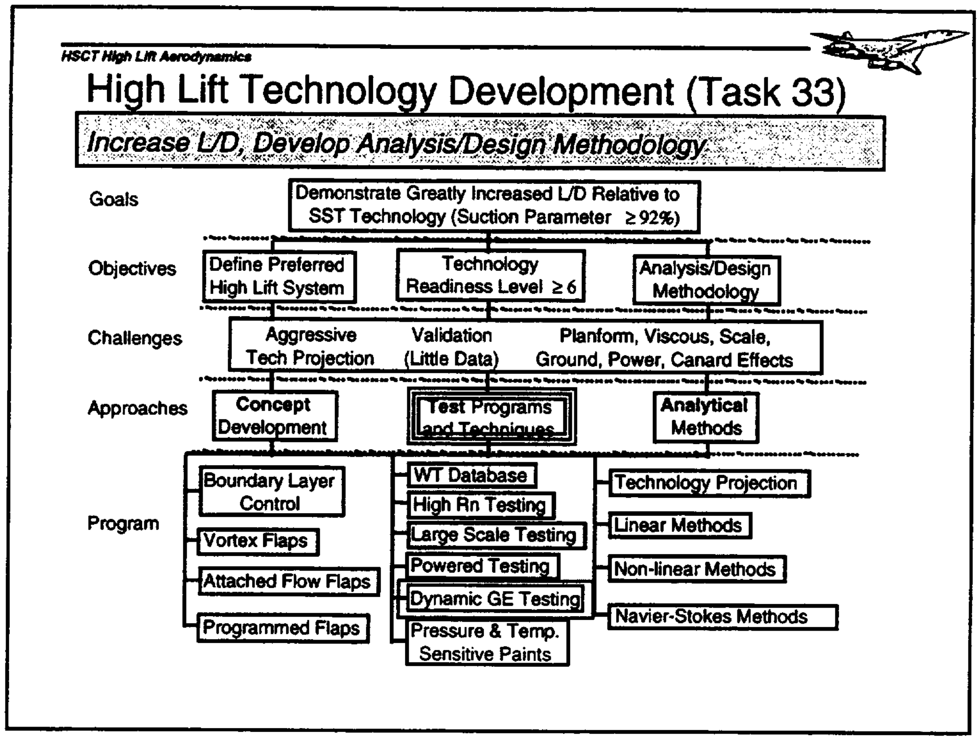

This study supports the Dynamic GE Testing Program under Test Programs and Techniques of the HSR High Lift Technology Development Task.

HSCT High Lift Aerodynamics

Outline

- General Test Information (Owens)
- Static Ground Effects (SGE) Data Analysis and Results (Powell)
- Dynamic Ground Effects (DGE) Data Analysis and Results (Owens)
- Comparison of Wind Tunnel and Flight Ground Effects Data (Curry)

This presentation is divided into four main sections. First, Lewis Owens (Langley Research Center) will cover some general Langley 14-by-22-Foot Subsonic Tunnel (14x22 ft) test information (LaRC Test 462 -- October '97). Next, Art Powell (Boeing-Long Beach) will present some of the analysis and results for the static ground effects (SGE) data, which provided a baseline for comparison with the dynamic ground effects (DGE) data. Lewis will follow with a presentation of the analysis and results for the dynamic ground effects data. Finally, Bob Curry (Dryden Flight Research Center) will present a summary and status of recent Tu-144 flight test ground effects results. He will also compare these results with data obtained from the wind tunnel test.

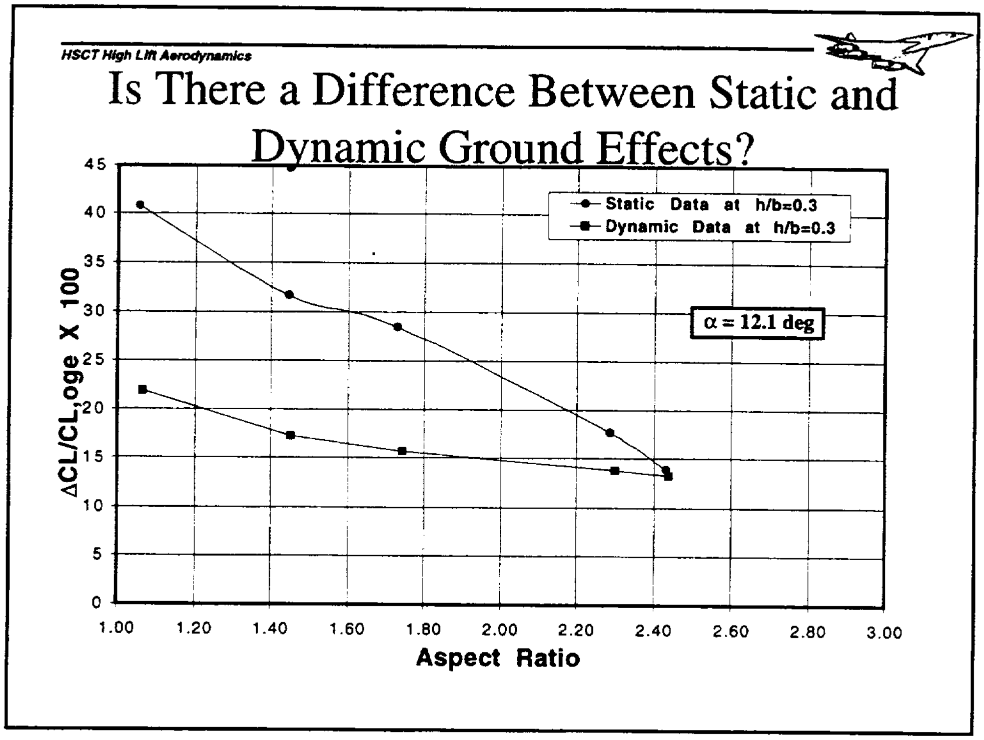

Previous ground effects data (University of Kansas) illustrates the potential for a difference between DGE and SGE. This plot of the percent increase in lift as a function of the aspect ratio is used to show that some wing planforms exhibit significant differences between DGE and SGE. At lower aspect ratios, the DGE lift increase may only be 50% of the SGE lift increase. If this happens to be the case for the HSCT planforms (aspect ratio currently about 2), then the expected SGE lift increments may over predict the flight (dynamic) ground effect. The significance of this over estimation is that the flight control surfaces may be under designed.

University of Kansas data reference:

R. C. Chang and V. U. Muirhead, "Effect of Sink Rate on Ground Effect of Low-Aspect-Ratio Wings," Journal of Aircraft, Vol. 24, No. 3, March 1987, pp. 176-180.

Test Objectives

- Shakedown the new 14'x22' DGE cart and instrumentation systems, and develop the overall system as a way of acquiring DGE data
- Determine the extent of DGE on HSCT planforms
- Understand how planform variables such as aspect ratio and sweep affect DGE

DGE cart hardware existed but had not been scheduled for use in the 14'x22' tunnel. The HSCT DGE/SGE difference question provided an opportunity to use this new cart. The HSR test was scheduled and a test plan was developed to meet three main test objectives. First, we had to develop experience to be able to effectively use the DGE cart. Each step toward operating the cart in the tunnel (for the first time) involved a major "debugging" effort. This shakedown process would also include validation of the DGE test technique by making comparisons with the Tu-144 flight test ground effects database. Second, we wanted to obtain DGE/SGE data on as many HSCT planforms as possible to try and provide an answer to the DGE/SGE difference question. Finally, we wanted to test a number of different low aspect ratio planforms to be able to understand the dominant geometry factors that may contribute to the potential DGE/SGE difference.

Dynamic Ground Effects Cart

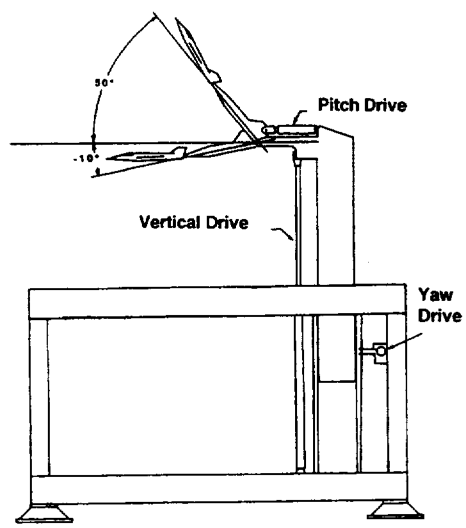

Here is a side view sketch of the DGE cart. The basic cart is similar to other 14'x22' model carts. The differences are primarily in the model support structure. A large support strut is hydraulically controlled (vertical drive) to vary the model height above the cart floor. Also, the strut has a hydraulic pitch drive that makes it possible to change the model attitude during a dynamic plunge. Finally, although not used in this test, a yaw drive allows the model to be yawed with respect to the oncoming flow (prior to DGE plunge) so that ground effects data can be obtained with angle of sideslip.

Basic Cart Performance

- Executes pre-programmed model trajectory
- Sink rates varying from 0 to 15 ft/sec
- Cart floor boundary layer minimized with tunnel boundary-layer removal system
- Height limits are 89 in. down to about 5 in. (depends on model pitch)
- Pitch limits are -10 degrees to +50 degrees (depends on model height)

Here are some of the basic performance parameters for the new DGE cart design. Note that we did have some operational problems with the cart. During the test, we were only able to reach sustained sink rates of about 9 ft/sec due to temporary "fixes" made to the hydraulic control system.

HSCT High Lift Aerodynamics

Models Tested

- Model #10: Elliptic wing planform with centerbody (AR=7.0)- No flaps deflected
- Model #7: Tu-144 wing planform (AR=1.627)- TE flaps deflected 10 deg
- Model #6: TCA wing planform (AR=2.027) - TE flaps deflected 10 deg

Originally, the test plan included 10 different flat-plate wing planforms (one high AR wing and nine low AR wings). Note that none of the wing planforms had wing twist or camber. The operational/training problems experienced with the new cart contributed to the reduction in the number of models that were tested. Only three models were tested. Model #10 was used to get an indication of the tunnel flow angularity with different model heights. This was done both statically and dynamically. Model #7 provided an opportunity to validate the wind tunnel DGE data by making comparisons to actual Tu-144 flight data. Model #6 provided an opportunity to assess the DGE/SGE differences for a current HSCT baseline wing planform.

Elliptic Wing Planform

All dimensions in inches.
Not to scale.

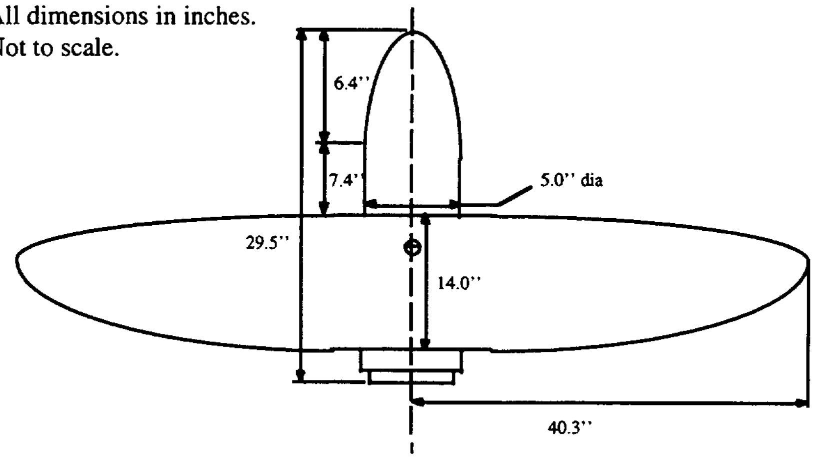

This is a sketch of model 10 wing planform with centerbody. The model was tested in the "high-wing" configuration such that the centerbody was under the wing. The dimensions are included to give a better sense of the model scale.

HSCT High Lift Aerodynamics

Tu-144 Wing Planform

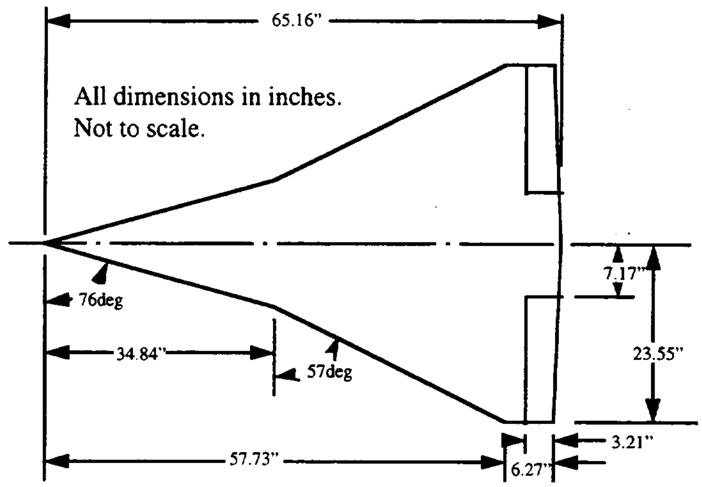

This is a sketch of the model 7 Tu-144 wing planform. The model was tested in the "low-wing" configuration with the balance/balance fairing mounting to the top of the wing. The dimensions are included to give a better sense of the model scale and location of trailing-edge flaps.

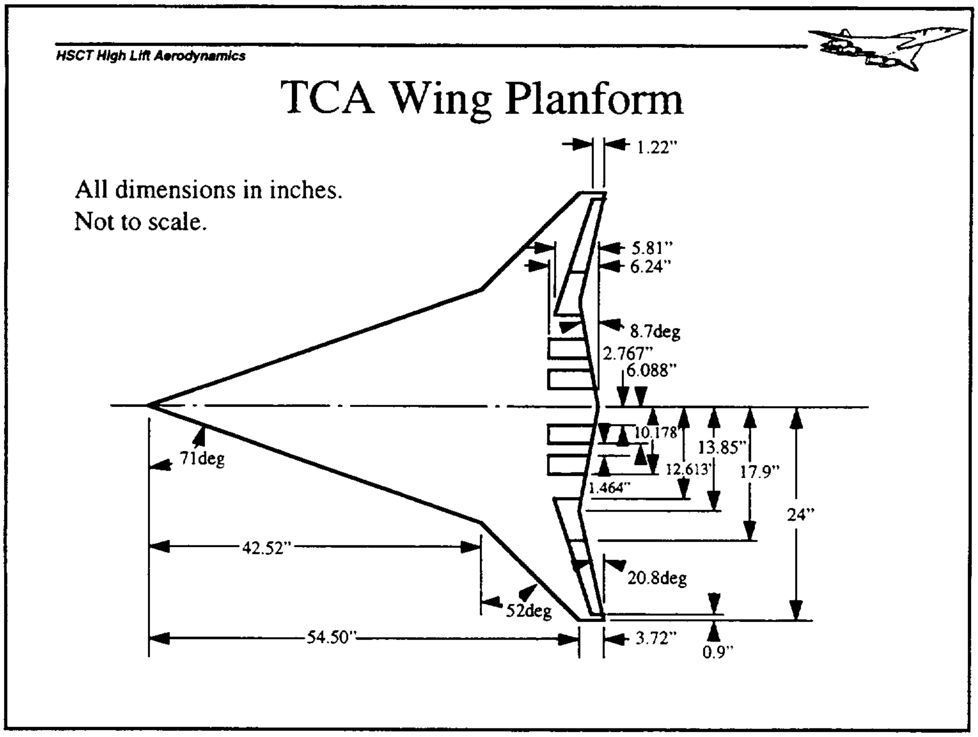

This is a sketch of the model 6 Technology Concept Airplane (TCA) wing planform. The model was also tested in the "low-wing" configuration with the balance/balance fairing mounting to the top of the wing. The dimensions are included to give a better sense of the model scale and location of trailing-edge flaps.

Wind Tunnel Measurements

- Six component force/moment balance
- Six model accelerometers
  - -3 linear accelerations
  - -3 angular accelerations
- Four sting accelerometers (data not used)
- Tunnel Optotrak system
  - -model height
  - -model pitch

The basic measurements provided during the wind tunnel test included a force/moment balance, accelerometers and an optical tracking system. The six model acceleration measurements were used in combinations to provide 3 linear and 3 angular accelerations of the model reference center. The four sting mounted accelerometer measurements tracked the model accelerations very closely and were not included in any of the inertial loads removal from the force/moment measurements.

HSCT High Lift Aerodynamics

Testing Ranges

- Longitudinal load ranges
  (NF: 1000 lbs.;PM: 4000 in.-lbs.; AF: 500 lbs.)
- Accelerometer range (10 g's)
- Tunnel velocity: 267 ft/sec
- Model sink rates
  (0, 1, 2.33, 4.67, 7, 9.33, 11.667 ft/sec)
- Gamma
  (0, 0.2, 0.5, 1, 1.5, 2, 2.5 degrees)
- Model AOA between 6 to 11 degrees
- h/b range
  (1.5 to 0.2)

Here is the range of variation of the major test condition parameters. Note that the flight path angle (Gamma) corresponds directly to model sink rate for a given tunnel velocity. The wind tunnel investigation did include some lower tunnel velocity test points, but none of those data have been analyzed yet and are not included in this presentation.

Data Corrections

- Static
  - -weight tare, balance woz
- Dynamic
  - -weight tare, balance woz
  - -model acceleration measurements used to remove inertial loads from balance load measurements
  - -angle of attack variation

Typical corrections were applied to the static data. The dynamic data included the same corrections plus those necessary to remove inertial loads and any angle-of-attack variation during the plunge.

Static Ground Effects

- Art Powell will present the next section

Static Ground Effects (SGE)

- Flow Angularity (Model 10)
- Lift and Moment (Models 7,6)

Objective: Best estimate of lift and pitching moment characteristics in static ground effect for comparison with dynamic values.

While Lewis, Sharon Graves (GWU JIAFS Graduate Student), and Bob processed the dynamic data, Art took on reducing the static data so we would have a basis of comparison.

Flow angularity was measured using Model 10, the AR=7 NACA 0012 elliptical wing. DACVINE, a higher-order panel method, was used to estimate zero-lift angle-of-attack, since this model had an underwing fuselage to house the balance.

The tunnel with DGE strut showed a downflow (of approximately 0.15 degrees) at the tunnel centerline, which decreased to near zero at the floor. The flow angularity was deemed too small to have a significant effect on the data for the lower AR wings.

Model 7, the Tu-144 planform, and Model 6, the TCA planform, were the only low-AR Models tested. Severe mechanical problems plagued the test throughout. Data quality was not judged good, but was felt to be sufficient to determine if any significant DGE effects existed.

Only lift and moment data were considered. Since the models had no camber, and no fuselage, and test Reynolds number so small, there was not sufficient motivation to study the drag variation with ground effect.

Overall agreement of static data with other sources was good.

Flow Angularity - Model 10

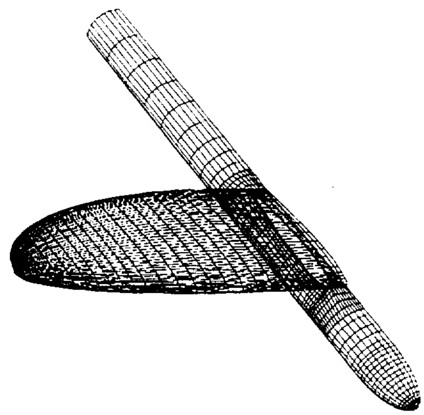

Model 10 consisted of an AR=7 elliptic wing with symmetric NACA0012 sections and a fuselage to accommodate the balance. Since this model had a steep lift-curve slope, it was ideal for probing tunnel flow angularity. The presence of the fuselage made the model slightly asymmetric with respect to lift, so DACVINE was used to determine its angle of zero lift at various heights. This, along with angle of attack sweeps taken at various heights, was used to determine the flow angularity. The figure is the geometry wireframe developed for the DACVINE analysis.

HSCT High Lift Aerodynamics

Static Lift Curves for Model 10

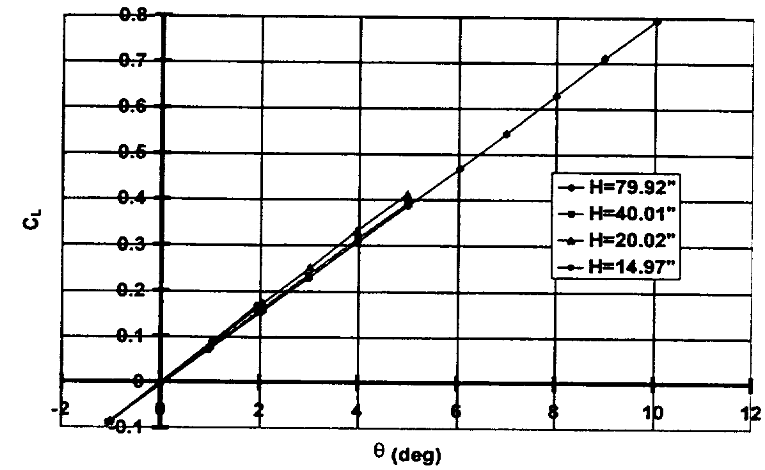

Lift data were taken at four heights, and the resulting lift curves are straight and pass close to the origin. The abscissa is really model attitude angle, not angle of attack. This distinction, which is usually ignored, is necessary in detecting tunnel flow angularity.

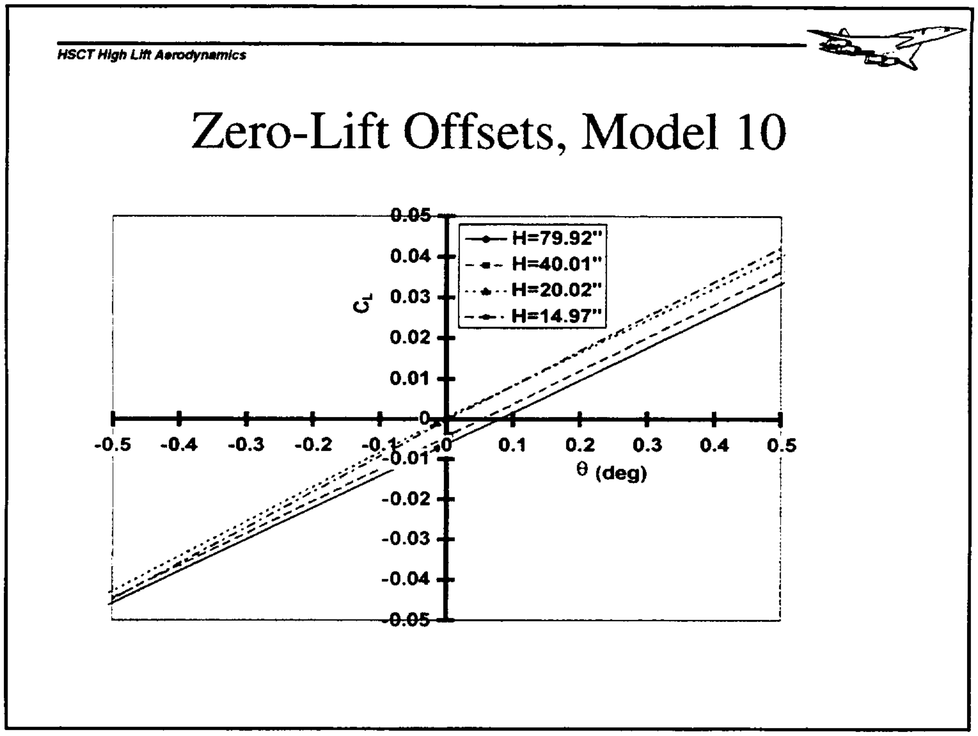

This figure is an expanded view near the origin for the lift curves of the last figure. As can be seen, the curves do not all exactly pass through the origin. There is some small positive angle of attack indicated at zero lift, which changes with height from the floor.

HSCT High Lift Aerodynamics

Tunnel Flow Angularity From Model 10

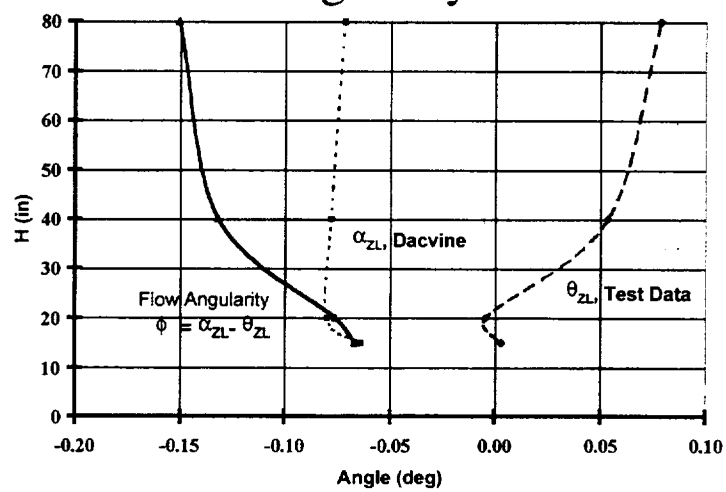

Tunnel flow angularity is calculated using the zero-lift angles of attack from DACVINE, and the zero-lift attitude angles from the test. The blue curve (solid line) is the resulting flow angularity for the tunnel with this cart and model in place. It is interesting to note that this is an apparent downflow, the opposite of what was found in the U&I test (LaRC442). The flow angularity was ignored in the DGE test because it was deemed insignificant for the dynamic measurements, but more importantly because the DGE test really only required that a difference be seen between static and dynamic data. An attempt is underway to extract "dynamic" flow angularity.

Model 7 Static Characteristics

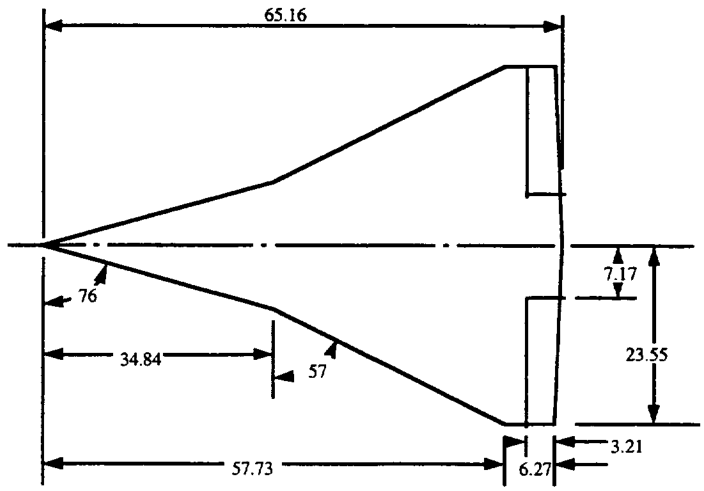

Model 7 was a flat wing of Tu-144 planform. Its leading edge was of small radius from centerline to tip. It featured flaps which were deflected 10 degrees for this test. The model was attached to the sting through a balance block and balance enclosed in a fairing and mounted to the model's upper surface. A 9-degree knuckle was used to provide some angle-of-attack capability near the groundplane. Model size is indicated above.

The model was run through angle-of-attack sweeps at six heights above the floor. Floor boundary layer suction was used.

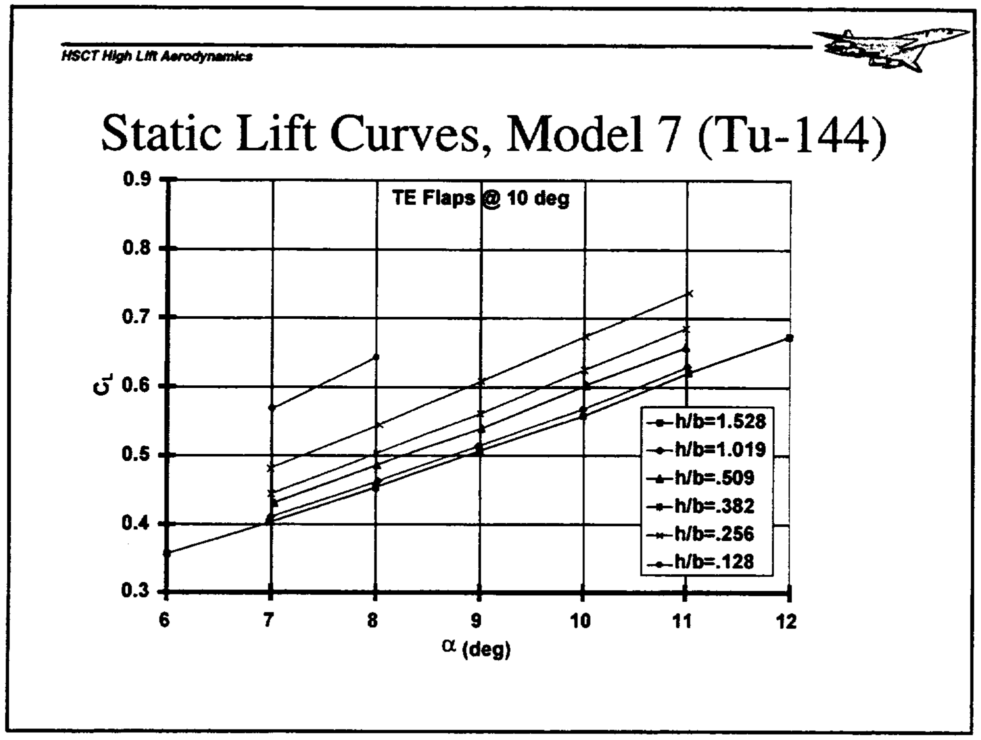

Model 7 static lift characteristics were measured at a number of discrete heights, which for comparison's sake have been normalized by the model span, 47.1". Each data point represents an average of 1200 samples, which eliminates sting vibration, a spurious effect present in most of the data. The data are shown in the region of interest to the DGE test, and landing maneuvers in general. The h/b=.125 data is limited in angle of attack due to clearance problems with the tunnel floor.

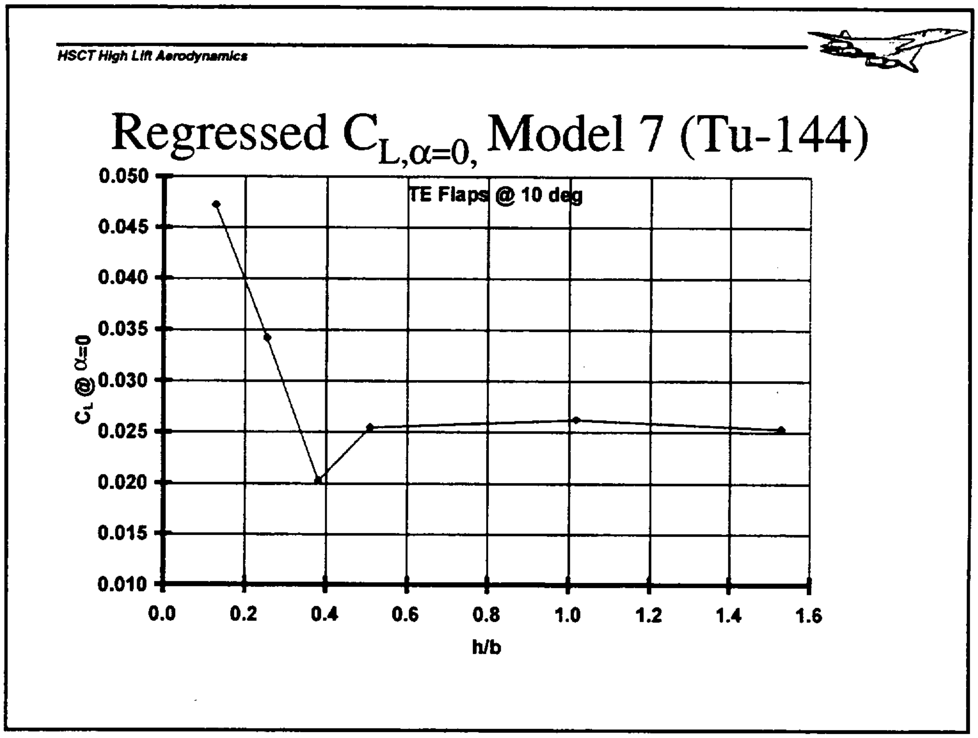

Regressing linearly the lift data in the 7-11 degree range allows the lift data to be generalized and interpolated, and although it was not strictly necessary in constructing the static ground effects characteristics, it is useful for data control. The lift at zero angle of attack asymptotes at higher h/b, which is reassuring.

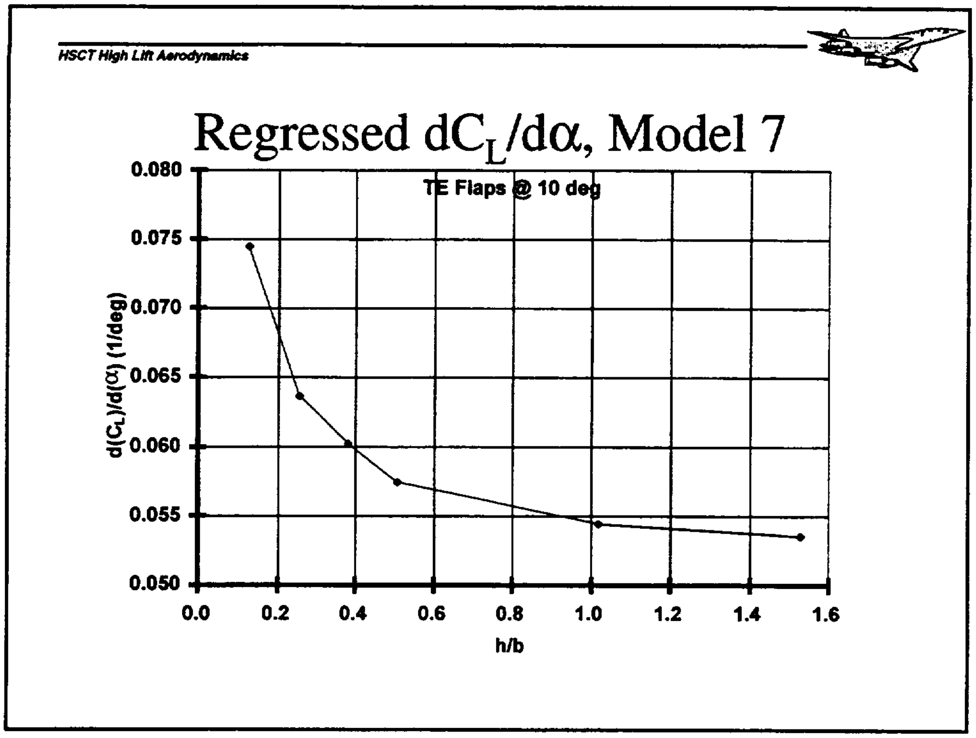

Regression coefficients were quite high for the Model 7 lift data. Again, the lift-curve slope asymptotes at high h/b, as expected. The increase in lift curve slope at low h/b values is substantial.

HSCT High Lift Aerodynamics

Normalized Lift Increment, Model 7

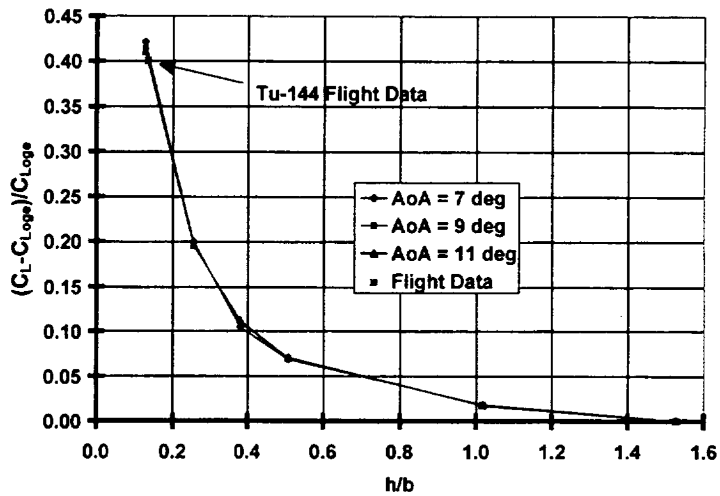

The regressed C_L @ α =0 and $dC_L/d\alpha$ vs. h/b curves were used to construct curves of C_L vs. h/b for 7, 9 and 11 degrees angle of attack. These were normalized by the free-air C_L and are presented here as normalized ground effect lift increment. The data compress well under the normalization. The data from this test were compared with data from the Tu-144 flight test, in which a series of landings were conducted at constant angle of attack. The agreement is very good, despite the fact that the Tu-144 data are for a dynamic maneuver of a full configuration, at vastly different Reynolds number, and powered. Also note the large (42%) ground effect lift increment for this planform.

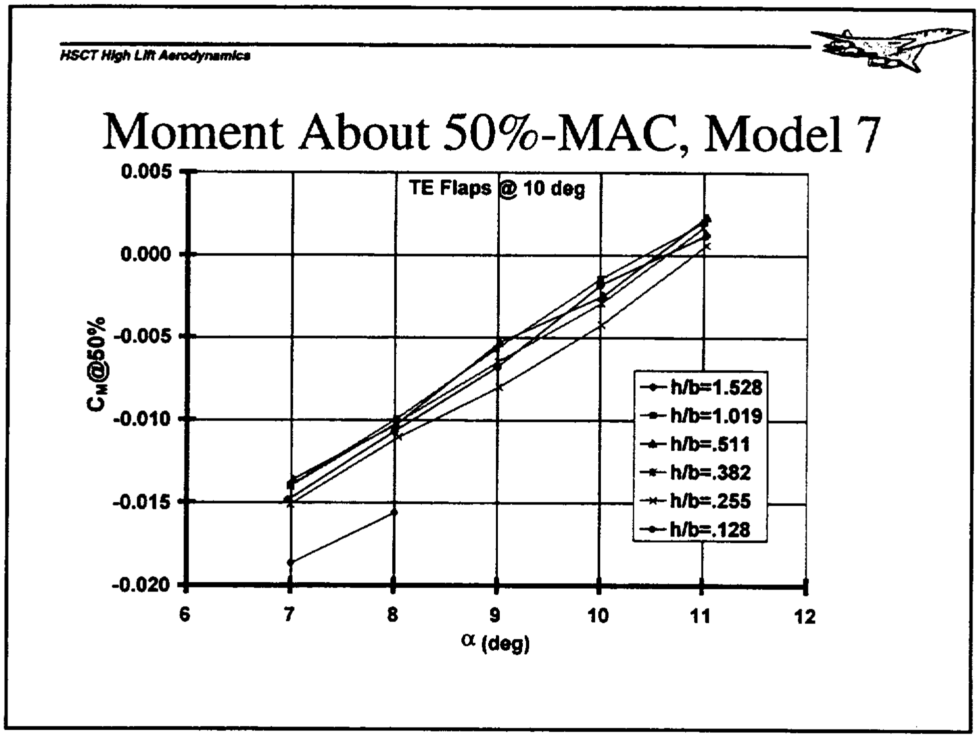

Pitching moment data about the 50%-MAC point are shown. The large positive slope indicates that the aerodynamic center for this angle-of-attack range is forward of the moment reference. The data do show a negative (nose-down) pitching moment increment as the groundplane is approached, which is what one would expect.

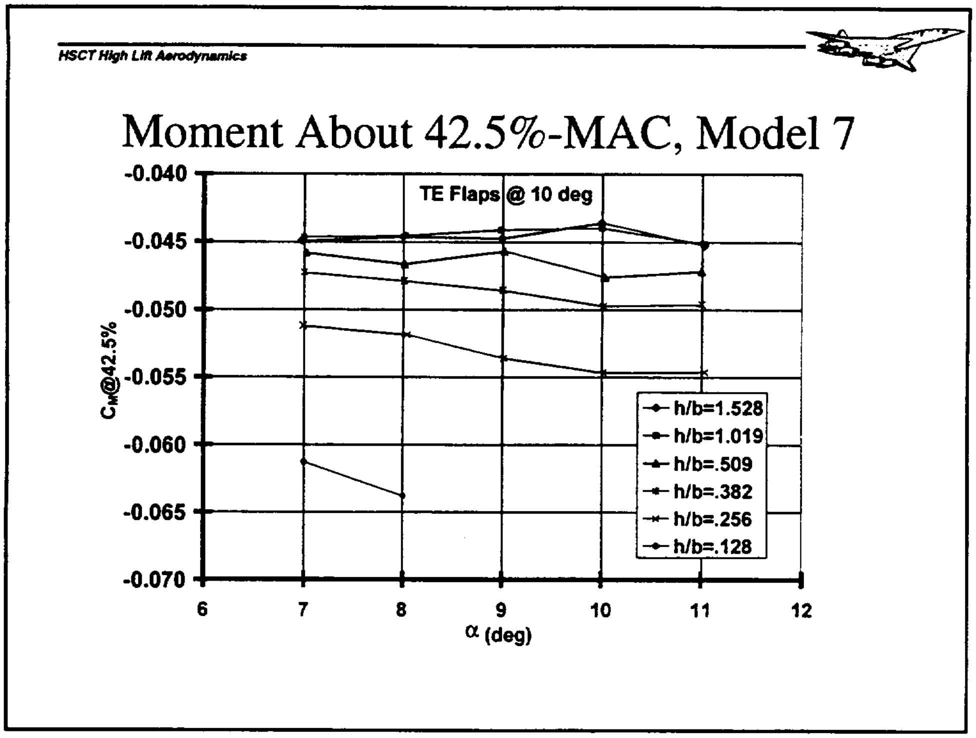

Re-referring the moment data to 42.5%-MAC essentially zeroes the moment slope, indicating this to be the approximate free-air aerodynamic center for this angle-of-attack range. Thus referred, the negative moment increment due to groundplane proximity is larger than in the previous figure. The normalized moment increment presented in the next slide will be based on this reference point.

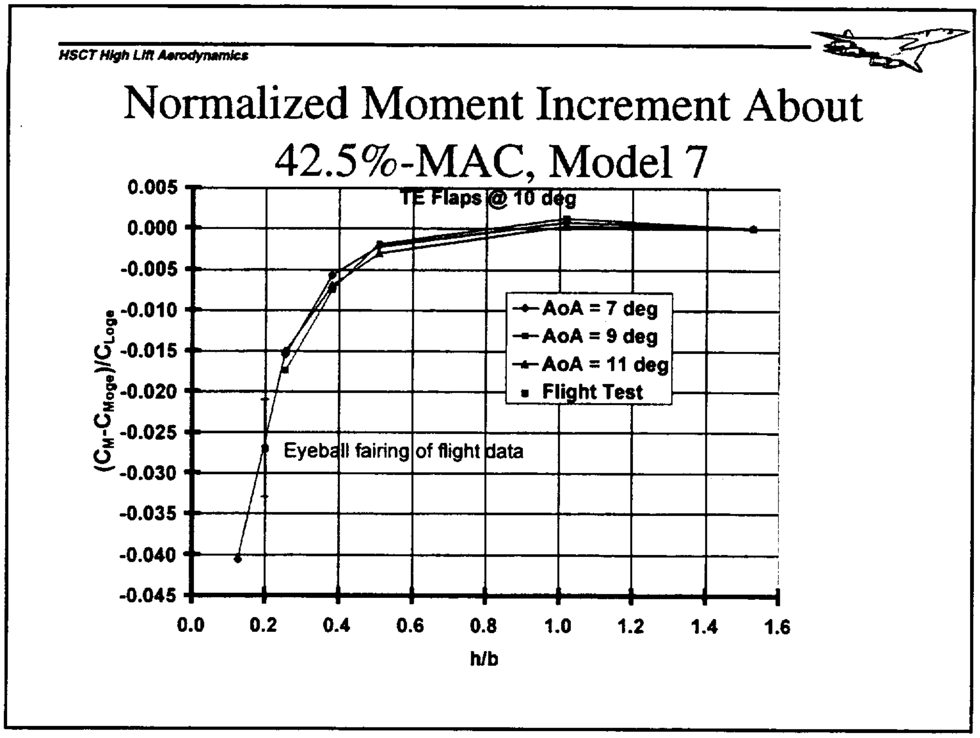

This figure shows the normalized moment increment about the aerodynamic center for Model 7. Following Curry, the ground-effect moment increment is normalized by the out-of-ground-effect (OGE) lift coefficient. The data compresses well under this normalization. One Tu-144 point is shown. This was taken from an eyeball fairing of rather noisy flight data. an indication of the noise level is shown by the error bar. Again, the agreement appears good, despite likely different flap settings.

Reference:

R. E. Curry, "Dynamic Ground Effect for a Cranked Arrow Wing Airplane," NASA TM-4799, August 1997.

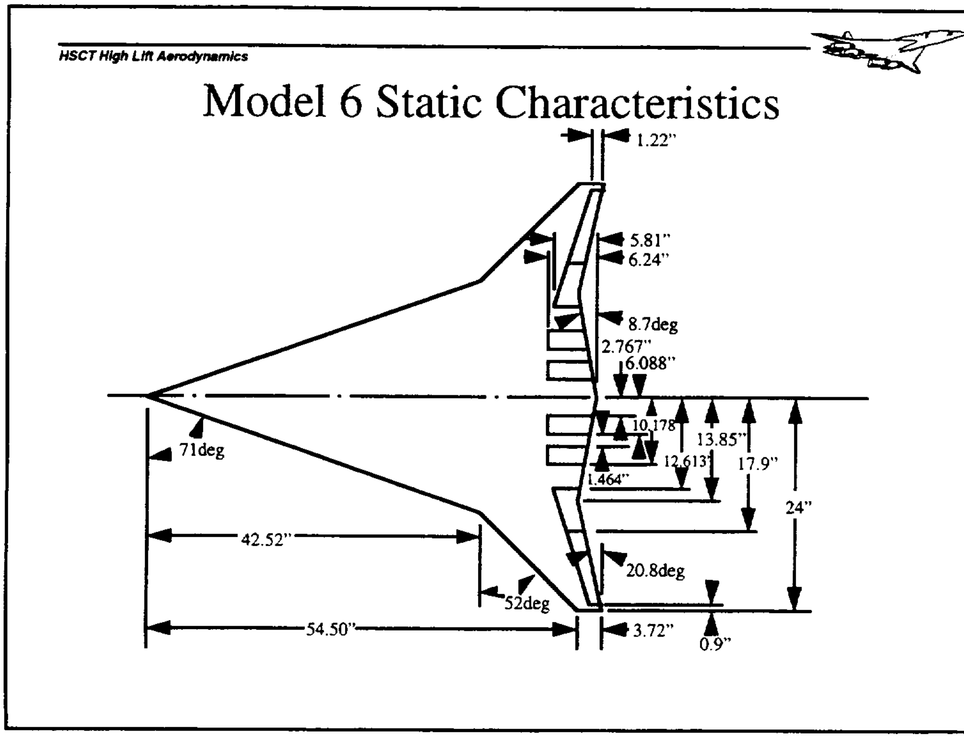

Model 6 was the TCA planform. It had no camber or twist, but featured 10-degree deflected trailing edge flaps. The leading edge radius was as large as the wing thickness allowed inboard of the leading-edge sweep break, and much smaller outboard. Like Model 7 it mounted to the sting via a faired balance block and balance on the upper surface. The 9-degree knuckle was used with this model as well.

This model was run through angle-of-attack sweeps at five heights above the floor. Tunnel boundary layer suction was used. In addition, static data was available at high h/b from certain dynamic runs before the plunges began. These data were also used to construct an estimate of the aerodynamic characteristics in static ground effect.

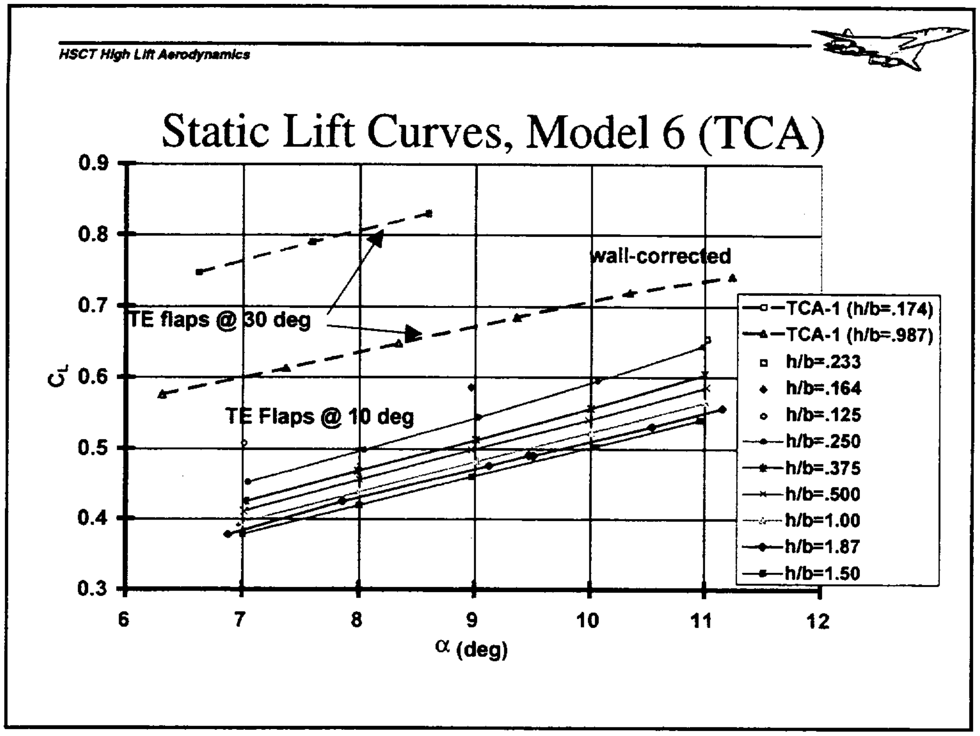

The Model 6 lift curves are presented in the angle of attack range of interest for DGE testing. Comparable lift curves from the TCA-1 (LaRC 14'x22' Test 449) are shown also. The h/b=.987 (TCA-1) data (Run 572) should be considered as free air data, since it includes wall corrections. The h/b=.174 (gear height) data (Run 350) was processed as ground effects data and was not corrected for the floor presence. Both of the TCA-1 curves are for 30 deg TE flaps, as opposed to the 10-degree TE flaps of the DGE model. The TCA-1 curves are for a full configuration, but without horizontal tail, while the DGE test data are for a flat wing planform only. The Reynolds numbers are also different: 7.8 million for the TCA-1 data versus only 4.7 million for the DGE test data. The h/b=.174 TCA-1 data was limited to below about 8.6 degrees by tailstrike.

The bulk of the DGE test data came from constant-height angle-of-attack sweeps. For these points, roughly 1200 data samples are averaged for each data point. Data at h/b=1.87 came from DGE runs prior to plunge start. Lift-curve data are available because plunges were taken at 7, 9 and 11 degrees angle of attack for Model 6. Typically, over 100 data samples were available for time-averaging prior to plunge start. This largely eliminates the effects of sting oscillations, if any.

A few individual data points at low h/b are shown near 7, 9, and 11 degrees angle of attack. These points, while unique in h/b, have turned out to be extremely useful, as will be seen.

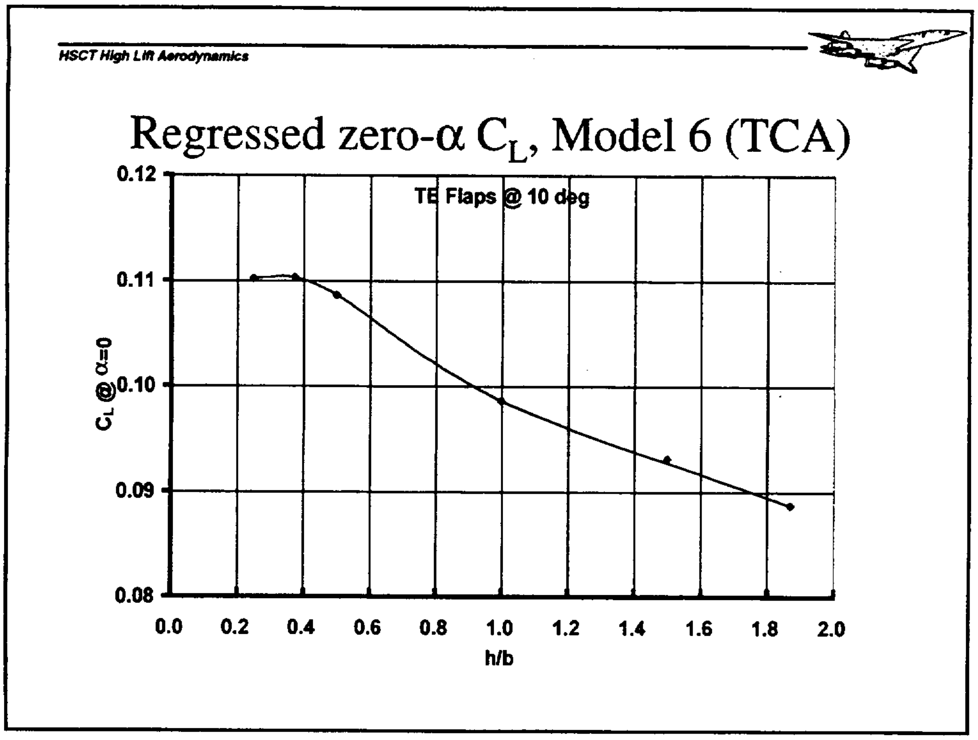

Each of the DGE test static lift curves was linearly regressed between 7 and 11 degrees. Regression coefficients "r" typically were quite good, with at least three "nines" past the decimal. The lift curves were represented as a zero-α C_L and lift curve slopes. The zero-α C_L data are presented here as a function of h/b. These data appear well-behaved and plausible.

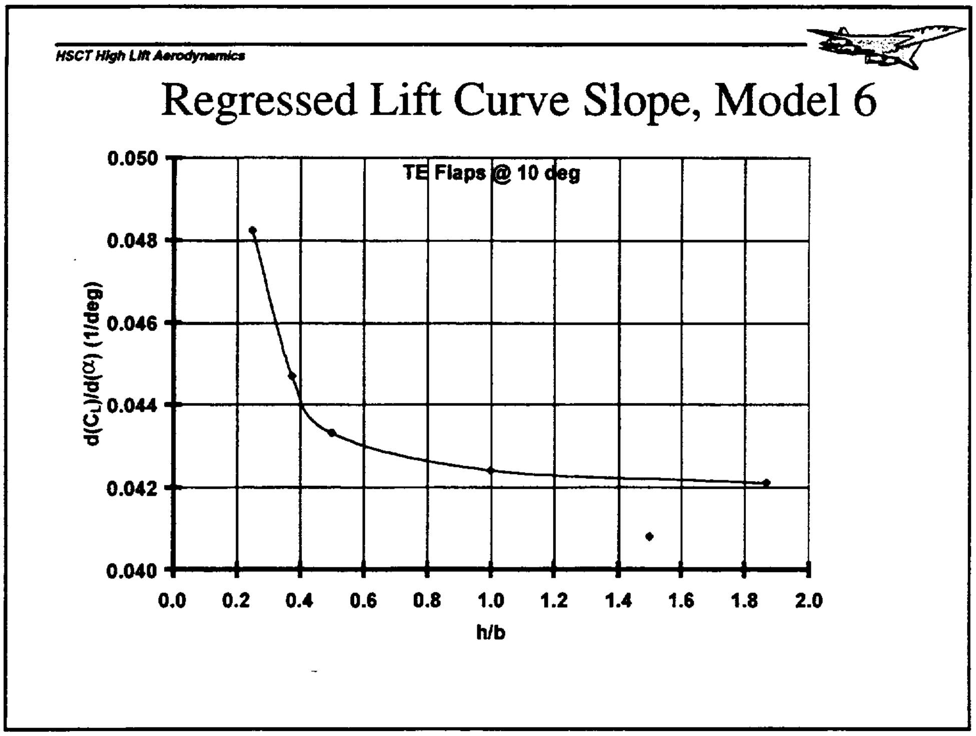

This plot shows the regressed lift-curve slopes of the Model 6 static ground effects data. One expects this curve to asymptote to some value as h/b approaches 2, which it does if the data point at h/b=1.5 is ignored. In the analysis, lift data at this h/b is excluded in favor of the h/b=1.87 data taken before plunge start on the dynamic runs.

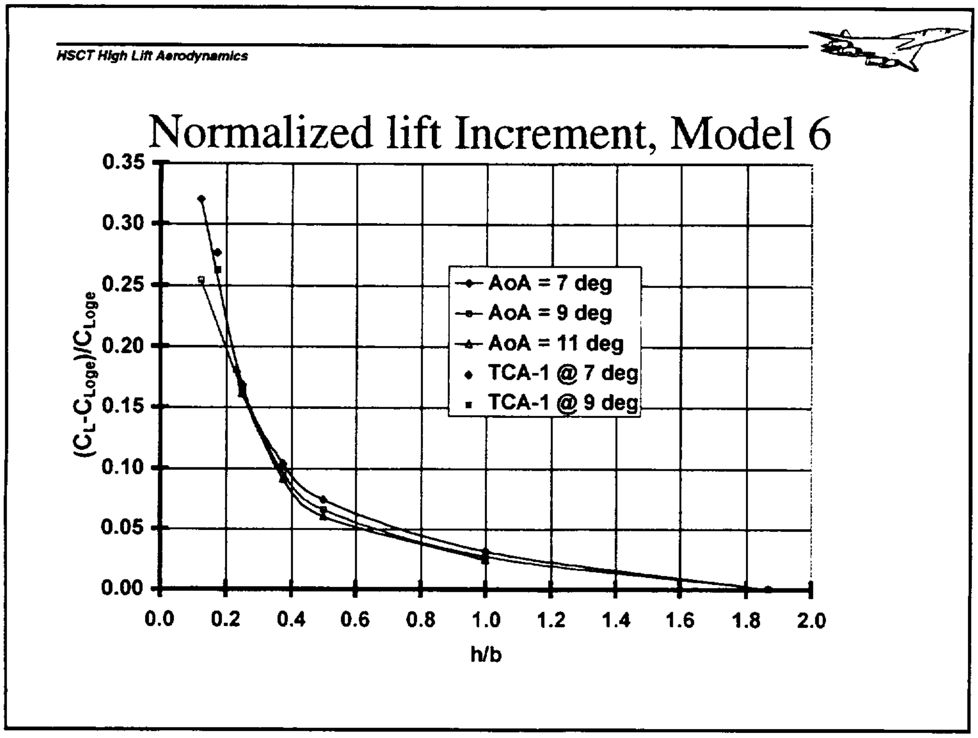

With the regressed data of the last two figures it is possible to put together plots of ground effect C_L increment versus h/b at constant angle of attack. This is a plot of that data, normalized by free-air C_L. Since the lowest h/b for which a lift curve could be constructed was 0.250, extension to gear height might seem difficult, except that the extra, unique data points at lower h/b were very close to the angles-of-attack for which the plot was made. A short extrapolation, using extrapolated lift-curve slopes makes the low h/b end of the curve accessible. The TCA-1 data are shown here for comparison, and show reasonable agreement with the DGE static data. The 9-deg TCA data required a short extrapolation, since the model was tailstrike limited to 8.6 degrees at h/b=.174.

Note that the static lift increment in ground effect for this planform is significantly lower (~25-30% compared to 42%) than it is for the Tu-144.

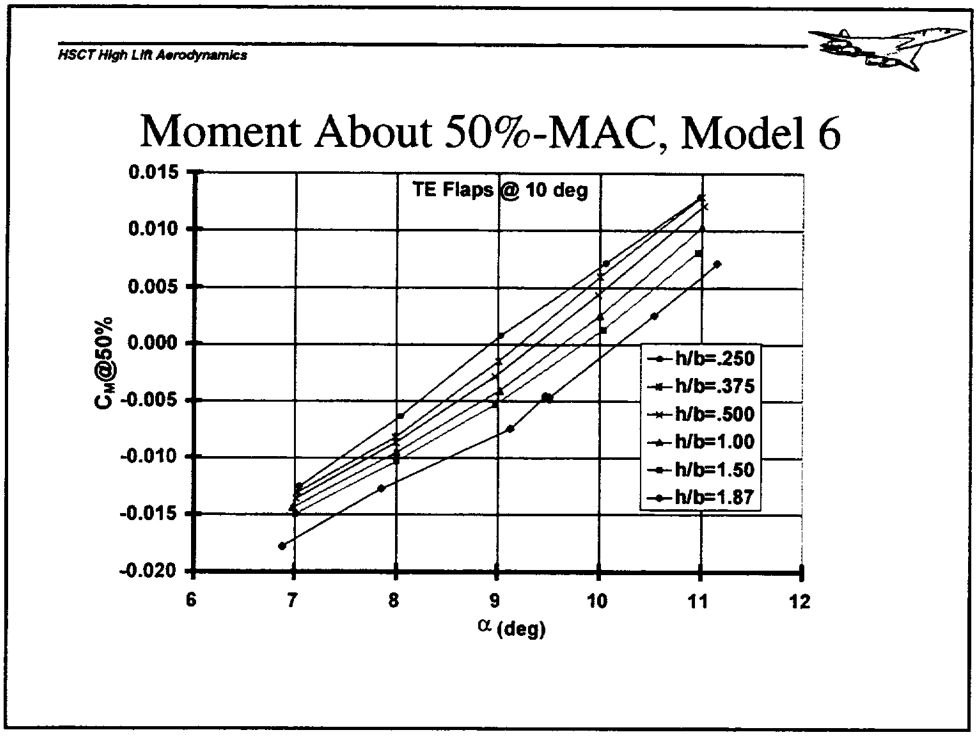

This is a plot of the pitching moment coefficient taken about the 50% MAC for Model 6. At this moment reference location, decreasing h/b causes a positive C_m increment. This and the positive slope suggests that the moment-reference center is well behind the aerodynamic center for this angle-of-attack range. Also, note that the h/b=1.87 data lie well below the other curves, which is counterintuitive. One would expect the curves to be close together at high h/b, near the edge of the ground effect regime.

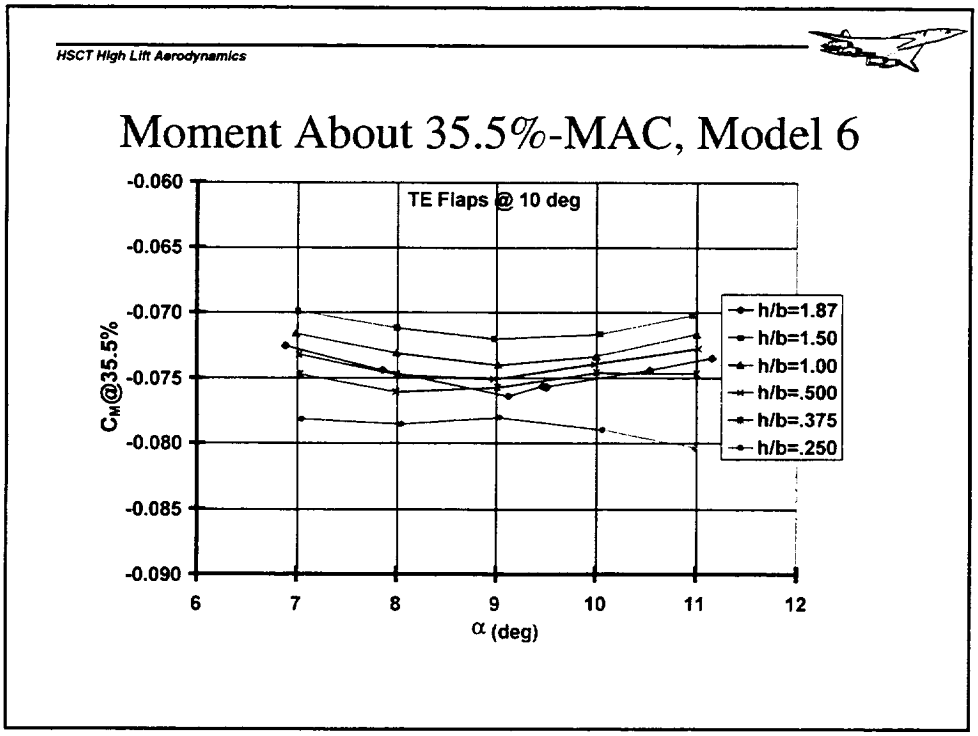

The moment data was re-referenced to 35.5% MAC, which reduced $dC_m/d\alpha$ to essentially zero for h/b=1.5. Taken about this reference point, most of the data exhibit a negative moment increment as the groundplane is approached. The data at h/b=1.87, taken from the dynamic runs prior to plunge start, do not follow this trend, which is counterintuitive and at odds with the other data. These data are therefore not used for OGE reference in normalizing the moment increment data.

HSCT High Lift Aerodynamics

Normalized Moment Increment About 35.5%-MAC, Model 6

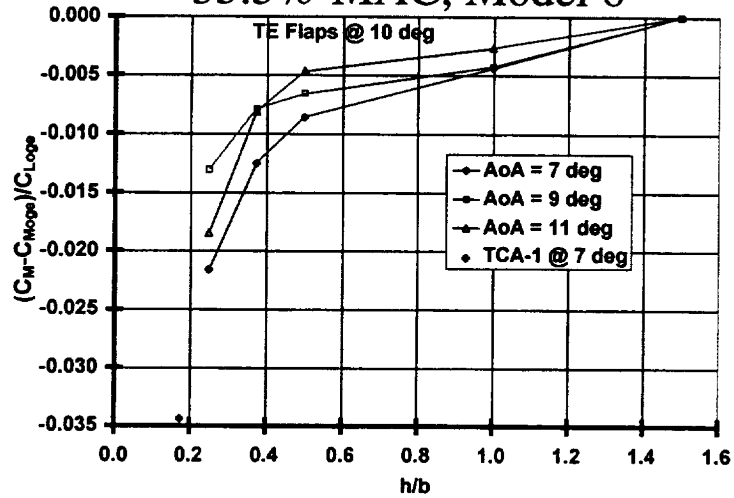

This figure shows the normalized moment increment due to static ground effect as measured for Model 6. The data show the expected trend of negative (nose-down) pitching moment increment as the groundplane is approached. The data does not collapse as well under the normalization as did those for Model 7. Limited data from TCA-1 appears to agree with the trend shown by these data.

HSCT High Lift Aerodynamics

Static Ground Effect Conclusions

- Flow angularity check shows small downwash, which was ignored in the DGE analysis.
- Model 7 data agrees with Tu-144 flight test.
- Model 7 lift and moment data compressed well under normalization.
- Model 6 data compares well with TCA-1.
- Model 6 moment data did not compress well under normalization.

The static data serve as a basis for comparison for the dynamic data. An examination of the tunnel flow angularity found, for the DGE strut and Model 10, a slight downwash of about .15 degrees near the tunnel centerline, which decreased as the tunnel floor was approached. Since the DGE test was principally a comparison of static and dynamic effects, and based on the assumption that flow angularity would be the same for dynamic conditions as for static conditions, the flow angularity was ignored for the purposes of this study.

The Model 7 static lift and moment data was quite consistent, agreed well with data from Tu-144 flight test, and collapsed well under normalization.

Model 6 static data was less consistent, but lift and moment increment data agreed reasonably well with TCA-1 wind-tunnel data. The lift data collapsed reasonably well under normalization, but the moment data did not.

Dynamic Ground Effects

- Lewis Owens will present the next section

Dynamic Ground Effects (DGE) Data Challenges

- Different sampling rates
  - -model height & pitch position (50 to 60 hertz)
  - -balance and accelerometers (150 hertz)
- Accelerations not completely zeroed
- Model/support system "ringing"
  - -during constant velocity segment
  - -most noticeable at high sink rates (>4 ft/sec)

Some aspects of the dynamic data acquisition/reduction presented real challenges. The data system was set up to acquire multiple channels of data that were each scanned at 150 hertz over an 8 second sampling period. Some of the more significant problems with the dynamic data included issues associated with sampling rates, zeroing initial accelerations and flexibility of the model support system. The position measurements were not sampled at as high a rate as the balance and acceleration measurements. This problem is obvious when either balance or accelerometer data is plotted versus height. Multiple data points are acquired at a given height measurement. The impact of this on the DGE plots is not considered significant for the height measurements, which results in small shifts in the data on the order of 0.01 to 0.07 in h/b depending on the sink rate of the run. The impact of reduced sampling rate on the pitch measurement is not as clear cut and may be contributing to problems with cleaning up the rest of the spread in the force/moment data already corrected for inertial loads. No corrections for these sampling rate problems have been made to any of the dynamic data presented. Another challenge included the initial zeroing of the model acceleration levels at the beginning of each dynamic plunge. We attempted to handle this with a combination of wind-off zero and theoretical corrections for changes in the gravity component with pitch, but this did not work. Sharon Graves and I ended up taking an average level at the beginning of each run to reference the accelerations. This appeared to work very well and allowed us to use the integrated accelerations to calculate the model's sink rate. Finally, model support system flexibility tended to shorten the constant velocity segment of the dynamic plunge trajectories and were associated with the larger spread in the data for higher sink rate runs. In the future, we plan for changes in the cart control system to help alleviate this situation.

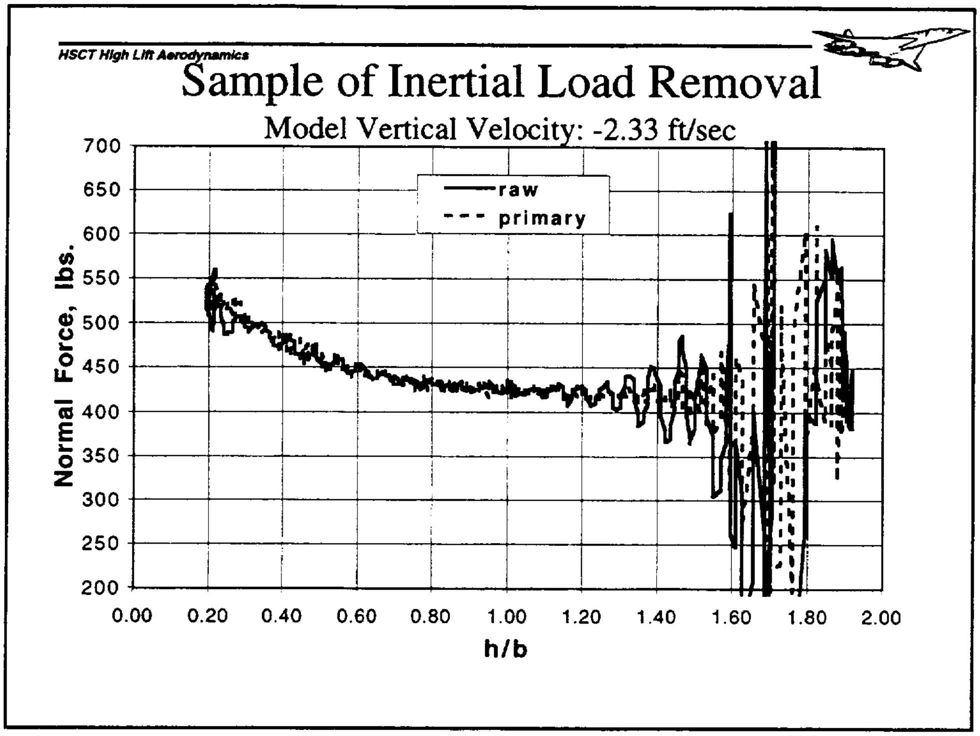

Here is a representative example of the effect of inertial load removal from the normal force balance measurements during a lower sink rate run. A run begins with the model resting at a position near the tunnel centerline, in this case at an h/b value of about 1.90. As the dynamic plunge starts, large excursions in the normal load is evidence of the rapid acceleration to the target sink rate. At an h/b level of about 1.30, the constant velocity segment of the trajectory is reached and the dynamic load excursions have diminished. The steady increase in the normal force level as h/b decreases is associated with the ground effect. At an h/b of about 0.3, the model begins decelerating and the raw normal force level is consistently lower than the corrected data. The dash curve represents the normal force data after corrections for the primary inertial loads. The amount of inertial load clean up is most evident in comparing the raw and primary curves near an h/b of 1.4 and below an h/b of 0.3. Between these two h/b values, the primary inertial load corrections routine does not have a significant impact on the raw data.

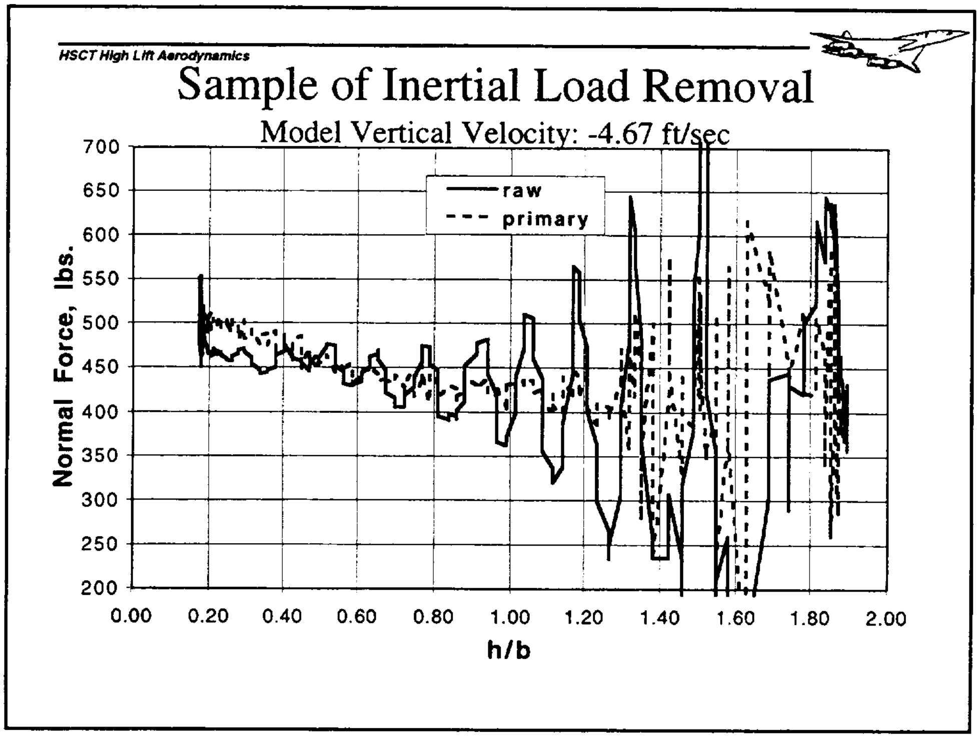

Here is a representative example of the effect of inertial load removal from the normal force balance measurements during a higher sink rate run. For the higher sink rate runs, the effect of removing the primary inertial loads is more evident throughout the plunge trajectory. Notice that the model deceleration starts earlier (h/b level of about 0.4) as compared with the previous plot for the lower sink rate run. Also note that the support system "ringing" is more prevalent throughout the plunge.

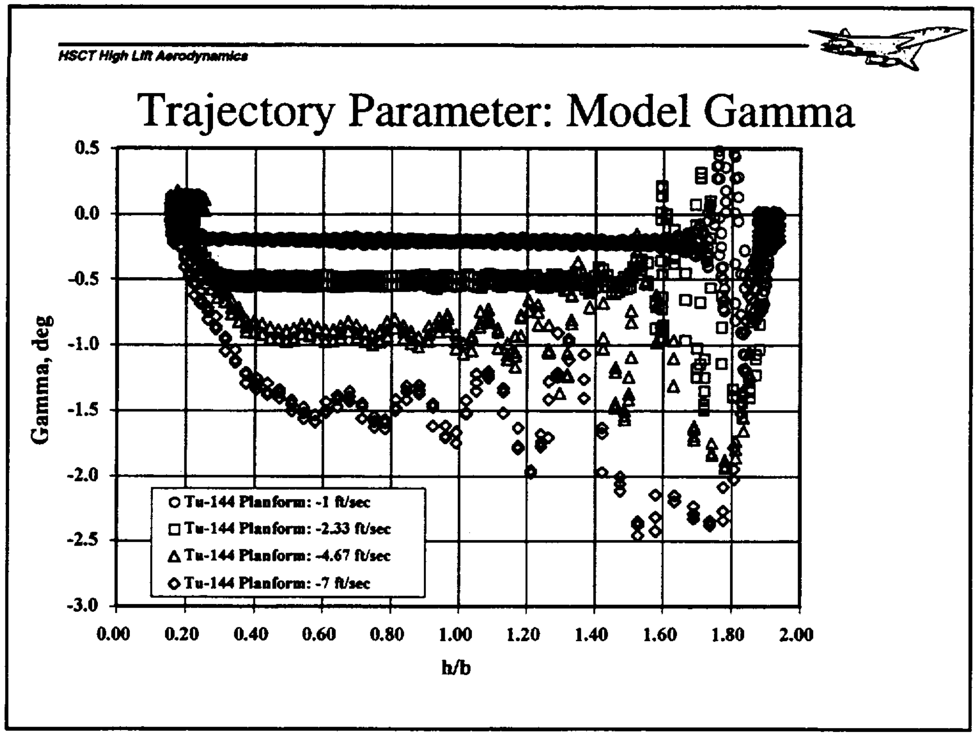

Here is a representative plot of the model glide path angle that resulted for the different dynamic plunge trajectories. The model sink rates were chosen to provide selected constant gamma for the given tunnel velocity (267 ft/sec). A significant feature of these trajectories is the long run of constant gamma for the lower sink rate runs. Notice that this constant gamma segment becomes shorter with increasing sink rate because the model support ringing persists to lower values of h/b. Also note that the model deceleration starts earlier (higher h/b values) as the sink rate increases, which further restricts or eliminates the constant gamma segment. Another noticeable feature in this data is associated with the reduced height sampling rate. For the sink rates greater than 1 ft/sec, the data symbols tend to cluster in groups of three showing that three accelerometer measurements were acquired before the height measurement was updated.

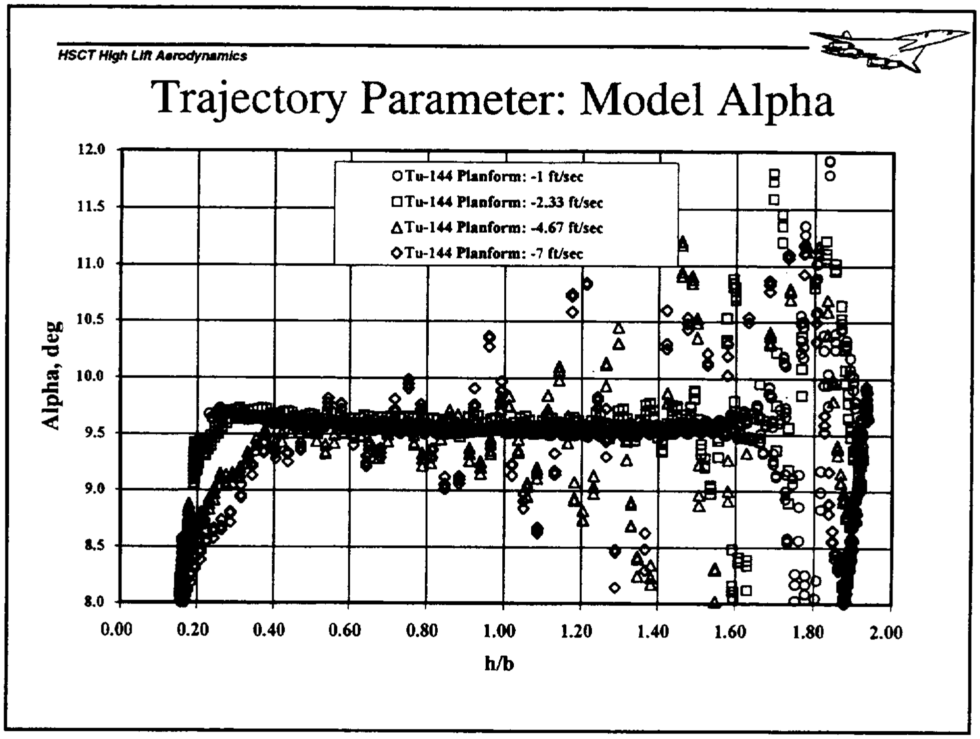

Here is a representative plot of the model angle of attack that resulted for the different dynamic plunge trajectories. As with the glide slope angle, the constant model alpha segment was longer for the lower sink rate runs. For the higher sink rate runs, the model alpha varied more significantly. Since the main point of this investigation was to try and isolate the ground effect (that is, look at lift variation with constant alpha), we decided to correct the lift data to a constant alpha to remove this effect. This correction involved compensating for the alpha variation by using the out-of-ground effect (OGE) lift curve slope. All of the DGE data that will be presented has been corrected to a constant alpha to make it comparable to the SGE data.

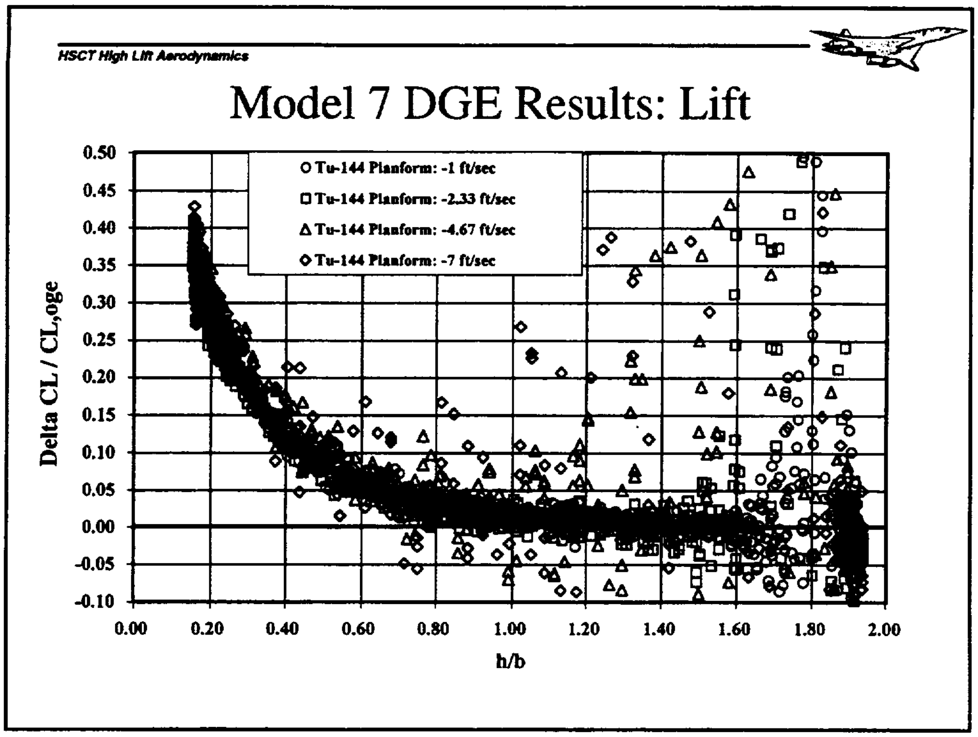

Here is a plot of the lift increment due to ground effect for the dynamic data obtained for Model 7. The cluster of data points at an h/b of 1.9 gives an idea of the variation in the lift levels while sitting statically before the start of the dynamic plunge. The data during the dynamic plunge tends to cluster in a solid trend indicating the ground effect levels on lift. The data points falling outside this trend are associated with the higher sink rate data. Keep in mind that up to h/b levels of 0.4, the model is decelerating for the higher sink rate runs so that the sink rate is not constant. From this DGE lift data, there is no indication of a significant change in the ground effect trend for varying sink rates.

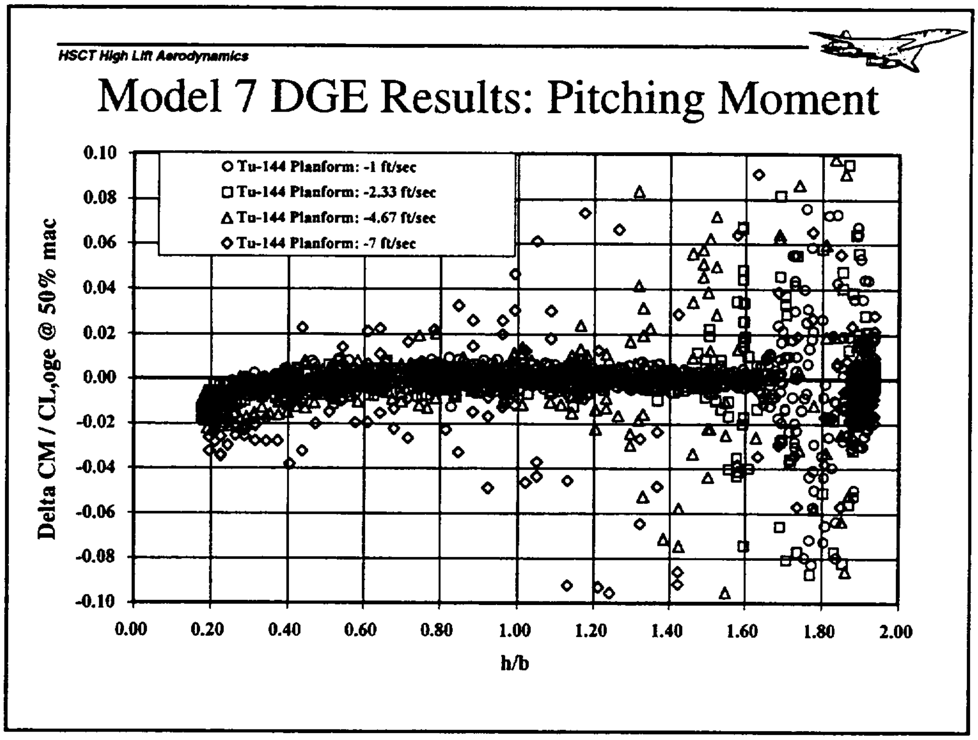

Here is a plot of the pitching moment increment due to ground effect for the dynamic data obtained for Model 7. The cluster of data points at an h/b of 1.9 gives an idea of the variation in the pitching moment levels while sitting statically before the start of the dynamic plunge. The data during the dynamic plunge tends to cluster in a solid trend indicating the ground effect levels on pitching moment. The ground effect trend on normalized pitching moment magnitude is about 2 percent. If this data were referenced to a moment center closer to the aerodynamic center (42% mac), then the magnitude of this effect would increase to about 5 percent.

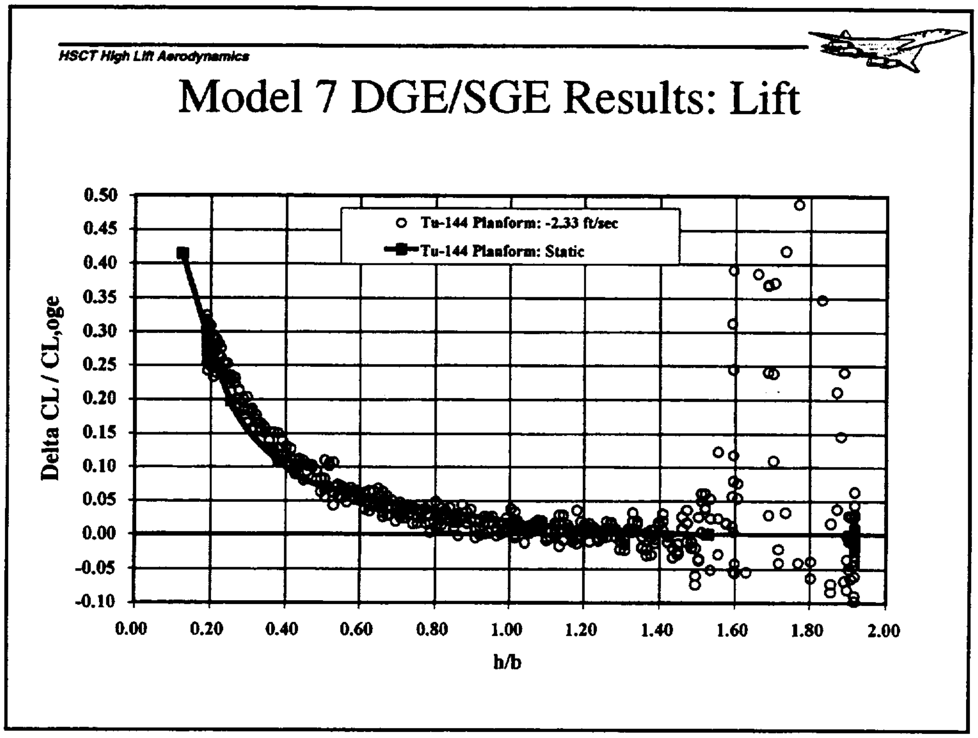

Since there did not appear to be any significant difference in the ground effect trend with different model sink rates, one of the lower sink rate DGE data runs was selected for comparison with the SGE data. This run was chosen because it was the highest sink rate run available in which the model deceleration did not begin until it was below an h/b of 0.3. This permits a comparison of DGE lift increase levels with those of the SGE in the more sensitive region of the ground effect trend. This comparison does not show that the DGE lift increase is significantly different from that of the SGE. (Recall that we are looking for differences indicating that the DGE lift increment is about 50 percent of that of the SGE at values of h/b of about 0.3.)

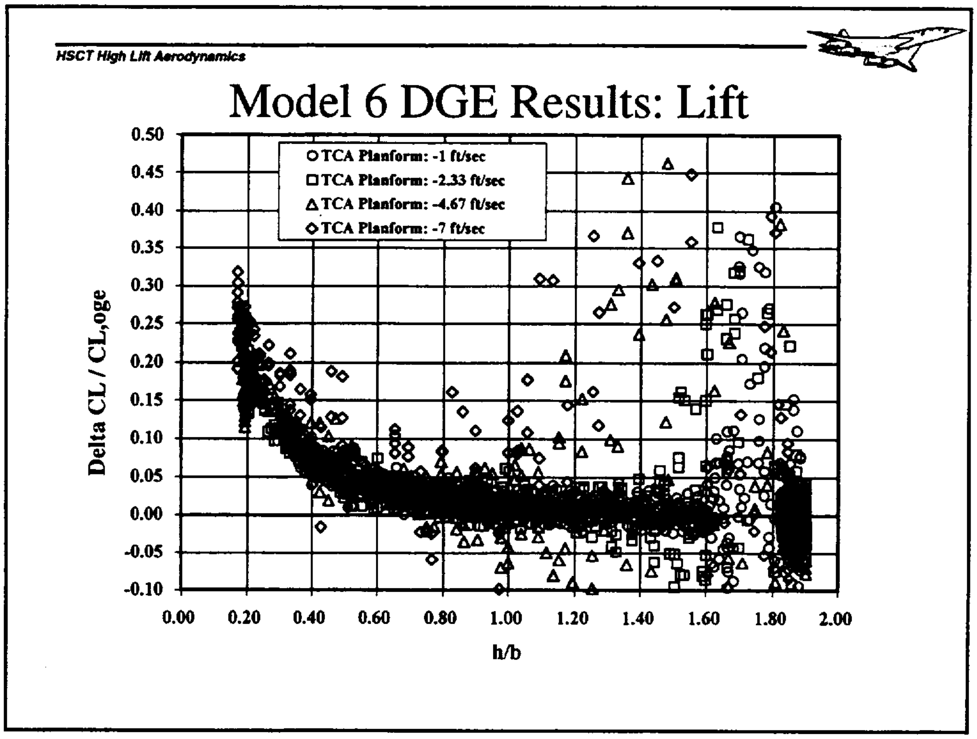

Here is a plot of the lift increment due to ground effect for the dynamic data obtained for Model 6. Again, the cluster of data points at an h/b of 1.9 gives an idea of the variation in the lift levels while sitting statically before the start of the dynamic plunge. The data during the dynamic plunge also tends to cluster in a solid trend indicating the ground effect levels on lift. The data points falling outside this trend are associated with the higher sink rate data. Keep in mind that up to h/b levels of 0.4, the model is decelerating for the higher sink rate runs so that the sink rate is not constant. From this DGE lift data, there is no significant change in the ground effect trend for varying sink rates. Note that the ground effect lift increase for this wing planform is below 15 percent at an h/b of 0.3 as compared to about 20 percent for Model 7. Also, the lift increment data for Model 6 appears to have a larger variation band than that for Model 7. Model 6 had a blunt inboard LE radius and Model 7 had a "sharp" LE. This geometry difference may contribute to the larger variation in the data for Model 6.

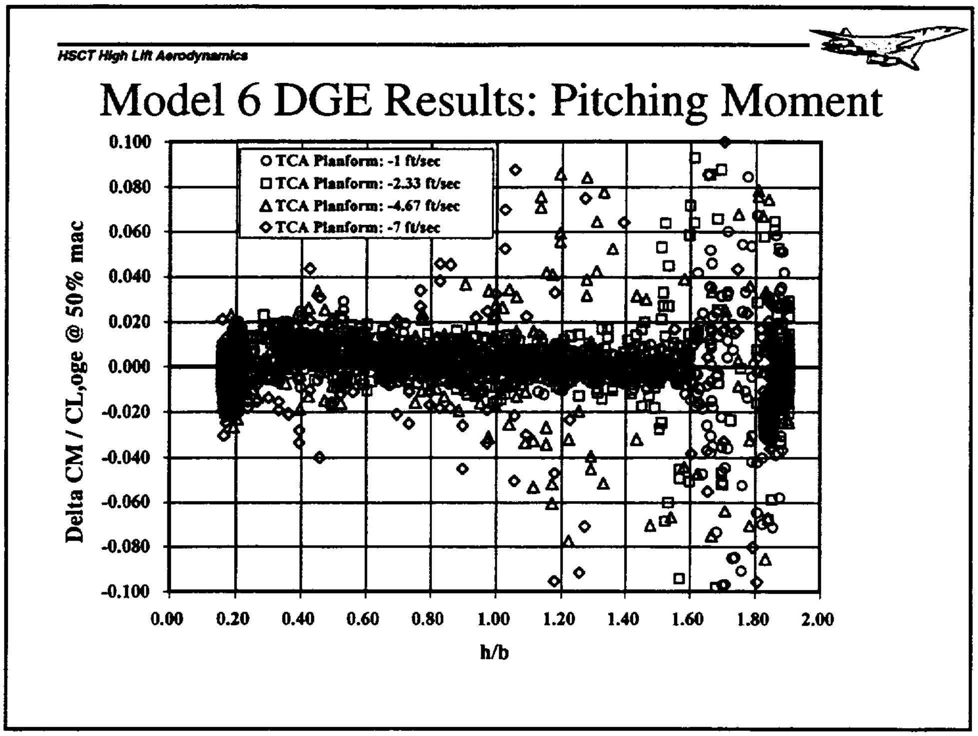

Here is a plot of the pitching moment increment due to ground effect for the dynamic data obtained for Model 6. The cluster of data points at an h/b of 1.9 gives an idea of the variation in the pitching moment levels while sitting statically before the start of the dynamic plunge. The data during the dynamic plunge was more scattered than that for Model 7. The ground effect trend on the pitching moment increment is not clear.

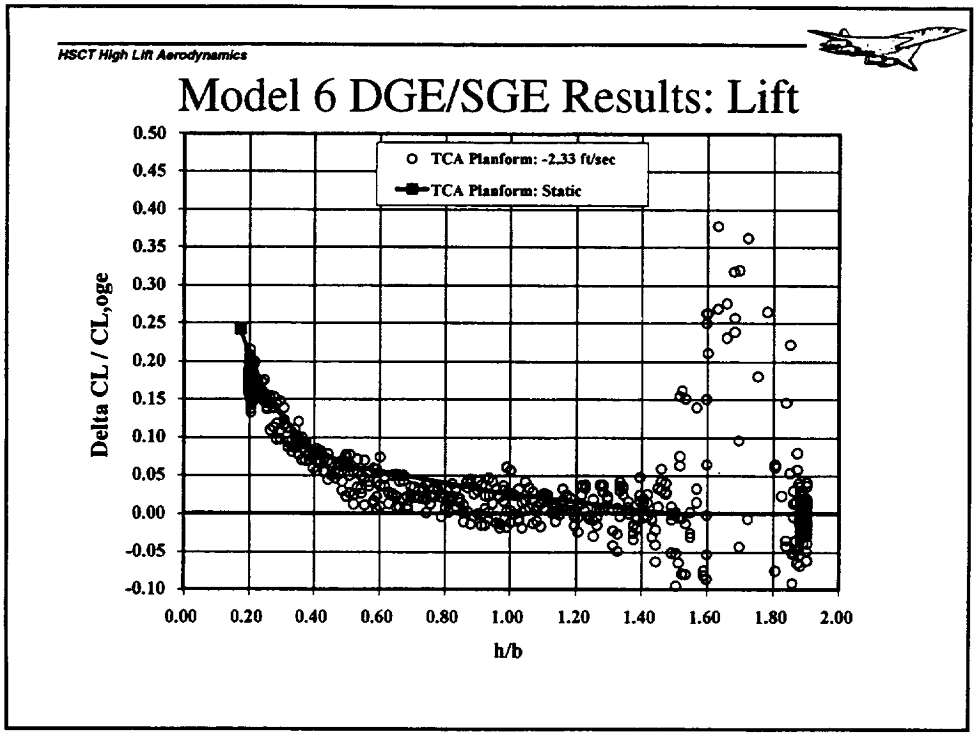

Since there did not appear to be any significant difference in the ground effect trend with different model sink rates, one of the lower sink rate DGE data runs was selected for comparison with the SGE data. This run was chosen to be consistent with that chosen for Model 7. This comparison also does not show that the DGE lift increase is significantly different from that of the SGE. (Recall that we are looking for differences indicating that the DGE lift increment is about 50 percent of that of the SGE at values of h/b of about 0.3.)

Why are SGE/DGE similar?

- Previous data indicated DGE/SGE lift increment ratio of about 50% for aspect ratios less than 2.0
- LE sweep or wing sweep-related factor may be the more important controlling parameter (especially with discontinuous LE)
- Other factors may include: AOA region, RN, flap configuration

The 14x22 ft DGE test did not show significant differences between SGE and DGE lift increment data. The previous KU data suggests that the models tested were in the aspect ratio range where this difference should be significant. A review of the KU database was performed to check for consistency and what factors may explain the difference in the findings. One difference noted was that the models tested in the 14x22 ft study had breaks in the wing planform LE while the KU data was based on planforms with no LE breaks. For continuous LE planforms, there is a direct correlation between the LE and the aspect ratio. For planforms with a LE break, this relationship is not as direct. Other differences were also noticed and considered in the review of the ground effects database. However, the LE sweep factor seemed to be consistent and deserved further examination.

University of Kansas data reference:

R. C. Chang and V. U. Muirhead, "Effect of Sink Rate on Ground Effect of Low-Aspect-Ratio Wings," Journal of Aircraft, Vol. 24, No. 3, March 1987, pp. 176-180.

Another Look at DGE/SGE wind-tunnel data

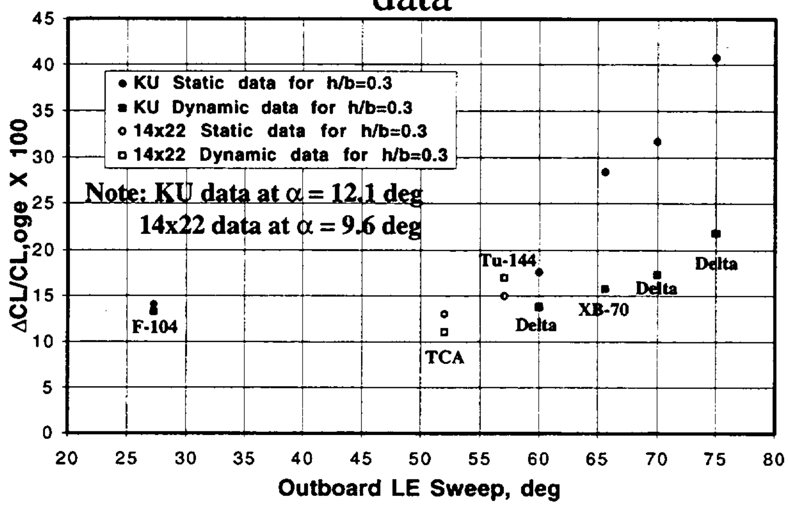

Here is another look at the University of Kansas wind-tunnel data plotted versus LE sweep (outboard LE for cranked wing planforms) instead of aspect ratio. Comparable SGE and DGE data points were added to show where they fall relative to the existing data. Note that both the TCA and the Tu-144 model data was placed considering the sweep of the outboard LE. If this is a proper way of looking at the differences between SGE/DGE data, then this may explain why the models tested in the 14'x22' study did not show any significant difference.

Computational Checks

- Unsteady 3-D seems to be predicting the similar DGE results as experiment for a 60 degree delta wing and the TCA wing
- Recommend using computational methods to investigate other factors (LE sweep, AOA region,...)

Two different analytical approaches, each developed by Winfried Feifel (Boeing) and Bill Dwyer (Northrup Grumman), were used to predict dynamic ground effects. Both the analytical and the experimental DGE results are consistent and show no significant difference between SGE and DGE for the TCA wing planform. It is interesting to note that Bill Dwyer showed some potentially significant DGE/SGE differences for the XB-70 wing, but unfortunately this work was not concluded due to funding constraints.

These analytical approaches provide an opportunity to explore other factors associated with low aspect ratio wings to gain a better understanding of when there may be significant differences between SGE and DGE testing techniques.

Dynamic Ground Effects: Flight Data

- Bob Curry will present the next section

HSCT High Lift Aerodynamics

Flight Data

- Flight data obtained for two similar vehicles
  - F-16XL experiment complete
  - TU-144, preliminary data available
- Data obtained Test Techniques
  - Instrumentation included both on-board sensors and differential GPS
  - Data was obtained during constant-angle-of-attack, constant-thrust approaches to the runway
- Data Analysis
  - Data corrected for variations in alpha and surface deflections
  - Flight results are shown as untrimmed, incremental changes in lift, and pitching moment coefficient relative to the 'out-of-ground-effect' lift coefficient

A flight experiment was conducted to provide additional information regarding ground effect characteristics for slender-wing, high-speed configurations. Flight data has been obtained for the F-16XL and the Tupolev TU-144 supersonic aircraft. Data from the TU-144 flight experiment will also be used to validate results from the DGE wind tunnel test technique.

A thorough discussion of the flight test techniques and data analysis process for the F-16XL is provided in NASA TM 4799. Similar methods are being used for the TU-144 flight experiment.

The data were obtained during approaches to the runway. Before each maneuver, the pilot began a stabilized descent at a pre-determined glide slope and angle of attack. The pilot attempted to hold the power and angle-of-attack constant for the remainder of the maneuver as the airplane descended into ground effect. Perturbations from the initial flight conditions were attributed to ground effect. Adjustments to angle-of-attack and elevon position which occurred during the maneuvers were accounted for in the extraction of ground effect increments.

Data were obtained for a variety of gross weights, flight path angles, flap and canard positions.

HSCT High Lift Aerodynamics

Test Configurations

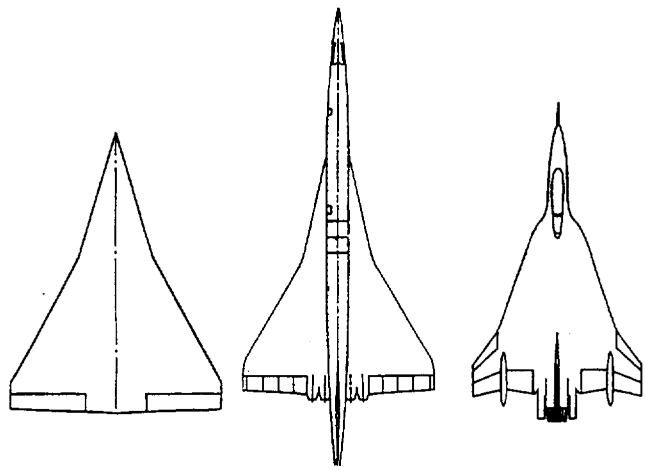

TU-144 planform   TU-144 airplane   F-16XL airplane

This figure shows three configurations for which static and dynamic ground effect data have been obtained. All of the wings have similar aspect ratio and similar inboard and outboard leading edge sweep.

The wind tunnel model is an uncambered, planform of the TU-144 wing. The trailing edge elevons were set at 10 degrees (trailing edge down) for all tests.

Flight data for the TU-144 was obtained using a research vehicle derived from an early production supersonic transport. The configuration has four turbojet engines mounted below the wing similar to 'HSCT' configurations. The airplane is normally landed with canard deployed, however, flight test data was obtained with the canard both deployed and retracted. Elevon positions were were about 9 deg (trailing edge down) during final approach for the majority of flight maneuvers. Slightly negative elevon positions (trailing edge up) were required during maneuvers with the canard retracted .

The F-16XL airplane is a high-performance, single-seat airplane with a cranked-arrow-wing designed for supersonic cruise flight. The single turbofan engine is located on the centerline. Because of the relatively large gear height relative to wing span, ground effect data at very low ratios of h/b could not be obtained with the F-16XL.

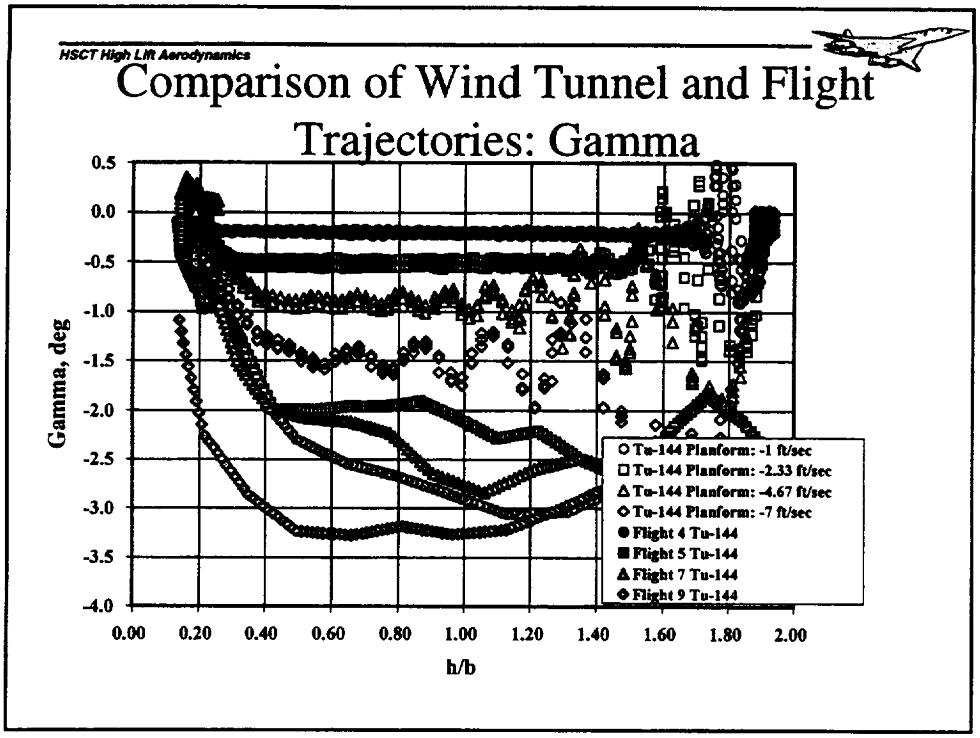

During flight testing, the flight path angle and vertical speed is generally constant as the airplane descends through altitudes above ground effect. Initial flight path angles for the flight maneuvers varied between about -2 and -3 deg. These sink rates correspond to vertical velocities of between 10 and 15 ft/sec. As the airplane passes through a height of about one span, the flight path angle and sink rate begins to decrease due to ground effect, until both parameters are nearly zero at touchdown

The variation of flight path angle with altitude during the flight test maneuvers is similar to the landing flare conducted during normal landings of the TU-144.

The DGE wind tunnel capability allowed data to be collected at a constant flight path angle in the presence of ground effect. Similar results have not been obtained in flight testing. The DGE wind tunnel flight path angles are generally lower than the sink rates experienced in flight.

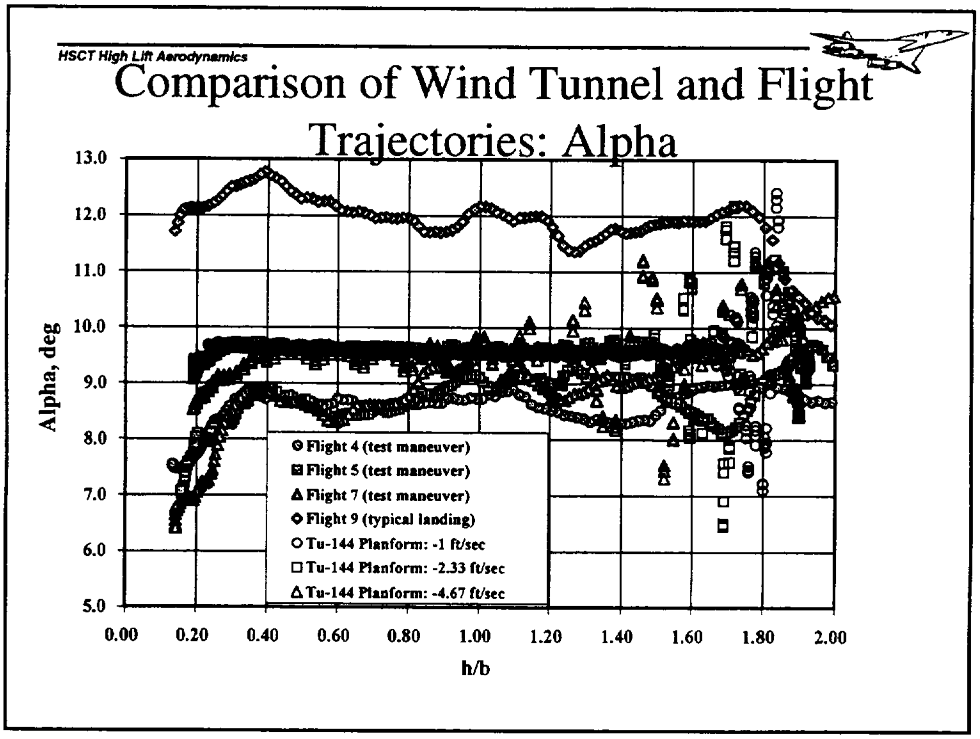

During the flight test maneuvers, the pilot attempts to hold angle-of-attack constant during the descent through ground effect. Atmospheric disturbances and the need to insure satisfactory conditions at touchdown cause some variations to occur. For most of the TU-144 flight maneuvers analyzed so far, there has been a decrease in alpha just prior to touchdown. Angle-of-attack is generally increased slightly during conventional landings. During the flight test maneuvers, the angle of attack was about 9 degrees.

Angle-of-attack was constant during a significant range of the DGE wind tunnel trajectories. As the model decelerated at the end of a run, the angle-of-attack decreased. The region of constant angle-of-attack was therefore smaller for the higher sink rate tests.

Analysis of both the wind tunnel and flight data sets account for any variations of angle-of-attack. Static measurements of lift and pitching moment derivatives with respect to angle-of-attack were used for these corrections.

Similar corrections are made to the flight data for any variation in elevon position which occurs during a maneuver.

As a result, the final wind tunnel and flight data sets represent untrimmed force and moment increments due to ground effect.

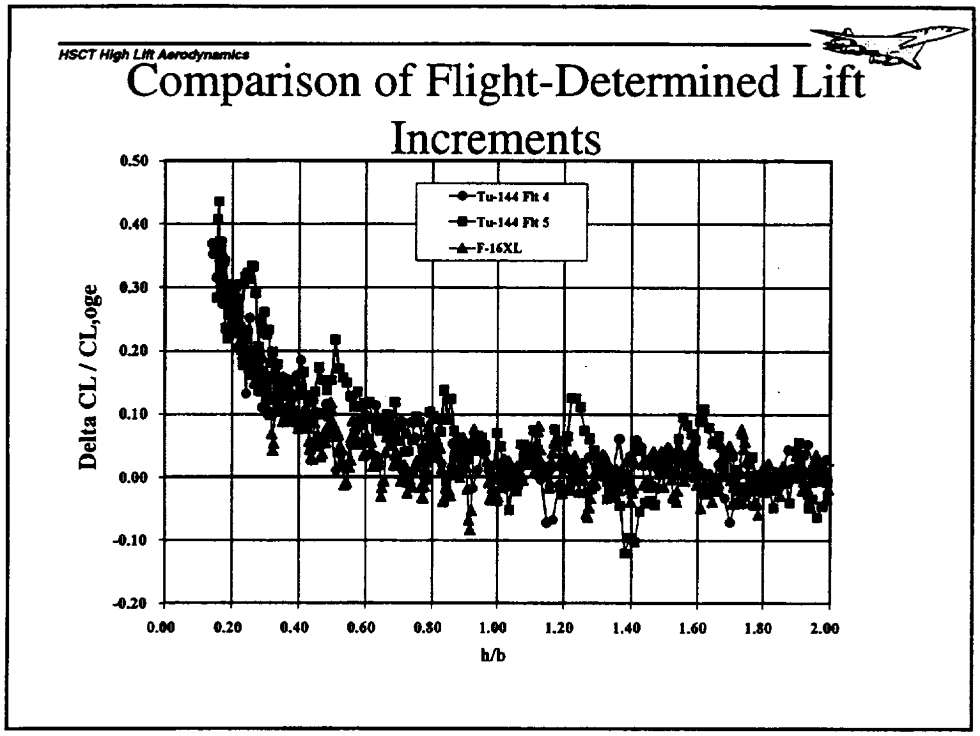

The incremental changes in lift coefficient due to ground effect from several flight maneuvers are repeatable within the noise level of the measurements. The primary sources of scatter in the data are felt to be noise in the accelerometer measurements and atmospheric disturbances.

Data for both the TU-144 and F-16XL compare favorably, despite differences in wing shape and engine configuration.

Comparison of Wind-Tunnel and Flight Lift Increments

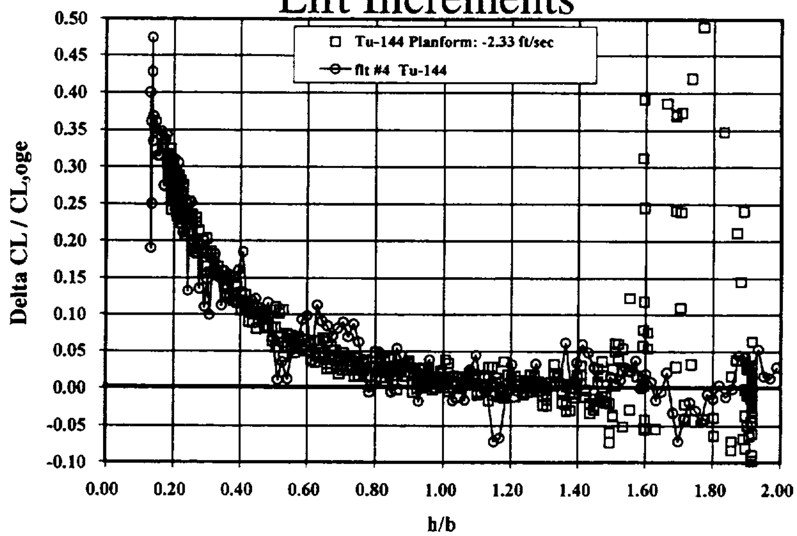

Preliminary comparisons of flight measured lift coefficient increments from flight and DGE wind tunnel testing show excellent agreement. The flight data shown was obtained at an initial sink rate of approximately 15 ft/sec with the canard deployed. The DGE data was obtained at a sink rate of about 2.33 ft/sec, wing planform only.

Additional correlations will be possible as more TU-144 flight data becomes available.

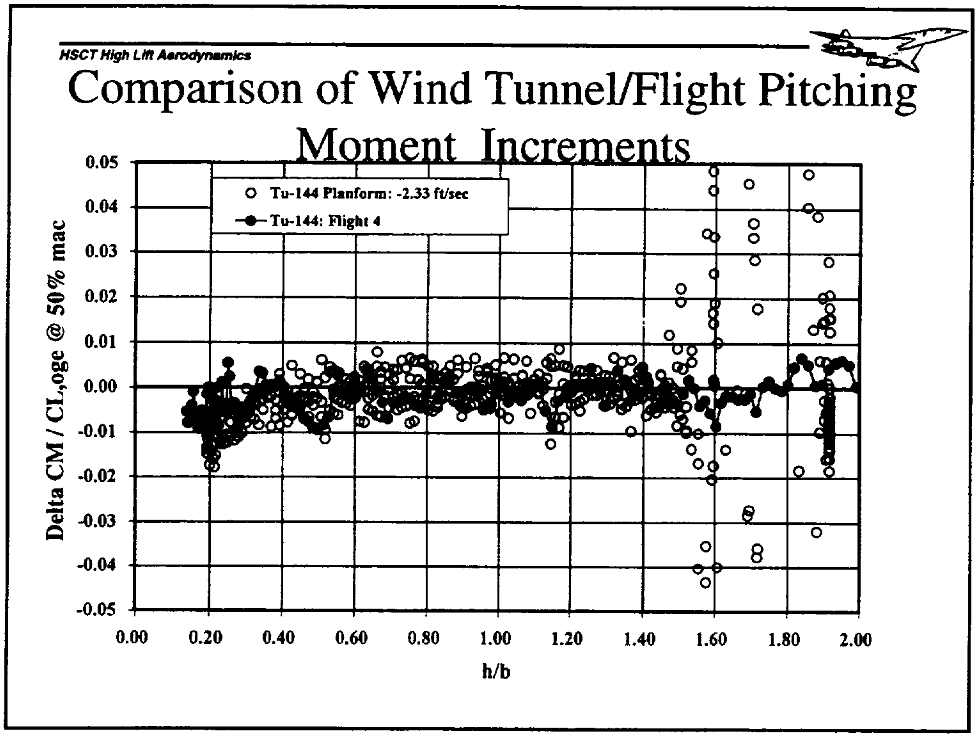

Both flight and wind-tunnel data indicated small levels of nose-down pitching moment in the presence of ground effect when referenced to 50% MAC.

The center of gravity for the aircraft is typically about 40% MAC and therefore the negative pitching moment due to ground effect is more significant for the flight vehicle.

Any differences between the wind tunnel and preliminary flight data are within the noise level of the flight measurements.

HSCT High Lift Aerodynamics

Status of Flight Testing

- TU-144 Flight Testing Still in Progress
- 17 flights completed to date, 9 ground effect maneuvers attempted
- Post-flight computations of mass properties and thrust estimates for most maneuvers still in progress
- Flight data set to be summarized in TU-144 final report

The TU-144 flight experiment is still in progress. A total of 18 flights are expected to be completed by the end of February.

The flight data set will be limited to about 8 to 10 good maneuvers. Although the airplane conducted fifteen flights, ground effect maneuvers were only attempted on certain flights due to test planning constraints, and it was also not possible to obtain more than one test point on a given flight.

Additional smoothing and trajectory reconstruction methods may be used to enhance the quality of the flight data. Final data analysis will not be possible until post-flight computations of mass properties and thrust have been provided by Tupolev. A summary of the flight experiment and electronic files containing flight data (in engineering units) will be available to the HSR project at the conclusion of the flight program.

HSCT High Lift Aerodynamics

Composite Data Set as a Function of Aspect Ratio, h/b=0.3

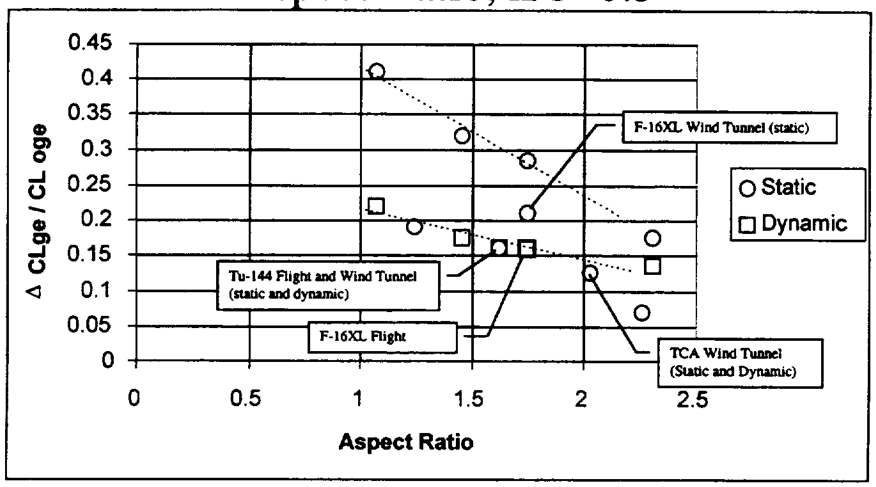

Shown in this figure is the composite ground effect data set from several tests plotted as a function of aspect ratio. As previously noted, there are two general trends.

One trend line consists of all the dynamic data as well as some static data. Another trend line consists of several static test points, with values approximately twice as great as the first trend line. The Tu-144 and TCA dynamic and static wind tunnel data, as well as the Tu-144 flight data all fall along the initial trend line. The dynamic flight data for the F-16XL also fits this trend, however, the corresponding F-16XL static wind tunnel data is significantly larger than the flight data.

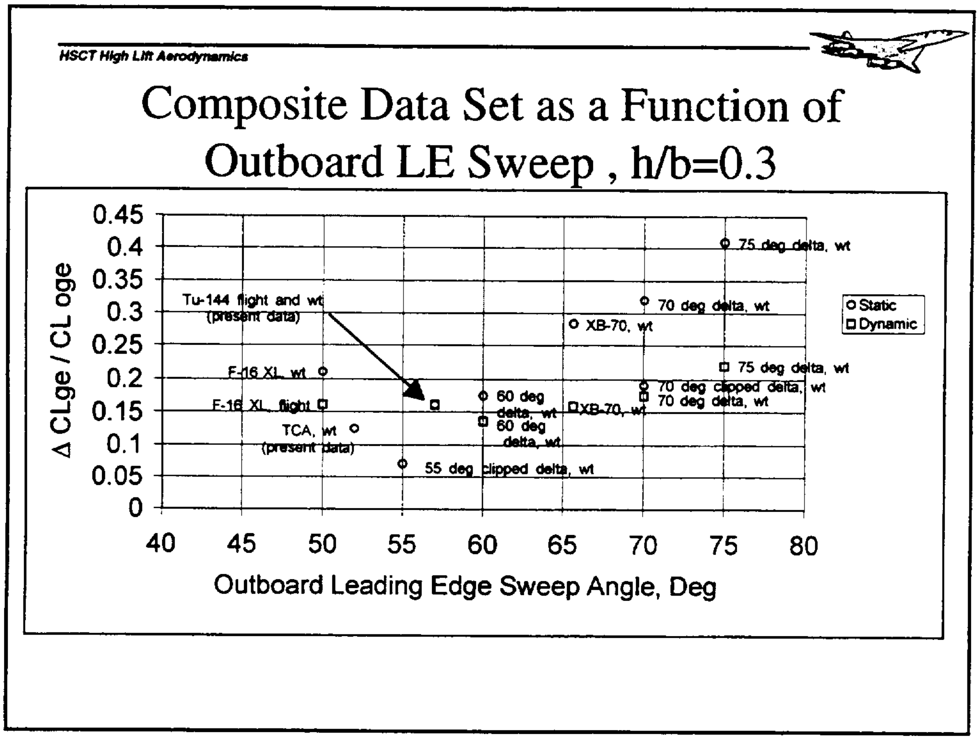

When the same data is plotted as a function of outboard leading edge sweep angle, both the Tu-144 and TCA data from the current study fit the trends fairly well. The F-16XL; however, appears to depart from the trend. It should be noted however, that the leading edge sweep breakpoint is relatively farther outboard for the F-16XL than for either the Tu-144 or the TCA model. Therefore it could be argued that the F-16XL data should be plotted against its inboard leading edge sweep angle (70 deg), which would result in a better fit to the trend. These observations suggest that ground effect, and the sensitivity to dynamic ground effect, may be indicated by a parameter which involves a weighted value of leading edge sweep.

The current data base is awkward to interpret since it includes an inconsistent variety of configurations and test facilities. In many cases, dynamic data for a configuration was obtained from flight or a dynamic facility and then compared against static data from a different wind tunnel facility. Only the University of Kansas low speed wind tunnel and the NASA Langley 14x22 ft DGE cart have the capability to provide parametric data under both static and dynamic conditions. So far, the Kansas data have distinctly indicated strong influences while the 14x22 ft data have indicated negligible differences due to dynamics. Further parametric testing with the 14x22 DGE system, especially with higher wing sweep angles, may help isolate the controlling parameters for dynamic ground effects.

HSCT High Lift Aerodynamics

Conclusions

- For the low aspect ratio wing planforms tested
  - no significant DGE/SGE differences
  - other parameters (besides AR) may be significant controlling factors in this difference (LE sweep)
- Wind tunnel and flight ground effects increment data for the Tu-144 compared well

For the HSCT wing planforms tested in the 14x 22 ft DGE test, no significant differences were found between DGE and SGE test techniques. From previous ground effects data, the aspect ratios of the model wing planforms tested were such that differences in DGE and SGE data were expected. Closer examination of all the data suggested that other factors (in addition to AR) may need to be controlled to better understand this difference. Comparisons of the ground effects increment data from the 14x22 ft DGE test and the flight test for the Tu-144 were good. These ground effects increments compared well even with a very basic model that represented only the wing planform of the Tu-144 aircraft.

HSCT High Lift Aerodynamics

Recommendations

- DGE cart needs to be reworked before it can be a routinely used in ground effects testing
- Follow-on DGE test
  - Check-out reworked DGE cart
  - Confirm current HSR DGE findings and provide an opportunity to validate DGE test technique
  - Expand parameter database for ground effects modeling for low aspect ratio wings (especially LE sweep influence)
- Computational parametric study of controlling factors
  - Unsteady 3-D, to study LE sweep influence on DGE/SGE differences
  - Steady-State method, check static ground effect levels

During this test, a list of items that need to be reworked was generated. Before this DGE cart can be routinely used in wind tunnel tests, these items need to be fixed. After these repairs are completed (current repair plan can be completed by Feb/Mar of 1999), a follow-on test would enable us to check-out the repairs. After a brief check-out, we could re-run the HSCT planforms already tested to confirm the current findings plus run the seven untested models to expand the ground effects database. This investigation would provide the opportunity to gain a better understanding of the differences between DGE and SGE test techniques as well as the knowledge necessary to decide when each is needed. In addition, a computational parametric study of some of the other potential factors would help the HSR community gain a better understanding of what factors need to be controlled in ground effects testing.

This page is intentionally left blank.

Potential Flow Analysis of Dynamic Ground Effect

W. M. Feifel

Boeing Commercial Airplane Group

Presented at

HSCT Airframe Annual Review

Los Angeles, February 1998

NASA HSR2 Contract No. NASI-20220

Task 33 4.3.2.4

Potential Flow Analysis of Dynamic Ground Effect

Interpretation of some flight test data suggests the presence of a 'dynamic ground effect'. The lift of an aircraft approaching the ground depends on the rate of descent and is lower than the aircraft steady state lift at a same height above the ground. Such a lift deficiency under dynamic conditions could have a serious impact on the overall aircraft layout. For example, the increased pitch angle needed to compensate for the temporary loss in lift would reduce the tail strike margin or require an increase in landing gear length.

Under HSR2 an effort is under way to clarify the dynamic ground effect issue using a multi-pronged approach. A dynamic ground effect test has been run in the NASA Langley 14x22 ft wind tunnel. Northup-Grumman is conducting time accurate CFD Euler analyses on the National Aerodynamic Simulator facility. Boeing has been using linear potential flow methodology which are thought to provide much needed insight in physics of this very complex problem.

The present report summarizes the results of these potential flow studies. The chart shows the outline of this report.

Potential Flow Analysis of Dynamic Ground Effect

Topics

I. Background and Objectives

II. Time Accurate Potential Flow Code UNSTEADY3D
    Description of Method
    Validation

III. Cropped Delta Wing
    Ground Effect Calculations
    Unsteady Pitching Motion

IV. TCA Wing and Tri-Surface Configuration

V. Conclusions and Recommendations

I. Background and Objectives

There are a number of flight test results from which the presence of a dynamic ground effect can be inferred. As a typical example, test data for the F-15 fighter airplane will be shown.

The objectives of the Boeing potential flow studies area are outlined below. While listed as separate tasks, the stated objectives have been addressed more or less simultaneously during the course of the investigations. Before hand it should be stated that even 'simple linear potential flow methods' become computationally very involved if time-accurate solutions rather than frequency domain solutions are needed. Dynamic ground effect is not a periodic problem and thus demands the time-accurate approach. The large amounts of computer time required limited both the complexity and the number of configurations analyzed during the present investigations.

I. Background and Objectives

- F-15 Flight Test Results

- Provide insight into the physics of dynamic ground effect
- Identify contributing factors other than the dynamic ground effect itself
- Validate analysis methods based on linear potential flow
- Apply methods to HSCT-type configurations

F-15 Dynamic Ground Effect Flight Test Results

The following excerpts from NASA Memorandum 4604 clearly summarizes the conclusions drawn from the F-15 flight test results:

In general, Figure 11 shows that ground effect becomes increasingly significant as sink rate decreases. The changes in the lift coefficient (Figure 11(a)) and the nose-down pitching moment (Figure 11(c)) increase with decreasing sink rate. These data also show that the changes because of ground effect decrease and approach zero as the sink rate increases. The change in the lift coefficient more than doubles from approximately 0.05 to over 0.1 as the sink rate decreases toward zero. The change in the nose-down pitching moment coefficient doubles from -0.008 to -0.016 for the 170kn with the flaps up configuration and more than quadruples from -0.008 to -0.038 for the 150kn with the flaps down configuration as the sink rate varies from the maximum to the minimum values.

The trends are not as clear for the drag coefficient (Figure 11(b)). The change in drag increased with decreasing sink rate from 0 to approximately 0.03. The large increase in drag at a sink rate of approximately 4 ft/sec may result from data scatter because of the greater sensitivity of calculating the small change in the drag force caused by ground effect.

Figure 11 also shows that the 150kn with the flaps down approach results in significant ground effects. This difference is most apparent for pitching moment (Figure 11(c)). Here, the 150kn with the flaps down values are approximately twice that of the 170kn with the flaps up values at the lower sink rates. This increase may result from a camber effect because of the flaps being down.

F-15 Dynamic Ground Effect Flight Test Results

Figure 11. Effect of approach speed, flap setting, and sink rate on change in F-15 aerodynamic coefficients caused by ground effect.

NASA Technical Memorandum 4604

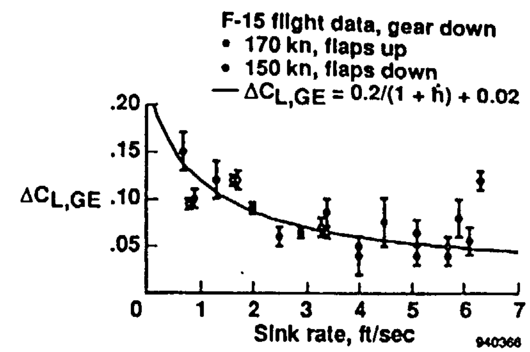

(a) Lift.

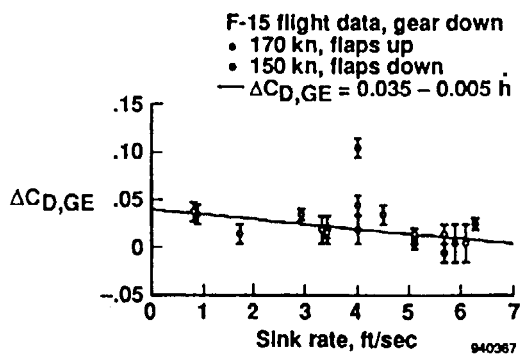

(b) Drag.

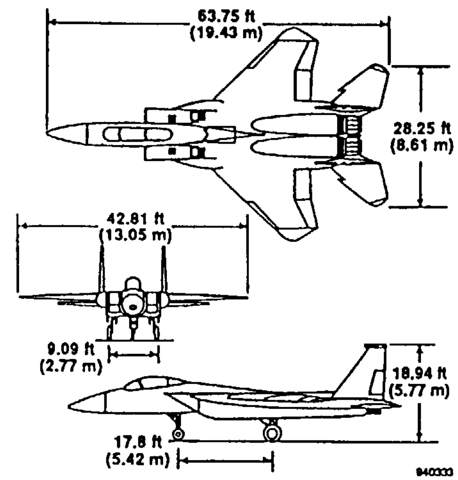

(a) F-15A.

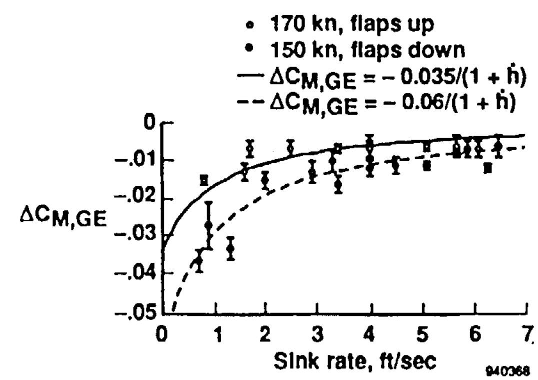

(c) Moment.

Lift of an Impulsively Started Two-Dimensional Flat Plate (Wagner's Function)

Much can be learned about unsteady aerodynamics by studying the Wagner function. This function, shown in the figure, describes the development of lift on an impulsively started 2d flat plate. The total lift is seen to consist of lift due to circulation and lift due to added mass effects. At the time $t = 0$, at the very onset of motion, the airfoil develops an infinite amount of lift for an infinite small length of time (similar to a Δ function). At the time $t = +0$ the circulation lift is zero, but already ½ of the final total lift is attained as a result of virtual mass effects. The circulation lift develops slowly due to the downwash induced by the startup vortices which travel downstream. The lift due to virtual mass decreases with time because it is proportional to the rate of change of flat plate circulation with time. Basically, the virtual mass forces are a result of the changes imposed on the entire flow field which was at rest at $t = -0$.

During the period of time when the lift of the flat plate starts building (actually an infinite length of time!), the potential flow drag of the flat plate is not zero. The drag consists of two components: (1) the vortex drag due to the downwash induced by the startup vortices and (2) the drag due to virtual mass lift which acts only normal to the flat plate surface.

It is important to note that only the lift associated with circulation produces a potential flow leading edge suction force on the flat plate. This means that at time $t = +0$ there is no circulation lift and thus no leading edge suction force, but the drag (due to added mass effects) is $C_d = \pi * \sin^2(\alpha)$. The fact that during transient conditions only the circulation part of lift is associated with a leading edge suction force may have important implications: Based on the Polhamus theorem (used, for example, in the modified form of "attainable leading edge suction" in the NASA Aero2S computer code), the strength of the leading edge suction force determines the lift due to leading edge vortex formation. If part of the lift of a delta wing is produced by virtual mass effects, the lower leading edge suction force would result in a reduced amount of Polhamus vortex lift if the leading edge flow is separated.

Lift of an Impulsively Started Two-Dimensional Flat Plate (Wagner's Function)

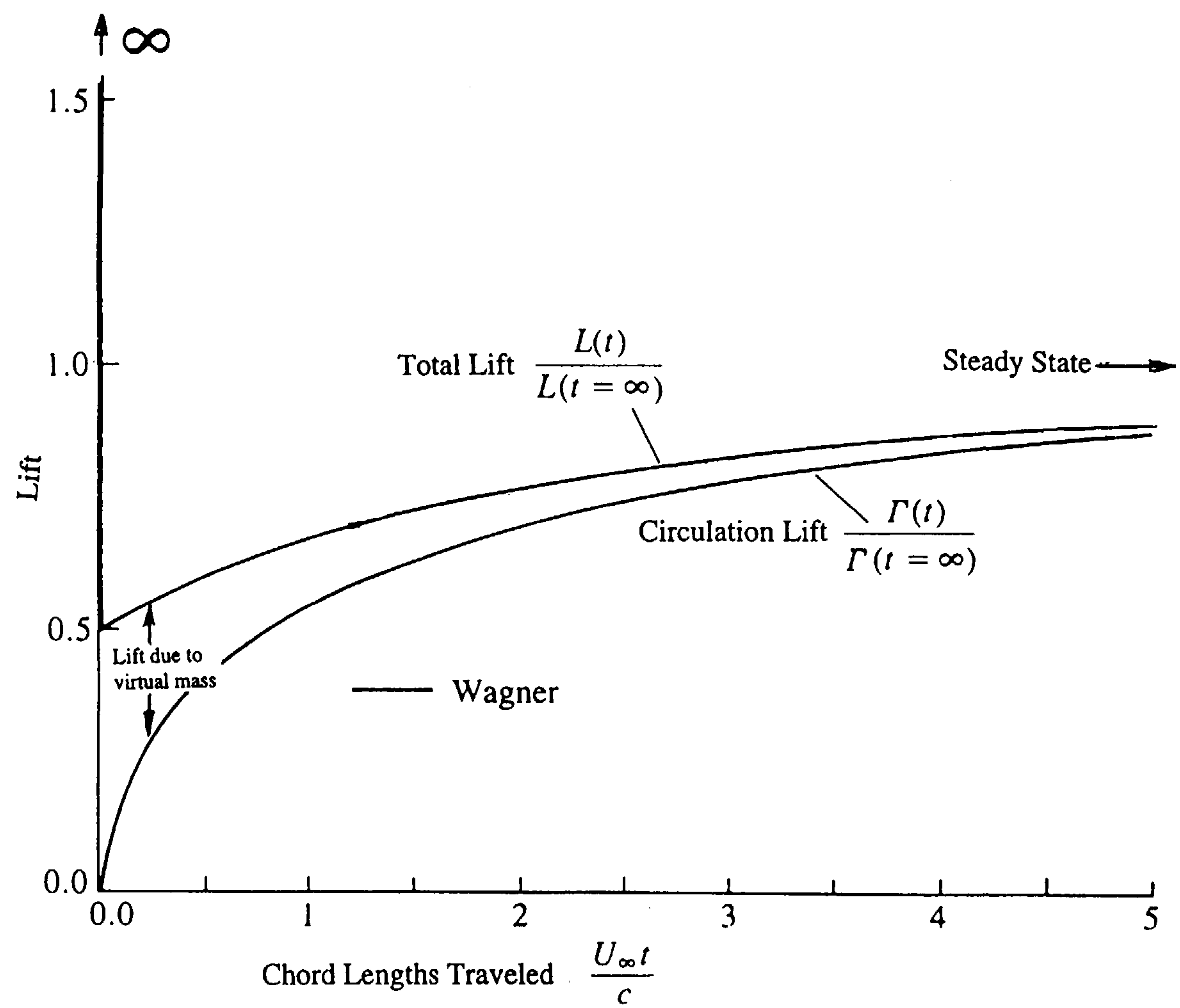

Dynamic Ground Effect Similarity Parameters

Important scaling parameters for dynamic testing are shown in this figure.

The most important parameter is the *nondimensional time*. It basically describes the number of chord lengths traveled before comparable states are achieved in model scale and full scale. This nondimensional time scale is important if, for example, flight test data are to be compared with wind tunnel data. Typically, the requirement that the nondimensional time scales be the same for the full scale and the model scale airplane is automatically satisfied if the *geometric similarities* listed in the figure are satisfied. As usual, it will be difficult to simultaneously satisfy all the *aerodynamic similarities*. Once a certain glide path angle, w/u_{∞} , has been specified the tunnel velocity is dictated by the attainable plunge velocity, w , of the plunge apparatus. However, attention has to be paid in the wind tunnel test to allow the model lift to adjust to the angle of attack change introduced once plunging commences. As will be explained later, a wing of aspect ratio 2 must have traveled about 5 chord lengths before steady state conditions are fully attained. Also, any oscillatory harmonic motion has to be scaled correctly.

Typically, oscillatory data (harmonic motion) are presented in terms of *nondimensional (reduced) frequency*.

Dynamic Ground Effect Similarity Parameters

Nondimensional time: (to collapse Wind Tunnel & Flight Test data)

Chord lengths traveled: $U_\infty * T/C = u_\infty * t/c$

Reduced frequency: $k = \dfrac{\Omega * C}{2U_\infty} = \dfrac{\omega * c}{2u_\infty}$

Geometric similarities: (must be matched in Wind Tunnel)

Wing geometry (must be similar)

Height above ground: $H/B = h/b$

Glide path angle: $W/U_\infty = w/u_\infty$

Attitude: $\alpha_{Airplane} = \alpha_{Model}$

Aerodynamic similarities: (should be matched in Wind Tunnel)

Mach Number

Reynolds Number

Nomenclature: (Upper case = Airplane, Lower case = Model)

T,t (sec) =	time
U,u (m/sec) =	free stream velocity
W,w (m/sec) =	vertical velocity
B,b (m) =	wing span
C,c (m) =	reference chord length
H,h (m) =	height above ground
Ω,ω (rad/sec) =	frequency of oscillation

II. Time-Accurate Potential Flow Code UNSTEADY3D

The Boeing UNSTEADY3D vortex lattice potential flow code has been used for most of the time dependent analyses discussed in this report.

A brief description of the code will be provided. Many of the validation cases run also served to further the physical understanding the unsteady flow phenomena.

II. Time-Accurate Potential Flow Code UNSTEADY3D

- Description of Method
  - Vortex Lattice/Quadrilateral Formulation
  - Polhamus Leading Edge Suction Theorem
- Validation Cases
  - Impulsively Started Flat Plate (Wagner Function)
  - Rectangular Low Aspect Ratio Wings
  - Heaving Airfoil (Theodorsen Function)
  - Low Aspect Ratio Plunging Wing in Ground Effect
- Findings

Description of Method

Time Accurate Boeing UNSTEADY3D Potential Flow Program

UNSTEADY3D has been derived from the Boeing A372 steady state vortex lattice code. In addition to the horse shoe type vortex singularities used in A372, the time dependent UNSTEADY3D code also employs quadrilateral vortex elements, as illustrated in the figure. The quadrilateral singularities describe the vorticity in the wake which consists of trailing and startup vortices. After every time step the wake vorticity is propagated down stream by one panel length, thus simulating the increasing separation with time between the wing and its startup vortex system. The computer code accumulates all new vorticity generated during a time step in a vortex system of known strength singularities. For every time step new vorticity generated on the wing is solved for subject to satisfying the wing boundary conditions which include the time dependent onset free stream flow and the velocities induced by the already existing known strength vortices. Once a steady state flow condition is attained, all vorticity resides in the known strength vortex system and no new vorticity is generated by the wing.

In time dependent flow the forces on the wing consist of forces associated with the wing circulation (as in steady state potential flow) and of inertia forces associated with the rate of change with time of the circulation lift. The inertia force is often referred to as added mass effect. UNSTEADY3D follows the method described in Katz, *Low Speed Aerodynamics*, for determining these added mass effects.

UNSTEADY3D uses a modified version of the A372 paneling scheme to generate the wing lifting and trailing vortex layout, automatically adapting to the step size prescribed for the time dependent analysis. As low order panel codes are sensitive to irregularities in the panel geometry, much care is taken to produce a 'good' panel layout. The shape of the wake can be defined as input. However, the wake shape is not altered as part of the solution process. For most analyses use of a straight wake, which is automatically generated by the code, has been found to be sufficiently accurate.

The code optionally computes the forces described by the Polhamus leading edge suction theorem, under the tacit assumption this theorem is still applicable in time dependent flow.

All computations were performed on a 200MHz PC. The code was compiled using the Microsoft Developer Studio FORTRAN environment.

Time Accurate Boeing UNSTEADY3D Potential Flow Program

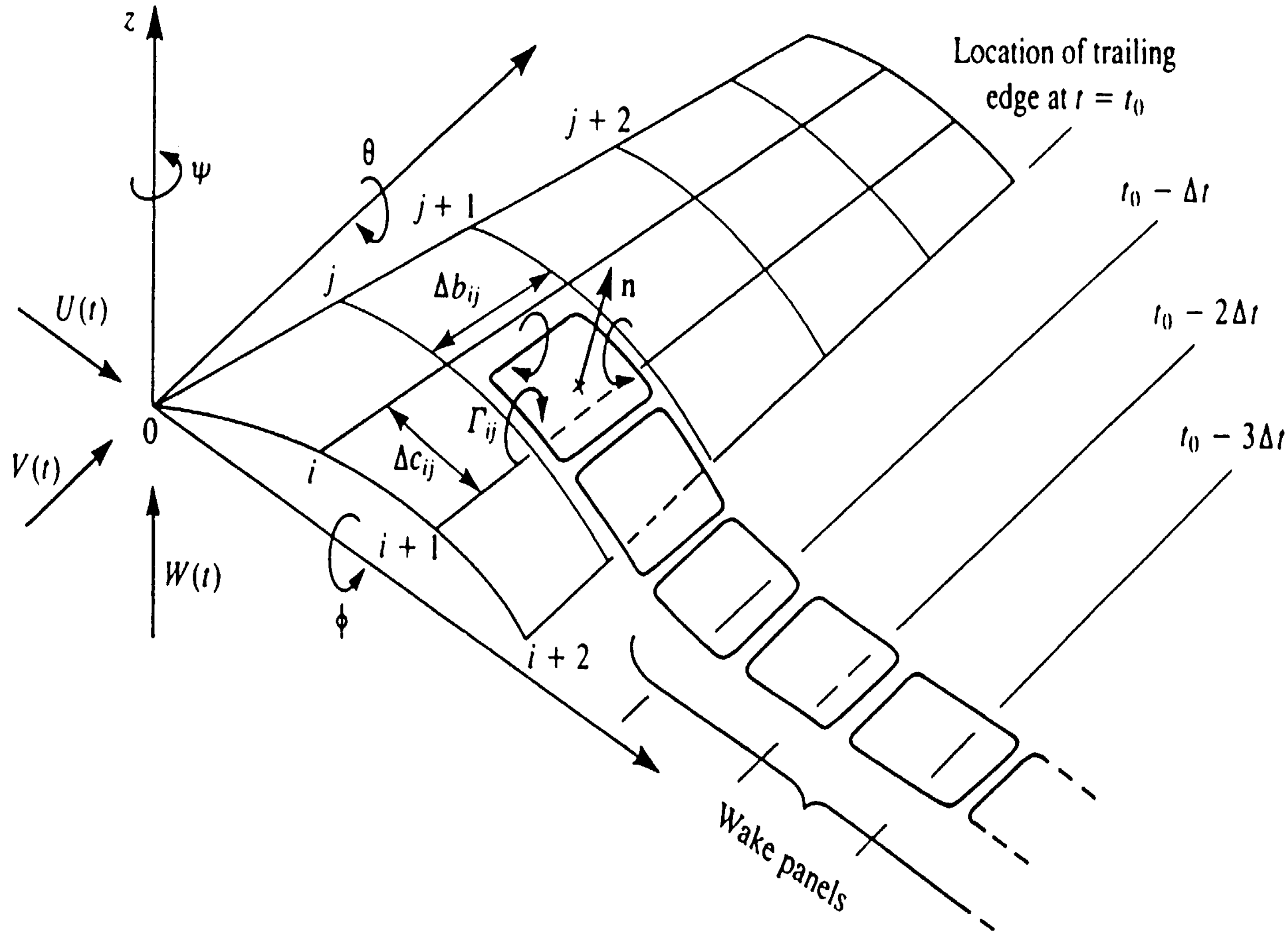

HLD403
Task 33 4.3.2.4/WMF

Polhamus Leading Edge Suction Theorem

The drag of a of a thin flat wing in frictionless flow is CL*tanα unless a forward facing force, C_T, is allowed to act on the wing leading edge. However, pressure forces can act only normal to a surface. Correspondingly, the leading edge suction force, C_S, is significantly larger than C_T if the wing is highly swept. Viscous effects limit the magnitude of the suction force that can be supported without incurring flow separation. If flow separation occurs and the leading edge is sufficiently swept a leading edge vortex develops. Experiments show that the formation of such a leading edge vortex significantly increases the lift, but also increases the drag of the wing.

Polhamus has shown that the observed increase in lift, ΔCL_{Vortex}, closely matches the magnitude of the leading edge suction force, C_S. Therefore the lift increments can be obtained by rotating the vector, C_S ,about the leading edge by 90 degrees such that it acts normal to the wing surface. Once the leading edge suction force is known, the changes in lift and drag are easily estimated based on Polhamus' theorem.

Polhamus Leading Edge Suction Theorem

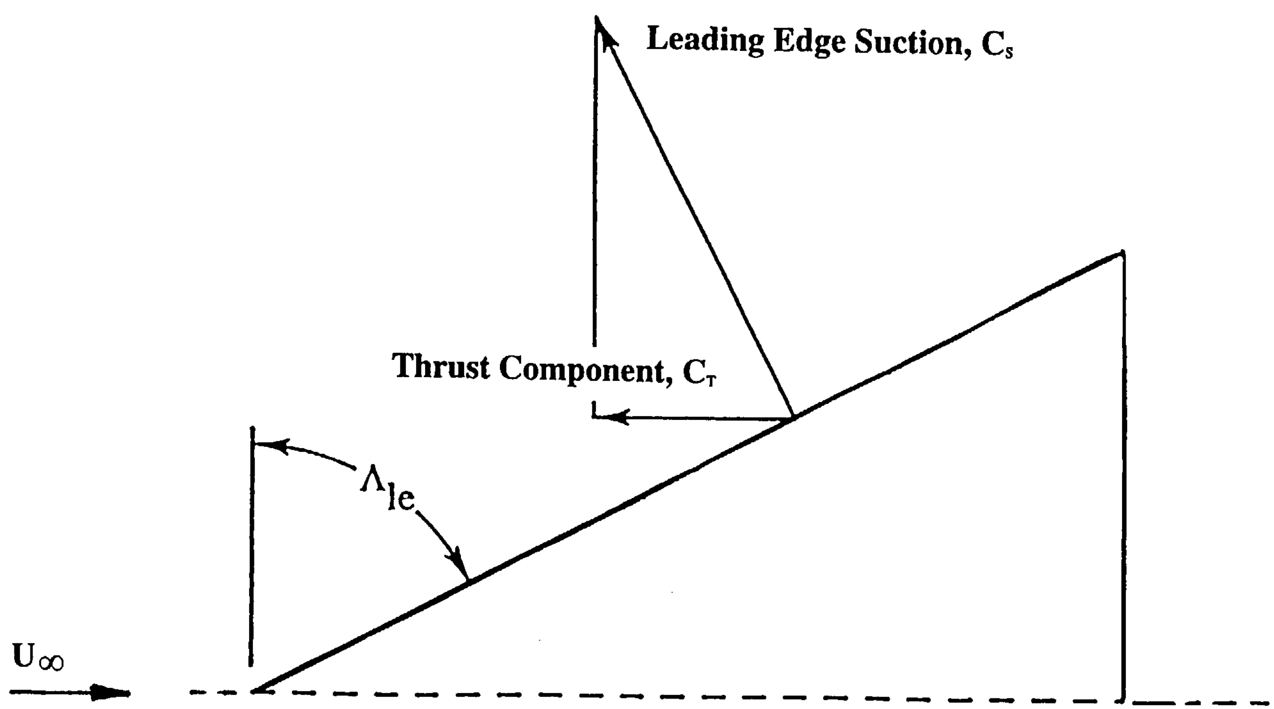

HLD403
Task 33 4.3.2.4/WMF

Validation of Time Accurate Vortex Lattice Method

Effect of Aspect Ratio on Lift of Impulsively Started Rectangular Wings

The figure shows the lift of impulsively started rectangular wings of varying aspect ratio. The solution for AR=400 compares well with Wagner's infinite span wing solution of the previous Figure. An important result of the computations is that low aspect ratio wings need to travel only a few chord lengths before the final lift level is attained. This behavior is attributed to the rapid decrease of the wake influence with time as the startup vortices are convected downstream. This will be explained later.

The first few time steps in the evaluation of the Wagner function are numerically difficult because of the initial spike of virtual mass lift and the initially very rapid growth of circulation lift. The rapid growth in circulation lift is associated with equally intense startup vortices in the wake region.

Effect of Aspect Ratio on Lift of Impulsively Started Rectangular Wings

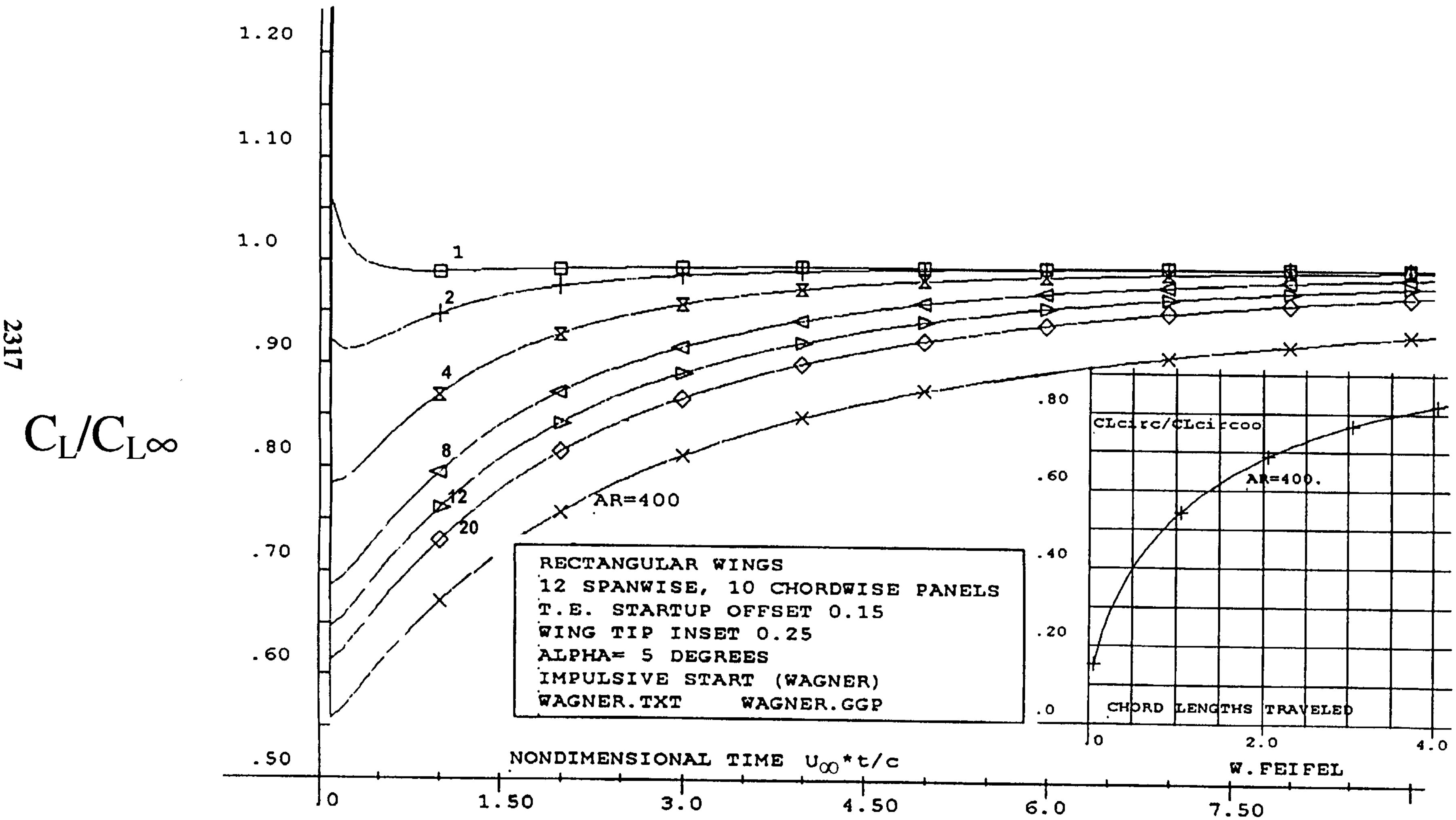

HLD403
Task 33 4.3.2.4/WMF

Downwash Induced by Startup Vortices

Low aspect ratio wings have been shown in the above analyses to adjust more rapidly to changes in the flow conditions. Examining Biot-Savart's vortex induction laws easily explains this behavior:

The downwash velocities induced at the point, P, by a startup vortex of the strength, Γ, is inversely proportional to the distance, a, and directly proportional to the term $(\cos\phi_1 - \cos\phi_2)$. For a 2-d airfoil this second term assumes the value 2, for a high aspect ratio wing the value of term is nearly 2 as long as the distance, a, is not very large. In the case of low aspect ratio wings, however, the angles ϕ_1 and ϕ_2 quickly approach nearly identical values when the startup vortices are convected down stream. Consequently the downwash induced at a low aspect ratio wing itself by its own startup vortex system diminishes very rapidly with time. This allows a more rapid buildup of circulation lift.

Downwash Induced by Startup Vortices

$$w = \frac{\Gamma}{4\pi a}(\cos\phi_1 - \cos\phi_2)$$

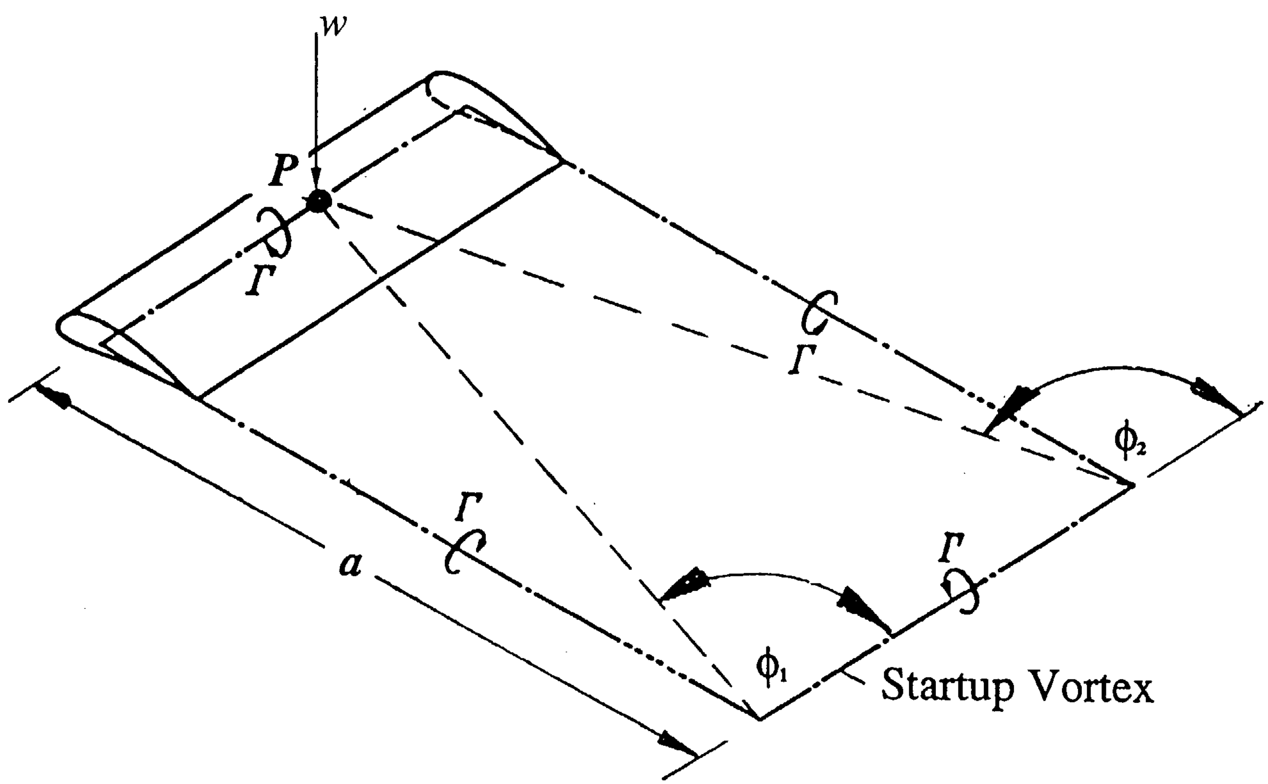

Effect of Aspect Ratio on Lift of Impulsively Started Rectangular Wings in Ground Effect

The figure shows the lift of wings of different aspect ratios in ground effect. The wing trailing edges are located 0.125 chord lengths above the reflection plane. In terms of chord lengths traveled, the final lift level is seen to be attained much faster in ground effect than in free air. A physical explanation for this behavior is the reduced influence of the vortices downstream of the trailing edge, as will be shown later.

Effect of Aspect Ratio on Lift of Impulsively Started Rectangular Wings in Ground Effect

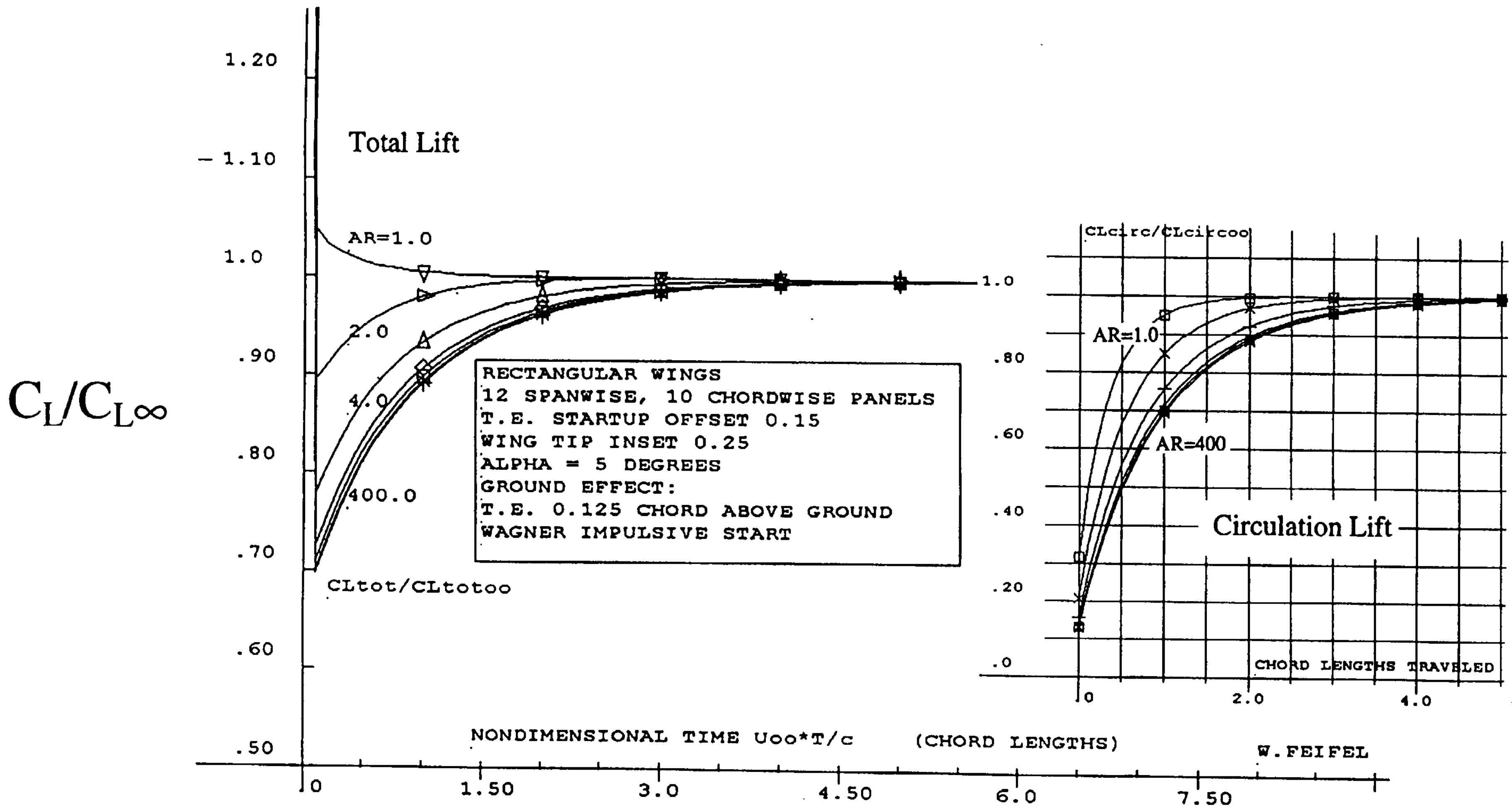

HLD403
Task 33 4.3.2.4/WMF

Vortex System of a Wing in Ground Effect

The figure depicts a simplified vortex system of a wing operating at the altitude, h, in ground effect. Computationally, the presence of the ground plane is simulated by introduction of an image of the wing. The image is located below the ground plane and the sense of its vortex circulation, Γ, is reversed.

The figure offers an easy physical explanation for the more rapid rate of change of lift when the wing operates near the ground: the downwash induced on the wing by of the vortices downstream of the trailing edge is lower than in free air. For example, the far field influence of the startup vortex is (nearly) canceled by the image of the startup vortex. This image vortex is located below the ground plane and rotates in the opposite direction. The two counter rotating vortices combined can be viewed as a weak doublet. The influence of a doublet diminishes proportional to $1/r^2$ while the influence of single vortex decreases with $1/r$, where r denotes the distance from the wing. The reduced downwash allows a much more rapid growth of the circulation lift. In addition, the virtual mass forces are initially higher because their magnitude is proportional to the rate of change of the circulation lift.

Vortex System of a Wing in Ground Effect

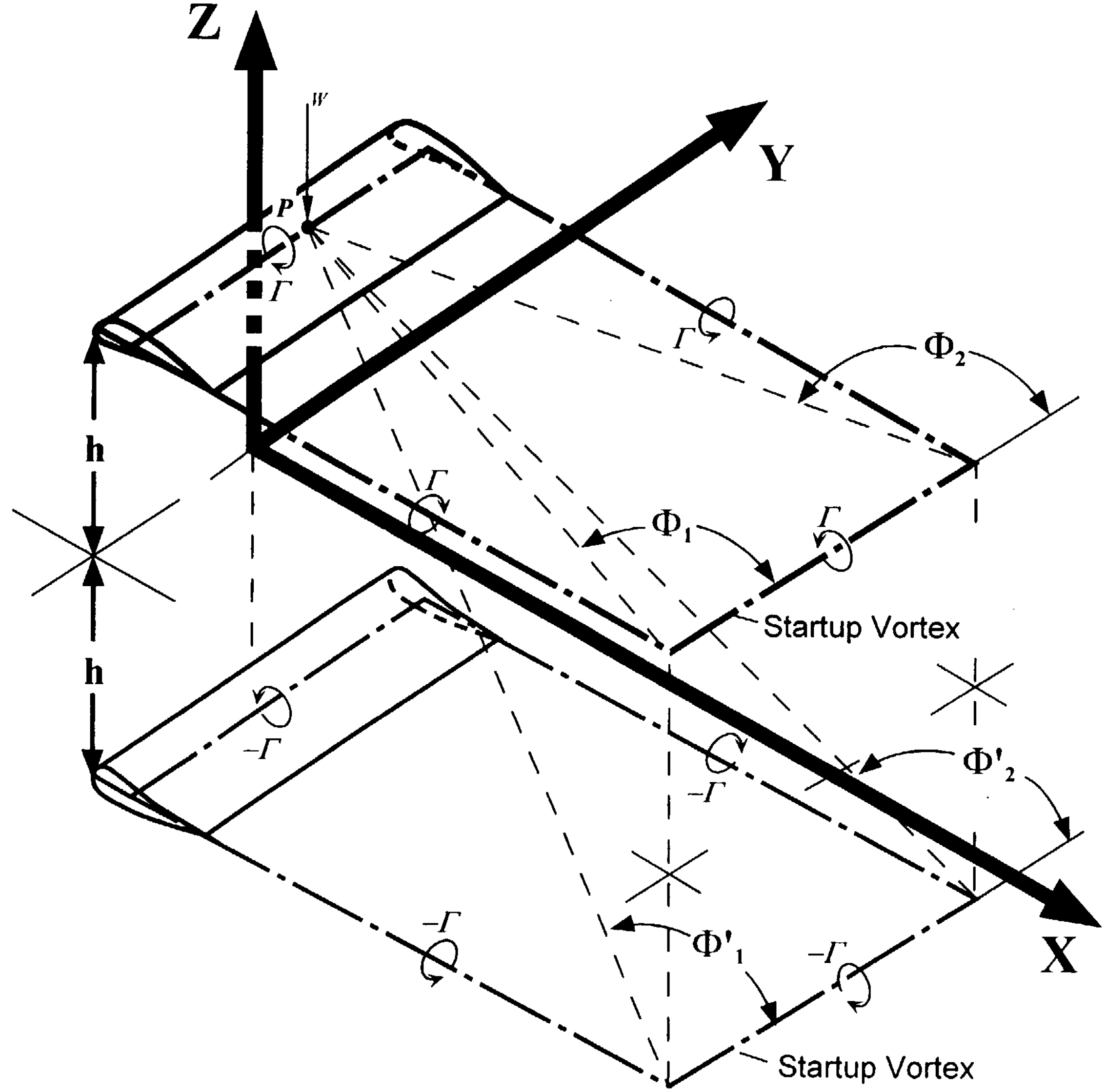

HLD403
Task 33 4.3.2.4/WMF

2-d Airfoil in Sinusoidal Plunging Motion / Effect of Number of Panels

The figure shows solutions obtained for a AR = 400 rectangular wing performing a ± 0.1 chord lengths amplitude sinusoidal plunging motion of the reduced frequency $k = \omega c/2U_{oo} = 0.5$. The maximum angle of attack excursions due to the plunging motion are $\Delta\alpha$ = +/-5.7 degrees. Superimposed to the plunging motion is a steady state angle of attack of $\alpha = 5$ degrees. Plunging is started at t=0. It initially causes a large Wagner-type response in lift. After about one wave length a steady state response is attained. Both total lift and circulation lift are seen to be virtually independent of the number of chordwise panels used in the analysis. Note the phase shift between total lift and circulation lift.

Steady state, an angle of attack excursion of $\Delta\alpha = 5.7$ degrees would correspond to a peak lift increment $\Delta C_l = \pm\, 0.62$. In the oscillating mode there is insufficient time to develop steady state flow, and thus the peak lift excursions are significantly smaller. The peak lift values become smaller as the frequency of the oscillation is increased. For the reduced frequency of k=0.5, UNSTEADY3D predicts a lift amplitude of $\Delta C_l = \pm 0.38$. The linearized theory due to Theodorsen predicts $\Delta C_l = \pm 0.40$ for a 2-d airfoil under same conditions. The agreement between the two methods appears to be adequate.

2-d Airfoil in Sinusoidal Plunging Motion / Effect of Number of Panels

Amplitude Predicted by:

- Theodorsen Linearized Theory $\Delta CL = \pm 0.40$
- Present Method $\Delta CL = \pm 0.38$

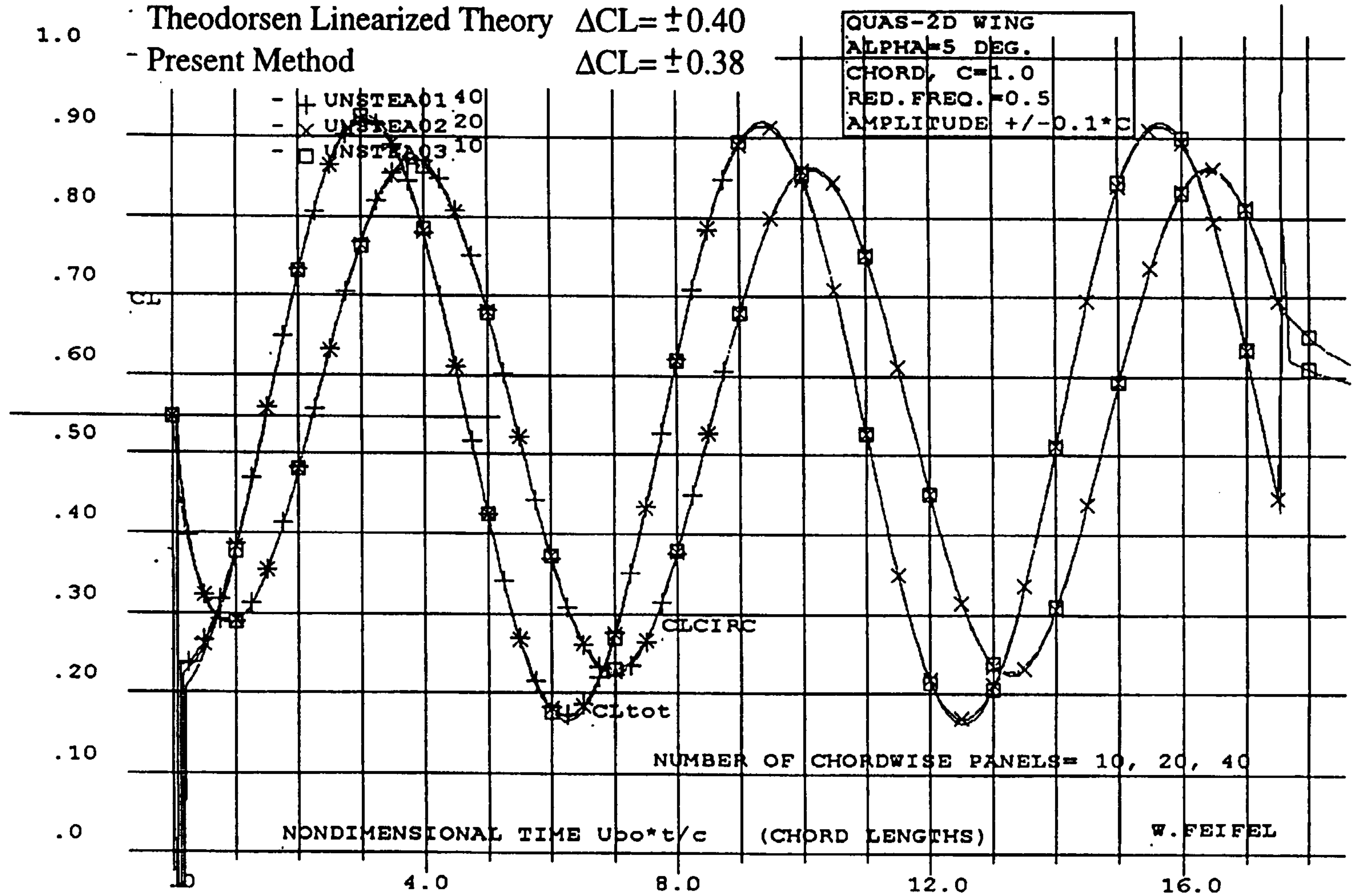

HLD403
Task 33 4.3.2.4/WMF

Rectangular Low Aspect Ratio Wing , AR=4, Performing Sinusoidal Plunging Motion 0.25 Chord Lengths Above The Ground

This somewhat crowded graph shows the UNSTEADY3D results for a low aspect ratio wing performing plunging oscillations close to the ground. In the present analysis the distance between the wing and the ground was varied with time to fully simulate the plunge effect. This results in lift excursions which are not fully symmetrical, as the ground effect is larger than the mean value during the lower portion of the plunging cycle and smaller during the balance of the plunging motion. The contribution of the virtual mass effect to the lift forces is seen to be quite significant.

Also listed in the figure is the lift variation obtained by Katz for the same condition. The excellent agreement between the two methods may be somewhat fortuitous as there are differences in the number of panels used. Also, there is a minor uncertainty how ground height was defined.

Rectangular Low Aspect Ratio Wing , AR=4, Performing Sinusoidal Plunging Motion 0.25 Chord Lengths Above The Ground

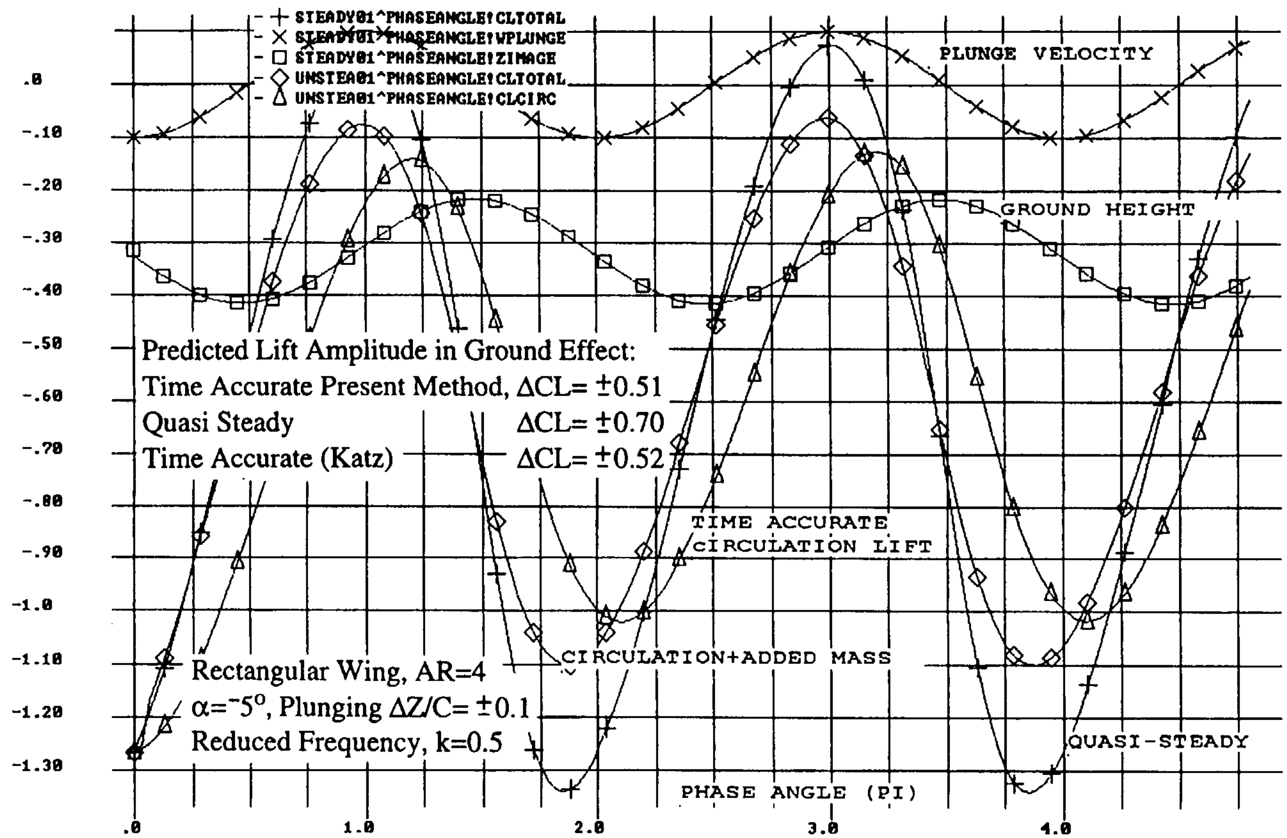

HLD403
Task 33 4.3.2.4/WMF

Lift of AR=4 Rectangular Wing Heaving in Ground Effect

As part of a study of race car front wings in ground effect, Katz has analyzed a low aspect ratio wing performing heaving motions close to the ground. Compared to his results for free air, the lift excursions are markedly increased. UNSTEADY3D predictions are in good agreement with his results.

Lift of AR=4 Rectangular Wing Heaving in Ground Effect

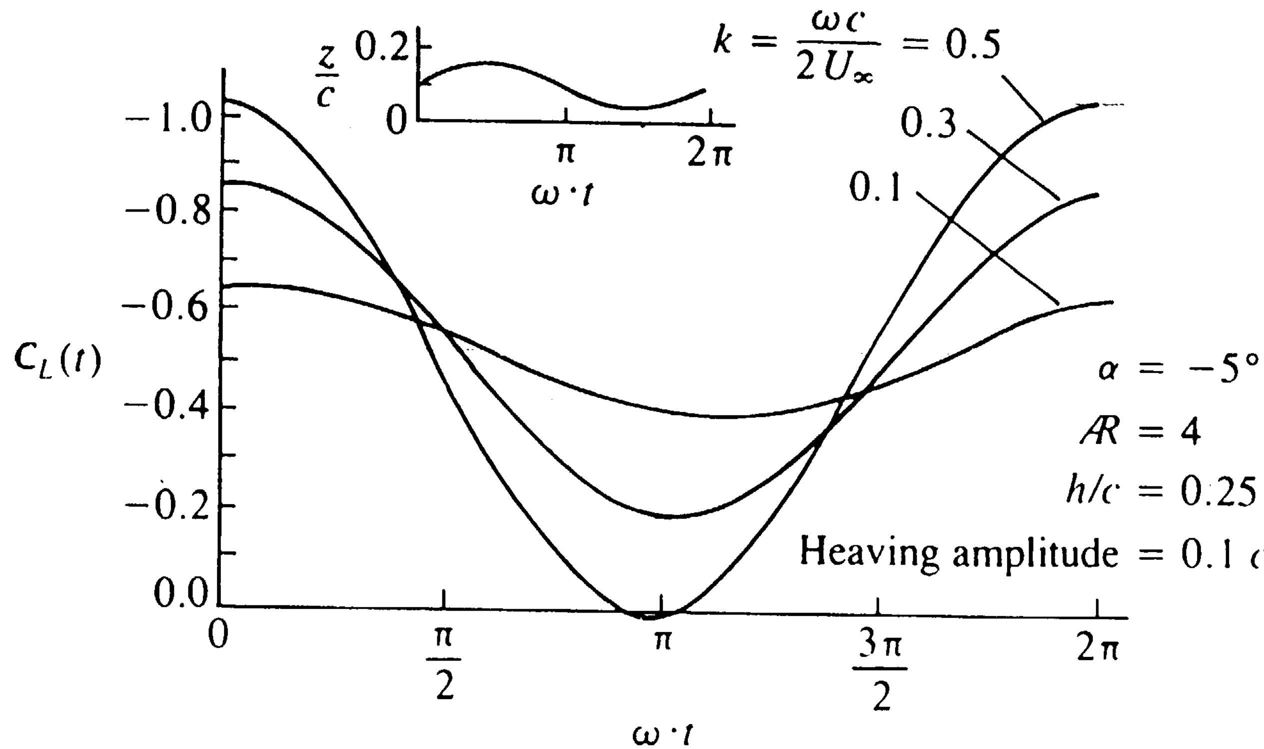

From: Katz, *Low-Speed Aerodynamics*

II. Findings

The figure summarizes the key findings of section II.

II. Findings

- Time dependent total lift consists of
  - Lift due to circulation
  - Lift due to added mass effects
- Added mass lift is proportional to the rate of change of circulation with time
- The number of chord lengths of travel required to attain steady state lift level decreases with wing aspect ratio
- The number of chord lengths of travel required to attain steady state lift decreases in ground proximity

III. Cropped Delta Wing

A number of investigations were made using a cropped delta wing because of its simple geometry. The wing was used to evaluate the lift characteristics in static and dynamic ground effect.

Also, the wing time accurate pitch stability derivatives were determined. These stability derivatives were used to investigate the effects of the wing pitch inertia on the time dependent lift response to an elevator deflection. This time response may be significant because elevon deflections commanded to compensate for changes in pitching moment due to ground effect may cause temporary changes in wing lift which could be interpreted as lift changes due to dynamic ground effect.

III. Cropped Delta Wing

- Ground Effect Calculations
  - Wing Geometry and Wake Layout
  - Descent Towards a Reflection Plane
- Unsteady Pitching Motion
  - Time Accurate Pitch Stability Derivatives
  - Time Accurate Pitch Motion
- Findings

Cropped Delta Wing Ground Effect Calculations

Cropped Delta Wing Geometry

Time accurate potential flow analysis in UNSTEADY3D becomes very computing intensive if complex configurations are to be analyzed which require a large number of panels for adequate geometry definition. The computing time also increases dramatically if a large number of time steps is to be performed, as with every time step the number of known strength singularities in the wake is increased. Therefore most of the analyses were run using a simple wing planform and steep descent angles, which minimize the number of time steps required to approach the ground. The wing pitch angle is 15 degrees, measured relative to the ground. The trailing vortex system, located parallel to the ground, was internally generated by UNSTEADY3D. Different wake locations require manual data input and have been found to slightly affect the lift levels, but have virtually no effect on lift increments. Most analyses were run using the automatic wake mode.

The figure illustrates the panel layout on the wing and of a small part of the wake. Also shown is the assumed location of the flap hinge line. Panels whose boundary points are located downstream of the hinge line will be treated as flap panels in some of the analyses to be shown later.

The point labeled X_N is the steady state wing neutral point ($dC_M/dC_L=0$) which has been obtained from potential flow analysis. A second point marked X_P defines the location of the axis pitching about which creates zero pitch lift ($dC_L/dq=0$), where q denotes the wing pitch rate. The location of X_P has also been obtained from potential flow analyses which will be discussed later.

Cropped Delta Wing Geometry

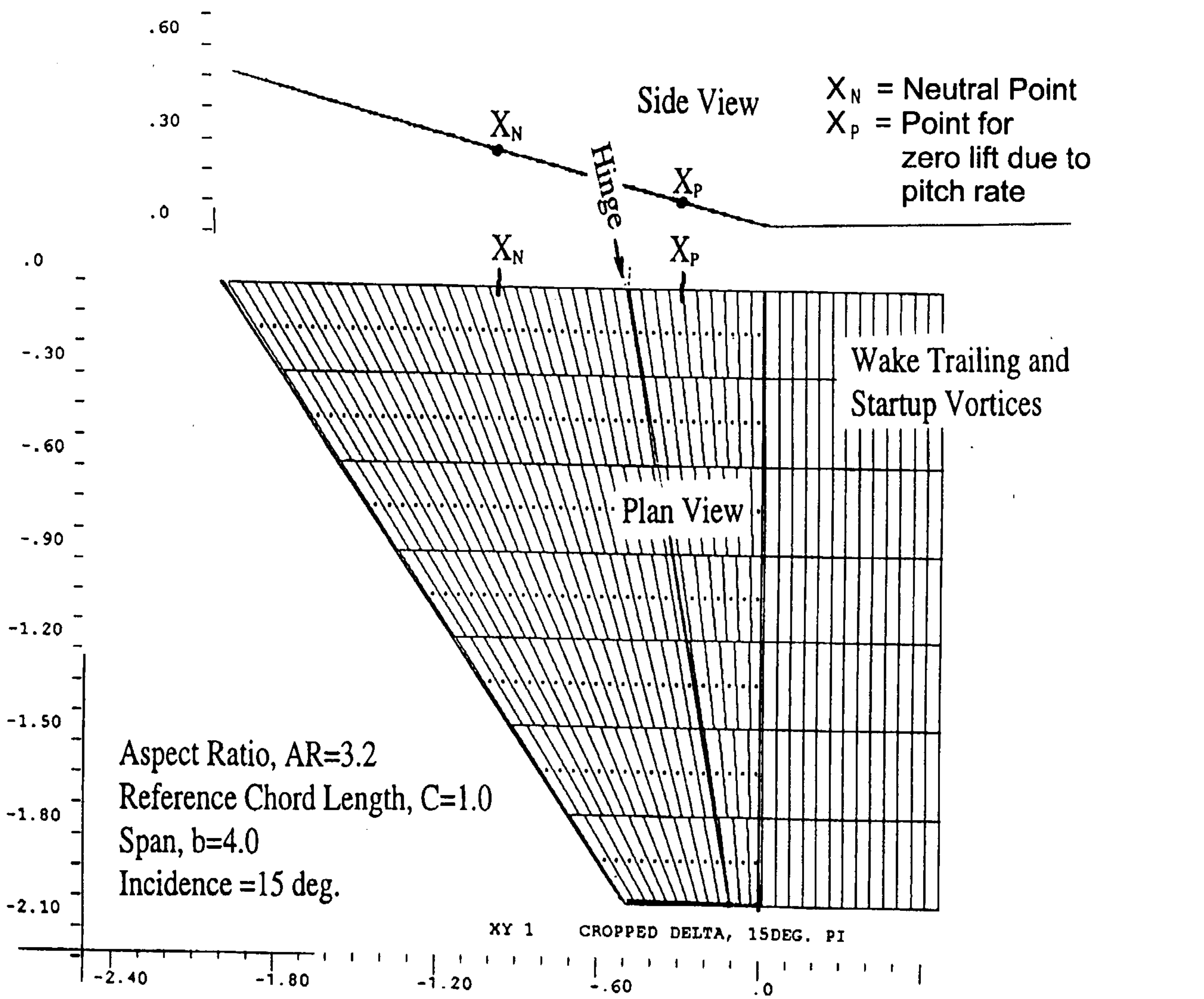

Aspect Ratio, AR=3.2
Reference Chord Length, C=1.0
Span, b=4.0
Incidence =15 deg.

Descent Profile for Cropped Delta Wing

The figure shows the descent profile used for all analyses. The wing trailing edge is located at z=0.0. The approach to the ground was simulated by moving the ground plane towards the airplane after every time step. At the start of the analysis the image plane was located z=3.0 chord lengths below the wing trailing edge, which corresponds to a height of 0.75 wing spans above the ground. The descent was stopped once the ground plane was located 0.13 wing spans below the wing. During the approach to the ground plane the airplane traveled a horizontal distance of 25 chord lengths. Note that the distance traveled is equivalent to nondimensional time.

During the entire flight the airplane attitude and angle of attack was maintained constant at 15 degrees. No aerodynamic angle of attack change due to plunging was introduced, thus the 15 degrees incidence included the angle of attack due to the plunging motion. Mathematically, this corresponds to panel boundary conditions of $\mathbf{u}_{\infty}*\mathbf{n}$ = constant, where $\mathbf{u}_{\infty}$ designates the free stream velocity vector , and $\mathbf{n}$ the panel surface normal vector. At the end of the trajectory when the plunging motion is stopped the aerodynamic angle of attack remains at α=15 degrees. In reality this would require a flare maneuver which would slightly change the airplane attitude relative to the ground in order to compensate for the vanishing sink rate, dh/dt. Within the assumptions of linearized theory these small attitude changes are small, because they only affect the location of the image singularities relative to the aircraft.

Descent Profile for Cropped Delta Wing

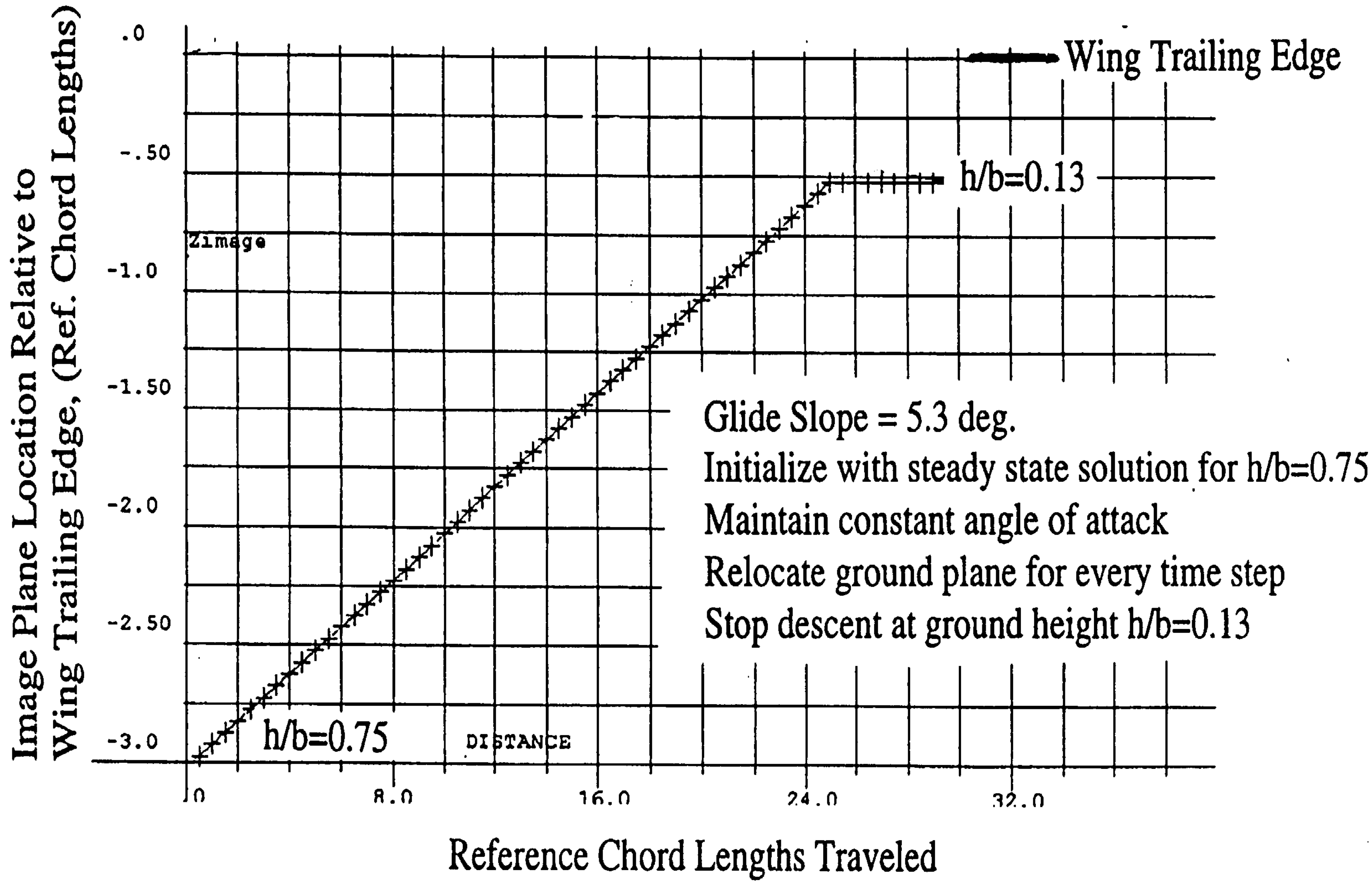

Cropped Delta Wing Lift During Constant Angle-of-Attack Descent Towards a Reflection Plane

The figure shows the predicted development of time dependent lift together with steady state solutions obtained for a number of different ground heights (diamonds). The differences between the steady state lift and the time dependent solution are surprisingly small. But it must be noted that the unsteady circulation dependent lift is definitely less than the steady state lift. The lift resulting from virtual mass effects virtually fully compensates for the loss in circulation lift. This finding is in agreement with the results obtained for the low aspect ratio rectangular wings which have been discussed in the previous figures.

Cropped Delta Wing Lift During Constant Angle-of-Attack Descent Towards a Reflection Plane

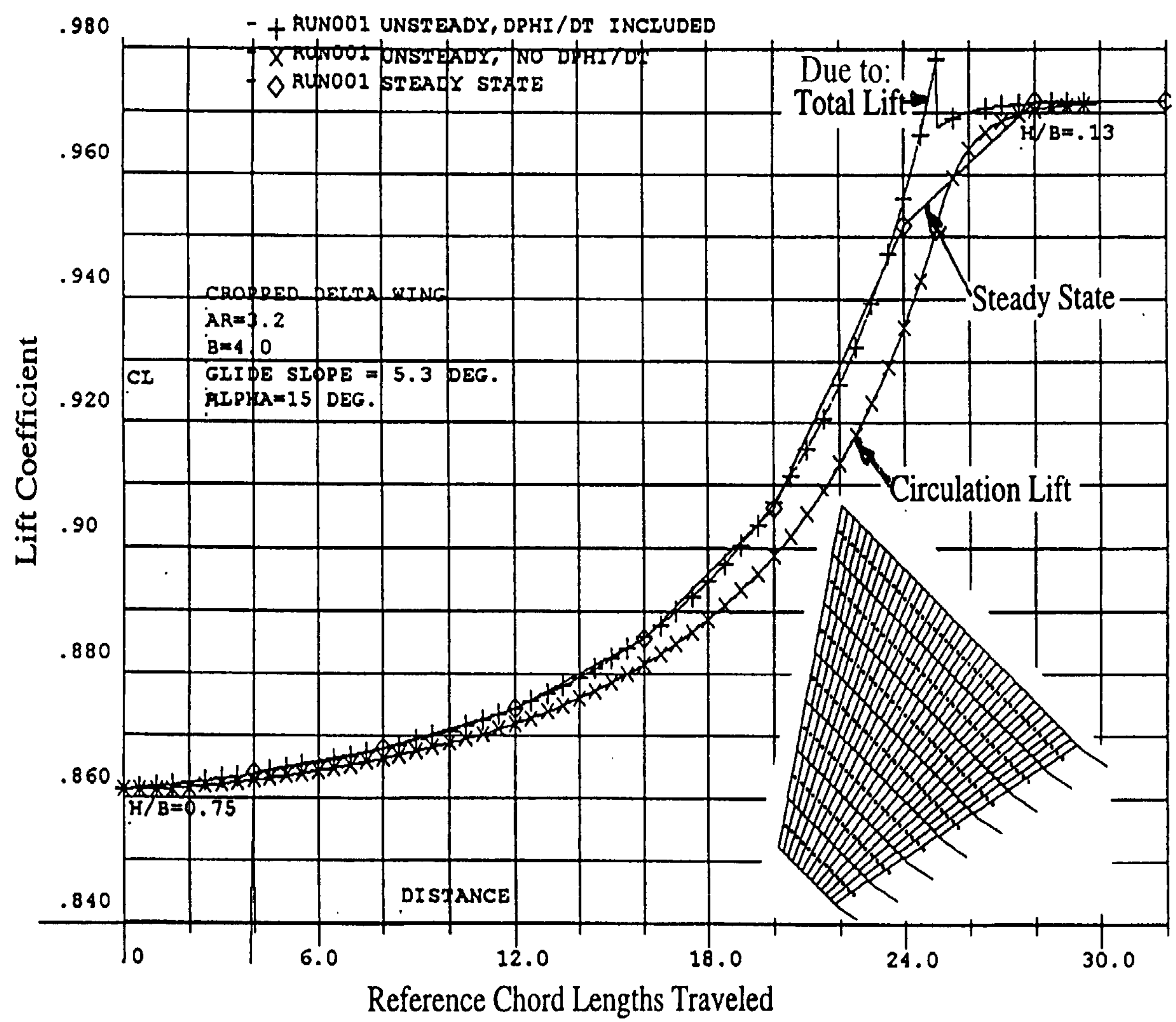

HLD403
Task 33 4.3.2.4/WMF

Cropped Delta Wing Induced Drag During Constant Angle-of-Attack Descent Towards a Reflection Plane

As the airplane approaches the ground, drag increases significantly over the steady state values for the same ground height, as shown in the figure. This drag increase is mainly due to virtual mass effects. Compared to the steady state solution the unsteady circulation induced drag is actually lower, mainly because the circulation lift itself is also lower. However, a few simple calculations indicate that, for example, at $h/b=0.13$, the unsteady circulation induced drag is higher than what would be expected from simply adjusting the steady state induced drag by the square of the ratio between time dependent and steady state circulation lift. This higher than expected circulation related induced drag in the unsteady mode must be attributed to the additional downwash induced by the time dependent startup and trailing vortices.

For an uncambered wing higher induced drag is equivalent to a reduction in leading edge suction force. This may be significant because the Polhamus leading edge suction theorem postulates that changes to the potential flow leading edge suction force will affect the leading edge vortex lift generated by wings with highly swept sharp leading edges. However, application of the Polhamus theorem has not been proven.

Cropped Delta Wing Induced Drag During Constant Angle-of-Attack Descent Towards a Reflection Plane

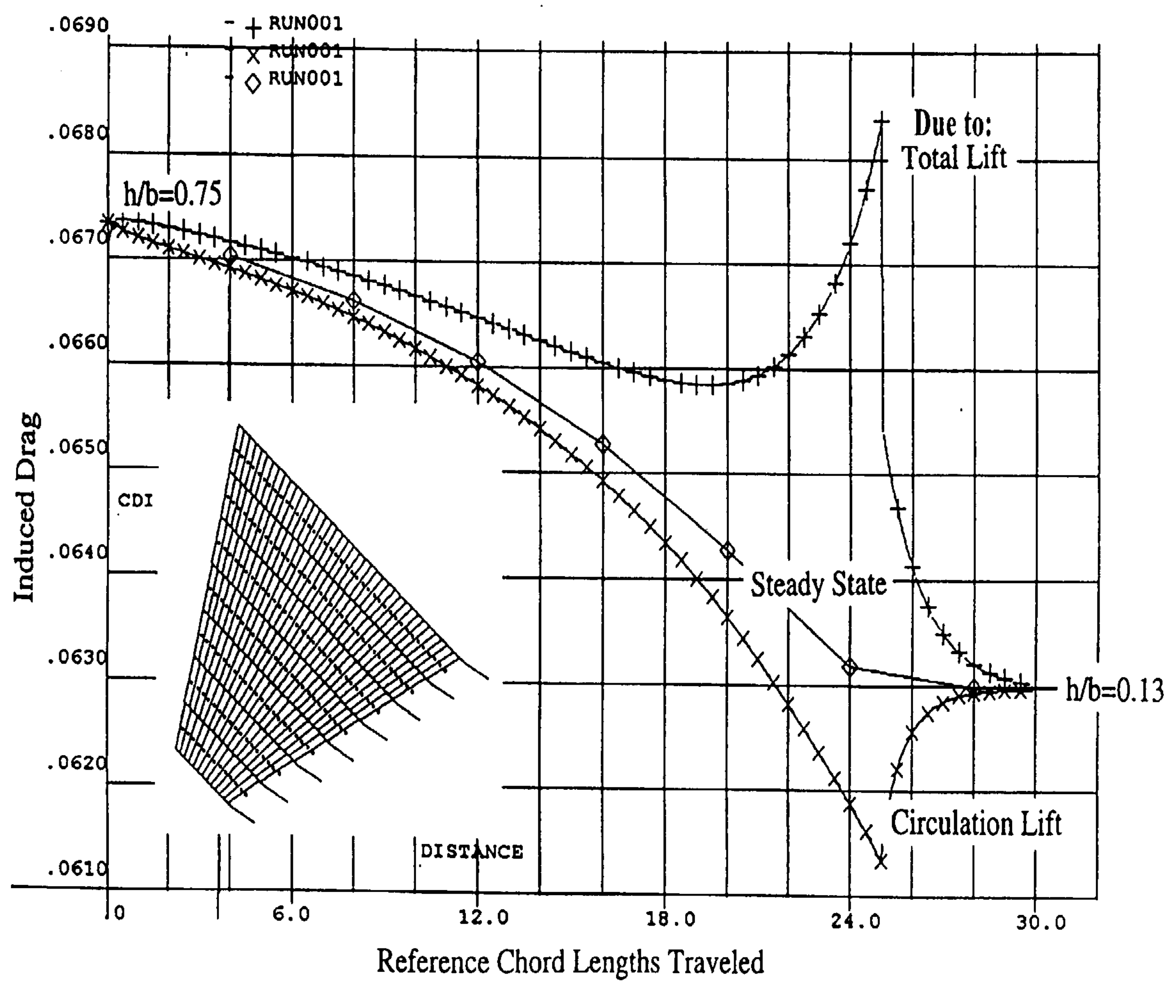

HLD403
Task 33 4.3.2.4/WMF

Unsteady Pitching Motion

Time Accurate Pitch Stability Derivatives

Landing maneuvers typically involve changes in pitch attitude for the landing flare, or at the very least, control surface deflections to compensate for the increased nose down aerodynamic pitching moment created by both static and dynamic ground effect phenomena. It was surmised, that lift transients associated with pitch control inputs could be interpreted as a 'dynamic ground effect'. Therefore it was decided to explore in more detail the aircraft response to pitch commands.

The investigations in this chapter describe an attempt to break the complex time dependent motions of a wing into a number of canonical functions which describe the time dependent aerodynamic responses to changes such as angle of attack, pitch rate, etc. If such a set of functions can be defined they could be used to synthesize a time accurate model flight profile, within the limits of linear superposition theory. The approach of linear superposition is commonly used to describe the steady state and quasi-steady stability and control characteristics of airplanes. Thus the analysis of an airplane could be performed very quickly, once the function shapes have been defined by running the lengthy time accurate potential flow code. One time accurate potential flow run in UNSTEADY3D would be necessary to define each individual function shape.

The following time accurate transfer functions were determined:

$dCL/d\alpha$	time dependent lift curve slope
dCM/dCL	time dependent neutral point position
$dCL/d\delta_F$	time dependent lift response to a flap deflection about flap hinge line
$dCM/d\delta_F$	time dependent pitching moment response to a flap deflection about flap hinge line
dCL/dq	time dependent lift response to pitch rate
dCM/dq	time dependent pitch damping

For the case of the cropped delta wing, all lift related functions proved to have shapes similar to a generalized Wagner function. The moment functions were nearly independent of time and were treated as constant for the quick preliminary analyses that will be described later.

Unsteady Pitching Motion of Cropped Delta Wing

Time Accurate Pitch Stability Derivatives

- **Explore time accurate lift response to pitch control inputs**
- **Account for airplane pitch inertia**
- **Quick integration scheme using time accurate transfer functions in free air:**

$dCL/d\alpha$	time dependent lift curve slope
dCM/dCL	time dependent neutral point position
$dCL/d\delta_F$	time dependent lift response to a flap deflection
$dCM/d\delta_F$	time dependent pitching moment response to a flap deflection
dCL/dq	time dependent lift response to pitch rate
dCM/dq	time dependent pitch damping

Time Dependent Lift and Pitching Moment of Cropped Delta Wing Impulsively Started in Free Air at 10 Degrees Angle-of-Attack

The figure shows the response of the cropped delta wing to an impulsive start at 10 degrees angle of attack. The circulation lift initially generates a large nose-up pitching moment, probably due to the initially strong downwash induced at the wing aft region by the startup vortices. This nose up moment is greatly reduced by the moment due to the virtual mass effects, which act farther aft on the wing. The location of the moment reference point, X_N, has been selected such that it forms the neutral point in free air once steady state conditions are attained. During the first 0.5 chord lengths of travel, the nose down pitching moment is appreciable. However, for the sake of simplicity this variation of CM has been neglected in the wing motion analyses that will be described later.

The variation of lift with time is somewhat similar to the shape of the Wagner function, except that the initial lift level is significantly higher than what would be predicted by the 2-d unsteady airfoil theory. After traveling one chord length the wing has already developed 87% of the final lift value. This finding is consistent with the results shown in previous figures for low aspect ratio rectangular wings.

Both the moment and the lift functions scale linearly with the angle of attack, which in turn defines the wing asymptotic lift level. Thus the shape of the functions is generic to this particular wing and therefore needs to be determined only once.

Time Dependent Lift and Pitching Moment of Cropped Delta Wing Impulsively Started in Free Air at 10 Degrees Angle-of-Attack

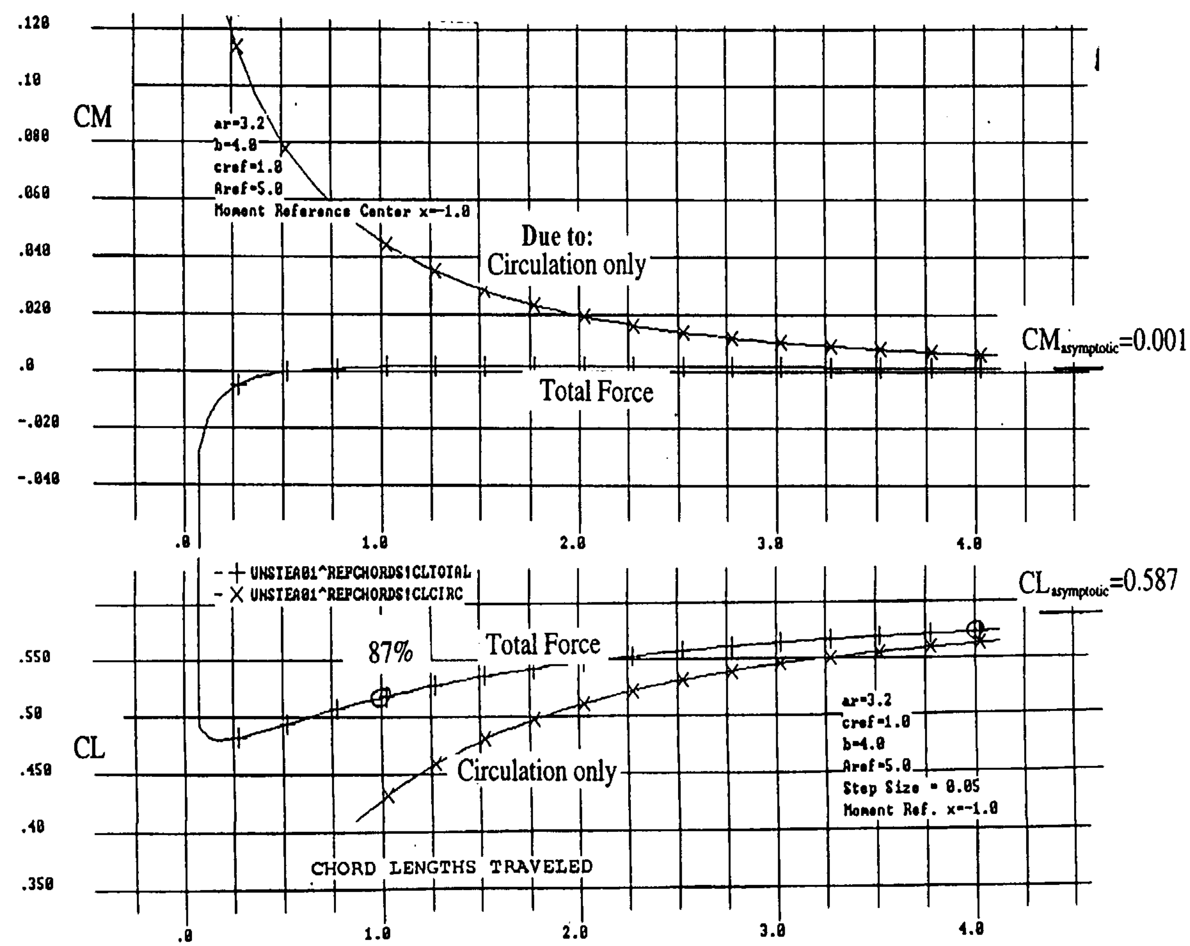

HLD403
Task 33 4.3.2.4/WMF

Steady State Chordwise Pressure Distribution of Cropped Delta Wing in Free Air at Zero Degrees Angle-of-Attack and 10 Degrees Flap Deflection

The figure illustrates how UNSTEADY3D assigns panels to a trailing flap region. First a uniform panel layout is generated for the entire wing planform; panels with boundary points located downstream of the hinge line are selected as flap panels. The dark shaded panels in the figure are flap panels. The chordwise pressure distribution is similar to that of a flat plate with a flap. Even at the wing tip, where the flap consists of only 3 panels, the shape of the pressure distribution appears to be 'reasonable'.

Steady State Chordwise Pressure Distribution of Cropped Delta Wing in Free Air at Zero Degrees Angle-of-Attack and 10 Degrees Flap Deflection

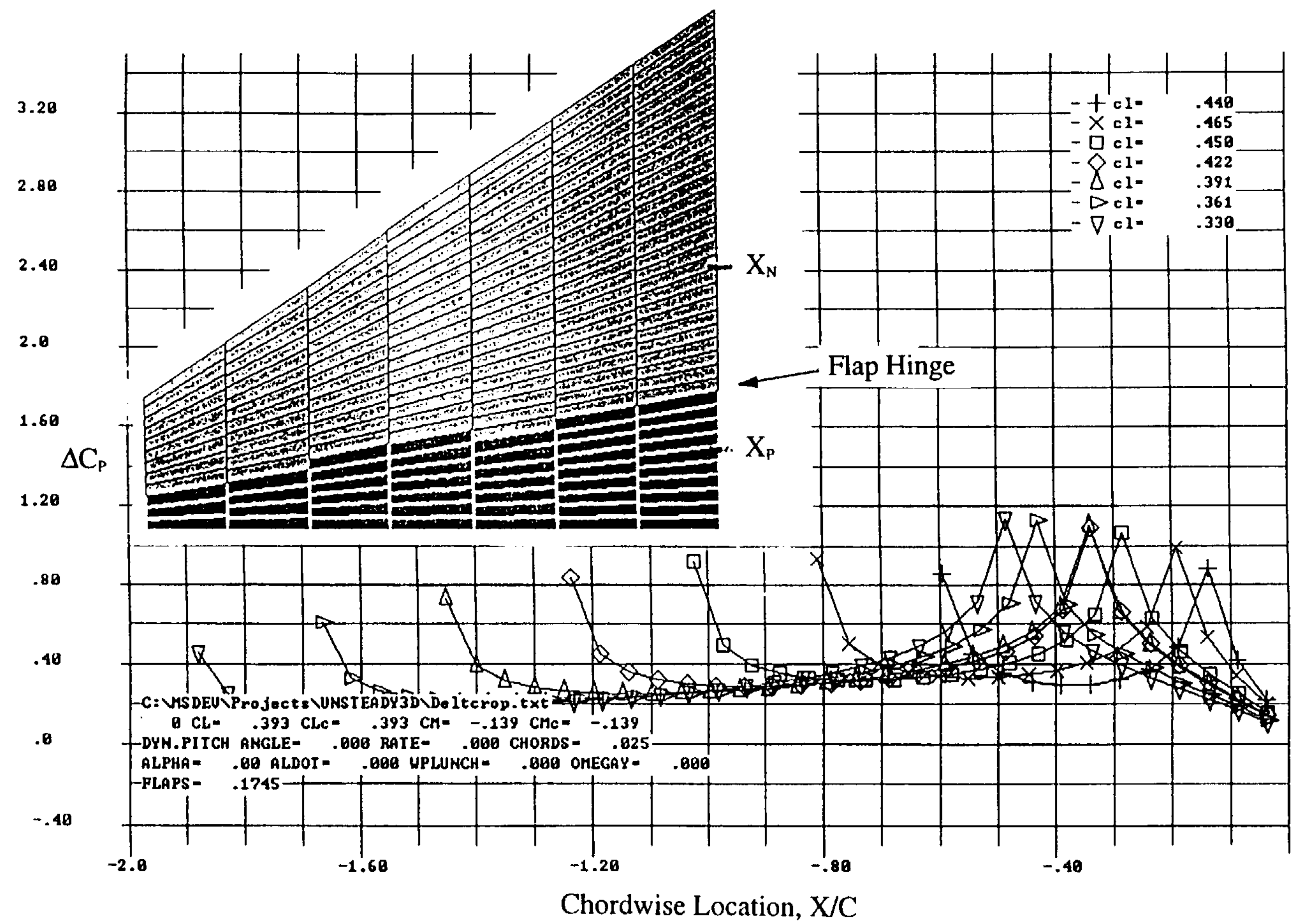

HLD403
Task 33 4.3.2.4/WMF

Effect of Pitch Rate on Dynamic Lift and Pitching Moment of Cropped Delta Wing in Free Air at Zero Degrees Angle-of-Attack

The UNSTEADY3D time accurate vortex lattice code has been extended to include computation of rate derivatives, such as pitch or yaw rates. These extensions have been incorporated because of a suspicion that a significant part of the 'dynamic ground effect' identified in flight test data may not be caused by the proximity of the ground, but rather results from the pitching maneuver the airplane has to perform close to the ground. A change in pitch attitude is associated with pitch rates which create time dependent 'pitch lift' and 'pitch damping'. Pitch lift depends on the location of the center of rotation and thus can be made zero. The pitch damping moment is the smallest when there is no pitch lift, but it can never be zero. The transient loads caused by changes in airplane attitude are time dependent responses, the shapes of which are very similar to Wagner functions.

Only on a computer is it possible to easily separate the effects of angle of attack, lift =f(α , time), and the rate of change of angle of attack, lift = f($d\alpha/dt$, time). The figure present the results of such a calculation.

The cropped delta wing is assumed to begin to pitch at the pitch rate ω=0.1 rad/sec about an axis located at the wing neutral point, X_N=-1.0. In the computer simulation this pitching motion is performed while maintaining a constant angle of attack, $\alpha = 0$ degrees! The pitching motion is impulsively started at time t=0. The figure shows the development of the pitch rate induced lift and moment as a function of nondimensional time (number of chord lengths traveled). The asymptotic lift coefficient due to the pitch rate is $\Delta CL_\omega = +0.236$. The associated pitching moment is CM=-0.077. The moment counteracts the pitching motion; it is therefore referred to as pitch damping moment. The shapes of both functions are identical to those found before for sudden changes in angle of attack or flap deflection.

For center of rotation located at X_P=-0.3, the pitch lift is found to be exactly zero. The pitching moment, however is still CM=-0.077. There is virtually no lift carried by the wing and thus there are no startup or trailing vortices. Consequently the pitch damping moment is independent of time. With this finding in mind, the lift and moment created by pitch rotation about an arbitrary axis can always be split into 2 components: A pure equivalent angle of attack change and a rotation about the point X_N. Depending on the location of the overall moment reference point, the pitch lift itself can create an additional pitch damping moment. Note that the equivalent angle of attack change is directly proportional to ω.

Effect of Pitch Rate on Dynamic Lift and Pitching Moment of Cropped Delta Wing in Free Air at Zero Degrees Angle-of-Attack

Impulsive Start. Omegay=0.1, Alpha = 0 = constant.

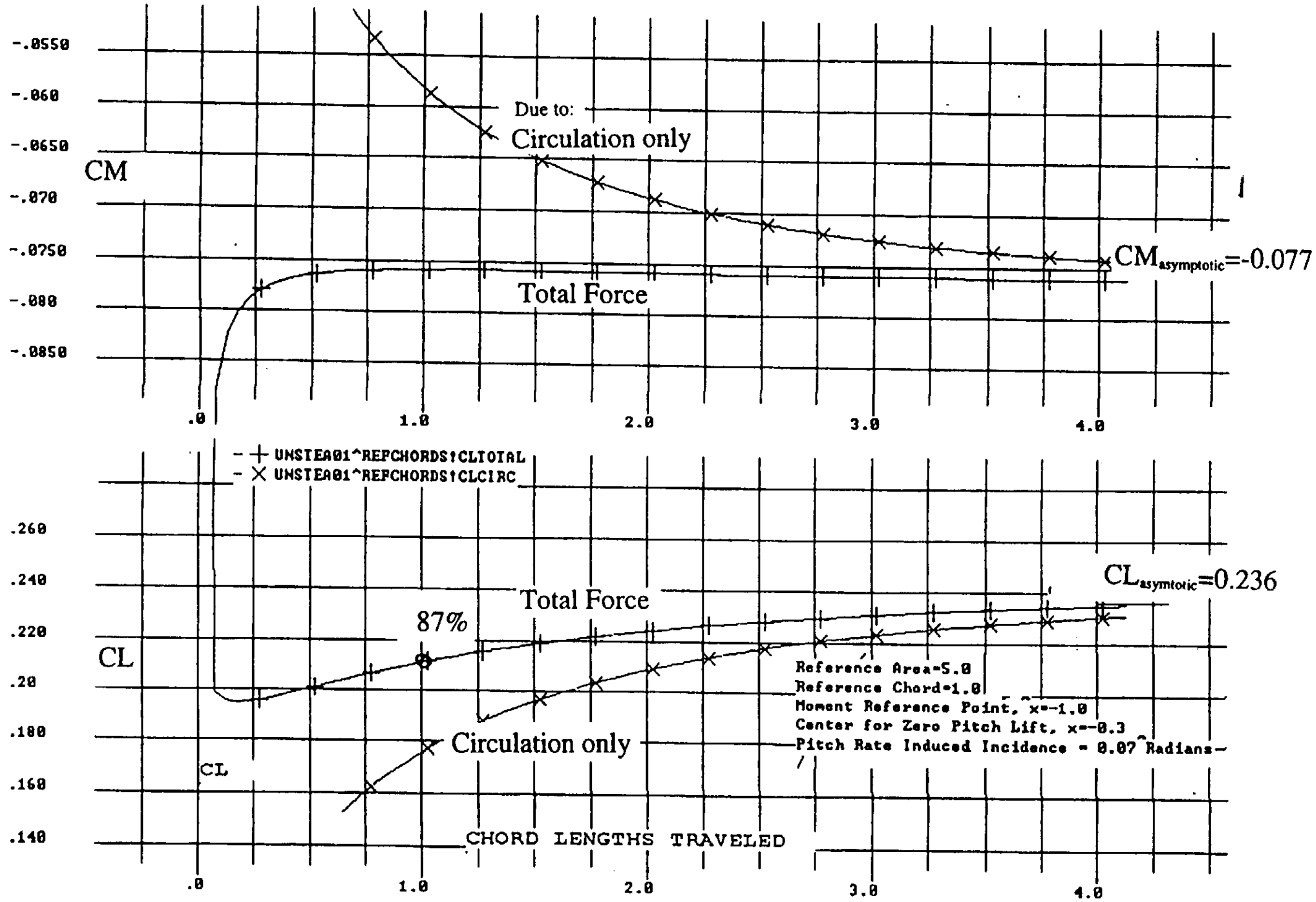

Effect of Pitch Rate on the Pressure Distribution About a Cropped Delta Wing in Free Air at Zero Degrees Angle-of-Attack

The figure shows the steady state pressure distribution about a cropped delta wing for the pitch rate, ω=0.1. Results are shown for two locations of the pitch axis.

The lower part of the figure shows the pressures when the pitch axis located at X_P=-0.3. This corresponds to the condition at which the pitch lift is zero and only a moment is generated. By visual inspection it can be verified that the lift of each chordwise strip is approximately zero. Yet the zero lift chordwise pressure distributions create a nose-down moment, the pitch damping moment. The shape of the chordwise pressure distributions is similar to that of a flat plate operating in a curved flow field, or, conversely, similar to pressure about a curved camberline airfoil flying in parallel flow. The pitching motion obviously has a pronounced impact on the pressure distribution near the wing leading edge. If a lifting airplane wing were to pitch about the point X_P (a *very* unstable airplane), the pitching motion would reduce the leading edge suction peak and thus could temporarily weaken the strength of leading edge vortex if such a vortex was present.

The upper part of the figure shows the pressure distribution if the pitch axis is located at the wing neutral point, X_N. As explained before, these pressure distributions contain two components (1) the pressure distribution due to rotation about the point X_N and (2) the flat plate type pressure distributions associated with the wing equivalent angle of attack, which above has been shown to be proportional to ω. Thus the pitching motion is seen to increase the suction peaks at the outboard part of the wing, while decreasing the inboard pressure peaks.

Effect of Pitch Rate on the Pressure Distribution About a Cropped Delta Wing in Free Air at Zero Degrees Angle-of-Attack

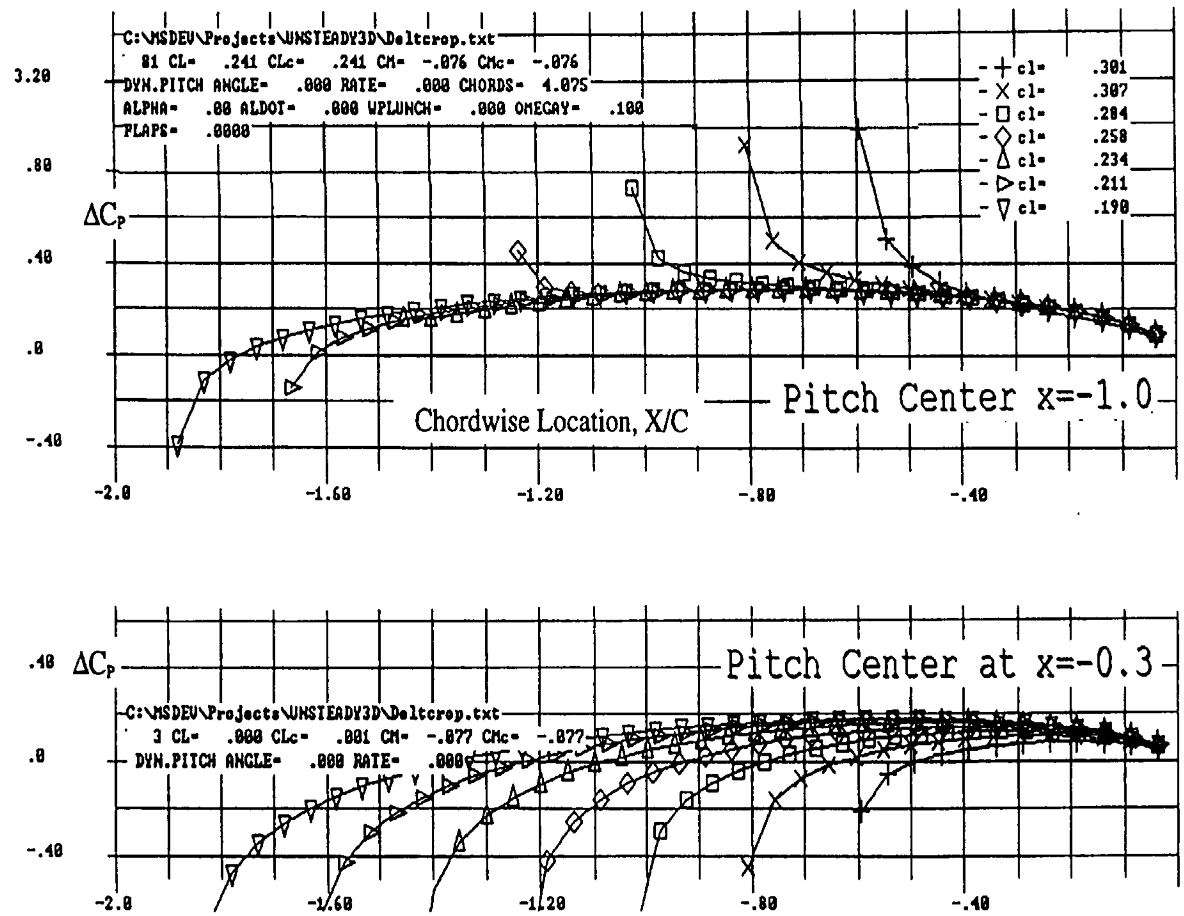

HLD403
Task 33 4.3.2.4/WMF

Time Accurate Pitch Motion

Time Accurate Analysis of Pitch Motion Due to a 10 Degree Sudden Flap Deflection of a Neutrally Stable Cropped Delta Wing

The canonical form for the time dependent stability derivatives allows the use of simple integration schemes for truly time accurate free air trajectory calculations. Compared to performing a trajectory analysis using the aerodynamics provided by interrogating for every time step the time accurate potential flow code, the computing time is reduced from many hours to a few seconds without sacrificing accuracy. At present this method can be used only out of ground effect because the time accurate canonical influence functions for changes in ground height have not yet been developed. However, time accurate analyses of maneuvers in free air may provide valuable insight in what to expect when maneuvering for the landing touch down.

Wings operating close to the ground experience a nose-down pitching moment. This nose-down moment is further increased by the added mass effects when the ground height changes with time. To trim and flare the airplane, the pilot uses elevator control deflections. These control deflections can produce brief initial responses which are counter to the pilot's intentions and thus will make the airplane more difficult to fly. This is illustrated in the figure showing the time accurate response of the cropped delta wing to a sudden downward deflection of the elevons when the center of gravity is located at the wing neutral point, X_N. The downward deflected elevator initially creates an upward lift force and a nose-down pitching moment. This moment causes the onset of a nose down pitch motion of the wing, the pitch acceleration of which depends on the wing pitch inertia and the magnitude of the moment. As the wing begins to rotate in pitch the rotation itself creates downward pitch lift and a pitch damping moment which counteracts the flap created moment. Integrated over time, the pitch rotation itself decreases the wing angle of attack which in turn creates downward lift. In the present analysis, it was assumed that the wing has a finite pitch inertia, but infinite mass. The assumption of infinite mass eliminates the need to account for the plunging motion of the wing as a result of the changes in lift.

The figure shows that the airplane will have traveled nearly 4 chord lengths before the downward lift commanded by the pilot actually begins to develop. For a large HSCT traveling at 150 knots this corresponds to a time delay of about 1 second!

Time Accurate Analysis of Pitch Motion Due to a 10 Degree Sudden Flap Deflection of a Neutrally Stable Cropped Delta Wing

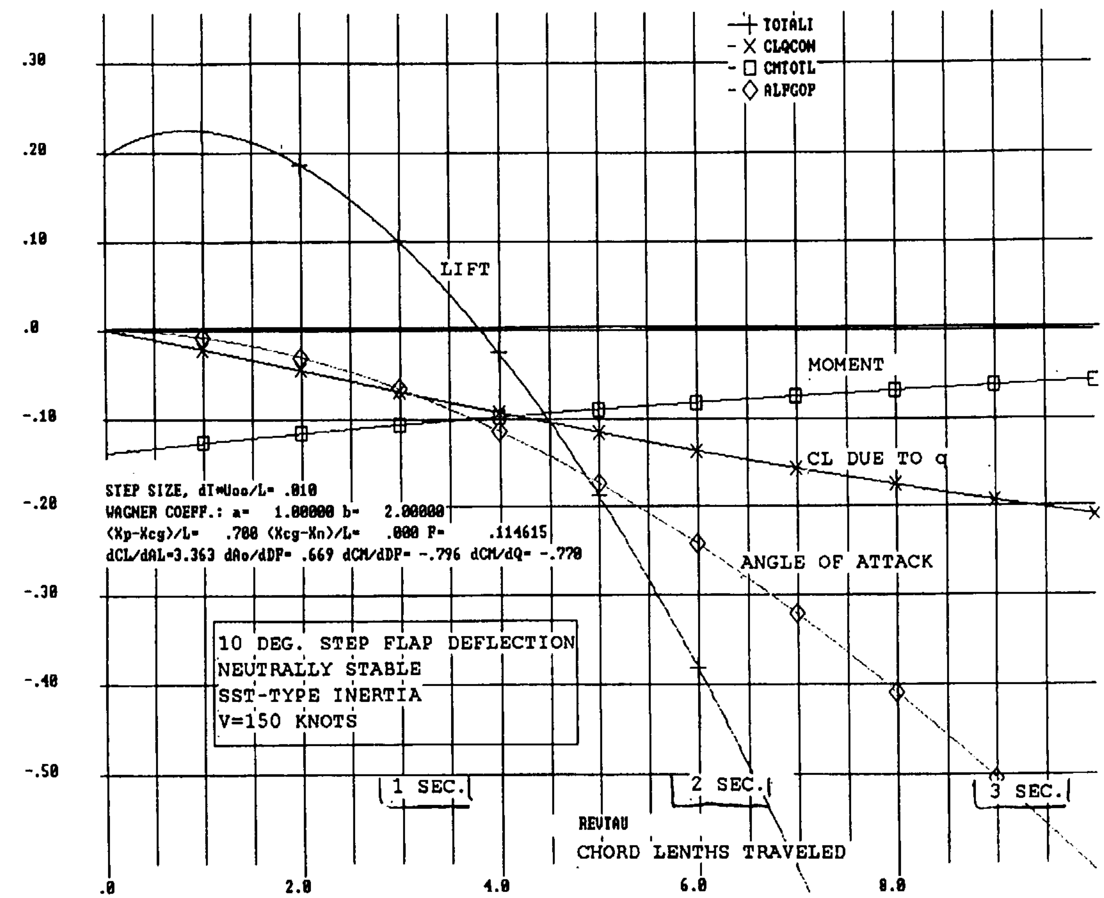

Quasi-Steady Analysis of Pitch Motion Due to a 10 Degree Sudden Flap Deflection of a Neutrally Stable Cropped Delta Wing

The analysis shown above was conducted using the 2-d Wagner function as the transfer function describing the time-accurate aerodynamics. Use of the 2-d Wagner function models a worst case scenario, as the response times for low aspect ratio wings are actually shorter. This has been explained before.

The present figure shows the wing response if quasi-steady aerodynamics are used, that is instant aerodynamic response to the wings instantaneous geometric operating conditions. The time required to develop the desired downward lift response is seen to be somewhat shorter than computed using unsteady aerodynamics. This indicates that neglecting time accurate aerodynamics will yield a slightly optimistic result. In both cases shown the pitch attitude diverges very quickly because the wing is neutrally stable and no autopilot algorithm was used in the analysis.

Quasi-Steady Analysis of Pitch Motion Due to a 10 Degree Sudden Flap Deflection of a Neutrally Stable Cropped Delta Wing

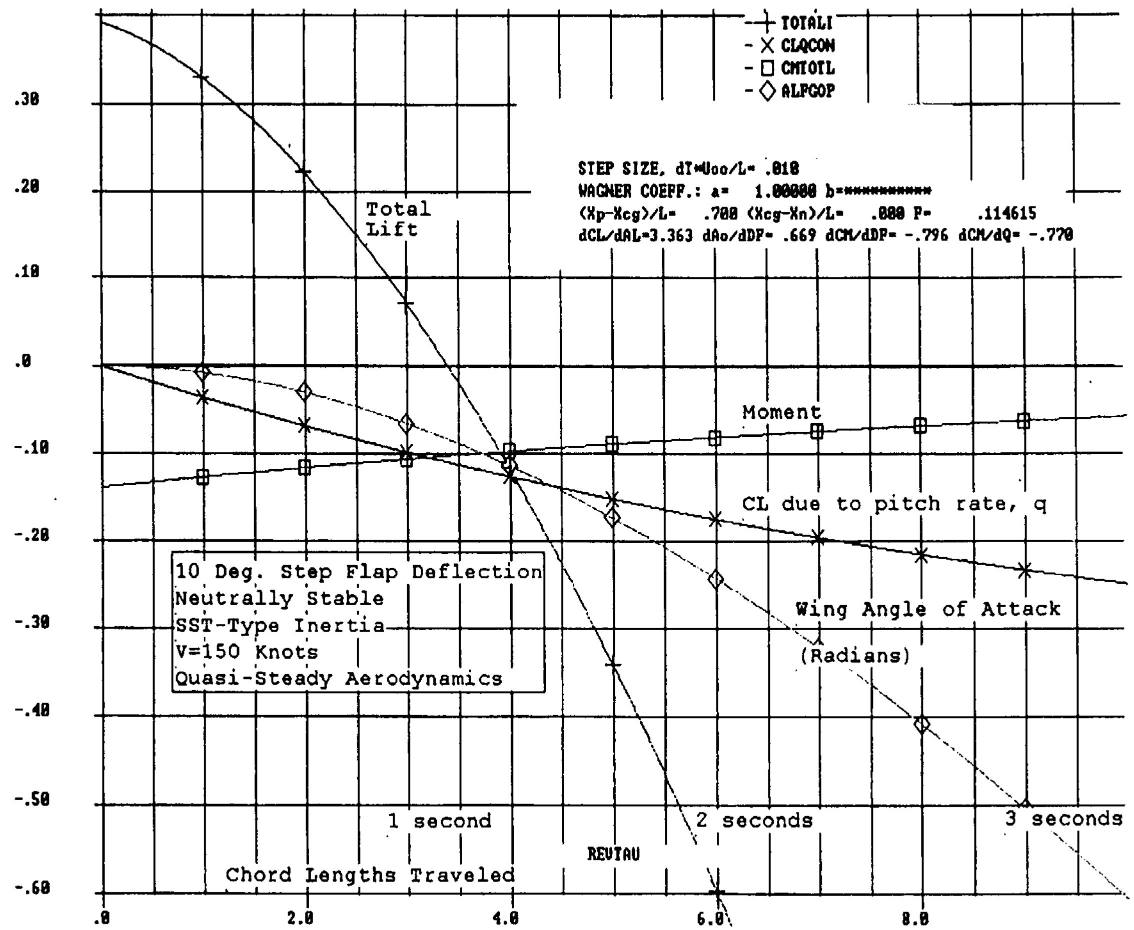

Quasi-Steady Analysis of Pitch Motion Due to a 10 Degree Sudden Flap Deflection of a 20% Stable Cropped Delta Wing

The figure shows the response of a (very) stable cropped delta wing with the center of gravity located 20% upstream of the neutral point, X_N. Given the same pitch inertia characteristics used in the previous analyses, the wing is seen to develop negative lift after less than 3 chord lengths of travel. This implies that the wing attains a negative incidence more quickly, a result of the nose-down moment created by the upward facing lift due to flap deflection. The lift acts at the neutral point, which is located 20% downstream of the center of gravity.

After an initial large overshoot the wing eventually settles at a lift coefficient, CL=-0.7, which represent the condition when all aerodynamic moments are balanced. Given the airplane aerodynamic characteristics, the amount of overshoot and the damping of the weather vane like oscillation greatly depends on the nondimensional inertia factor, F, which accounts for the air density, ρ, the airplane wing reference area, A_{ref}, the reference chord length, l, and pitch inertia, I_{yy} :

$$F=(0.5\ \rho\ A_{ref}\ l^3)/I_{yy}$$

Changing the magnitude of F (for example by changing the airplane pitch inertia), profoundly effects the wing pitch dynamics. The effect of increasing F on wing behavior will be illustrated next.

Quasi-Steady Analysis of Pitch Motion Due to a 10 Degree Sudden Flap Deflection of a 20% Stable Cropped Delta Wing

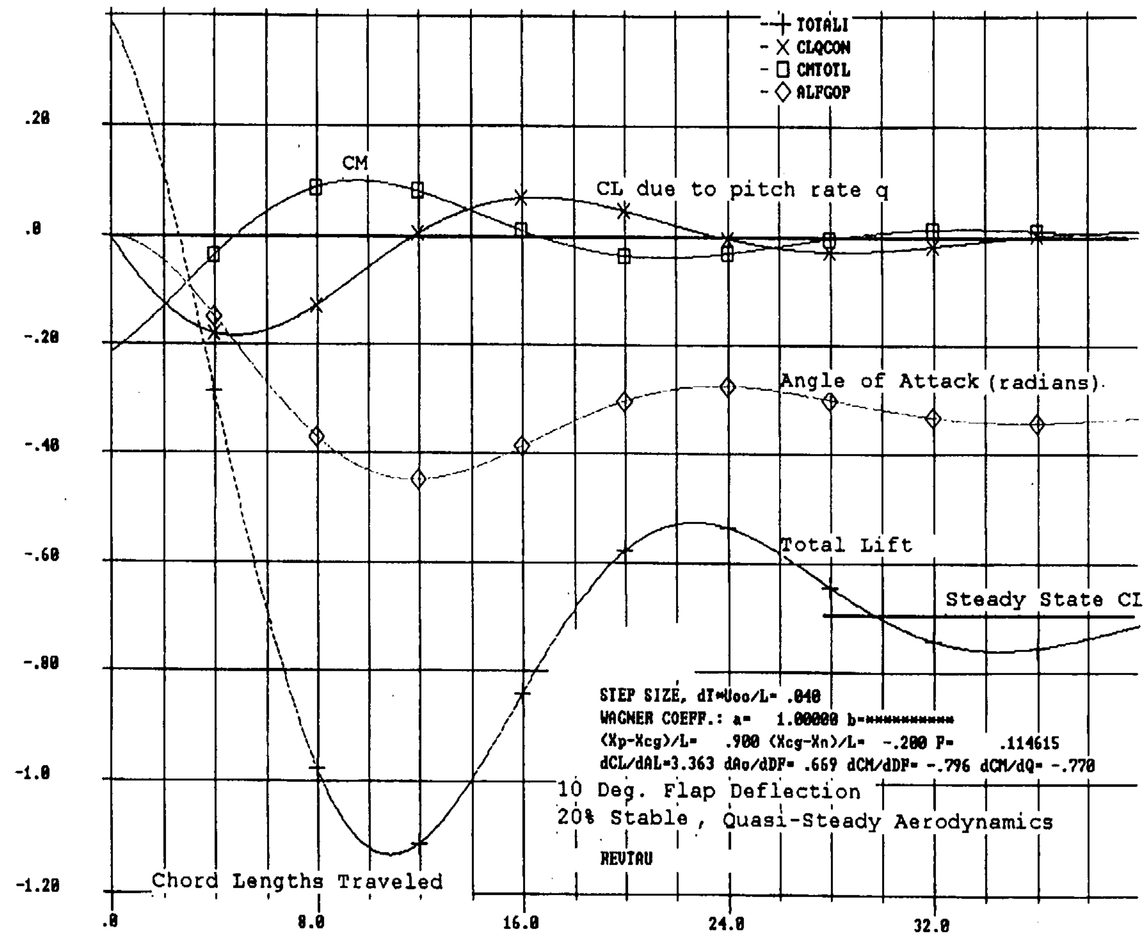

HLD403
Task 33 4.3.2.4/WMF

Quasi-Steady Analysis of Pitch Motion Due to a 10 Degree Sudden Flap Deflection of a 20% Stable Cropped Delta Wing With Reduced Pitch Inertia

The figure illustrates wing behavior if the pitch inertia factor F is four times larger than the value used in the previous calculations. Assuming that the geometry of the airplane remained unchanged, this amounts to a reduction of the pitch inertia by a factor of four. The computations indicate that for the same 10 degree flap deflection input, negative lift is obtained after 1 chord length of travel. Also, the wing settles with little overshoot at the new steady state lift level, CL=-0.7.

Based on this preliminary investigation it must be concluded that the magnitude of the inertia factor F can have a significant impact on how the airplane handles in ground effect. Also, there should be a large impact due to the type of pitch control used. The impact of control surfaces on transient lift varies greatly if canards, conventional horizontal tails, and tri-surface configurations were considered in addition to a tailless delta wing.

The F15 horizontal tail is very closely coupled to the wing, thus the time response of the wing/horizontal tail combination to an elevator deflection may be very similar to that of a single low aspect ratio cropped delta wing. Deflecting the elevator to compensate for the nose-down moment due to ground effect will initially reduce wing lift and cause the aircraft to settle. This behavior could be interpreted by the pilot as an adverse ground effect.

Quasi-Steady Analysis of Pitch Motion Due to a 10 Degree Sudden Flap Deflection of a 20% Stable Cropped Delta Wing With Reduced Pitch Inertia

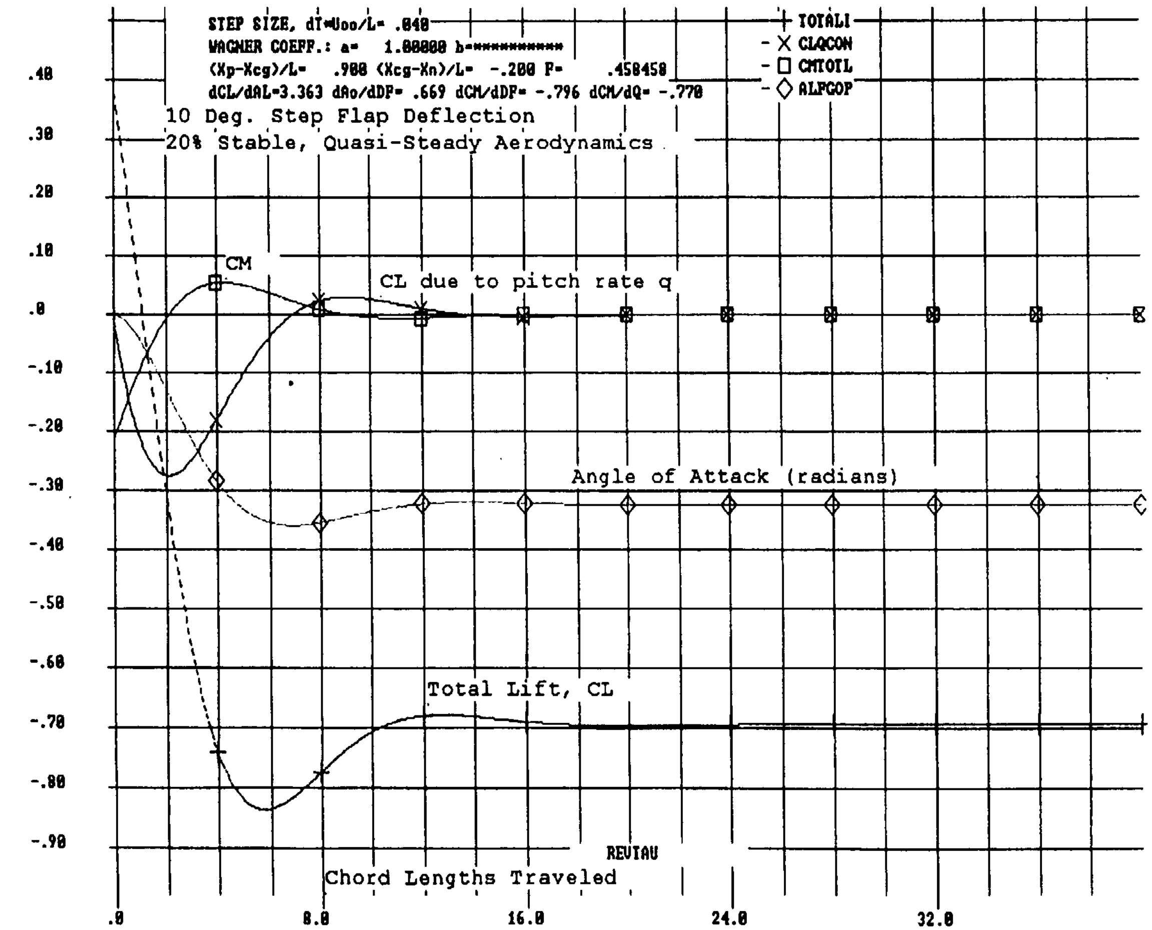

HLD403
Task 33 4.3.2.4/WMF

III. Findings for Cropped Delta Wing

This figure summarizes the key results obtained from the time accurate cropped delta wing analyses.

III. Findings for Cropped Delta Wing

- Time accurate circulation lift + added mass lift $\approx$ quasi steady lift
- Time accurate induced drag is higher than quasi steady drag
- In free air, the conventional steady state stability and control derivatives can be replaced by canonical (Wagner-type) transfer functions allowing quick time accurate analyses
- Eigen-pitch-damping is independent of time (pitch about point X_P)
- Lift due to pitch rate is eliminated by pitching about the point X_P
- Elevon deflections for lift control initially produce not intended reversed lift excursions which
  - depend on airplane pitch inertia
  - may explain difficult landing characteristics of Concorde

IV. TCA Wing and Tri-Surface Configuration

TCA Wing Panel Layout for Time Accurate Analysis

The TCA wing planform was one of the configurations evaluated in the NASA Langley 14x22 ft wind tunnel during a dynamic ground effect test series run in October 1997. To aid in test planning and to provide a better understanding of the many factors contributing to ground effect aerodynamics, the TCA wing planform was selected for analysis in UNSTEADY3D.

A tri-surface configuration is one of the options under consideration for pitch control and improved ride quality. Such a configuration has been analyzed at the conclusion of the present dynamic ground effect study. The results will be shown later.

The figure illustrates the vortex lattice paneling layout for the TCA wing. The panel spacing was setup somewhat coarsely in order to conserve computer time.

IV. TCA Wing Panel Layout for Time Accurate Analysis

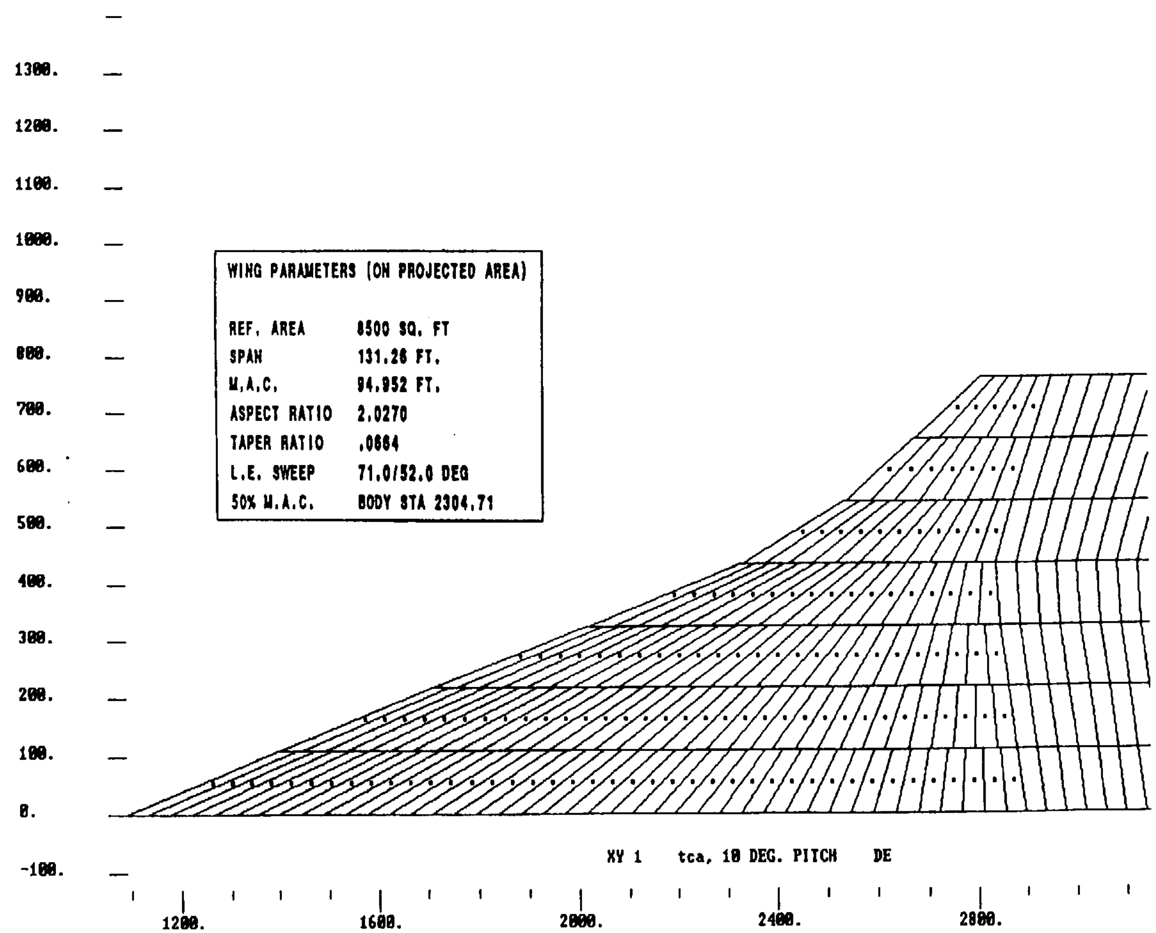

HLD403
Task 33 4.3.2.4/WMF

Comparison of TCA Predicted Ground Effect With Wind Tunnel Data

The figure shows the computed lift as a function of ground height for quasi-steady and time accurate conditions. The theoretical lift values have been nondimensionalized using the steady state lift in free air as reference condition. Ground height is measured relative to 50% MAC and has been nondimensionalized by wing span.

The theoretical static and dynamic ground effect curves are seen to be virtually identical. There are some minor differences between the wake models used for the static and the dynamic analyses, respectively. These modeling differences should cause less than 1% variation in lift. The theoretical prediction of a negligible dynamic effect for the TCA agrees with the observations made for all the other low aspect ratios analyzed so far.

Also shown in the graph are the results obtained in the NASA Langley 14x22 ft tunnel for the static TCA ground effect. The agreement with theory is excellent. No loss of leading edge suction was assumed in the theoretical predictions. It is not known if a leading edge vortex was present in the experiment. At the time of writing this report, no dynamic experimental data had become available.

Comparison of TCA Predicted Ground Effect With Wind Tunnel Data

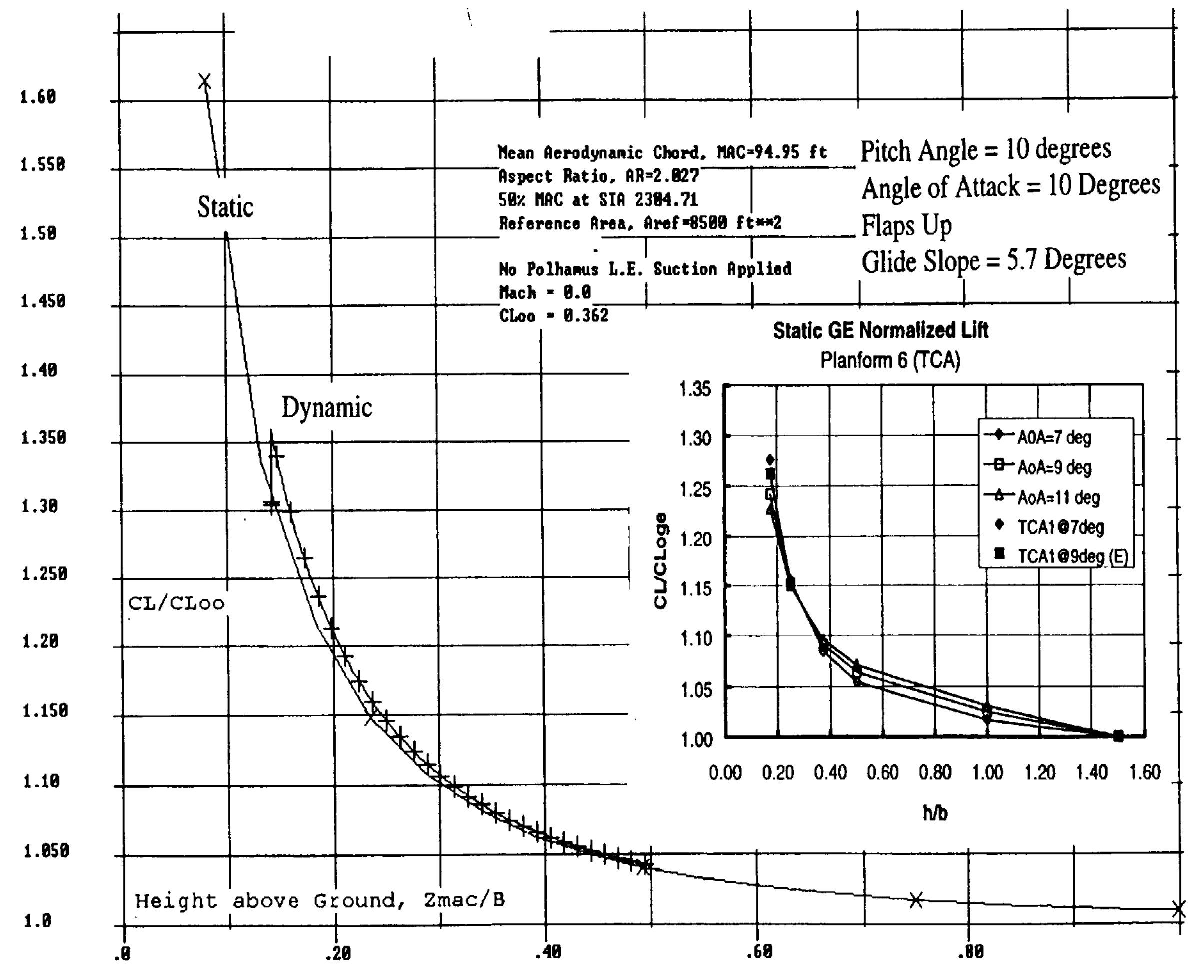

HLD403
Task 33 4.3.2.4/WMF

Polhamus Leading Edge Vortex Lift Increment in Static and Dynamic Ground Effect

Application of the Polhamus theorem to time dependent flows is based on the unproved assumption that development of leading edge vortices follows the same time scale as the underlying unsteady potential flow. If the airplane depends on the formation of leading edge vortex lift, but the leading edge vortex takes a relatively long time to establish itself, then the airplane would initially experience only the potential flow lift variations; there would be a shortfall of lift. Formation of vortex lift is associated with a separation of the boundary layer. Since boundary layer separation takes time to develop - consider the CL_{max} overshoot of rapidly pitching attached flow wings - it is conceivable that such a mechanism temporarily reduces the lift of highly swept wings.

The graph presents the computed variation of leading edge vortex lift in ground effect under static conditions and for time accurate 5.7 degree glide path angle. As expected, the leading edge vortex lift increment is slightly smaller during the dynamic approach conditions than during steady state level flight in ground effect. Because of the high leading edge sweep of the TCA wing, the overall Polhamus lift increment is appreciable. Steady state lift in free air is increased from $CL_{no\ Polhamus} = 0.362$ to $CL_{Polhamus} = 0.448$. At a ground height of H/B=1.0 the computed steady state lift, including the Polhamus effect, is $CL_{Polhamus} = 0.452$. This very small difference between the lift in free air and at H/B=1.0 provides proof that starting time accurate descent analyses at that ground height will cause only a minimal error.

Polhamus Leading Edge Vortex Lift Increment in Static and Dynamic Ground Effect

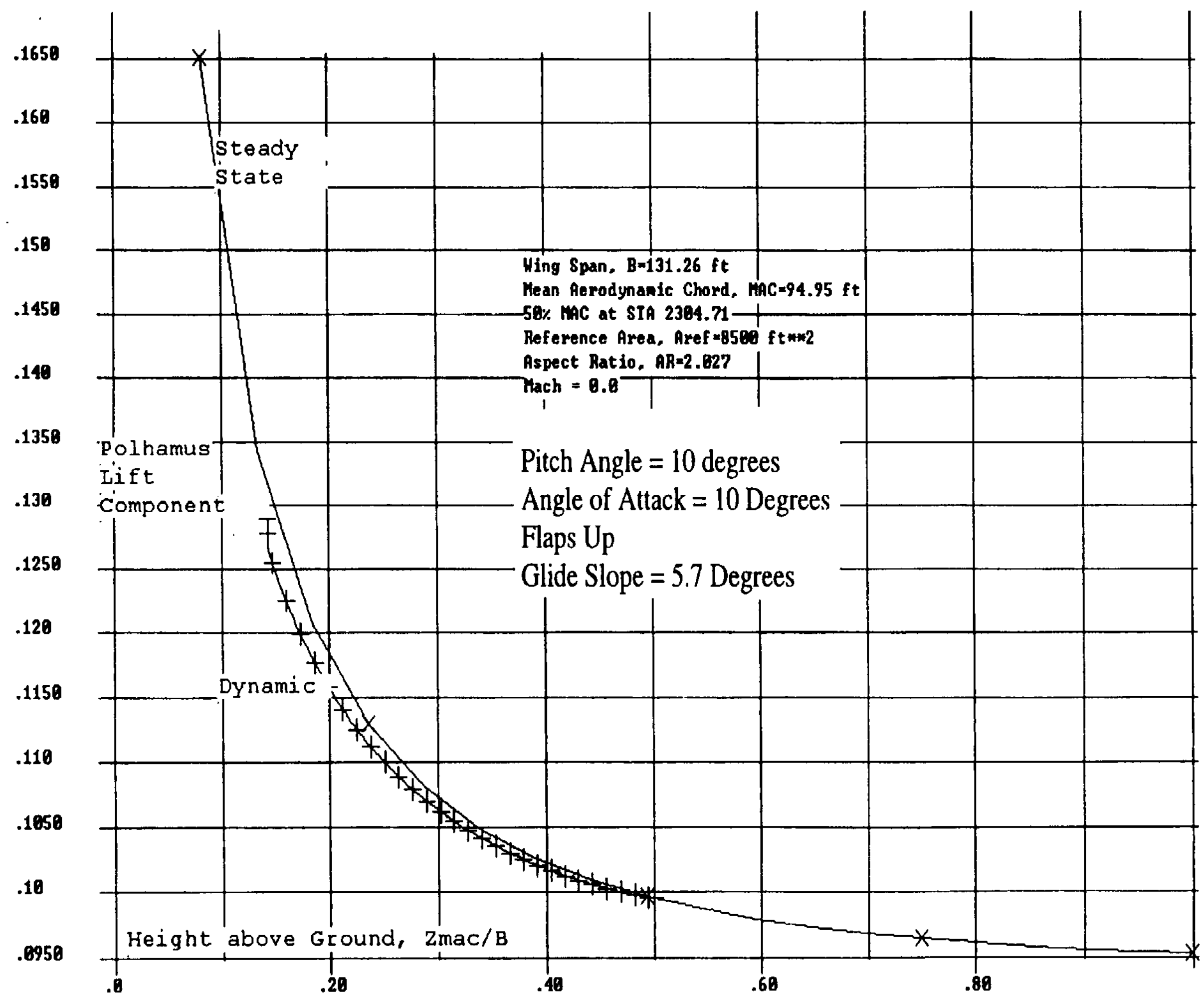

HLD403
Task 33 4.3.2.4/WMF

TCA Normalized Pitching Moments

All pitching moment data shown for the TCA wing are referenced to 50% MAC (mean aerodynamic chord). The term -dCM/dCL defines the location of the wing actual neutral point relative to the somewhat arbitrarily selected 50% MAC reference. Assuming that the center of gravity is located at 50% MAC, the wing is unstable if the neutral point is located upstream (forward) of 50% MAC.

As the wing approaches the ground, the neutral point (which for a flat wing coincides with the center of pressure) is seen to move aft; the wing becomes statically *less unstable*. This behavior is seen to be slightly more pronounced in dynamic ground effect. It is caused by the lift due to added mass effects, which act farther aft on the wing. Also, the amount of neutral point travel is seen to be larger if a leading edge vortex (Polhamus effect) is present.

The term (CM -CMoo)/CLoo can be interpreted as the amount of neutral point shift due to ground proximity. The predicted 2% aft shift of the TCA wing neutral point between free air and the ground height, H/B=0.2, is quite significant, considering that the airplane overall CG travel is only about 5%. In particular, control input required to retrim the airplane may cause a configuration dependent temporary loss of lift, as has been explained earlier. This temporary reduction in airplane lift, while real, may falsely be interpreted as a lift loss due to dynamic ground effect. To verify this contention, a time accurate analysis of the specific airplane configuration coupled with an autopilot algorithm would be necessary. This was beyond the scope of the present study.

Also shown in the graph are experimental data obtained for the TU144 wing in the October 1997 NASA Langley14x22 ft wind tunnel test. While different in planform from the TCA, the trend of the wind tunnel data is well reproduced by the UNSTEADY3D analysis. When comparing experimental and theoretical data, one must bear in mind that potential flow theory in general does not accurately predict pitching moments for viscous flows. Also, the coarse panel layout used in the present analysis introduces additional inaccuracies.

TCA Normalized Pitching Moments

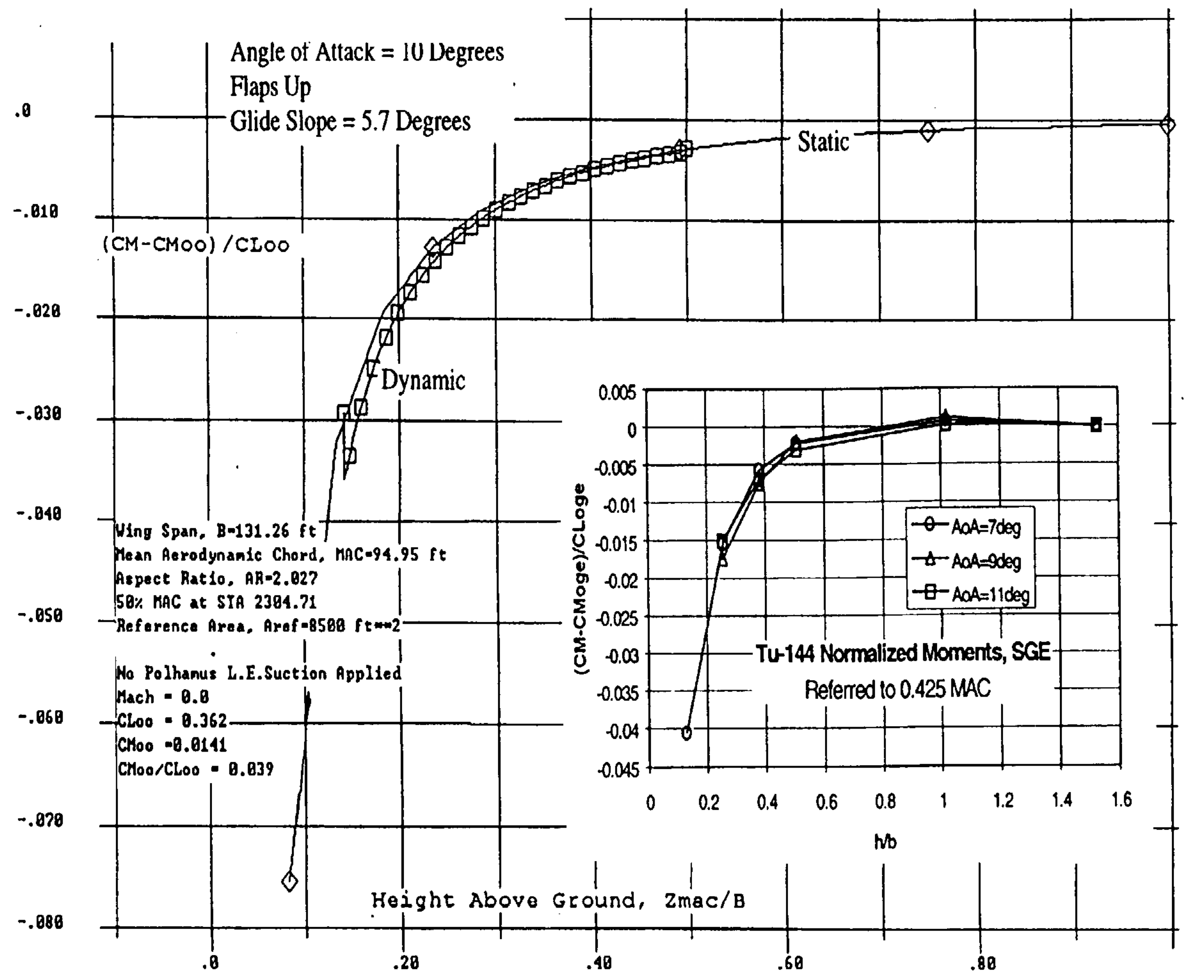

HLD403
Task 33 4.3.2.4/WMF

TCA Induced Drag Factors in Static and Dynamic Ground Effect

Under dynamic conditions there are two source for drag: (1) drag due to circulation and (2) drag due to added mass effects.

(1) The drag due to the dynamic circulation lift component is lower than the induced drag at steady state conditions. This caused by two effects:

a) For the same amounts of circulation lift, the wing must be closer to the ground in the unsteady case. Closer to the ground the downwash is decreased, thus saving induced drag.

b) In the time dependent case the trailing vortices have not yet traveled downstream to 'infinity', thus the amount of induced downwash will be lower in the unsteady case.

(2) The pressures due to added mass effects act normal to the wing surface. However, there is no leading edge suction due to added mass effects. This causes a large amount of drag. Therefore the overall drag is dramatically higher in the case of dynamic ground effect.

The induced drag characteristics of a wing are commonly described by the, k - factor, where

$$k = CD_i/CL^2.$$

In the present figure the wing total drag shown before has been recast in this term. CD_i/CL^2 is seen to decrease with ground proximity, clear evidence that the induced drag is decreased due to the ground effect. Also, under static conditions the ground effect is seen to be more beneficial than during the 5.7 degree dynamic glide path. For reference, the free air elliptic induced drag factor has been added to the graph. The theoretical free air drag of the TCA wing is seen to be somewhat higher than the theoretical minimum. Higher than elliptic induced drag is to be expected. However, use of only 7 spanwise panels in the UNSTEADY3D analysis has possibly decreased the accuracy of the induced drag predictions.

TCA Induced Drag Factors in Static and Dynamic Ground Effect

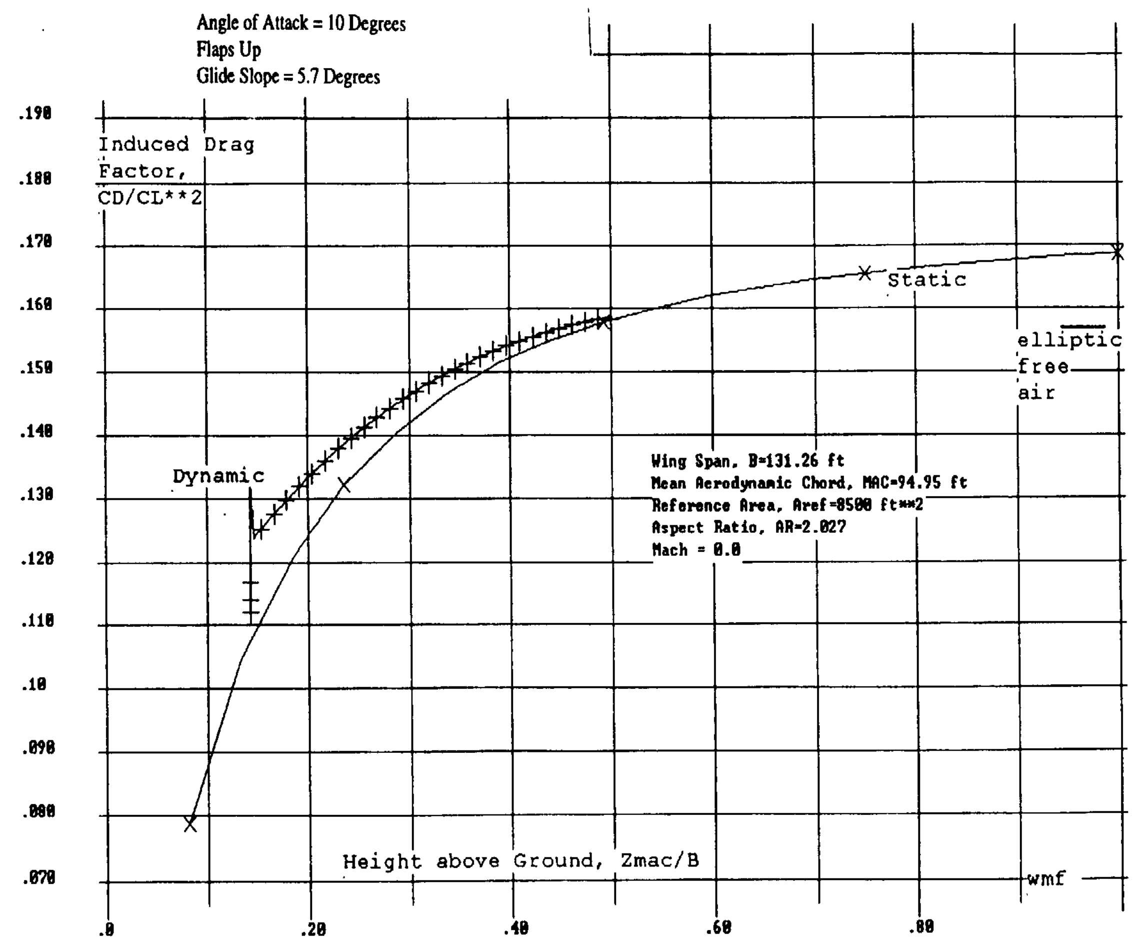

HLD403
Task 33 4.3.2.4/WMF

TCA Wing Lift Response to Sudden Change in Ground Height

The difference between steady state and time dependent dynamic ground effect increases with the airplane rate of descent toward the ground. At zero rate of descent (flight parallel to the ground) the dynamic effects vanish. Conversely, the dynamic effects are the largest for very steep glide slope angles. An upper limit of the rate of descent toward the ground and thus the largest dynamic ground effect occurs in what may referred to as an "air craft carrier landing", where the ground height changes abruptly. This limiting condition was investigated in UNSTEADY3D.

The figure shows the development of lift when, after a steady state flight at H/B=0.5, CL=0.376, the ground height is abruptly reduced to H/B=0.14. In the example shown the jump in ground height occurred at the nondimensional time equivalent to 0.15 chord length of distance traveled. Total lift is seen to rapidly approach the new steady state conditions associated with the reduced ground height.

TCA Wing Lift Response to Sudden Change in Ground Height

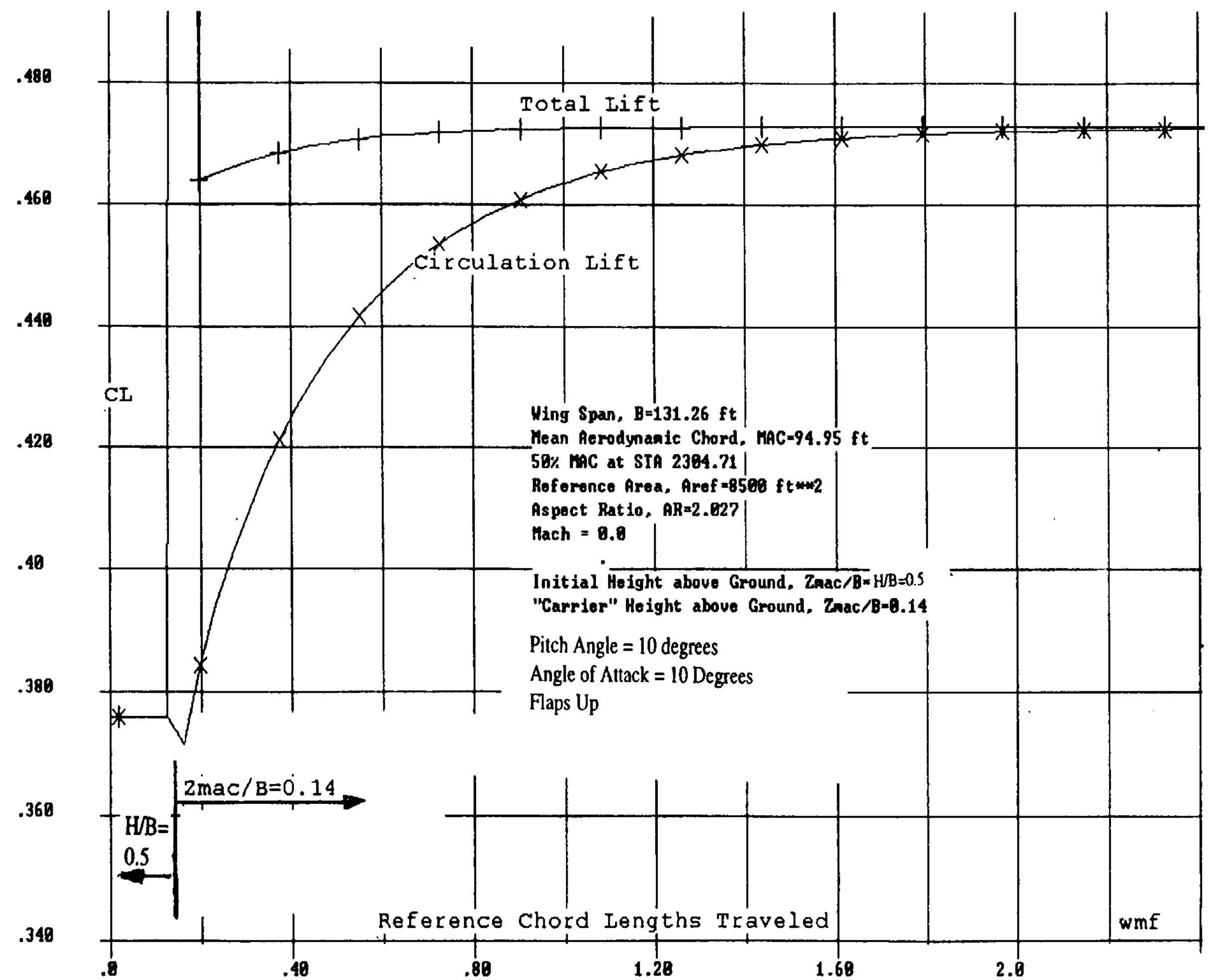

Change of TCA Wing Chordwise Pressure Distribution Due to a Sudden Change in Ground Height

The increase in nose down pitching moment with decreased ground height is easily explained by examining the chordwise pressure distributions shown in the figure. Most of the lift and pitching moment increase due to ground proximity is caused by additional load carried on the aft portion of the wing.

Change of TCA Wing Chordwise Pressure Distribution Due to a Sudden Change in Ground Height

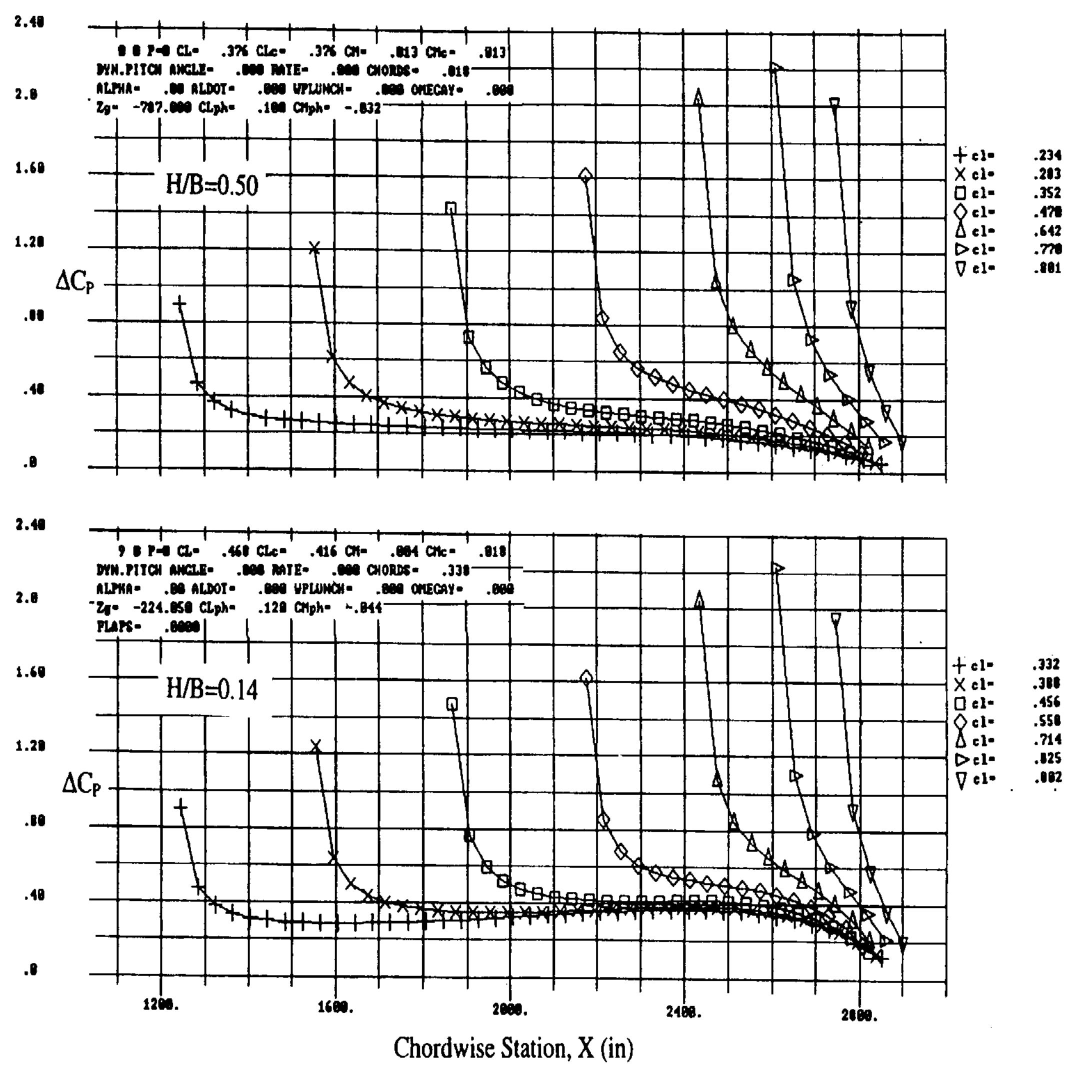

HLD403
Task 33 4.3.2.4/WMF

Tri-Surface Airplane Pressure Distributions Due to a Sudden Canard Deflection

The analyzes presented in previous charts showed that in ground effect the center of pressure is shifted aft by up to 3% MAC relative to its location in free air. Deflection of the wing elevons, a horizontal tail, a canard surface, or a combination of these three devices could be used to compensate for the nose down pitching moment. The figure shows a tri-surface airplane configuration formed by addition of two low aspect ratio rectangular control surfaces to the TCA wing. All three surfaces are planar, except that they are vertically staggered by 40 inches (3.5%MAC) in order to avoid numerically singular points between interacting wakes. In the following free air analysis, only the canard will be used as a pitching moment effector.

At the nondimensional time τ=0 (the equivalent of chord lengths traveled) all three surfaces are positioned at zero degrees angle of attack. At τ=0.05 the incidence of the canard is suddenly increased to α_{canard}=10 degrees.

At τ=0.3 the chordwise pressure distribution about the canard surface is seen to have nearly fully developed. Also shown is the approximate location of the canard startup vortices, which at that particular instant induce a small amount of upward flow on the main wing.

At τ=1.6 the startup vortices have traveled farther downstream and are now located somewhat upstream of the wing trailing edge. Both the canard trailing and startup vortices induce a downward flow on the forward part the wing which now develops a negative lift force.

At τ=2.3 the bulk of the startup vortices is located between the wing trailing edge and the leading edge of the horizontal tail. The upwash induced at the tail causes a temporary upward lifting force on the tail.

At τ=2.8 both the startup and trailing vortices have traveled downstream of t
he tail, which now carries a downward load. Nearly steady state conditions will be attained shortly thereafter.

Tri-Surface Airplane Pressure Distributions Due to a Sudden Canard Deflection

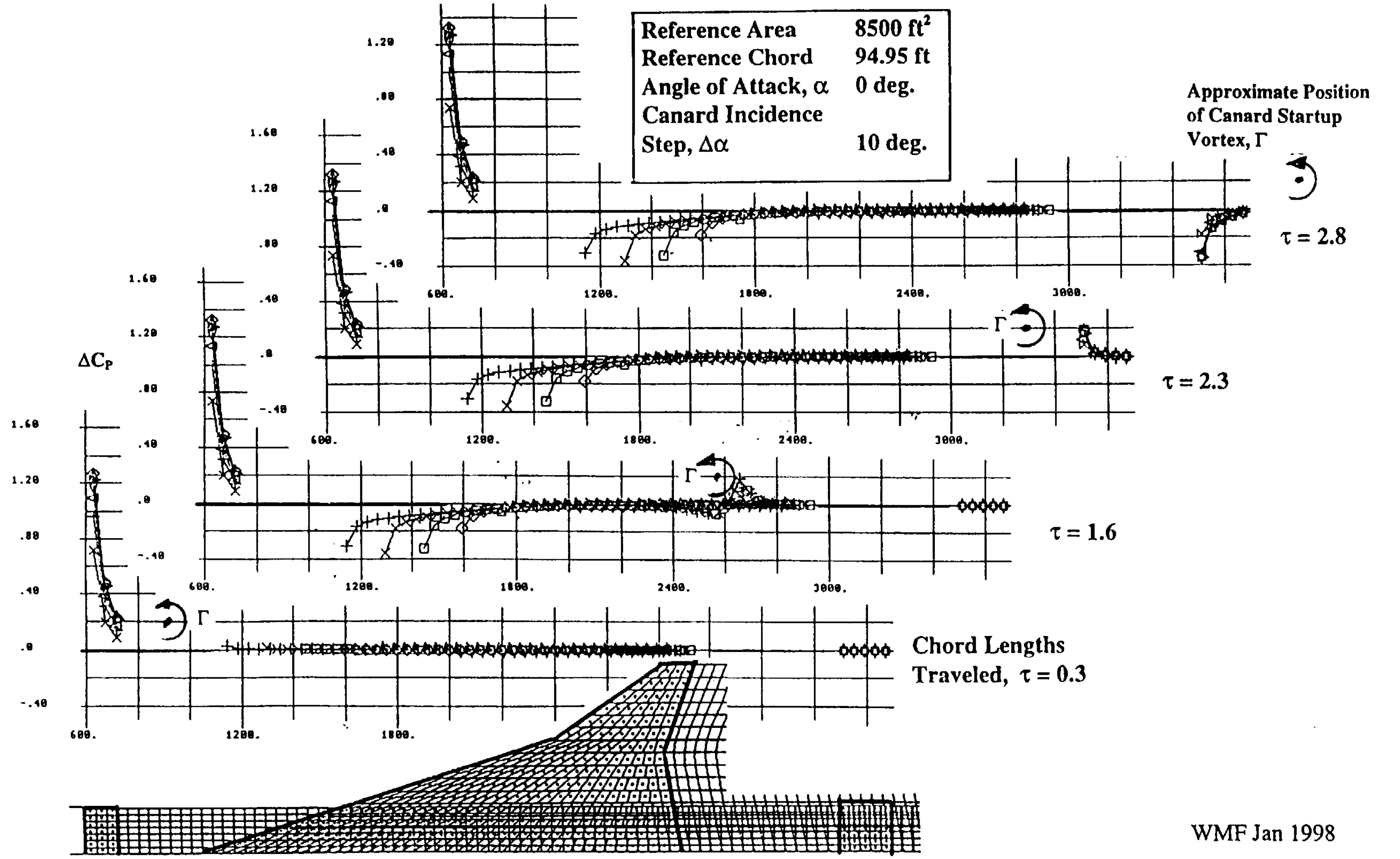

WMF Jan 1998

HLD403
Task 33 4.3.2.4/WMF

Tri-Surface Airplane Lift and Pitching Moment Due to a Sudden Canard Deflection

The figure presents the airplane time dependent lift and pitching moment characteristics associated with the above pressure distributions. Initially, a large positive lift increment and a nose up pitching moment is generated by the sudden 10 degree canard deflection at the nondimensional time τ=0.05.

Up to the time τ=0.5 lift and moment continue to increase as a result of the upflow induced on the wing by the canard startup vortices. Subsequently, lift is reduced by the growing downwash on the wing as the canard vortices travel farther downstream. Note the reduction in lift due to added mass effects. The added mass forces act in the aft region of the wing and cause a nose-down moment.

When the canard startup vortices approach the tail, the induced upflow creates for a short period of time an upward tail lift force at approximately τ=2.5. The tail lift briefly creates a nose down pitching moment.

Once the canard vortices have traveled past the horizontal tail the induced downwash very rapidly creates a downward tail force which is associated with a nose up moment. Nearly steady state conditions are approached past τ=3. Note that the downwash of the lifting canard eventually results in negative lift for the entire configuration.

In summary, the canard deflection creates initially a positive increment in lift, which is followed shortly thereafter by a loss in lift. Such an airplane handling characteristic could be interpreted by the pilot as an adverse dynamic ground effect.

The trisurface analysis yields a few important findings:

1) In the case of low aspect ratio configurations, positive lift of the canard creates a downwash field which causes a significant loss in lift of the main wing. This can result in a small net loss of overall lift.
2) Moments and lift vary greatly with time during the first few chord lengths of travel after a canard deflection.
3) There is a strong time dependent interaction between the canard wake vortices and the horizontal tail. This interaction can most likely not be ignored if these surfaces are to be used for control of ride quality or to suppress fuselage bending modes.

Tri-Surface Airplane Lift and Pitching Moment Due to a Sudden Canard Deflection

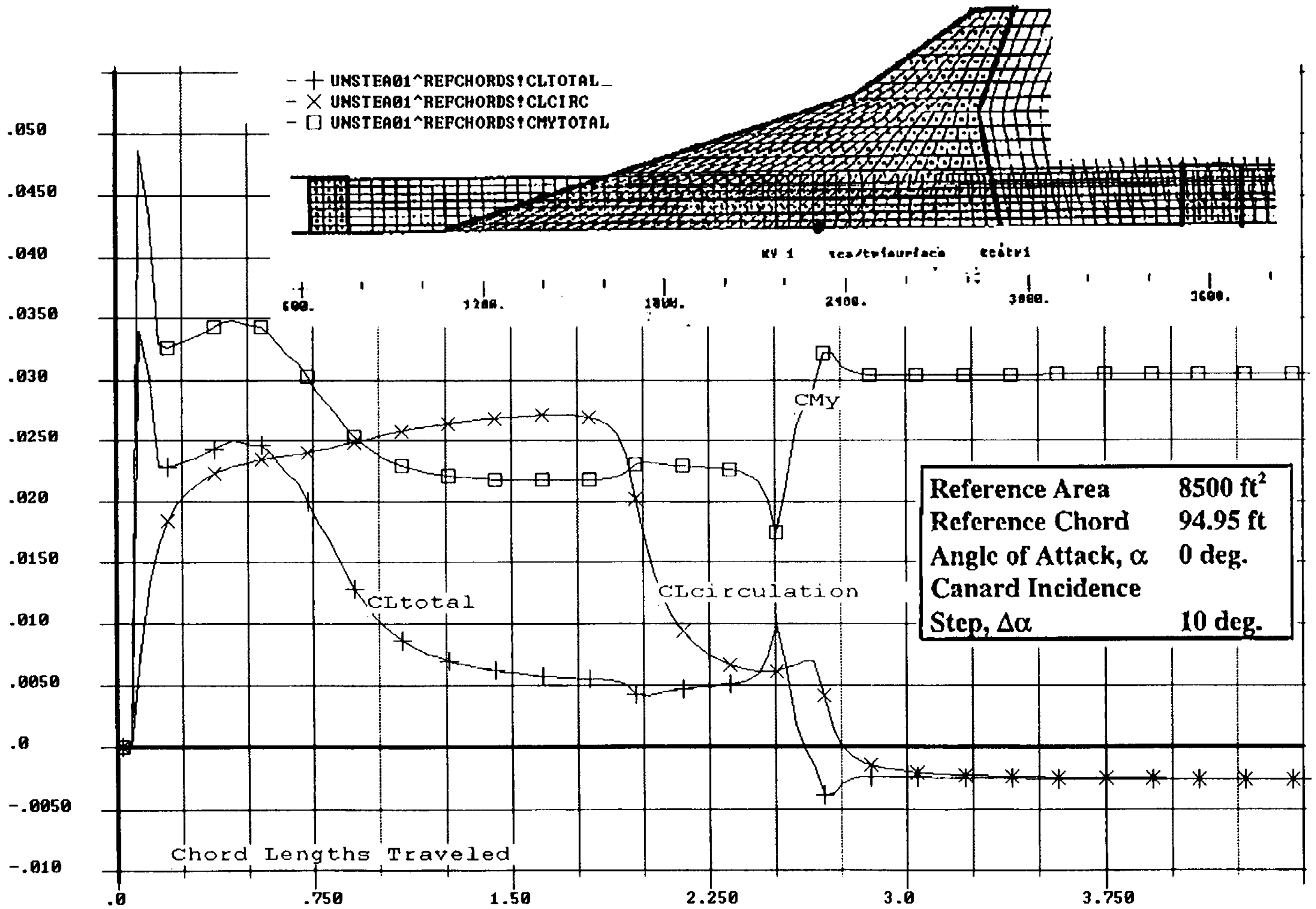

HLD403
Task 33 4.3.2.4/WMF

IV. Findings from TCA Analyses

The figure summarizes the findings from the TCA analyses.

IV. Findings from TCA Analyses

- Changes in total lift (circulation + added mass) due to dynamic ground effect are small
- Polhamus leading edge vortex lift is reduced in dynamic ground effect
- Large shift in center of pressure associated with static ground effect is aggravated by dynamic effects
- Induced drag is increased by dynamic ground effect
- Tri-surface airplane overall lift can be decreased by upward lift of the canard
- Significant variation of lift and moment during the initial 3 chord lengths of travel
- Strong interactions between canard and horizontal tail (ride quality control issue)

V. Conclusions

Time accurate potential flow results obtained from UNSTEADY3D are in good agreement with the very limited data base of known theoretical solutions. However, all known 'exact' analytical solutions are only for 2-d airfoils out of ground effect. Discretization problems may have contaminated the accuracy of 3-d wing data found in literature used for comparison. At present, even relatively coarse panel layout schemes result in long computer run times in the time accurate mode. These inherent difficulties associated with time accurate analyses impede rapid program check out, and limit the number of cases that can be evaluated.

All the data cases run indicate that the dynamic effects on lift in potential flow are relatively small for low aspect ratio wings. However, pitch control input required to compensate for the increased nose down pitching moment in ground effect, may cause a transient loss in lift which could be interpreted as lift loss due to ground effect.

The figure summarizes the key findings of the dynamic ground effect study.

V. Conclusions

1) While generally small, the influence of dynamic ground effect on lift is largest for steep glide path angles and disappears in steady level flight.

2) Virtual mass effects significantly increase induced drag in dynamic ground effect.

3) The large aft shift of the center of pressure in ground effect is slightly aggravated by dynamic effects.

4) The number of chord lengths of travel needed to approach steady state lift conditions decreases with wing aspect ratio. This effect is more pronounced in ground proximity.

5) Assuming applicability of the Polhamus leading edge suction force theorem, the leading edge vortex lift of highly swept wings is slightly reduced in dynamic ground effect.

6) Depending on the airplane pitch inertia, control inputs for pitch trim can produce a temporary loss in lift which - erroneously - could be interpreted as lift loss due to dynamic ground effect.

7) In order to separate lift due to angle of attack from lift due to pitch rate in dynamic wind tunnel tests, the wing must be pitched about "the point of zero pitch lift, X_P, (the ¾ point in 2-d flow, free air)".

8) Tri-surface configurations exhibit highly complex time aerodynamic responses to canard deflections.

Recommendations

The Figure lists a few recommendations for future work.

Recommendations

- Analyses shown are for infinite speed of sound. Estimate influence of Mach number.
- At present only rudimentary trajectories have been analyzed. Implement simple auto pilot algorithm for realistic analysis of statically unstable configurations characterized by linearized transfer functions.
- Refine the use of linearized time accurate transfer functions for stability and control derivatives. This will allow subsequent configuration analyses at a reasonable computational level of effort.
- **Reanalyze flight test data trying to account for time accurate transients due to control inputs.**
- **Analyze NASA Langley 14x22 ft ground effect data knowing what characteristic behavior to look for.**

This page intentionally left blank.

Dynamic Ground Effects Simulation Using OVERFLOW-D

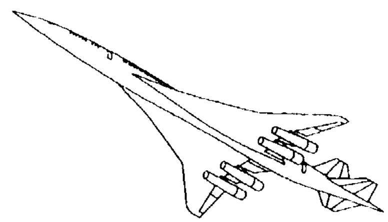

Bill Dwyer
Northrop Grumman Corporation
Bethpage, NY

NORTHROP GRUMMAN

HSR Task 33 Technology Chart

This work is being performed under the Non-Linear Methods portion of the High Lift Analysis Methods technology area. This work is being performed under HSR Contract NAS1-20220, Task 33, Subcontract ZA0867, supervised by Paul Meredith at Boeing-Seattle.

High Lift Technology Development (Task 33)

Increase L/D, Develop Analysis/Design Methodology

Goals
- Demonstrate Greatly Increased L/D Relative to SST Technology (Suction Parameter ≥ 92%)

Objectives
- Define Preferred High Lift System
- Technology Readiness Level ≥ 6
- Analysis/Design Methodology

Challenges
- Aggressive Tech Projection
- Validation (Little Data)
- Planform, Viscous, Scale, Ground, Power, Canard Effects

Approaches
- **Concept** Development
- **Test** Programs and Techniques
- **Analytical** Methods

Program
- Concept Development
  - Boundary Layer Control
  - Vortex Flaps
  - Attached Flow Flaps
  - Programmed Flaps
  - Canards
- Test Programs and Techniques
  - WT Database
  - High Rn Testing
  - Large Scale Testing
  - Powered Testing
  - Dynamic GE Testing
  - Pressure & Temp. Sensitive Paints
- Analytical Methods
  - Technology Projection
  - Linear Methods
  - [redacted]
  - Navier-Stokes Methods

NORTHROP GRUMMAN

Outline Of Presentation

This presentation is broken into 5 logical sections. The Background Information section describes the technical issues being address by this study. The Approach section describes the organization of the contract effort which was laid out as the most effective means of quantifying, with validated methods, the magnitude of dynamic ground effects for the TCA configuration. The Validation Case section describes the analysis of the XB-70 configuration in both static and dynamic ground effect, with comparisons to wind tunnel and flight test data. The TCA Analysis section then describes the application of the same codes and methodologies to the TCA in both static and dynamic ground effect. Comparisons are made between the static and dynamic, as well as to early static data from a recent wind tunnel test on the TCA configuration. Finally, the work to date is summarized and the future direction of this study is outlined.

NORTHROP GRUMMAN

Outline of Presentation

- Background Information
- Approach
- Validation Case (XB-70)
- TCA Analysis
- Summary and Conclusions

NORTHROP GRUMMAN

Background Information

Wind tunnel and flight test data for ground effects data shows a difffering magnitude of induced effects for static and dynamic data. Existing literature shows that as the aspect ratio of a vehicle descreases, the difference between static and dynamic ground effects increases with the magnitude of dynamic ground effects being smaller than the static. Both wind tunnel and flight test data show this general trend as demonstrated on wings of aspect ratio between 1.0 and 2.5 with the difference between the two decreasing as the aspect ratio increases. This difference raises concerns that the low aspect ratio of the TCA wing my lead to sizable errors in predicting ground effects using only static methods.

NORTHROP GRUMMAN

Background Information

- Dynamic Ground Effect Differs From Static Ground Effect For Low Aspect Ratio Wings.
  - DGE Lift Increments Are Less Than SGE
- Data From Various Configurations Support This Claim
- Desire is to Quantify the Effect For The TCA

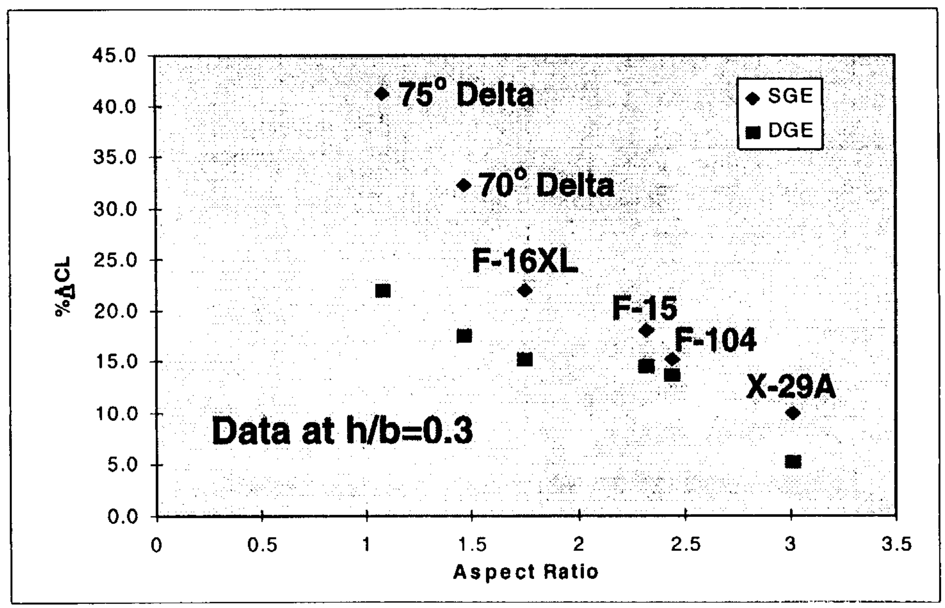

NORTHROP GRUMMAN

Background Information
Continued

The increasing speed of computers has made possible the application of compute intensive time-accurate fluid dynamics analysis over 3-D configurations. This increase in computational power has been accompanied by the development of analytical tools capable of modeling complex, moving-body configurations. One of these tools is the Euler/Navier-Stakes code, OVERFLOW. It has the required time varying metric computations and boundary conditions coupled with automated tools to maintain inter-block connectivity s the solution progresses and the bodies move. Northrop Grumman personnel are experienced in the use of this code, particularly in the unique approaches to interblock connectivity and the software used to perform this task.

NORTHROP GRUMMAN

Background Information

Continued

- **Computers and Attendant Methods Have Advanced to the Point Where 3-D, Time-Accurate, Moving Body Analyses Have Become Feasible**
- **OVERFLOW-D**
  - Existing Version of Popular CFD Solver Capable of Solving the Given Problem
  - Has Moving Metric Boundary Conditions and Coupled Domain Connectivity Routines
- **Northrop Grumman Personnel Experienced With All Associated Software Tools**

OVERFLOW-D

The OVERFLOW-D flow solver used in this study is an early version of the popular flow solver written by Pieter Buning. It has several flow solver options available, with the ARC3D central difference solver used for this study. It is a multi-block code which uses overset grids for domain decomposition. This method allows for efficient modeling of complex configurations. The particular version of the code used in the current study had been modified by Bob Meakin of NASA-Ames. To incorporate a SIXDOF routine and the domain connectivity functions within the flow solver itself. This allows for a complete iteration of flow solver, vehicle position updates, and updates of interblock connectivity information to be performed within a single code, which provides for efficient use of computational resources. This code has been demonstrated on several time-accurate moving body simulations, with perhaps the most notable being an analysis of the V-22 with spinning rotors in vertical flight.

OVERFLOW-D

- Core Solver is Early Version of OVERFLOW, Written By Pieter Buning
- Has Subroutine Callable SIXDOF and Overset Grid Connectivity Routines
- Grid Connectivity Performed by DCF3D
  - Written by Bob Meakin
  - Cuts Holes Using Analytic Shape Functions
  - Ran 10X Faster Than The Then Current Version of PEGSUS
  - Uses GDCF to Set Up Inputs For Analytic Shapes
- Demonstrated Capabilities on V-22 With Spinning Rotors in Vertical Flight

GDCF and DCF3D

DCF3D is an acronym for Domain Connectivity Function in 3-Dimensions. It was written as an alternative to PEGSUS, which was the standard routine accompanying the OVERFLOW code. DCF3D organizes the input grid data into an octree data structure based on integer truncation of the 3-D floating point coordinate locations. This allows for an efficient search method to locate interpolants for grid boundary points. DCF3D uses analytic shapes to cut holes in grids. These shapes can include spheres, cylinders, planes, boxes, cones, ellipsoids, and frustrums. An accompanying code called GDCF was written to facilitate the layout of these analytic functions. GDCF provides a graphical display of the shapes so that they may be placed interactively. The GDCF program writes a namelist file, which is used as input to the DCF3D routine. The DCF3D routines have been coded into the OVERFLOW-D package. The namelist written by GDCF is included as an input when running OVERFLOW-D with moving bodies.

NORTHROP GRUMMAN

GDCF and DCF3D

- DCF3D Written as Faster Alternative to PEGSUS
- Uses Octree Data Structures to Quickly Find Neighborhood of Search Points
- Holes Are Cut Using Analytic Shape Functions
- These Shape Functions are Created Using GDCF
  - Cuts Holes Using Sphere, Cylinders, Planes, Boxes, Cones, and Frustrums
  - Allow s For Arbitrary Size and Orientation of These Shapes
  - Software Writes a Namelist File Containing Shape Parameters Used as Input to DCF3D
- DCF3D Coded as a Subroutine Call to Within OVERFLOW-D

Approach to Problem

The decision was made to model the ground effects using an inviscid (Euler) solver. It was felt that this would be capable of capturing the time dependent variations of the pressure field, without requiring an overly large model. This approach would make the best use of available computational resources. 500 CPU hours on the NAS Cray C-90 where available for this study. It was estimated that each time-accurate solution would require approximately 30 CPU hours.

The actual analysis was to be broken into three tasks. The initial task was a code validation effort. A computational comparison between static and dynamic ground effects would be made for a configuration with existing empirical data. This configuration was the XB-70, for which existed both wind tunnel and flight test data for static and dynamic ground effects. A wing/body model was deemed sufficient for capturing the majority of the controlling aerodynamic characteristics without complicating the geometry too much. Upon completion of the validation study and quantification of the code capability to predict dynamic ground effect a similar study was to be performed on a wing/body model of the TCA configuration. The TCA was to be analyzed with deflected trailing edge flaps, as this is the normal landing configuration. Finally, upon completion of the TCA study, a higher aspect ratio, conventional transport wing configuration was to be analyzed to determine the range of applicability of the code for dynamic ground effects analysis, with an eye toward accommodating any future modifications to the TCA configuration.

Approach To Problem

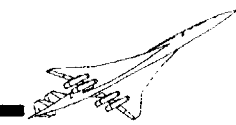

- **All Analyses To Be Run Inviscid (Euler Solver)**
  - Should Model Time Dependent Pressure Field Variations
  - Minimize Model Size to Contain CPU Usage
  - Given 500 CPU hours on NAS C-90
- **Validate Time-Accurate, Moving-Body Analysis Capability on Configuration With Available Empirical Data (XB-70)**
  - XB-70 Has Both Wind Tunnel and Flight Test Data Available for SGE and DGE
- **Model TCA Configuration**
  - Run Several Descent Rates
- **Model High Aspect Ratio Wing To Determine Range of Applicability of the Code**

NORTHROP GRUMMAN

XB-70 Analysis

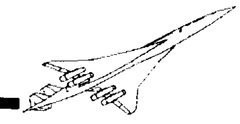

The XB-70 is a 1.75 aspect ratio delta wing configuration. The delta wing has a small break in the leading edge very near the wing apex. The leading edge sweep of the wing is 65.6°. The overall vehicle length is 194 ft with a wing span of 105.0 ft. The wing has a very small leading edge radius giving rise to leading edge vortex flow at angle of attack. The wing is a low-wing configuration, with the apex standing off from the fuselage on a boundary layer diverter. The configuration used a flapped canard for longitudinal control. This canard was not modeled in this study. The engine inlets and engines themselves were mounted under the wing. There were also omitted from this analysis. The configuration had trailing edge flaps, which were used as high lift devices, but were left undeflected for this study.

NORTHROP GRUMMAN

XB-70 Analysis

Configuration Description

- Length - 194.0 ft
- Span - 105.0 ft
- Aspect Ratio - 1.75
- Wing Planform - Delta Wing, 65.6° Sweep

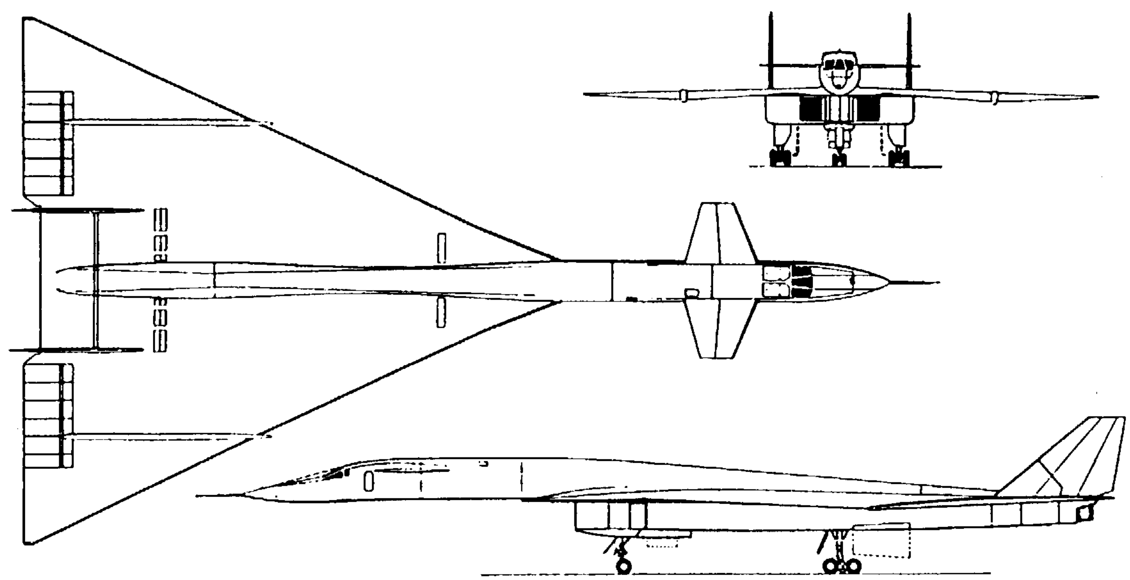

NORTHROP GRUMMAN

XB-70 Model Description

The model was created as a system of overset grids, as required by the OVERFLOW solver. The domain was decomposed into near-field body fitted grids overset into orthogonal background grids. The wing was modeled using a C-H topology, with the C direction wrapping around the wing leading edge and mapping to itself in the wake plane.

XB-70 Model Description

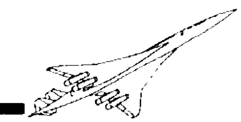

- Overset Grid Utilizing Near-Field Body and Background Grids
- Built a Wing/Body Model With Undeflected Flaps
- Used a C-H topology to Model the Wing
- 8 Blocks
  - 6 Blocks Covering the Body
  - 2 Background Grids
- 674000 Grid Points

NORTHROP GRUMMAN

XB-70 Model

Grid Scheme

The fuselage was modeled as a series of 3 grids broken into forward, mid, and aft fuselage sections. Additionally, a patch grid was used to resolve the underside wing-centerline juncture, and a collar grid was used to resolve the geometry near the wing apex/fuselage juncture. The background grid was built as a nearly orthogonal grid, with slight clustering in the streamwise, and spanwise directions to concentrate points near the vehicle. The spacing of the background grid was set in all three coordinate directions to match the outer spacing of the body fitted grids around the vehicle. This spacing in the off-body direction was 30-40 inches. This matching of spacing between connected grids allows for more continuous resolution of the flow field through the grid junctions. This spacing was carried in the vertical direction to the ground to accommodate vehicle translation from a non-dimensional height (h/b) of 1.0 to 0.2. The background grids vertical resolution increased near the ground to a spacing of approximately 10 inches. A cutting plane was placed 50 inches above the ground to keep the near field body grids from penetrating the ground.

XB-70 Model

Grid Scheme

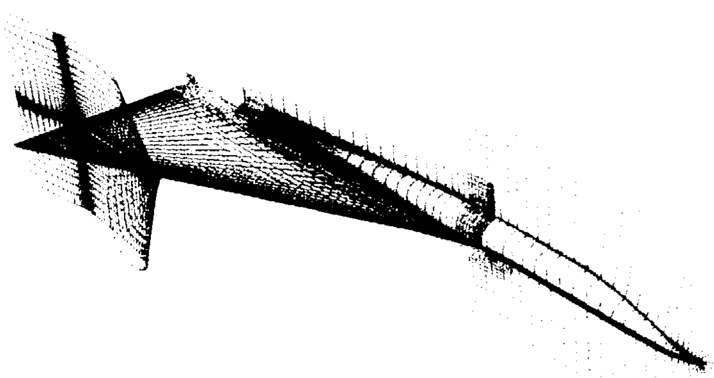

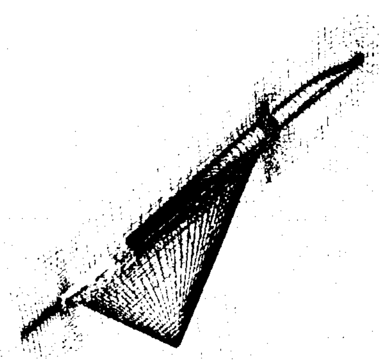

NORTHROP GRUMMAN

XB-70 Steady-State Convergence

Each of the steady state solutions required approximately 6000 iterations. The time step was limited somewhat by convergence of the wing block which required a smaller time step due to the clustering of the grid cells along the length of the sharp leading edge. Each solution required approximately 10 CPU hours on the NAS Cray C-90. All blocks converged at least three orders of magnitude. The collar grid near the wing apex was held up in converging its residual to machine zero by a few points oscillating near the stagnation point at the wing leading edge. The solution was stopped before all blocks had a residual which reached machine zero because the lift and drag coefficients had both converged to four decimal places.

XB-70 Steady-State Convergence

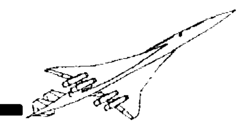

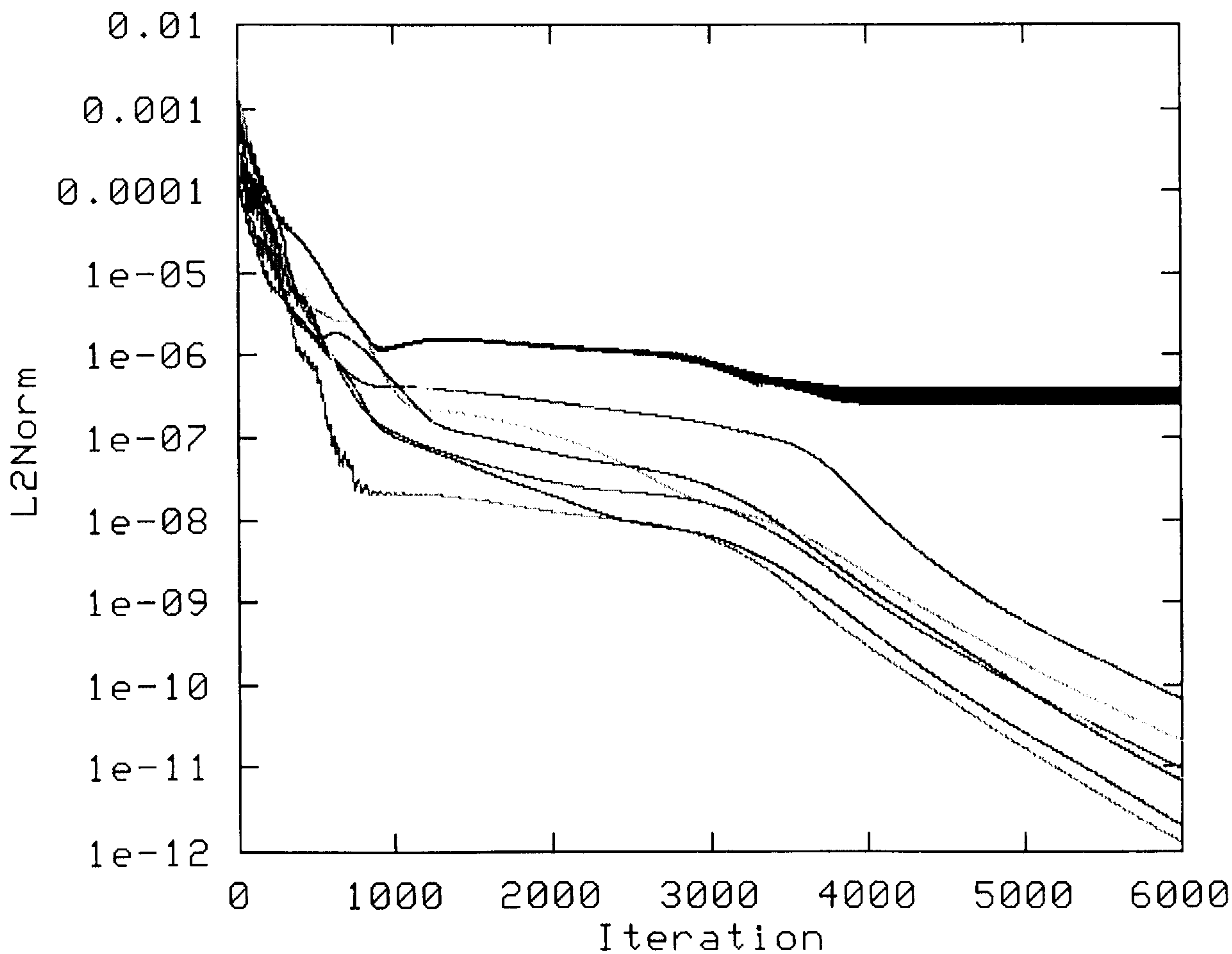

NORTHROP GRUMMAN

XB-70 Freestream Solution

The freestream solution for the XB-70 configuration at 9° angle of attack shows the upper surface of the wing dominated by the separated leading edge vortex flow. The only noticeable flow feature on the wing lower surface is the variation in wing section thickness as outlined by the pressure change on the aft portion of the lower wing.

XB-70 Freestream Solution

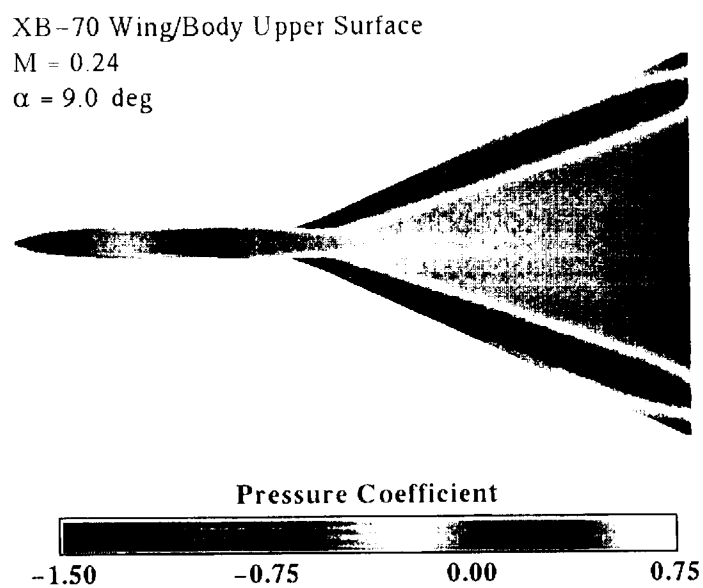

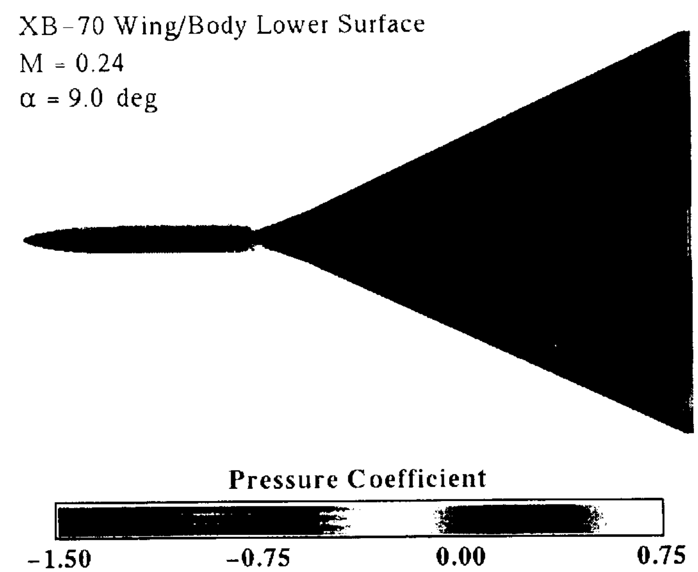

NORTHROP GRUMMAN

XB-70 Ground Pressure Plots

All of the ground height cases converged as well as the freestream condition. The pressure plots over the vehicle did not show much visibly discernable difference from the freestream pressure contours. The variation in these cases is best illustrated by the ground pressure variations. As can be seen in the plots, the high pressure footprint becomes more pronounced as the vehicle descends, and when it gets low enough (as indicated by the h/b=0.2 case) the low pressure associated with the leading edge vortex begins to become visible on the ground pressure pattern as well.

XB-70 Ground Pressure Plots

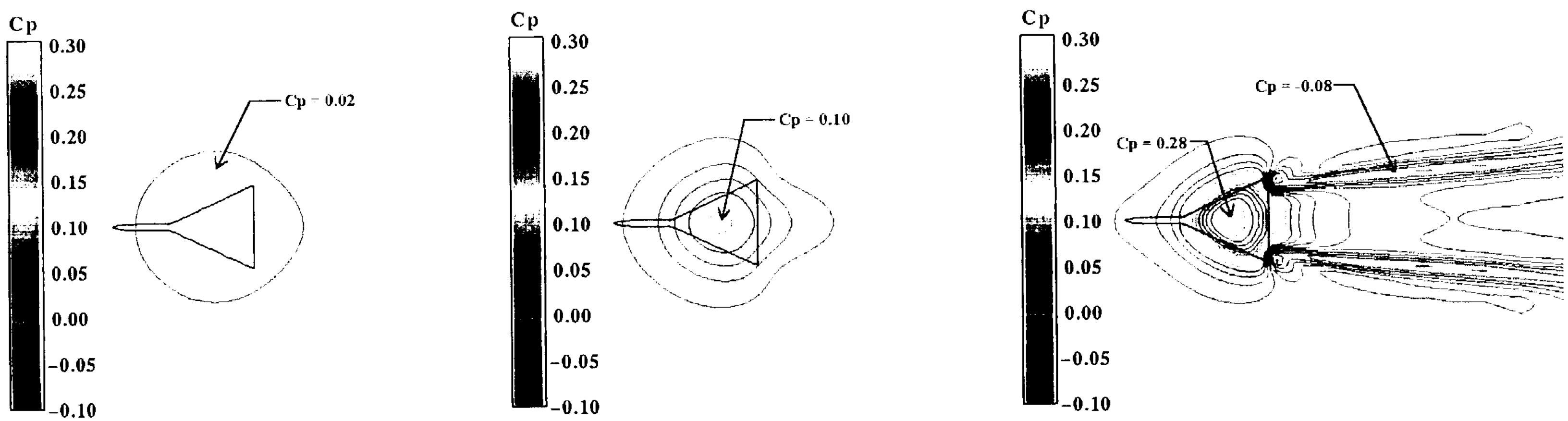

h/b=1.0 h/b=0.5 h/b=0.2

NORTHROP GRUMMAN

XB-70 Steady-State Solutions

The induced ground effects were calculated from the integrated pressure force coefficient data. The surface pressure was integrated using the FOMOCO utilities written by William Chan of NASA-Ames. The parameter called %ΔCL was calculated as

$$\%\Delta CL = (CL - CL_{Free}) / CL_{Free} * 100$$

The results from the three different ground heights was plotted against static ground effects data from a Kansas University wind tunnel test* of the XB-70 configuration. The induced lift coefficient compared well with the computational results. This was encouraging enough to proceed on to the dynamic solution.

*Lee, P.H., Lan, C.E., and Muirhead, V.U. “An Experimental Investigation of the Dynamic Ground Effect,” NASA-CR-4105, Dec. 1987.

NORTHROP GRUMMAN

XB-70 Steady State Solutions

- Solutions Obtained at M=0.24, $\alpha = 9^{o}$
- Data Compared Well With XB-70 Wind Tunnel Data From Kansas University

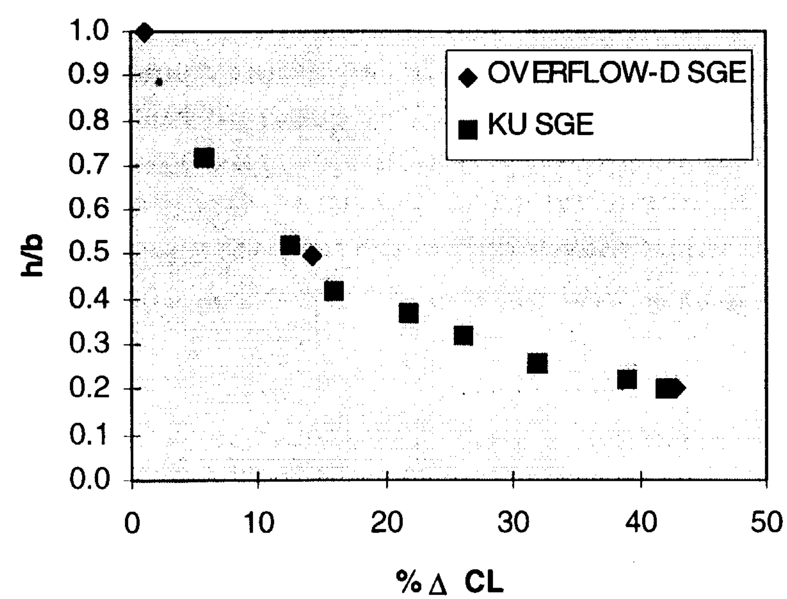

NORTHROP GRUMMAN

XB-70 Time-Accurate Solution

The time-accurate model was run at a constant descent rate of 12 ft/s. This was driven by the initial desire to run 12 ft/s and 2 ft/s on the TCA configuration. The 12 ft/s would require the least computational time, as it models the shorter duration of real time, so it was chosen. The solution was to be run at a freestream Mach number of 0.24 and angle of attack of 9°. This corresponded to an actual freestream Mach number of 0.2397 and a vehicle pitch attitude of 6.4°. The glide slope was accounted for in the application of the time-accurate boundary condition which accounts for the surface velocity and adds it to the local surface normal, to determine the actual surface tangency condition to be enforced. The solution was initialized by running the steady-state flow solver with the vehicle descending at the 12 ft/s rate, without it's vertical position being updated between iterations. After the lift and drag coefficients had converged at this condition, the time-accurate flow solver was turned on and the vehicle was allowed to descend. During the course of the solution the SIXDOF solver was replaced by a routine which prescribed the vehicle position as a function of time. The solution required approximately 19000 iterations to reach the h/b=0.2 position. The entire solution required 40 CPU hours, with 10 of the hours required to obtain the initial condition.

NORTHROP GRUMMAN

XB-70 Time-Accurate Solution

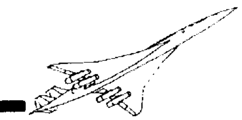

- Ran a Constant Descent Rate of 12 ft/s
- Initialized the Solution to Converged Lift Coefficient at h/b=1.0
- Then Started Time-Accurate Solution, Allowing The Vehicle to Descend
- Solution Required 30 CPU Hours on Cray C-90
- Modeled 7.25 Seconds of Real Time in 0.00036 Second Increments
  - Model Translates 0.0522 Inches At Each Time Step

NORTHROP GRUMMAN

XB-70 Time-Accurate Solution

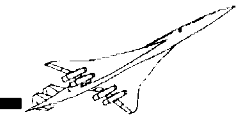

A complete flow solution and grid were saved every 100 iterations during the run. This allowed for effective post-processing of the solution file to extract the force data. After the force coefficients where calculated for each solution, the resultant values had to be rotated by the glide slope angle to maintain their proper definition. The induced lift coefficient data was plotted against the static data, and it was found the dynamic solution did produce lower induce lift values over most of the height range. There is a slight positive shift in the lift coefficient data at the h/b=1.0 condition which is not completely understood. Several potential causes of this are under investigation.

NORTHROP GRUMMAN

XB-70 Time-Accurate Solution

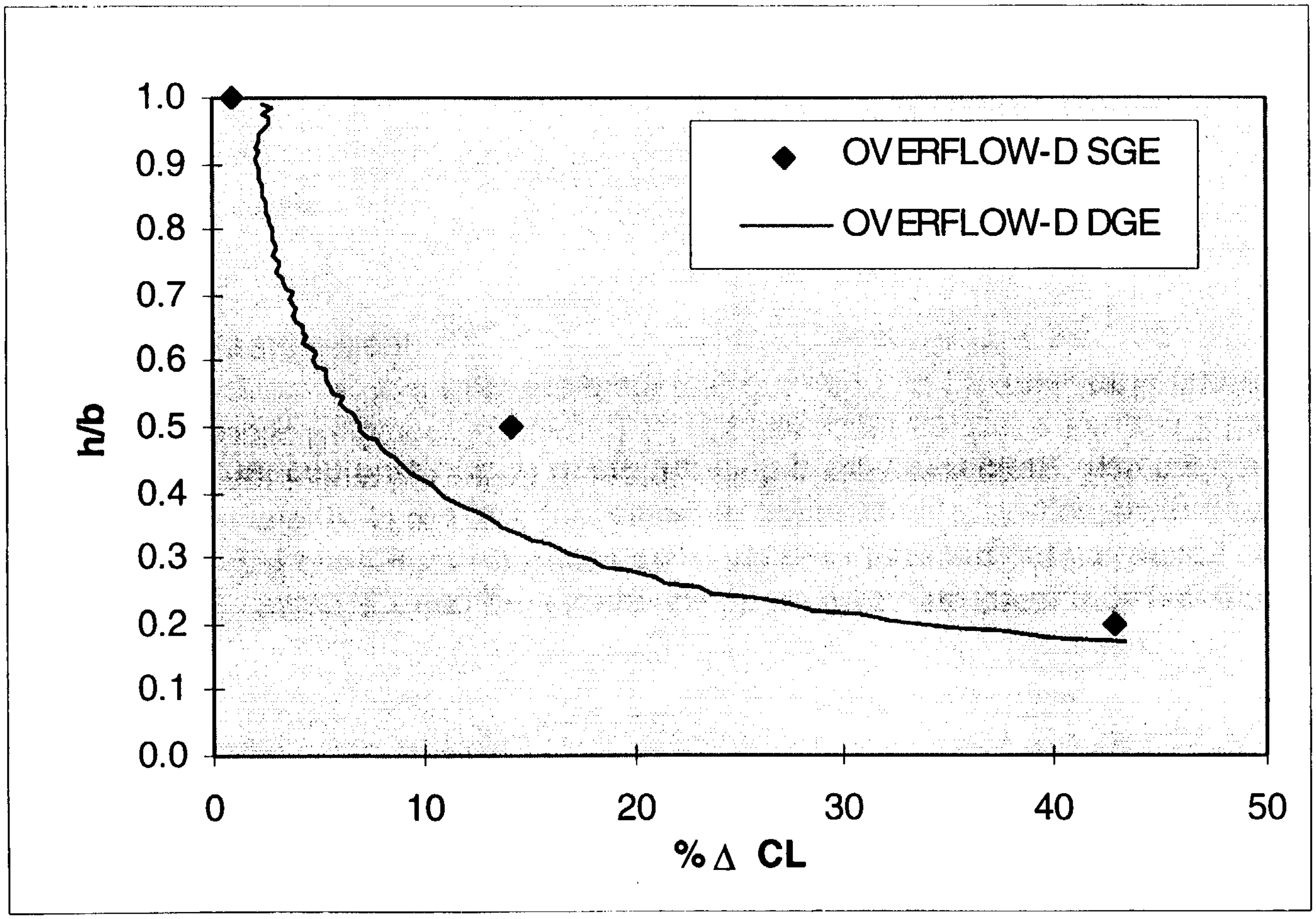

NORTHROP GRUMMAN

XB-70 Time-Accurate Solution

Comparison to Data

The dynamic ground effect data was then compared to the empirical data. For h/b values greater than 0.3, the OVERFLOW code under-predicts the amount of induced ground effect, and for values greater than 0.3, it over-predicts the induced lift coefficient. It was noted that the OVERFLOW data did not follow the same trajectory as the flight test data. The flight test data followed a nearly parabolic trajectory starting at 12 ft/s descent rate, but ending at 2 ft/s. It was decided that a trajectory closer to that of the flight test data should be analyzed computationally to provide a proper code verification.

XB-70 Time-Accurate Solution

Comparison to Data

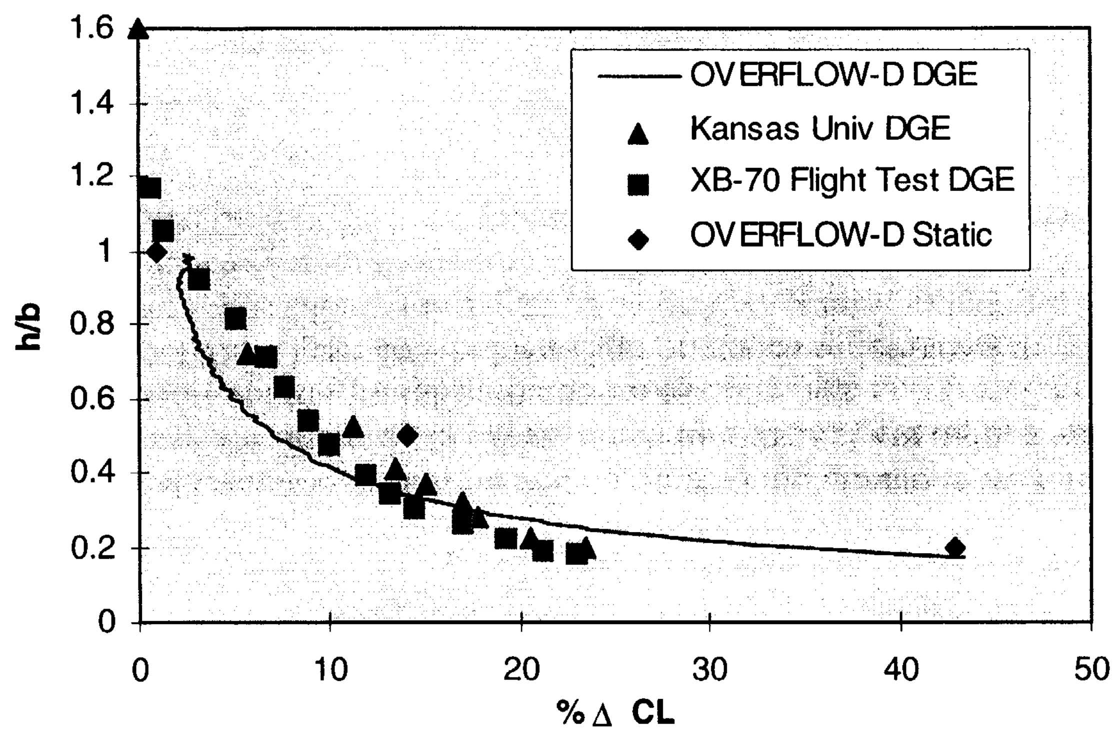

NORTHROP GRUMMAN

XB-70 DGE vs SGE

Surface Pressures at h/b=0.5

A comparison of the plotted surface pressures shows no distinguishable difference between the static and dynamic cases at the h/b=0.5 condition which had the largest difference in induced ground effects. Comparison of the ground pressure footprint shows some minor differences in the pressure coefficient contours near 0.0, but the high pressure regions match closely.

XB-70 DGE vs SGE

Surface Pressures at h/b=0.5

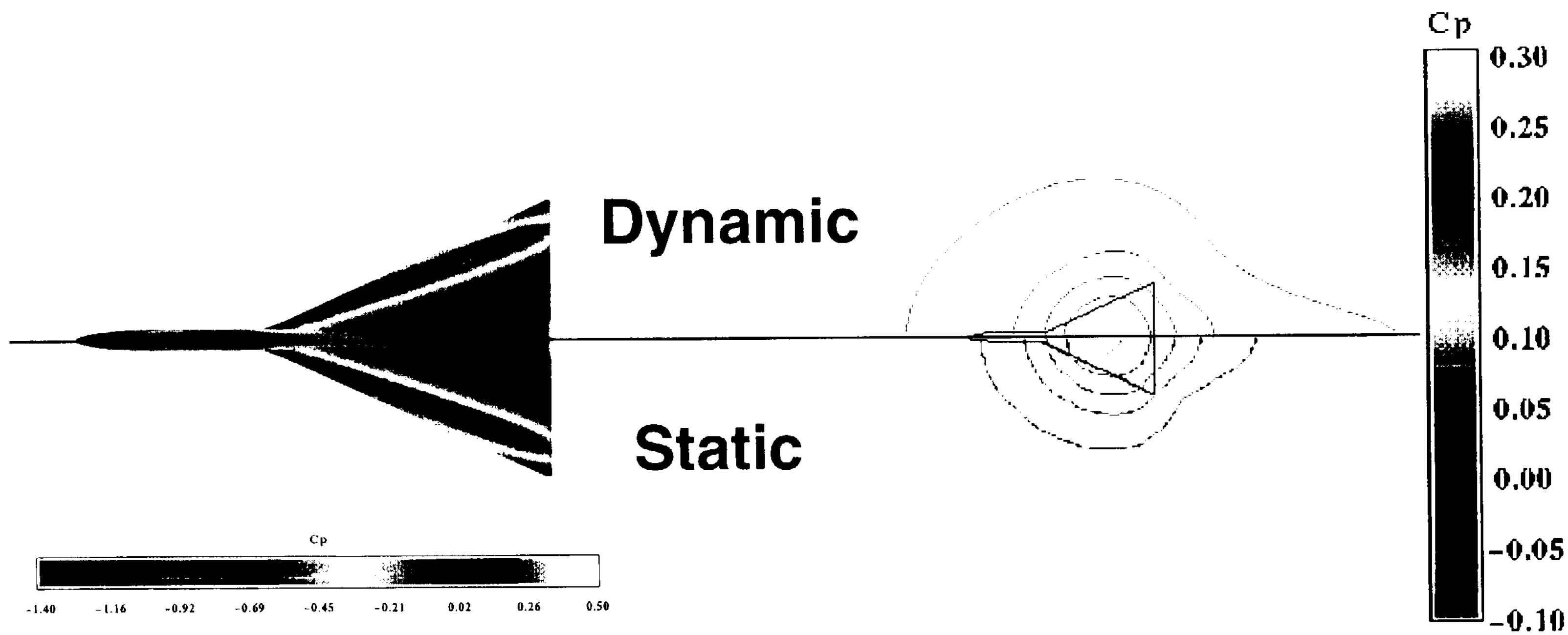

NORTHROP GRUMMAN

XB-70 Data Reduction

In post-processing the data, the major emphasis on verifying the solutions was in making comparisons of the induced ground effects. After pausing to digest the data, it was realized that the level of the lift coefficient for the freestream case was quite high compared to that expected for a wing of aspect ratio 1.75. Upon further investigation it was determined that the major source of the error was insufficient resolution of the leading edge vortex flow, causing a "smearing" of the pressure peak over a larger region of the leading edge than expected. It was decided that before proceeding, the grid should be modified to bring the lift coefficients more in line with the expected values.

XB-70 Data Reduction

- References Being Used Were All Ground Effects Papers
- All The Data Presented in The Form of $\%\Delta C_L$
- When Data Was Finally Discovered For XB-70, Found That Steady-State C_L For Free Air Was Very High (0.53 calculated vs 0.36 expected)
- Investigation Showed Insufficient Resolution of The Leading Edge Was Smearing Pressure Peak
- Decided to Modify Grid to Better Resolve Leading Edge

NORTHROP GRUMMAN

XB-70 Finer Wing Grid

It was determined that a different grid topology would provide better resolution of the wing leading edge. That topology was a "stacked-O" grid with all spanwise points collapsing to the wing vertex at the centerline, which provides good resolution for the high gradients in this region. This topology also orients the major direction of the grid lines with the major flow features of the wing, naturally providing better resolution of those features. This new topology required many more grid points to properly resolve the leading edge.

XB-70 Finer Wing Grid

- Wing Was Regridded Using a Stacked-O Topology
- New Model Was 10 Blocks, 1E6 Grid Points

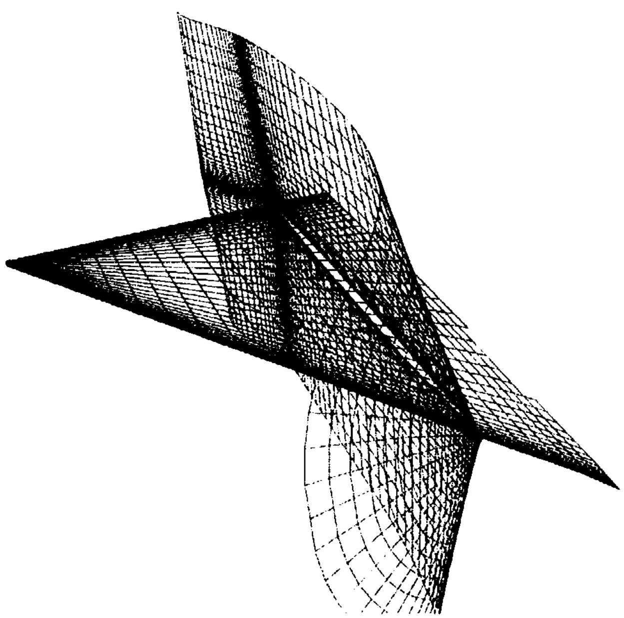

C-H Topology

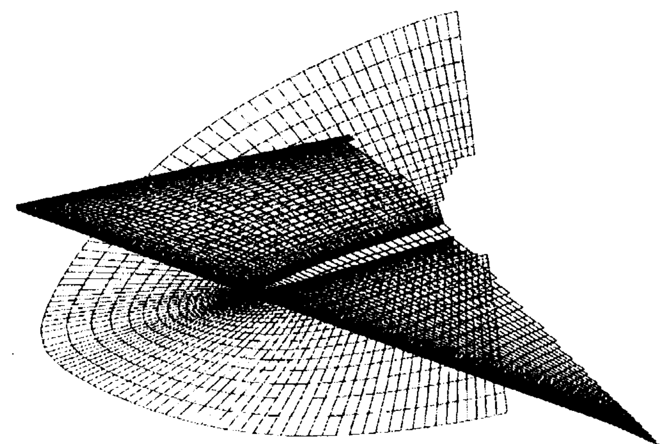

Stacked-O

NORTHROP GRUMMAN

XB-70 Second Model

The steady-state freestream condition was repeated with the resultant lift coefficient of 0.382. Additionally, the new wing grid was run alone to determine the lift curve slope prediction. The wing alone produced a lift curve slope of 0.0399 vs the predicted 0.040 for a wing of aspect ratio 1.75. This was deemed sufficiently accurate. The resultant values of static ground effect decreased the h/b=0.5 and 0.2 cases with the h/b=0.5 case showing the largest percentage change.

XB-70 Second Model

- **Repeated Steady-State Runs**

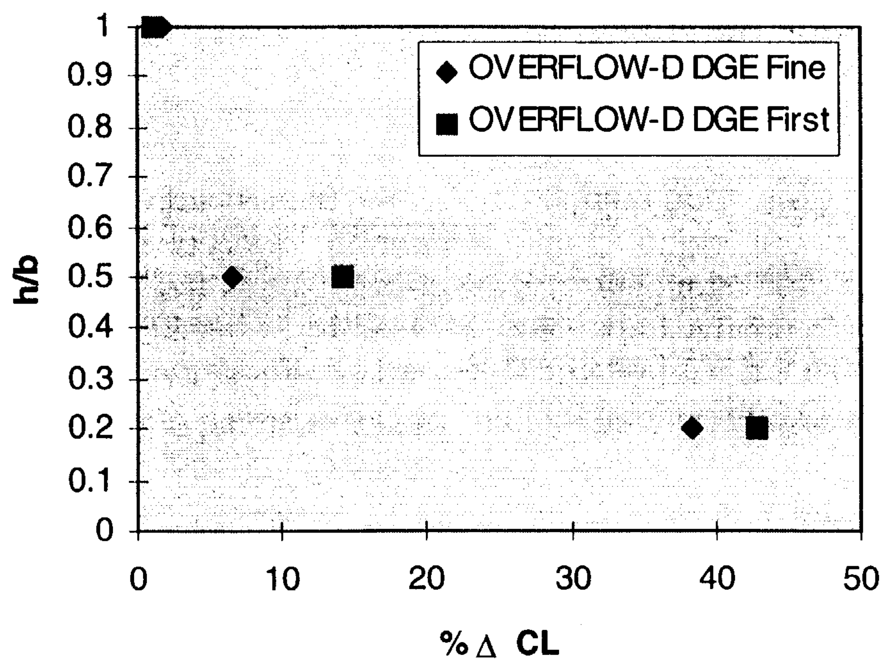

NORTHROP GRUMMAN

XB-70 Solution Comparisons

Comparison of the the solutions from the C-H grid and the stacked-O topology reveal that the stacked-O grid gives better refinement of the low pressure over the wing upper surface, and a better definition of the point of origin, which was at the wing leading edge break. Also it is noted that the finer grid predicts higher pressures over the aft portion of the upper surface, contributing to the lower integrated lift coefficient.

XB-70 Solution Comparisons

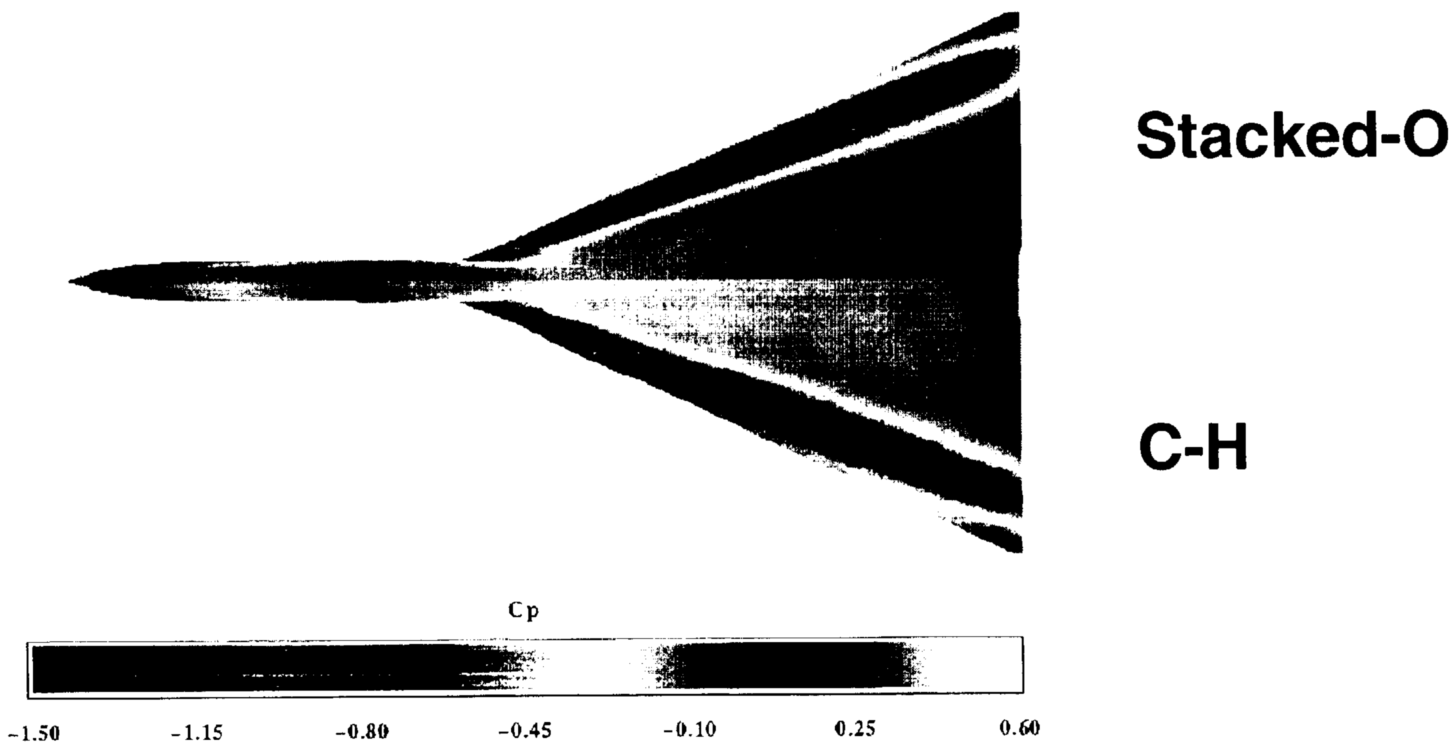

NORTHROP GRUMMAN

XB-70 Fine Model Time-Accurate

The new XB-70 model with the highly resolved wing leading edge was attempted to be run with the time-accurate solver. The solution was to follow the same trajectory as that of the flight test data. Unfortunately, the global time step was being severely limited by the small grid cells and very high gradients near the wing apex. When an allowable time step was finally determined it was calculated that the solution would require the entirety of the remaining CPU budget for the study, so the analysis was terminated in favor of continuing on to the TCA configuration.

XB-70 Fine Model Time-Accurate

- Unable to Get The Model to Run at a Reasonable Time Step
- Global Time Step Was Being Limited By The Small Cells Resolving the Leading Edge Flow
- Estimated CPU Time to Solution with An Allowable Time Step Would Use Remainder of CPU Allocation
- Decided to Move On To Solution On TCA Model

NORTHROP GRUMMAN

TCA Model Description

The TCA configuration was modeled as a wing/body configuration with deflected trailing edge flaps. The flaps were deflected to 25° to produce the same additional lift from the inviscid flow solver, as those that would be produced by a 30° deflection of the real flaps in the landing configuration. The flaps were deflected using the original HSR distributed TCA lines. The rotations were performed about the given hinge lines. The gaps created in the upper surface were filled in with conic sections providing slope continuity to both edges of the gap. The lower surfaces of the flaps were intersected at the natural line of intersection created by the deflection. The exposed edges of the flap and wing were covered with planar surfaces.

TCA Model Description

- Wing/Body Model With Deflected Trailing Edge Flaps
- Flaps Deflected 25° to Mimic Viscous Results of 30° Deflection
- Faired Upper Surface Wing Gaps With Round Surfaces (Surface Tangency at Both Gap Ends)
- Intersected Lower Surfaces
- Gridded Exposed Wing and Flap Edges

NORTHROP GRUMMAN

TCA Model Description

Continued

The grid was made of 33 blocks, broken into near-field and background grids. There were 26 near field grids and 7 background grids. The main background grid was made as an orthogonal grid with sufficient spacing in all three coordinate directions to sufficiently match those of the outer spacings of the body grids to provide smooth solution definition through the interfaces at the various ground heights to be run.

TCA Model Description

Continued

- 33 Blocks, 1.1E6 Grid Points

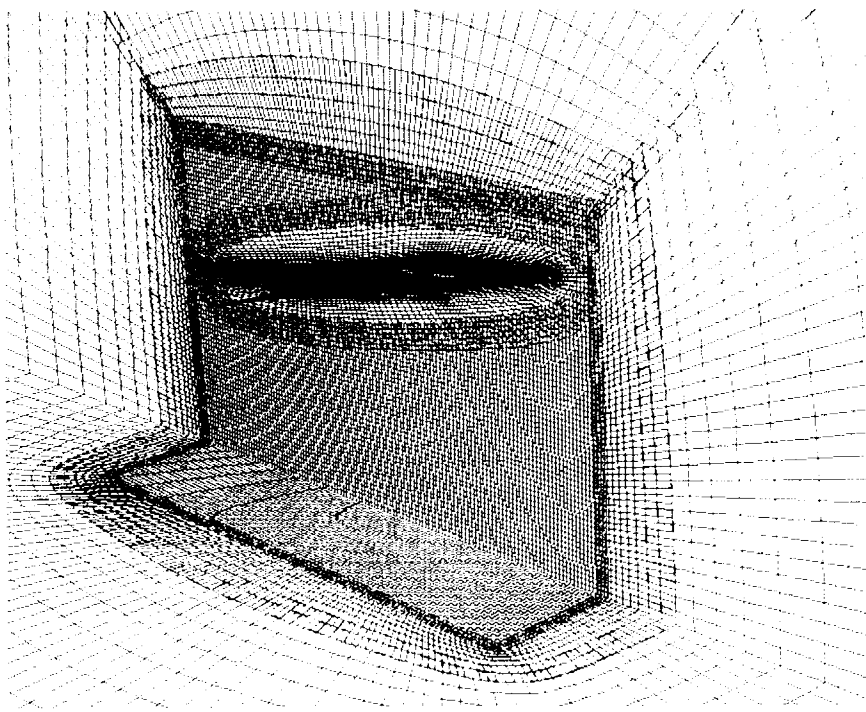

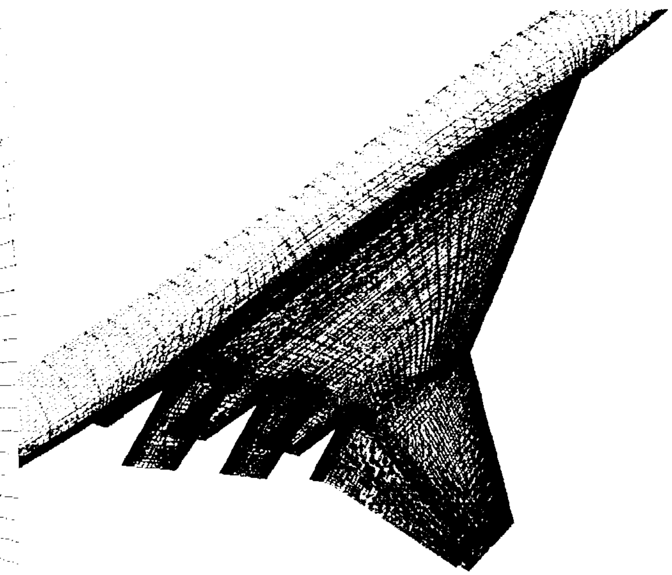

NORTHROP GRUMMAN

TCA Model - Flap Grids

The wing was gridded using a C-H topology. The C-H was used despite the lesson learned on the XB-70 because the C-H is more "point efficient" and it was felt that the rounded leading edge over the inboard portion of the wing would provide attached flow, and hence the C-H would be sufficient. Each exposed flap or wing edge had it's own grid. The flaps cut holes in the main wing grid which was gridded with undeflected flaps.

TCA Model - Flap Grids

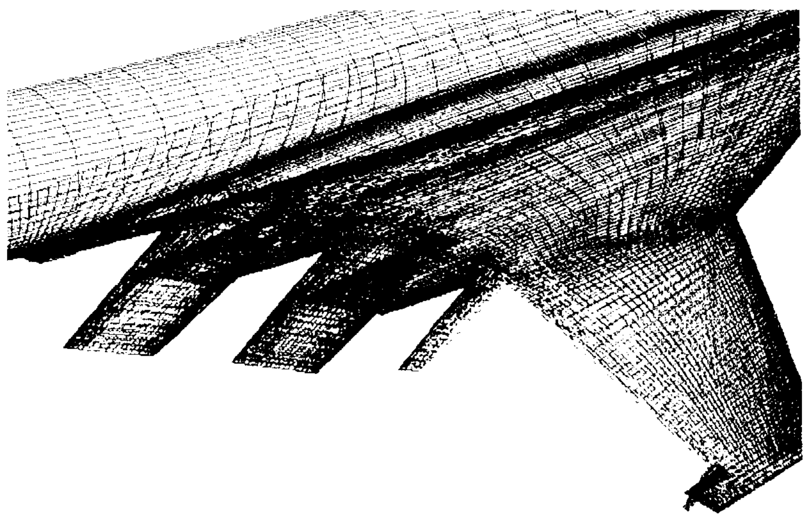

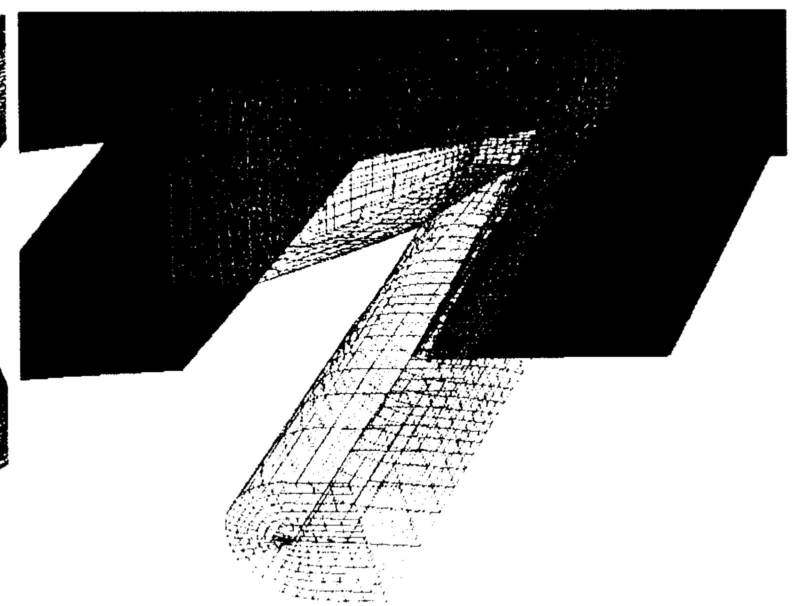

NORTHROP GRUMMAN

TCA Steady-State Solutions

The target condition for the analyses with the TCA configuration was a specified lift coefficient of 0.634. Three angles of attack were run before it was deemed that an acceptably close lift coefficient had been achieved. After the freestream angle of attack was determined the various ground heights were run statically (steady-state solver).

TCA Steady-State Solutions

- Ran Heights of Freestream and h/b=1.157, 0.657, 0.357, 0.2
- Angle of Attack Was Targeted to Give C_L=0.634
- Ended Up Using $\alpha = 11.5^{\circ}$ Which Produced Freestream C_L=0.614 And Was Deemed Usable

NORTHROP GRUMMAN

TCA Steady-State Convergence

All blocks tended to converge toward machine zero, but the solutions were terminated when the integrated lift and drag coefficients had stabilized to four decimal places. The TCA configuration was able to converge in about half the number of iterations as the XB-70 model, due to the fact that a higher minimum CFL number could be used.

NORTHROP GRUMMAN

TCA Steady-State Convergence

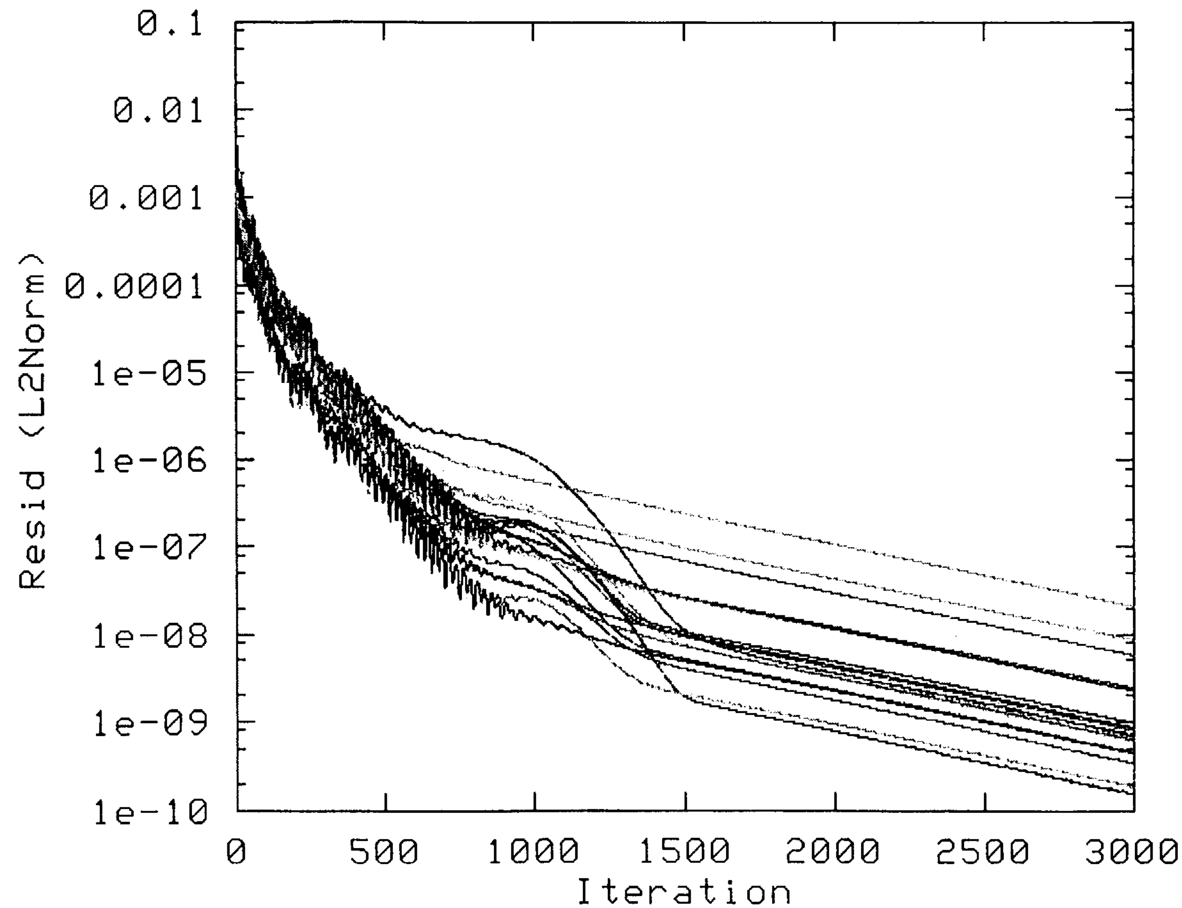

NORTHROP GRUMMAN

TCA Freestream Solution

The converged solution at α=11.2° is plotted to show pressures and flow patterns. Although this is not the final angle of attack used, it demonstrates the same salient flow features. Nearly the entire portion of the inboard wing appears to have attached flow. Only along the leading edge, just inboard of the leading edge break is there evidence of a leading edge vortex forming. Then it appears to break off of the configuration and travel over the thin outboard wing section. There is evidence of a vortex burst or wing separation over the outboard panel in seeing the upstream traveling particle trace. The inboard flaps appear to maintain attached flow, with suction peaks shown over the hinge lines.

TCA Freestream Solution

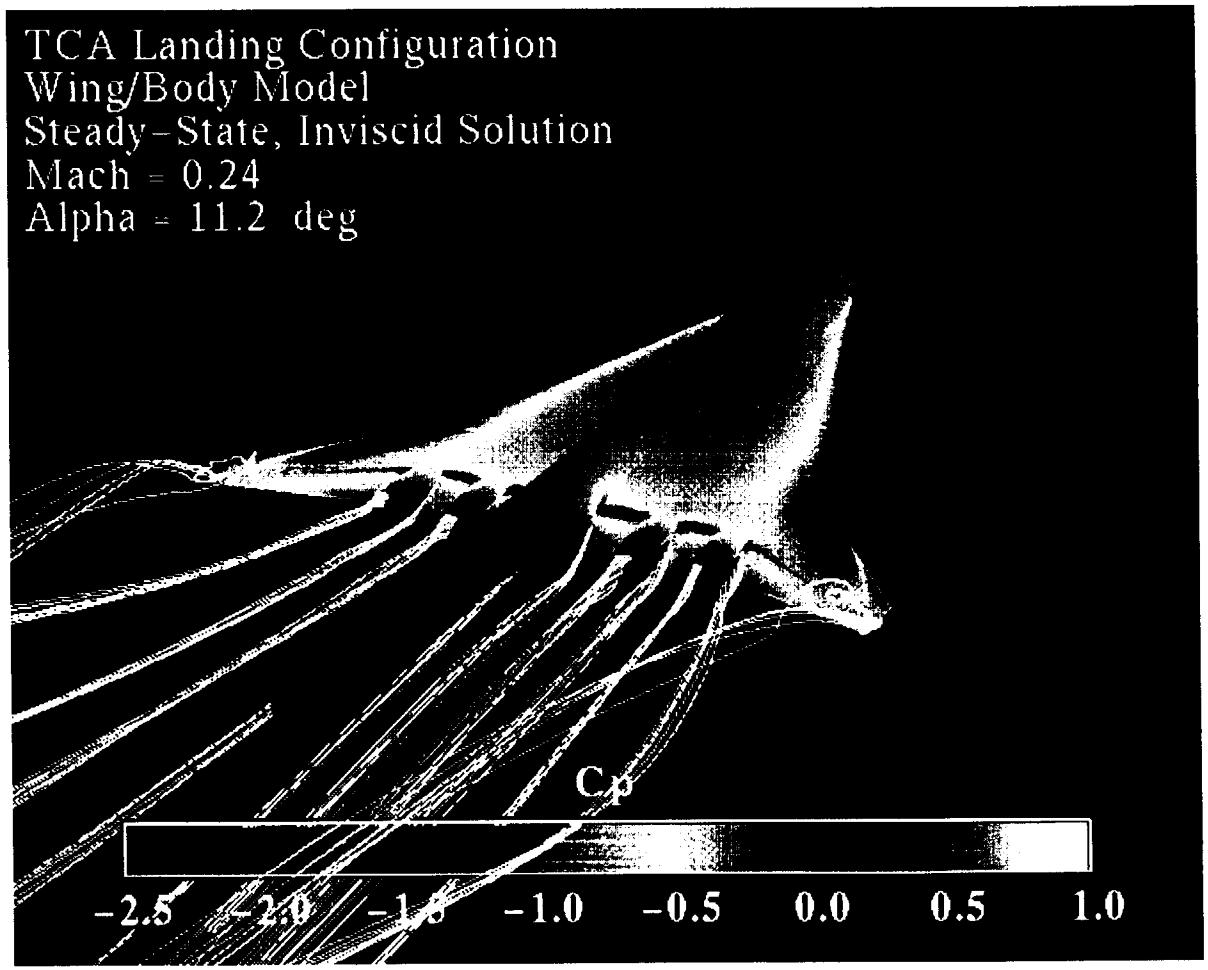

NORTHROP GRUMMAN

TCA SGE Pressure Footprints

The ground pressures show the increasing influence of the TCA configuration with decreasing height. The contours show the same character as those demonstrated by the XB-70 ground pressure patterns. Initially the high pressure field from the underside of the wing can be seen on the ground, then as the vehicle descends the low pressure region from the wing tip can be seen. It should be noted that the irregularities in the contours behind the vehicle are attributed to the block interface region. At each of the successive interfaces moving downstream the grid is coarsened by a factor of 2 to save points. This coarsening has been shown to effect local pressure patterns but not have an effect on the overall solution. To investigate this a downstream grid refinement study was performed. The grid was not coarsened behind the vehicle and the freestream solution was rerun. The integrated performance coefficients changed insignificantly.

NORTHROP GRUMMAN

TCA SGE Pressure Footprints

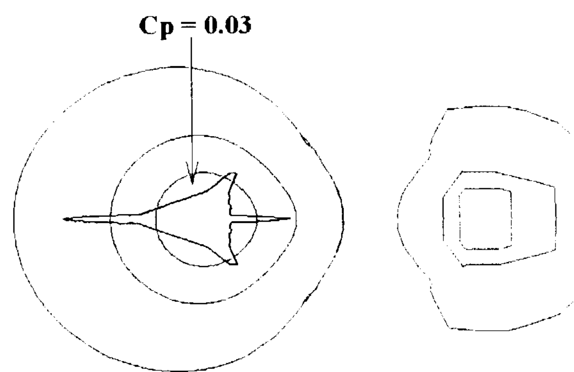

h/b=1.157

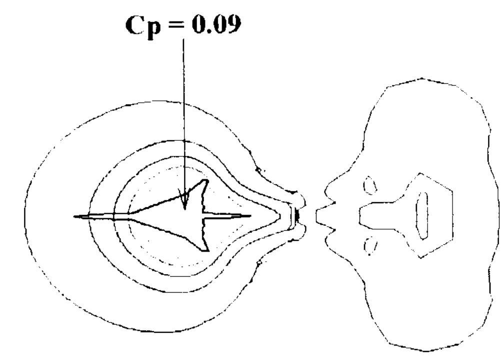

h/b=0.657

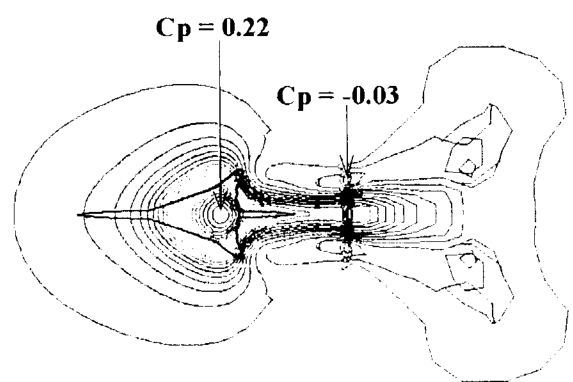

h/b=0.357

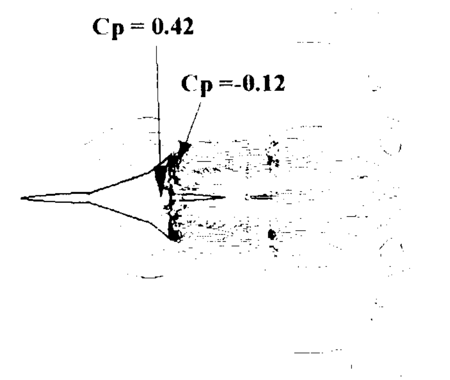

h/b=0.2

NORTHROP GRUMMAN

h/b=0.2 Ground Pressure and Traces

The next three figures show the ground pressures under the vehicle at a height of h/b=0.2. It also shows particle traces emanating from the wing leading edge, and over the flaps and flap edges. This figure shows the outward sweeping motion of traces along the ground. Only those traces very near to the centerline remain there. All others get swept up into the vortex pattern off the outer wing panel.

h/b=0.2 Ground Pressure and Traces

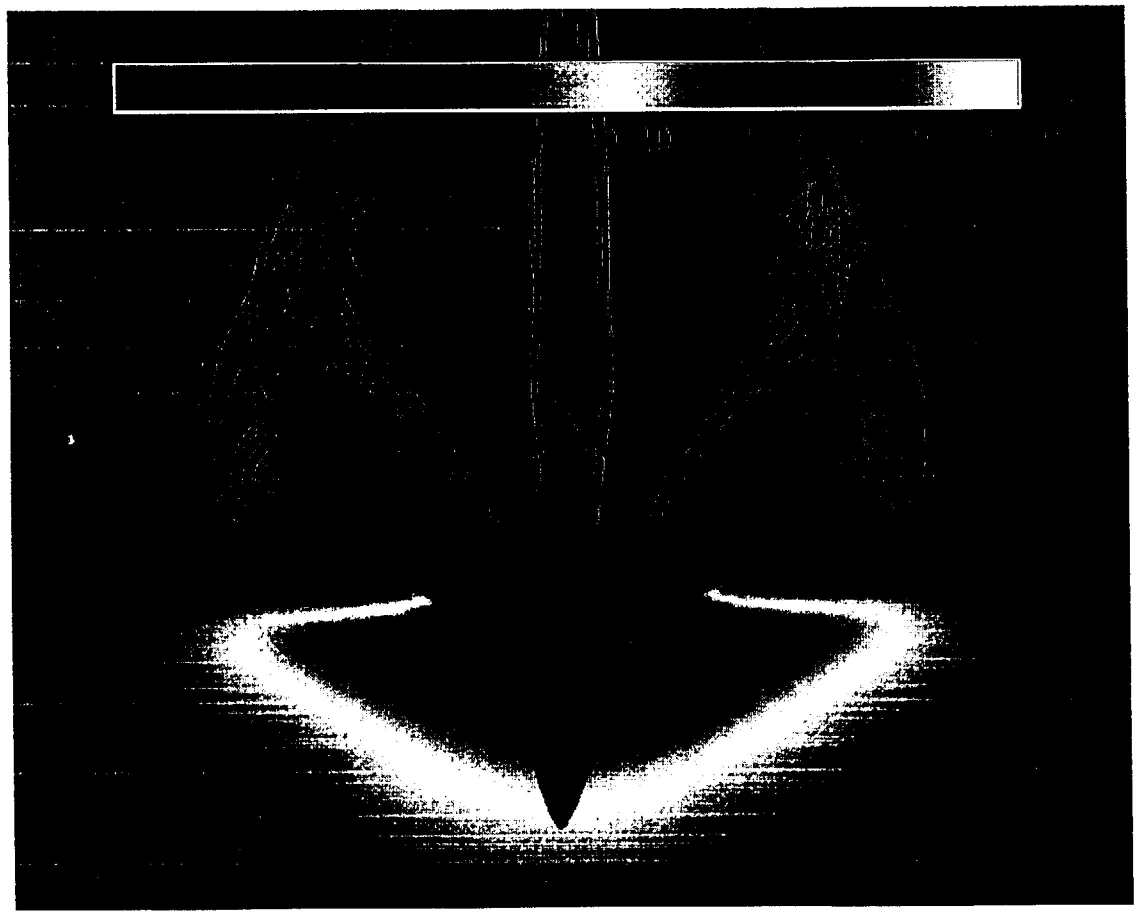

NORTHROP GRUMMAN

h/b=0.2 Ground Pressures and Traces

This figure illustrates the attached flow over the two inboard flaps. The outboard flap has attached flow only over the inboard half. The outboard half of the flap has separated flow interacting with the vortex field over the outboard panel. Also evident is the extended high pressure region downstream of the wing trailing edge created by the empennage. Finally, the irregular pressure patterns created by the deflected trailing edge flaps can be seen on the ground.

h/b=0.2 Ground Pressures and Traces

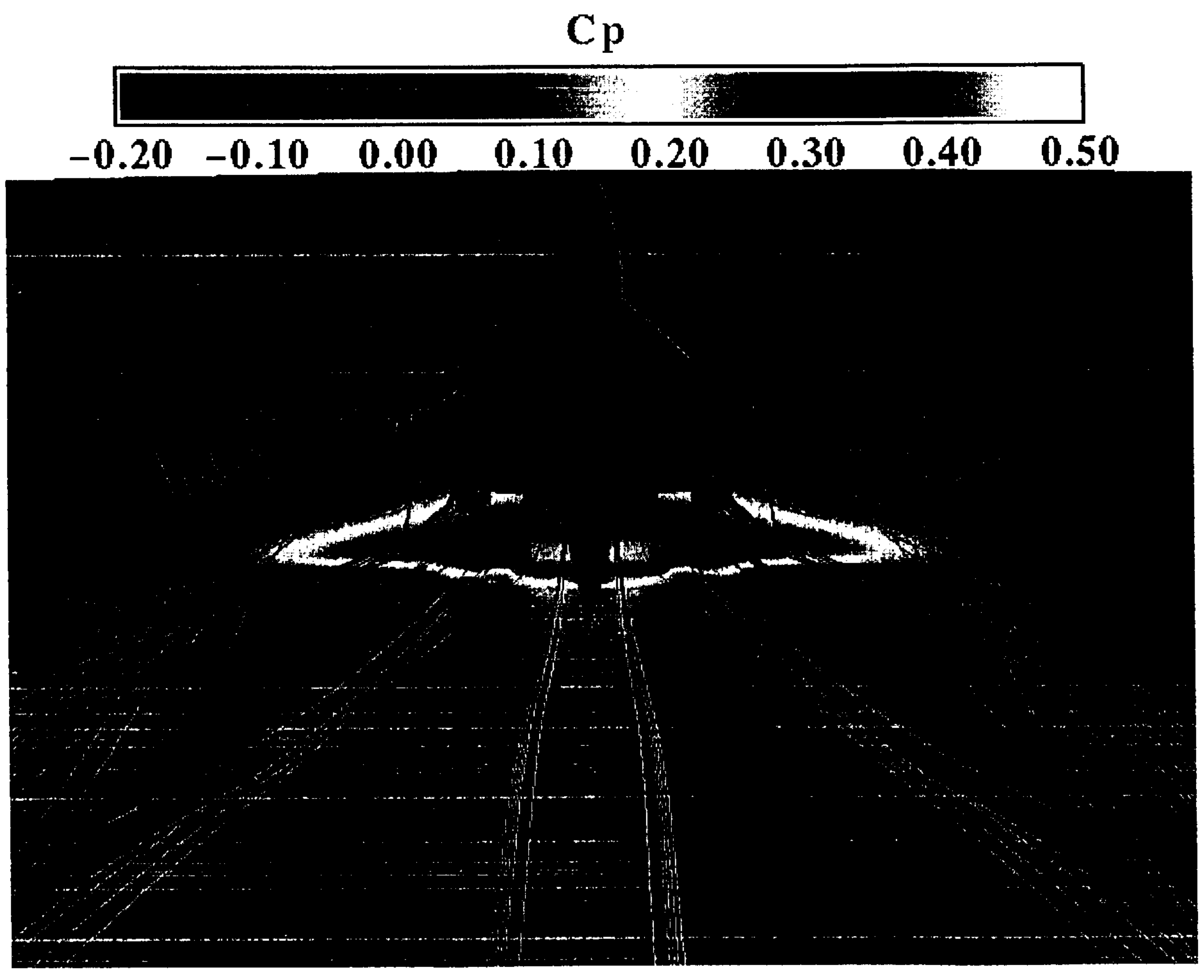

NORTHROP GRUMMAN

h/b=0.2 Wing Close-up

The wing close-up view shows the vortex flow off the wing. The entire inboard wing leading edge does not maintain fully attached flow. The leading edge vortex actually begins inboard of the break. The outer half of the outboard wing panel has separated flow, with the circulation in that region feeding into the detached leading edge vortex from the main wing panel.

h/b=0.2 Wing Close-up

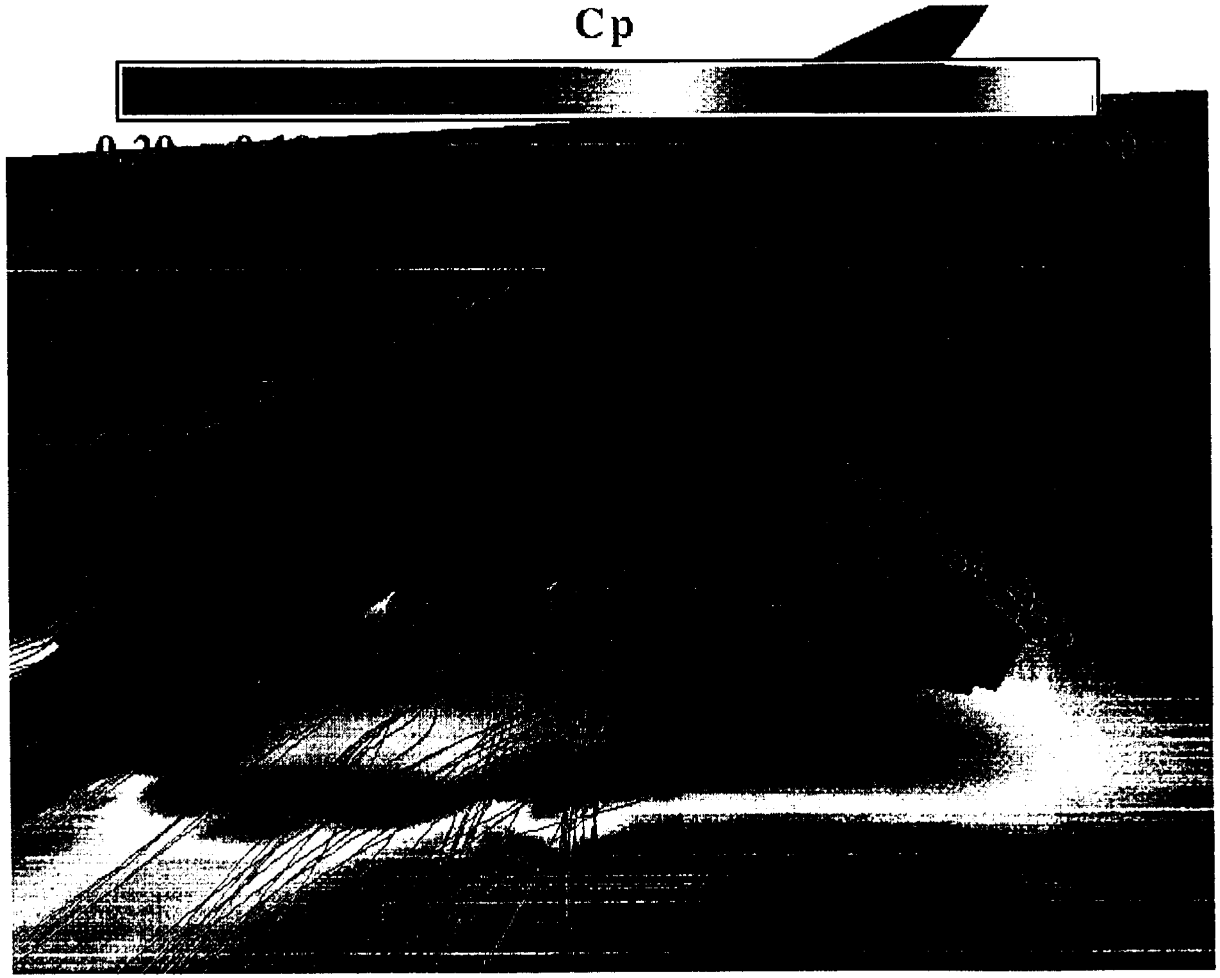

NORTHROP GRUMMAN

TCA SGE Comparisons

The static lift increment data from the OVERFLOW analysis is plotted against data from a recent HSR memo from Art Powell of Boeing-Long Beach presenting static ground effect data extracted from the recent HSR dynamic ground effects wind tunnel test. The computational results seem to agree fairly well with the experimental data, with a slight under-prediction of the induced lift at h/b=0.657.

TCA SGE Comparisons

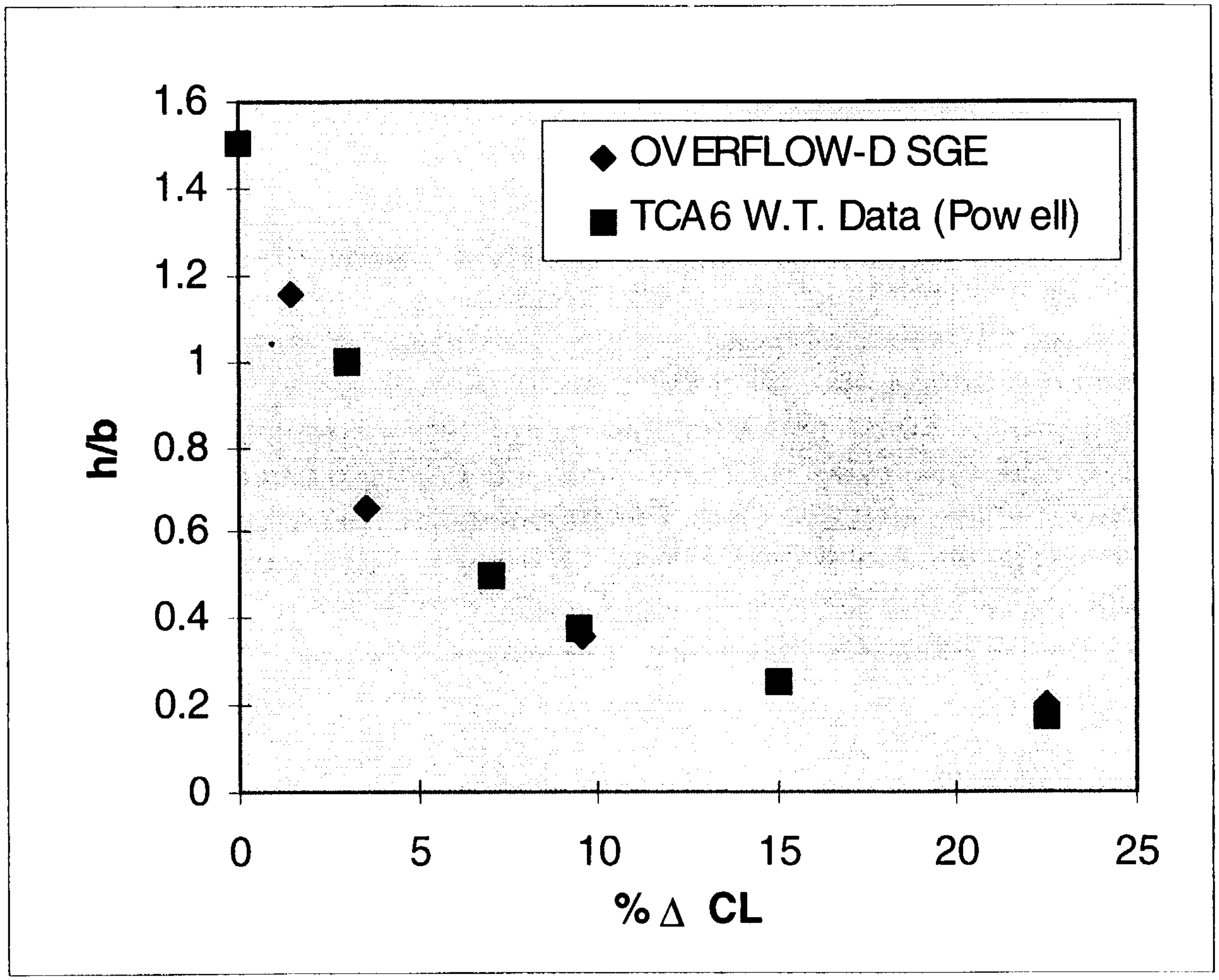

NORTHROP GRUMMAN

TCA Dynamic Solution Flight Path

A trajectory of a typical TCA landing was devised. The trajectory began with a 3° glide slope (13.8 ft/s sink rate) at h/b=1.0 and ended with a sink rate of 4 ft/s at h/b=0.17 with a parabolic profile fitted between. At each iteration when the vehicle height and velocity were adjusted the pitch attitude was also changed to maintain constant angle of attack. After beginning the dynamic descent condition an error was detected in the calculation of the vehicle ground heights. The location of the vehicle from the HSR distribution database was used as h/b=0.0 instead of the actual value of h/b=0.157. This error is what gave rise to the odd values of non-dimensional height used in this study. After the error was detected the trajectory was corrected by descending the vehicle at a constant velocity until it was back on the originally calculated trajectory, then allowed to continued it's smooth sink rate variation. Subsequently, the static case for the actual h/b=0.2 was calculated.

NORTHROP GRUMMAN

TCA Dynamic Solution Flight Path

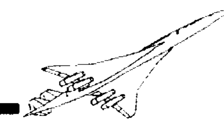

- Devised Flight Path To Start With a Glide Slope of 3° (13.8 ft/s) at h/b=1.0, and End With A Sink Rate of 4 ft/s at h/b=0.17
- After Starting The Dynamic Solution An Error Was Found in h/b Calculations
- The Trajectory Was Modified During the Run to Account For The Error
- This is The Reason For the Odd h/b Values Used. The h/b=0.2 Steady-State Case Was Run After Discovering The Error

NORTHROP GRUMMAN

TCA Dynamic Solution Flight Path

Continued

These figures show the effect on the descent and velocity profiles of the height calculation error. The descent profile most clearly shows the region where sink rate was held constant. The variation is not detectable in the plotted flight path. The flight path plot shows that 15 seconds of real time were modeled in the dynamic analysis.

TCA Dynamic Solution Flight Path

Continued

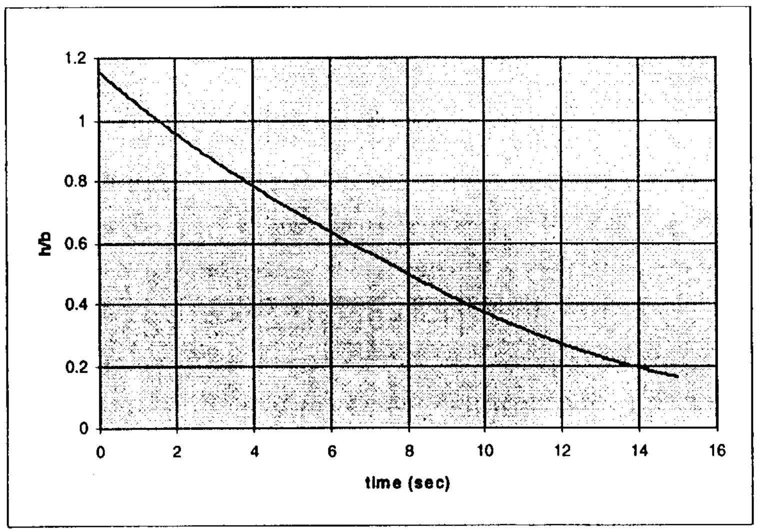

Flight Path

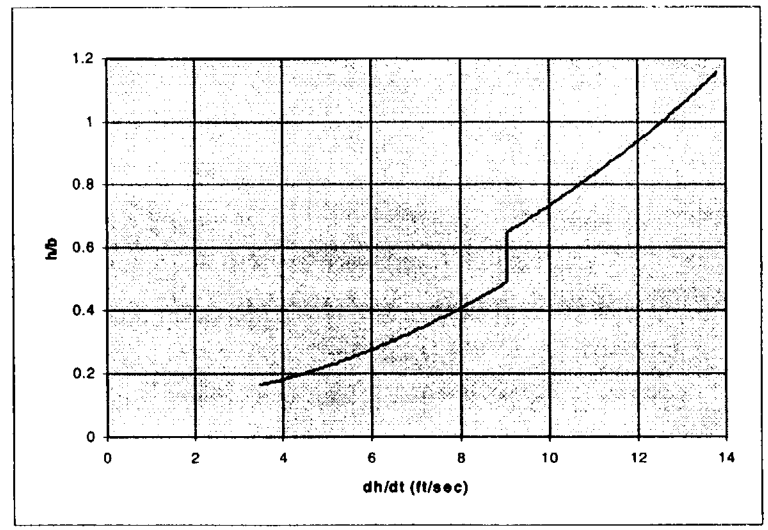

Descent Profile

NORTHROP GRUMMAN

TCA DGE Results

The dynamic solution required 58 CPU hours to complete, with 8 hours required for the initial solution and 50 hours to complete the trajectory. The solution used a real time step of 0.00069 seconds. This time step resulted in a vehicle descent of 0.114 inches/time step at the largest sink rate. The solution was initialized in the same manner as the XB-70. The steady-state solution at h/b=1.157 required 4500 iterations to achieve. The complete dynamic trajectory required 21700 iterations. The dynamic data shows very little difference from the static ground effect lift increments. In fact the dynamic increments are slightly higher at the higher ground heights due to a jump in the data just after beginning the descent. This jump is currently being investigated.

TCA DGE Results

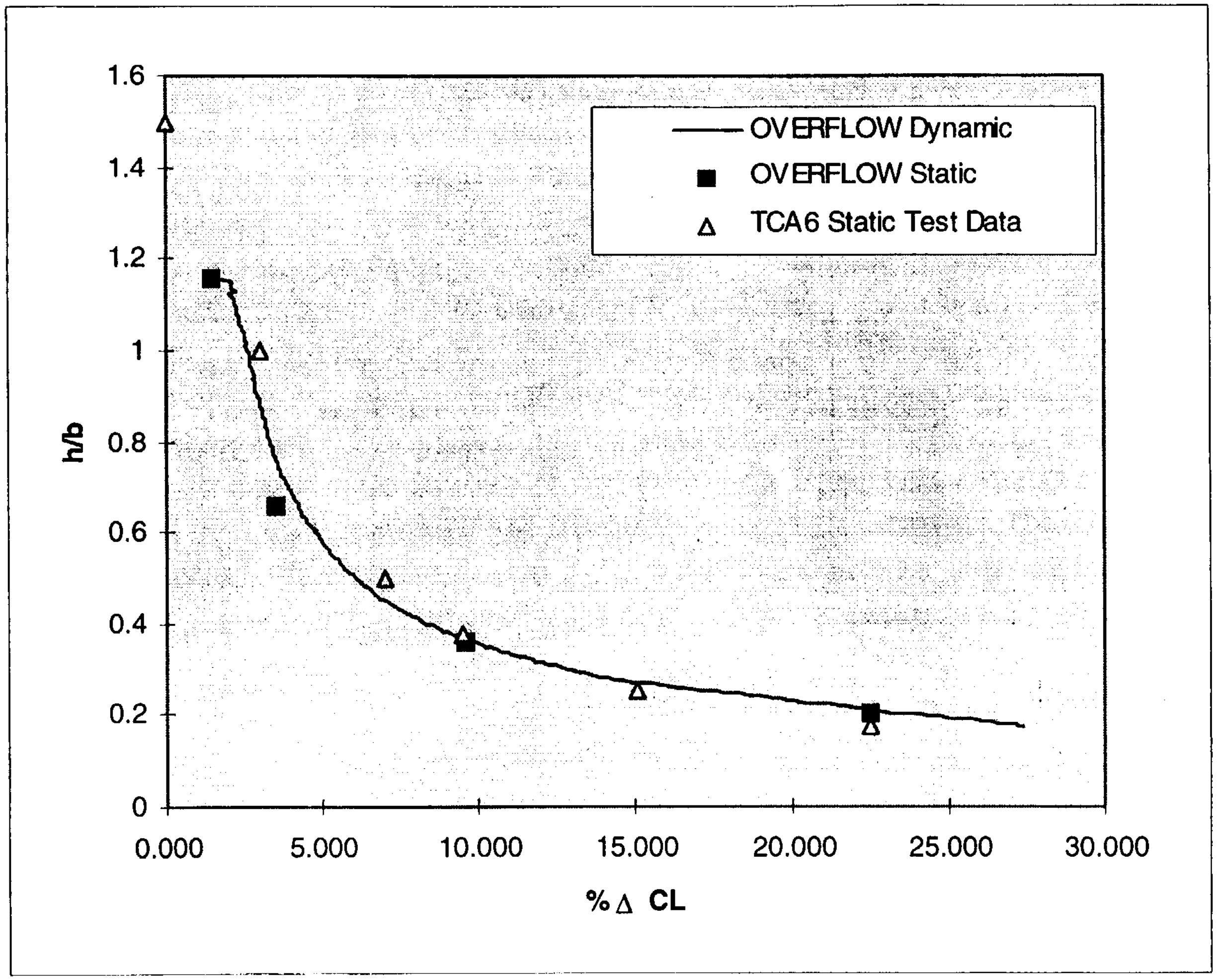

NORTHROP GRUMMAN

TCA DGE With Constant Descent

After obtaining the surprising result showing little difference between the static and dynamic cases, a constant descent rate was run. The TCA configuration was held on a constant 3° glide slope (sink rate = 13.8 ft/s) all the way to the ground. This data, surprisingly, nearly over-plotted the variable descent rate case. The results of the analyses where discussed with Bob Meakin to make sure that the analysis methodology was not flawed. It was suggested that before beginning the descent of the vehicle, the time accurate solver should be run for several hundred iterations at the constant height condition. This change was made, as well as an increase in the frequency of connectivity updates. It had been found that the TCA model required a much larger CPU expenditure to complete the DCF3D routine calls. Therefore, the frequency of connectivity updates was decreased to every 10 iterations, which would have meant a recomputation of inter-grid interpolants every 1 inch of translation, as opposed to every 0.1 inches. To address this issue, the DCF3D calls were made every iteration. The results of this computation are plotted in the figure, label as Initial Time-Acc. The only noticeable difference is that the solution did not make a discontinuous jump to the higher initial lift increment values. Instead it slowly merged with the previous analyses. The solution continued to track the previous solutions, so the analysis was stopped.

NORTHROP GRUMMAN

TCA DGE With Constant Descent

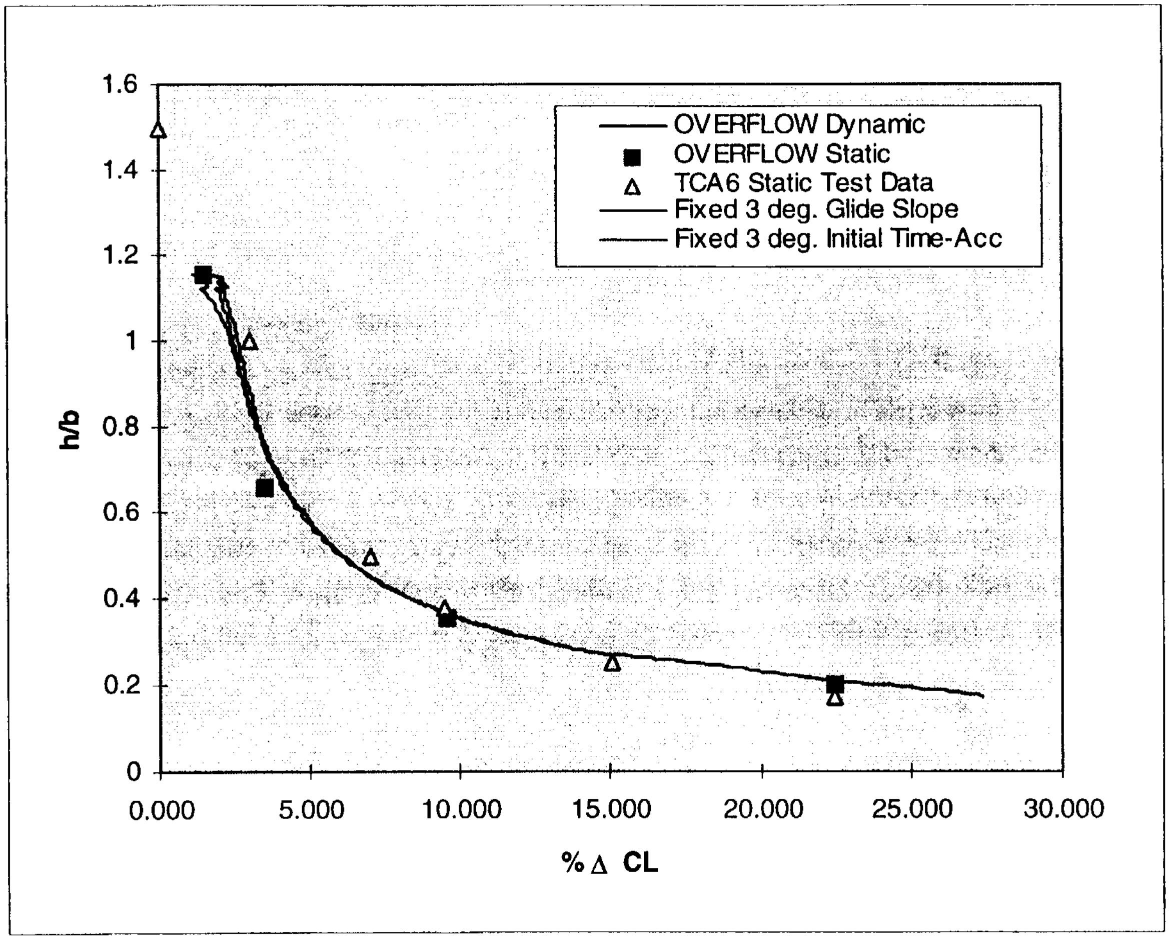

NORTHROP GRUMMAN

TCA DGE Results

The resultant increments due to ground effects on CD and Cm are shown. The drag curve resembles that of the lift curve, with the larger difference between static and dynamic largely due to the fact that the freestream value of drag provides a numerically smaller value to normalize with. The pitching moment curves show a greater disparity in the data. All of the curves show an increase in nose-down pitching moment. The most interesting point to note is the very different character of the curve exhibited by the constant descent rate case compared to the variable descent, compared to the relative similarity of the lift and drag coefficient comparisons. This point deserves further investigation.

TCA DGE Results

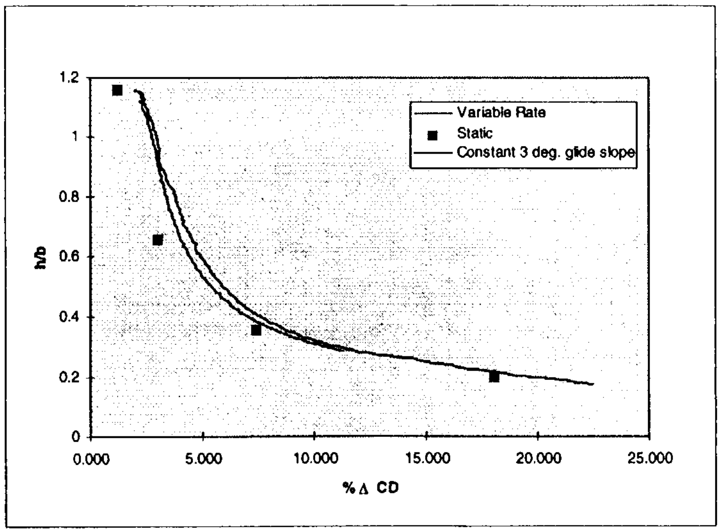

Drag Increment Comparisons

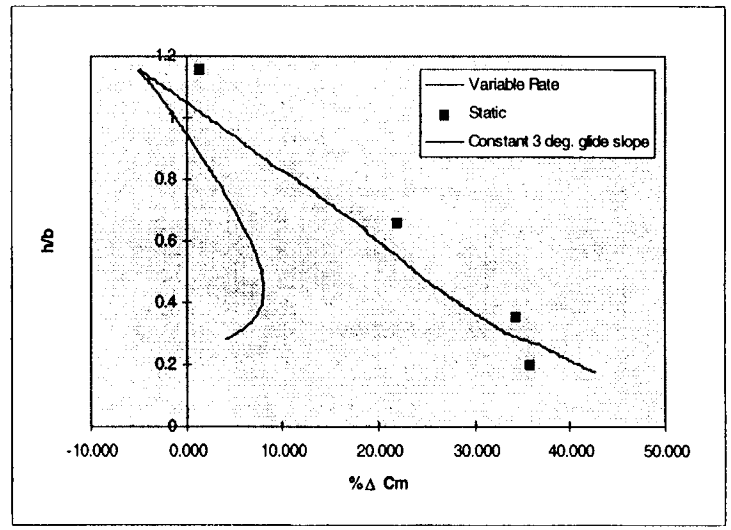

Pitching Moment Comparisons

NORTHROP GRUMMAN

DGE Current State of Affairs

This study is still in progress with several questions that need to be answered.

NORTHROP GRUMMAN

DGE Current State of Affairs

- **Questions Remain**
  - **Would a Time-Accurate Solution on the Finer XB-70 Grid Differ From the Initial Solution?**
  - **Empirical Data Suggests That Wings Dominated by Vortex Lift Show Greater Difference Between DGE and SGE**
    - The XB-70 Differs From TCA in That XB-70 Wing Flowfield is Dominated by Leading Edge Vortex, TCA Main Wing is Attached Flow
    - Does This Suggest Less Difference Between DGE and SGE for TCA?
  - **Would Better Refinement of Downstream Flow Structures Change Time-Accurate Results?**
  - **Are The DGE Characteristics Tied to Viscous Phenomena?**

NORTHROP GRUMMAN

Next Steps

A prerequisite to continuing this study is to find additional CPU time. The current CPU budget is nearly gone. All future efforts should be directed at answering the questions raised by the previous analyses.

NORTHROP GRUMMAN

Next Steps

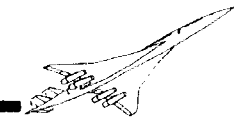

- Need More Computer Time
  - Currently Pursuing Leads
- Pursue Fine Grid, Time-Accurate XB-70 Model
  - Conclusively Demonstrate Ability to Predict DGE
- Modify Current TCA Model to Incorporate Additional Lessons Learned From Further Validation Work
- Incorporate Results From DGE Wind Tunnel Test Into Knowledge Base
- Perhaps Pursue Investigation of Vortex Lift on Simplified Models (TCA Wing With Sharp LE)

NORTHROP GRUMMAN

This page is intentionally left blank.

Recent Results in the Study of Static Ground Effect Using an Inviscid Unstructured Grid Code

Steven F. Yaros
NASA Langley Research Center

Presented in the HL ITD Team Workshop
at the Biannual Airframe Technical Review
held February 9-13, 1998 at the Westin Hotel,
Los Angeles Airport

This page is intentionally left blank.

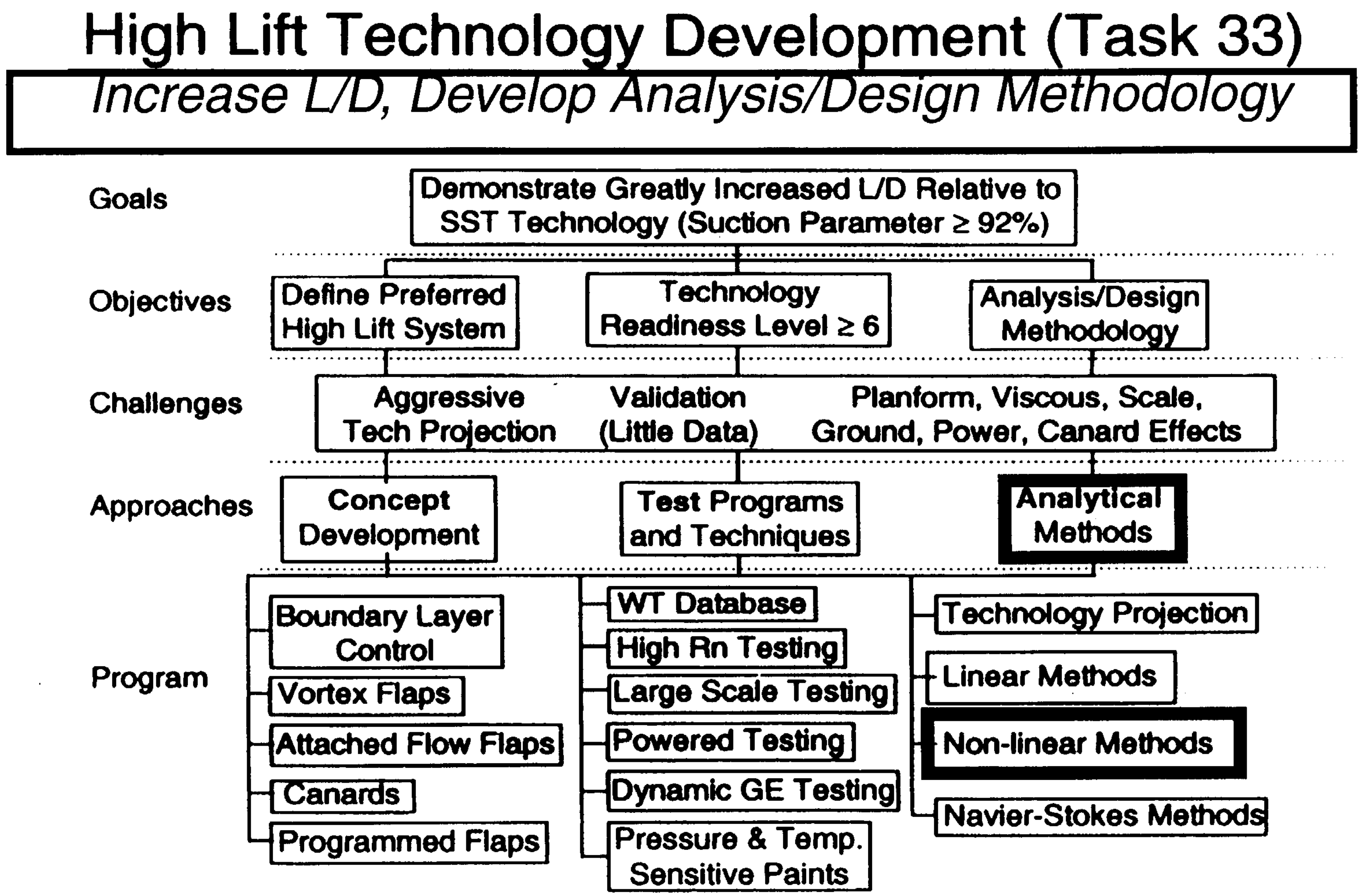
High Lift Technology Development (Task 33)
Increase L/D, Develop Analysis/Design Methodology
Goals
Demonstrate Greatly Increased L/D Relative to SST Technology (Suction Parameter ≥ 92%)
Objectives
Define Preferred High Lift System
Technology Readiness Level ≥ 6
Analysis/Design Methodology
Challenges
Aggressive Tech Projection
Validation (Little Data)
Planform, Viscous, Scale, Ground, Power, Canard Effects
Approaches
Concept Development
Test Programs and Techniques
Analytical Methods
Program
Boundary Layer Control
Vortex Flaps
Attached Flow Flaps
Canards
Programmed Flaps
WT Database
High Rn Testing
Large Scale Testing
Powered Testing
Dynamic GE Testing
Pressure & Temp. Sensitive Paints
Technology Projection
Linear Methods
Non-linear Methods
Navier-Stokes Methods

This page is intentionally left blank.

Summary

- CFD Approach - TetrUSS
- Wind Tunnel Data
- Results

The TetrUSS system, developed at NASA LaRC, enables one to take a vehicle from its surface definition to its analyzed solution. The important parts are the shape definition, accomplished in GRIDTOOL; the initial front and volume grid generation in VGRID; the flow solver USM3D, and the various ways used to post-process the computational results.

TetrUSS

Tetrahedral Unstructured Software System

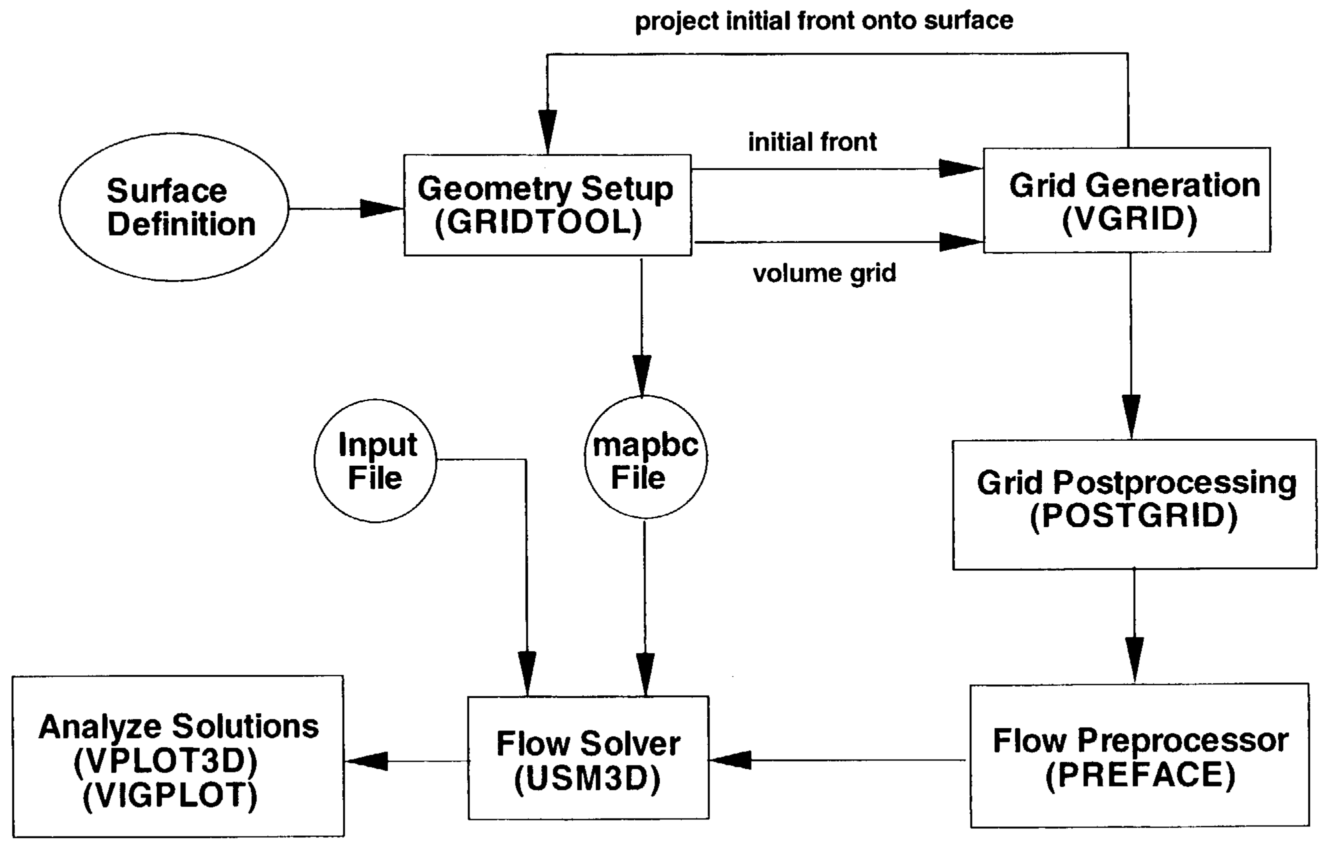

The box shown here is the semi-span representation of the NASA LaRC 14-by-22-foot Subsonic Wind Tunnel. The model is the TCA in its lowest position at an angle of attack of 8 degrees. The lines with the arrows represent a typical patch...the vehicle is composed of many smaller patches. The tetrahedra are background sources that can be used to control the size and distribution of the tetrahedra during the volume grid generation.

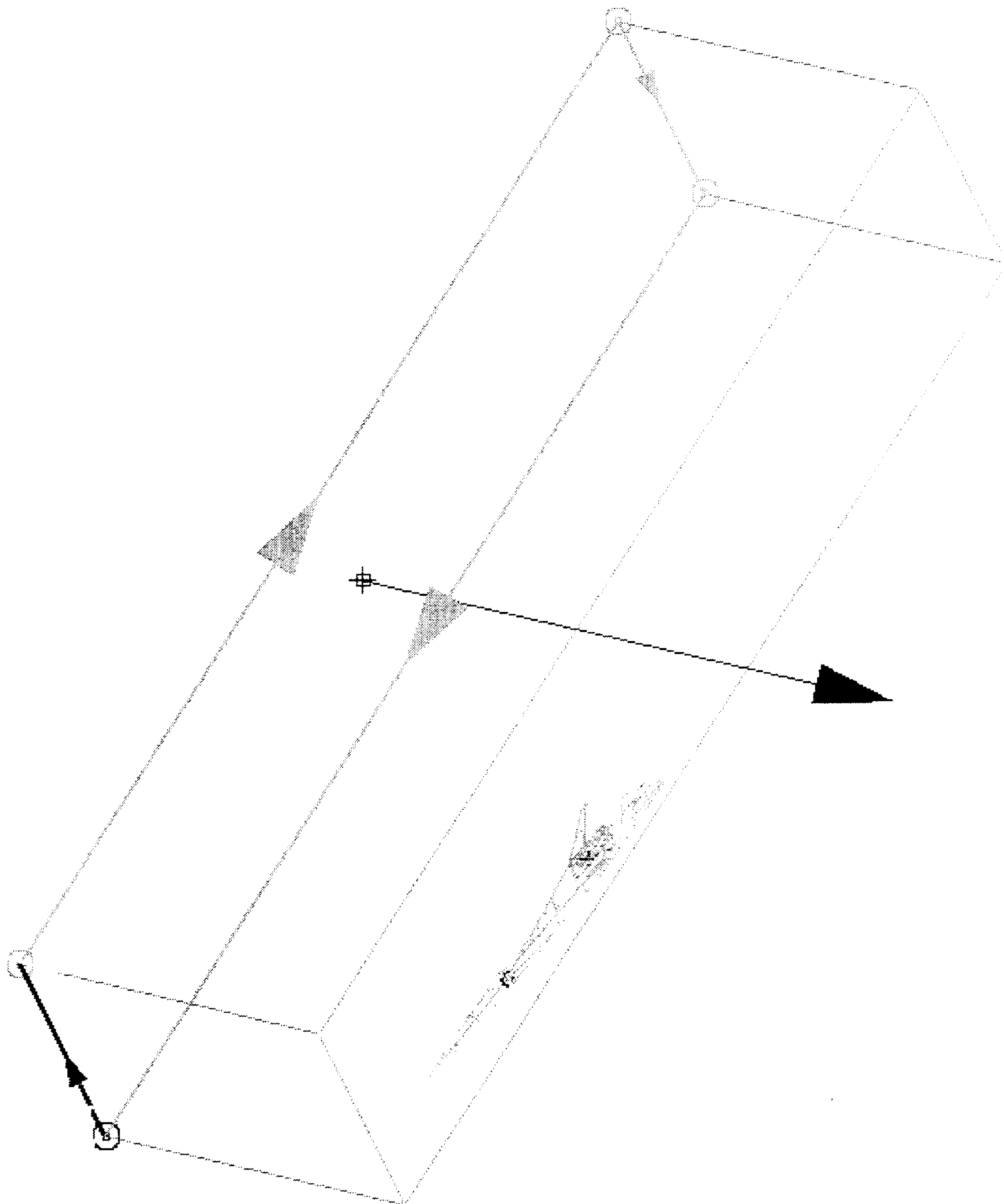

This view is a close-up of the triangulation on the plane of symmetry for the free-stream condition at an angle of attack of zero degrees. Of particular note is the fine detail of the mesh near the body, a result of the background sources specified in the initial front development. This grid distribution served as a model for emulation when other wall conditions were specified.

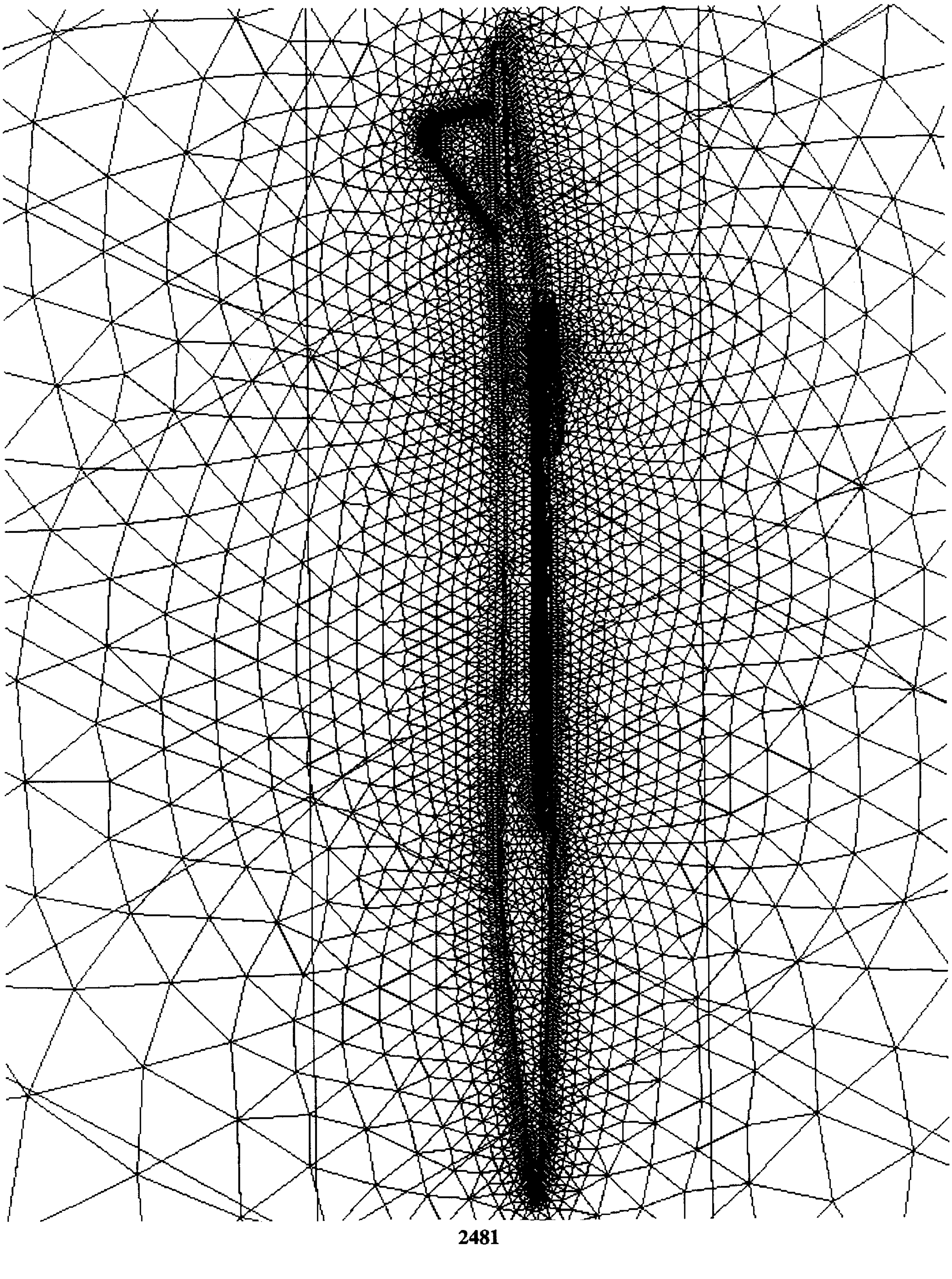

The result of running the flow solver USM3D is shown in these plots. This was one of the more difficult cases, with approximately 3000 iterations required for convergence of the solution. The varying of the CFL number in the first plot indicates the sensitivity of the convergence rate to this number. The solution was accepted after about three orders of magnitude decrease of the log of the residual.

TCA at Alpha=8 Degrees in the "Lo" Position

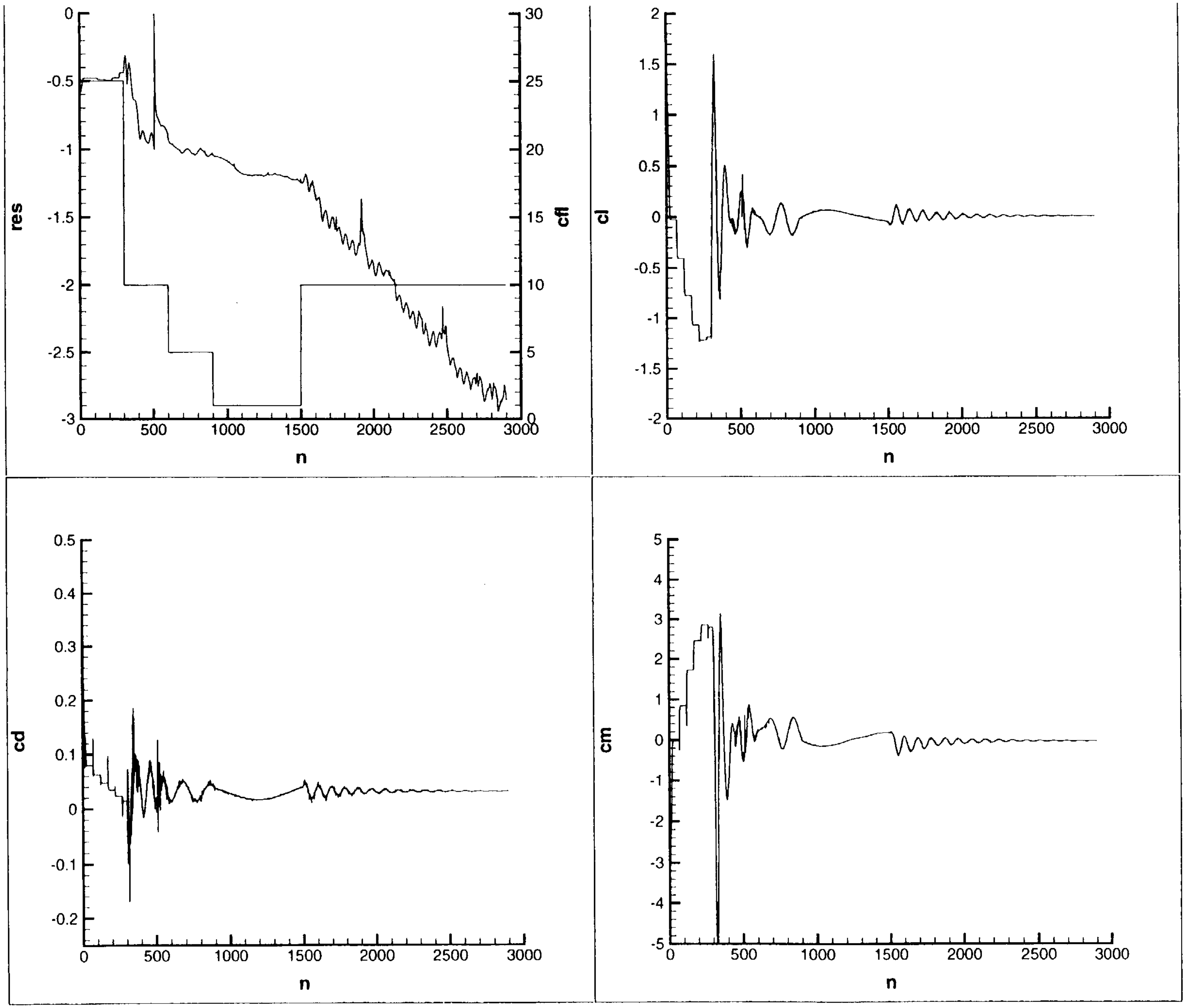

As the initial grid was shrunk from a free-stream ("big box") size to a representation of the 14-by-22 wind tunnel, an effort was made to keep the grid as stable in size as possible, especially near the vehicle. Measuring and trying to adjust tetrahedra sides proved to be inaccurate, so a method of counting cells in a given volume was adopted. It was felt that if the number of cells in the wind tunnel box approximated the number of cells in the same size box in the original "big box", the cell sizes should be reasonably similar throughout the volume. The background sources on the vehicle were not changed at all. The table shows our initial attempt to perform the above cell matching. Note the relative insensitiviy of the coefficients even though the cell sizes did vary. Note also the devastating result of removing an innocuous side source on the number of cells in the volume.

Initial Grid Study Summary 17Jan98

Grid ID Description	Comments	Z max Z min Y max	BG source size	Total number of cells	Approx. cell edge size	Comments	C_L C_D C_M
TCA-17 "Big Box" Centered	Arbitrary large free stream grid	10251 -10251 10251	3000 3000 3000	751315	0.6-0.8	There are 743976 to 746014 cells in the WT Box volume	0.1171 0.01189 -0.2610
TCA-18 "WT Box" High pos.	Source size linearly adjusted	2136.6 -1343.4 2610	625 393 764	737608	0.6	Edge size too small	0.1208 0.01159 -0.2692
TCA-19 "WT Box" High pos.	Source size increased 50%	2136.6 -1343.4 2610	937.5 589.5 1146	390337	0.7	Bigger edge size, but loss of definition near A/C	0.1210 0.01211 -0.2694
TCA-20 "WT Box" High pos.	Side source value back to 764	2136.6 -1343.4 2610	937.5 589.5 764	582046	0.6-0.8	Definition regained near A/C	0.1208 0.01185 -0.2691
TCA-21 "WT Box" High pos.	Side source removed	2136.6 -1343.4 2610	937.5 589.5 XXX	>>1.4M	XXXX	Grid not completed, as there were indications the number of cells would be huge	XXXX

This page and the next show the trial-and-error procedure used to determine the source sizes for the model in its highest position in the wind tunnel. The "RWT" nomenclature indicates a refinement of the wind tunnel box, in that the length of the test section and the position of the model were modified to match the 14-by-22 foot wind tunnel exactly.

“Real Wind Tunnel” High-Position Grid Study Summary, 23Jan98

Grid ID Description	Comments	X range Y range Z range	BG source size	Approx. cell edge size	Comments	C_L C_D C_M
TCA-17 “Big Box” Centered	Arbitrary large free stream grid.	-10251,0,10251 -10251,10251,10251 -10251,0,-10251 -10251,10251,-10251 10251,0,10251 10251,10251,10251 10251,0,-10251 10251,10251,-10251 2295.22,10251,171.417	3000 3000 3000 3000 3000 3000 3000 3000 3000	0.6-0.8	There are 751315 cells total and 743849 to 745790 cells in the RWT-hi volume.	0.1171 0.01189 -0.2610
TCA-22 “RWT Box” High pos.	Source size linearly adjusted according to distance from A/C rotation point.	-1476.94,0,2136.6 -1476.94,2610,2136.6 -1476.94,0,-1343.4 -1476.94,2610,-1343.4 10523.06,0,2136.6 10523.06,2610,2136.6 10523.06,0,-1343.4 10523.06,2610,-1343.4 2295.22,10251,171.417	860 828 809 794 1789 1525 1737 1492 765	1.0-1.2	174607 cells total in the RWT-hi volume. Need to decrease the size of the BG sources.	0.1184 0.01413 -0.2633
TCA-23 “RWT Box” High pos.	Source size decreased by factor of 2 from TCA-22.	Same as TCA-22.	Half TCA-22	0.6-0.7	472950 cells. Need to make the source sizes still smaller.	0.1207 0.01218 -0.2689
TCA-24 “RWT Box” High pos.	Source size decreased by factor of 3 from TCA-22.	Same as TCA-22.	1/3 TCA-22	0.5	920680 cells. Need something between this case and TCA-23.	0.1207 0.01170 -0.2691

This page is intentionally left blank.

Grid ID Description	Comments	X range Y range Z range	BG source size	Approx. cell edge size	Comments	C_L C_D C_M
TCA-25 "RWT Box" High pos.	Source size decreased by factor of 2.65 from TCA-22.	Same as TCA-22.	1/ 2.65 TCA -22	0.6	745844 cells. This is close to the number (743849 to 745790) in RWT-hi volume.	0.1205 0.01183 -0.2685

This page and the next summarize the same procedure for the model at an angle of attack of zero in its lowest position. The thought occurred that it would be better to increase the resolution of the grid underneath the model near the wall in anticipation of aggravated flow in that area, but it was decided to go with the original cell-counting criterion at this time. A short side study will be done to look at the effect of refining the grid.

"Real Wind Tunnel" Low-Position Grid Study Summary 26Jan98

Grid ID Description	Comments	X range Y range Z range	BG source size	Approx. cell edge size	Comments	C_L C_D C_M
TCA-17 "Big Box" Centered	Arbitrary large free stream grid.	-10251,0,10251 -10251,10251,10251 -10251,0,-10251 -10251,10251,-10251 10251,0,10251 10251,10251,10251 10251,0,-10251 10251,10251,-10251 2295.22,10251,171.417	3000 3000 3000 3000 3000 3000 3000 3000 3000	0.6-0.8	There are 751315 cells total and 710471 to 719847 cells in the RWT-lo volume.	0.1171 0.01189 -0.2610
TCA-26 "RWT Box", model in Low position	Source size linearly adjusted from the "successful" high-position case, TCA-25.	-1476.94,0,3422.8 -1476.94,2610,3422.8 -1476.94,0,-57.2 -1476.94,2610,-57.2 10523.06,0,3422.8 10523.06,2610,3422.8 10523.06,0,-57.2 10523.06,2610,-57.2 2295.22,10251,171.417	543 521 54 53 1127 960 115 99 289	0.55	There are 1045078 cells in this grid, about 50% "too many" compared to the number of points in the TCA-17 reference box above.	0.1401 0.00991 -0.3149
TCA-27 "RWT Box", model in Low position	Increase source sizes by 50% from their TCA-26 values.	Same as TCA-26.	3/2 TCA-26	0.65-0.8	544932 cells. Need to interpolate between this case and TCA-26 to get approximately 715000 cells.	0.1407 0.01030 -0.3158

This page is intentionally left blank.

Grid ID Description	Comments	X range Y range Z range	BG source size	Approx. cell edge size	Comments	C_L C_D C_M
TCA-28 "RWT Box", model in Low position	Increase source sizes by 1/3 from their TCA-26 values.	Same as TCA-26.	4/3 TCA-26	0.7	656505 cell, a bit short of the desired 715000, but just capable of being run as a batch job.	0.1404 0.01016 -0.3153

This is the model in the wind tunnel at 8 degrees angle of attack in the highest postion. With such close solid walls it is not enough just to specify the angle of attack, as the incoming flow would cascade over the wind tunnel floor, which would also be at 8 degrees according to the USM3D flow algorithm. It is also necessary to rotate the wind tunnel walls down 8 degrees to present a consistent flow configuration. Both the wind tunnel wall and the plane of symmetry surface grids are shown in this picture.

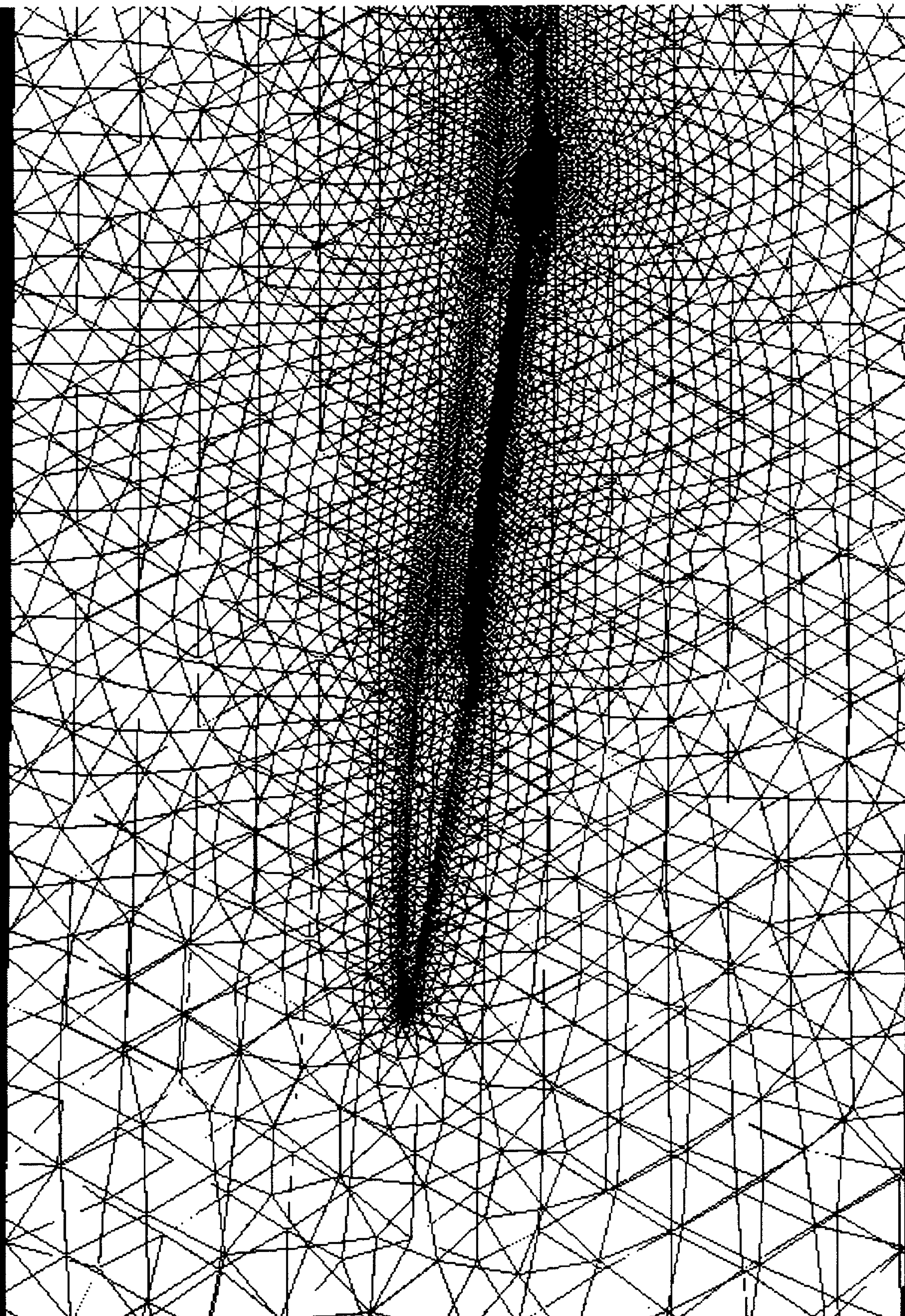

The first page shows the starting cases used to step the high and low position models from zero to eight degrees angle of attack. The number of cells remained essentially the same in both the high and low cases after rotation, so these grid configurations were used . Note the rotated box coordinates.

"Real Wind Tunnel" Alpha=8 degrees Summary, 02Feb98

Grid ID Description	Comments	X range Y range Z range	BG source size	Approx. cell edge size	Comments	C_L C_D C_M
TCA-25 "RWT Box" **High** pos.	Reference case used to start grid search for alpha=8, hi-position configuration. Reference configuration, alpha=0.	-1476.94,0,2136.6 -1476.94,2610,2136.6 -1476.94,0,-1343.4 -1476.94,2610,-1343.4 10523.06,0,2136.6 10523.06,2610,2136.6 10523.06,0,-1343.4 10523.06,2610,-1343.4 2295.22,2610,171.417	325 312 305 300 675 575 655 563 289	1.0-1.2	745844 cells total in the RWT-hi volume. 500 iterations.	0.1184 0.01413 -0.2633
TCA-28 "RWT Box", model in **Low** position	Increase source sizes by 1/3 from their TCA-26 values. Reference configuration, alpha=0.	-1476.94,0,3422.8 -1476.94,2610,3422.8 -1476.94,0,-57.2 -1476.94,2610,-57.2 10523.06,0,3422.8 10523.06,2610,3422.8105 23.06,0,-57.2 10523.06,2610,-57.2 2295.22,10251,171.417	724 695 72 71 1503 1280 153 132 385	0.7	656505 cell, a bit short of the desired 715000, but just capable of being run as a batch job. 600 iterations.	0.1404 0.01016 -0.3153

This page is intentionally left blank.

Grid ID Description	Comments	X range Y range Z range	BG source size	Approx. cell edge size	Comments	C_L C_D C_M
TCA-29 "RWT Box" **High** pos.	Rotated grid to allow for alpha=8 degree flow.	-1705.165,0,1617.168 -1705.165,2610,1617.168 -1220.843,0,-1828.965 -1220.843,2610,-1828.965 10178.053,0,3287.245 10178.053,2610,3287.245 10662.375,0,-158.888 10662.375,2610,-158.888 2303.785,2610,196.093	Same as TCA-25.	-----	Gives 750173 cells...OK to run since it's close to the 745844 cells of TCA-25. 2900 iterations.	0.2909 0.03184 -0.6248
TCA-30 "RWT Box" **Low** pos.	Rotated grid to allow for alpha=8 degree flow.	-1884.169,0,2890.851 -1884.169,2610,2890.851 -1339.847,0,-555.282 -1339.847,2610,-555.282 9999.048,0,4560.928 9999.048,2610,4560.928 10483.371,0,1114.795 10483.371,2610,1114.795 2124.780,2610,1469.779	Same as TCA-28.	-----	Gives 642946 cells. This value is pretty close to the 656505 cells of TCA-28. 1700 iterations.	0.3423 0.03185 -0.7408

This page is intentionally left blank.

Wind Tunnel Data

- From NASA LaRC 14- by 22-Foot Subsonic Wind Tunnel, test 449 ("TCA-1")
- Force and Moment data available on HSR ADAPT system
- Free-air and Ground-effect data separated for ease of access

The USM3D results for angles of attack of zero and eight degrees are presented for the highest and lowest model heights, 78 and 14 inches, respectively. the wind tunnel data are presented at all five model heights. It appears there is some question about the wind tunnel data at a height of 14 inches, but it has not been resolved. The USM3D results appear to be consistent with the wind tunnel data. The drag coefficient was not corrected for skin friction, which would raise the curve approximately 0.0900. The moment reference point is slightly in error for the USM3D results, and it is anticipated that movement to the correct location will eliminate the discrepancies.

TCA-1 WT GE Data, LE=30, TE=20

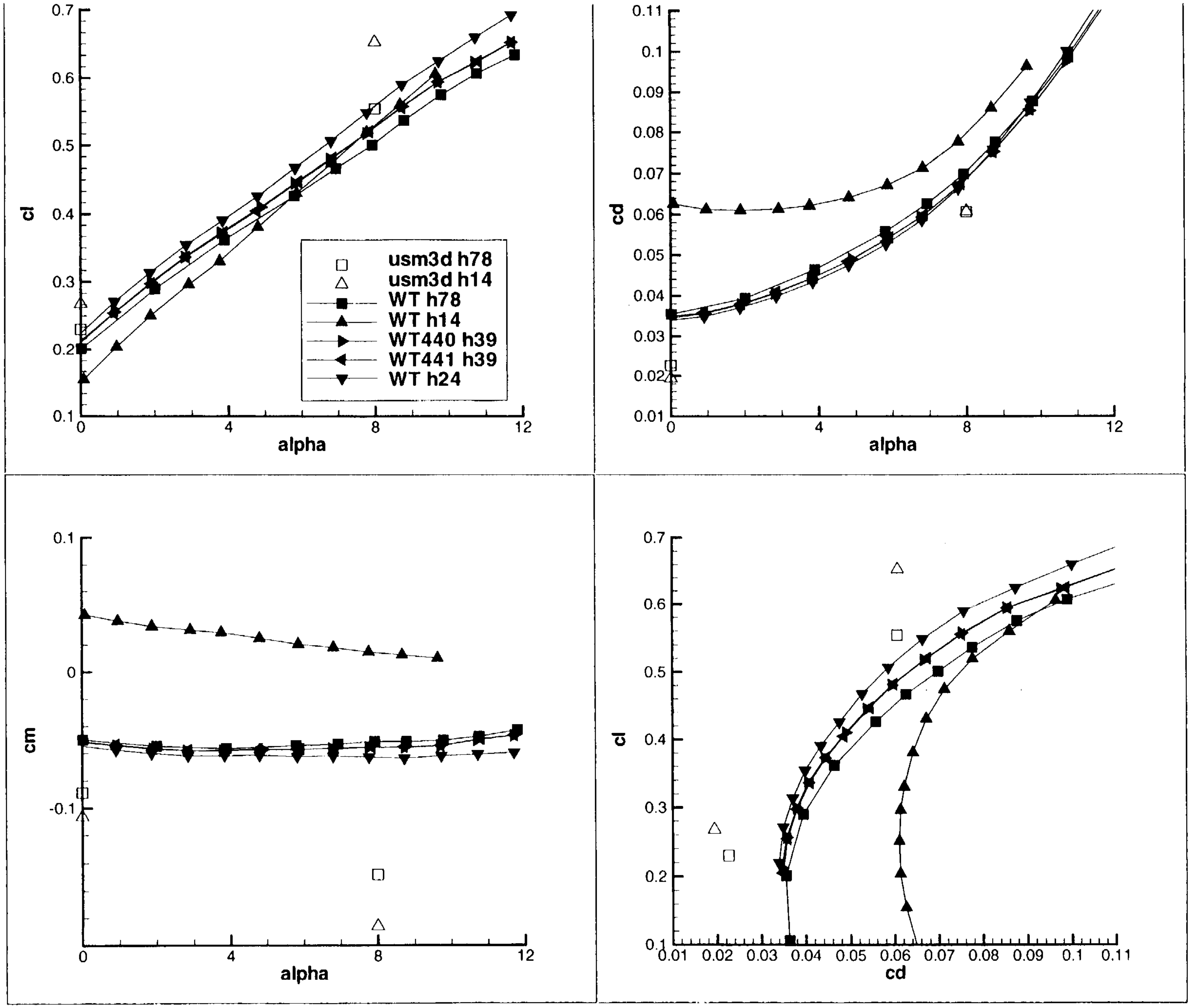

These curves of the wind tunnel data for a different flap arrangement were examined to see if there was any inconsistent behavior of the data at low model heights as on the previous page, but there did not seem to be any.

TCA-1 WT GE Data, LE=0, TE=30

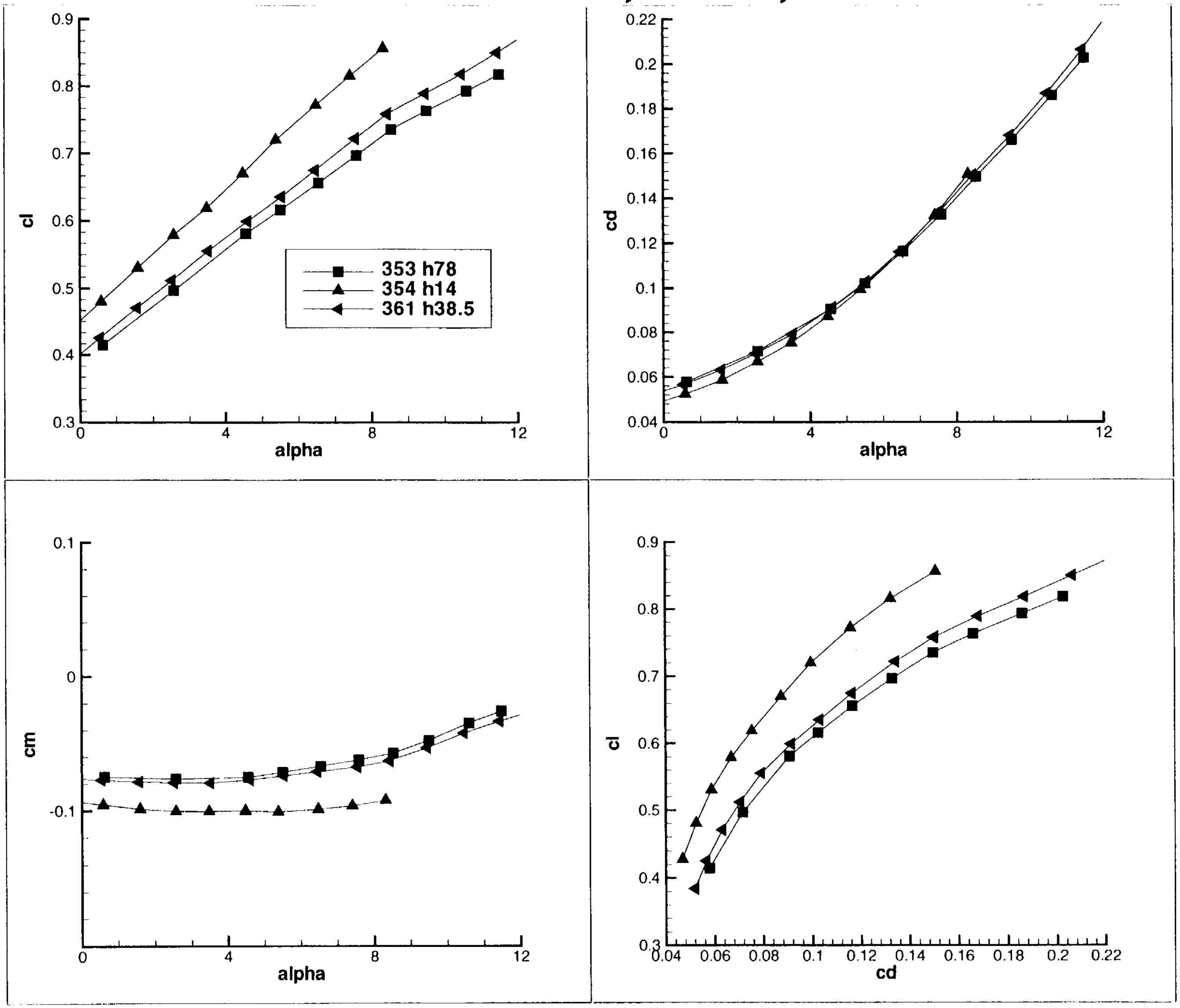

This page is intentionally left blank.

Plans for the Immediate Future

- Investigate wind tunnel data reduction and CFD parameter specifications to reconcile differences between the two
- Further computations to augment the height/alpha matrix
- Add powered nacelles to the analysis and compare with data from test 455 ("TCA-2")

This page is intentionally left blank.

Potential Flow Analysis of the Mark-XVI Flow Survey Probe

Eric J. Roth
Boeing Commercial Airplane Group
Seattle, Washington

High Speed Research Program
Airframe Annual Review

February 10, 1998

This page intentionally left blank.

High Lift Technology Development (Task 33)

Increase L/D, Develop Analysis/Design Methodology

Goals	Demonstrate Greatly Increased L/D Relative to SST Technology (Suction Parameter ≥ 92%)		
Objectives	Define Preferred High Lift System	Technology Readiness Level ≥ 6	Analysis/Design Methodology
Challenges	Aggressive Tech Projection	Validation (Little Data)	Planform, Viscous, Scale, Ground, Power, Canard Effects
Approaches	**Concept** Development	Test Facilities and Techniques	Analytical Methods
Program	Boundary Layer Control Vortex Flaps Attached Flow Flaps Programmed Flaps Canards	WT Database High Rn Testing Large Scale Testing Powered Testing Dynamic GE Testing Pressure & Temp. Sensitive Paints	Technology Projection Linear Methods Non-linear Methods Navier-Stokes Methods

ptm - 02/03/98

Overview

This page intentionally left blank.

Overview

- Introduction
- Geometry
- Analysis Configuration
- Results
- Summary

Introduction

A flow survey probe is an important tool for investigating the complex flow field around a wind tunnel model. It is especially useful for quantitative measurements of profile and induced drag. These separate measurements, which cannot be distinguished using a force balance, are necessary for CFD validation.

The cost of using a flow survey probe includes not only the hardware and software, but also the staff required to operate it. If modifications need to be made to the existing hardware, cost will increase as well.

Installing the traverser is simple, especially if holes are drilled into the mounting surface prior to installation. Installation time in this case could be on the order of 45 minutes.

A major drawback of any flow survey system is the possibility of aerodynamic influence. It is important that the traverser, whose purpose is to measure the flow field created by the model, not alter that flow field and give inaccurate data. Any changes to the flow field must be taken into account.

Introduction

Why use a flow survey probe?

- Flow field, wake measurements
- Separation between profile and induced drag
- CFD validation (TCA-4)

What are the drawbacks?

- Cost
- Installation time
- Possible aerodynamic influence

Mark-XVI Information

With these swift traverse rates, complete surveys can be performed in 20-30 minutes, with final data available ten minutes after the survey is complete.

Either a 5-hole probe or a pitot tube may be used.

By specifying a user-defined path for the traverser, survey time can be reduced. The traverser can simply skip over regions that may have otherwise been "pre-programmed", but that are unimportant to the current researcher.

Setting the boundary of the traverser will avoid potentially damaging and costly collisions between the probe and tunnel walls or model.

Because of its portability, the Mark-XVI traverser can be used in different low speed wind tunnels.

Mark-XVI Information

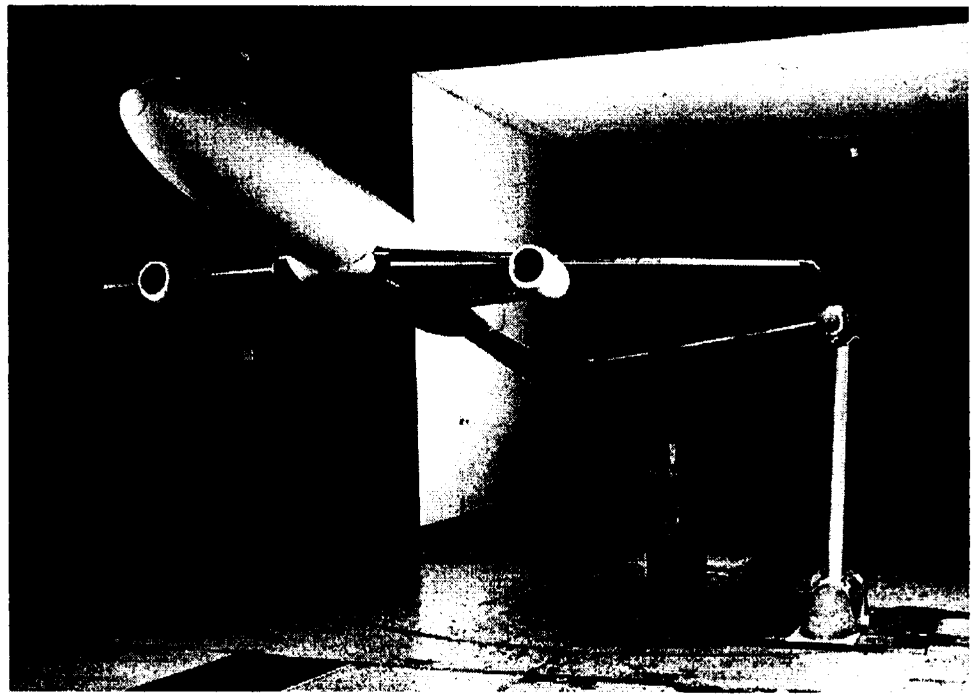

- Capable of accurate quantitative surveys at traverse rates up to 25 inch/sec
- Various interchangeable probes may be used
- Operator specified traverser path and boundary
- Portable

Mark XVI Geometry

Components

The cannon, upper arm, and probe can translate forward and aft allowing for surveys of body stations up to 36 inches apart.

Mark XVI Geometry

Components

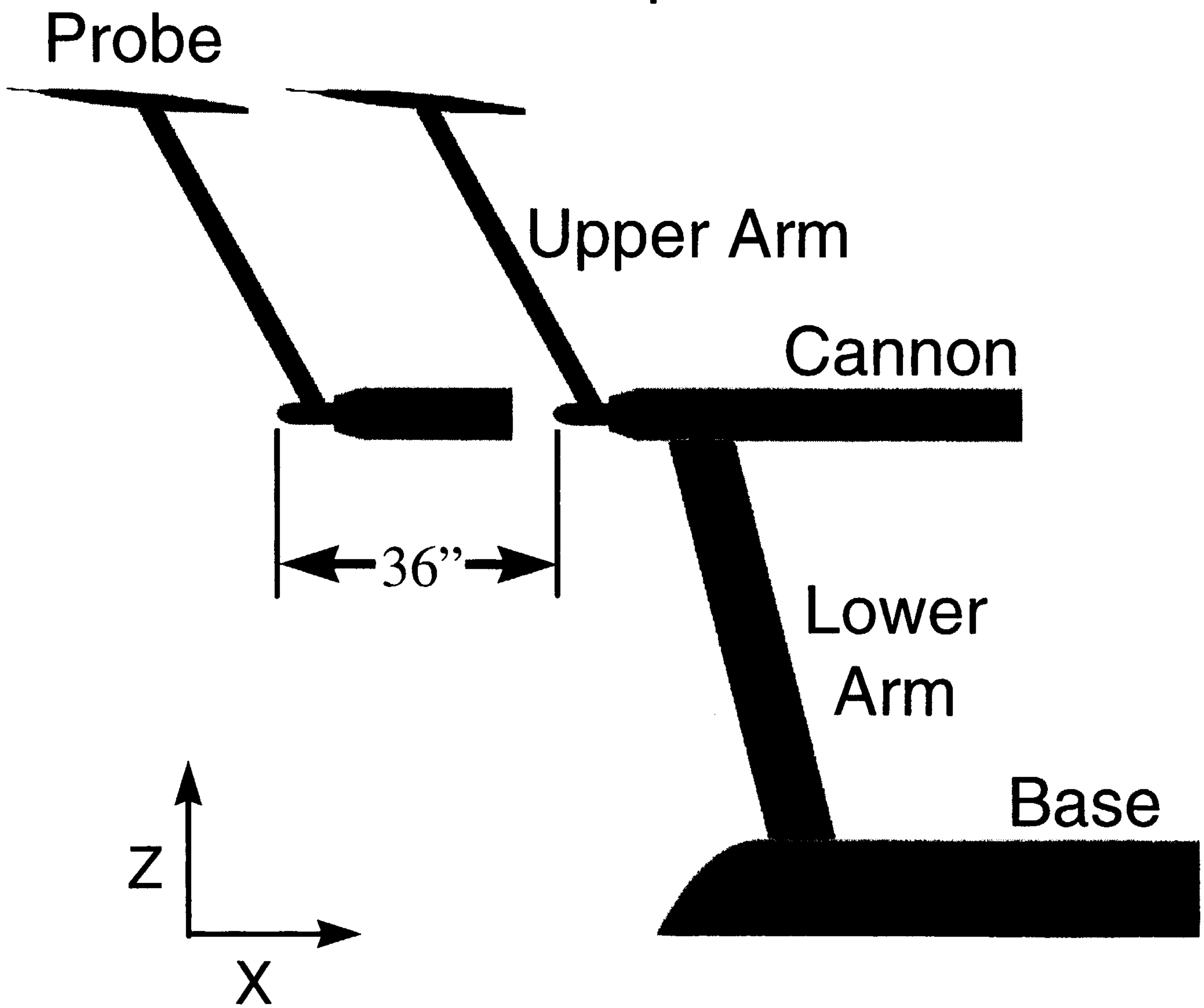

Mark XVI Geometry

Range of Motion

The “double rotary” design consists of two linked struts. The lower arm rotates about the base of the traverser while the upper arm rotates about the cannon. The probe, therefore, can be positioned anywhere between the 102” outer radius and the 18” inner radius.

Because the traverser is located entirely within the test section, there are no tunnel wall penetrations and the total blockage of the traverser remains constant.

Mark XVI Geometry

Range of Motion

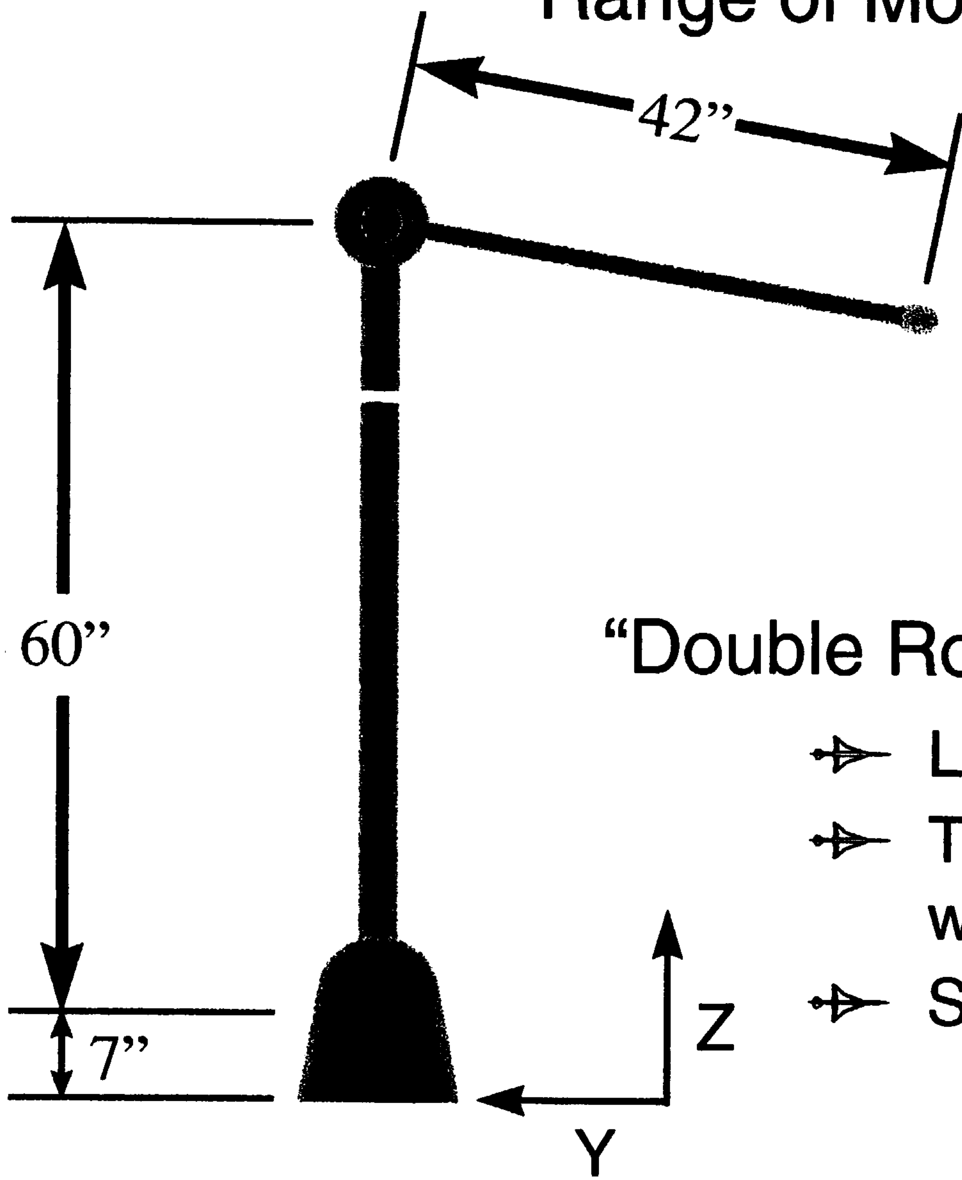

“Double Rotary” design allows for:

- Low total blockage
- Traverser located entirely within the test section
- Single point attachment

Analysis Configuration

The purpose of this analysis was to use computational fluid dynamics (CFD) to determine what influence the traverser may have on the TCA model, in terms of pressures, forces, and moments. The guidelines outlined below were set both to correspond with the proposed configuration that the CFD team will be testing during the TCA-4 test, as well as simplify the paneling of the traverser. When input into the potential flow code, these panel corner points define the configuration geometry.

A previous analysis of the traverser alone (without a TCA model) was modeled with both the upper and lower arms vertical. Paneling on the cannon's circumference was divided equally into 36 10° arc-segments. Therefore, when rotating the nose of the cannon to reposition the upper arm and probe for this current analysis, maintaining multiples of 10° satisfied the abutment requirements of the potential flow code.

Rotating the lower arm would have required re-paneling the base of the traverser. To avoid this, the lower arm was simply kept in the vertical position.

Analysis Configuration

- 5% TCA model at $\alpha = 10^\circ$
- Model height at tunnel centerline (tunnel not actually modeled)
- Flaps 30/10, tail & nacelles OFF
- Base of traverser placed on tunnel floor ($z=0.0$), 60 inches off centerline
- Upper arm deflection angle must be multiple of 10°
- Lower arm of traverser remains vertical

Analysis Configuration

One Little Problem

With the configuration set up based on the proposed guidelines, it was noticed that the upper arm of the traverser would collide with the wing of the model before the probe could even come close to the wing surface. This would not only cause errors in the code, but it also draws attention to the fact that, if the traverser is used in TCA-4, the configuration cannot be tested as originally desired. Changes to the configuration must be made for probe positions where this problem occurs, mainly over the leading edge flap and slightly aft of the hingeline.

Analysis Configuration

One Little Problem

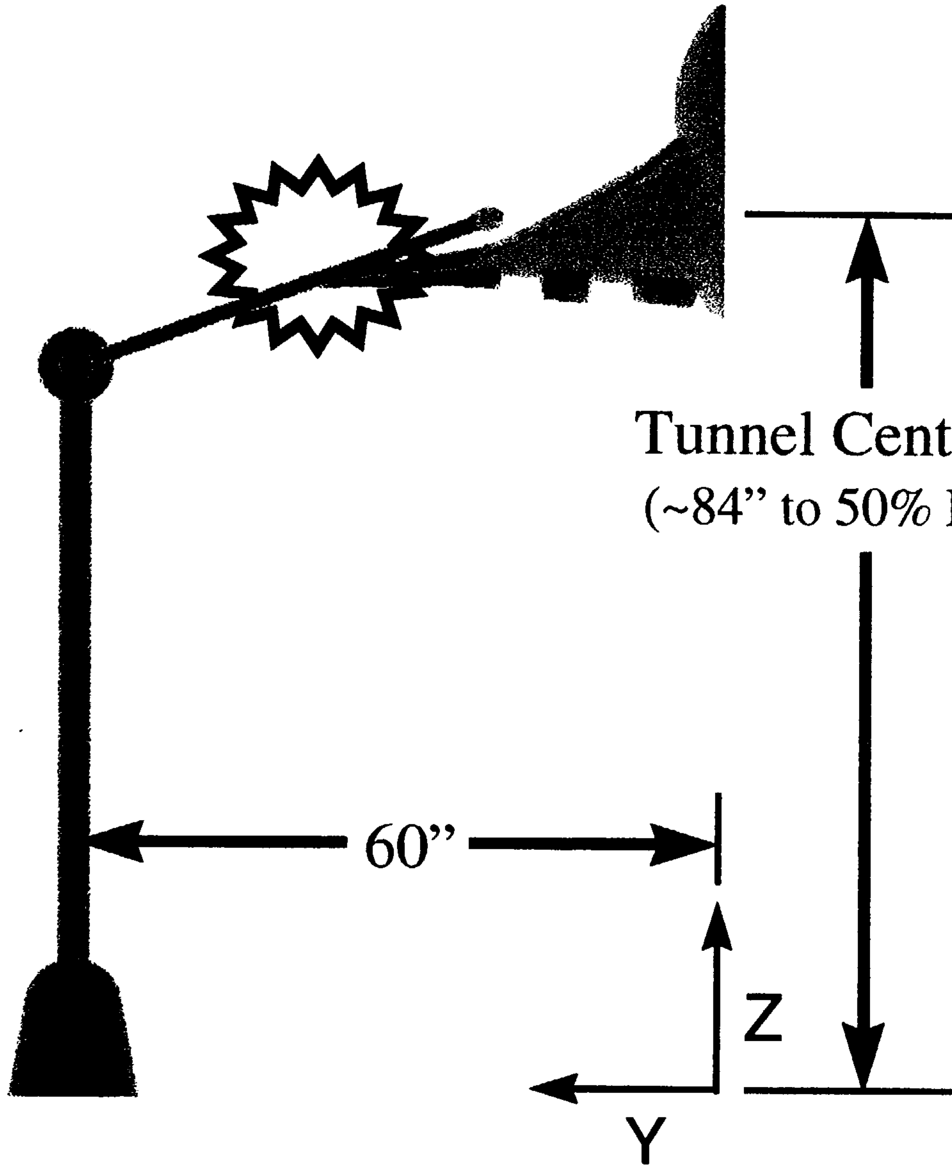

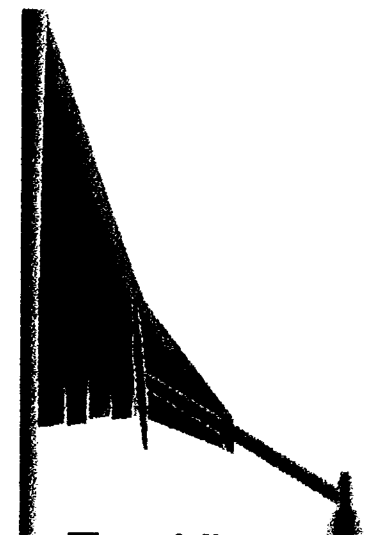

- Upper arm positioned 20° above horizontal
- Probe tip located aft of leading edge

Analysis Configuration

One Simple Solution

In order to solve the problem of the wingtip engulfing the traverser, the model had to be lowered 21 inches from its original height. As far as the potential flow code is concerned, this means nothing. But in the wind tunnel itself, ground effect may become significant.

Other solutions that were proposed in solving this problem included building new hardware for the traverser, such as longer arms, which costs additional money. Placing the entire traverser on a “soapbox” would also work.

One way to allow surveys of the entire upper surface without concern for striking the model would be to mount the traverser from the ceiling of the tunnel. The main problem with this is hoisting a several hundred pound structure and mounting it upside down.

Analysis Configuration

One Simple Solution

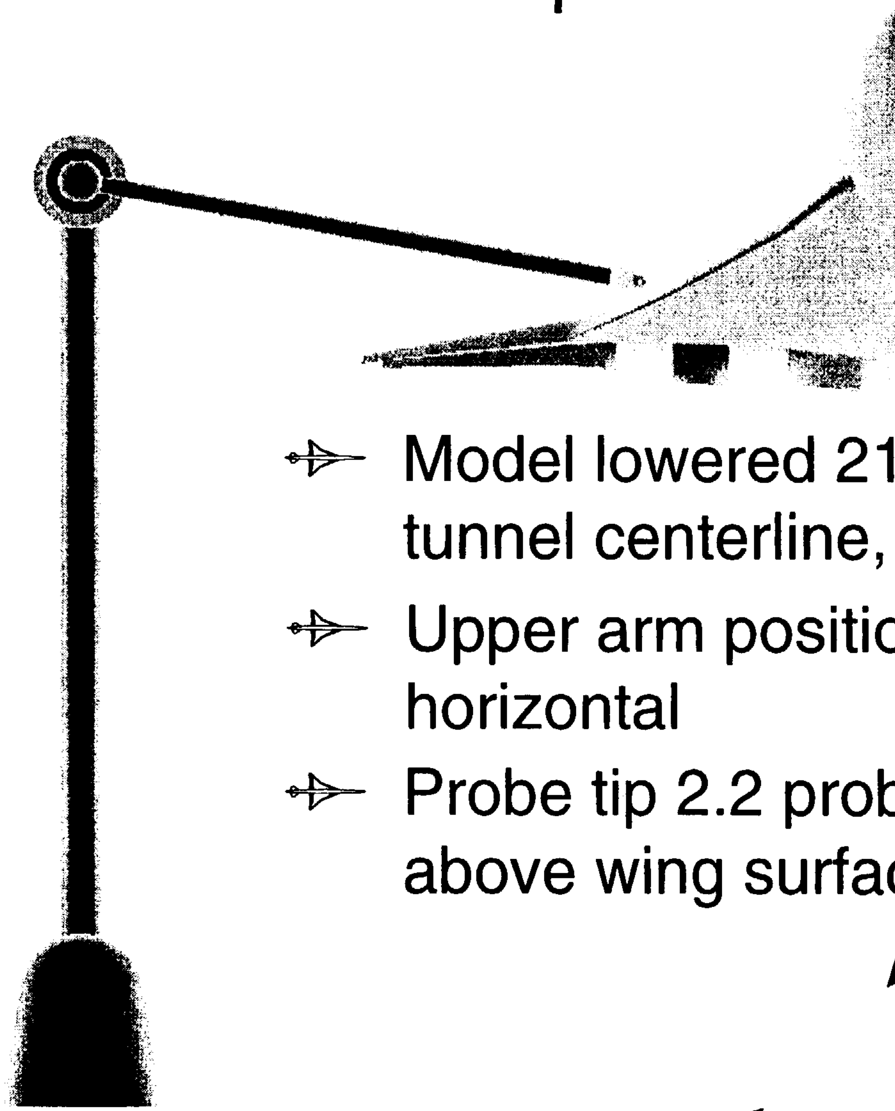

- Model lowered 21 inches from tunnel centerline, $\alpha = 10^{\circ}$
- Upper arm positioned 10° below horizontal
- Probe tip 2.2 probe-diameters above wing surface (0.6")

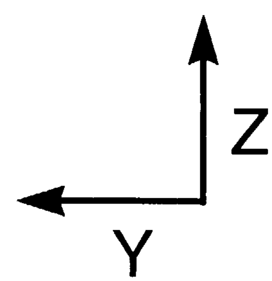

Results

The Code: A502

The wireframe shown illustrates the panels that were created to model the traverser and airplane geometry. For clarity, however, this wireframe is less dense than the actual input deck which consisted of 7922 panels.

Solutions provided by A502 include flow directions, pressures, and Mach numbers on the surface, forces and moments.

Results

The Code: A502

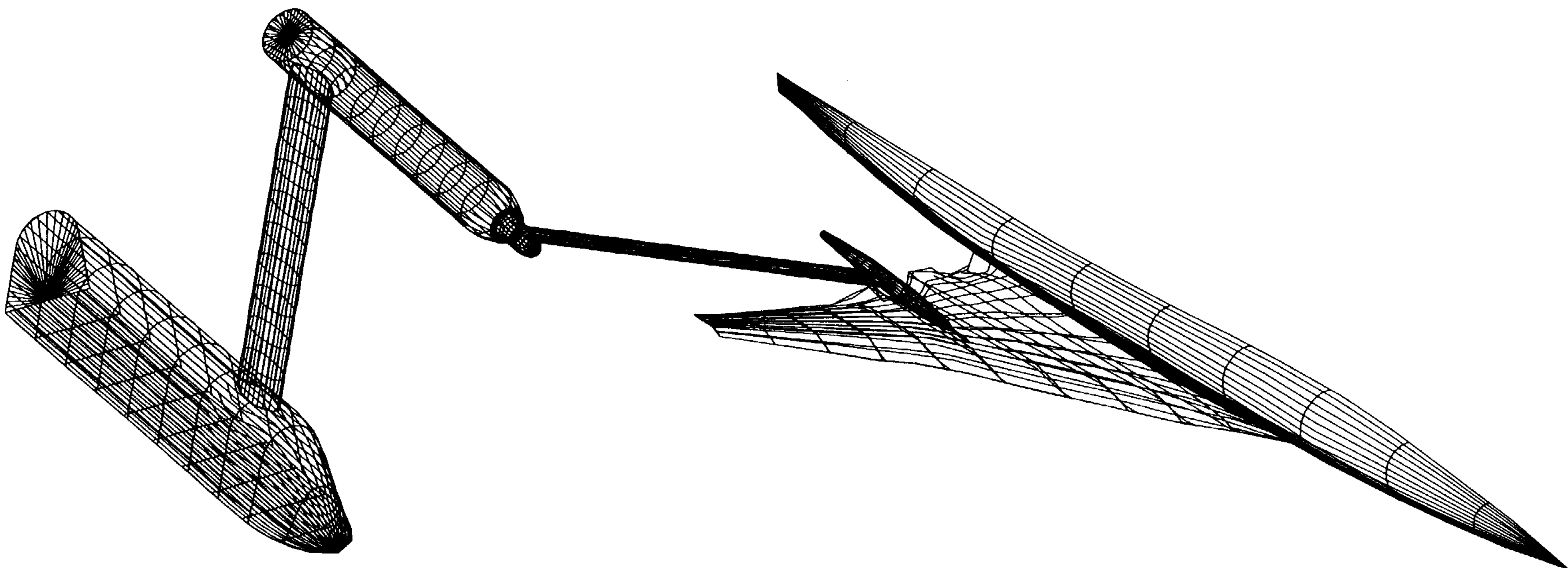

- Calculates flow properties, forces, and moments about arbitrary 3-D configurations
- Uses higher-order panel method to solve linearized potential flow boundary value problem

Pressure Distribution

Traverser Surface

This figure simply illustrates that there is nothing out of the ordinary occuring on the traverser surface. Flow is accelerated over the upper and lower arms (which have elliptical cross sections) causing the pressure to decrease. Stagnation occurs at the leading edges of the arms as well as the forward regions of the base and cannon.

Pressure Distribution

Traverser Surface

- Cannon in full forward position
- Both upper and lower arms vertical

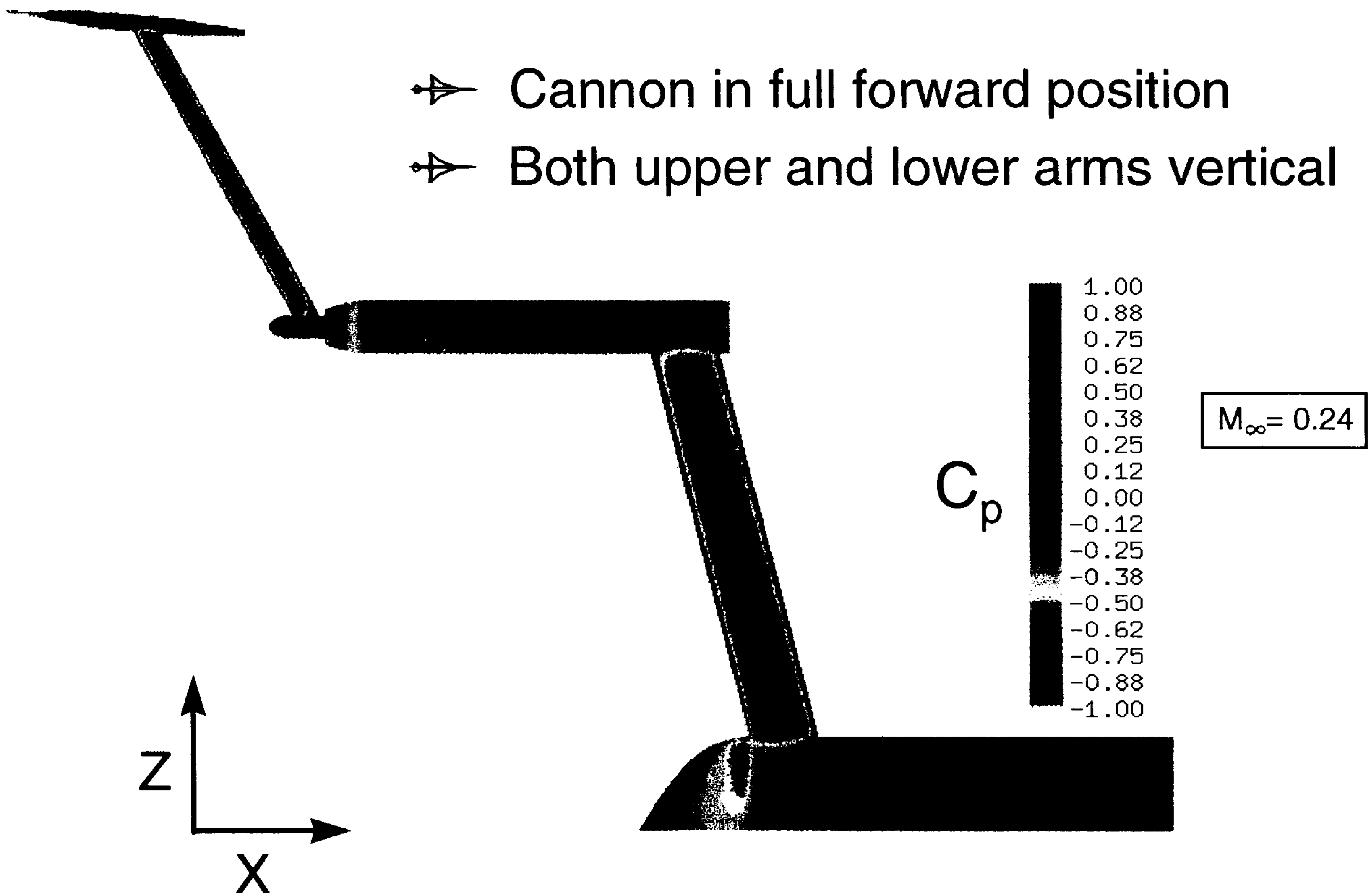

ejr - 2/10/98

Traverser Effect on Pressures

Inboard Location

At locations inboard of the probe and upper arm, there is little effect due to the traverser on the pressure distribution over the wing.

In the cross sectional view at this location, the probe appears to be deceivingly close to the upper surface of the wing. It should be noted, however, that the probe is not actually positioned above the wing at this particular spanwise station.

Traverser Effect on Pressures

Inboard Location

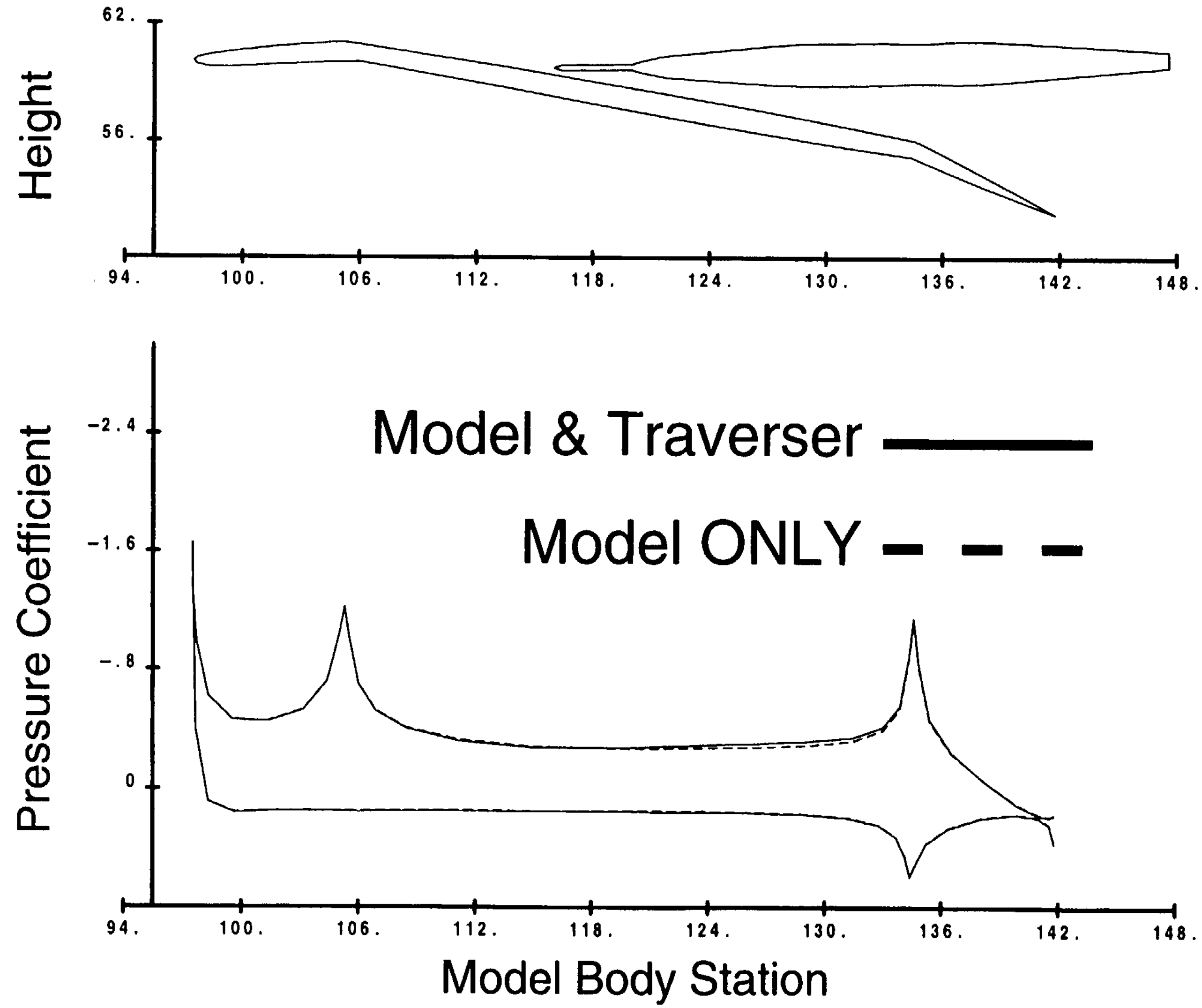

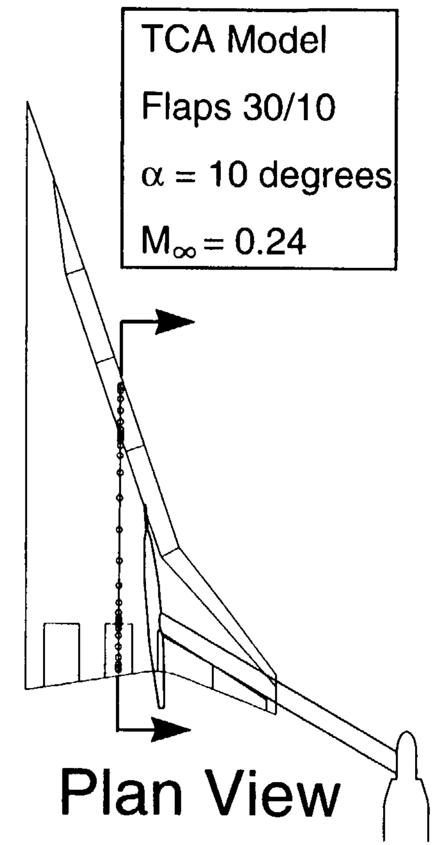

Traverser Effect on Pressures

Mid-Span Location

The probe and upper arm create a channel with the upper wing surface causing the pressure distribution on the upper wing to decrease as the flow is accelerated through this region.

At a spanwise location directly beneath the probe, the point being measured is essentially unaffected by the traverser despite this "channeling" effect. For this particular location, the probe is surveying just forward of the leading edge hingeline.

Traverser Effect on Pressures

HSCT High Lift Aerodynamics

Mid-Span Location

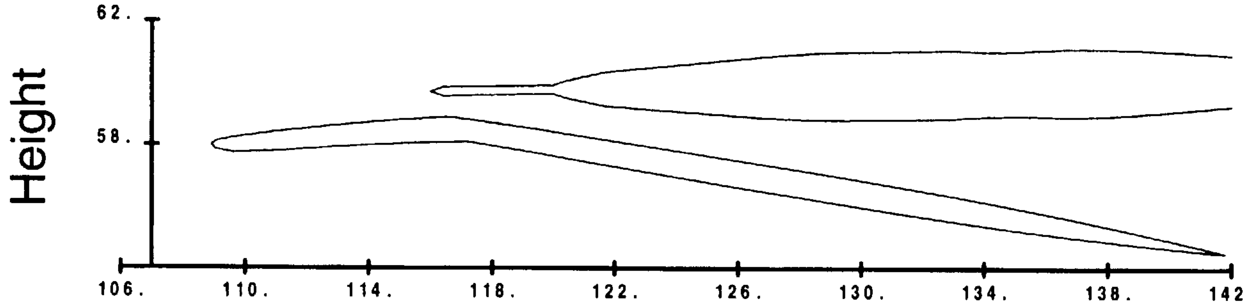

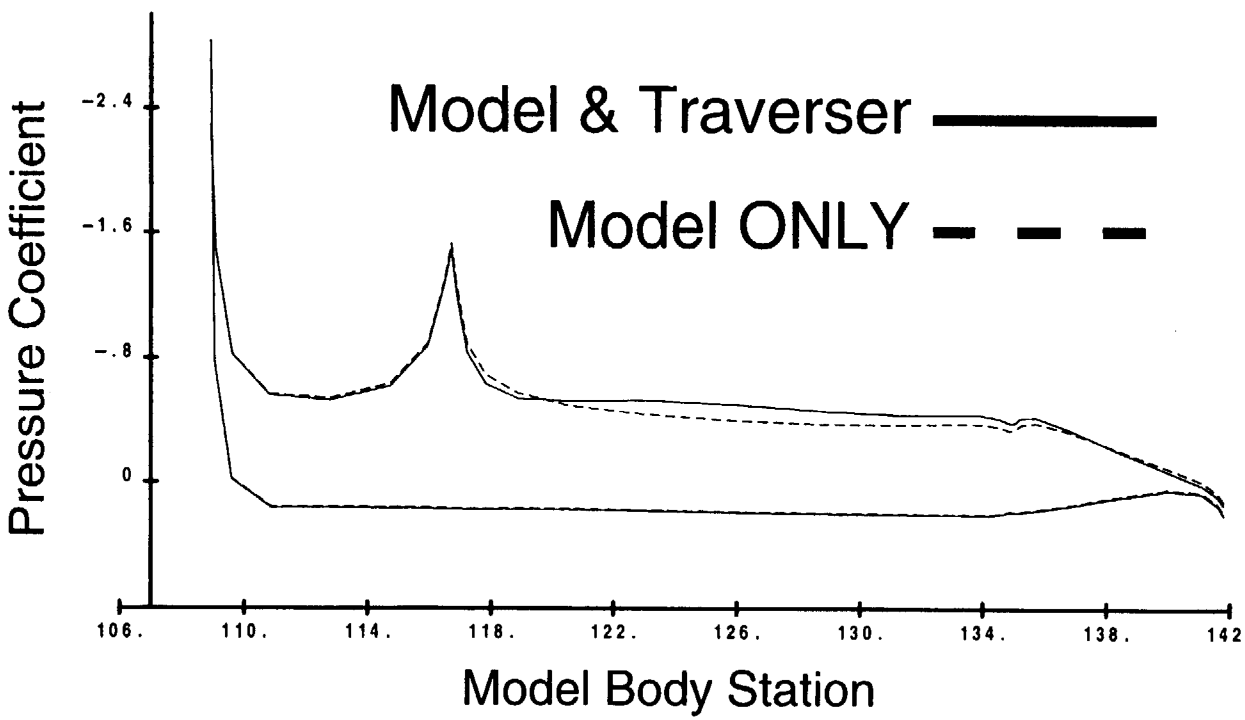

TCA Model
Flaps 30/10
$\alpha = 10$ degrees
$M_\infty = 0.24$

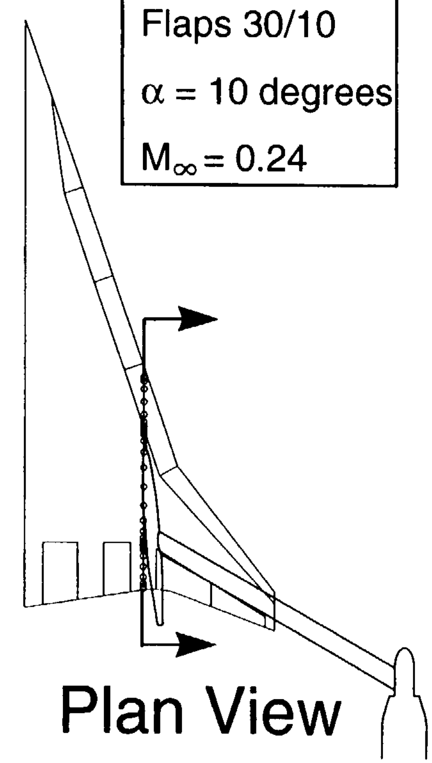

Traverser Effect on Pressures

Outboard Location

The traverser continues to influence the pressure distribution along the upper surface of the wing causing the pressure to decrease.

Traverser Effect on Pressures

Outboard Location

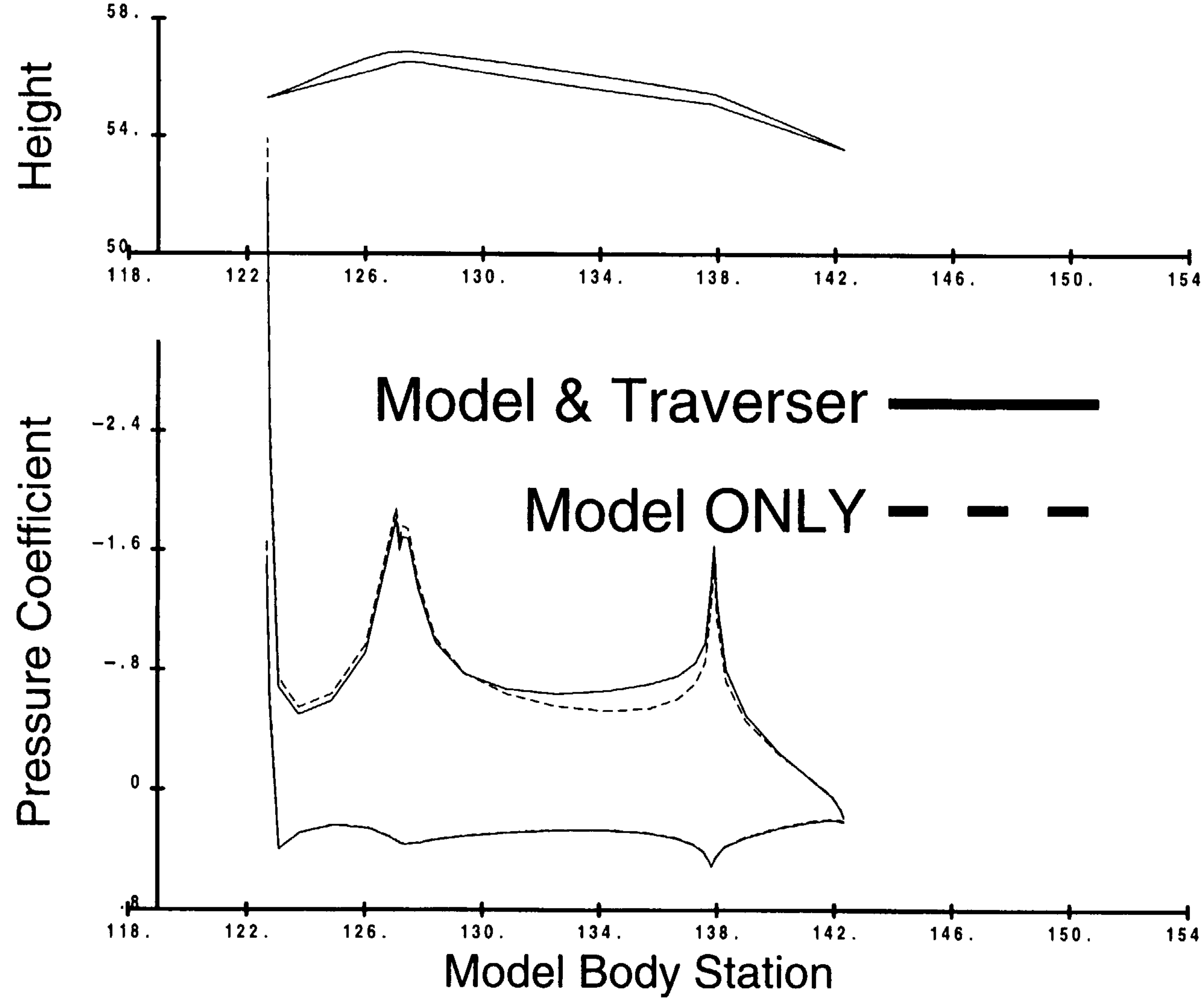

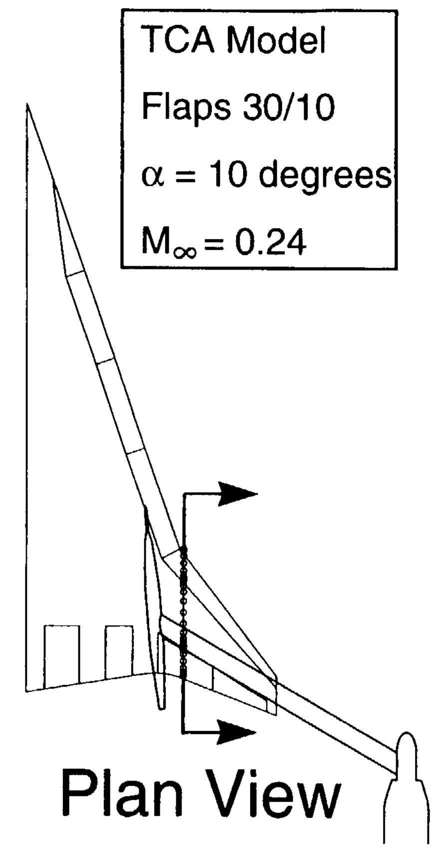

Traverser Effect on Pressures

Pressure Difference

The probe and upper arm of the traverser create a channel with the upper surface of the wing, causing the flow to accelerate through it. This figure illustrates the net result of these effects over the entire spanwise distribution. Pressures on the lower surface of the wing are only slightly affected by the traverser, showing differences at least an order of magnitude smaller than those on the upper surface.

Traverser Effect on Pressures

HSCT High Lift Aerodynamics

Pressure Difference

$$\Delta C_p = C_{p_{\text{model \& traverser}}} - C_{p_{\text{model ONLY}}}$$

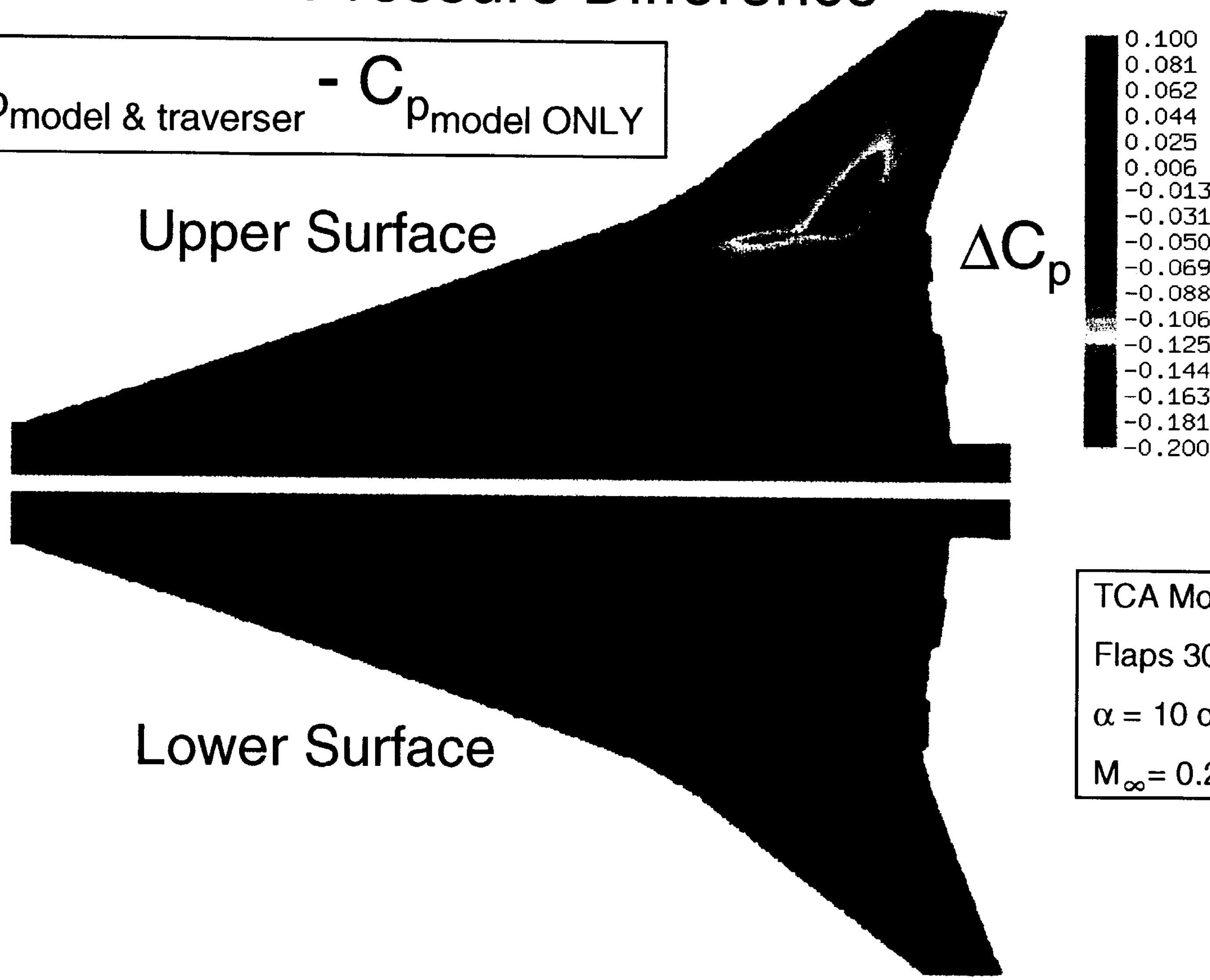

TCA Model

Flaps 30/10

α = 10 degrees

M_∞ = 0.24

ejr - 2/10/98

Traverser Effect on Forces & Moments

HSCT High Lift Aerodynamics

The accelerated flow caused by the traverser over the upper surface of the wing creates an increase in lift by 1.4%. This also causes induced drag to increase by 3.8%.

Because the lift increase is mainly concentrated on the outboard portion of the wing, aft of the center of gravity, nose-down pitching moment is increased. This change is equivalent to 2.0° of horizontal stabilizer.

Model ONLY	Model & Traverser
$C_L = 0.492$	$C_L = 0.499$
$C_{Di} = 0.0425$	$C_{Di} = 0.0441$
$C_M = 0.0144$	$C_M = 0.0056$

ejr - 2/10/98

Traverser Effect on Forces & Moments

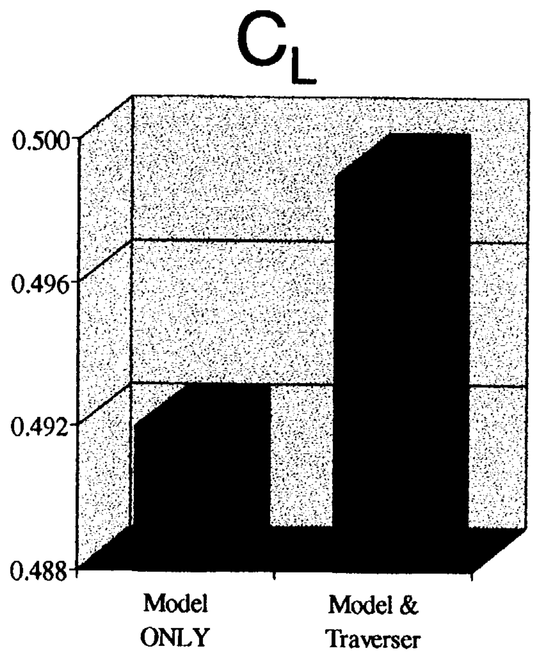

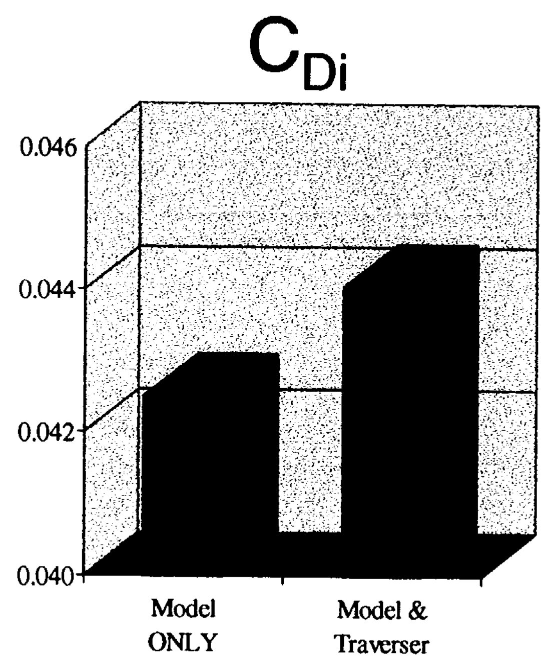

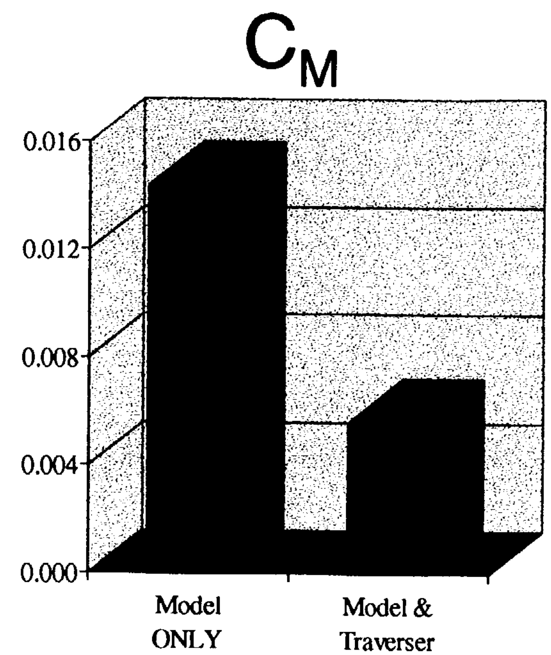

Influence of the traverser causes (on a full model):

- C_L increase by 1.4%
- C_{Di} increase by 3.8%
- ΔC_M equivalent to 2.0° of horizontal stabilizer

Summary

This page intentionally left blank.

Summary

- Pressures at the point being surveyed are relatively unchanged by the probe's presence
- Lift, drag, and nose-down pitching moment increase due to the presence of the traverser
- Changes are necessary to the model's position or the traverser itself in order to survey some locations on the model

This page is intentionally left blank.

HSR
High Speed Research

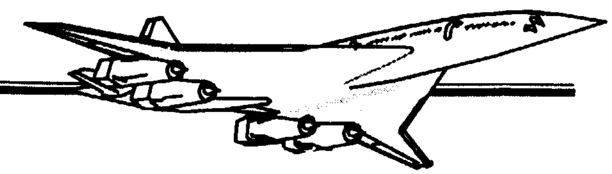

Aerodynamic Design of Inboard Sealed Slats for the TCA-3 Wind Tunnel Test

High Lift Aerodynamics
Robert C. Griffiths

Airframe Annual Review
February 10, 1998

High Lift Technology Development (Task 33)

Increase L/D, Develop Analysis/Design Methodology

This page intentionally left blank

High Lift Technology Development (Task 33)

Increase L/D, Develop Analysis/Design Methodology

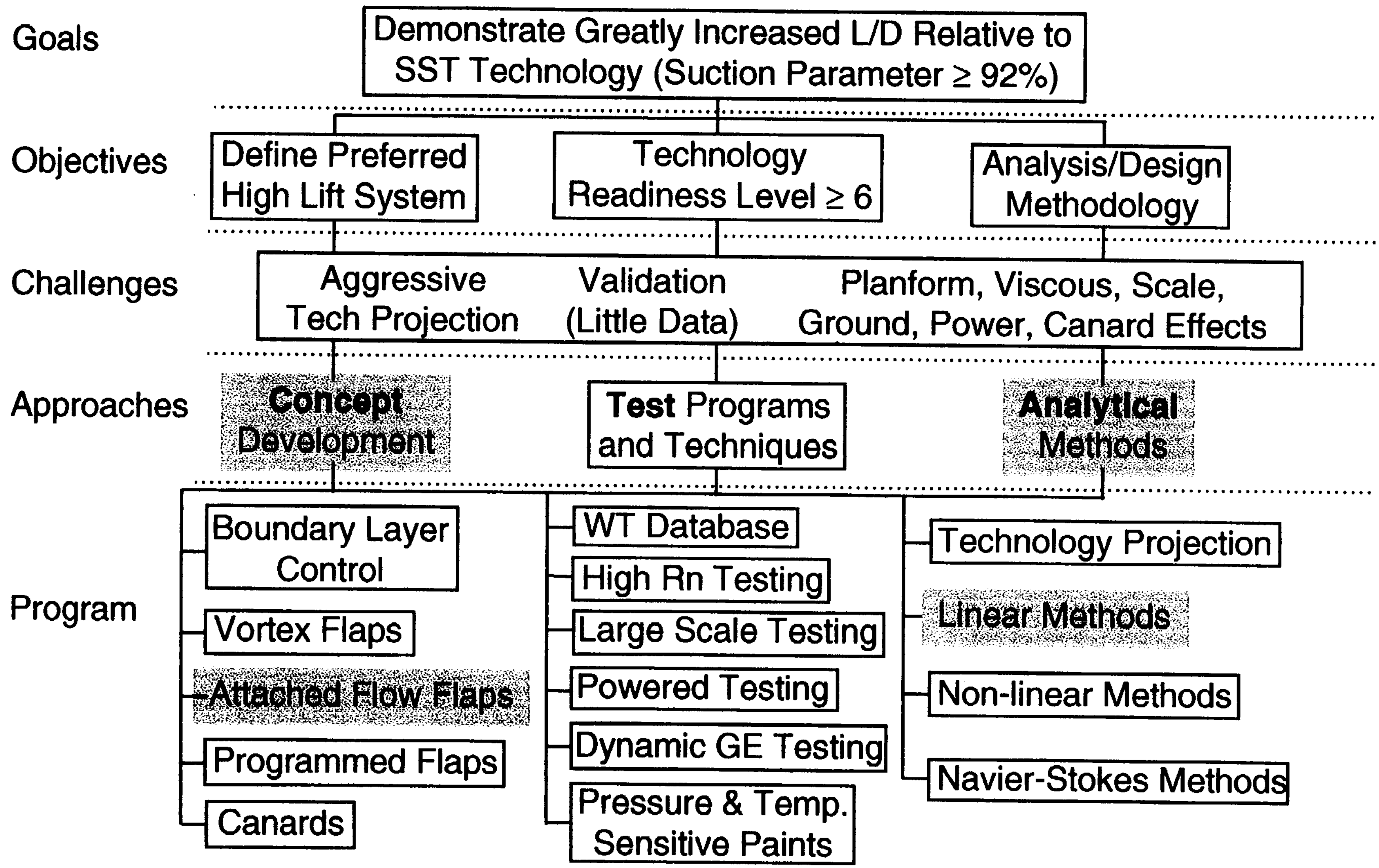

Introduction

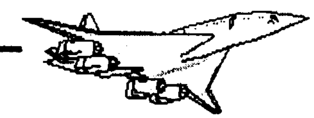

The goal of this study was to design inboard leading edge devices that would improve the baseline plain flap performance (airplane L/D). Sealed slats were selected to focus the study on because of the success seen with these devices on the sharp outboard leading edge and because of the aerodynamic benefits inherent in the sealed slat concept.

Ultimately, the result of this study was to choose the best leading edge designs, build them and test them in TCA-3.

Included in this discussion are reasons as to why sealed slats work, design constraints, approach taken, and computational results.

Introduction

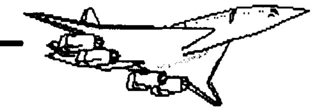

- Goal of this study: increase L/D by improving the flow on the inboard wing
- Sealed slats to increase performance - experience
- Theory - why sealed slats work
- Practical constraints - design issues - approach
- Results
- Conclusions

Why We Care About L/D

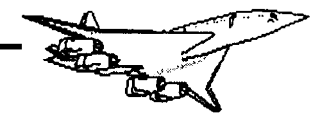

This chart shows sensitivity of MTOW to changes in L/D. For example, a 30 count improvement in drag at climbout CL of 0.5 is equivalent to approximately a 5% improvement in L/D, or 10,000 pounds MTOW.

The PTC is seen to be less sensitive than TCA.

The major impact to MTOW comes from engine size (increased thrust) or wing area at a given L/D.

Why We Care About L/D

BOEING

HSCT High Lift Aerodynamics

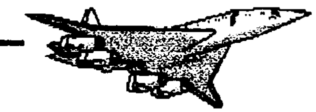

PTC Sensitivity to Climbout L/D
Sized to Stage III -5 dB

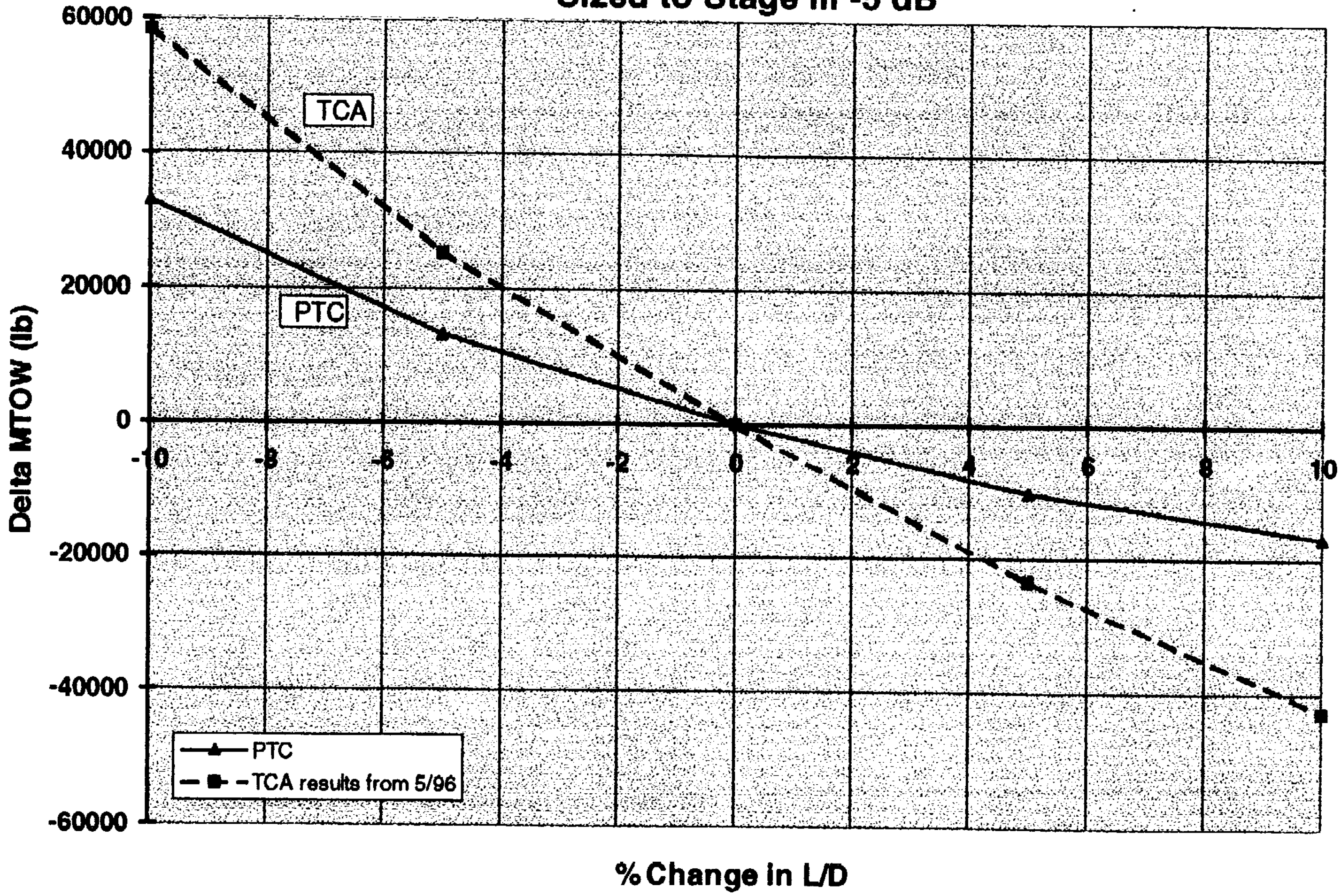

BOEING

HSCT High Lift Aerodynamics

Sealed Slat Concept

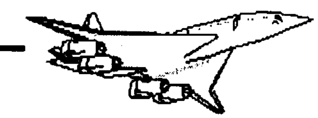

The idea of including a sealed slat device on an HSR configuration has been studied in the mechanical systems area. Previous studies have shown that it is mechanically viable to include a sealed slat on the sharp outboard leading wing panel. Installing a sealed slat device on the inboard wing would be easier still due to an increased in allowable space (leading edge is rounded, therefore there is more room for mechanical systems). The drawback to either an inboard or outboard sealed slat device is the added OEW due to additional hardware required - the slat would need to "buy it's way on" with increased performance.

The chart shows approximately a 4% L/D benefit when compared to the baseline plain flaps (based on TCA-1 wind tunnel data).

Sealed Slat Concept

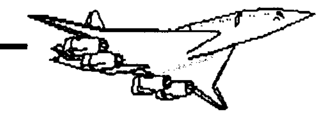

L/D increased by nearly 4% for both TCA & REF. H

viable mechanical system

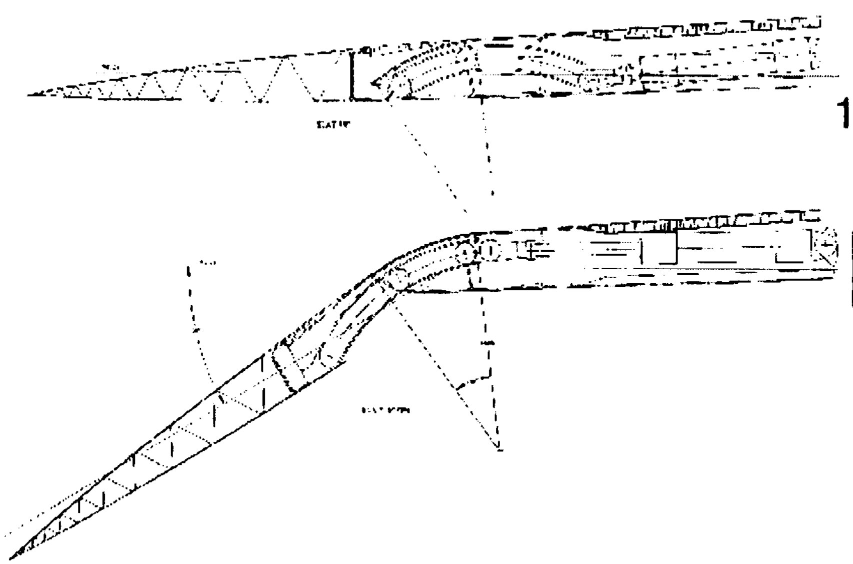

TCA-1 (NASA #449) Test Data

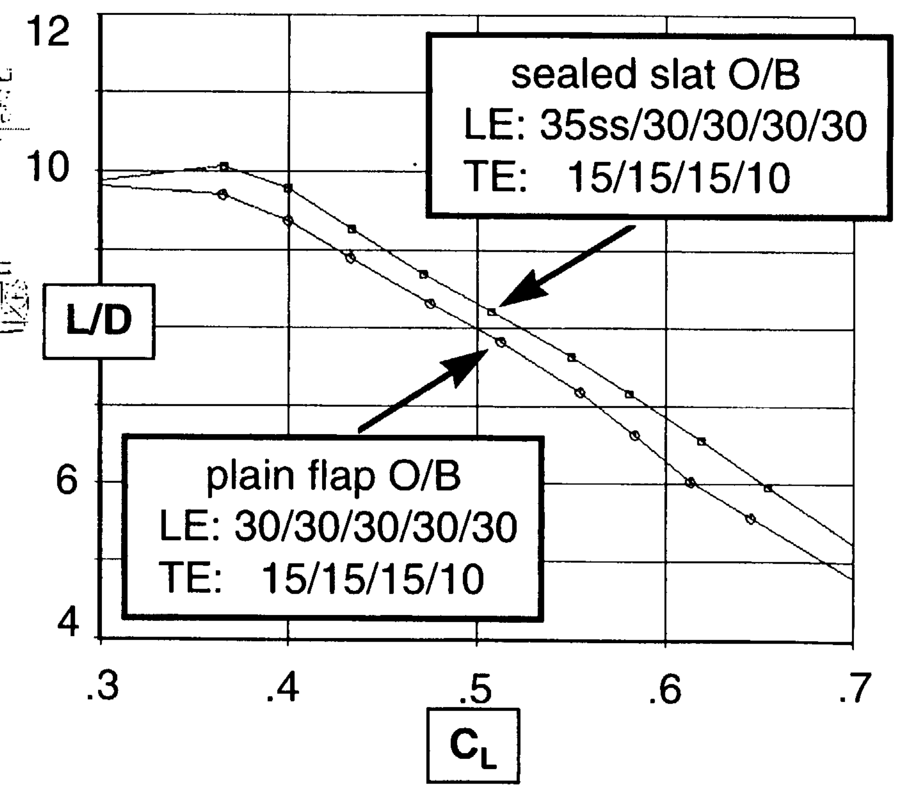

Sealed Slat Concept

The sealed slat has a hingeline that is below the wing; therefore, when the flap (slat) is deflected, Fowler motion occurs adding a small amount of wing area and increasing the hingeline radius. The added area reduces the angle-of-attack required for a given lift, and therefore the required flap deflection. Reduced flap deflection results in a more forgiving upper surface curvature.

The increased radius of a sealed slat results in a pressure gradient less likely to cause separation. The pressure peaks at both the leading edge and hingeline can be studied with a potential code to help predict separation tendencies.

Sealed Slat Concept

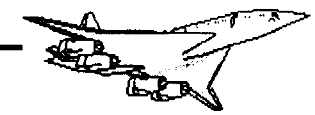

how sealed slats help performance

- Increased flap chord due to fowler motion:
  - Additional area decreases required AOA for given CL
  - Better L/D at given CL
  - Increased hingeline radius
- Increase hingeline radius - reduce hingeline pressure peak
- Proper LE flap deflection - reduce leading edge peak

Theory

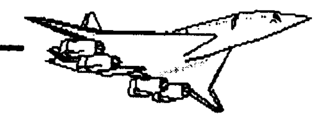

The adverse pressure gradient associated with a sharp hingeline results in separation or vortex formation; this gradient is moderated with a more generous hingeline. Note the leading edge peak is not reduced due to the sharp leading edge and the lower surface attachment line.

The inboard (subsonic) leading edge of an HSCT configuration is blunt; this will help the flow negotiate the leading edge and reduce the chance of separation (at a reasonable angle-of-attack) at the leading edge. As the attachment line approaches the leading edge hilite, the leading edge pressure peak will be reduced. This condition helps indicate when an ideal local angle-of-attack (flap deflection) is approached.

Increasing hingeline radius helps the flow negotiate the upper surface curvature at the flap break.

HSCT High Lift Aerodynamics

Theory

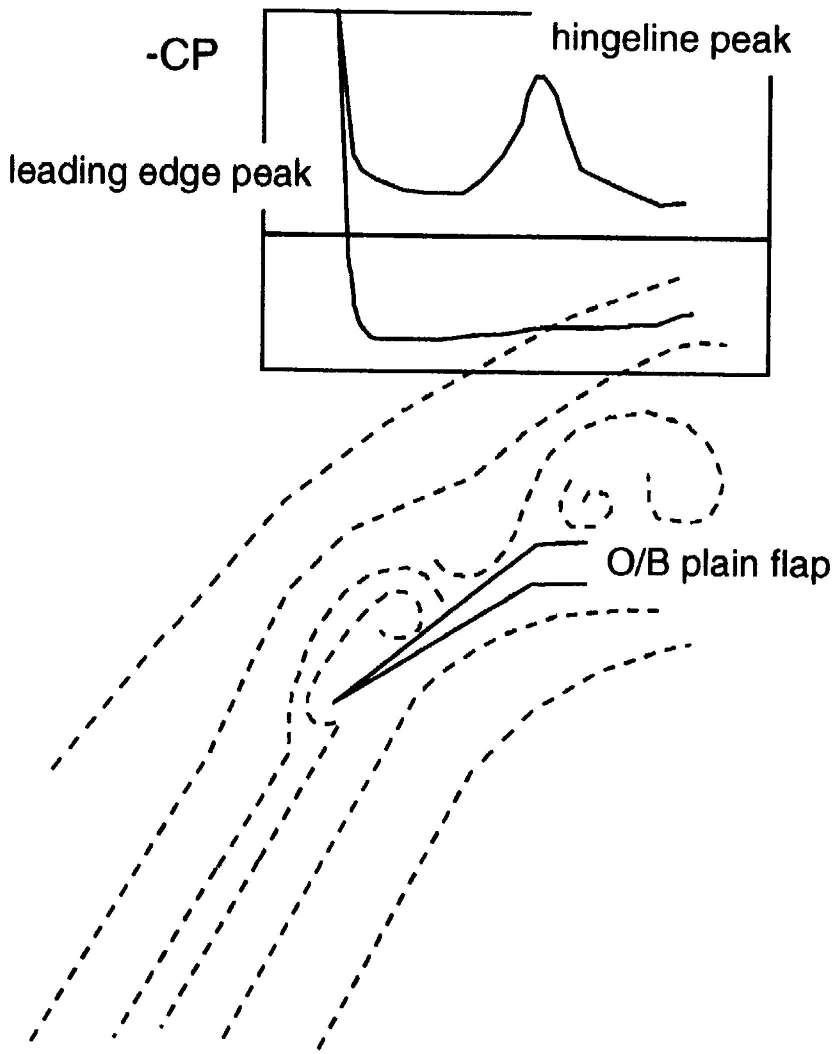

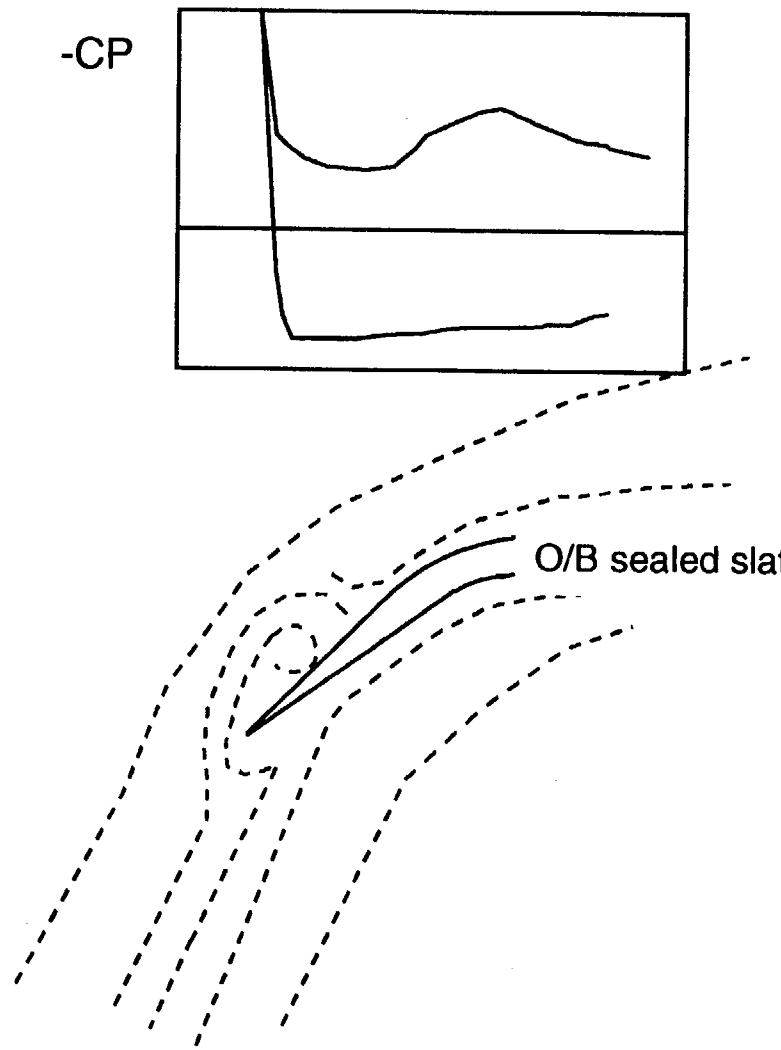

Theory Put to Work

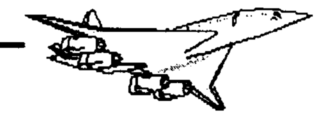

Test results from NASA #437 (Reference H configuration) show the improvements seen in both L/D and CD at the reference CL of 0.55 when replacing the baseline plain flap with a device with a larger hingeline radius (the outboard sealed slat) or a combination round leading edge and generous hingeline curvature ("attached flow flap").

(Note: a CL of 0.55 is referenced to Wimpress area).

Theory Put to Work

(Ref H) NASA #437 Test Results of Different "Best" Leading Edges -
increased hingeline concepts show improvement over baseline

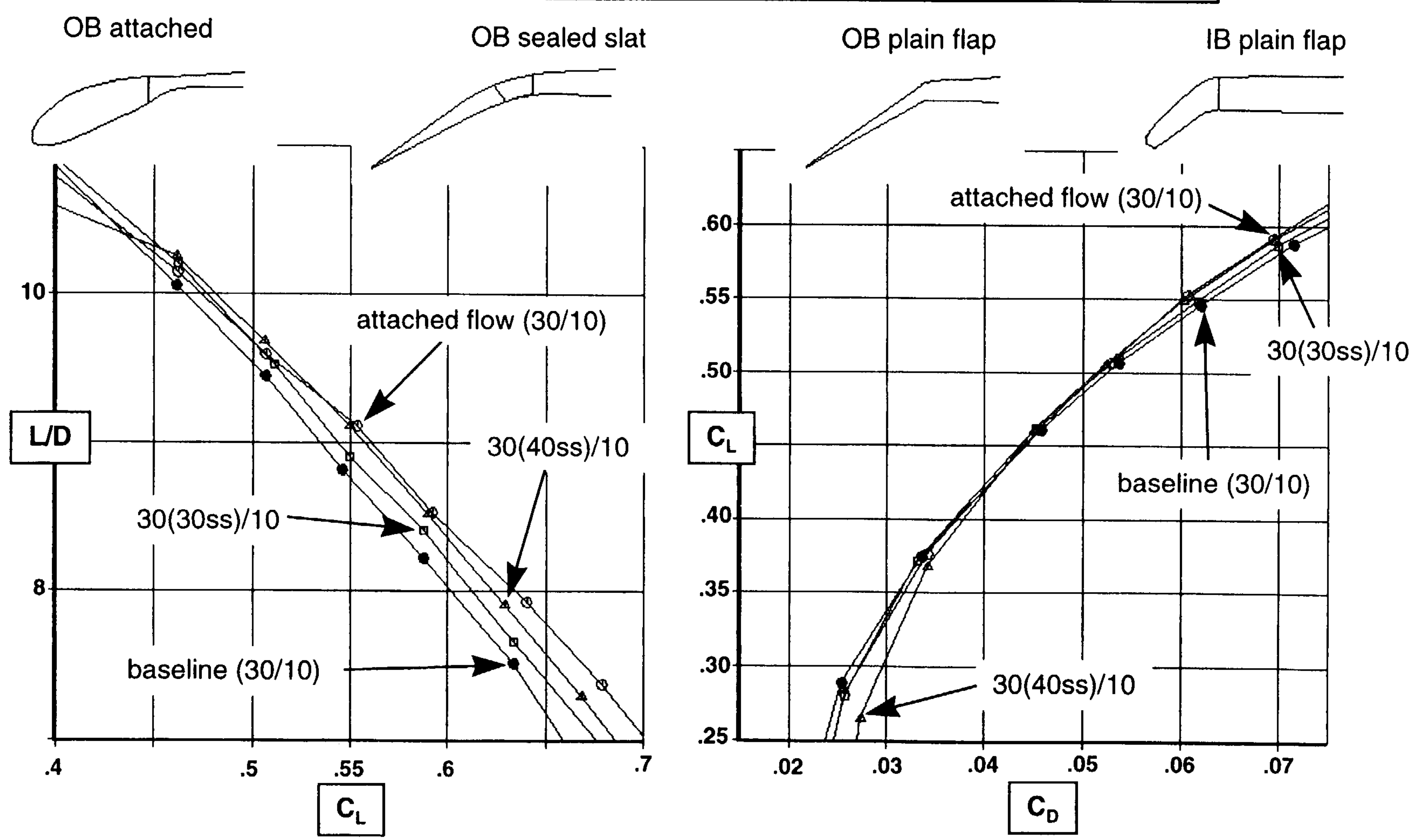

Design Study Constraints

The study was constrained by both physical and time considerations.

The goal was to have lofts available within one month from the start of the study so that new parts could be built and tested during TCA-3. Consideration was given to make sure the new parts fitted up with any existing mating parts. Finally, any new design would need to be considered practical from a mechanical systems point of view.

BOEING

Design Study Constraints

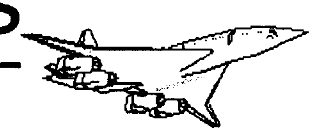

HSCT High Lift Aerodynamics

- Physical constraints:

  - new parts must fit up with existing O/B parts (sealed slats / plain flaps)

  - design must be reasonably practical from a mechanical systems point of view

- Time constraint: 1 month from start to loft

  - in-house paneller

  - potential code (A502)

Model Geometry

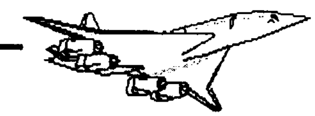

The design study was limited to the inboard wing region shown.

Model Geometry

Inboard leading edges focus of study -
new parts must mate up with existing outboard parts

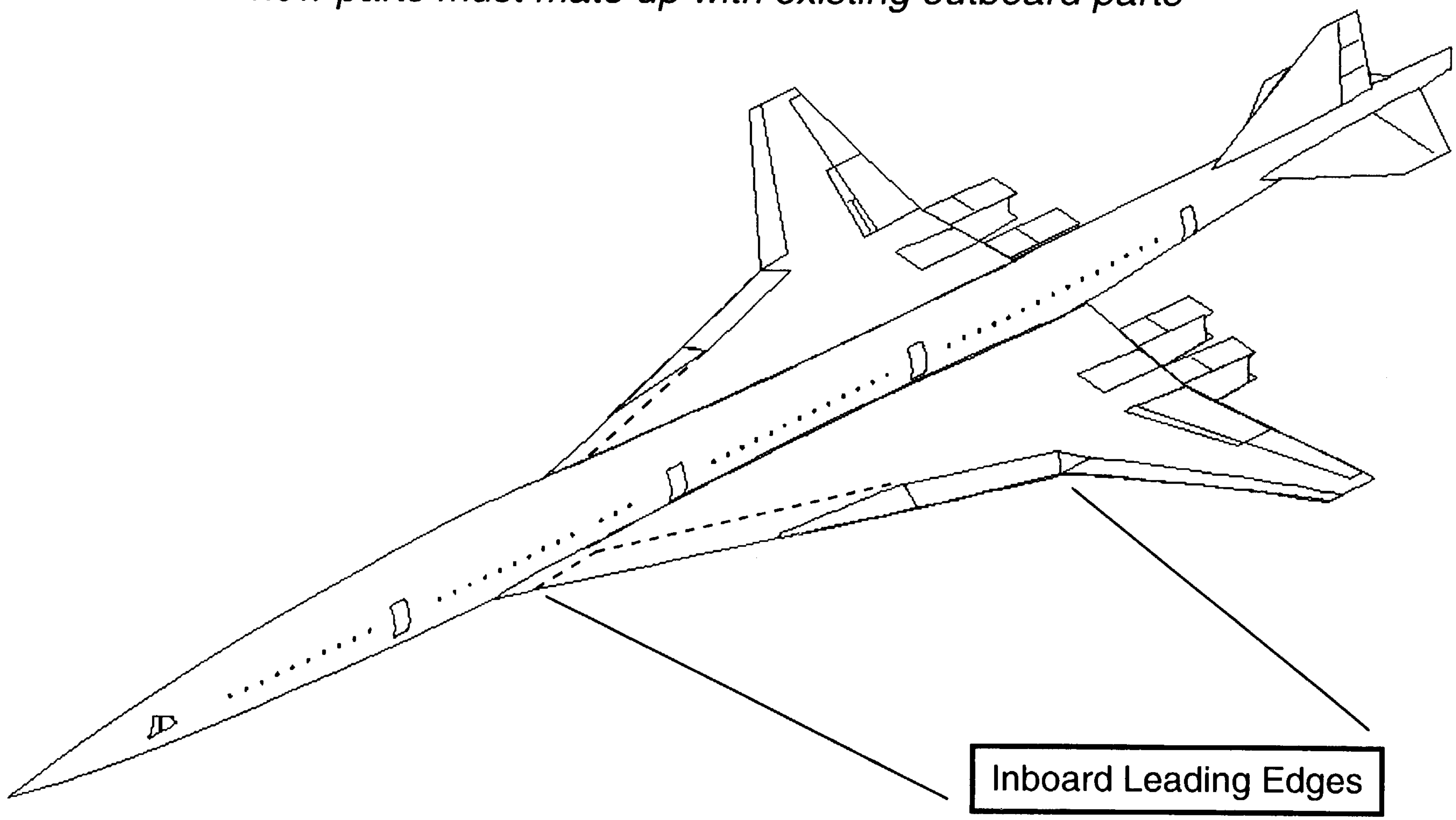

Panelling Process

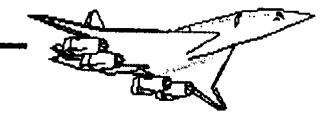

Having access to a fairly robust paneller made possible analysis of multiple configurations in the short amount of time available.

Special thanks to Keith Ebner for his work in creating the paneller!

Panelling Process

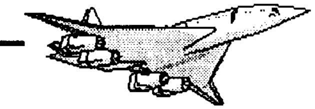

Required:
wing & body lofts, wing planform corner points, flap corner points and hingelines

interactive - package allows editing of geometry

Generates grids for:
deflected LE and TE flaps, wing spar, body

Creates wakes for body, wing and flap edges

generates input deck for A502 program

launch A502

solution!

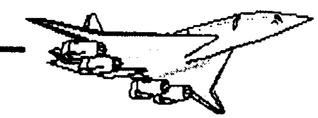

Sample Gridding

Sample configurations - panelled and shaded.

Sample Gridding

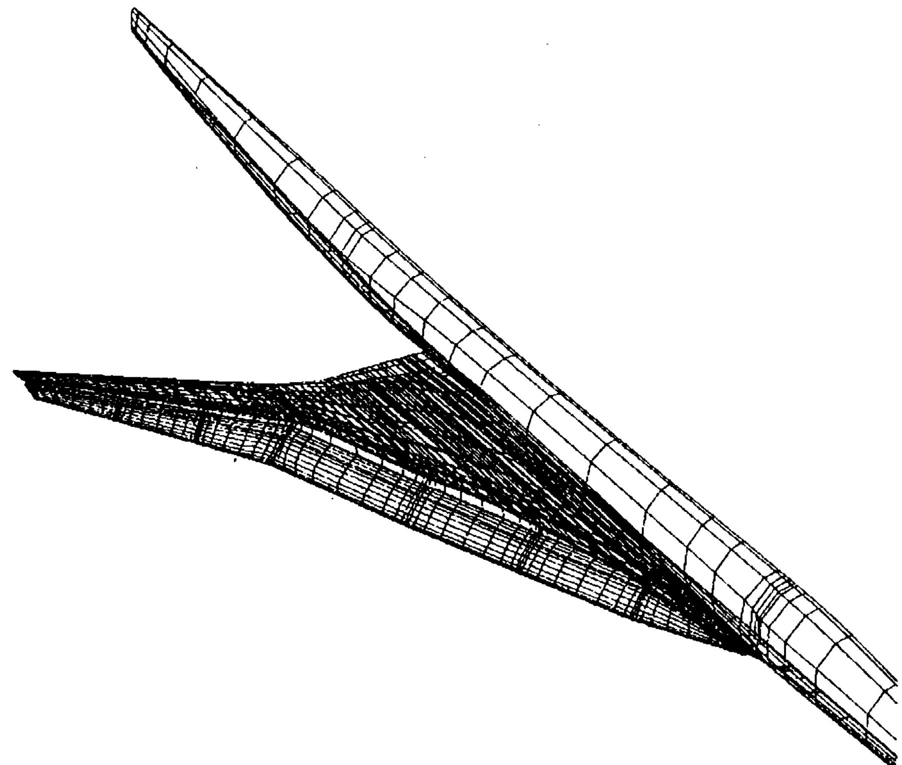

Geometries Analyzed

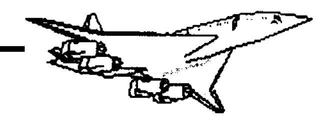

This is a listing of all geometries analyzed. Included in the study were partial span, and full span flap configurations along with a combination of plain flaps and sealed slats.

Of these, results of three configurations will be shown here:

1. 35 degree full span sealed slats.
2. 45 degree full span sealed slats.
3. 35 degree sealed slats outboard and 30 degree plain flaps inboard.

Geometries Analyzed

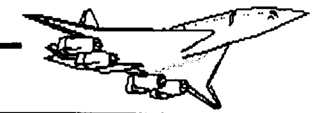

all configurations run with 15/15/15/10 (O/B -> I/B) trailing edges

Sealed Slat Runs

***(35ss/35ss/35ss/35ss/35ss)**	**35 sealed slat full span**
(40ss/40ss/40ss/40ss/40ss)	35 sealed slat full span
***(45ss/45ss/45ss/45ss/45ss)**	**45 sealed slat full span**
(35ss/30ss/30ss/30ss/30ss)	35ss/30ss sealed slat full span
***(35ss/30/30/30/30)**	**35ss/30 sealed slat - plain full span**
(35ss/30/30/0/0)	35ss/30 sealed slat - plain partial span

Plain Flap Runs

(30/30/30/30/30)	30 plain flap full span
(35/35/35/35/35)	35 plain flap full span
(45/45/45/45/45)	45 plain flap full span
(35/30/30/30/30)	35/30 plain flap full span
(30/30/30/0/0)	30 plain flap partial span
(35/30/30/0/0)	35/30 plain flap partial span

BOEING

HSCT High Lift Aerodynamics

Representative CP's

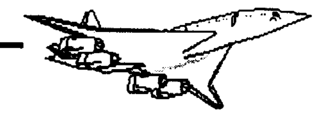

Representative pressure distributions are shown at two different spanwise locations, the cuts are roughly normal to the flap leading edge.

Both flap configurations shown here have a 35 degree sealed slat on the outboard leading edge. The inboard flaps on one are 30 degree plain; the other has 35 degree sealed slats. Both have 15/15/15/10 trailing edge flaps (O/B ->I/B).

The 35 degree full span case shows a reduction in the LE peak relative to the 30 degree inboard plain flap case, indicating 35 degrees is closer to an ideal flap deflection.

The upper surface hingeline pressure peak of the 35 degree inboard sealed slat is reduced relative to the 30 degree inboard plain flap. In addition, the hingeline pressure peak can be seen to be spread over a larger region of the flap, indicating the presence of a more favorable presure gradient.

Neither flap configuration is over-deflected.

Representative CP's

HSCT High Lift Aerodynamics

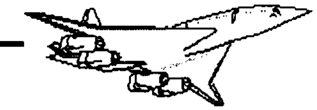

full30/35 vs. full35ss35ss

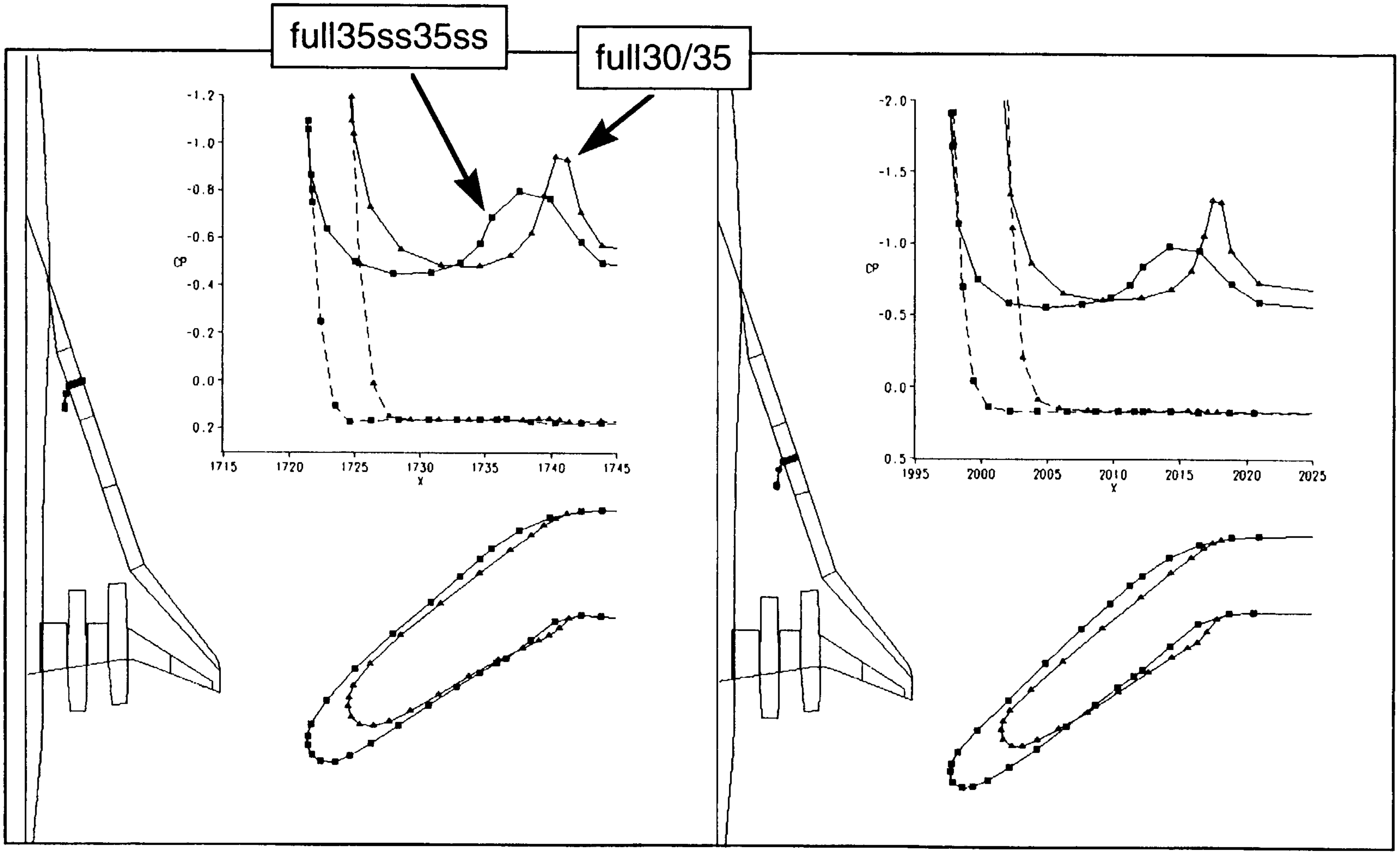

Representative CP's

Representative pressure distributions are shown at two different spanwise locations, the cuts are roughly normal to the flap leading edge.

One of the flap configurations shown here has a 35 degree sealed slat on the outboard leading edge and 30 degree plain flaps on the inboard wing. The other has full span 45 degree sealed slats. Both have 15/15/15/10 trailing edge flaps (O/B ->I/B).

The 45 degree full span case shows a reduction in the LE peak relative to the 30 degree inboard plain flap case, indicating 45 degrees is closer to an ideal flap deflection.

The upper surface hingeline pressure peak of the 45 degree inboard sealed slat is reduced relative to the 30 degree inboard plain flap. In addition, the hingeline pressure peak can be seen to be spread over a larger region of the flap, indicating the presence of a more favorable presure gradient.

Neither flap configuration is over-deflected.

Representative CP's

BOEING

HSCT High Lift Aerodynamics

full30/35 vs. full45ss45ss

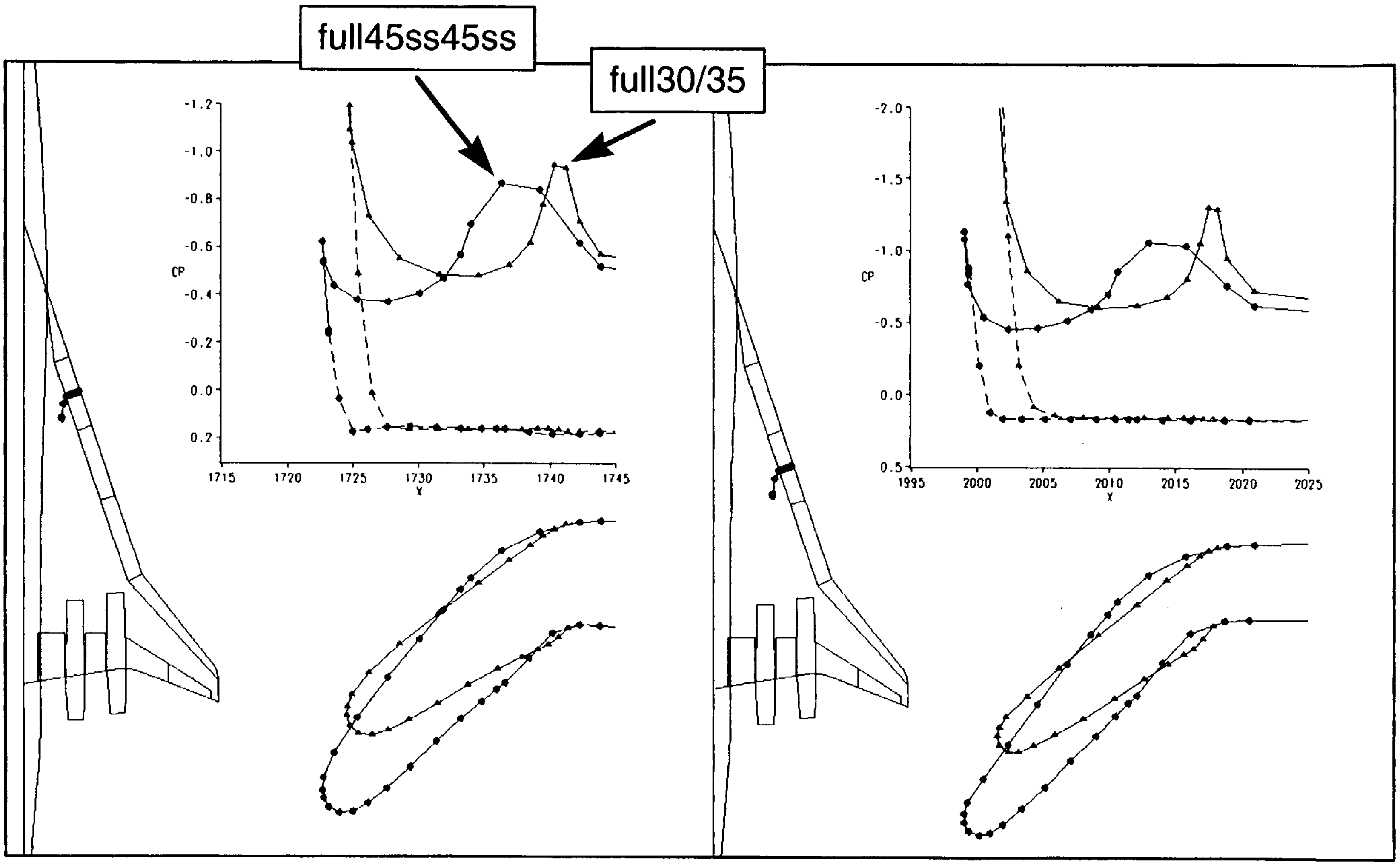

Representative CP's

BOEING

HSCT High Lift Aerodynamics

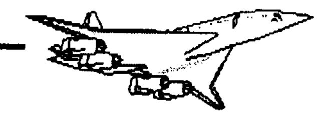

Representative pressure distributions are shown at two different spanwise locations, the cuts are roughly normal to the flap leading edge.

One of the flap configurations shown here has full span 35 degree sealed slats; the other has full span 45 degree sealed slats. Both have 15/15/15/10 trailing edge flaps (O/B ->I/B).

The 45 degree full span case shows a reduction in the LE peak relative to the 35 degree full span sealed slat case, indicating 45 degrees is closer to ideal flap deflection. However, the upper surface hingeline of the 35 degree sealed slat is reduced relative to the 45 degree sealed slat, indicating that there is a trade of hingeline to leading edge peaks (or flap deflection for upper surface curvature) for these 2 sealed slat configurations.

Both configurations have a lower surface attachment line; there was some concern that commonly deflected full span flaps / slats would result in an over-deflection of the inboard flaps.

Representative CP's

BOEING

HSCT High Lift Aerodynamics

full35ss35ss vs. full45ss45ss

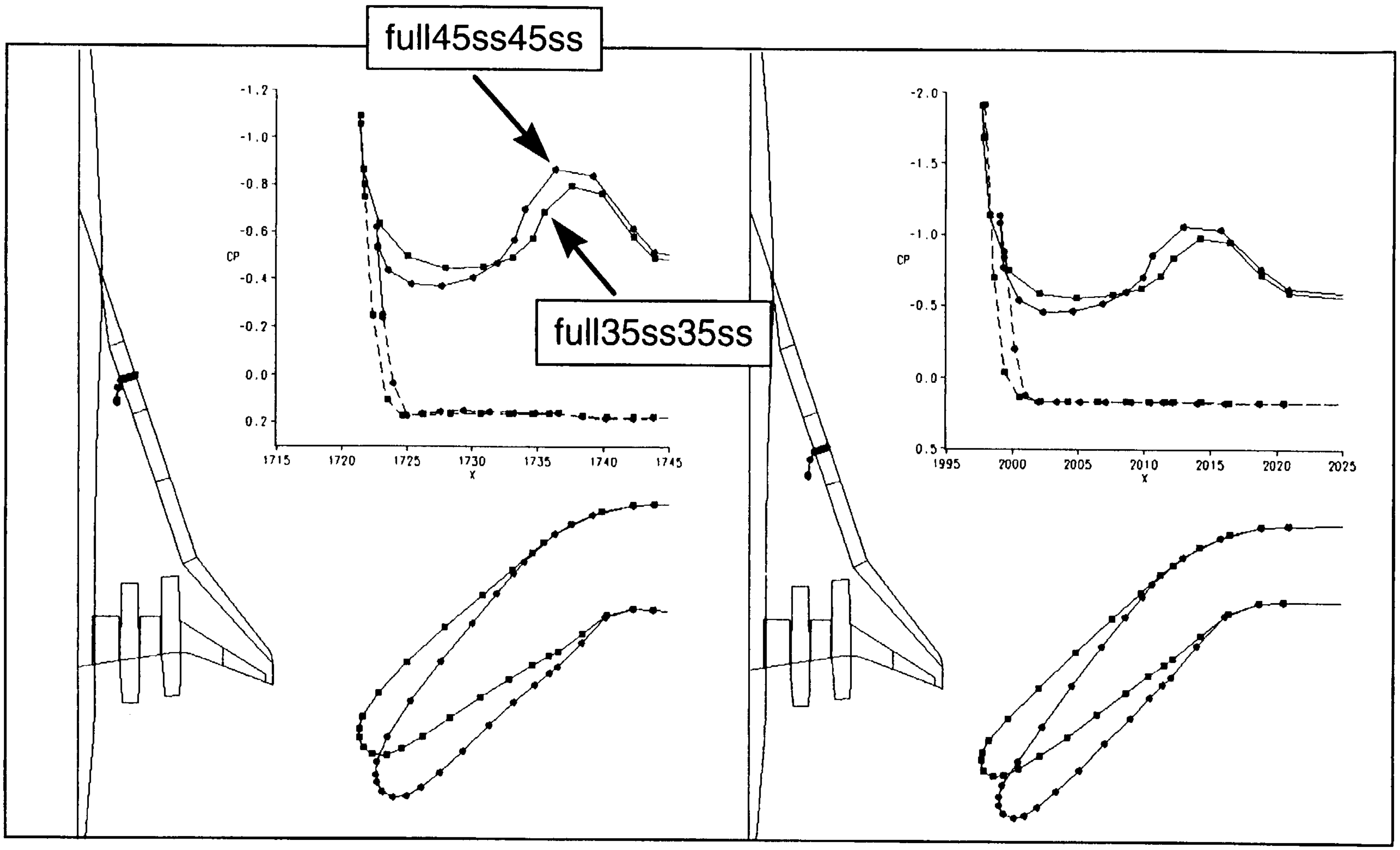

TNS3DMB Force Results

Shown are TCA results from the Navier-Stokes code TNS3MDB, courtesy of Allen Chen of Boeing-Seattle and Anthony Saladino of Dynacs.

The chart on the left shows the drag improvement when changing inboard flaps from 30 degree plain flaps to 35 degree sealed slats. The outboard flaps were 35 degree sealed slats for both configurations. Also, the trailing flaps were (from outboard to inboard) 15/15/15/10. At a C_L of 0.5, C_D is reduced by about 55 counts.

TNS3DMB Force Results

HSCT High Lift Aerodynamics

The Two Configurations:

LE: O/B 35ss, I/B 35ss
TE: 15/15/15/10 (O/B -> I/B)

And

LE: O/B 35ss, I/B 30plain
TE: 15/15/15/10 (O/B -> I/B)

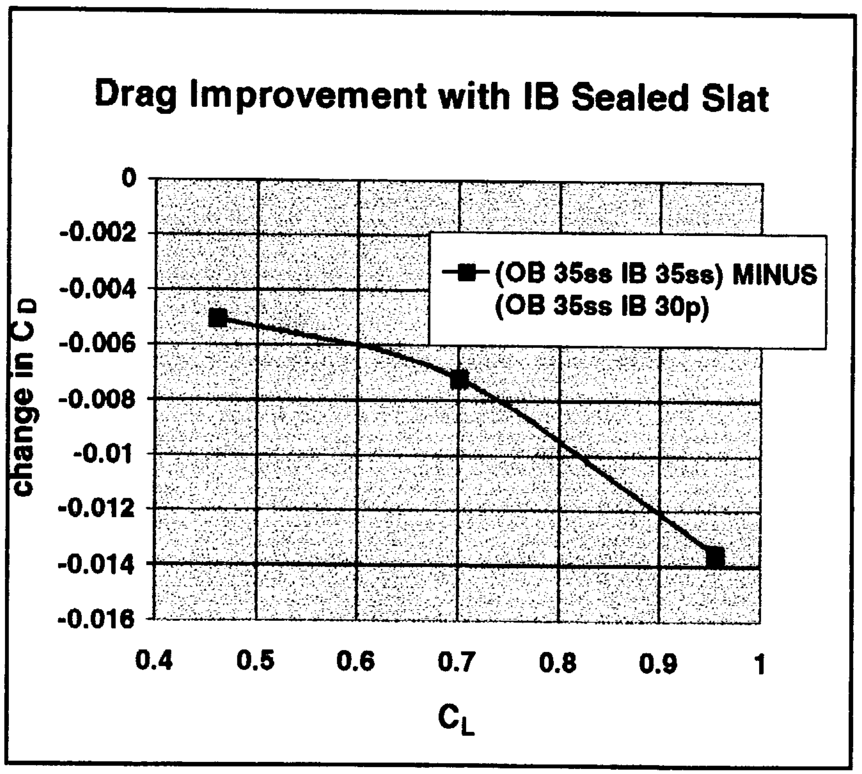

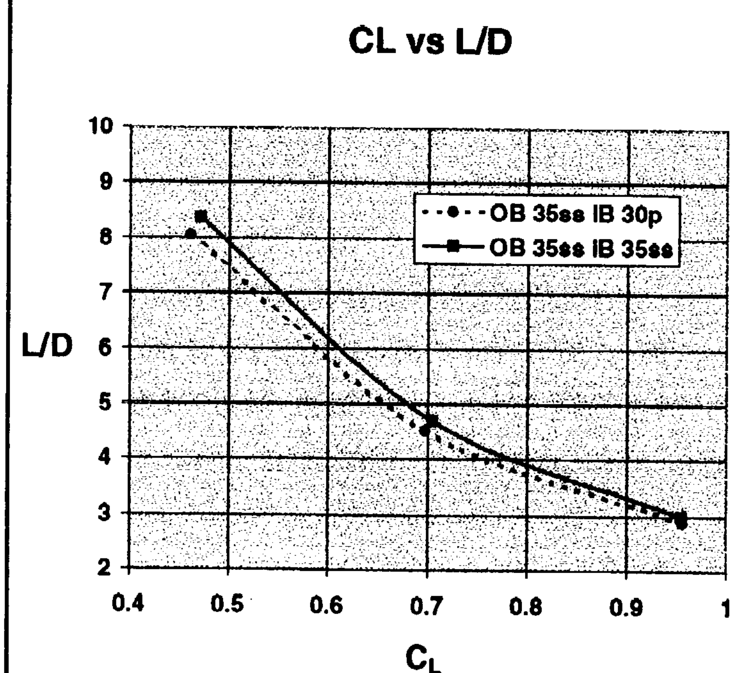

BOEING

New Sealed Slat Hardware

HSCT High Lift Aerodynamics

This picture was taken during the TCA-3 new part checkout at the Boeing wind tunnel shop facilities. The region highlighted in the photo shows an end view of the new 35 degree sealed slat with the more generous hingeline.

New Sealed Slat Hardware

BOEING

HSCT High Lift Aerodynamics

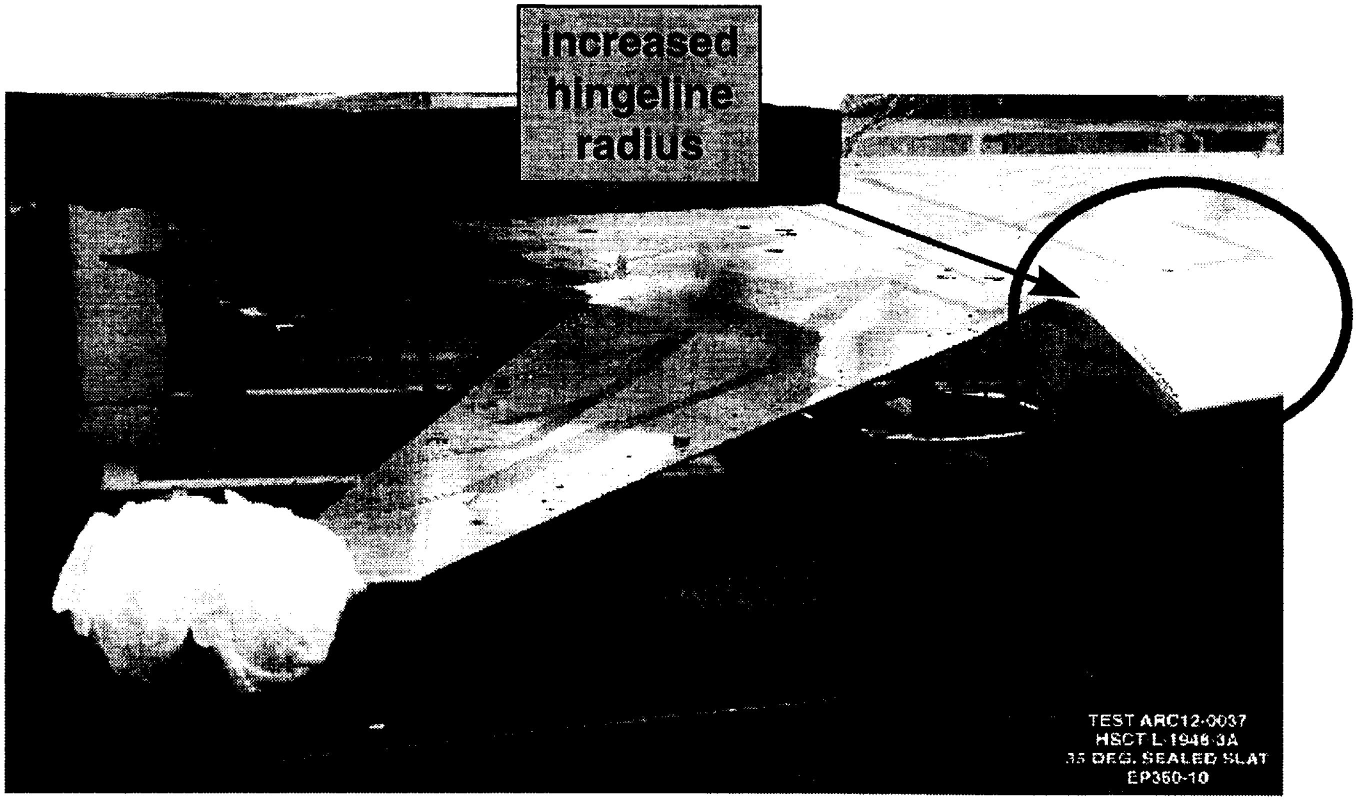

BOEING

New Sealed Slat Hardware

HSCT High Lift Aerodynamics

These 2 photos were taken at the Boeing wind tunnel during the TCA-3 new part checkout in November 1997.

The photo on the left shows the new inboard 45 degree sealed slat fitted up with the existing outboard 45 degree sealed slat.

The photo on the lower right shows some interference between the new inboard 35 degree sealed slat and the existing outboard 35 degree sealed slat.

New Sealed Slat Hardware

BOEING

HSCT High Lift Aerodynamics

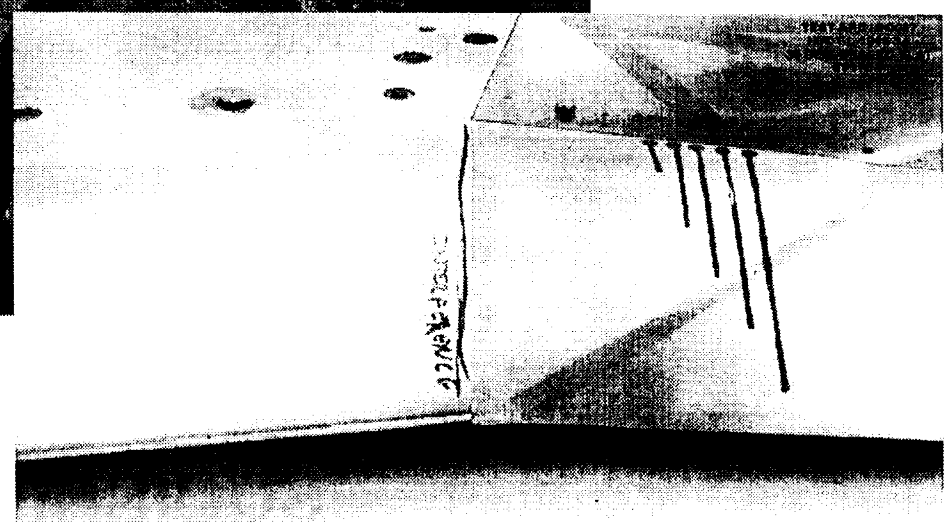

BOEING

HSCT High Lift Aerodynamics

Conclusions

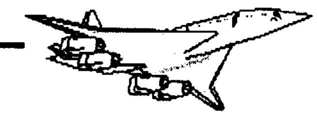

The use of the Boeing in-house paneller and a potential code worked well in achieving a quick turn around to a leading edge design problem.

Constant deflection flaps are beneficial from a systems point of view; based on calculated pressure distributions, the inboard flaps were not over-deflected when set to the same angle as the outboard flaps.

Navier-Stokes results confirmed the potential code design choice; sealed slats show an improvement in L/D over a plain flap configuration.

The bottom line will be whether or not the sealed slats buy their way onto the airplane. The trade in added complexity and weight must be offset by the improved performance seen in L/D.

Conclusions

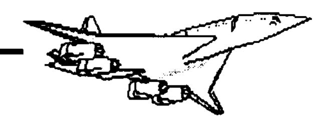

- Approach taken worked well in achieving quick design solution
  - Potential code, paneller
- Inboard flaps not over-deflected when set to same angle as outboard flaps
- Constant deflection flaps are beneficial from a systems POV
- N-S results confirm design choice
- 1998 TI study to determine whether sealed slats buy their way onto the airplane

This page is intentionally left blank.

Navier-Stokes Results for HSCT High-Lift Configurations

Anthony J. Saladino
Dynacs Engineering Co., Inc.

Allen W. Chen
Boeing Commercial Airplane Group

HSR Airframe Annual Review
February 10, 1998
Los Angeles, California

This presentation summarizes the effects of flap span and outward wing sweep on the Ref. H, and sealed slats vs. plain flaps on the TCA.

In each of the three tasks, CFD was used to determine if it can duplicate the wind tunnel results and explain the phenomena.

Each task has its own conclusions. Final recommendations are made based upon the conclusions of the three tasks.

Outline

- Objectives
- Task 1 - Effect of Inboard LE Flap Span (Ref. H)
- Task 2 - Effect of Outboard Wing Sweep (Ref. H)
- Task 3 - Effect of Inboard Sealed Slats (TCA)
- Conclusions and Recommendations

It's the long term goal to make the codes an integral part of configuration design. Running codes and comparing results with test data are the means to establish confidence in computed results.

Some of the configurations to be tested in TCA-4 were influenced by Navier-Stokes solutions.

Details of flow physics such as vortex formation, streamlines, and skin friction that are important to design are generally not available or difficult to obtain in tests.

Objectives for Navier-Stokes Solutions

- To make the codes an integral part of configuration design
- To reveal flow details that are not available or difficult to obtain in tests

Outline of task 1.

Task 1: Effect of Inboard LE Flap Span (Ref.H)

- Background
- Geometry and grid generation
- Flight conditions, flow solver and postprocessing
- Results
- Conclusions

We'd like to understand why. If the Navier-Stokes results match the test data, future designs may be done by computations.

Why the LE Flap Span Study (Ref. H)

- Test data from Test 429, 14x22 Wind Tunnel, showed that partial span leading edge flaps performed almost as good as the full span leading edge flaps.

The wind tunnel data from the 14x22 Test 429 was obtained on a 6% scale model of the Ref. H, run with the configuration wing/body/nacelles/vertical tail. Run 251 has LE flaps 30° along the full span, and Run 254 has the two most inboard LE flaps undeflected. Both have TE flaps deflected 10°.

The surface grid was constructed with Boeing's Aero Grid and Paneling System (AGPS). Points were clustered around the wing leading edge, the wing trailing edge, the flap hinges, and flap side edges. There are 121 points from wing LE to TE for each longitudinal grid. There are 113 longitudinal grid lines from the wing root to the wing tip. The four-block volume grid has 5.6 million points. Boeing here means Boeing/Seattle.

Turnaround time for the batch job on vn ranges from 4 hours to 40 hours. CPU time for the full-span case was two hours. The grid smoothing parameters were adjusted for the partial-span case, which resulted in a reduction of CPU time to one hour.

Geometry and Grid Generation for Task 1

- Ref. H wing/body. Flap geometry to match the ones which were tested. Wind tunnel test run log provided the information.
- Surface grid generated by Boeing using AGPS, with zero thickness along the outboard wing leading edge, the entire wing trailing edge, and the wing tip.
- Four-block volume grid generated by Boeing with a batch job on von Neumann

This page intentially left blank

Grid Generation

Upper Surface Grids for Ref. H, W/B Flaps, LE 30/TE 10
(every other grid line shown)

full–span LE flap

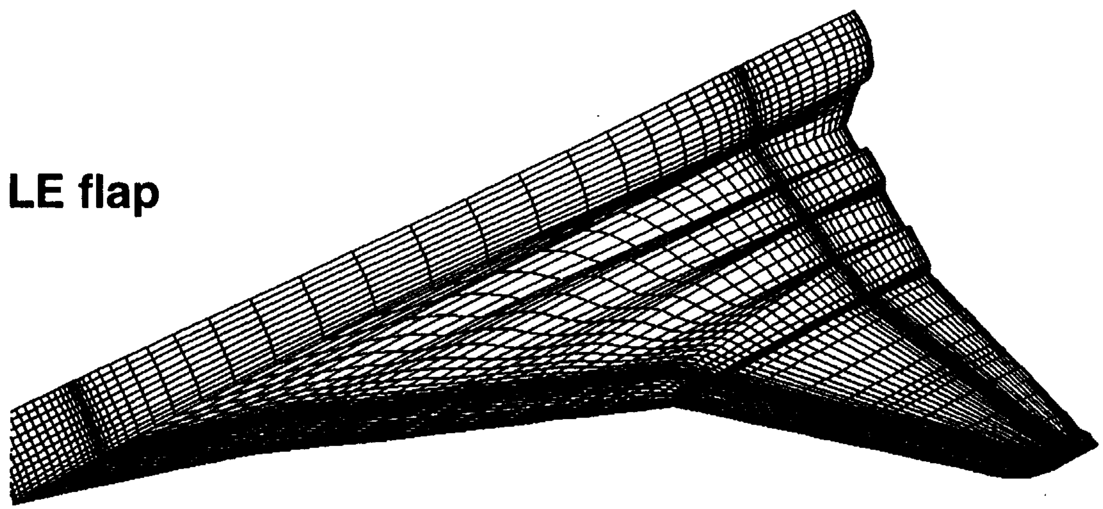

partial–span LE flap

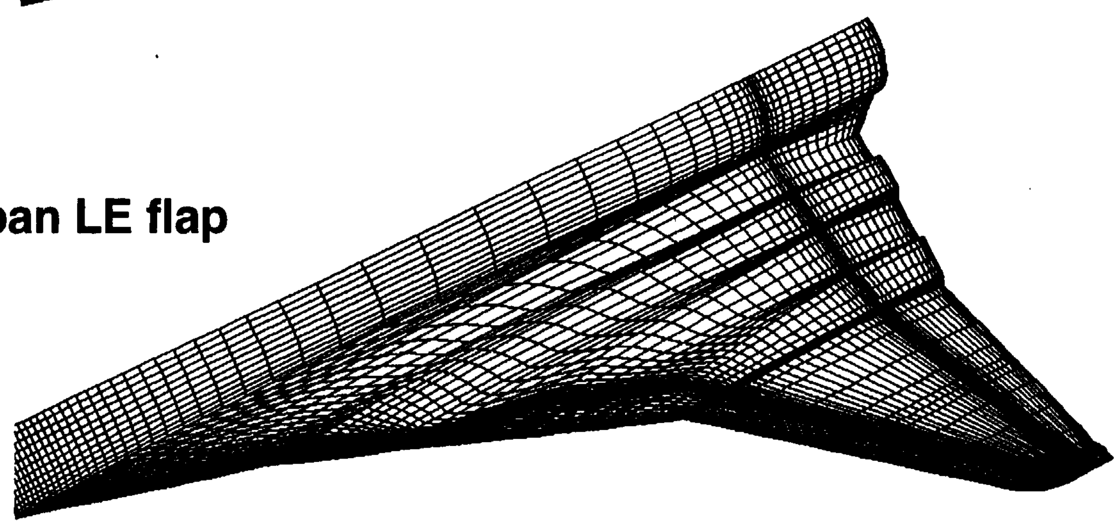

Dynacs ENGINEERING CO INC

The CPU time is 12.9 hours on the NAS C-90. Turnaround time is two-four days.

The flap edges are approximated in the grid. The upper and lower surfaces of the flap edges merge to a point, leading to flap gap regions of zero thickness. The flap gaps are set to a flow-through boundary condition.

Viscous computation with Spalart-Allmaras turbulence model.

Flight Conditions, Flow Solver, and Postprocessing

- Mach 0.242, Re 8 M to match the conditions at 14x22 wind tunnel
- Angle of attack (10°) to match the test data from Test 429
- Flow computed by Dynacs using TNS3DMB
- Postprocessing by Dynacs using FAST, Tecplot, and Kaleidagraph

This page intentially left blank

Results for Task 1

- Total pressure surveys
- Wing pressures
- Forces and moments compared with test data
- Drag analyses

The total pressure distribution at seven body stations and one station downstream of the trailing edge are shown with the local total pressure normalized by the free stream total pressure. It may be seen that the partial-span case has a noticeable vortex emanating from the inboard wing leading edge where the leading edge flap was not deflected. The full-span case, on the other hand, does not have such a noticeable vortex-like behavior even though there is a much smaller area further inboard which has lower total pressure. The full-span case leaves a wake with more energy than the partial-span case. This translates into more drag for the partial-span case.

Total Pressure Ratio Contours and Streamlines

Ref. H, W/B, Flaps LE 30/TE 10, Mach 0.24, Alpha 10 Deg., Re 8.8M/MAC
4-Block Viscous TNS3DMB

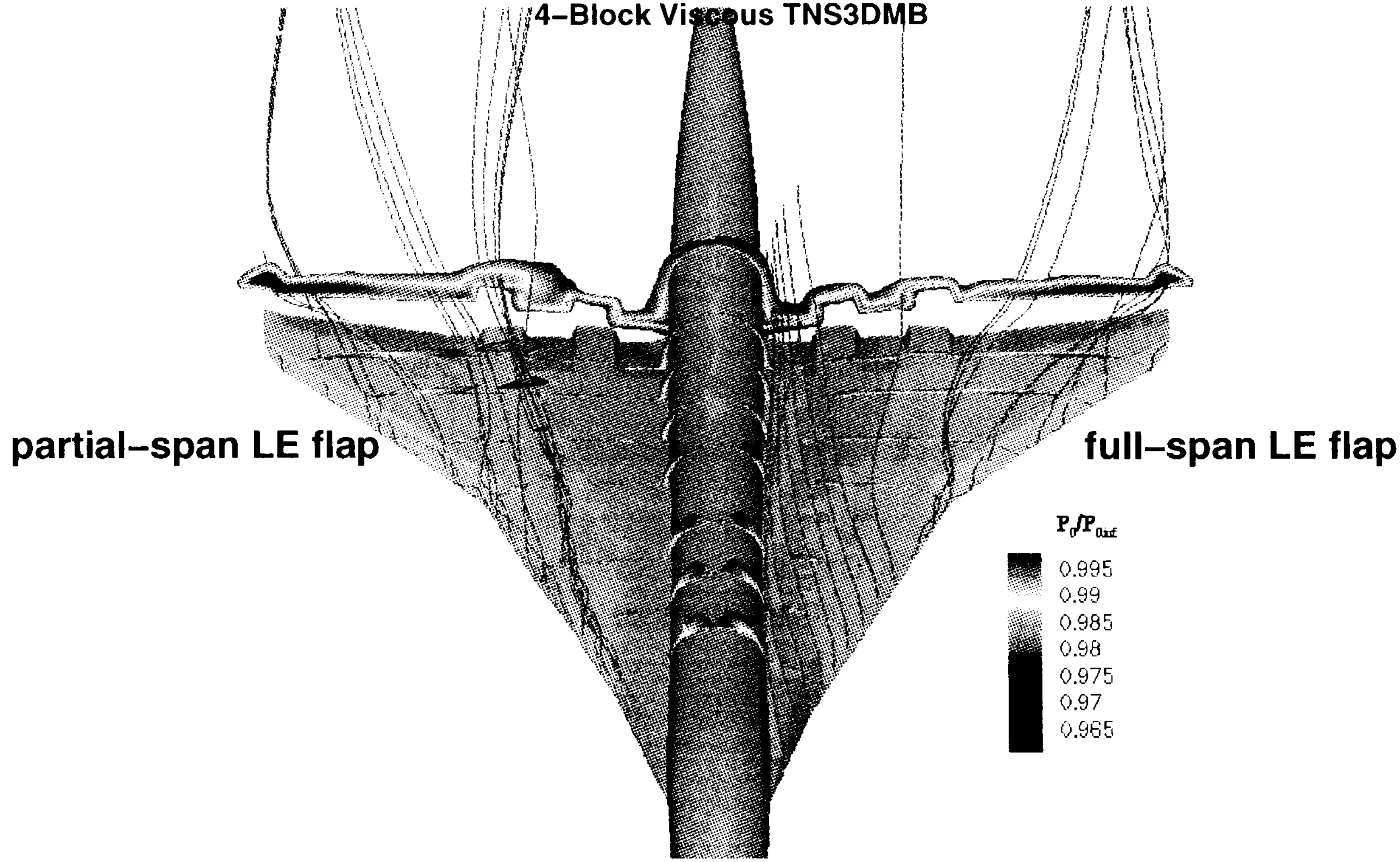

The differences between the full-span and the partial-span LE flap cases are greatest on the inboard wing. In the partial-span LE flap case there is a region of low pressure that starts at the most inboard deflected LE flap and extends downstream and spanwise. The software that was used to generate the figure does not allow the reversal of the C_P scale.

Upper Surface Pressure Coefficient

Ref. H, W/B, Flaps LE 30/TE 10, Mach 0.24, Alpha 10 Deg., Re 8.8M/MAC
4-Block Viscous TNS3DMB

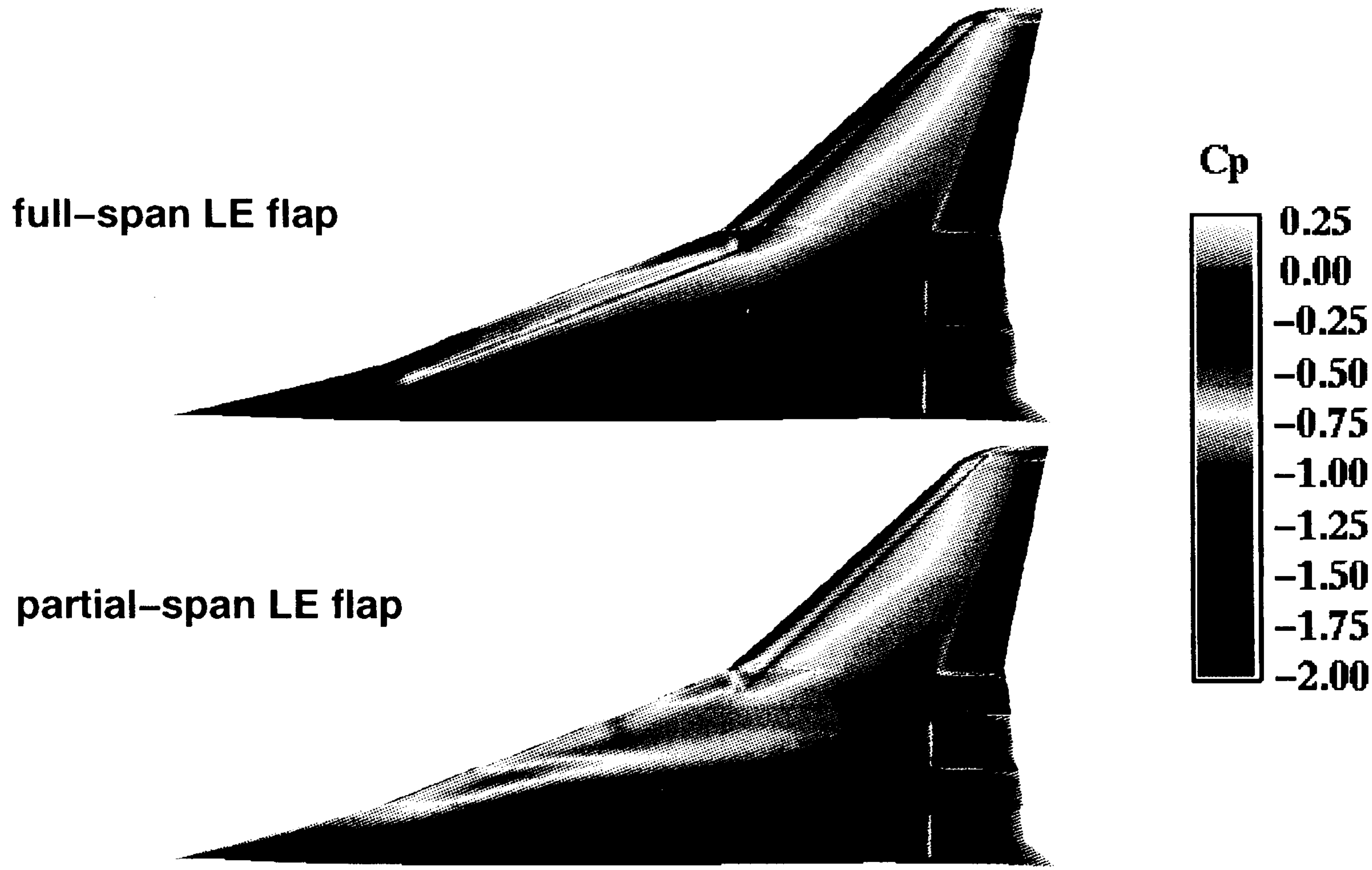

Results from TNS3DMB indicate that the full-span LE flap case has a lower lift coefficient than the partial-span LE flap case at the same angle of attack. The same trend is observed in the 14x22 Test 429 data, although the amount is much more than that of the CFD results.

Lift Coefficient vs. Alpha

Ref. H, Mach 0.24, Alpha 10 Deg.

Flaps LE Full–Span 30/30/30/30/30/30, Partial–Span 0/0/30/30/30/30; TE 10
NASA Langley 14 x 22 Wind Tunnel, W/B/N/V, Re 8M/MAC
TNS3DMB, W/B, Re 8.8M/MAC

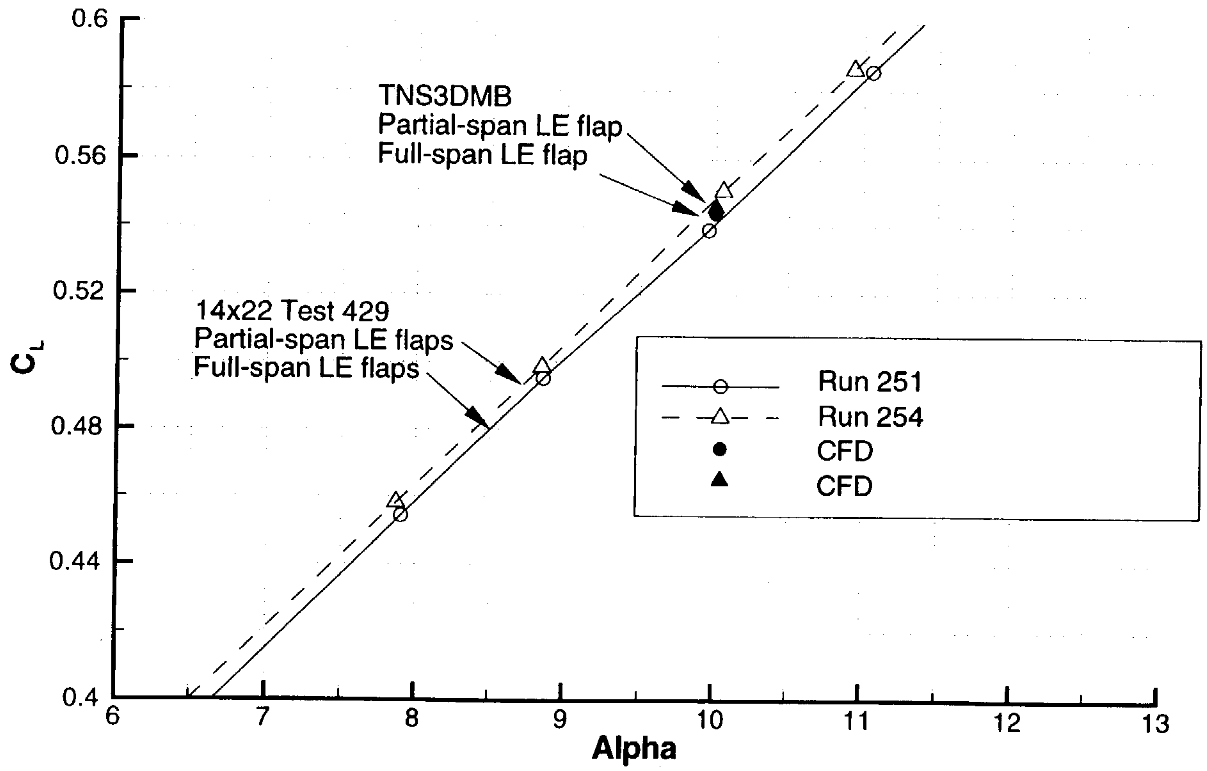

At a given angle of attack such as 10° the full-span inboard LE flap case generated lower drag than the partial-span inboard LE flap case in both CFD and the wind tunnel. For a given lift coefficient such as 0.55 the full-span LE flap generated much lower drag in CFD but slightly higher drag in the wind tunnel. Pressure distributions presented later show where the contribution comes from.

Lift Coefficient vs. Drag Coefficient

Ref. H, Mach 0.24, Alpha 10 Deg.

Flaps LE Full–Span 30/30/30/30/30/30, Partial–Span 0/0/30/30/30/30; TE 10
NASA Langley 14 x 22 Wind Tunnel, W/B/N/V, Re 8M/MAC
TNS3DMB, W/B, Re 8.8M/MAC

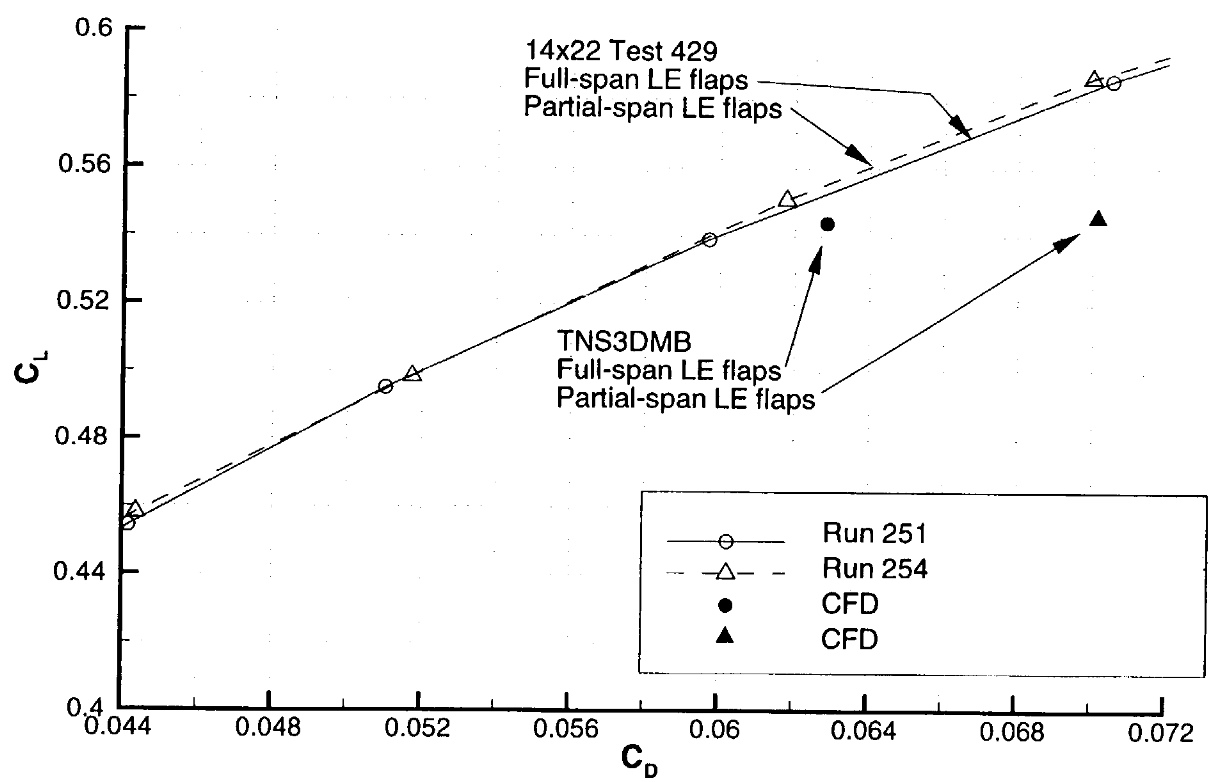

The TNS3DMB results show the same trend as the test data but the difference in pitching moment coefficient between the full-span and the partial-span LE flap cases is twice that of the 14x22 Wind Tunnel data.

Lift Coefficient vs. Moment Coefficient

Ref. H, Mach 0.24, Alpha 10 Deg.

Flaps LE Full–Span 30/30/30/30/30/30, Partial–Span 0/0/30/30/30/30; TE 10
NASA Langley 14 x 22 Wind Tunnel, W/B/N/V, Re 8M/MAC
TNS3DMB, W/B, Re 8.8M/MAC

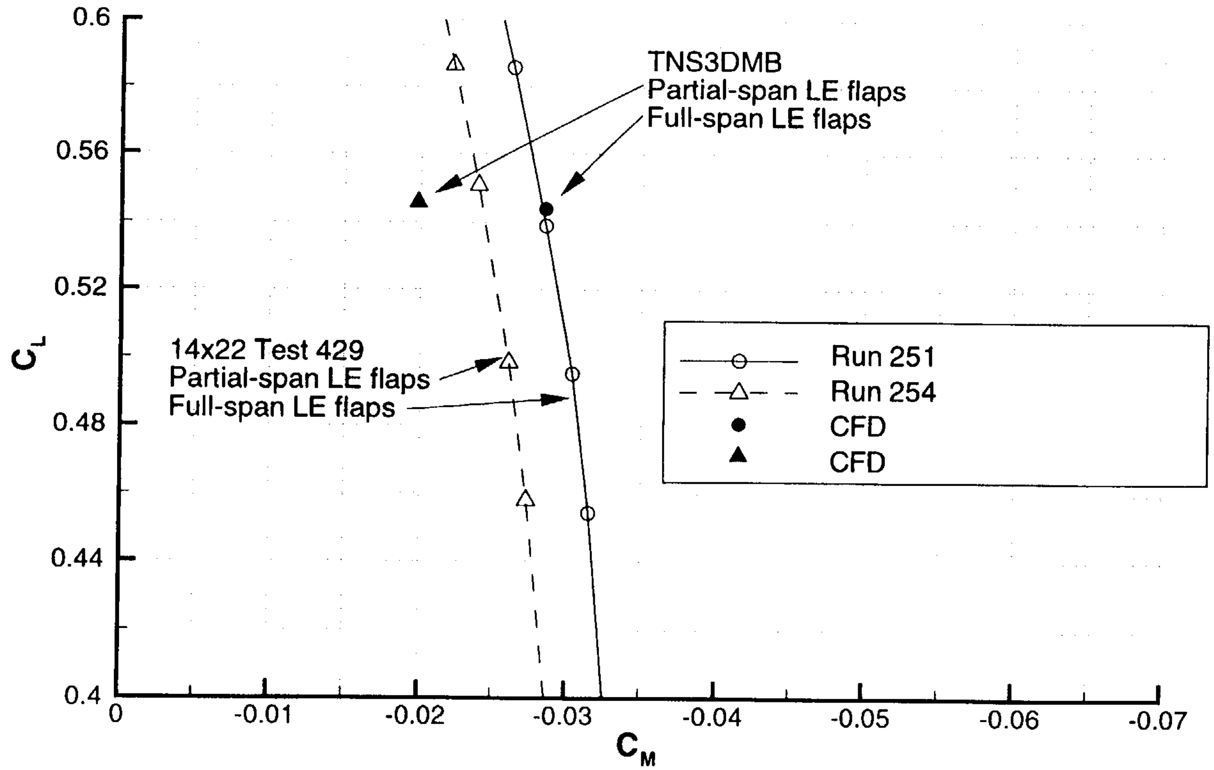

CFD generated a lower L/D than the test data for a given C_L, mainly due to the higher drag. Although the C_L is slightly larger for the partial-span compared to the full-span case, the L/D is much lower due to greater drag. Also, in the CFD results the difference between the full-span inboard LE flap and the partial-span inboard LE flap is significant, while test data show nearly identical L/D for both geometries.

Lift Coefficient vs. L/D

Ref. H, Mach 0.24, Alpha 10 Deg.

Flaps LE Full–Span 30/30/30/30/30/30, Partial–Span 0/0/30/30/30/30; TE 10
NASA Langley 14 x 22 Wind Tunnel, W/B/N/V, Re 8M/MAC
TNS3DMB, W/B, Re 8.8M/MAC

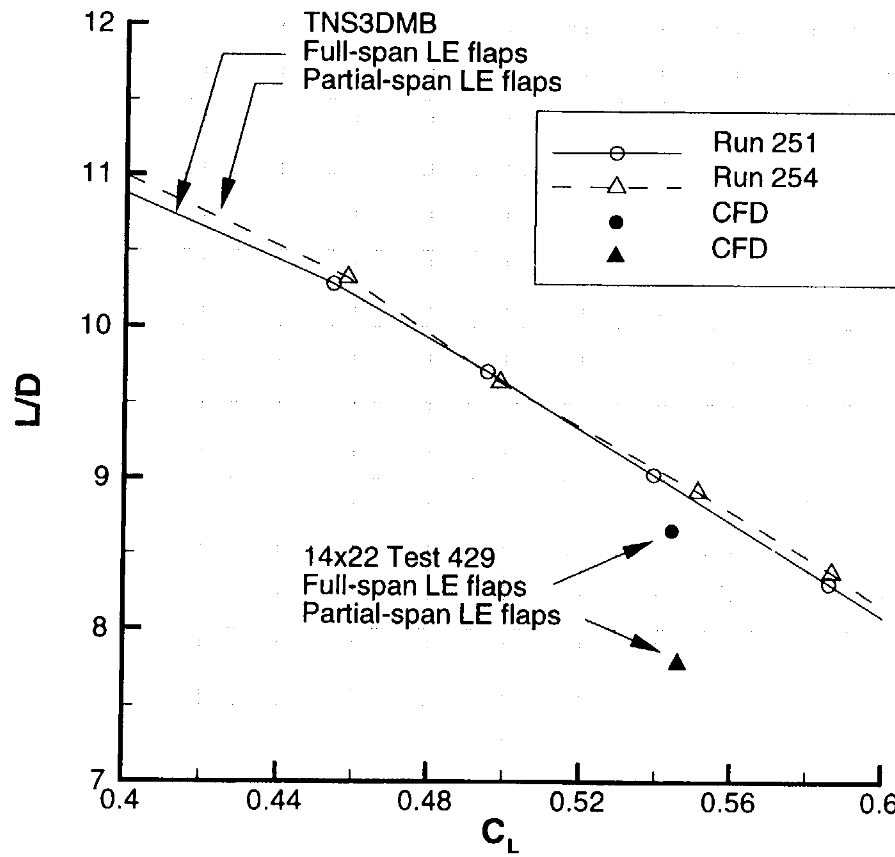

The majority of the difference in drag between the two configurations is in pressure drag, 0.0072. The difference in the skin friction is less than 0.0001.

The following pages show further analyses of the source of this difference in pressure drag.

Drag Coefficient Components

Ref. H, W/B, Mach 0.24, Alpha 10 Deg., Re 8.8 M/MAC
Flaps LE Full-Span 30/30/30/30/30/30, Partial-Span 0/0/30/30/30/30; TE 10
4-Block Viscous TNS3DMB

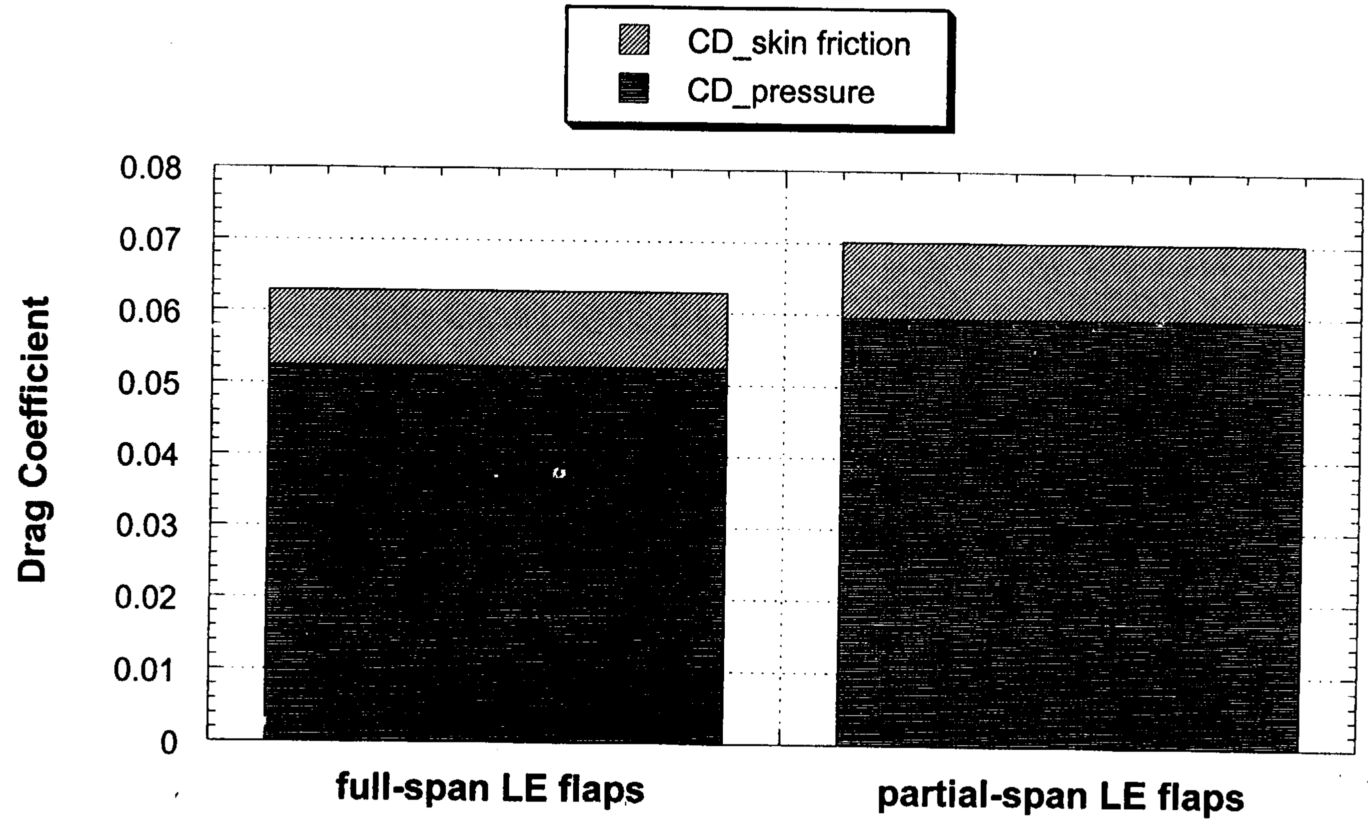

Dynacs Engineering Co., Inc.

Spanwise distributions of section lift coefficient and pressure drag coefficient are presented, with the coefficients being normalized with respect to the local chord.

The section lift coefficient for the full-span case is less than that of the partial-span LE case for part of the inboard wing. It is higher on the outboard wing. the section drag coefficient for the full-span case is less than that for the partial-span case on both the inboard and the outboard wing. The partial-span inboard LE flaps start at approximately BBL 240.

Spanwise Distribution of Section Lift and Drag Coefficient

Ref. H, W/B, Mach 0.24, Alpha 10 Deg., Re 8.8M/MAC

Flaps LE Full–Span 30/30/30/30/30/30, Partial–Span 0/0/30/30/30/30; TE 10

4–Block Viscous TNS3DMB

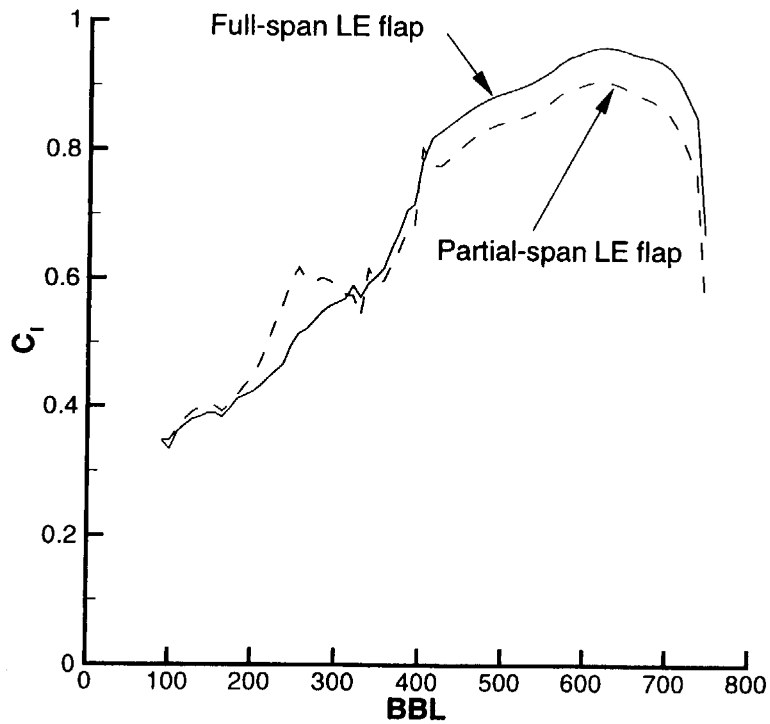

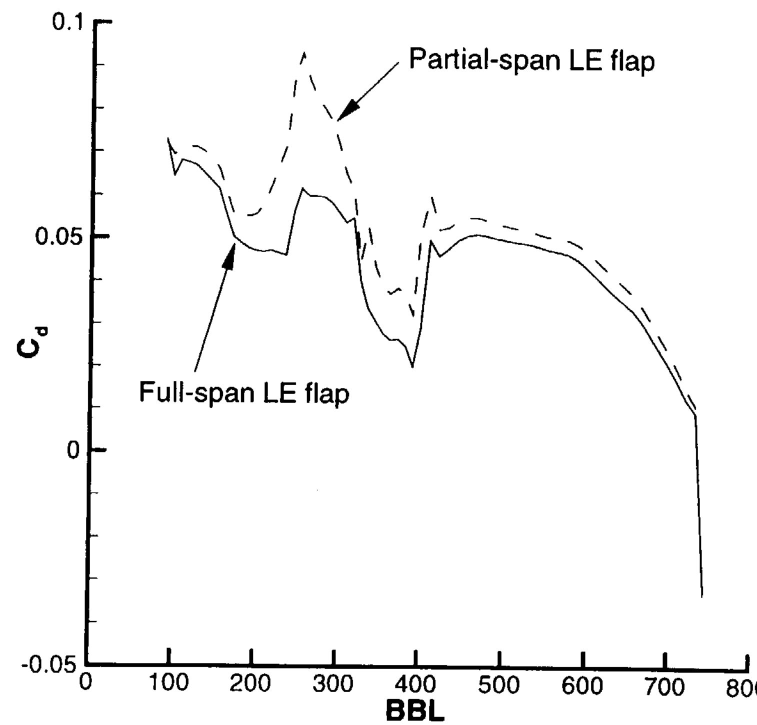

As a means of identifying the source of the larger pressure drag of the partial-span LE flap case compared with the full-span LE flap case, a suction loop plot is presented as C_P versus z'/c. The areas enclosed by the curves represent drag due to pressure. Two representative suction loop plots are shown in this and the next page. The partial-span case has a huge drag loop and a very small suction loop at maximum z'/c. The full-span case has a smaller drag loop and a noticeable suction loop.

Section Pressure Distribution
Ref. H, W/B, Mach 0.24, Alpha 10 Deg., Re 8.8M/MAC
Flaps LE Full–Span 30/30/30/30/30/30, Partial–Span 0/0/30/30/30/30; TE 10
4–Block Viscous TNS3DMB

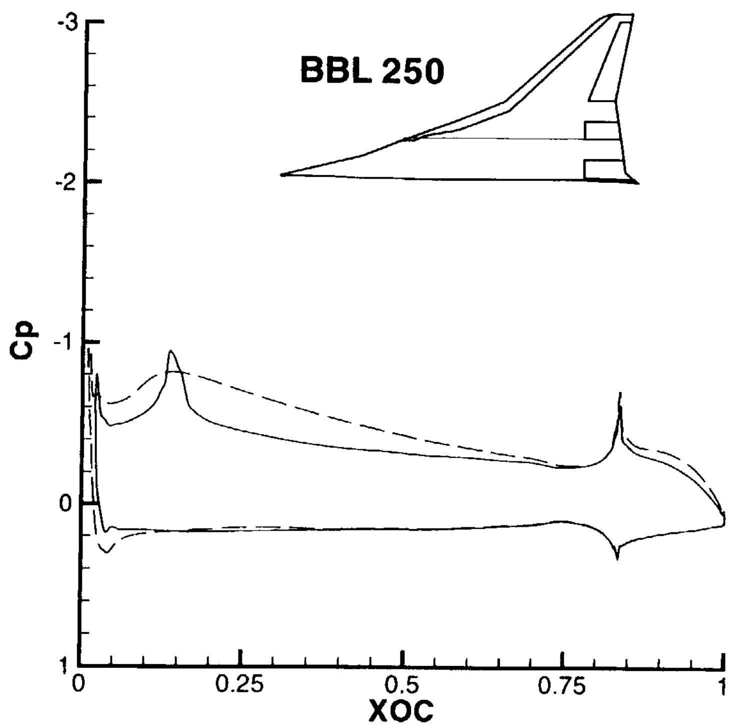

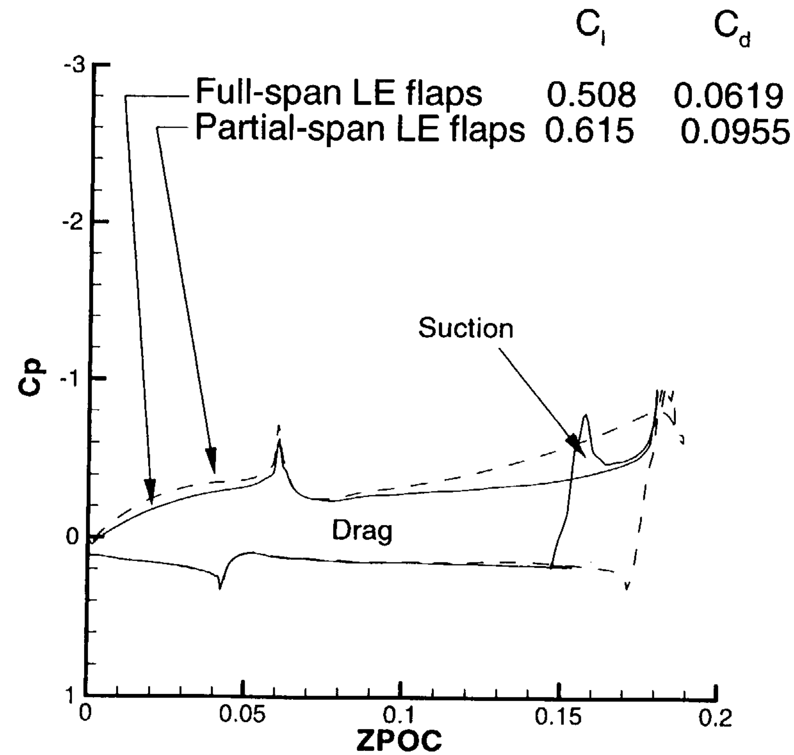

Dynacs ENGINEERING CO. INC

The full-span inboard LE flap case has 5% more lift and 6% less drag at this section. This is typical for the entire outboard wing.

Section Pressure Distribution

Ref. H, W/B, Mach 0.24, Alpha 10 Deg., Re 8.8M/MAC
Flaps LE Full–Span 30/30/30/30/30/30, Partial–Span 0/0/30/30/30/30; TE 10
4–Block Viscous TNS3DMB

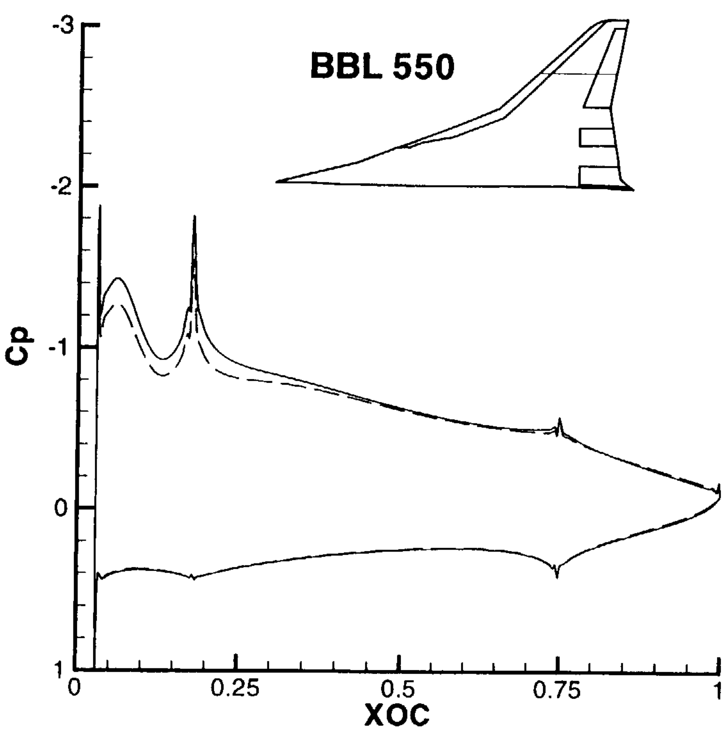

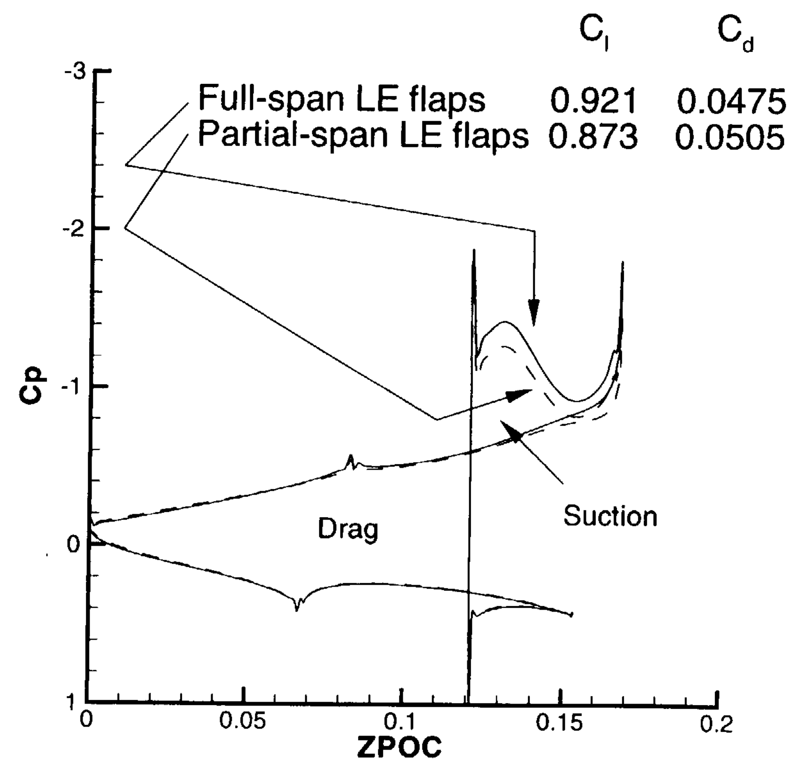

Dynacs ENGINEERING CO. INC

TNS3DMB results did not match the test data perfectly, but had the similar increments between the two configurations.

A detailed flow field survey from TNS3DMB shows vortical flow on the inboard wing with the partial-span inboard LE flap. Surface pressure distributions show this vortical flow has a large contribution to the pressure drag.

Conclusions – Task 1

- Navier-Stokes solutions from TNS3DMB compared favorably with test data
- TNS3DMB showed full-span flaps had better performance than partial-span flaps
- Vortical flow has a large contribution to the pressure drag

Outline of task 2.

Task 2: Effect of Outboard LE Sweep (Ref. H)

- Background
- Geometry and grid generation
- Flight conditions, flow solver and postprocessing
- Results
- Conclusions

If the Navier-Stokes results match the test data, future designs may be done by computations. Some of the configurations to be tested in TCA-4 were guided by Navier-Stokes solutions.

Why the Outboard LE Sweep Study (Ref. H)

- TCA was exercising an outboard LE sweep study
- Ref. H test data available from Test 429, 14x22 wind tunnel

The wind tunnel data from the 14x22 Test 429 was obtained on a 6% scale of the Ref. H, run with the configuration wing/body/nacelles/vertical tail. Runs 122, 123, 186 and 187 have an outboard LE sweep angle of 48°, and Runs 166 and 167 have an outboard LE sweep angle of 38.9°. The LE flaps are deflected 0/0/30/30/30/30, and all of the TE flaps are deflected 10°. The aspect ratio is the same for each configuration (AR = 2.3673).

Surface grid generation shifted to Dynacs. The surface grid was constructed with Boeing's Aero Grid and Paneling System (AGPS). Points were clustered around the wing leading edge, the wing trailing edge, the flap hinges, and flap side edges. There are 121 points from wing LE to TE for each longitudinal grid. There are 113 longitudinal grid lines from the wing root to the wing tip. The four-block volume grid has 5.6 million points. Boeing here means Boeing/Seattle.

Turnaround time for the batch job on vn ranges from 4 hours to 40 hours. CPU time is one hour.

Geometry and Grid Generation for Task 2

- Ref. H W_6(48° outboard LE sweep)/body and W_7(38.9°)/body. Flap geometry to match the ones which were tested.
- Surface grid modified from a previous case by Dynacs using AGPS, with zero thickness along the outboard wing leading edge, the entire wing trailing edge, and the wing tip.
- Four-block volume grid generated by Boeing with a batch job on von Neumann.

This page intentially left blank

Grid Generation

Upper Surface Grids for Ref. H, W/B, Flaps LE 30/TE 10
(every other grid line shown)

48 deg outboard sweep

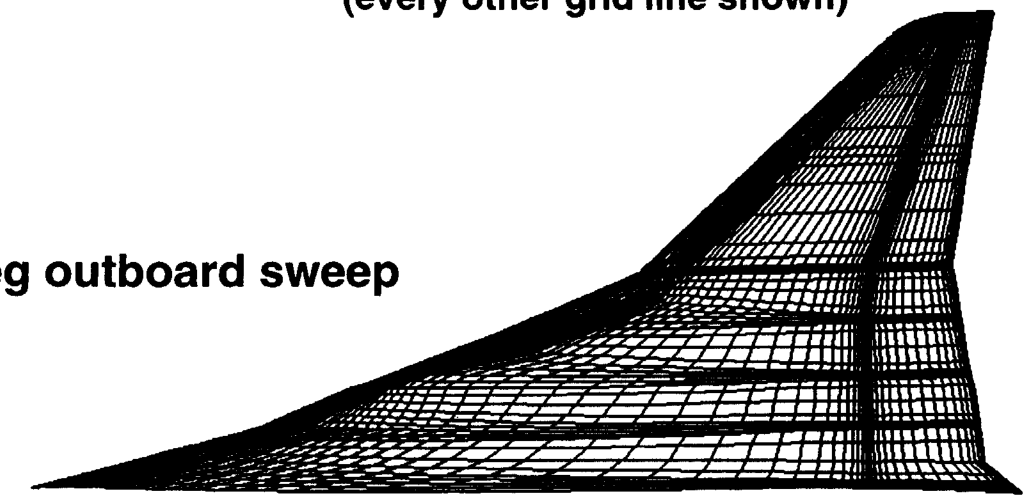

38.9 deg outboard sweep

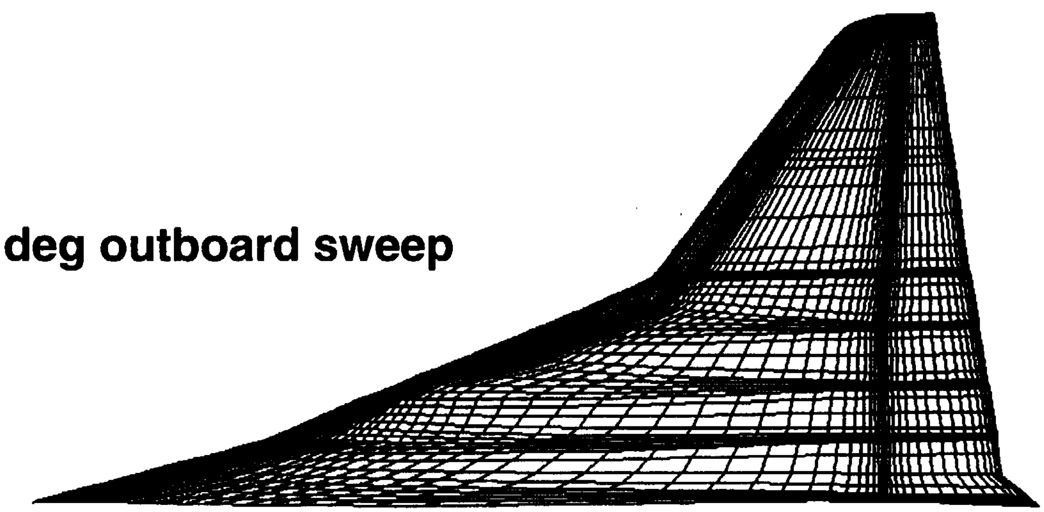

The CPU time is 13.0 hours on the NAS C-90. The clock time is 2.1 hours. Turnaround time is one day.

Boeing here means Boeing/Seattle.

The flap edges are approximated in the grid. The upper and lower surfaces of the flap edges merge to a point, leading to flap gap regions of zero thickness. The flap gaps are set to a flow-through boundary condition.

Viscous computation with Spalart-Allmaras turbulence model.

Flight Conditions, Flow Solver, and Postprocessing

- Mach 0.242, Re 8 M to match the conditions at 14x22 wind tunnel
- Angle of attack (10°) to match the test data from Test 429
- Flow computed by Dynacs using Boeing's version of TNS3DMB with multi-tasking
- Postprocessing by Dynacs using FAST, Tecplot, and Kaleidagraph

This page intentially left blank

Results for Task 2

- Total pressure surveys
- Wing pressures
- Forces and moments compared with test data
- Drag analyses
- Particle traces
- Skin friction

The total pressure distributions at seven body stations and one station downstream of the TE are shown with the local total pressure normalized by the free stream total pressure. A vortex, apparent in both cases, emanates from the inboard wing where the LE flap was not deflected. A vortex exists near the planform break, which seems to lose more energy in the W_6 (48° outboard LE sweep) case than in the W_7 (38.9° outboard LE sweep) case as it approaches the trailing edge. A noticeable difference exists between the two configurations in the vortex aft of the tip; there is more energy in the tip vortex of W_7 compared with the tip vortex of W_6, resulting in less drag for W_7.

Total Pressure Ratio Contours and Streamlines

Ref. H, W/B, Flaps LE 30/TE 10, Mach 0.24, Alpha 10 Deg., Re 8.8M/MAC

4-Block Viscous TNS3DMB

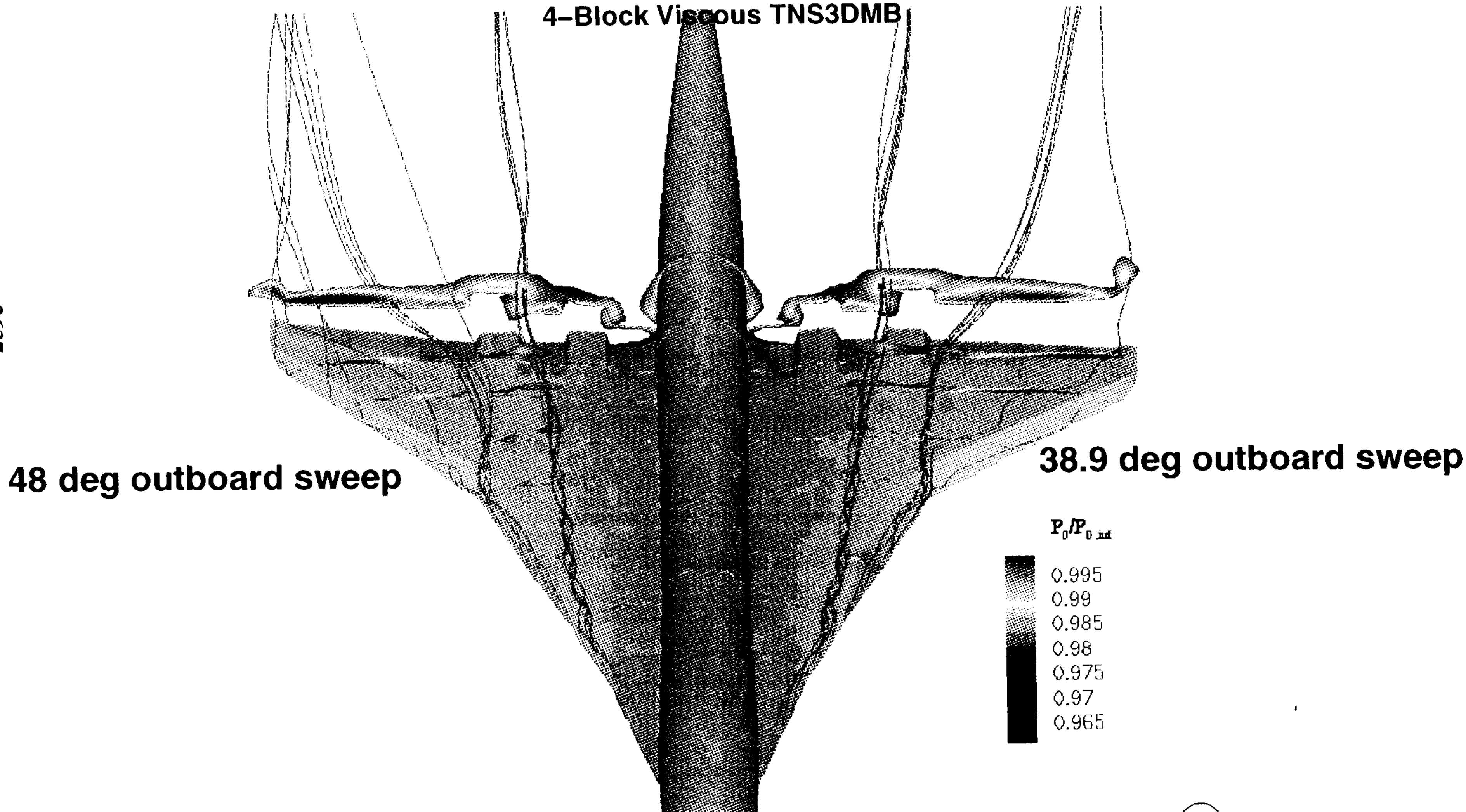

The differences between the W_7 (38.9° outboard LE sweep) and the W_6 (48° outboard LE sweep) cases are greatest on the outboard wing. The region of low pressure covers more of the outboard wing in the W_7 case than in the W_6 case. The software that was used to generate the figure does not allow the reversal of the C_p scale.

Upper Surface Pressure Coefficient

Ref. H, W/B, Flaps LE 30/TE 10, Mach 0.24, Alpha 10 Deg., Re 8.8M/MAC
4–Block Viscous TNS3DMB

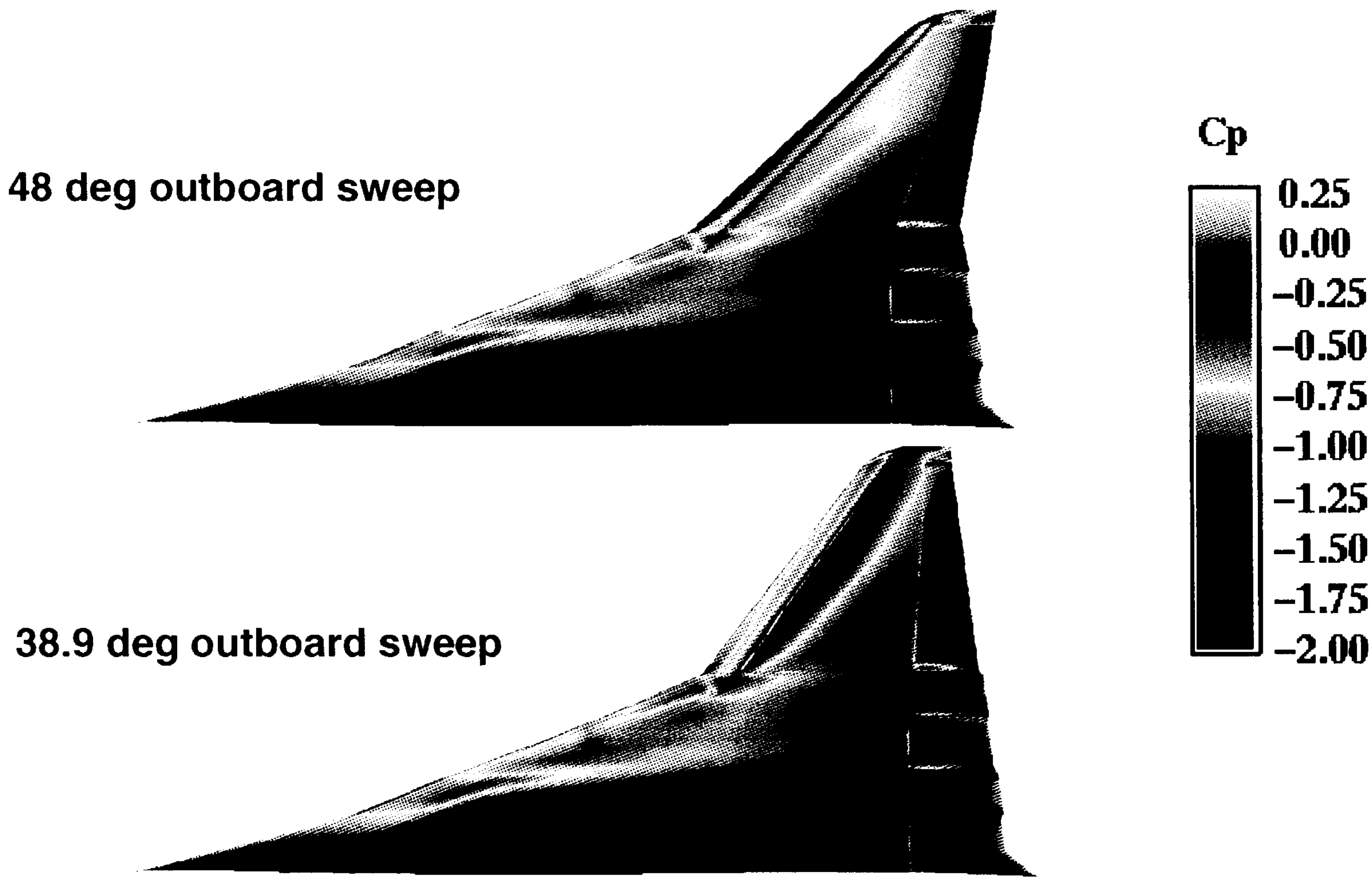

Dynacs ENGINEERING CO. INC.

Results from TNS3DMB indicate that the W_7 (38.9° outboard LE sweep) case has a higher lift coefficient than the W_6 (48° outboard LE sweep) case at the same angle of attack. The same trend is observed in the 14x22 Test 429 data, although the amount varies, due to the range of W_6 data in the repeat runs.

Lift Coefficient vs. Alpha

Ref. H, Flaps LE 0/0/30/30/30/30 TE 10, Mach 0.24, Alpha 10 Deg., Re 8M/MAC
NASA Langley 14 x 22 Wind Tunnel, W/B/N/V
TNS3DMB, W/B

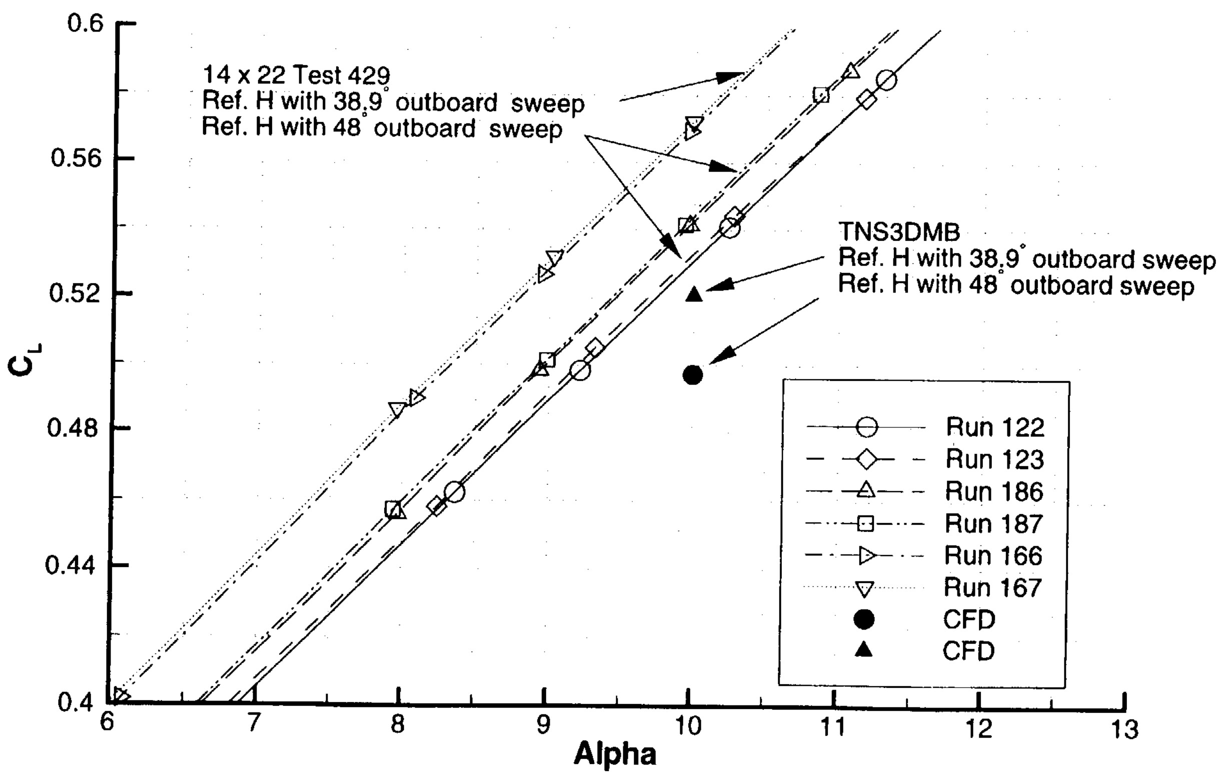

Dynacs Engineering Co. Inc.

At a given angle of attack such as 10° the W_6 (48° outboard LE sweep) configuration generated lower drag than the W_7 (38.9° outboard LE sweep) configuration in both CFD and the wind tunnel. Pressure distributions will be presented later to show how the drag varies on the outboard wing of each configuration.

Lift Coefficient vs. Drag Coefficient

Ref. H, Flaps LE 0/0/30/30/30/30 TE 10, Mach 0.24, Alpha 10 Deg., Re 8M/MAC
NASA Langley 14 x 22 Wind Tunnel, W/B/N/V
TNS3DMB, W/B

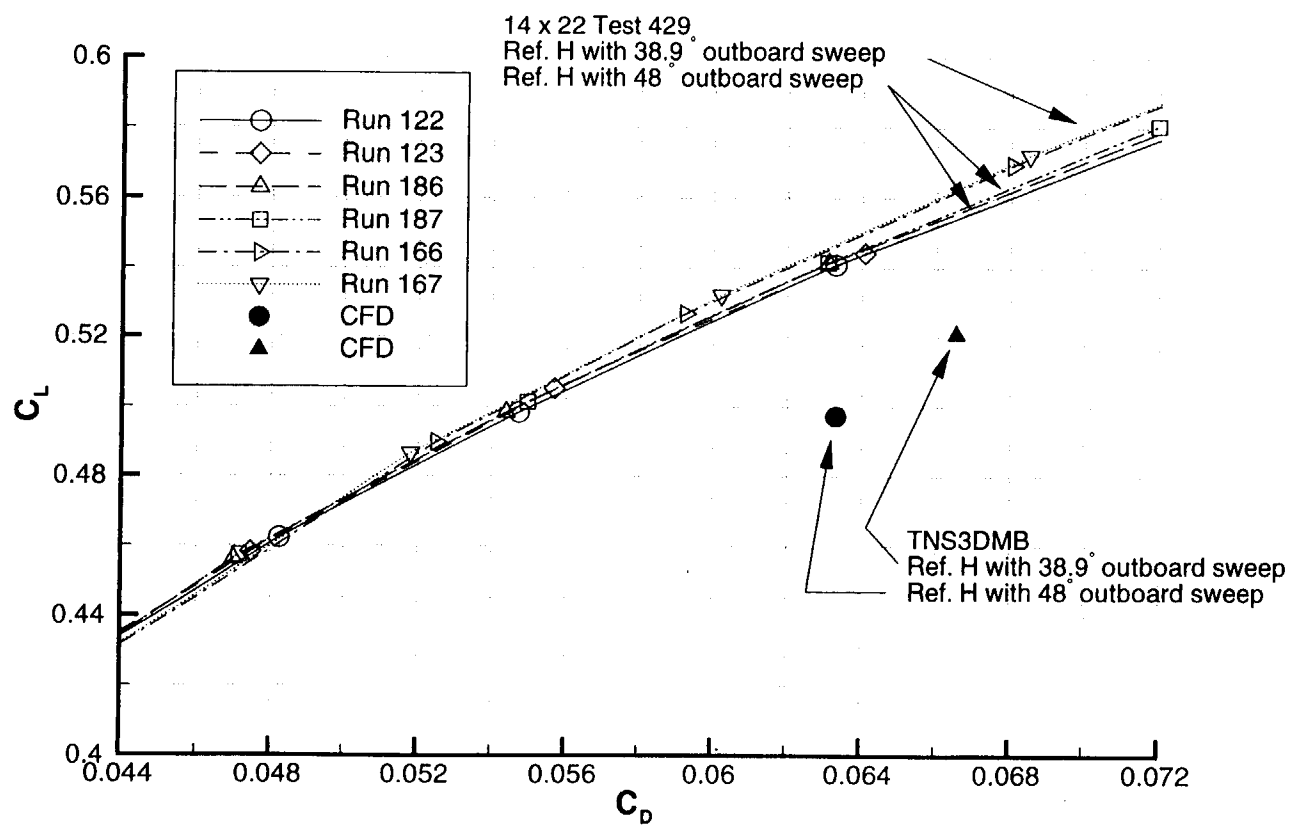

The TNS3DMB results show the opposite trend as the test data, with more nose-up moment on the W_6 (48° outboard LE sweep) configuration. The difference in pitching moment coefficient between the W_7 (38.9° outboard LE sweep) configuration and the W_6 configuration cases is larger in the 14x22 Wind Tunnel data.

Lift Coefficient vs. Moment Coefficient

Ref. H, Flaps LE 0/0/30/30/30/30 TE 10, Mach 0.24, Alpha 10 Deg., Re 8M/MAC
NASA Langley 14 x 22 Wind Tunnel, W/B/N/V
TNS3DMB, W/B

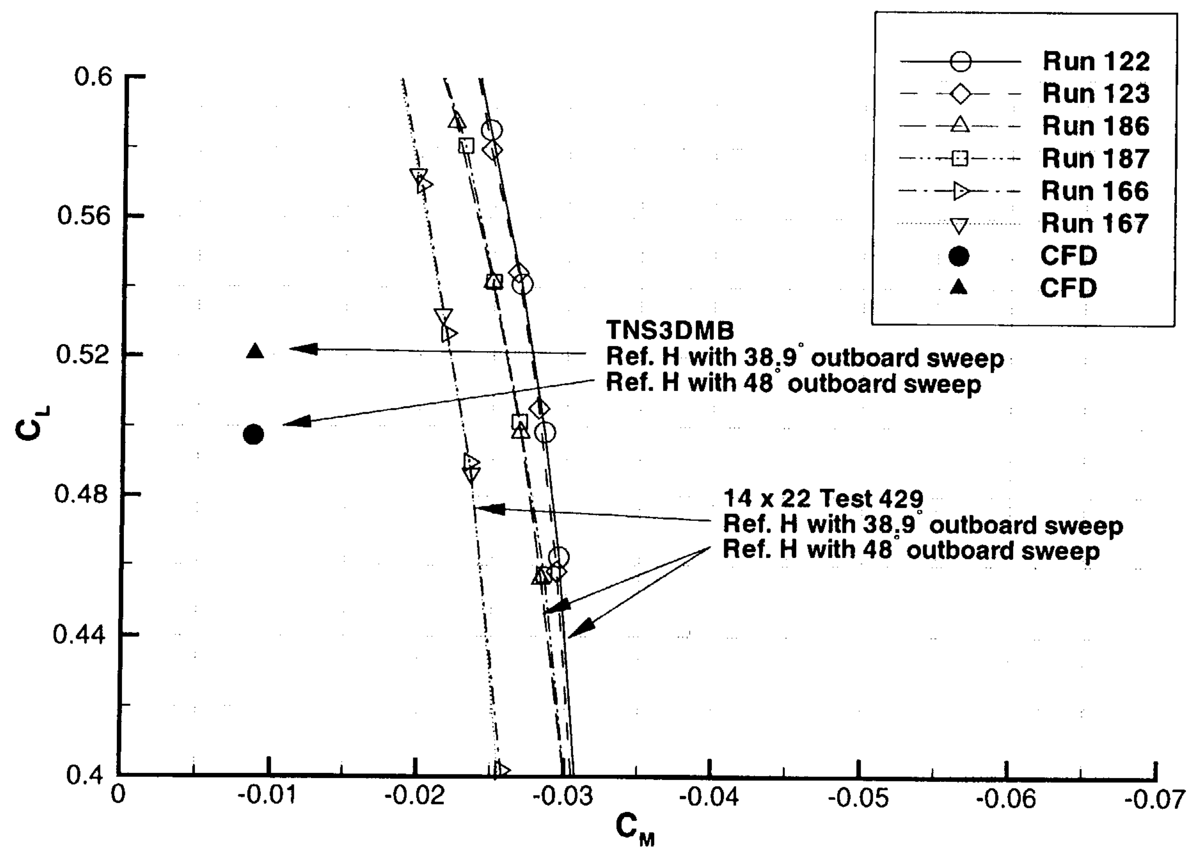

Dynacs Engineering Co. Inc.

The data show a greater L/D for the W_7 (38.9° outboard LE sweep) configuration compared to the W_6 (48° outboard LE sweep), while CFD indicates that W_7 has a slightly lower L/D than W_6. Also, CFD generated a lower L/D than the test data for a given C_L, mainly due to the higher drag. The difference between the W_7 configuration and the W_6 configuration is greater for the CFD results.

L/D vs. Lift Coefficient

Ref. H, Flaps LE 0/0/30/30/30/30 TE 10, Mach 0.24, Alpha 10 Deg., Re 8M/MAC
NASA Langley 14 x 22 Wind Tunnel, W/B/N/V
TNS3DMB, W/B

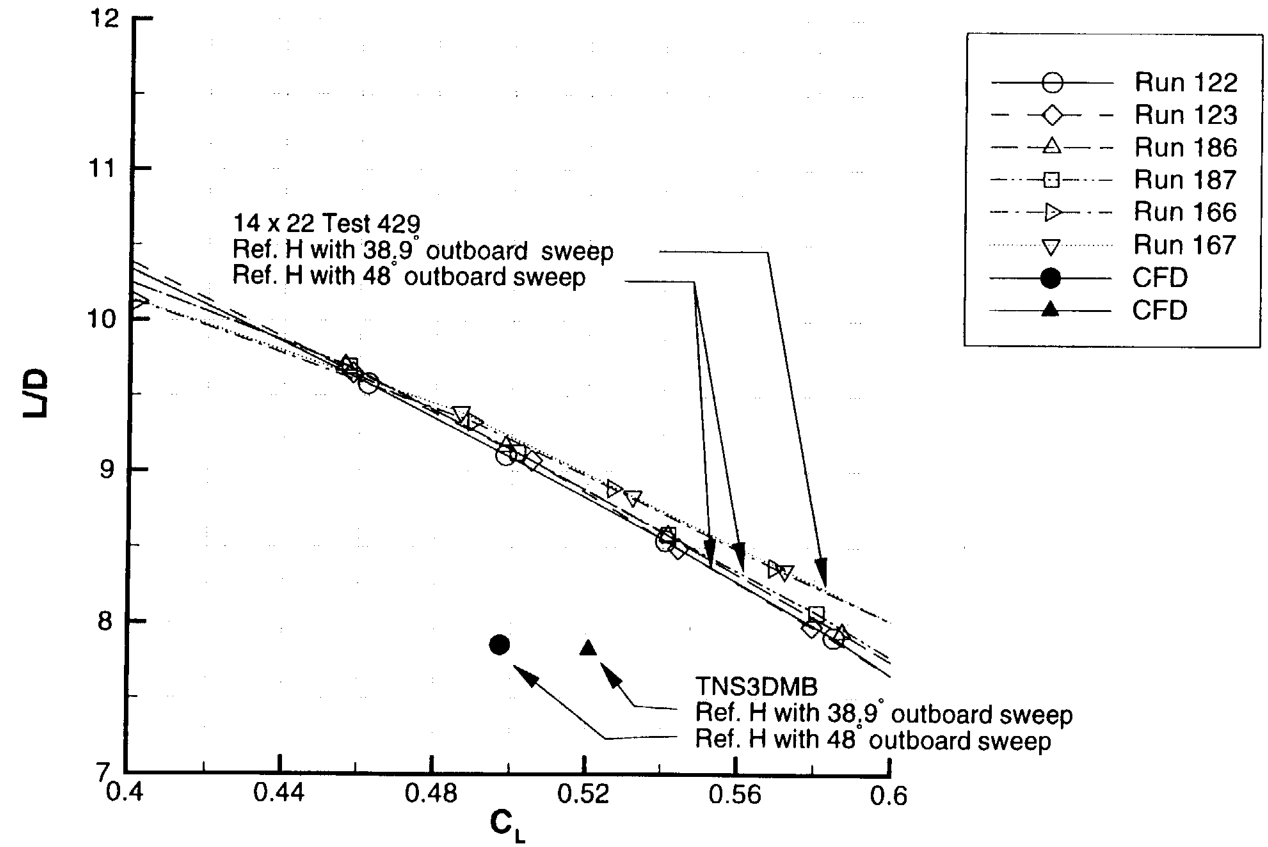

The majority of the difference in drag between the two configurations is in pressure drag, 0.0033. The difference in skin friction drag is less than 0.0001.

Drag Coefficient Components

Ref. H, W/B, Mach 0.24, Alpha 10 Deg., Re 8 M/MAC
Flaps LE 0/0/30/30/30/30 TE 10
4-Block Viscous TNS3DMB

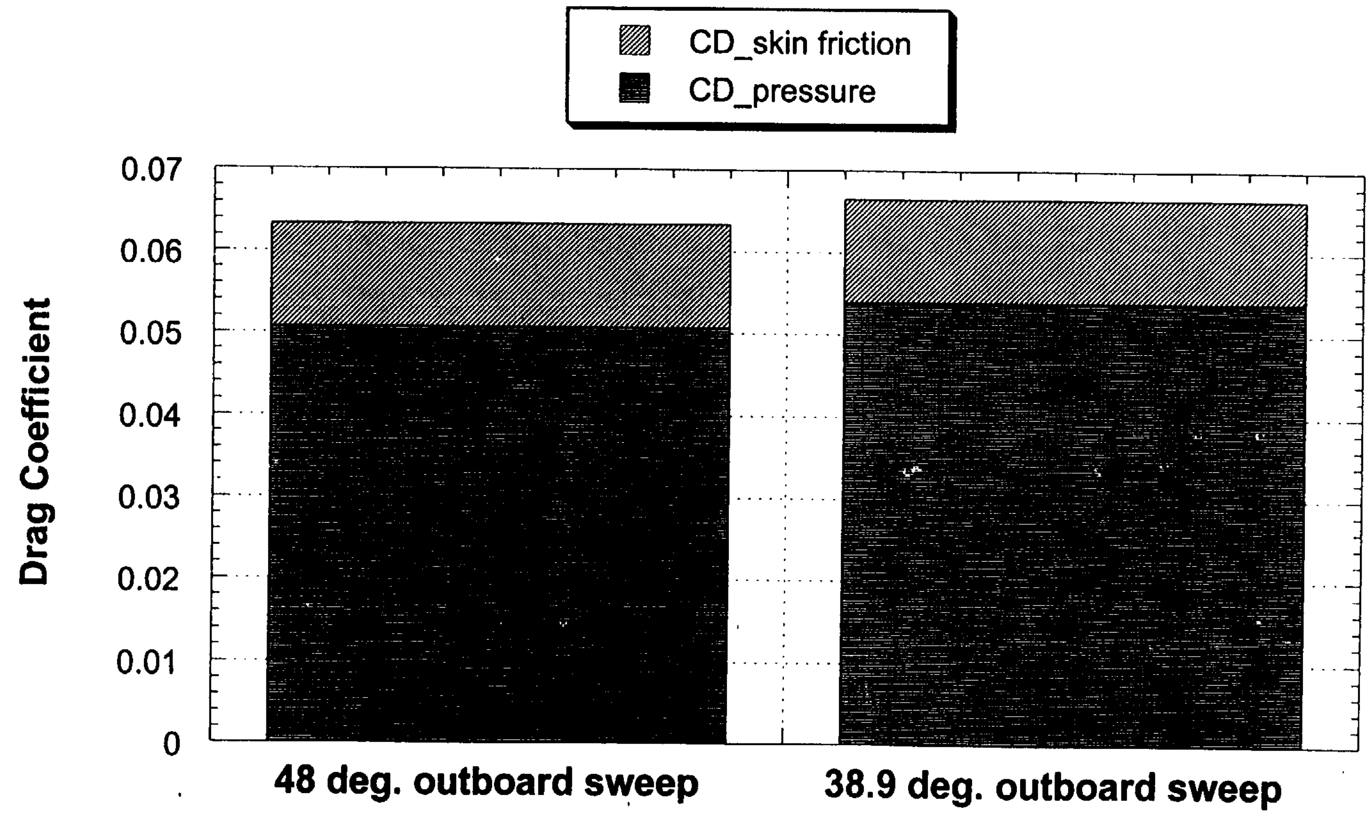

Dynacs Engineering Co., Inc.

Spanwise distributions of section lift coeficient and pressure drag coefficient are presented, with the coefficients being normalized with respect to local chord.

The section lift coefficient for the W_7 (38.9° outboard LE sweep) case is greater than that of the W_6 (48° outboard LE sweep) case throughout the entire wing span. The difference is greater on the outboard wing. The section drag coefficient for the W_7 case is higher than that for the W_6 case on almost the entire wing span. It is lower from the planform break to BBL 560. The planform break starts at approximately BBL 407.

Spanwise Distribution of Section Lift and Drag Coefficient

Ref. H, W/B, Flaps LE 0/0/30/30/30/30 TE 10, Mach 0.24, Alpha 10 Deg., Re 8M/MAC

4–Block Viscous TNS3DMB

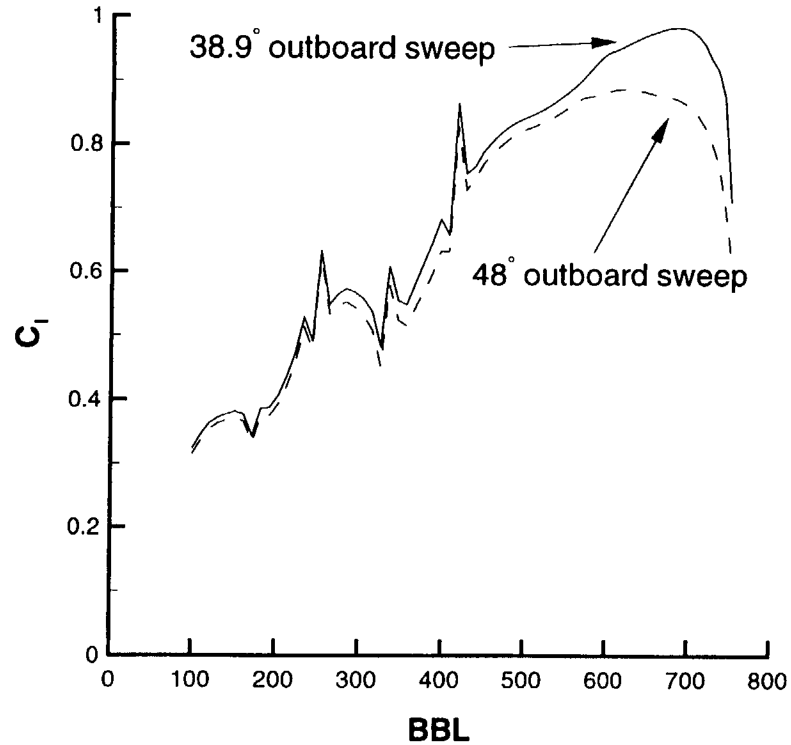

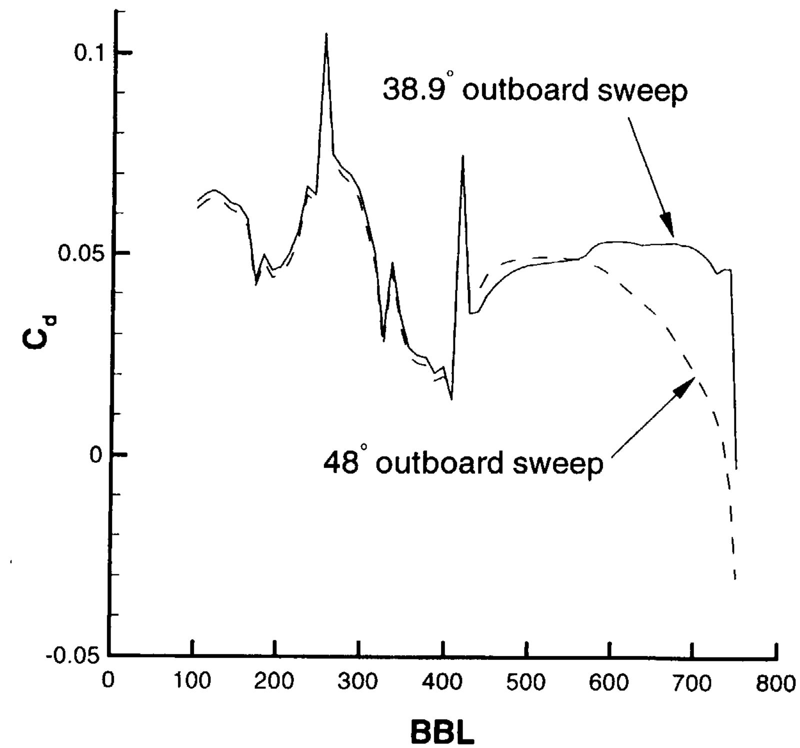

Dynacs Engineering Co. Inc.

Suction loop plots (C_p vs. z'/c) are made to identify the regions on the W_7 (38.9° outboard LE sweep) that contribute to the larger pressure drag compared with the W_6 (48° outboard LE sweep) configuration. The areas enclosed by the curves represent drag due to pressure. The lift and drag coefficients are nearly the same at this section.

Section Pressure Distribution

Ref. H, W/B, Flaps LE 0/0/30/30/30/30 TE 10, Mach 0.24, Alpha 10 Deg., Re 8M/MAC
4–Block Viscous TNS3DMB

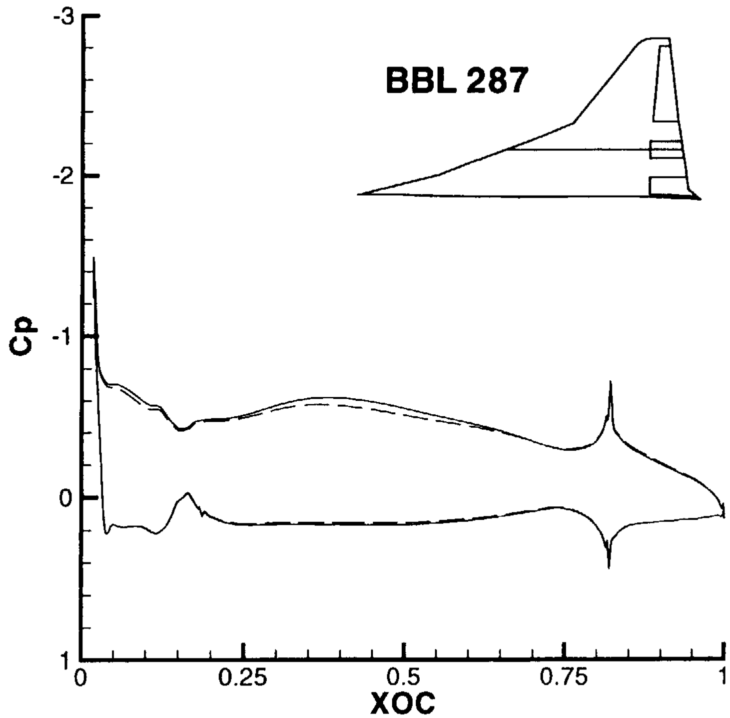

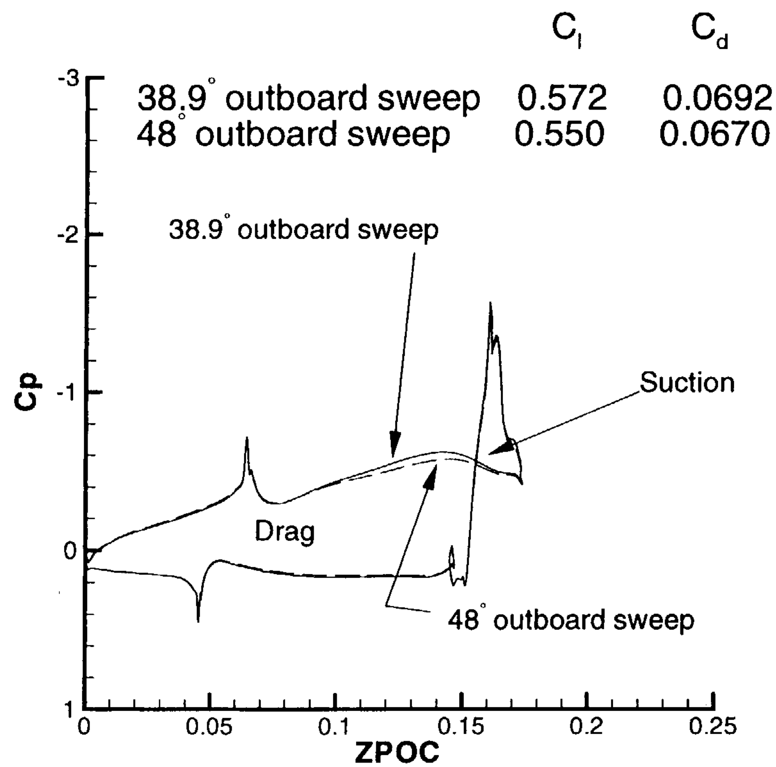

The W_7 (38.9° outboard LE sweep) case has 5% greater lift and 12% greater drag than the W_6 (48° outboard LE sweep) case. This trend is typical for sections outboard of BBL 560.

Section Pressure Distribution

Ref. H, W/B, Flaps LE 0/0/30/30/30/30 TE 10, Mach 0.24, Alpha 10 Deg., Re 8M/MAC

4–Block Viscous TNS3DMB

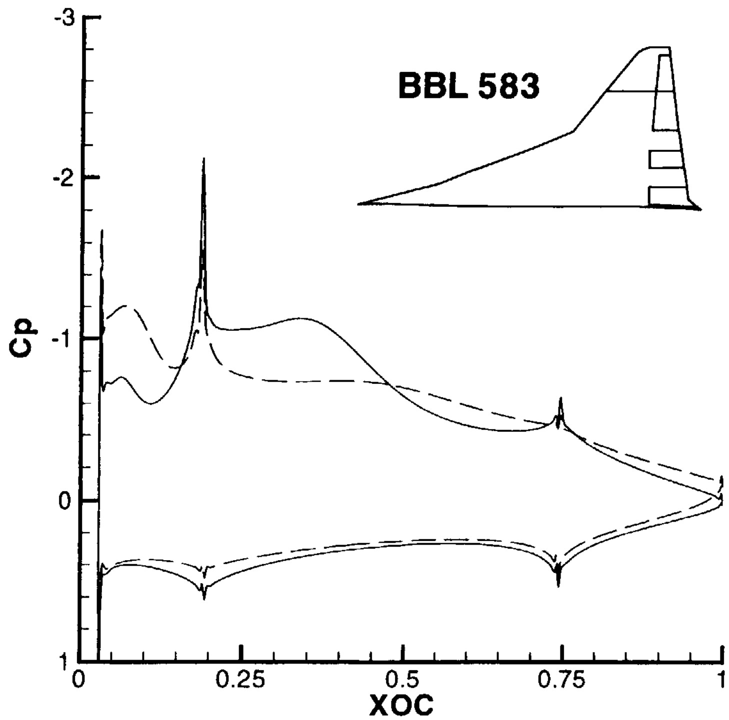

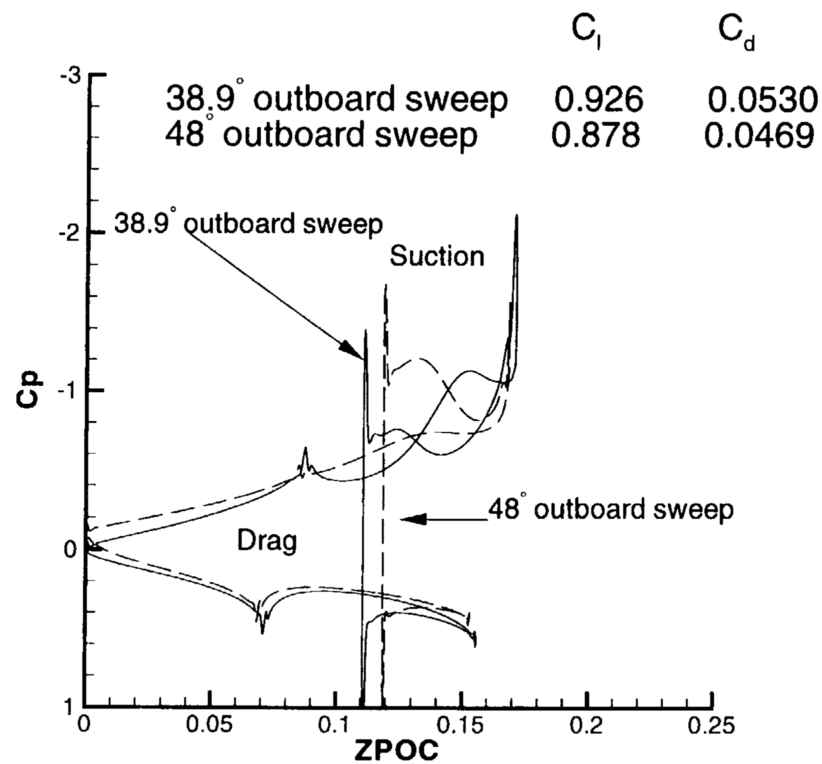

The suction at the LE hinge is greater for W_7 (38.9° outboard LE sweep). The W_7 results indicate the existence of a vortex: at STA 2252 near 2YOB of 0.50, and at STA 2321 near 2YOB of 0.44. A vortex occurs at STA 2252 near 2YOB of 0.70, and at STA 2321 near 2YOB of 0.62. A similar vortex exists for W_6 (48° outboard LE sweep), although it lies further outboard compared to that on the W_7 configuration.

Section Pressure Distribution

Ref. H, W/B, Flaps LE 0/0/30/30/30/30 TE 10, Mach 0.24, Alpha 10 Deg., Re 8M/MAC
4–Block Viscous TNS3DMB

solid lines (38.9° outboard sweep), dashed lines (48° outboard sweep)

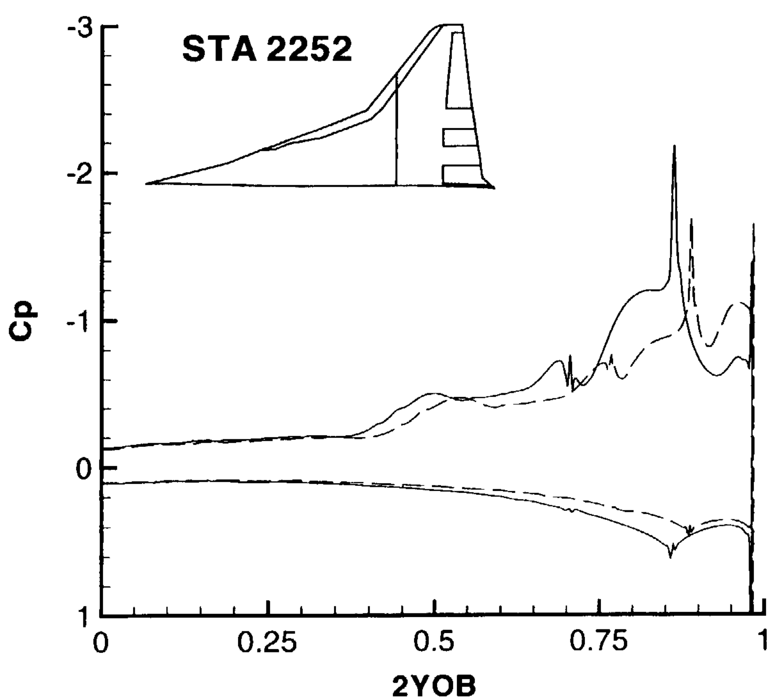

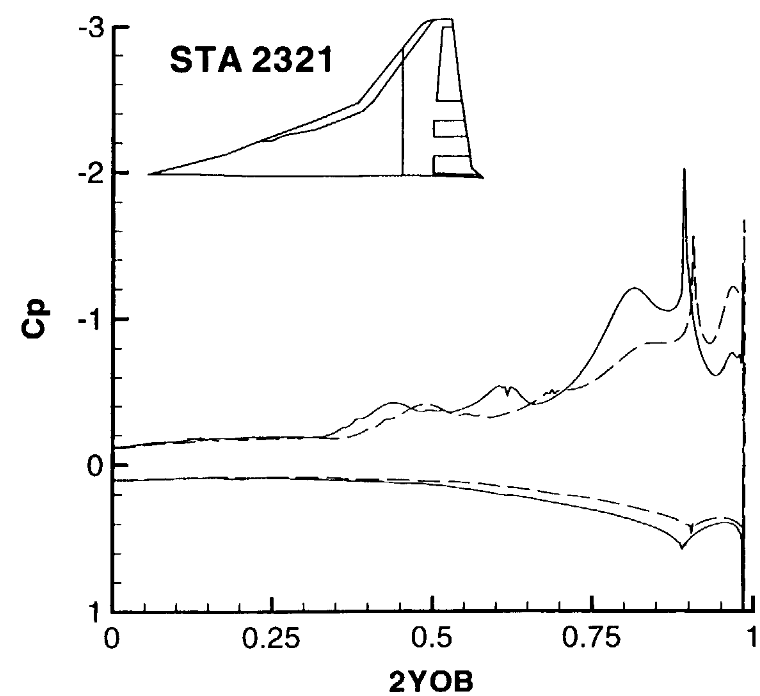

Dynacs ENGINEERING CO. INC

Particle traces on a layer two computational cells off the wing upper surface show dissimilar patterns for W_7 (38.9° outboard LE sweep) and the W_6 (48° outboard LE sweep) cases, specifically on the outboard wing. In the case of the reduced sweep angle, a greater percentage of the outboard LE region undergoes spanwise flow. The clustering of streamlines near the beginning of the inboard LE flap is an indication of the vortical flow seen previously on the off-body total pressure and streamline figure on page 53.

Particle Traces 2 Grid Cells Above the Upper Wing Surface

Ref. H, W/B, Flaps LE 30/TE 10, Mach 0.24, Alpha 10 Deg., Re 8.8M/MAC

4-Block Viscous TNS3DMB

48 deg outboard sweep

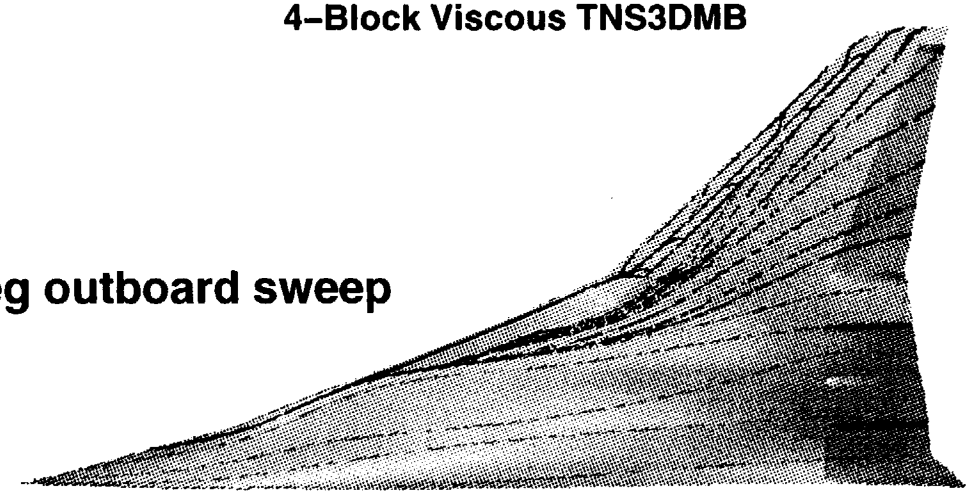

38.9 deg outboard sweep

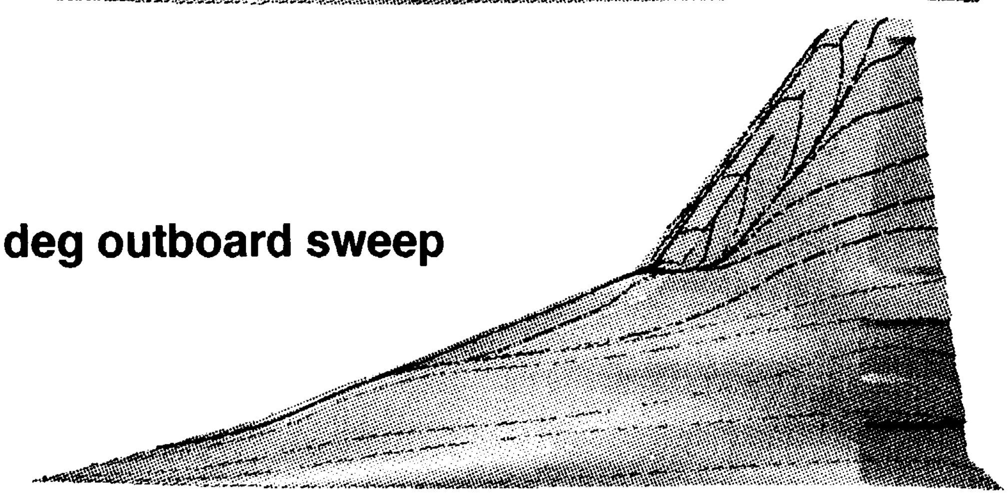

The major difference in the coefficient of skin friction in the streamwise direction occurs on the outboard wing. This clearly indicates that the propensity for separation is greater in the outboard LE region for the reduced wing sweep (38.9° outboard LE sweep case). The effect of skin friction on the particle traces was seen in the previous figure.

Upper Surface Streamwise Component of Skin Friction Coefficient

Ref. H, W/B, Flaps LE 30/TE 10, Mach 0.24, Alpha 10 Deg., Re 8.8M/MAC
4–Block Viscous TNS3DMB

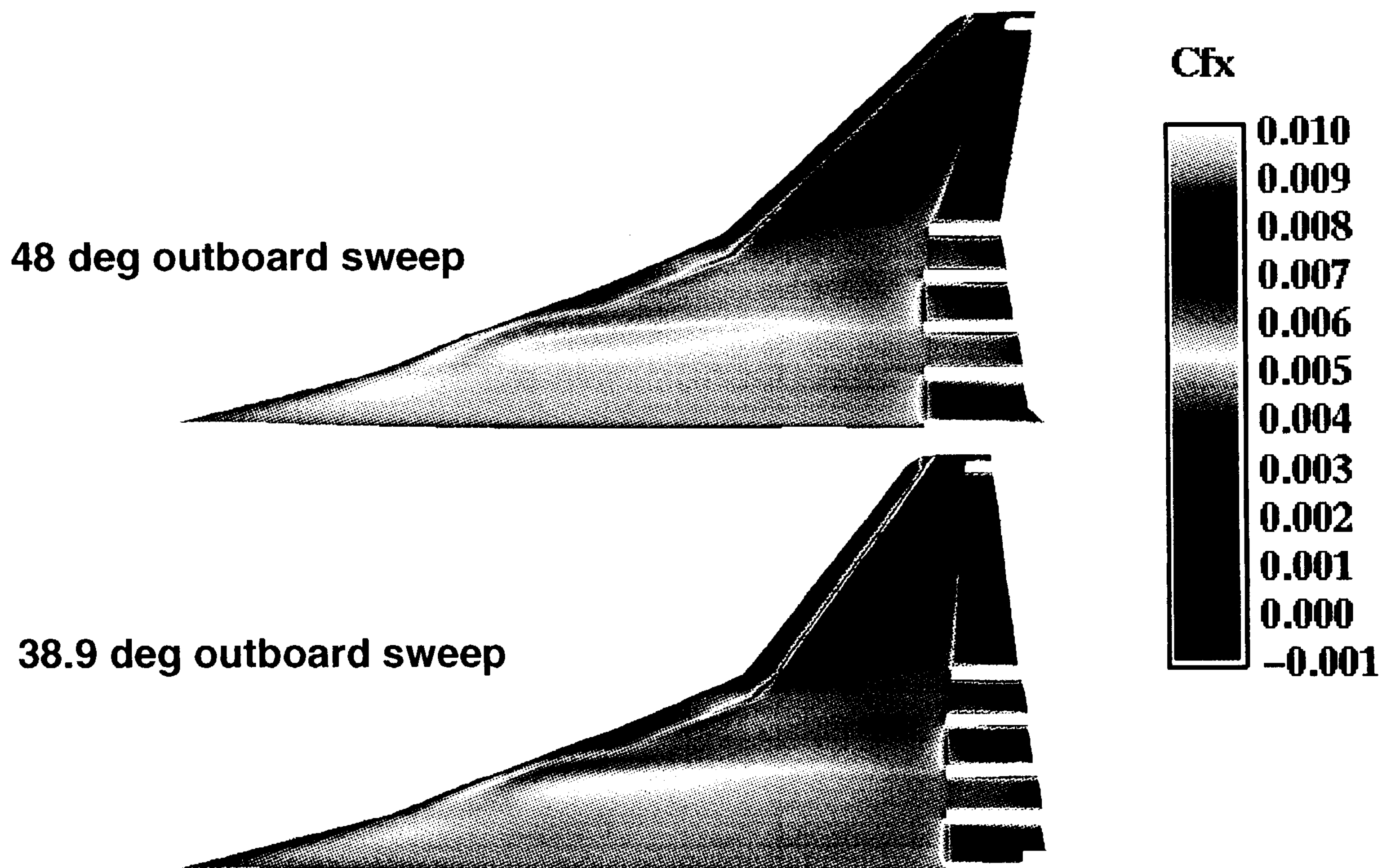

Dynacs Engineering Co. Inc

TNS3DMB results did not match the test data perfectly, but had the similar increments between the two configurations.

A detailed flow field survey from TNS3DMB shows vortical flow on the inboard wing of the W_6 (48° outboard LE sweep) and W_7 (38.9° outboard LE sweep) configurations. The vortex has a larger spanwise component for the larger sweep case.

The performance is greater for the reduced wing sweep, at the expense of more spanwise flow on the outboard wing.

Conclusions – Task 2

- Navier-Stokes solutions from TNS3DMB compared favorably with test data
- Performance was improved with reduced wing sweep
- Greater tendency for outboard LE hinge separation for reduced wing sweep

This page intentionally left blank

Task 3: Effect of Inboard Sealed Slats (TCA)

- Background
- Geometry and grid generation
- Flight conditions, flow solver and postprocessing
- Results
- Conclusions

We'd like to understand why. If the Navier-Stokes results match the test data, future designs may be done by computations.

Why the Inboard Sealed Slats Study (TCA)

- Sealed slats have shown good performance before on the outboard wing
- Sealed slats were proposed to be used on the inboard wing for TCA-3 test

Both configurations have 35° sealed slats on the outboard wing. The type of LE device is used in what follows to differentiate between the two configurations: 30° full-span plain flaps, and 35° full-span sealed slats.

Points were clustered around the wing leading edge, the wing trailing edge, the flap hinges, and flap side edges. There are 121 points from wing LE to TE for each longitudinal grid. There are 113 longitudinal grid lines from the wing root to the wing tip.

The surface grid was constructed with Boeing's Aero Grid and Paneling System (AGPS). Boeing here means Boeing/Seattle.

The turnaround time for the batch job on an SGI Indigo^2/IMPACT 10000 was 50 minutes. The CPU time is 45 minutes.

Geometry and Grid Generation for Task 3

- Two TCA W/B with 35° sealed slats for the outboard wing. One case has a 30° plain flap for the inboard wing, a configuration tested in Test 449 at 14x22. Another case has a full span 35° sealed slats to be tested at Ames 12-ft Pressure Tunnel.
- Surface grid generated by Boeing using AGPS, with zero thickness along the outboard wing leading edge and the entire wing trailing edge.
- Four-block volume grid generated by Boeing with a batch job on an SGI workstation.

This page intentionally left blank

Grid Generation

Upper Surface Grids for TCA, W/B, Outboard Sealed Slats 35°/TE 10/15/15/15
(every other grid line shown)

Inboard Plain Flaps 30°

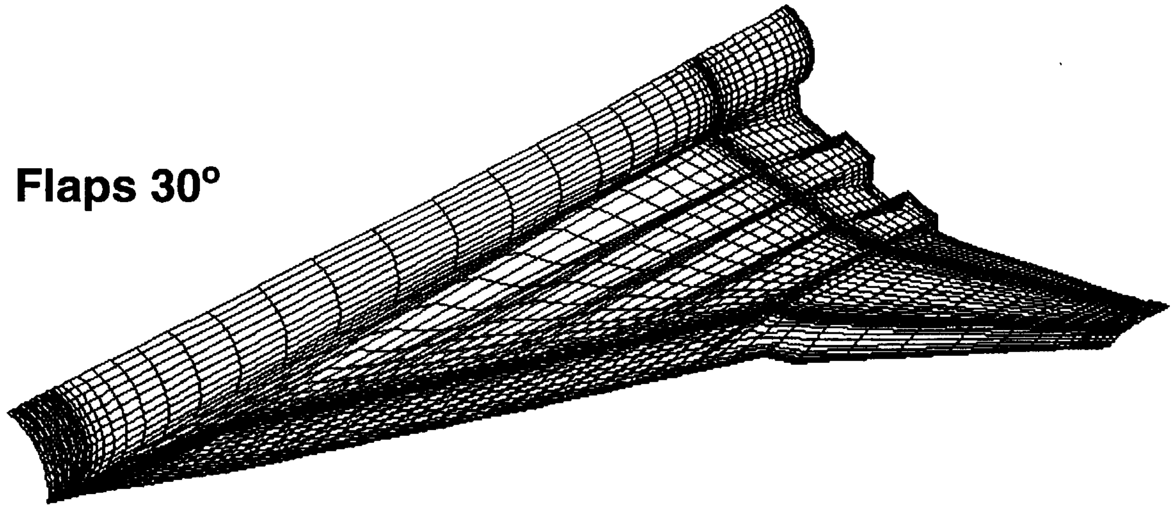

Inboard Sealed Slats 35°

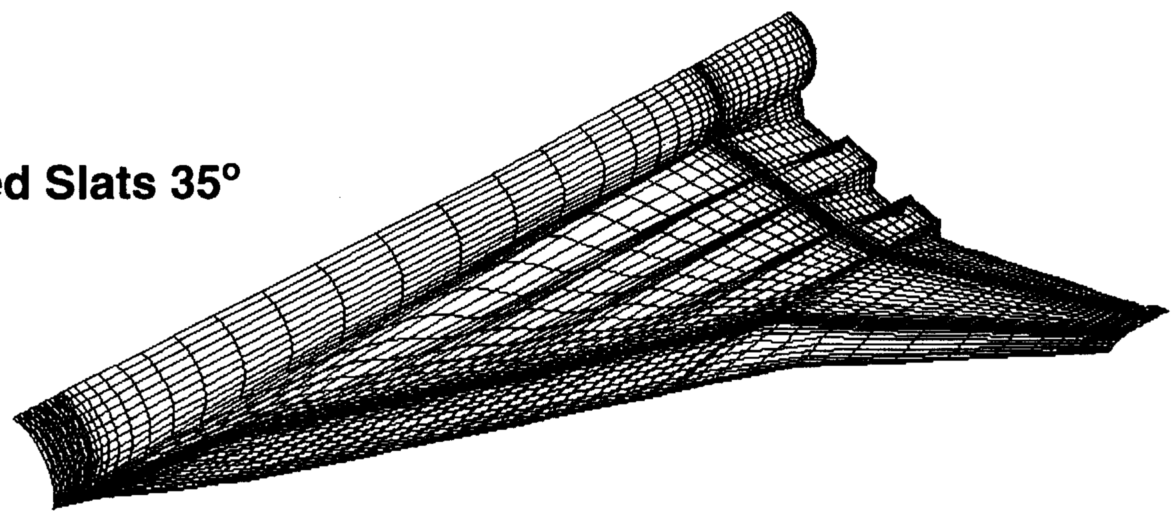

Dynacs Engineering Co. Inc

The CPU time is 12.8 hours on the NAS C-90. The clock time is 2.5 hours. The turnaround time is generally overnight if von neumann is not heavily loaded.

Boeing/Seattle started to use FIELDVIEW.

The flap edges are approximated in the grid. The upper and lower surfaces of the flap edges merge to a point, leading to flap gap regions of zero thickness. The flap gaps are set to a flow-through boundary condition.

Viscous computation with Spalart-Allmaras turbulence model.

Flight Conditions, Flow Solver, and Postprocessing

- Mach 0.247, Re 8 M to match the conditions at 14x22 wind tunnel
- Angles of attack (10°, 16°, 22°) to match the test data from Test 449
- Flow computed by Boeing using Boeing's version of TNS3DMB with multi-tasking
- Postprocessing by Boeing and Dynacs using FIELDVIEW, FAST, Tecplot, and Kaleidagraph

Wind tunnel data for outboard sealed slats only are available from Langley 14x22 Test 449.

Wind tunnel data for both inboard and outboard sealed slats will be available from Ames 12-ft Test 037.

Results for Task 3

- Total pressure surveys
- Forces and moments compared with test data whenever available

The total pressure distribution at six body stations and one station downstream of the trailing edge are shown with the local total pressure normalized by the free stream total pressure. The figure shows that the full-span sealed slats leave a wake that has more energy than the one with outboard sealed slats only. Areas of low total pressure above the wing indicate well-behaved flow and may be difficult to survey experimentally.

Total Pressure Ratio Contours and Streamlines

TCA, W/B, Outboard Sealed Slats 35°/TE 10/15/15/15, Mach 0.247, Alpha 16 Deg., Re 7.9M/MAC
4-Block Viscous TNS3DMB

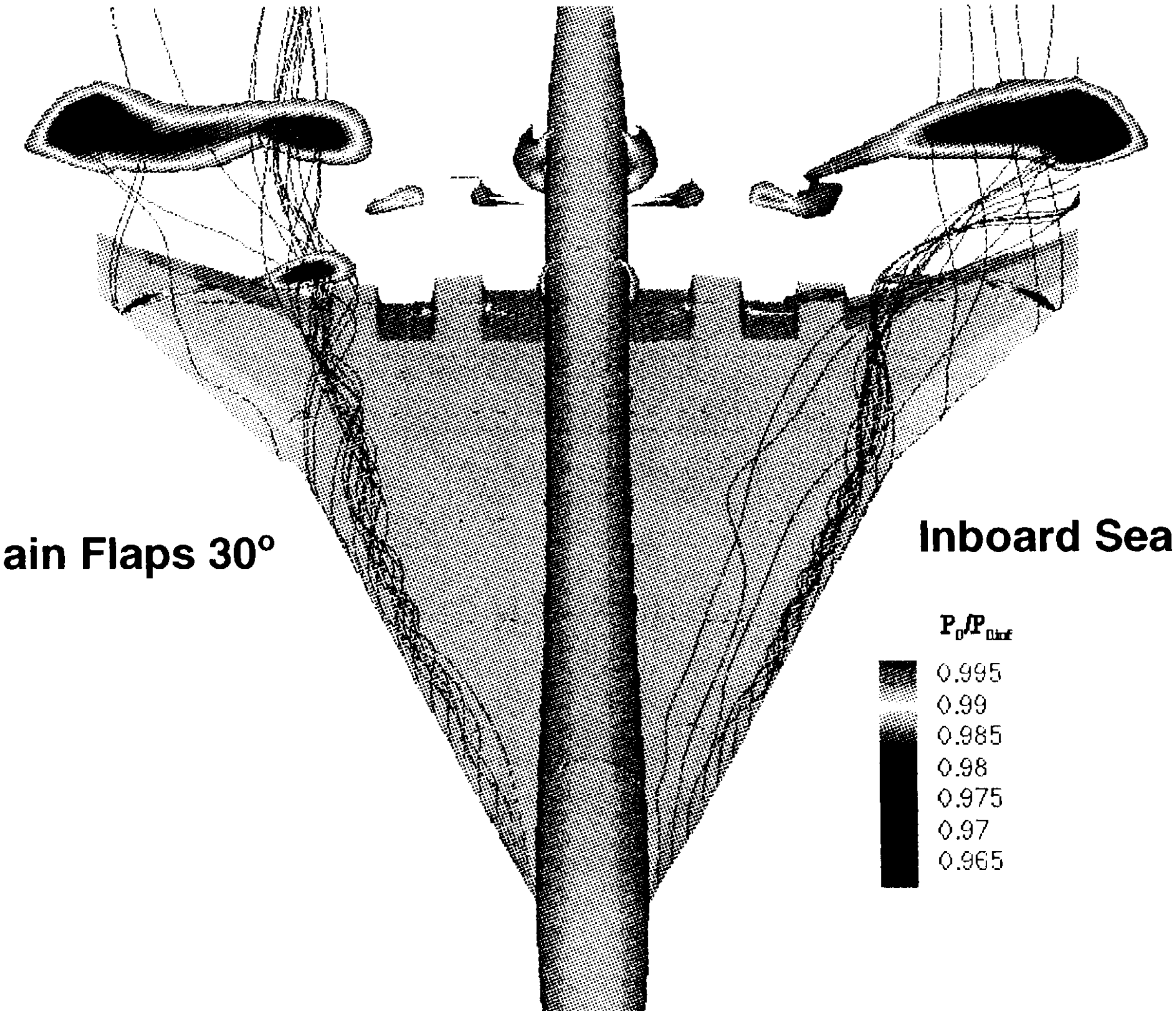

Inboard Plain Flaps 30°

Inboard Sealed-Slats 35°

Dynacs ENGINEERING CO. INC.

The outboard slat case was analyzed for three angles of attack. The computed lift coefficient is lower than the test data at 10°, which has been observed previously when this version of TNS3DMB was used.

The computed lift curve slope is higher than test data, for unknown reasons.

The inboard slat and outboard slat case was also analyzed for the same three angles of attack. The lift coefficient of 10° angle of attack is higher than the outboard slats-only case. The benefit diminishes at higher angles of attack.

Effect of Inboard LE Device
TCA With 35 deg. outboard sealed slat, TE 10/15/15/15

Mach 0.247, Re 7.9 M/MAC
NASA-Langley 14x22 Tunnel, Test 449, Run 202, W/B/N/V
TNS3DMB W/B

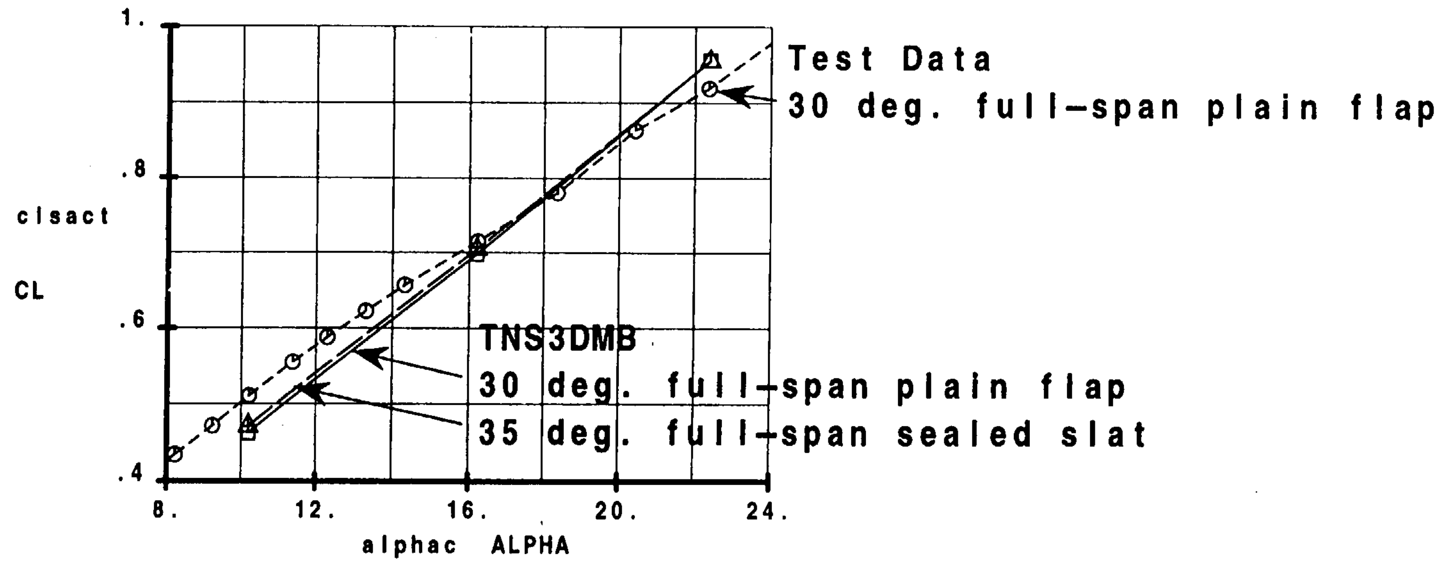

The full-span sealed slat generated more lift and less drag than the outboard sealed slat case at 10° and 16° angle of attack. It generated approximately the same lift but less drag at 22° angle of attack. Test data fromTCA-3, which is ongoing, will indicate how the full-span sealed slat performs.

Effect of Inboard LE Device
TCA With 35 deg. outboard sealed slat, TE 10/15/15/15

Mach 0.247, Re 7.9 M/MAC
NASA–Langley 14x22 Tunnel, Test 449, Run 202, W/B/N/V
TNS3DMB W/B

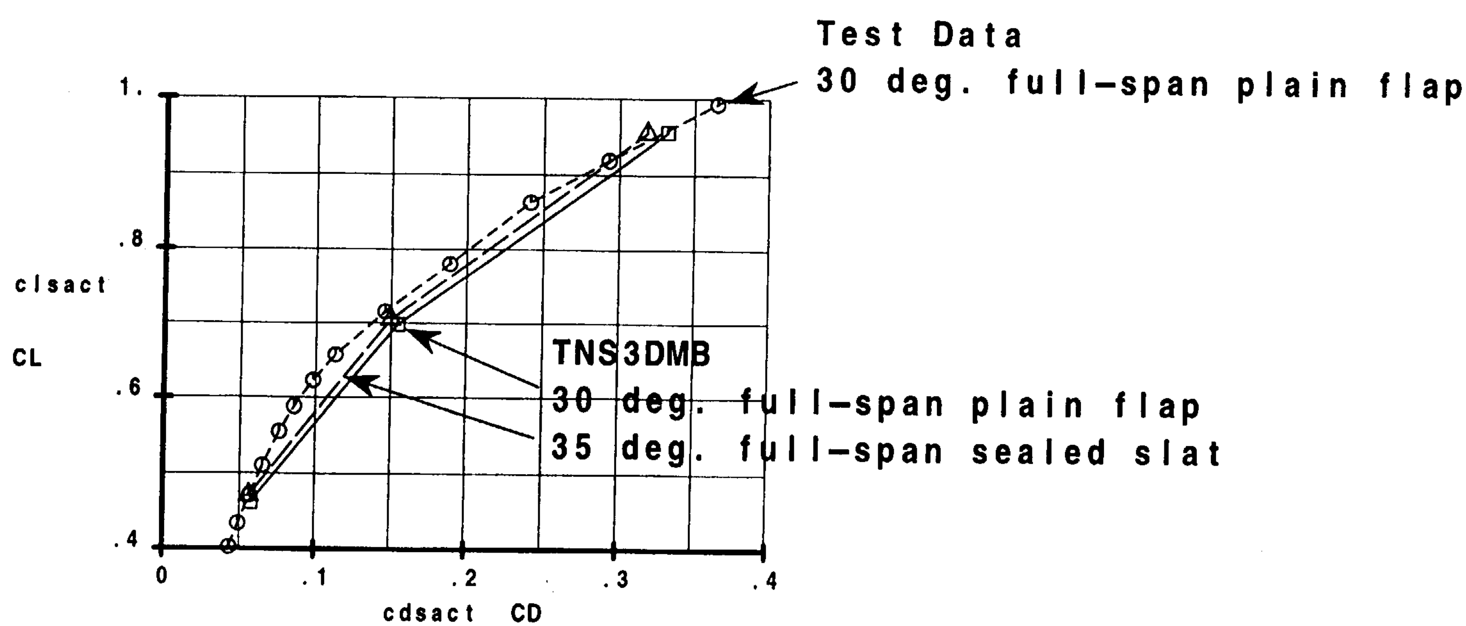

The full-span sealed slat generated approximately the same pitching moment as the outboard sealed slat-only case except at the highest angle of attack, 22°.

Effect of Inboard LE Device
TCA With 35 deg. outboard sealed slat, TE 10/15/15/15

Mach 0.247, Re 7.9 M/MAC
NASA–Langley 14x22 Tunnel, Test 449, Run 202, W/B/N/V
TNS3DMB W/B

Test Data
30 deg. full–span plain flap
TNS3DMB
30 deg. full–span plain flap
35 deg. full–span sealed slat

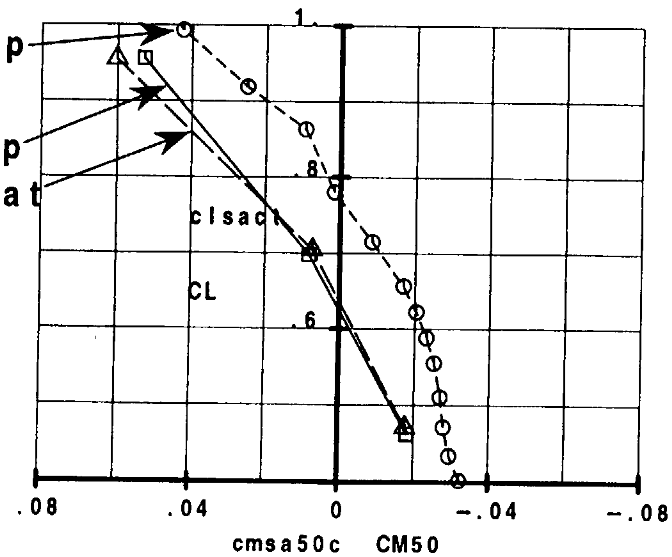

Dynacs Engineering Co., Inc.

The computed LOD (lift-to-drag ratio) vs. C_L form curves that generally follow the test data. Again, the ongoing TCA-3 test will provide more information.

Effect of Inboard LE Device
TCA With 35 deg. outboard sealed slat, TE 10/15/15/15
Mach 0.247, Re 7.9 M/MAC
NASA–Langley 14x22 Tunnel, Test 449, Run 202, W/B/N/V
TNS3DMB W/B

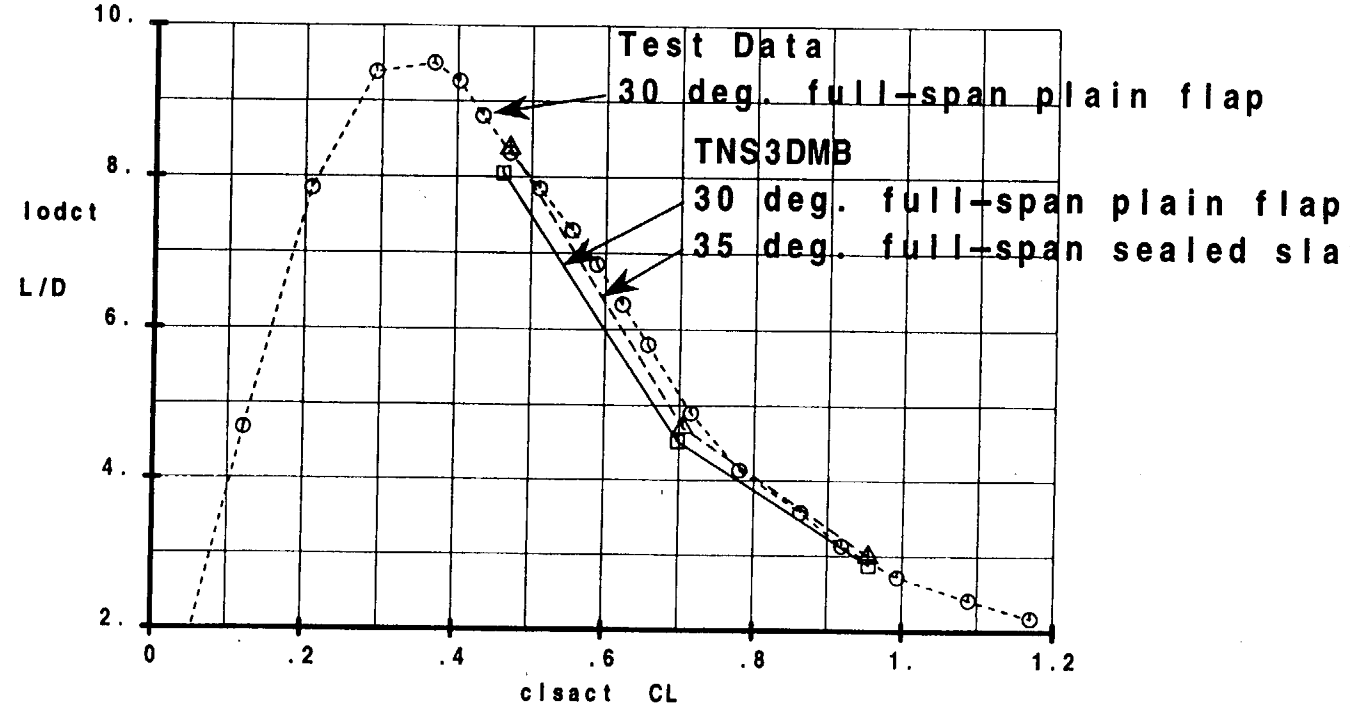

TNS3DMB results did not match the test data perfectly. A different post-processor was used on one of the solutions and it improved the $C_L(\alpha)$ result.

Pressure sensitive paint (PSP) results may be available from theTCA-3 test.

Skin friction on the forebody may be available from the TCA-3 test.

Conclusions – Task 3

- Fair agreement between Navier-Stokes solutions and the test data for configurations that have been tested
- Sealed slats improve the performance
- Data from TCA-3 test will add more information

TheTNS3DMB results did not match the test data perfectly. They consistently showed a more nose-up pitching moment compared to that of the corresponding wind tunnel results. Differences between all of the force and moment comparisons can be attributed in some degree to the configuration differences between the wind tunnel model (W/B/N/V) and the CFD grid (W/B). The increment between configurations is somewhat believable, which will make the code a useful design tool.

Wind tunnel flow details, which the Navier-Stokes code validation needs, are scarce. There have been many, many wind tunnel tests for HSR in the past several years but code validation data were always regarded as low priority. This situation needs to change if the codes are going to get better.

The PSP method could be used to aid in pressure visualization; this may be useful on thin outboard wings where pressure tapping may be difficult. Skin friction can be obtained from oil film interferometry.

Conclusions and Recommendations

- Fair agreement between Navier-Stokes solutions from TNS3DMB and test data. The post-processor may need to be re-examined.
- Surface pressure data from the wind tunnel were not available for the configurations analyzed.
- Future wind tunnel tests should provide more data for CFD validation runs. Ideally, measurements would include surface skin friction, and off-body properties such as velocity components and/or total pressures.

This page intentially left blank

Code Calibration Applied to the TCA High-lift Model in the 14x22 Wind Tunnel

(Simulation With and Without Model Post-Mount)

HSR Airframe Technical Review
High-Lift Performance
Los Angeles, CA
February 9-13, 1998

Wendy B. Lessard - LaRC

This research falls under the Analysis/Design Methodology under High Lift Development (Task 33) and is a Navier-Stokes computational method for analyzing the flow field about the Technology Concept Airplane (TCA).

High Lift Technology Development (Task 33)

Increase L/D, Develop Analysis/Design Methodology

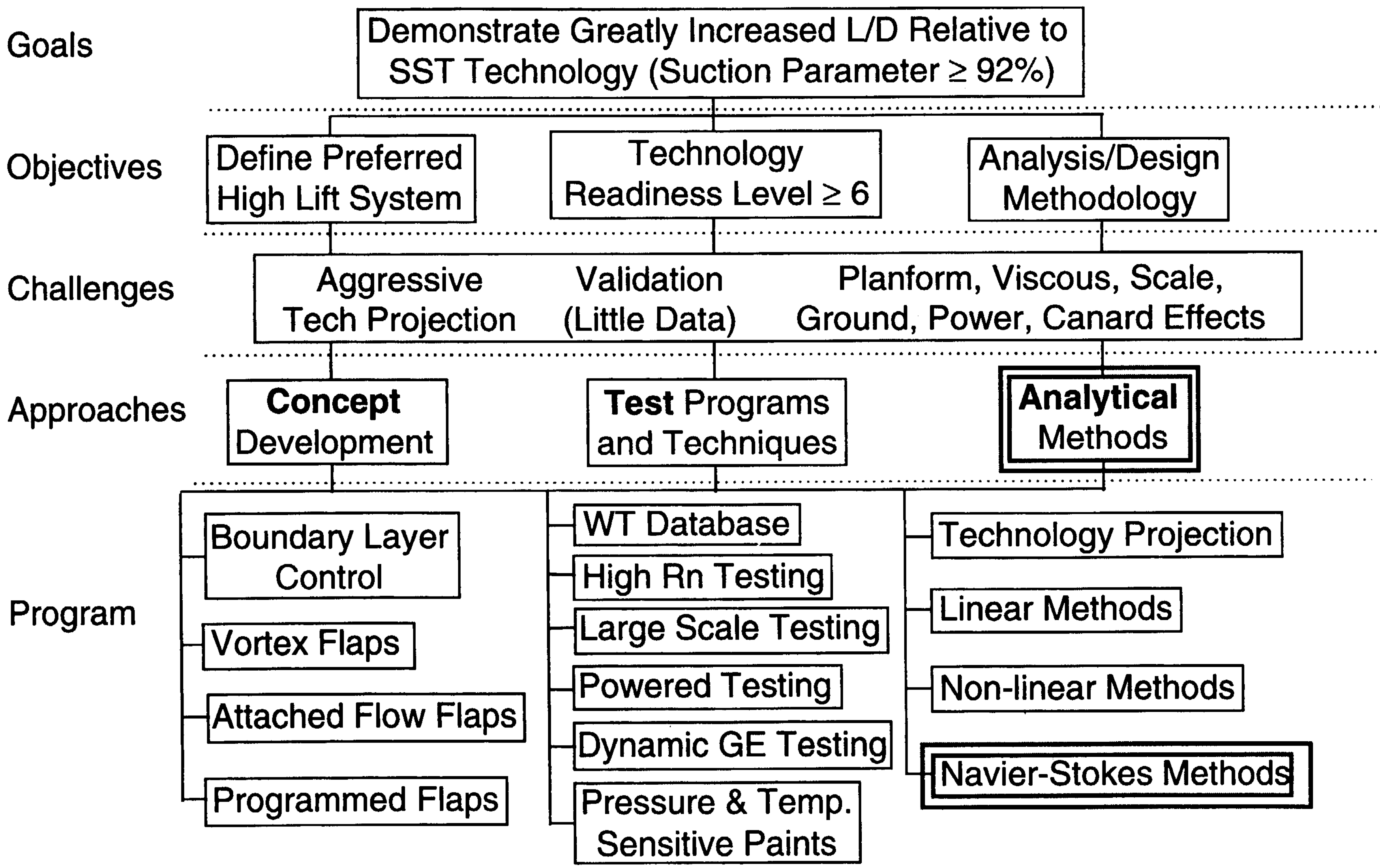

The outline of this presentation is self-explanatory

HSR High-Lift TCA Configuration

Outline

- **Objective & Approach**
- **Results**
  - TCA in free air
  - TCA with post-mount
- **Summary & Conclusions**

The objective of this study is to calibrate a Navier-Stokes code for the TCA (30/10) baseline configuration (partial span leading edge flaps were deflected at 30 degs. and all the trailing-edge flaps were deflected at 10 degs). The computational results for several angles of attack are compared with experimental force, moments, and surface pressures.

The code used in this study is CFL3D; mesh sequencing and multi-grid were used to full advantage to accelerate convergence. A multi-grid approach was used similar to that used for the Reference H configuration allowing point-to-point matching across all the trailing-edge block interfaces. From past experiences with the Reference H (ie, good force, moment, and pressure comparisons were obtained), it was assumed that the mounting system would produce small effects; hence, it was not initially modeled. However, comparisons of lower surface pressures indicated the post mount significantly influenced the lower surface pressures, so the post geometry was inserted into the existing grid using Chimera (overset grids).

HSR High-Lift TCA Configuration

Objective & Approach

- **Objective** - To calibrate a proven Navier-Stokes code for a low-speed high-lift TCA Configuration in terms of assessing its value to predict forces and moments as well as surface pressures.

- **Approach** - Solve the turbulent flow field of the TCA highlift baseline (30/10) configuration using CFL3D. A multi-block grid approach is used (similar to the Ref H) and a Chimera (overset grid) technique is used to account for mid-tunnel mount effects.

The model without the post-mount was simulated first and the resources needed are shown on this slide.

HSR High-Lift TCA Configuration

Results

$M = 0.243$, $Re = 8$ million

- **Model without post-mount**
  - Multi-block grid containing 26 blocks
  - Solutions obtained for $\alpha = 6, 8, 10, \& 12$ deg
  - Memory required - 265 MW (multi-tasked)
  - Average run time 30 hours or 12.5 μsec/cell/iteration
  - 2.5 - 3 order decrease in residual magnitude

The TCA (30/10) surface grid plotted in the symmetry plane is shown in this figure. The grid is composed of 26 blocks, 53 point-to-point matching interfaces, and 3 patched boundaries. The grid used a C-O/O-H type of topology and contains over 6 million grid points.

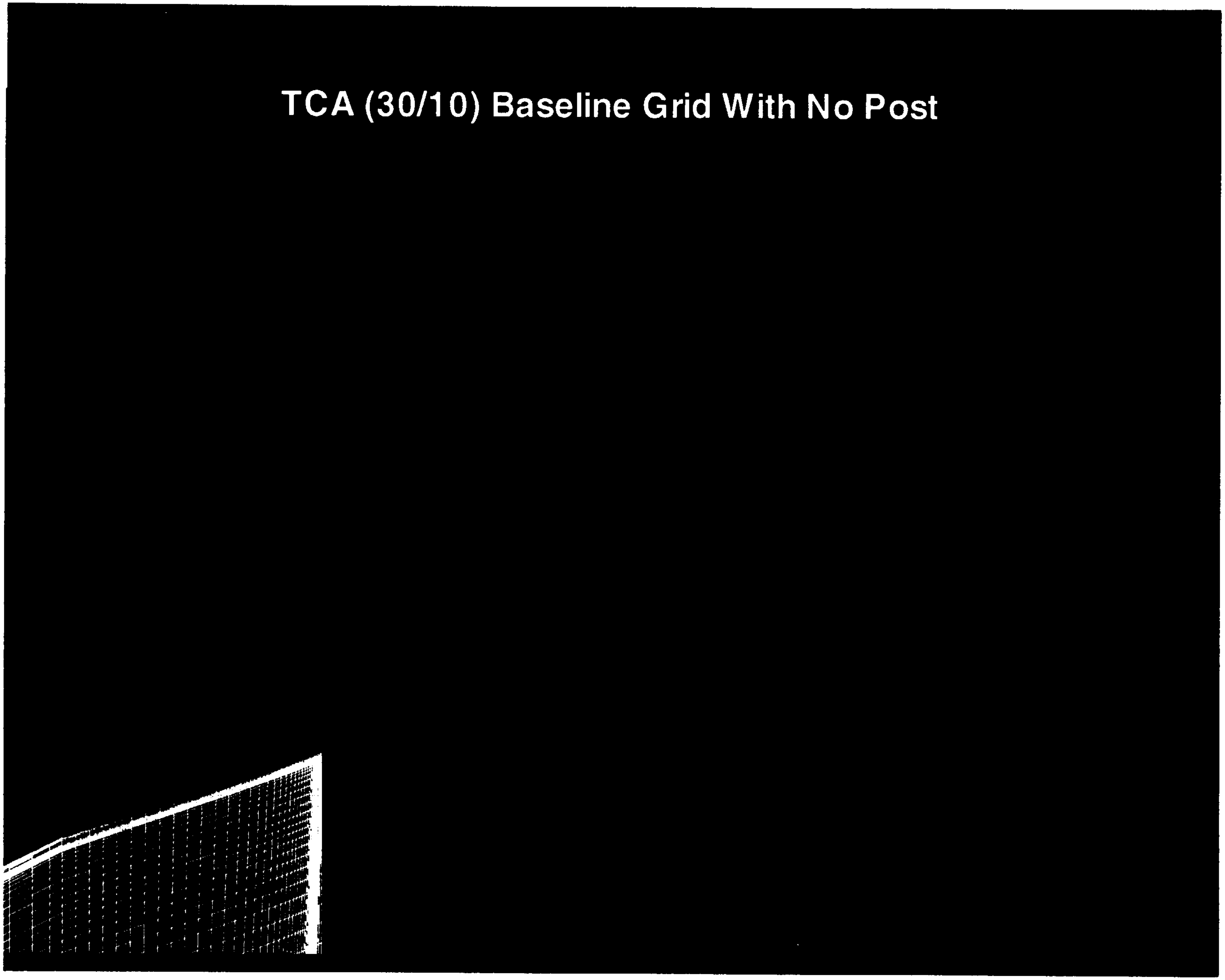
TCA (30/10) Baseline Grid With No Post

The spanwise computational surface pressures were extracted from the solution and compared with the Langley 14x22 ft wind-tunnel data, T449. The first three fuselage stations compare fairly well. However, the discrepancies between pressures seen on the lower surface for the aft three stations were quite alarming, and the experimental pressure data was considered suspect. It was thought that the upward drifting of the experimental data (on the lower surface, aft of station 100.5) may be due to a possible leak in the atmospheric reference line, since the previous solutions obtained on the Reference H configurations showed flat pressure distributions on the lower surface. Future investigation of the pressure data did not indicate any error.

Spanwise Pressure Distributions for TCA (30/10) With No Post-Mount

M = 0.243, α = 8°, Re = 8 mil

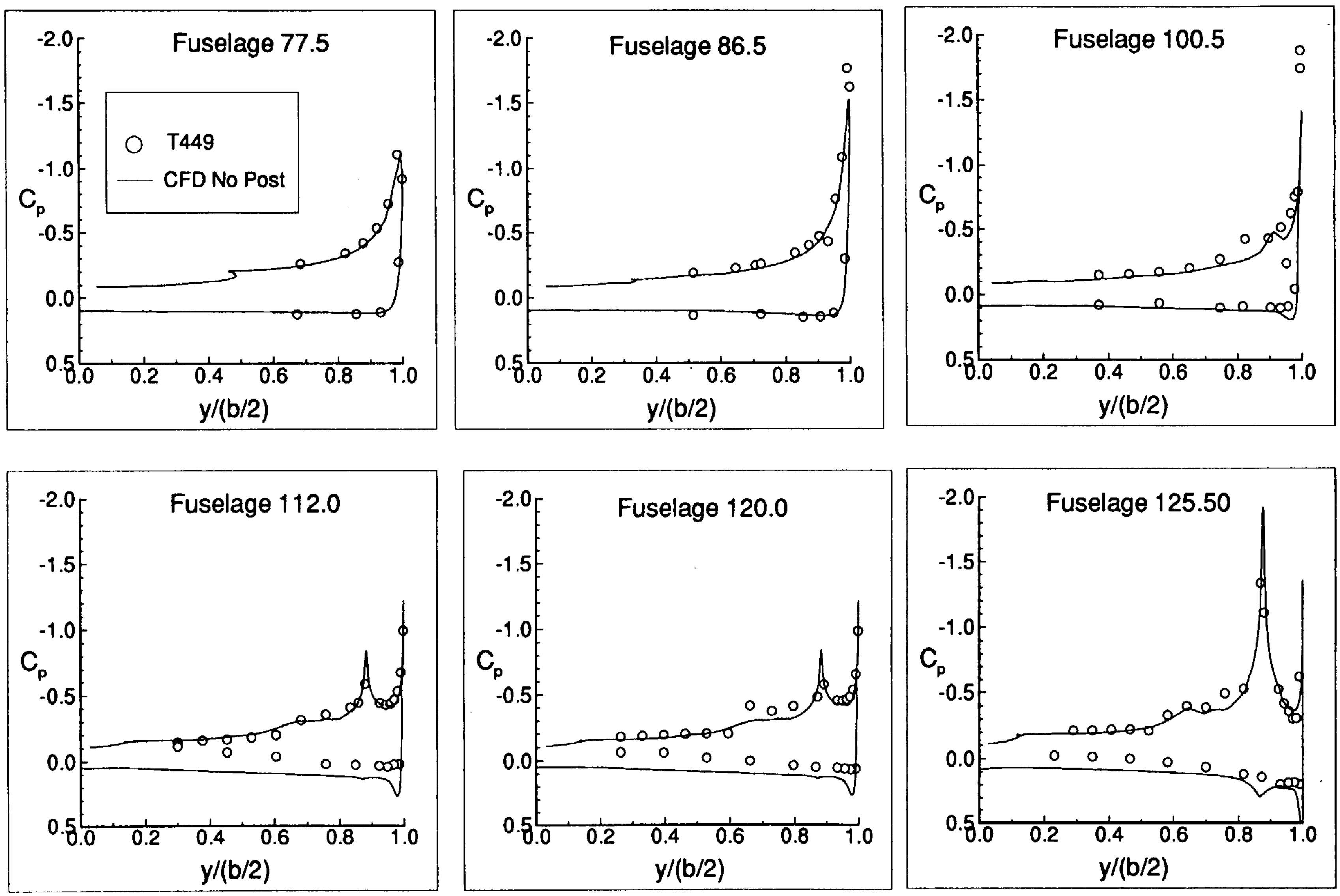

The post effects were considered next; Allen Chen from Boeing (using the panel code A502) showed that the post appeared to be effecting the lower surface more than previously expected. Consequently, the post geometry was inserted into the grid. The resources needed for this case are listed on this slide.

HSR High-Lift TCA Configuration

Results

M = 0.243, Re = 8 million

- **Model with post-mount**
  - Multi-block grid containing 28 blocks, post inserted with overset grids.
  - Solutions obtained for $\alpha = 6, 8, \& 10$ deg
  - Memory required - 275 MW (multi-tasked)
  - Average run time 45 hours or 13 μsec/cell/iteration
  - 2.5 - 3 order decrease in residual magnitude

A global view of the TCA (30/10) configuration mounted on the post is shown. The post is inserted into an intermediate block which has a grid distribution comparable to the surrounding global grid in order to facilitate interpolation of the overset regions.

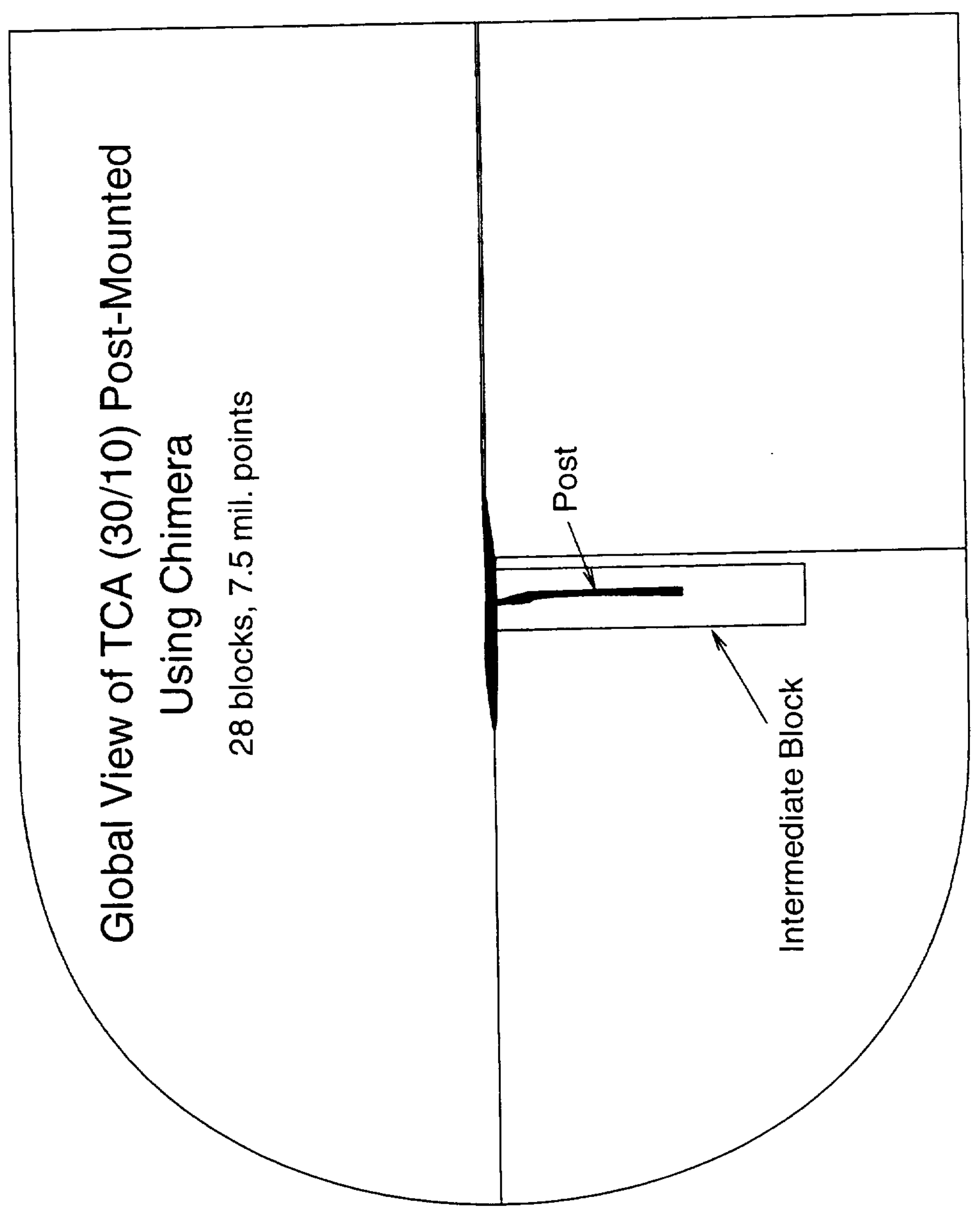
Global View of TCA (30/10) Post-Mounted
Using Chimera
28 blocks, 7.5 mil. points
Post
Intermediate Block

A close-up view of the model support, which interfaces with the lower wing surface. The post and intermediate overset grids are also shown.

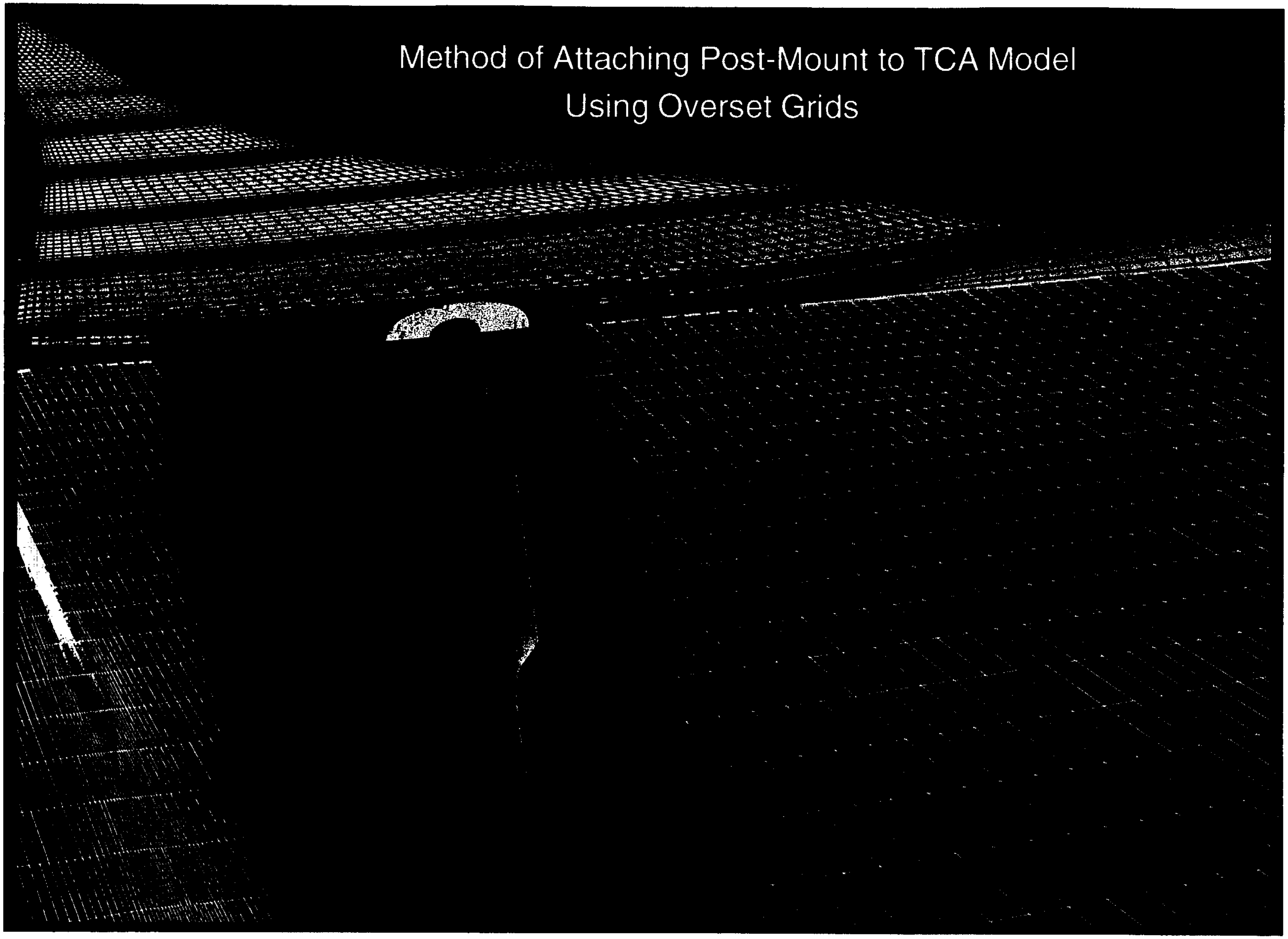
Method of Attaching Post-Mount to TCA Model
Using Overset Grids

A more global view of the TCA (30/10) surface grid and post is shown on the left of this slide. The solution at $\alpha = 8$ deg is shown on the right, and depicts surface pressure contours on the model and post.

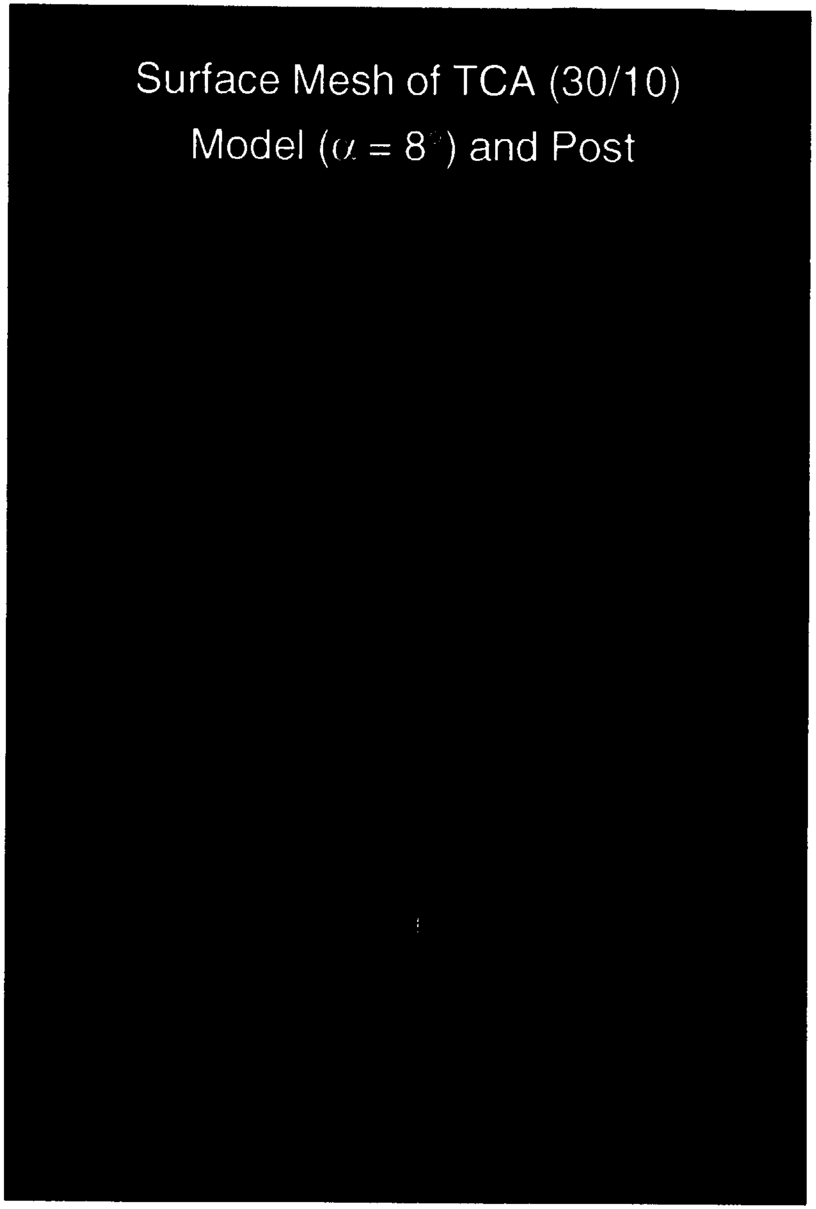
Surface Mesh of TCA (30/10)
Model ($\alpha = 8°$) and Post

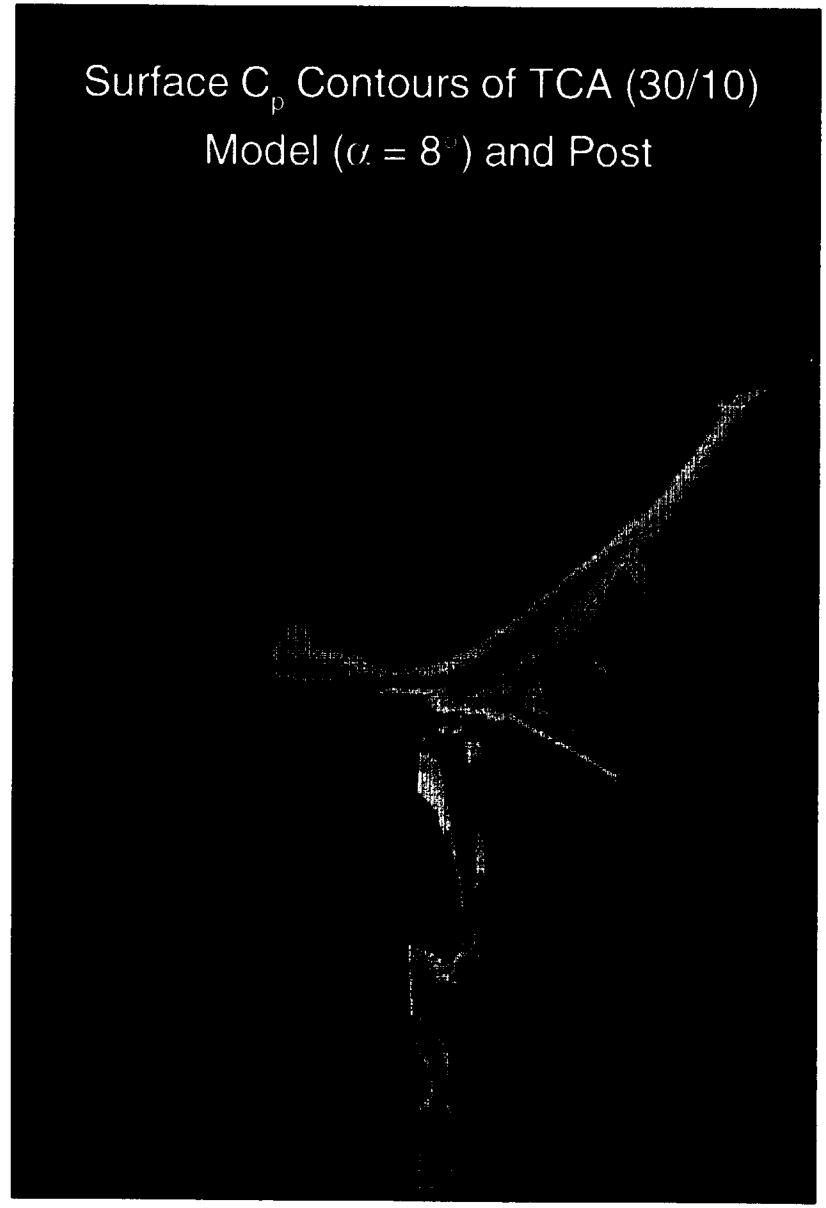
Surface C_p Contours of TCA (30/10)
Model ($\alpha = 8°$) and Post

The pressure contours are plotted in the symmetry plane and on the lower configuration surface. The continuity of the contour lines as they pass from one overset region to another is evident.

Pressure Contours Plotted in the Overset Grid Regions

The lower surface pressure contours (shaded and lines) at $M = 0.243$, $Re = 8$ mil., and $\alpha = 8$ deg is shown with the post-mount (upper plot) and without (lower plot) the post-mount The wake generated by the post creates a strong pressure field which in turn decreases the pressure coefficients on the surface and lowers the lift.

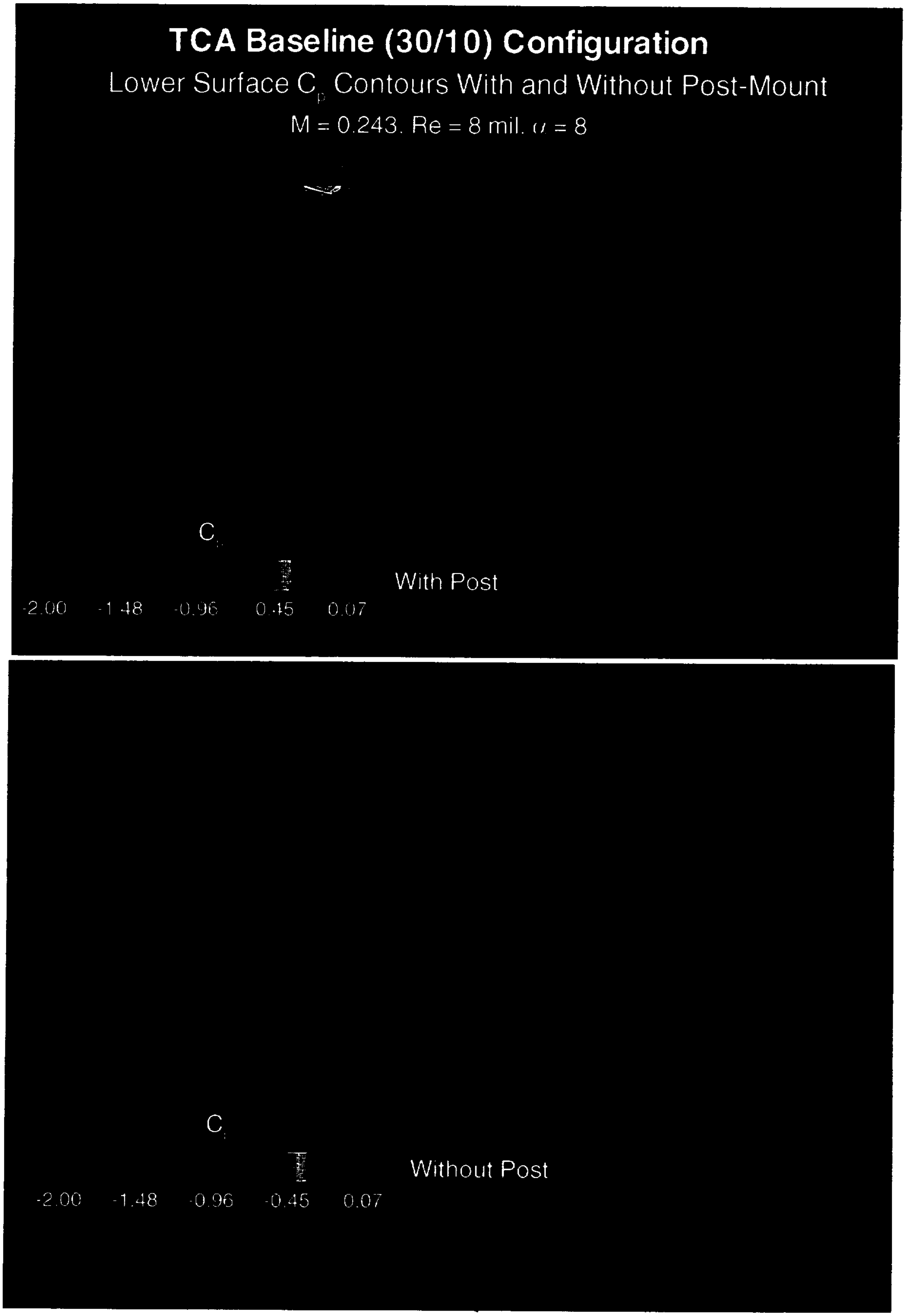
TCA Baseline (30/10) Configuration
Lower Surface C_p Contours With and Without Post-Mount
M = 0.243. Re = 8 mil. α = 8
C_p
With Post
-2.00 -1.48 -0.96 0.45 0.07
C_p
Without Post
-2.00 -1.48 -0.96 -0.45 0.07

The upper surface pressure contours (shaded and lines) at $M = 0.243$, $Re = 8$ mil., and $\alpha = 8$ deg are shown with the post-mount (upper plot) and without the post-mount (lower plot). Comparison of contours with and without the post reveal some substantial differences in the pressure.

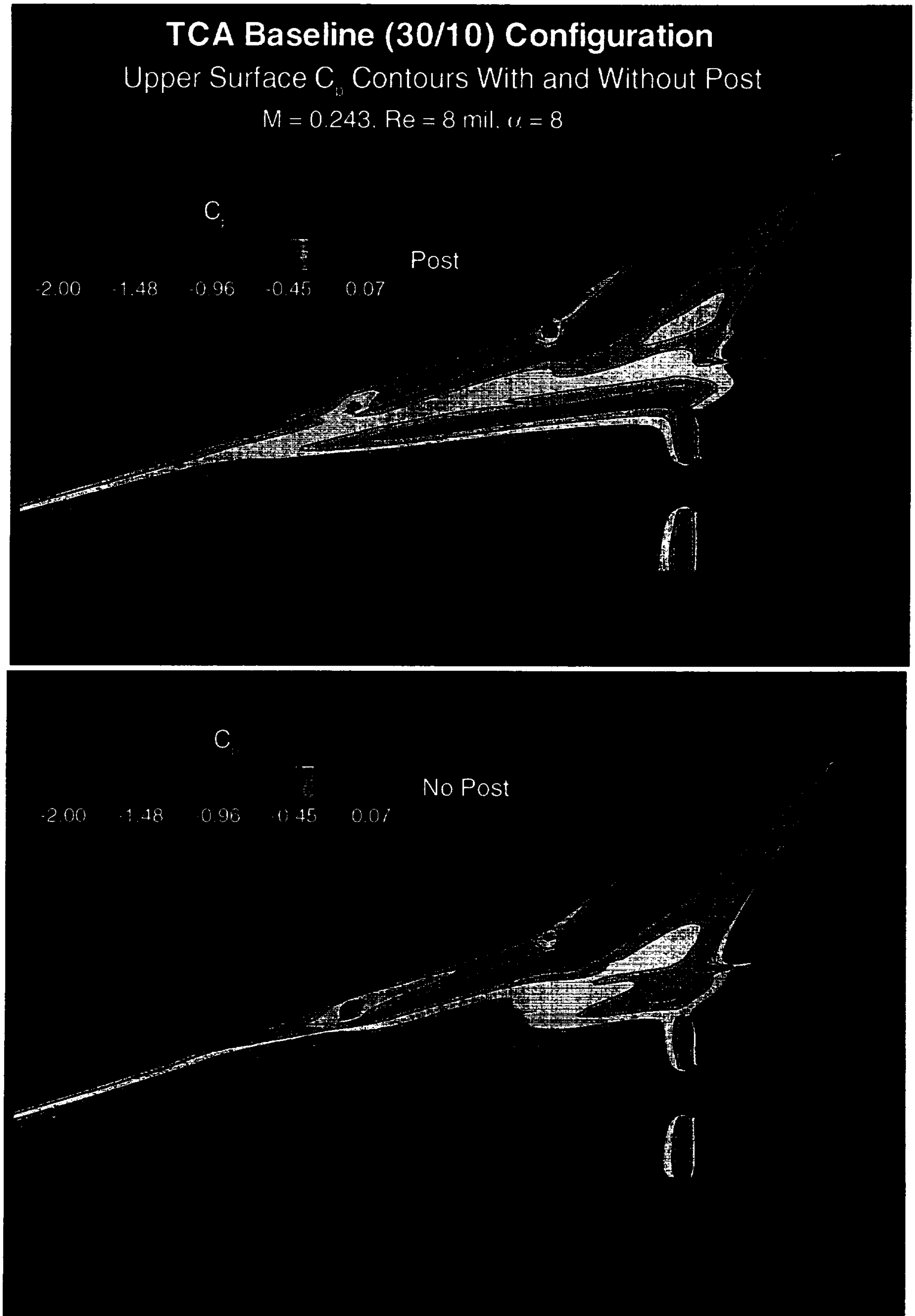
TCA Baseline (30/10) Configuration
Upper Surface C_p Contours With and Without Post
M = 0.243. Re = 8 mil. α = 8
C
Post
-2.00 -1.48 -0.96 -0.45 0.07
C
No Post
-2.00 -1.48 -0.96 -0.45 0.07

The chordwise pressure distributions with and without the post-mount are compared at $M = 0.243$, $Re = 8$ mil, and $\alpha = 8$ deg. A dramatic improvement in the computational pressure distributions inboard of BL 22.5 are seen when the post is added.

Chordwise Pressure Distributions for TCA (30/10)
With and Without Post-Mount

M = 0.243, α = 8°, Re = 8 mil

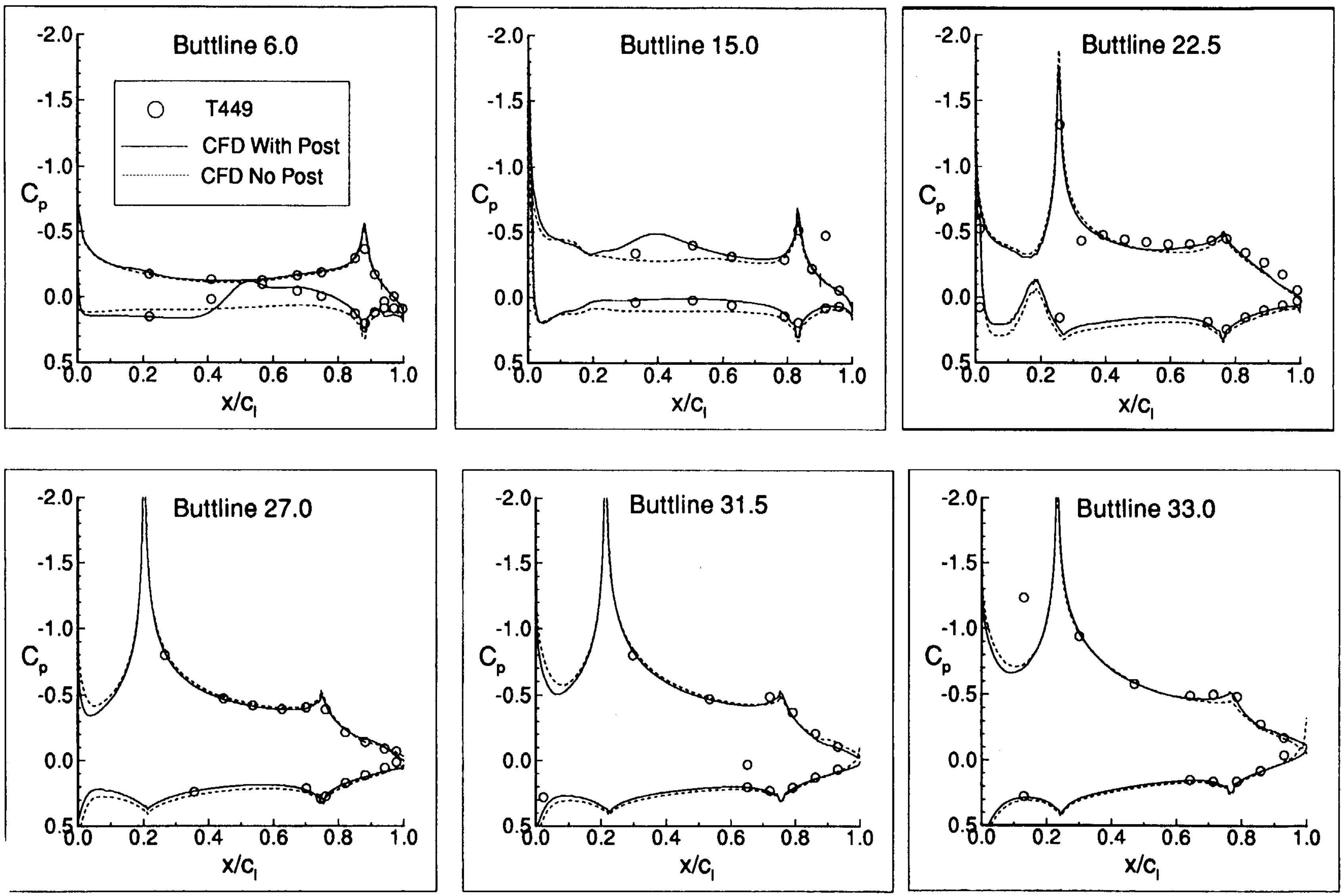

The spanwise pressure distribution for the TCA (30/10) with and without the post at the same conditions are shown. A dramatic improvement in both the upper and lower surface pressures from station 100.5 and aft is again seen.

Spanwise Pressure Distributions for TCA (30/10) With and Without Post-Mount

M = 0.243, α = 8°, Re = 8 mil

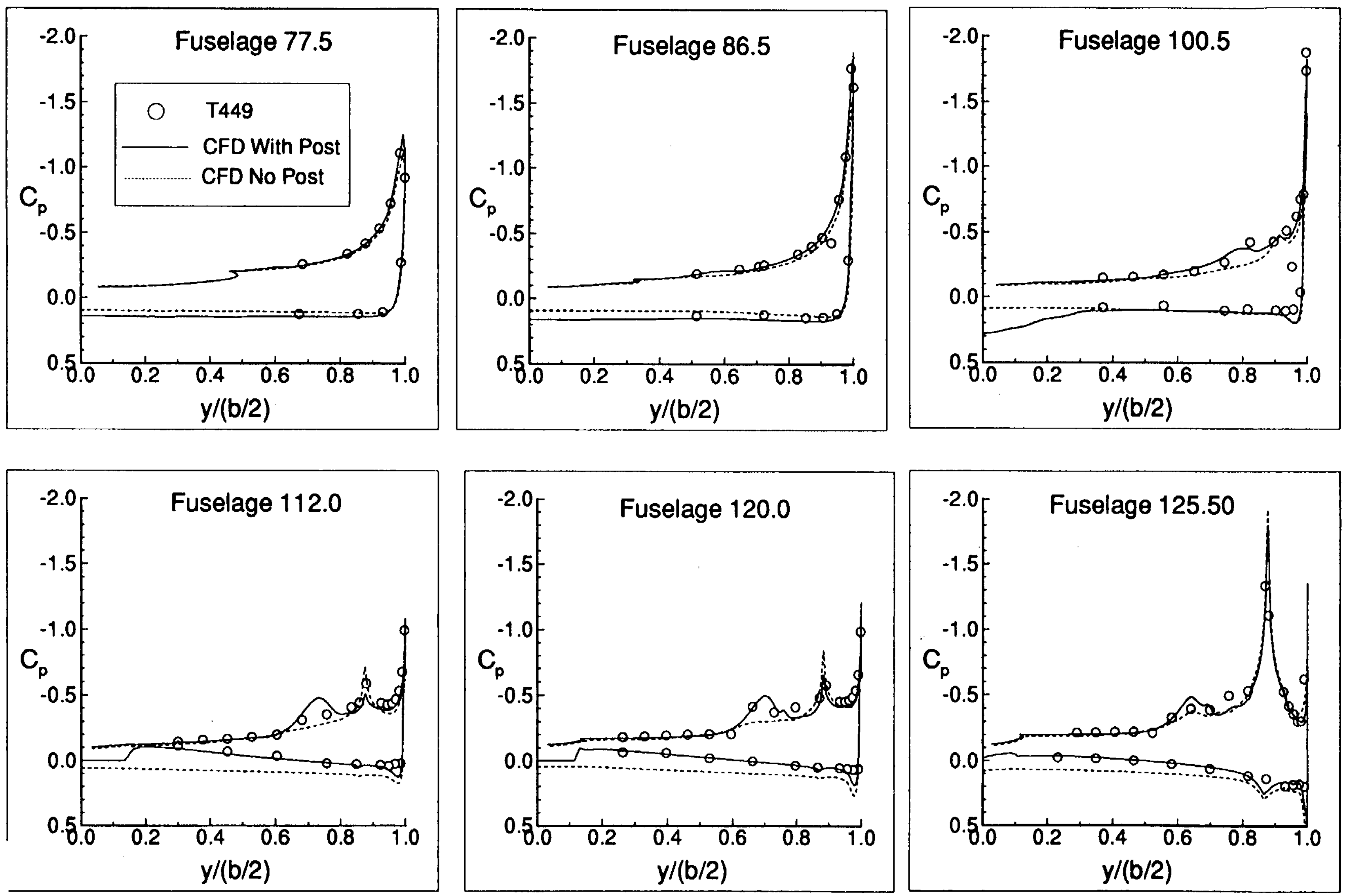

The experimental interference effects due to the post were corrected using the results obtained from the strut interference test performed at Langley, T442. As the photograph shows, the Reference H model was tested inverted with and without the image post to obtain the mounting effects.

The Model

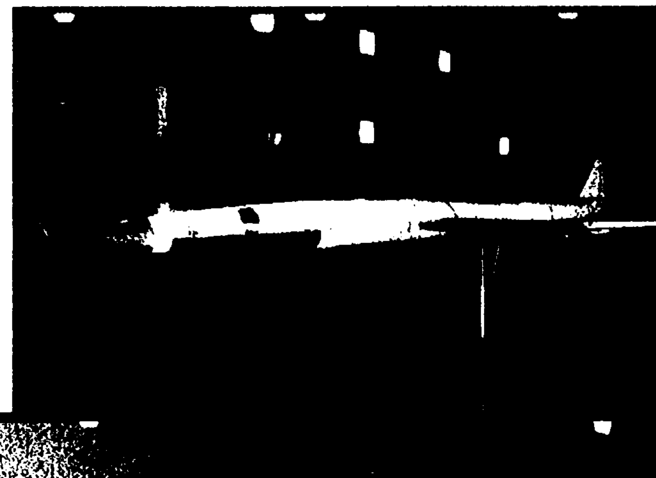

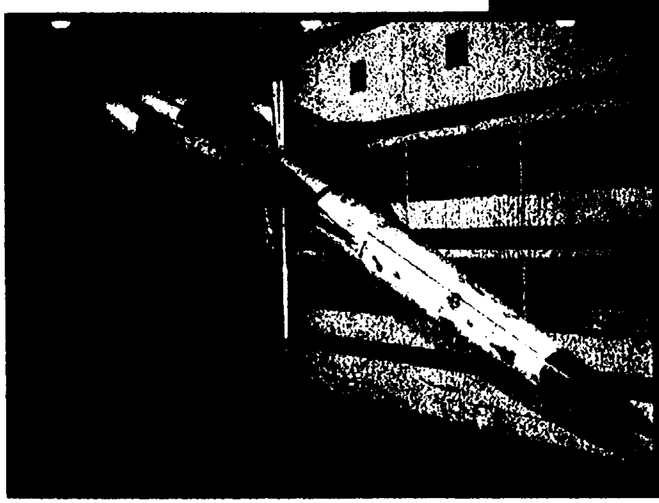

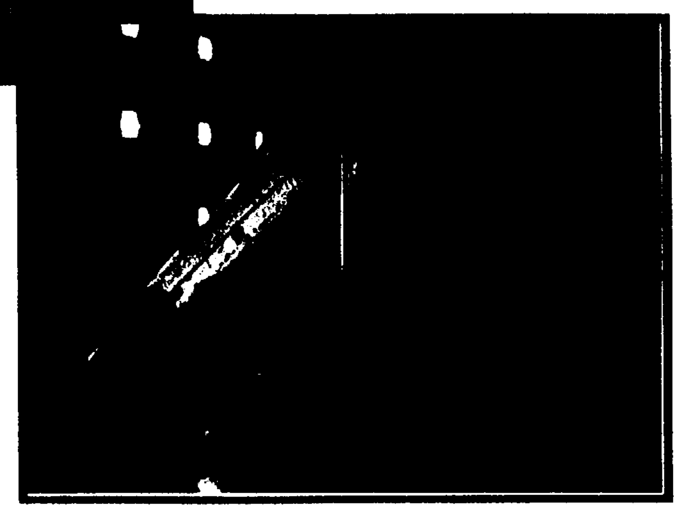

The next four figures present forces and moments of computational and experimental high-lift TCA configurations. The code CFL3D is used to calculate the free air case (model only) and the model with the post-support. This is compared to experimental data, which was corrected for free air and for free air without post-mount corrections. (Note the corrected pitching moment for the post was not available and therefore not included in the C_m vs a plot). Very good agreement is seen for both scenarios, and the code's ability to predict the increments due to the post-mount interference is excellent.

C_L Comparisons With and Without the Post-Mount

TCA (30/10) Baseline, M = 0.243, Re = 8 mil.

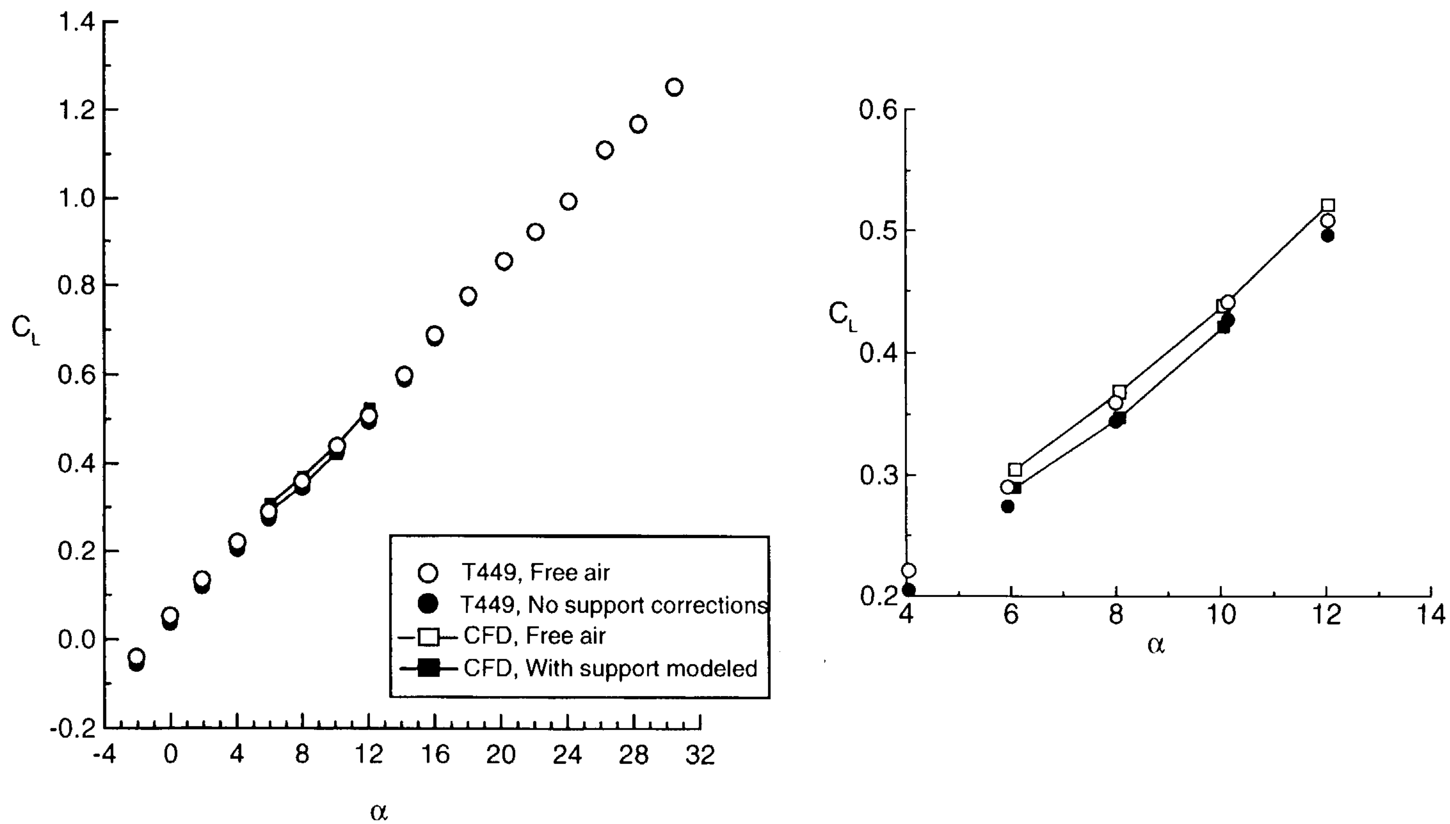

This page is intentionally left blank.

C_D Comparisons With and Without the Post-Mount

TCA (30/10) Baseline, M = 0.243, Re = 8 mil.

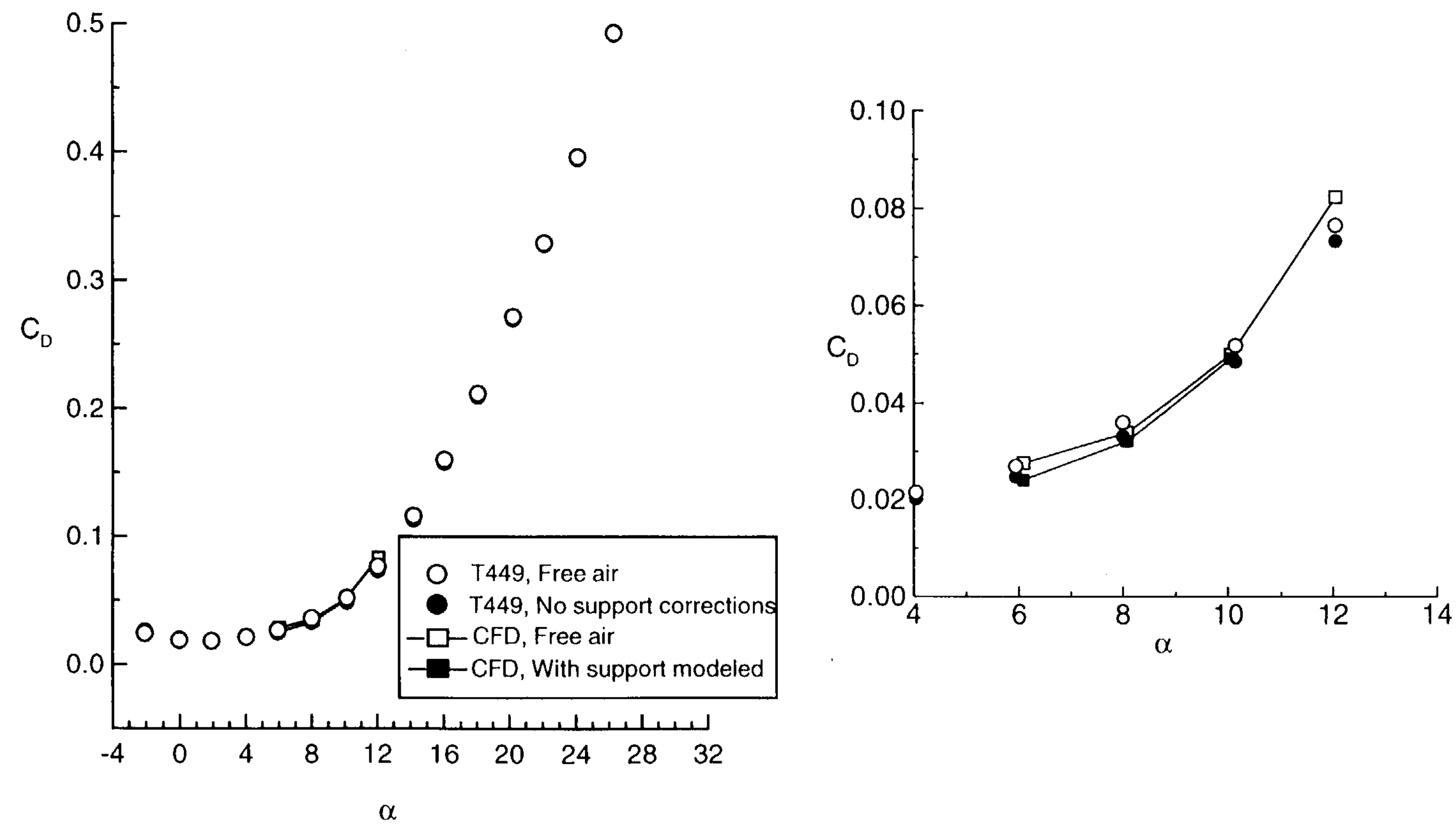

This page is intentionally left blank.

Drag Polar Comparisons With and Without the Post-Mount

TCA (30/10) Baseline, M = 0.243, Re = 8 mil.

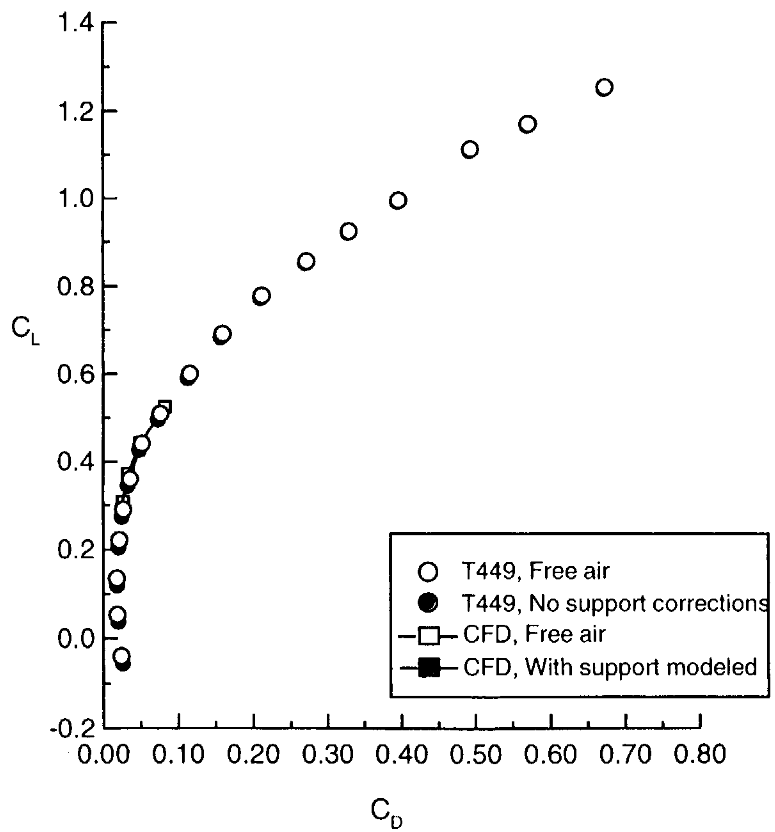

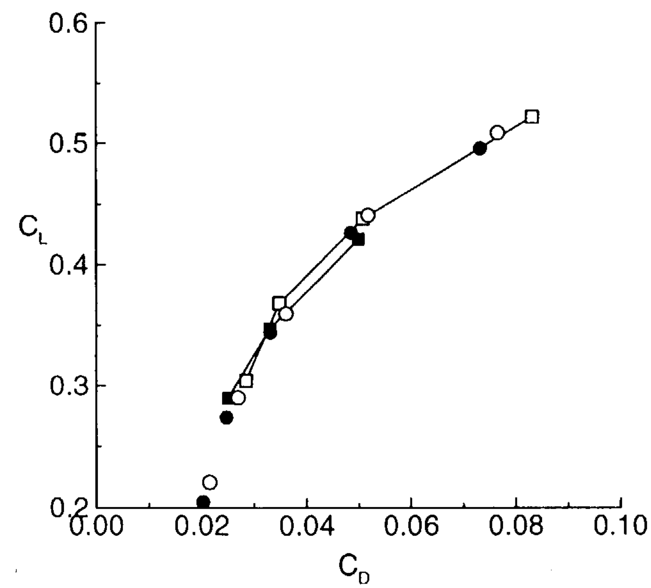

This page is intentionally left blank.

C_m Comparisons With and Without the Post-Mount

TCA (30/10) Baseline, M = 0.243, Re = 8 mil.

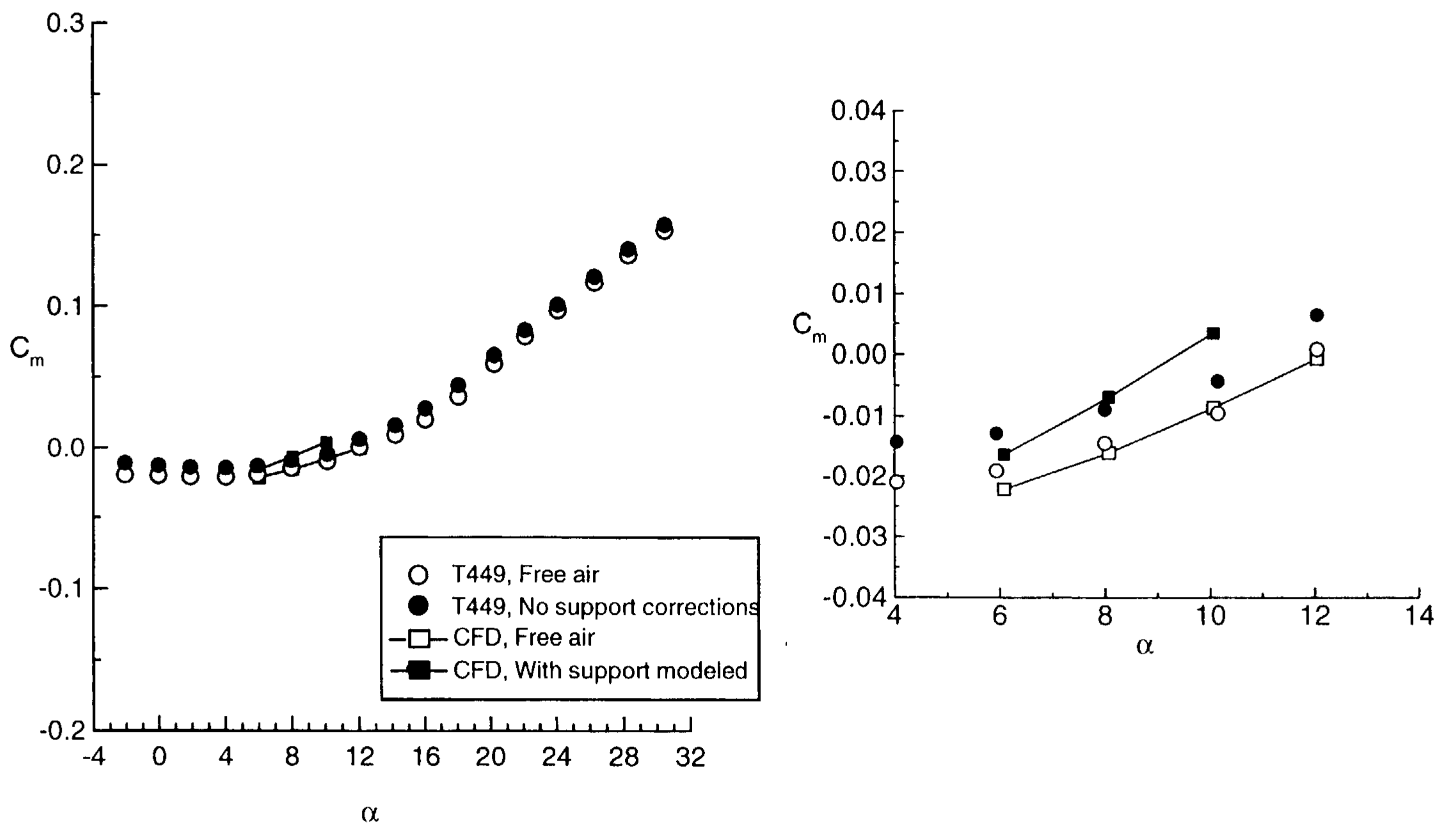

The present post-mounting system used for the Reference H and TCA creates a strong wake which dramatically effects the model's surface pressures, in addition to causing notable differences in the forces and moments. The lower surface pressures obtained from the Reference H test were confined to the leading edge of the wing; therefore the pressure values which extend over the full lower wing span were never measured. However, it is now known that the flow field was not being accurately captured when the Reference H was modeled without it's post-mount. The lesson here is that fairly good force and moment comparisons may be obtained on a configuration, but that does not validate or confirm that one has accurately solved the flow field. This is clearly evident from the pressure distribution plots shown in this presentation.

Very good results were obtained from the post/no-post cases, not only in terms of absolute values but also increments. The code could also be calibrated against and may provide useful insight into the wind-tunnel corrections that were also made.

HSR High-Lift TCA

Summary & Conclusions

- Very good agreement seen in force and moment comparsions with and without the post.
- Surface pressure distributions correlate better with experiment when the post was included in the analysis.
- The TCA post-mount geometry should be modeled in all calculations since it has been shown to create an extensive pressure field which effects the lower and upper flowfield.
- Addition of wind-tunnel walls in the calculations would provide a calibration of the experimental wall correction.

This page is intentionally left blank.

Aerodynamic Analysis of TCA Wing/Body/Nacelle High Lift Configurations

Xuetong Fan
Paul Hickey
ASE Technologies, Inc.

High Speed Research Program
Airframe Technical Review
Westin Hotel, Los Angeles Airport
February 9–13, 1998

This presentation includes the work completed at ASE Technologies, Inc. in the CFD analysis of HSCT TCA Wing/Body/Nacelle High Lift configurations.

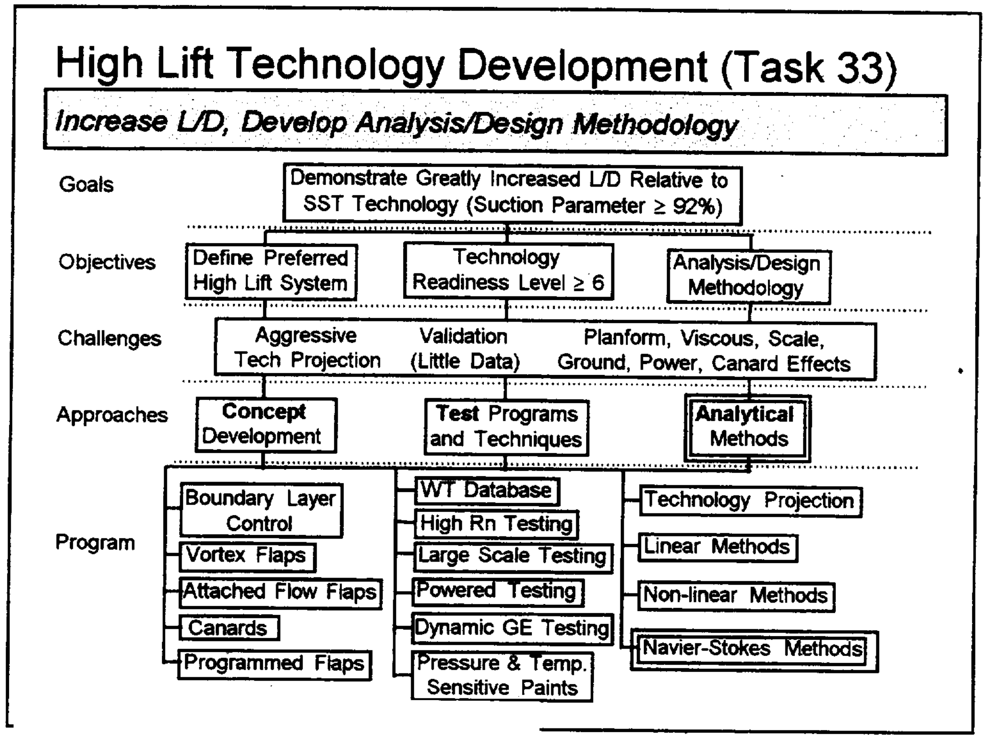

In the High Lift Technology Development program (Task 33), this work falls in the category of Navier-Stokes Methods under Analytical Methods. We hereby acknowledge the support and help from Roger Clark and David Yeh of Boeing Long Beach.

Objectives

- Develop CFD Models for aerodynamic analysis of HSCT TCA Wing/Body/Nacelle (WBN) high lift configurations
  - Construct multi–block CFD grids to include nacelles and diverters with and without deflected LE/TE flaps
  - Obtain converged CFL3D solutions for the TCA WBN models
- Evaluate the effect of nacelle installation on the aerodynamic performance of HSCT TCA high lift configurations
  - Identify and analyze important flow characteristics due to nacelle installation to support Propulsion Airframe Integration (PAI) effort
  - Provide flow and performance data related to nacelle effect to supplement wind tunnel test

The objectives of this work are two fold. The first objective is to develop efficient CFD modeling procedures for the TCA high lift configurations with nacelle installation. The second objective is to evaluate the effect of nacelle installation on the aerodynamic performance of the TCA high lift configurations.

To achieve the first objective, we will build multi–block CFD grids to include nacelles and diverters in the TCA high lift configurations with and without deflected LE/TE flaps. And then we will use CFL3D to obtain fully converged turbulent solutions for the TCA W/B/N models.

For the second objective, we will, from the CFD solutions, identify and analyze important flow characteristics due to nacelle installation to support Propulsion Airframe Integration. We will also provide flow and performance data for the TCA W/B/N configurations to supplement wind tunnel test.

Outline

- TCA 0/0 WBN Model
  - Model description
  - Convergence history
  - Comparison with wing/body solution and test data
  - Flow characteristics
- TCA 30/10 WBN Model
  - Model description
  - Convergence history
  - Comparison with wing/body solution and test data
  - Flap loading analysis
  - Flow characteristics
- Summary

We completed two CFD models for the TCA W/B/N configurations: TCA 0/0 and TCA 30/10. In this presentation, we will describe the multi-block CFD models for the two W/B/N configurations and show the CFL3D solutions. We will compare our CFL3D solutions for W/B/N with the respective CFL3D solutions for W/B obtained at Boeing Long Beach for the same flap settings. We will also compare the CFD solutions with the available test data to illustrate nacelle effect. We will use flow visualization to show the important flow characteristics, especially in the vicinity of nacelles and diverters. For the TCA 30/10 W/B/N configuration, we will examine the span loading of the deflected TE flaps. A brief summary of this work is included at the end of this presentation.

TCA 0/0 WBN Model Description

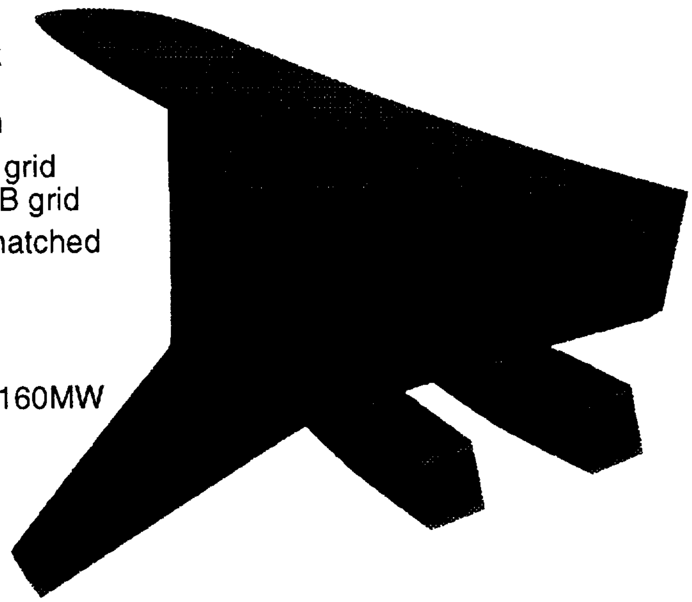

- Based on single–block TCA 0/0 W/B grid provided by David Yeh
- Nacelle/Diverter (N/D) grid face–matched with W/B grid
- Mostly 1–to–1 point–matched between N/D blocks
- Model size: 20 blocks 4 million grid points
- Memory requirement: 160MW
- Minimum viscous spacing: 0.002 in

The construction of TCA 0/0 W/B/N grid is based on the TCA 0/0 W/B grid provided by David Yeh. A portion of the W/B grid is removed to make room for nacelles and diverters (N/D). The N/D blocks interface with the W/B grid in a face–matched manner using the RONNIE pre–processor in CFL3D. Between the N/D blocks, 1–to–1 point–match is used as much as possible. The final model for TCA 0/0 W/B/N has 20 blocks with 4 million grid points. It requires 160 MW of memory on Cray C–90 to run the CFL3D flow solver for this model. The minimum viscous spacing in the W/B/N model is 0.002 inches to be consistent with the W/B grid.

TCA 0/0 WBN Model

Contour of y+ off model viscous surfaces
(Mach #=0.3, Re=$8x10^6$, AOA=10 degrees)

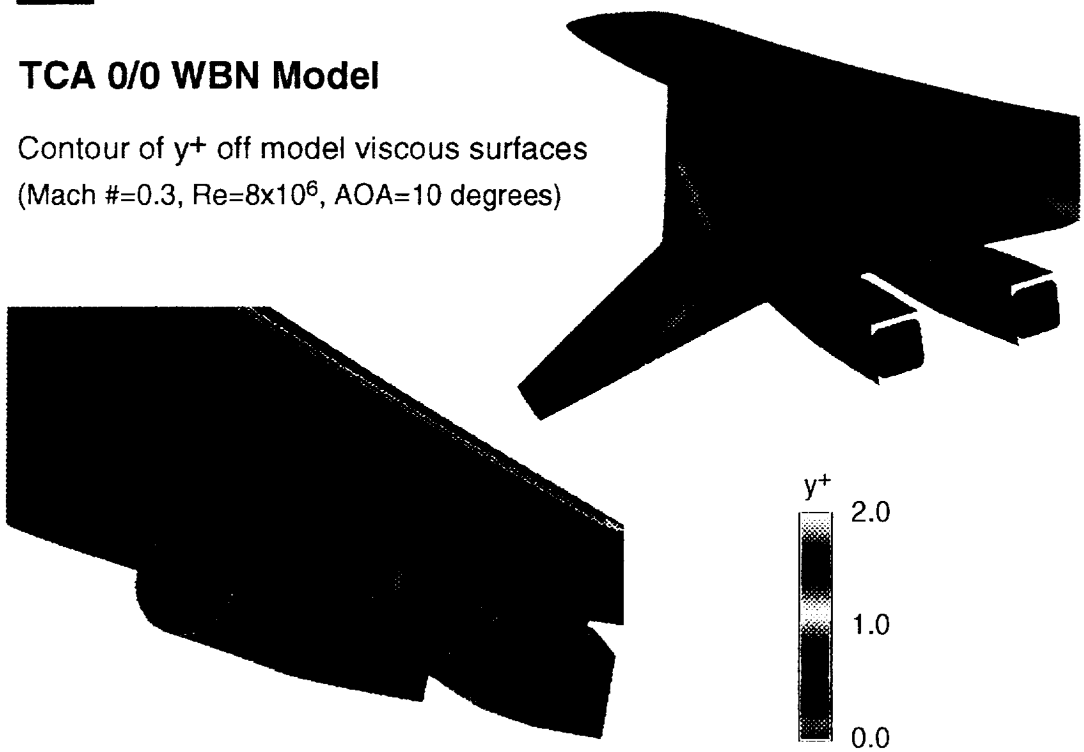

With the minimum viscous spacing of 0.002 inches, the y+ values for the first grid points off model solid surfaces are in the order of 1.0, which is appropriate for the Baldwin–Lomax turbulence model. The flow condition for the y+ results are: Mach No. = 0.3, Re = 8 million, and Angle of Attack = 10 degrees.

CFL3D Convergence History

(TCA 0/0, Mach #=0.3, Re=8x10^6, AOA=10 degrees)

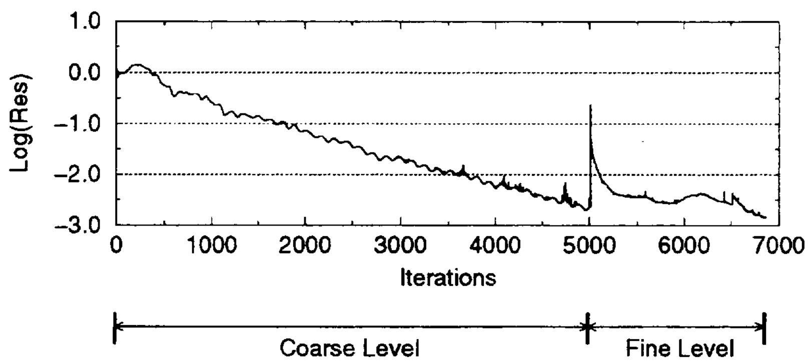

- 2–level grid sequencing; 2–level multi–grid on fine level
- Total CPU Usage: 42 hours on Cray C–90
  (9 hours on coarse level and 33 hours on fine level)

The convergence history of the CFL3D solution for the TCA 0/0 W/B/N model is shown here. Two–level grid sequencing was used and two–level multi–grid was applied on the fine grid level. Extensive iterations were performed on the coarse grid level for debugging purposes, which used 9 hours of CPU time on Cray C–90. After 500 iterations on the fine level, we adopted David Yeh's modification to the Baldwin–Lomax turbulence model with Degani–Schiff option. It has been proven that Yeh's modification can better simulate the vortical flow above the wing upper surface. For simplicity, we only used his modification in the block around the leading edge and above the wing upper surface in the W/B/N model. This modification caused the predicted lift coefficient to increase gradually, which is why extensive (and expensive) iterations were run on the fine grid level. The 1800 iterations on the fine grid level used 33 CPU hours on Cray C–90.

CFL3D Convergence History

(TCA 0/0, Mach #=0.3, Re=8x10^6, AOA=10 degrees)

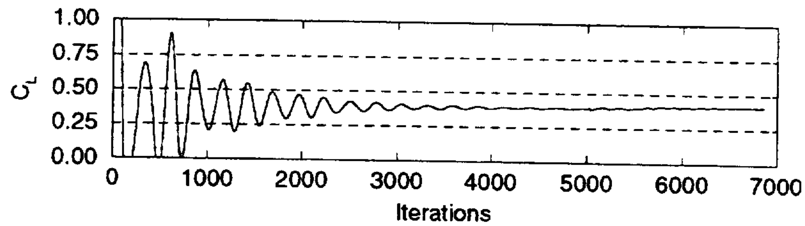

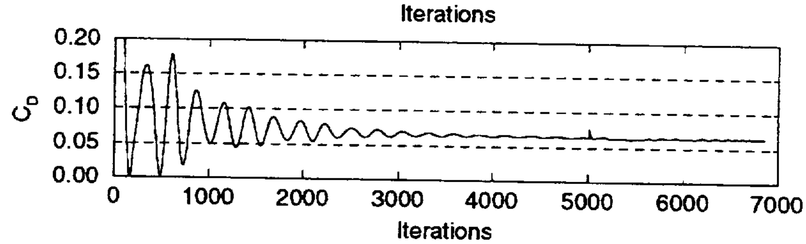

The convergence history for C_L and C_D for the TCA 0/0 W/B/N model is shown here. For the last 200 iterations, the peak–to–valley variations in C_L and C_D are within 2% of their mean values, which are comparable to the level of convergence achieved in the W/B model. Since our W/B/N model is based on the W/B grid, it is unlikely for the W/B/N solution to converge much better than the W/B solution.

Comparison with W/B Solution and Wind Tunnel Data

(TCA 0/0, Mach #=0.3, Re=8x10^6, AOA=10 degrees)

Lift Coefficient (C_L)

C_L	W/B	W/B/N	ΔC_L
CFL3D	0.3850	0.4116	0.0266
Experiment	0.3749	0.3711	–0.0038

Drag Coefficient (C_D)

C_D	W/B	W/B/N	ΔC_D
CFL3D	0.0599	0.0634	0.0035
Experiment	0.0606	0.0616	0.0010

The integrated coefficients, C_L and C_D, for the TCA 0/0 W/B/N model are shown in the above tables, together with those from the W/B solution and wind tunnel experiments. Considerable discrepancies are found between the CFD solutions and the experimental data. Further and more detailed investigation is necessary to understand and possibly eliminate the discrepancies. It is noted that the C_D values from both the W/B/N CFD solution and the test data have been corrected for the nacelle interior friction forces and the nacelle base pressure forces.

Comparison with W/B Solution and Wind Tunnel Data

(TCA 0/0, Mach #=0.3, Re=8x10^6, AOA=10 degrees)

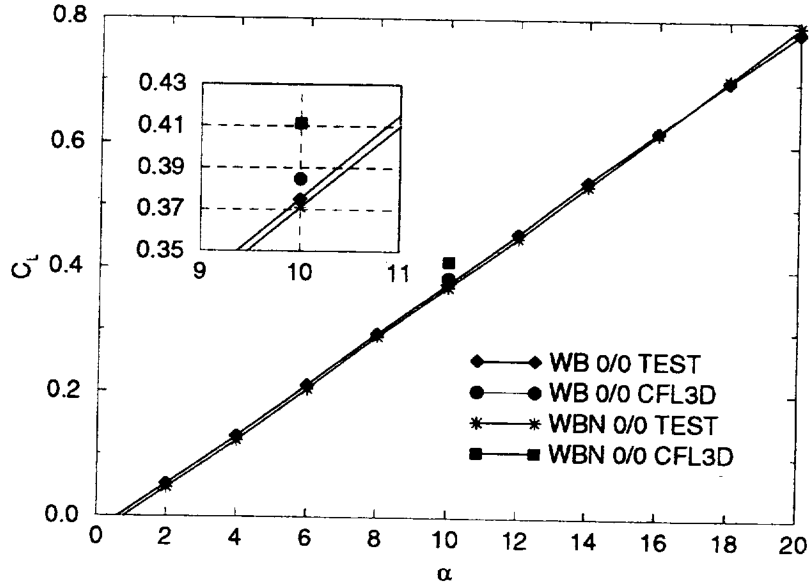

This figure shows the relative locations of the lift coefficients on the lift curve. It is noted that for the angles of attack (AoA) up to 16 degrees, wind tunnel test shows decreases in C_L, whereas the CFD solution predicts an opposite trend at AoA of 10 degrees.

Comparison with W/B Solution and Wind Tunnel Data

(TCA 0/0, Mach #=0.3, Re=8x10^6, AOA=10 degrees)

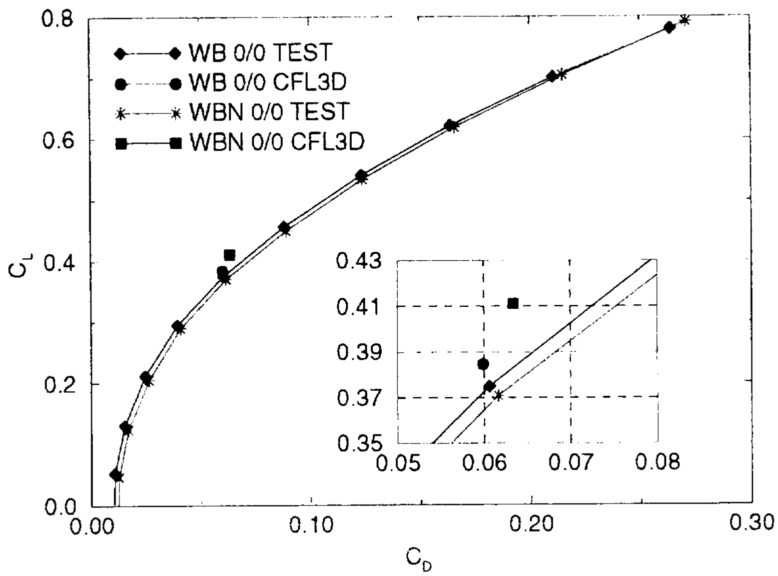

This figure shows the relative locations of the lift and drag coefficients on the drag polar.

ASE Technologies, Inc.

TCA 0/0 CFL3D Solutions:

(Mach #=0.3, Re=8x10^6, AOA=10 degrees)
Cp on wing upper surfaces

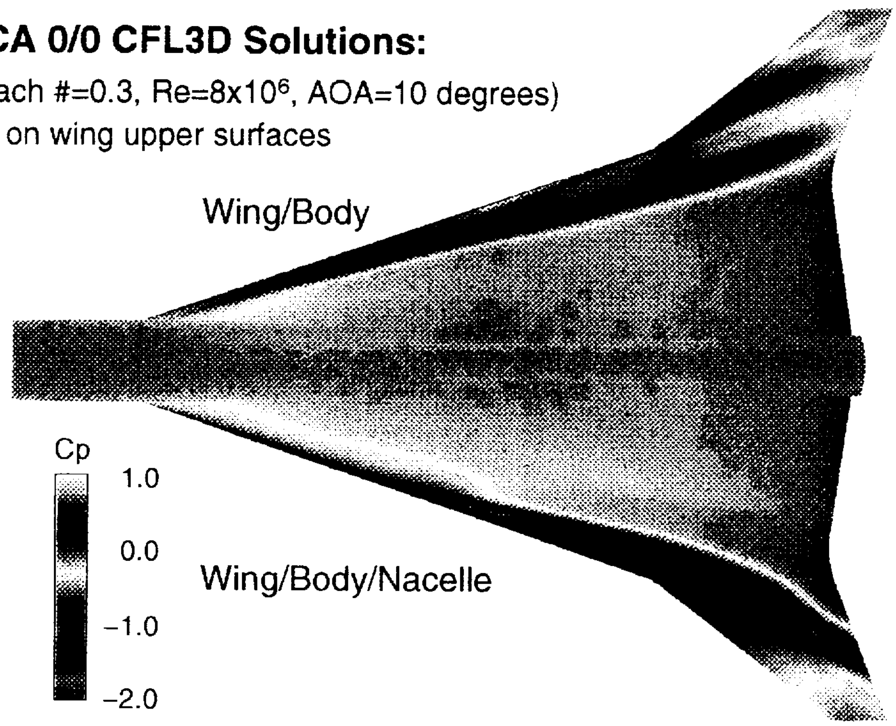

This slide shows the pressure coefficient contour on the wing upper surfaces for the W/B and W/B/N CFD models. With nacelles installed, the CFD solution shows similar leading edge vortices but with enhanced strength, compared to the W/B solution. This enhancement resulted in the increment in the predicted lift coefficient for the TCA 0/0 WBN configuration.

TCA 0/0 CFL3D Solutions:

(Mach #=0.3, Re=8x10^6, AOA=10 degrees)
Cp and limiting streamlines on wing lower surfaces

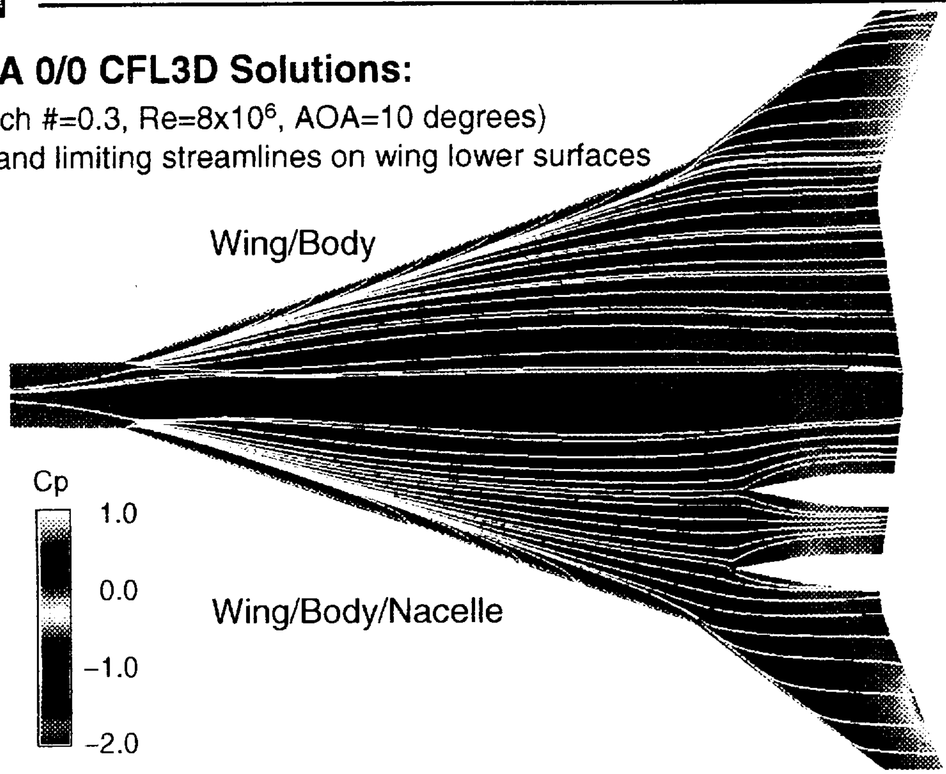

On the wing lower surface, the pressure coefficient distributions and the limiting streamlines are very similar between W/B and W/B/N solutions, except for around the diverters. For the W/B/N case, the limiting streamlines indicate possible flow separation near the leading edges of the diverters.

TCA 0/0 WBN CFL3D Solutions:

(Mach #=0.3, Re=$8x10^6$, AOA=10 degrees)

Normalized total pressure downstream of nacelle inlets

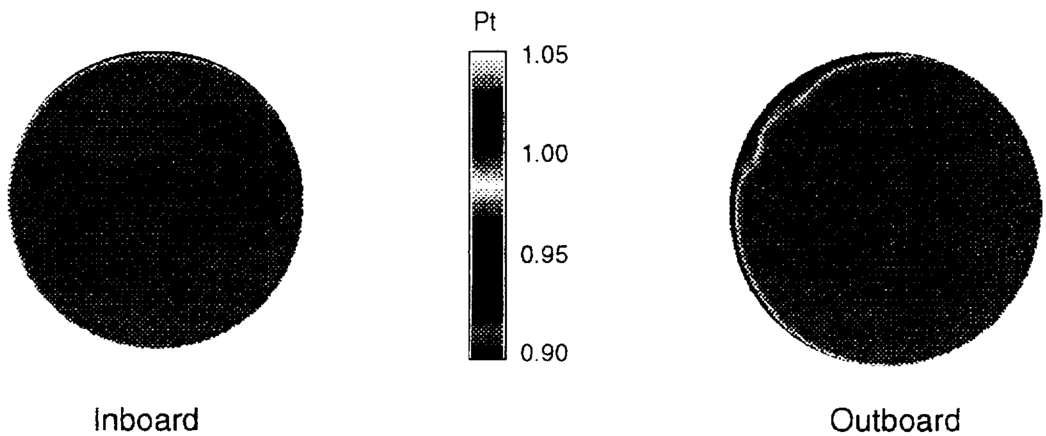

This figure shows the total pressure contours in the nacelle interior cross sections just downstream of the nacelle leading edge. Local flow separation is apparent at the entrance to the outboard nacelle which may impact the outboard engine performance.

TCA 0/0 WBN CFL3D Solutions:

(Mach #=0.3, Re=8×10^6, AOA=10 degrees)

Limiting streamlines around nacelle leading edge

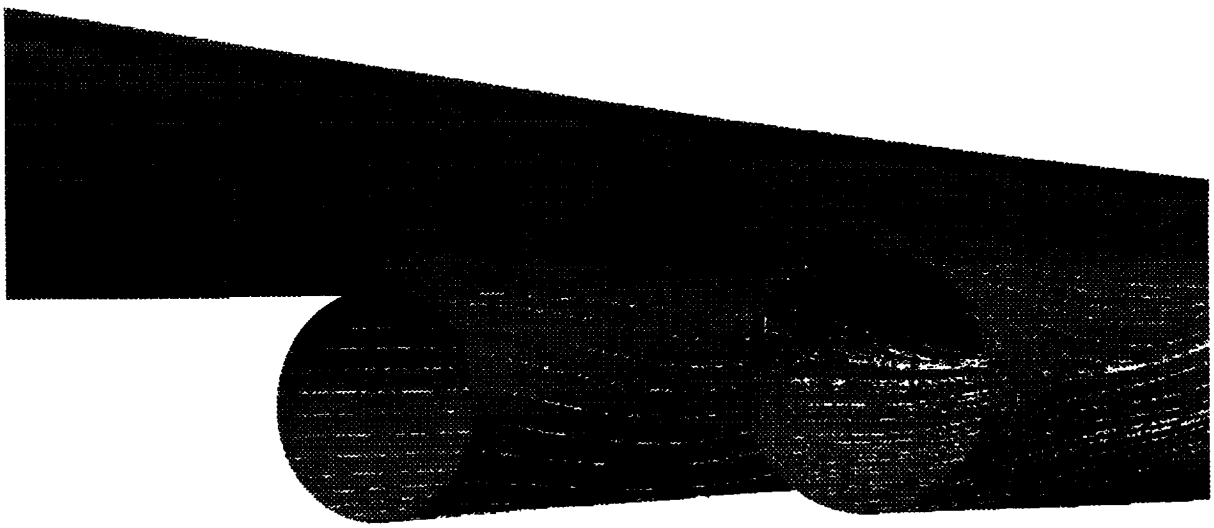

Examination of the limiting streamlines near the leading edge of the outboard nacelle further confirms the local flow separation.

TCA 30/10 WBN CFD Model

- Based on single-block TCA 30/10 W/B grid provided by David Yeh
- Buffer zones were used to 1-1 match with W/B grid in spanwise locations
- Nacelle/Diverter grid face-matched with buffer zones and W/B grid
- Mostly 1-to-1 point-matched between N/D blocks

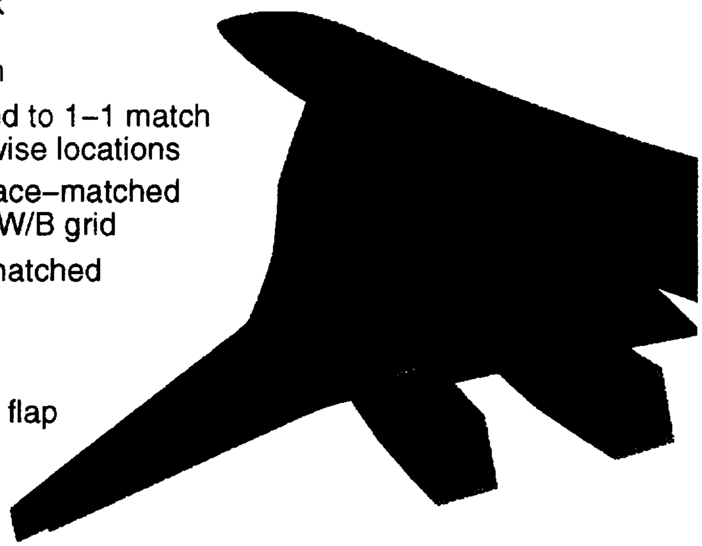

Major challenges

- "Web" approach to TE flap deflection not feasible
- Close proximity of deflected TE flaps to nacelles and diverters

The W/B/N model for the TCA 30/10 configuration is based on the TCA 30/10 W/B grid provided by David Yeh. To improve the interfacing quality between the W/B grid and the N/D grid, we used buffer zones between them at spanwise locations. These buffer zones 1-to-1 point-match with the W/B grid and face-match with the N/D grid on flat surfaces for higher interpolation accuracy. Between the N/D blocks, mostly 1-to-1 point-match is used.

The major technical challenge for the TCA 30/10 W/B/N configuration is the modeling of the deflected TE flaps. With nacelles installed, the "web" approach used by David Yeh for the W/B model is not feasible. In addition, due to the close proximity of the deflected TE flaps to the nacelles and diverters, it is difficult to obtain high quality grid that can accurately simulate the potentially complicated flows in that region.

TCA 30/10 WBN Model

Modeling the deflected TE flaps with wedges

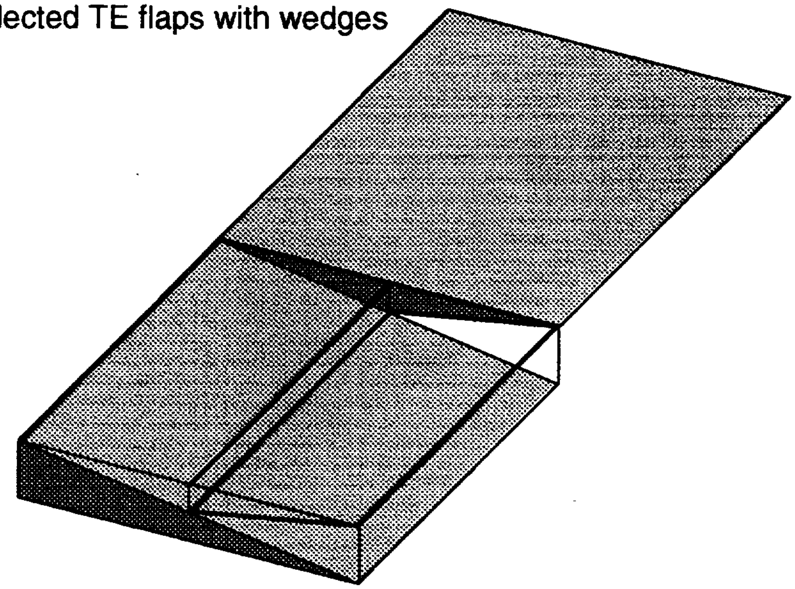

Our approach to the problem is to use three wedges for each region above the upper surfaces of the deflected flaps, as shown in the above figure. These wedges fill in the space created by TE flap deflection and at the top flush with the wing upper surface. The side surfaces of the undeflected wing segments and the openings between the wing and the deflected TE flaps are accurately modeled with this approach.

TCA 30/10 WBN Model

Modeling the deflected TE flaps with wedges

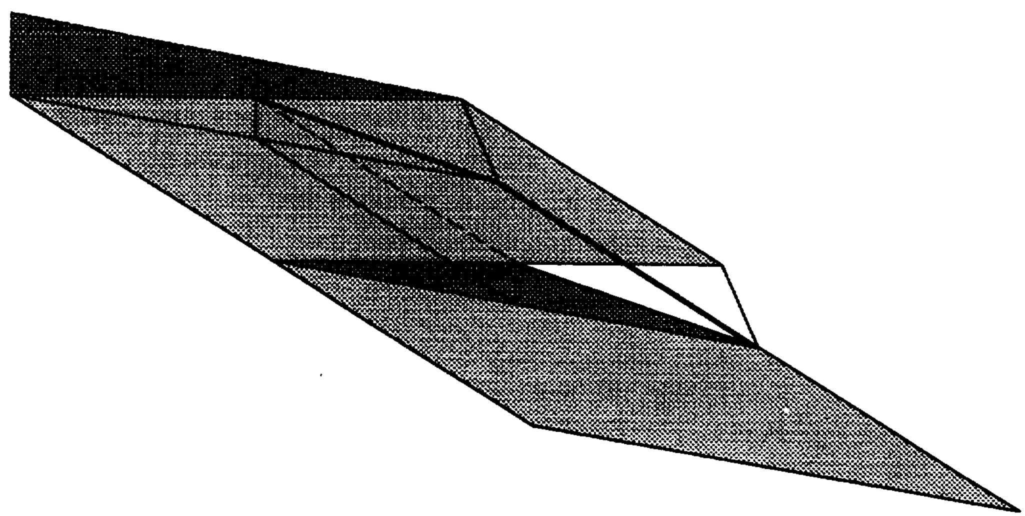

Underneath the wing, another three wedges are used for each region between the deflected TE flaps. The bottom surface of these wedges are flush with the lower surfaces of the deflected TE flaps. Through the openings created by the TE flap deflections, 1–to–1 point-match is established between the upper and lower wedges.

TCA 30/10 WBN Model

- Model size: 50 blocks (including 21 wedges); 6 million grid points
- Memory requirement: 255MW

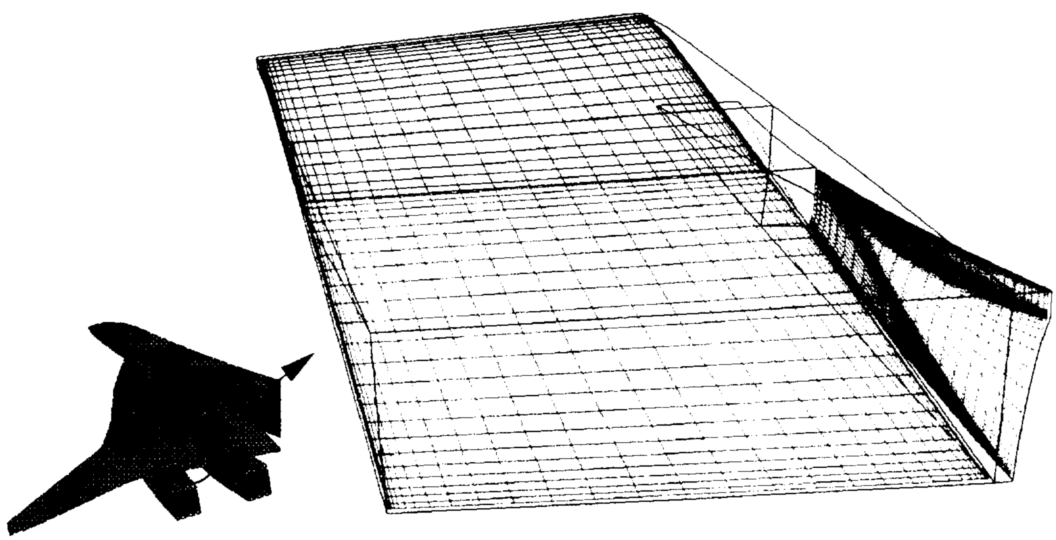

This figure shows the actual wedge grid in one of the deflected TE flap regions. It is noted that one side for each set of the lower wedges will lie on the side surfaces of the nacelles and diverters. The final grid for the TCA 30/10 W/B/N configuration consists of 50 blocks including 21 wedges and a total of about 6 million grid points. It requires 255 MW of memory on Cray C–90 to run the CFL3D solver for this model.

CFL3D Convergence History

(TCA 30/10, Mach #=0.3, Re=8x10^6, AOA=10 degrees)

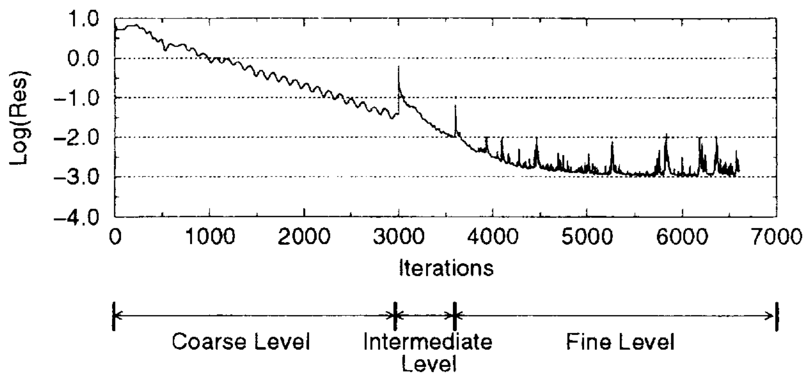

- 3-level grid sequencing
- 2-level multi-grid on intermediate and fine levels
- CPU Usage: 54 hours on Cray C-90 (2 hours on coarse level; 2 hours on intermediate level; 50 hours on fine level)

With the improved accuracy for the patched grid interfaces in the TCA 30/10 W/B/N model, we are able to run 3-level grid sequencing with 2-level multi-grid on the intermediate and fine grid levels. We completed 3000 iterations on the coarse grid level and 600 iterations on the intermediate level which used 2 CPU hours each on Cray C-90. After switching to fine grid level after 3600 iterations, however, fluctuations started to appear in the residual history. Various means were tried to elliminate the fluctuations with no success. Examination of the flow field revealed that local flow fluctuations exist only in the wedge regions. After 6300 total iterations, we adopted David Yeh's modification to the turbulence model and completed another 300 iterations. All the fine level iterations used 50 CPU hours on Cray C-90.

CFL3D Convergence History

(TCA 30/10, Mach #=0.3, Re=8x10^6, AOA=10 degrees)

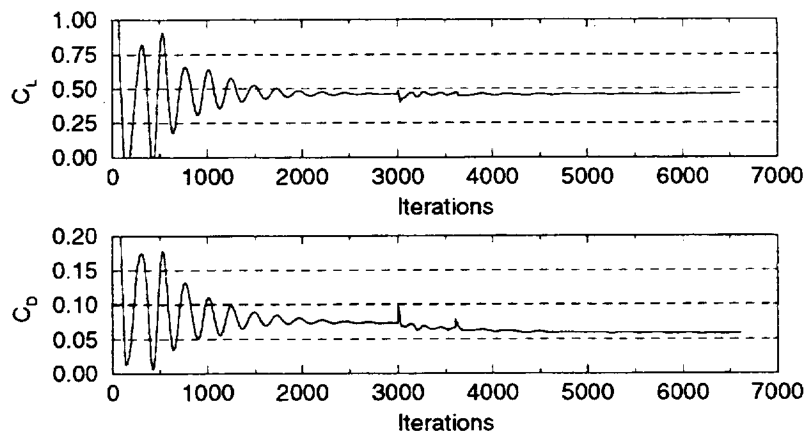

This figure shows the convergence history for the integrated lift and drag coefficients for TCA 30/10 W/B/N model. The local fluctuations in the flow field near the deflected TE flaps have no apparent effect on the integrated coefficients. In addition, Yeh's modification to the turbulence model is not affecting the solution due to the weakness of the LE vortices for the TCA 30/10 configurations. For the last 200 iterations, the peak–to–valley variations in C_L and C_D are within 2% of their mean values respectively, which are comparable to the level of convergence achieved in the TCA 30/10 W/B CFD model.

Comparison with W/B Solution and Wind Tunnel Data

(TCA 30/10, Mach #=0.3, Re=8x10^6, AOA=10 degrees)

Lift Coefficient (C_L)

C_L	W/B	W/B/N	ΔC_L
CFL3D	0.4421	0.4635	0.0214
Experiment	0.4260	0.4697	0.0437

Drag Coefficient (C_D)

C_D	W/B	W/B/N	ΔC_D
CFL3D	0.0501	0.0571	0.0070
Experiment	0.0505	0.0602	0.0097

The integrated coefficients, C_L and C_D, for the TCA 30/10 W/B/N model are shown in the above tables, together with those from the W/B solution and wind tunnel experiments. Discrepancies are found between the CFD solutions and the experimental data in terms of lift and drag increments due to nacelle installation. Further and more detailed investigation is necessary to understand and possibly eliminate these discrepancies. It is noted that the C_D values from both the W/B/N CFD solution and the test data have been corrected for the nacelle interior friction forces and nacelle base pressure forces.

Comparison with W/B Solution and Wind Tunnel Data

(TCA 30/10, Mach #=0.3, Re=8x10⁶, AOA=10 degrees)

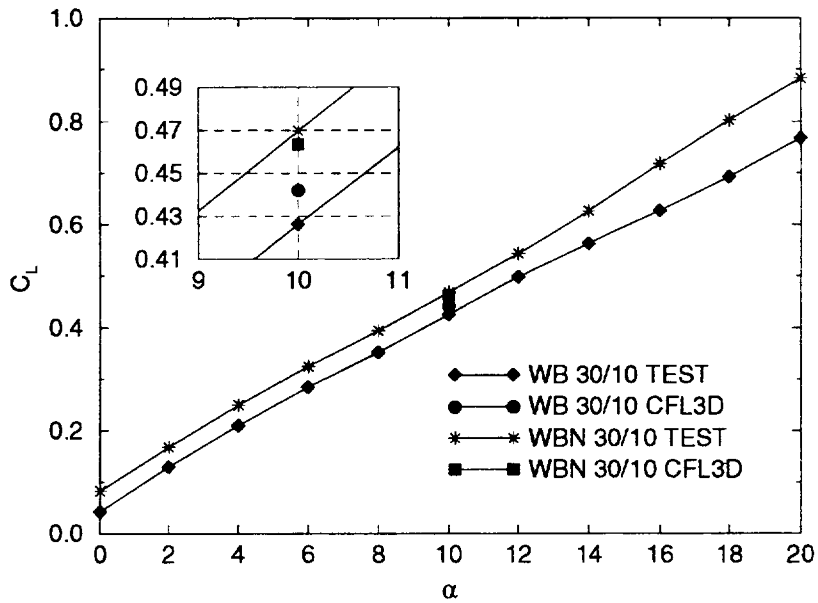

This figure shows the relative locations of the lift coefficients on the lift curve. For TCA 30/10 configurations, both CFD analysis and wind tunnel experiment show an increase in C_L due to nacelle installations, although the CFD solution predicts a much smaller increment in C_L than test data at AoA of 10 degrees.

Comparison with W/B Solution and Wind Tunnel Data

(TCA 30/10, Mach #=0.3, Re=8x10^6, AOA=10 degrees)

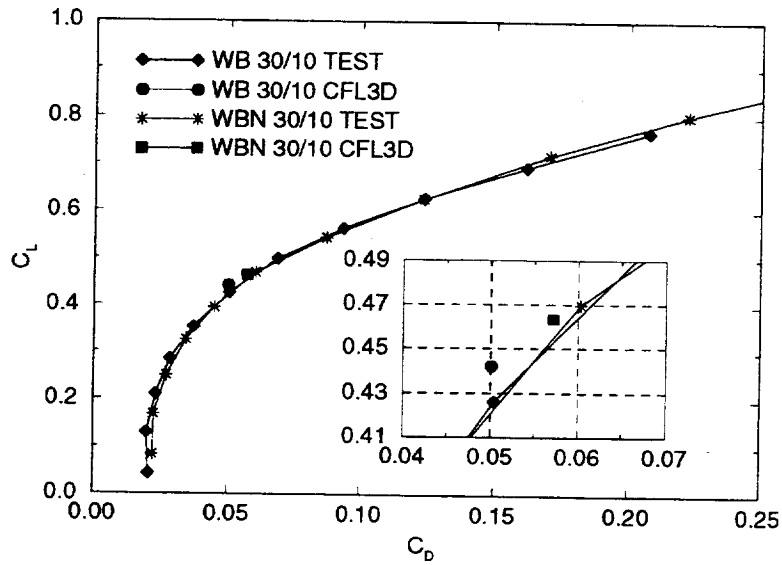

This figure shows the relative locations of the lift and drag coefficients on the drag polar for the TCA 30/10 W/B and W/B/N configurations.

Comparison with W/B Solution

(TCA 30/10, Mach #=0.3, Re=8x10^{6}, AOA=10 degrees)

Cp on wing upper surface

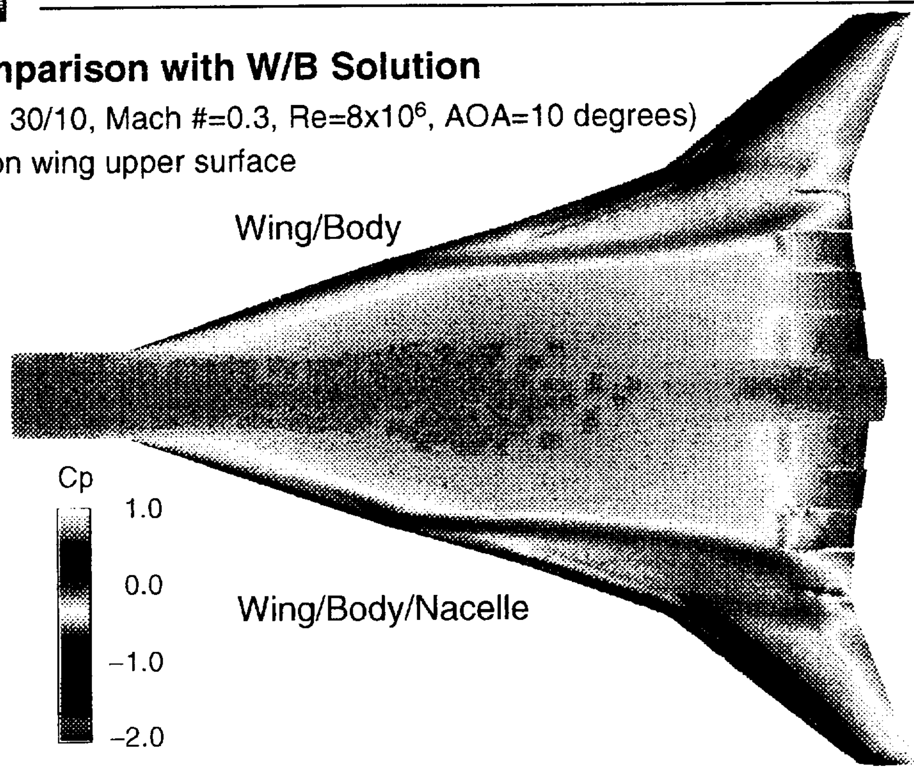

The pressure coefficient contour on the wing upper surface for the TCA 30/10 W/B/N model is similar to that for the W/B model due to the weakness in the vortices around the deflected leading edge. The nacelles have very little effect on the overall pressure distribution on the wing upper surface. Local "hot spots" can be seen near the deflected TE flaps which are responsible for the residual fluctuations in the convergence history.

Comparison with W/B Solution

(TCA 30/10, Mach #=0.3, Re=8x10^{6}, AOA=10 degrees)
Cp and limiting streamlines on wing lower surface

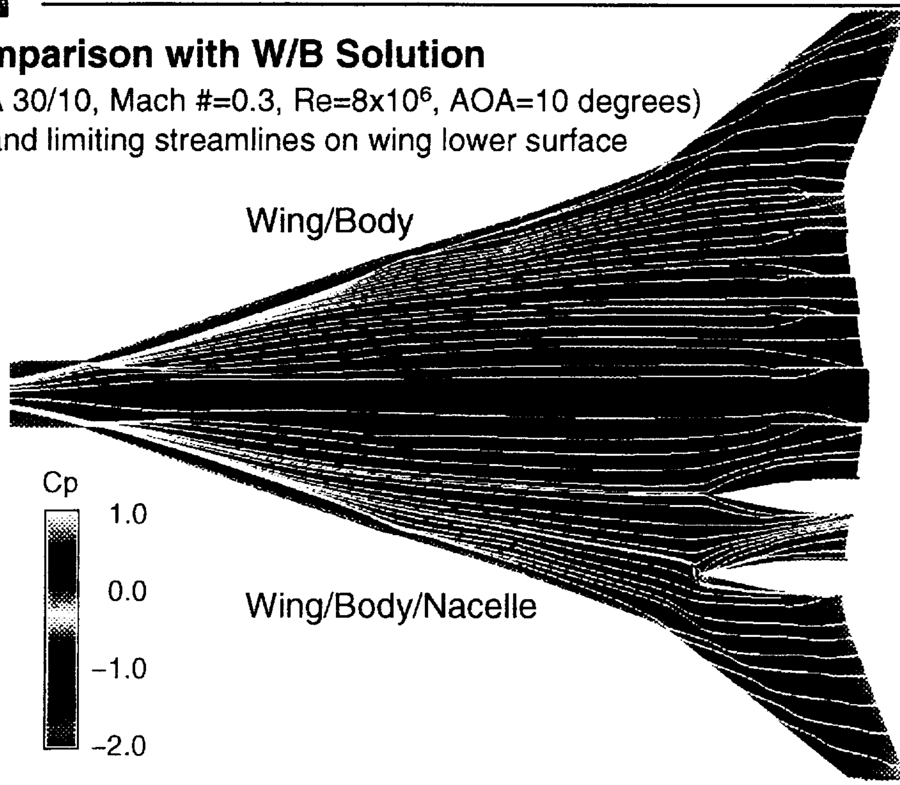

On the wing lower surface, the pressure coefficient distributions and the limiting streamlines are very similar between the W/B and W/B/N solutions, except for around the diverters. For the W/B/N case, the limiting streamlines indicate possible flow separation near the leading edge of the diverters. Local flow acceleration can be seen between the inboard and the outboard nacelles.

TCA 30/10 WBN CFL3D Solutions:

(Mach #=0.3, Re=8x10^{6}, AOA=10 degrees)
Normalized total pressure downstream of nacelle inlets

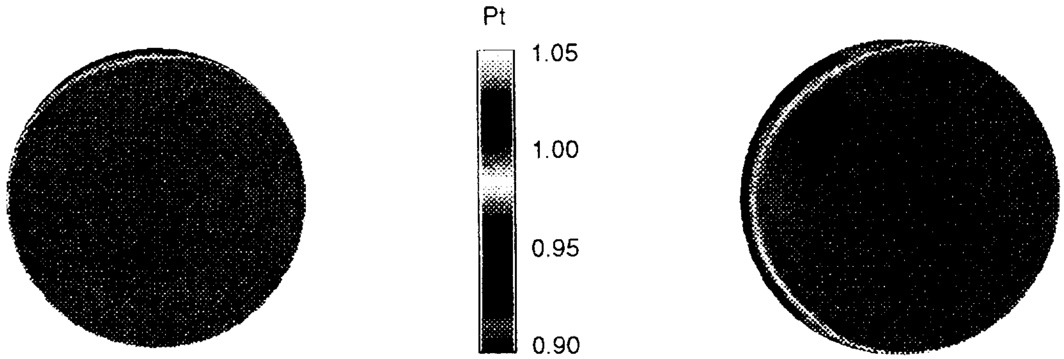

Inboard   Outboard

This figure shows the total pressure contours in the nacelle interior cross sections downstream of the nacelle leading edge. Local flow separation is apparent at the entrance to the outboard nacelle which may impact the outboard engine performance. Flow separation also exists, though not severe, at the entrance to the inboard nacelle.

Comparison with W/B Solution: Flap Span Loading

(TCA 30/10, Mach #=0.3, Re=8x10^6, AOA=10 degrees)

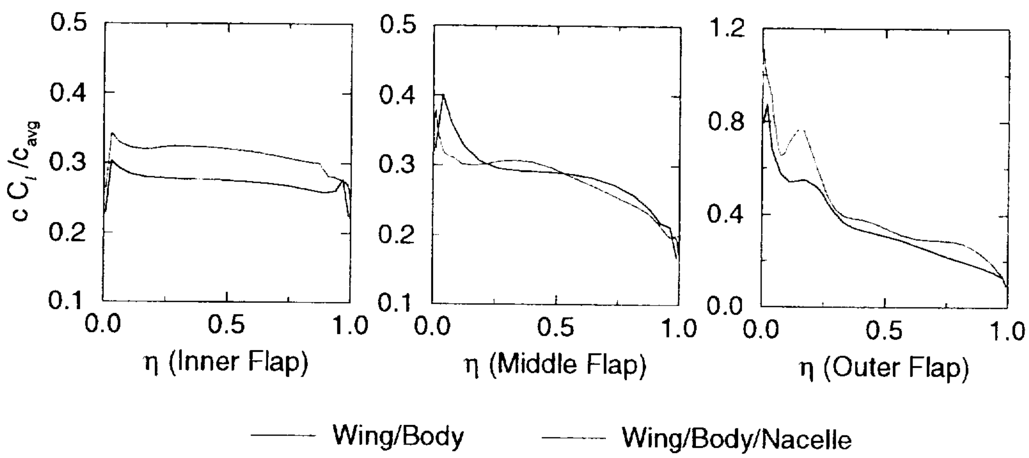

This slide shows the effect of nacelles on the span loading of the deflected TE flaps. It is expected that the nacelles will work like end–plates to the wing or flap segments, which will usually cause an increase in span loading. This end–plating effect is apparently seen for the inner and outer flaps but not for the middle flap.

TCA 30/10 WBN CFL3D Solutions:

(Mach #=0.3, Re=8x10^6, AOA=10 degrees)
Cp on lower surfaces of deflected middle flaps

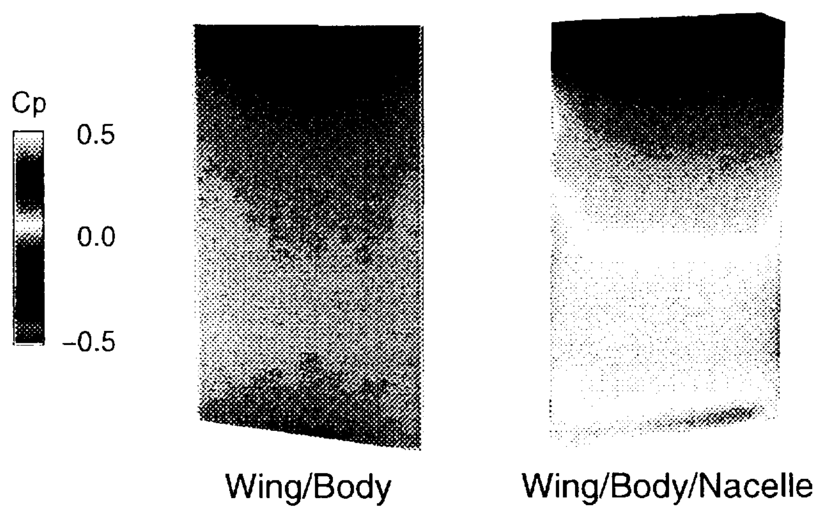

Further examination of the pressure distribution on the lower surface of the deflected middle flap shows relatively lower overall pressure for W/B/N case compared to the W/B case. This is the result of local flow acceleration between the inboard and outboard nacelles. The flow acceleration and end-plating effect tend to offset each other in the span loading on the middle flap.

Summary

- Developed CFD Models for TCA Wing/Body/Nacelle (W/B/N) high lift configurations including 0/0 and flaps 30/10.
- Obtained converged CFL3D solutions for the TCA W/B/N models at Mach No.=0.3, Re=8×10^6, AOA=10 degrees.
- CFD solutions provide insight into the effect of nacelle installation on the aerodynamic performance of TCA high lift configurations.
  - Impact on overall flow field and aerodynamic parameters
  - Local flow separation on nacelles/diverters
  - Span loading and flow characteristics near deflected TE flaps
- Comparison between CFD results and wind tunnel data reveals discrepancies in aerodynamic coefficients. Further investigation is warranted.

In summary, we developed two CFD models and obtained converged CFL3D solutions for the TCA Wing/Body/Nacelle high lift configurations including flaps 0/0 and 30/10. CFD solutions make it possible to examine in detail and understand in depth the effect of nacelle installation on the aerodynamic performance of HSCT TCA high lift configurations. Preliminary comparison with wind tunnel test data reveals discrepancies in the integrated aerodynamic coefficients. We will perform further investigation into the CFD solution as well as the test data.

Canard Integration for CFD Analysis of HSCT High Lift Configurations

David T. Yeh
Boeing, Long Beach

HSR Airframe Technical Review
High Lift Aerodynamics
at
Los Angeles, CA
February 9–13, 1998

BOEING

This page is intentionally left blank.

High Lift Technology Development (Task 33)

Increase L/D, Develop Analysis/Design Methodology

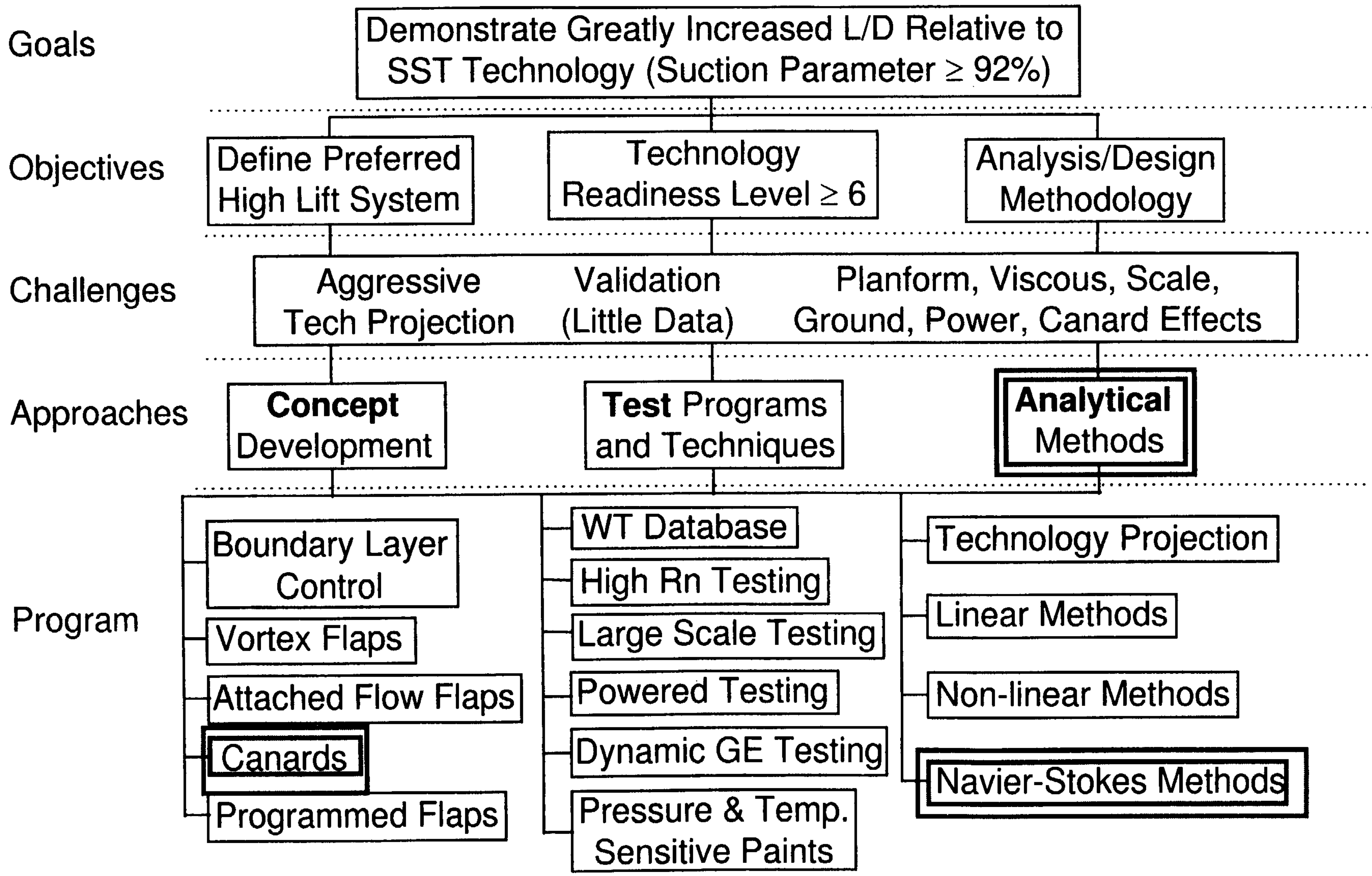

Outline

This report starts with the description of the objectives for canard integration analysis, followed by the numerical approach. The methodologies behind the automated canard modeling procedure are described and the integration process to obtain the numerical solutions is then summarized. A sample solution is presented and analyzed for the TCA wing/body/canard configuration with a part span leading edge flap deflected at 30 degrees and the trailing edge flaps deflected at 10 degrees at a high lift condition. This report concludes with a summary and future plans.

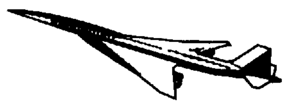

OUTLINE

- Objectives
- Approach
- Automated Canard Modeling Procedure
- Numerical Solution Process
- Sample Solution
  - TCA W/B/C 30/10 Configuration at α=10° (Part span LE flaps)
- Summary and Future Plans

BOEING

Objectives

The objective for the current study is to develop the numerical capability to model the canard surface for high lift configurations; and to evaluate the canard flow characteristics and its impact on the high lift performance.

OBJECTIVES

- Investigate canard vortex characteristics
- Analyze canard influence on the wing
- Support upcoming TCA–4 test (May '98)
- Evaluate high lift performance through parametric studies

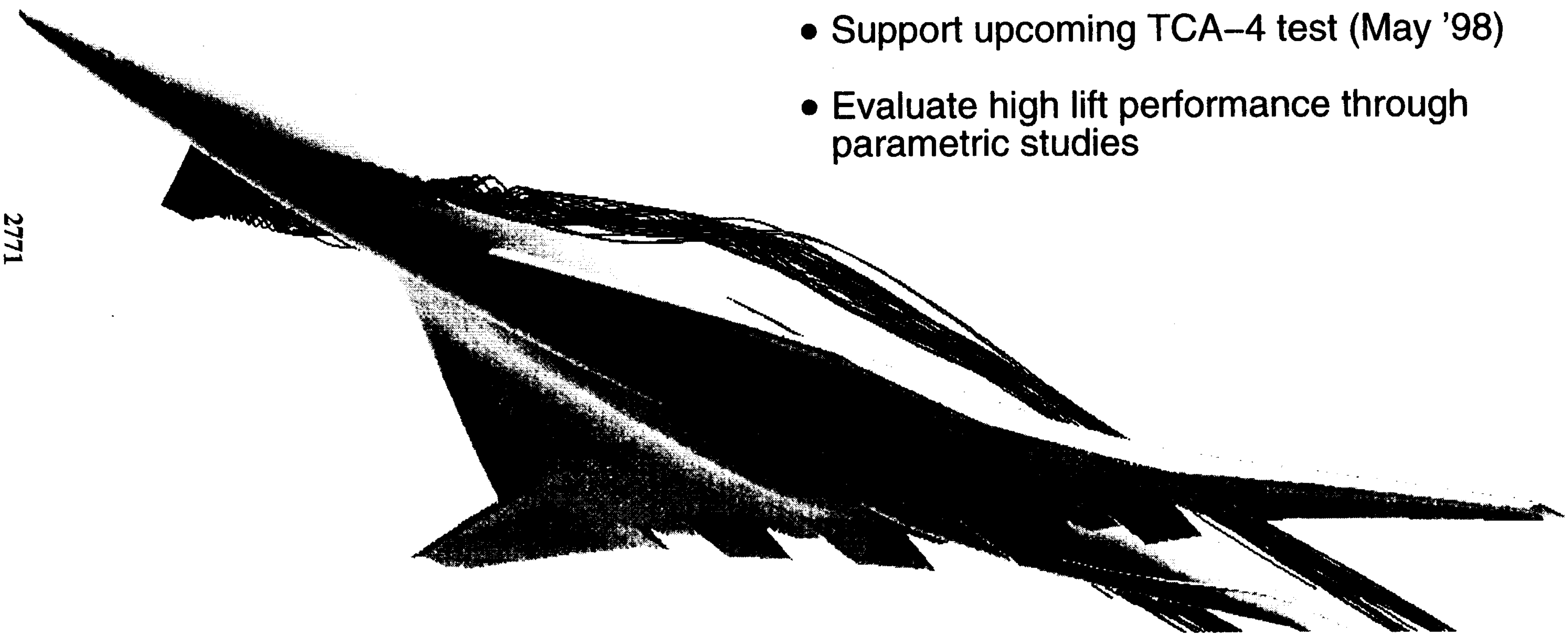

BOEING

Approach

The approach is to utilize the overset approach to integrate various canard models with high lift configurations. An automated gridding procedure is developed and utilized for the current analysis. This procedure is also applicable for future parametric studies. NASA developed CFL3D/MAGGIE codes are used for simulation of the physical phenomena. The numerical solution is analyzed to evaluate canard/wing vortex characteristics and the corresponding high lift performance. The numerical procedure will be extended to support the upcoming TCA-4 test, and code validation will be conducted as the test data becomes available.

APPROACH

HSCT Aerodynamics, Long Beach

- Utilize overset approach
- Develop an automated gridding procedure for various canard configurations
- Utilize CFL3D/MAGGIE for flow analysis
- Evaluate canard/wing vortex characteristics at high lift conditions
- Validate numerical solution based on upcoming TCA4 test (May 1998)

BOEING

W/B/C Modeling Using Overset Approach

The advantage of using the overset approach is that various canard configurations can be easily integrated into an existing CFD model or future models as the configuration evolves. Currently, the canard surface is added to a TCA wing/body configuration with deflected part span leading-edge flaps and trailing-edge flaps for demonstration.

W/B/C Modeling Using Overset Approach

HSCT Aerodynamics, Long Beach

- Easily integrated into an exsting CFD model
  (*i.e.*, W/B/Flaps, W/B/../..)

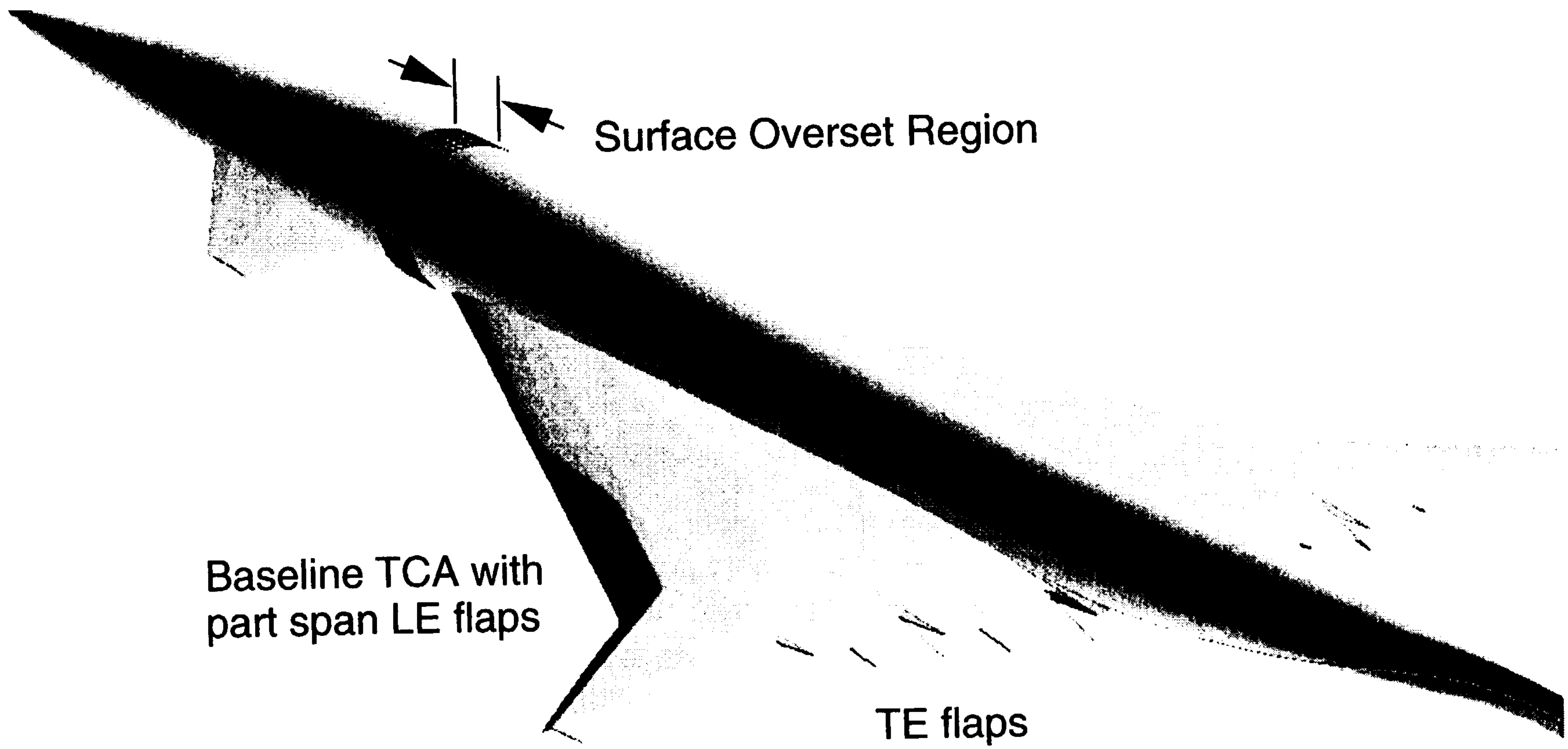

Automated Canard Modeling Procedure

An automated canard modeling procedure has been developed to efficiently generate canard/forebody grids for CFD analysis. Canard configurations can be different in a variety of ways such as planform, position, deflection angles mounted on a forebody with or without a wiping surface. The automated procedure will reduce the gridding time significantly for sensitivity studies of various canard configurations.

Automated Canard Modeling Procedure

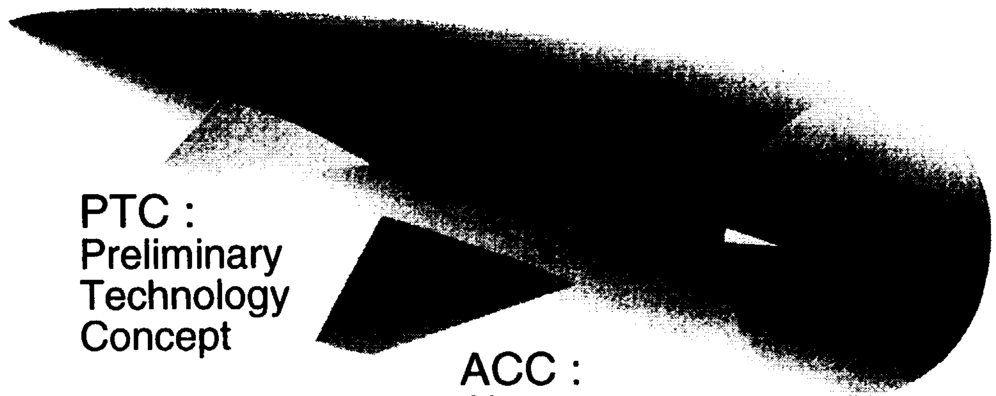

Reduce gridding time for sensitivity studies
- Planforms (LE/TE sweep, AR, Size)
- Vertical positions (High, Mid, Low mount)
- Horizontal locations
- Dihedral/Anhedral angles
- Deflection setting (δ)
- Aft elevator modeling
- Forebody/wiping surface

BOEING

Automated Procedure for Canard Surface Integration

This chart summaries the process that is involved in the automated canard modeling procedure. The only input required is the surface grids of a forebody and a canard surface. This procedure will first combine the surface grids, deflect the canard through a user specified angle, calculate the trim curve and generate a combined surface grid. A CFD volume grid will also be generated automatically using an algebraic grid generation tool. Once the forebody/canard volume grid has been generated, a zonal connectivity file will be created using MAGGIE code for CFD analysis. The following few pages will be focused on the details of each step.

Automated Procedure for Canard Surface Integration

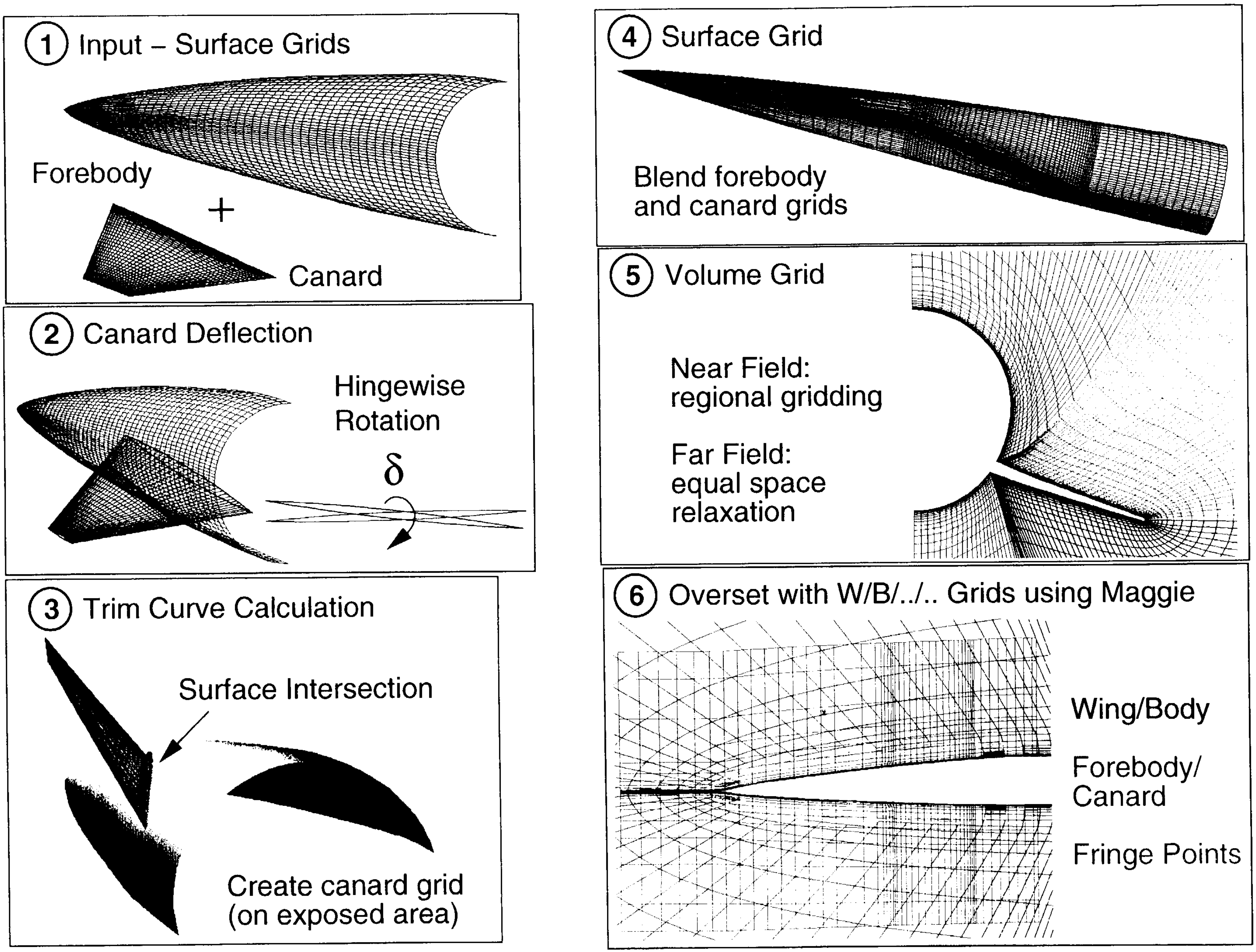

Surface Geometry Definition for Modeling Canard Surface

The first step of the procedure is to combine the forebody and the canard surface grids together. The surface geometries can be obtained from any configuration of interest. Once the canard surface is available, the canard surface grid is extrapolated to the centerline so that a trim curve can be computed.

Surface Geometry Definition for Modeling Canard Surfaces

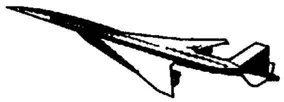

HSCT Aerodynamics, Long Beach

1.1 Input – Surface Grids

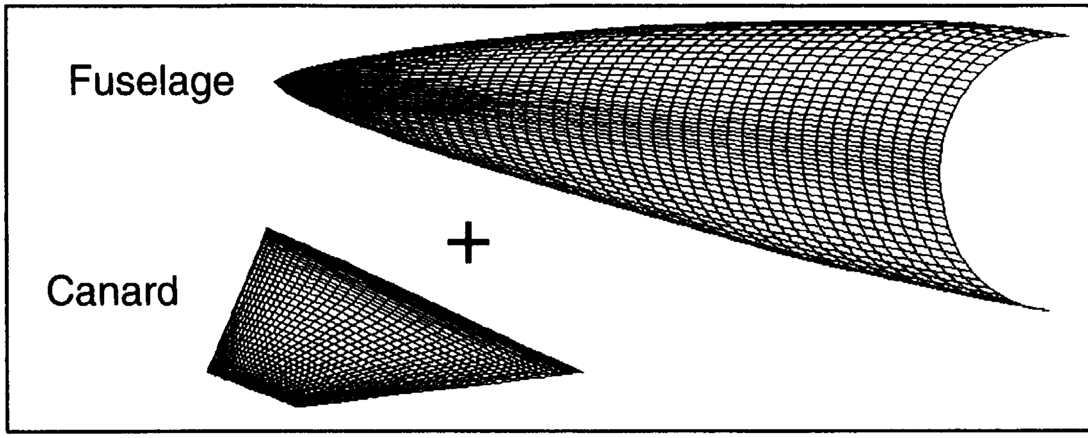

1.2 Extrapolate Canard Grid to the Centerline

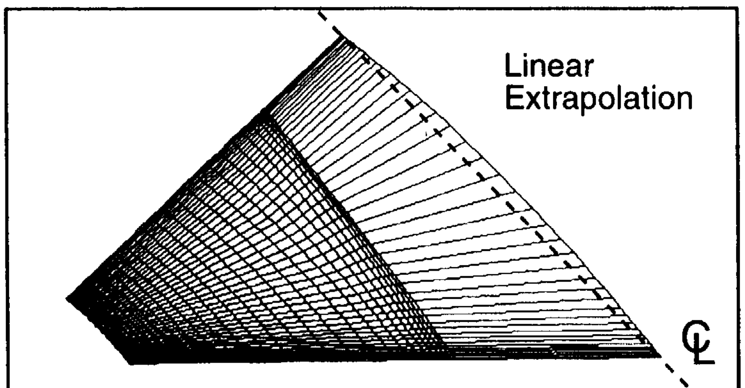

BOEING

Canard Manipulation for Sensitivity Studies

The numerical capability to move the canard surface around has been implemented for future sensitivity studies. The canard manipulation consists of a translation and rotation. The canard surface can be moved around in the upstream or downstream, and upward or downward directions through a translation process, while the dihedral angle is modified through a chordwise rotation. Once a desirable position is obtained, the canard is deflected in the hingewise direction based on a user specified angle.

Canard Manipulation for Sensitivity Studies

HSCT Aerodynamics, Long Beach

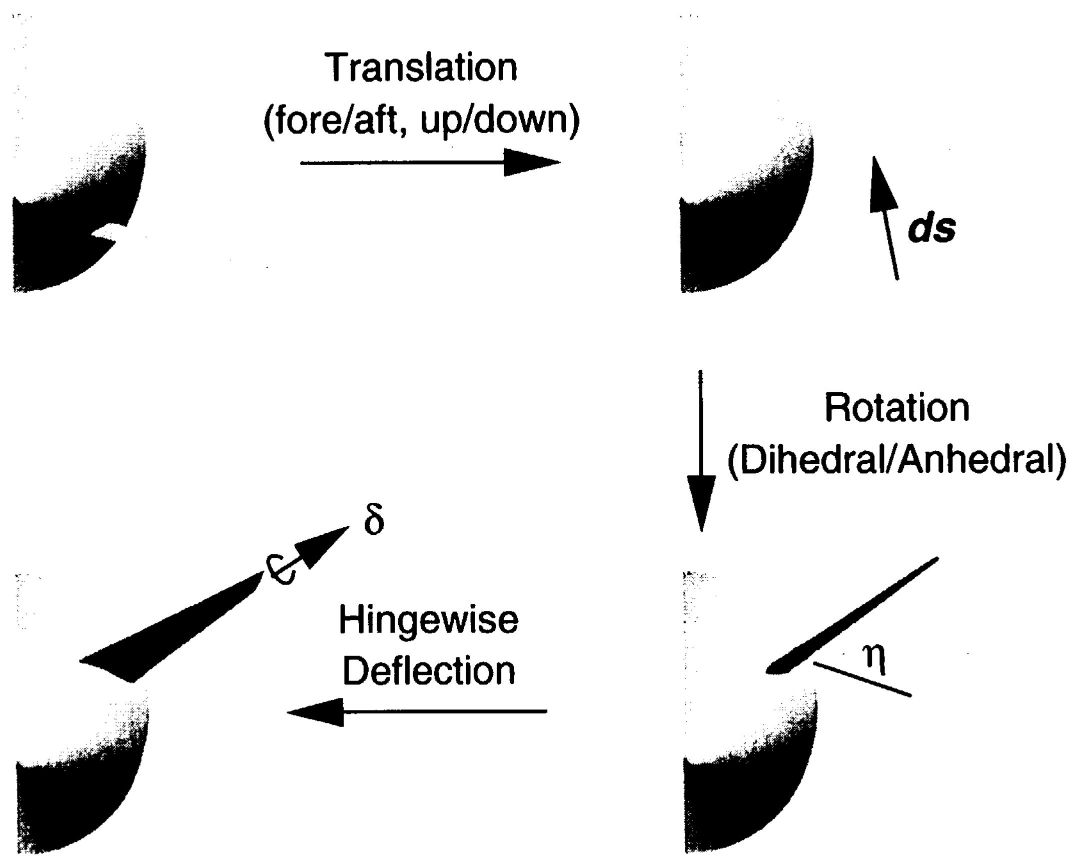

Canard Translation Process

The translation process is provided to move the canard forward or backward and upward or downward from the original location. The first step is to find a reference point on the fuselage which is located at the intersection of the hinge axis and the fuselage. The total displacement of the reference point consists of two vectors. One vector is obtained by sliding the reference axially along the fuselage surface. The second vector is determined by moving the reference point vertically through an user specified circumferential angle. Once the total displacement is found, the canard surface points are linearly translated to the new location.

Canard Translation Process

HSCT Aerodynamics, Long Beach

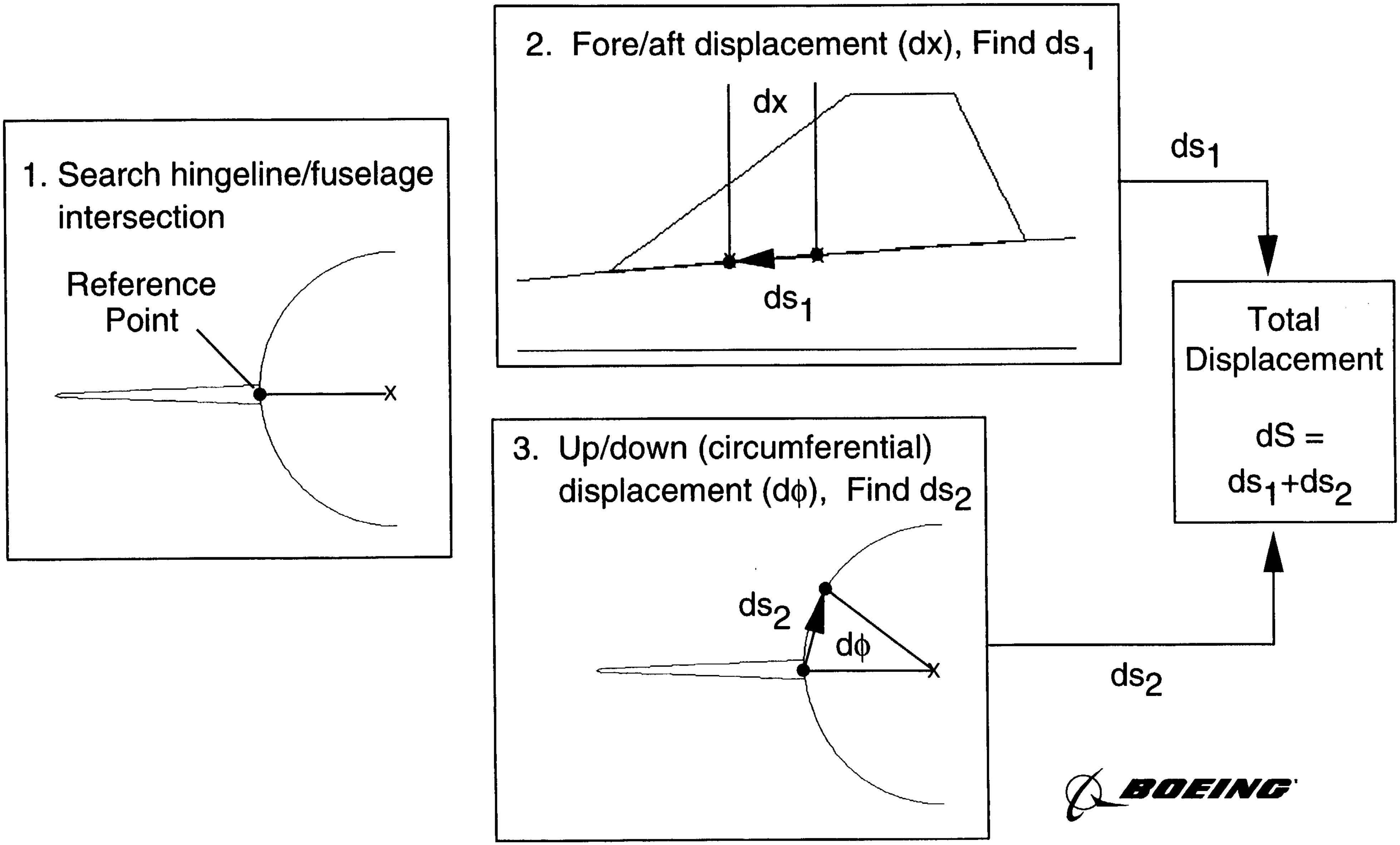

BOEING

Canard Dihedral/Anhedral Setting Modification

Two options have been implemented in the procedure to change the canard dihedral angle. The first option is to rotate the canard from the original geometry which may consist an initial dihedral/anhedral angle. The second option is to first reset the dihedral angle to zero (project onto the horizontal plane) and then rotate the canard from the waterline. For either case, the rotation is performed about the axis of the canard root chord.

Canard Dihedral/Anhedral Setting Modification

(1) Rotate from the original geometry

(2) Rotate from the horizontal plane

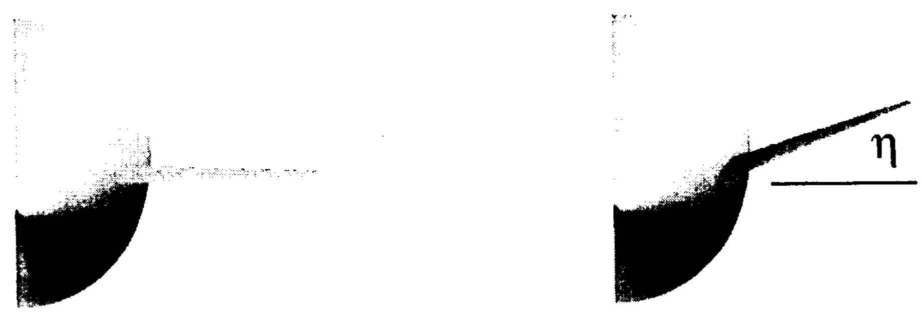

BOEING

Canard Hingewise Deflection

Canard deflection is performed in the hingewise direction. A hinge line typically lies perpendicular to the local tangent in order for the canard to rotate freely. Once the canard is deflected, the locus of the root chord lies along the local tangent which would result a gap between the canard and a rounded fuselage. A wiping surface on the fuselage will minimize the gap for a range of deflection angles.

Canard Hingewise Deflection

Canard Hinge Axis is Defined by 2 Points

- Low Mount ACC Canard

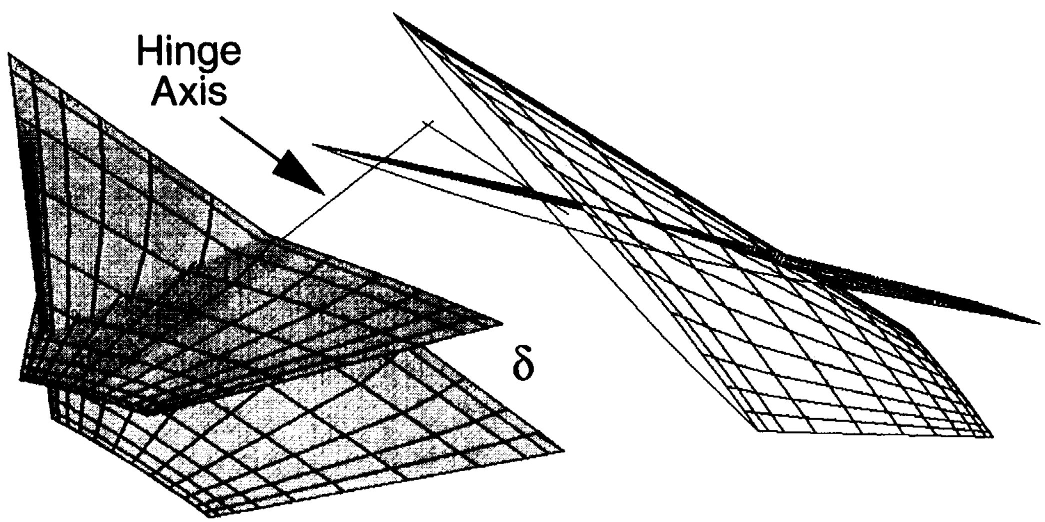

- Typical Hinge Line ⊥ Local tangent

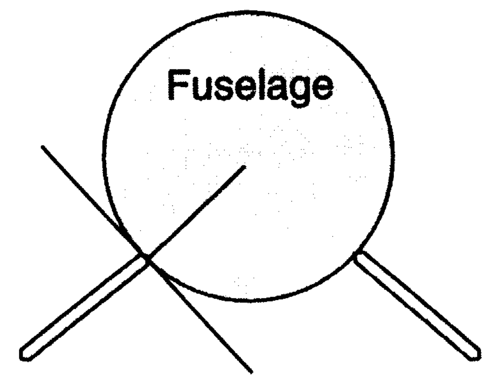

Wiping Surface:
Reduce Canard/Fuselage Gap

BOEING

Numerical Procedure for Trim Curve Calculation

Once the canard has been moved and deflected to the desirable position, a trim curve is then calculated to define the intersection curve between the two surfaces. Each point on the trim curve is located through the search of the intersection between the canard segment and the fuselage. The intersection is located when the line segment passes through the fuselage panel. The trim curve is then obtained by combining the intersection points. The trim curve would not be found if the surfaces either do not intersect or they intersect tangentially.

Numerical Procedure for Trim Curve Calculation

HSCT Aerodynamics, Long Beach

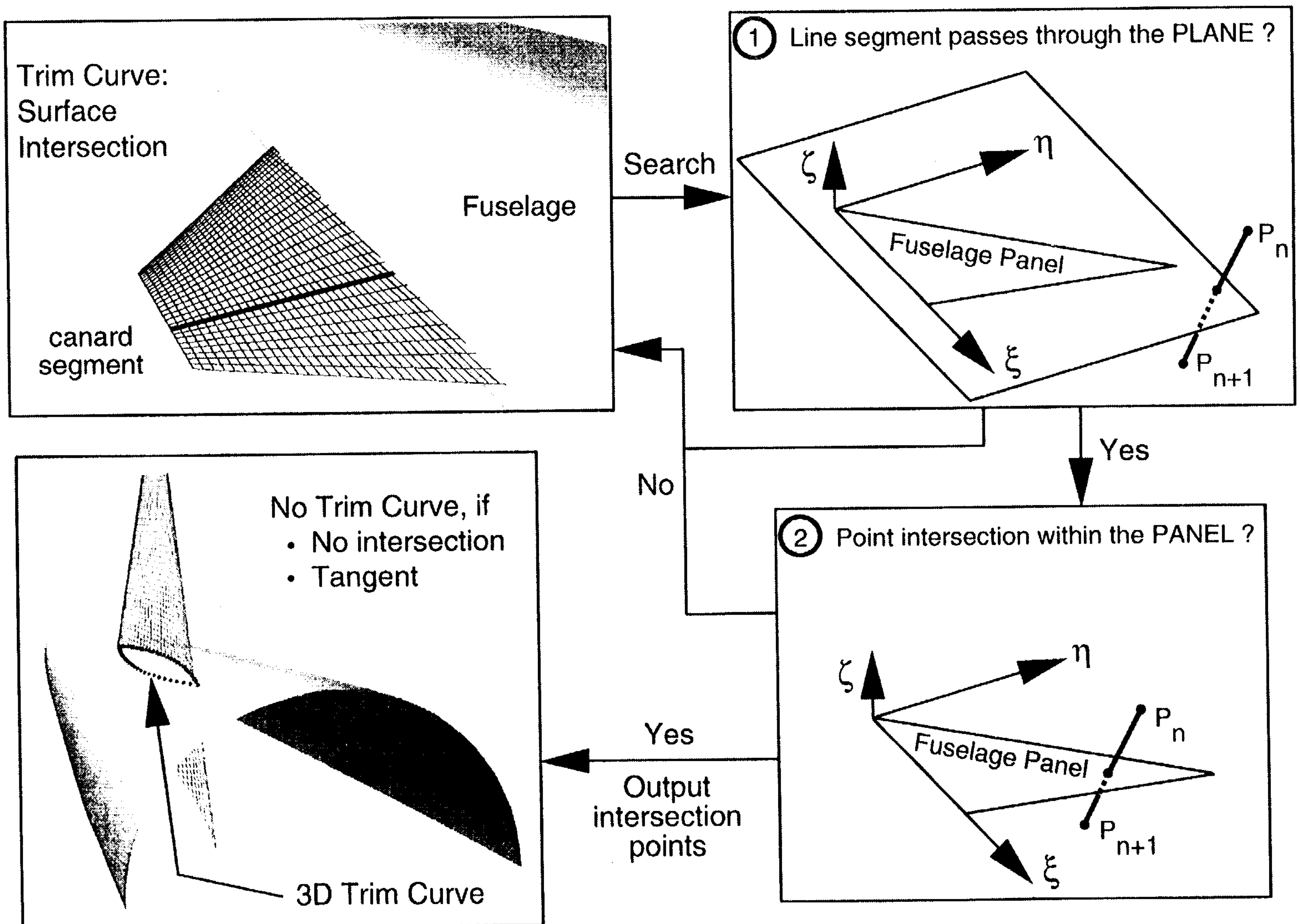

Surface Grid Construction Procedure

To blend the fuselage and canard grids together, the fuselage surface grids that are upstream and downstream of the canard are first generated based on the original fuselage definition. In the canard region, the upper and lower surfaces of the fuselage are gridded separately based on the trim curve grid distribution.

The second step in the surface grid generation is to create artificial wake surfaces upstream and downstream of the canard surface.

Surface Grid Construction Procedure

HSCT Aerodynamics, Long Beach

- **Create Fuselage Grid**
  1. Upstream of canard apex
  2. Downstream of canard TE
  3. Canard region
     - 3.1 Upper
     - 3.2 Lower

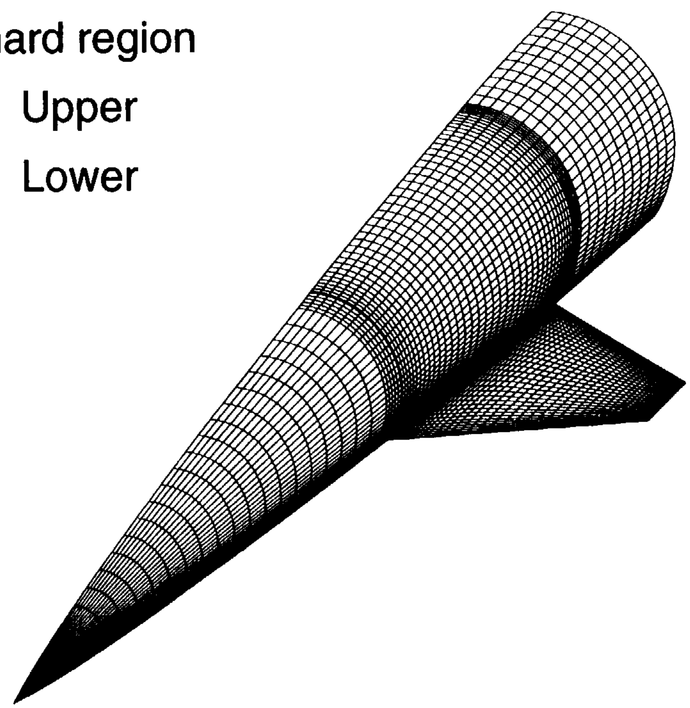

- **Create Wake Surfaces**
  1. Upstream of the canard
  2. Downstream of the canard

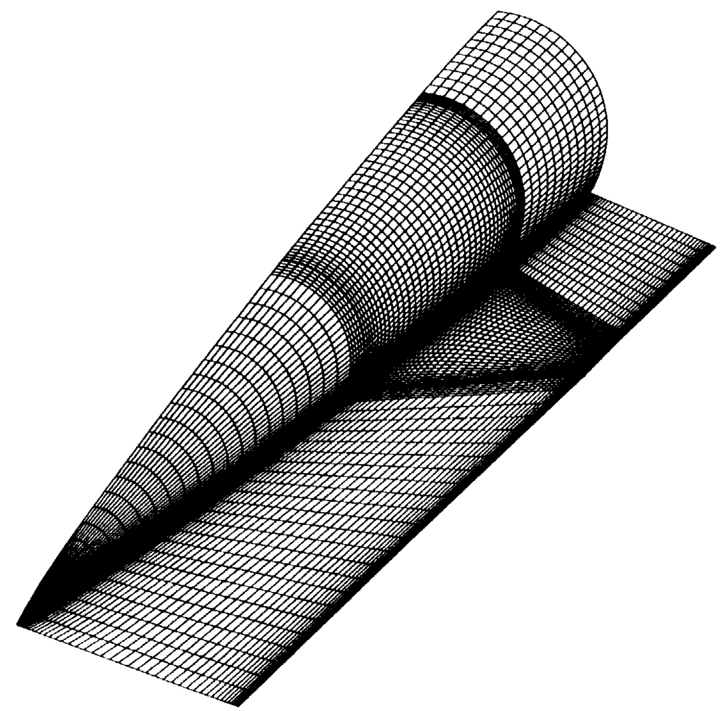

BOEING

Sectional Volume Grid Generation

The volume grid generation for the forebody and canard configuration is divided into 2 regions. In the inner region, 4 subregions are temporarily created based on the surface normals at canard/fuselage junction and at the tip. The subregions are created so that the boundaries can be used to guide the grid lines through sharp corners and avoid grid line crossing. In the far field, the grid cells are relaxed to a more uniform distribution. Once the forebody/canard grid is complete, they are combined into a single block. The size of the outer boundary is controlled by the user in order to overset with an existing CFD model.

Sectional Volume Grid Generation

HSCT Aerodynamics, Long Beach

- Near Field:
  Divided into 4 regions based on the normals calculated at the root and the tip

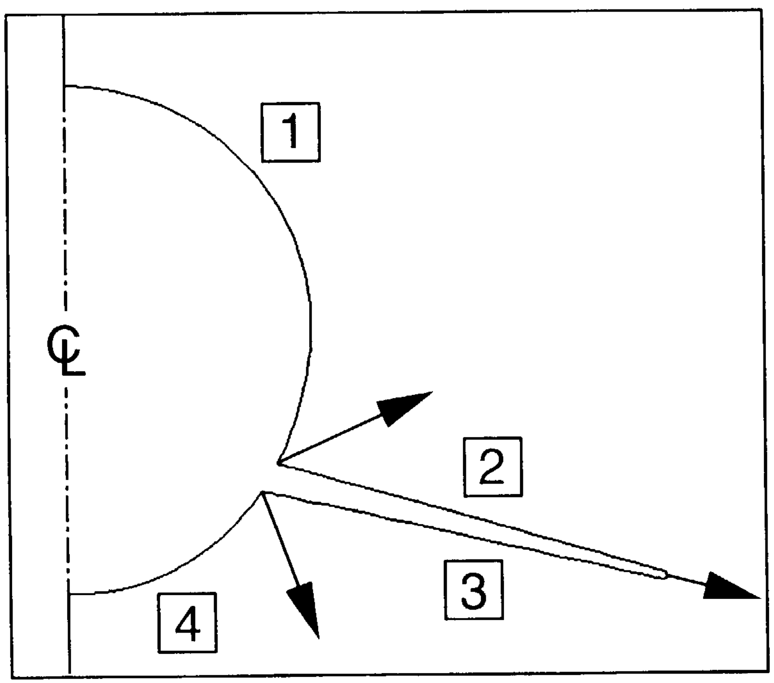

- Far Field:
  Grid cells are relaxed to uniform distribution

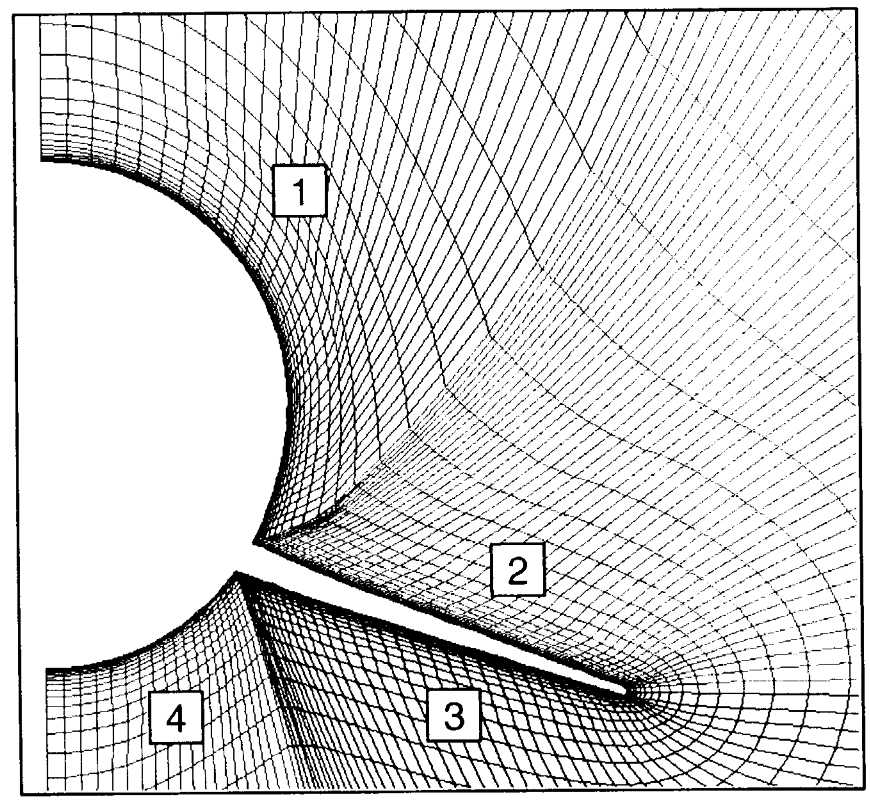

BOEING

Forebody/Canard Volume Grid

The resultant forebody/canard volume grid is a single zone grid with an O-H grid topology. The grid has an O-type in the circumferential direction and an H-type in the axial direction. The size of the outer boundary for the forebody/canard is chosen such that it is away from the boundary layers and the flow regions with large gradient. In addition, it should provide a sizable overlap region in order to get a quality stencil (extrapolation points) through compatible grid sizes across the blocks.

Forebody/Canard Volume Grid

Grid Typology
O–type : Circumferential Dir
H–type : Axial Dir

Grid Size
101 X 41 X 141
axial X normal X cir

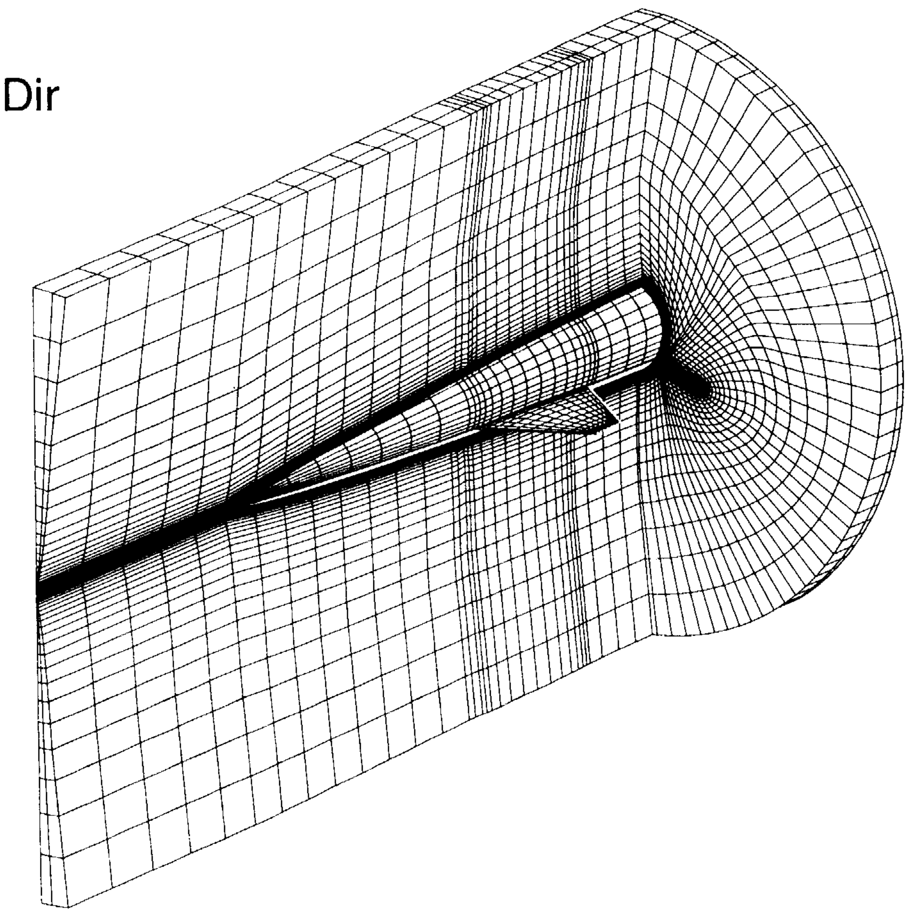

Numerical Integration Procedure for W/B/C Configurations

The numerical integration procedure for the current study is illustrated in the figure. The TCA grids obtained from the automated flap deflection procedure and the canard procedure are combined to form overset grids. The overset grids are fed into MAGGIE code to establish the zonal communication between the forebody/canard and wing/body/flap grids for CFL3D flow analysis.

Numerical Integration Procedure for W/B/C Configurations

HSCT Aerodynamics, Long Beach

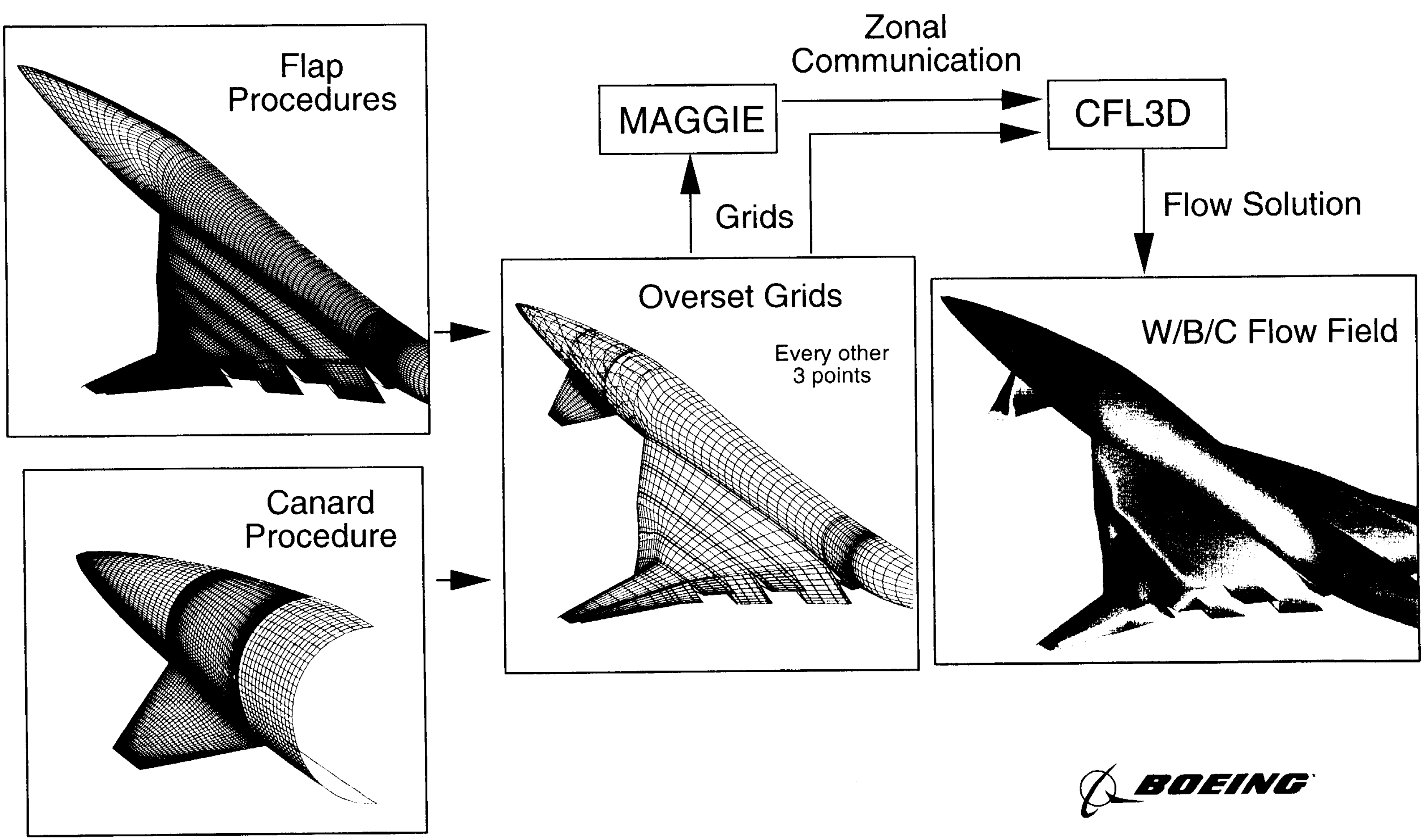

BOEING

Create Overset Connectivity Using MAGGIE

MAGGIE is a pre-processor code for using the chimera (overset) option of the CFL3D code. MAGGIE cuts holes in the wing/body grid to accommodate the forebody/canard grid. The zonal communication is then generated so that the wing/body solution will feed into the forebody/canard grid through its outer boundary. The influence of the forebody/canard solution will pass to the wing/body grid through the fringe points that are generated associated with the hole creation in the wing/body grid. The flow information will pass back and forth between these zones until the solution is converged.

Create Overset Connectivity Using MAGGIE

HSCT Aerodynamics, Long Beach

W/B – Wing/Body Grid
F/C – Forebody/Canard Grid
Fringe Points

1. Cut W/B to accommodate F/C
2. W/B Sol'n --> F/C outer boundary
3. F/C Sol'n --> W/B through fringe points

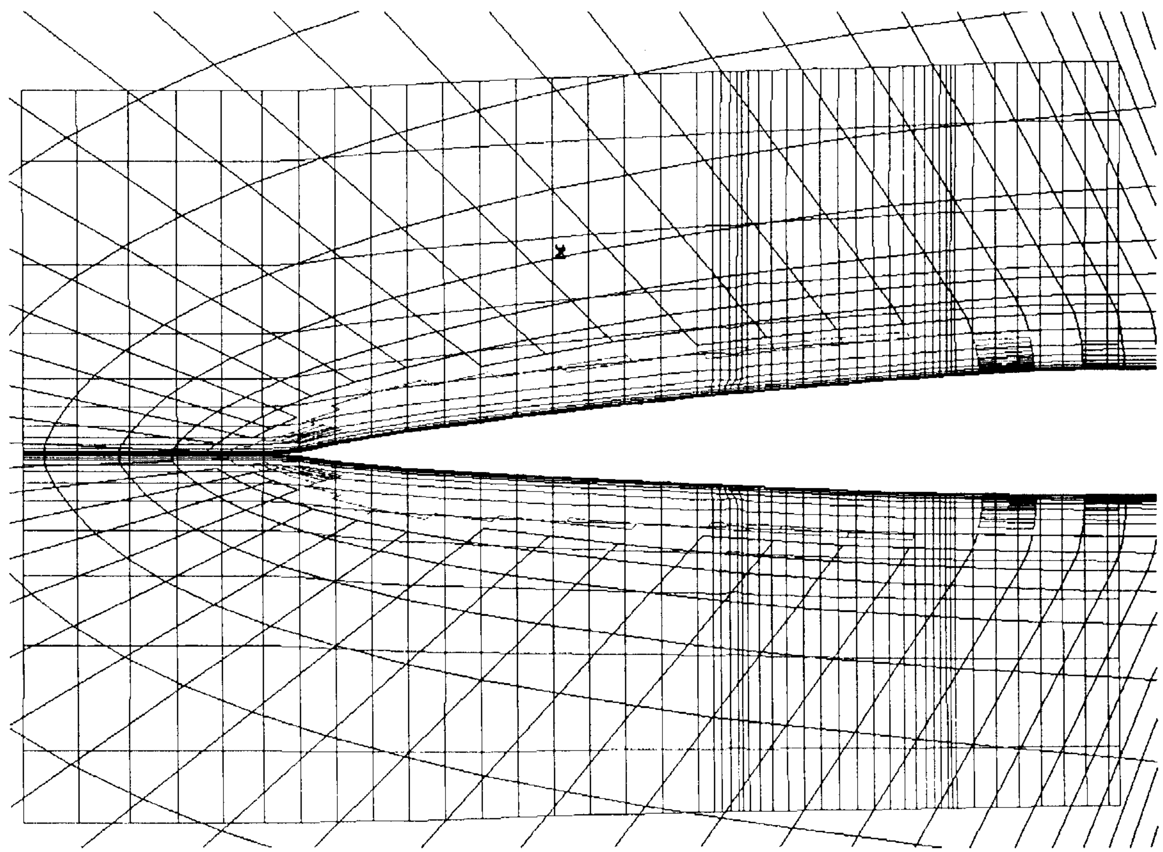

BOEING

TCA W/B/C Geometry for High Speed Model

The automated canard integration procedure provides a fast and efficient way for canard study. This procedure has been utilized by the Configuration Aerodynamics group and successfully applied for various canard positions at M=2.4 for sensitivity studies. The results of the numerical analysis were utilized for defining the canard positions and the plan of test for an upcoming wind tunnel test.

TCA Wing/Body/Canard Geometry

TCA Wing/Body with PTC (v2) Canard, $i_c = 0.0°$

View at $\alpha = 0.0°$

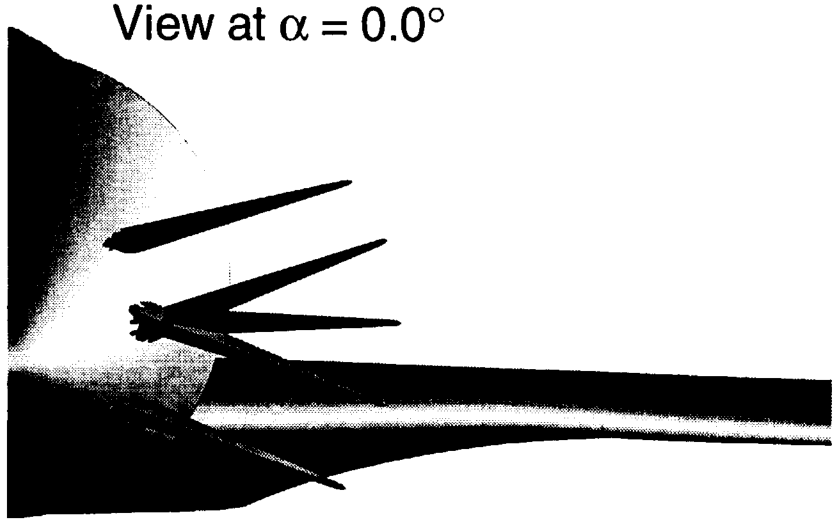

View at $\alpha = 3.5°$

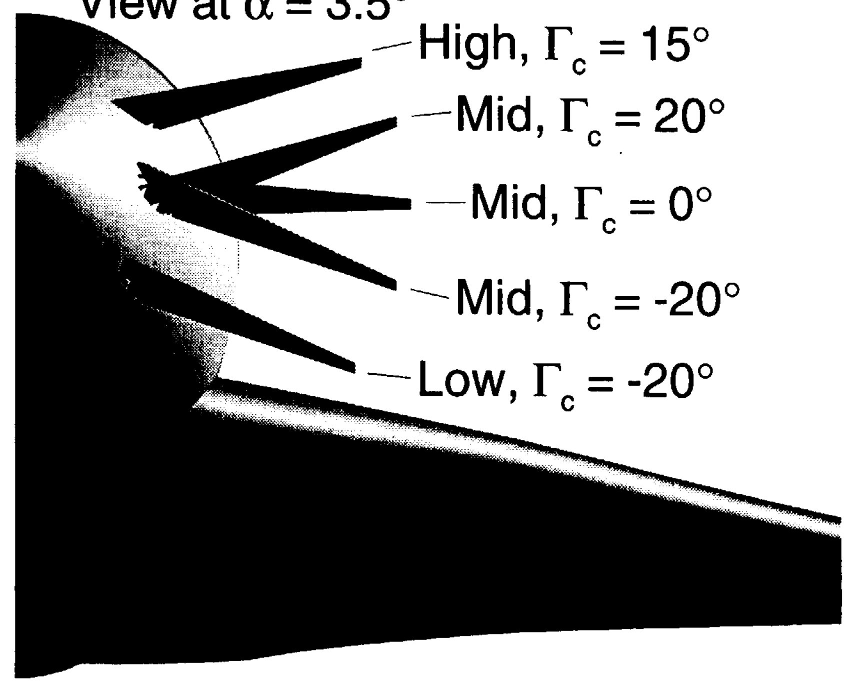

View at $\alpha = 0.0°$

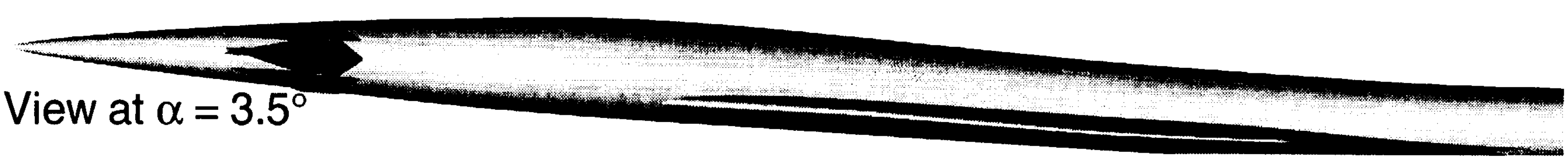

View at $\alpha = 3.5°$

JOH, 12-15-97

Flow Solution for TCA W/B/C Configuration

A numerical solution of a TCA wing/body/canard configuration has been obtained. The TCA 30/10 high lift configuration with part span leading-edge flaps and coupled with a low mounted ACC (alternate controls concept) canard has been analyzed. The numerical simulation was performed at the free stream condition of $M=0.3$, $\alpha=10$ degrees, with Reynolds number of 8 million. The ACC canard was used because the preliminary technology concept (PTC) canard geometry for the current configuration was not available during the time of development.

The focus of this study is to provide a preliminary assessment of the canard flow characteristics, its influence on the wing, and its impact on the high lift performance.

Flow Solution for TCA W/B/C Configuration

HSCT Aerodynamics, Long Beach

M=0.3, AoA=10 deg, Re=8 million

Canard : ACC with δ=0 deg

Wing : TCA baseline 30/10 Configuration
with part span LE flaps

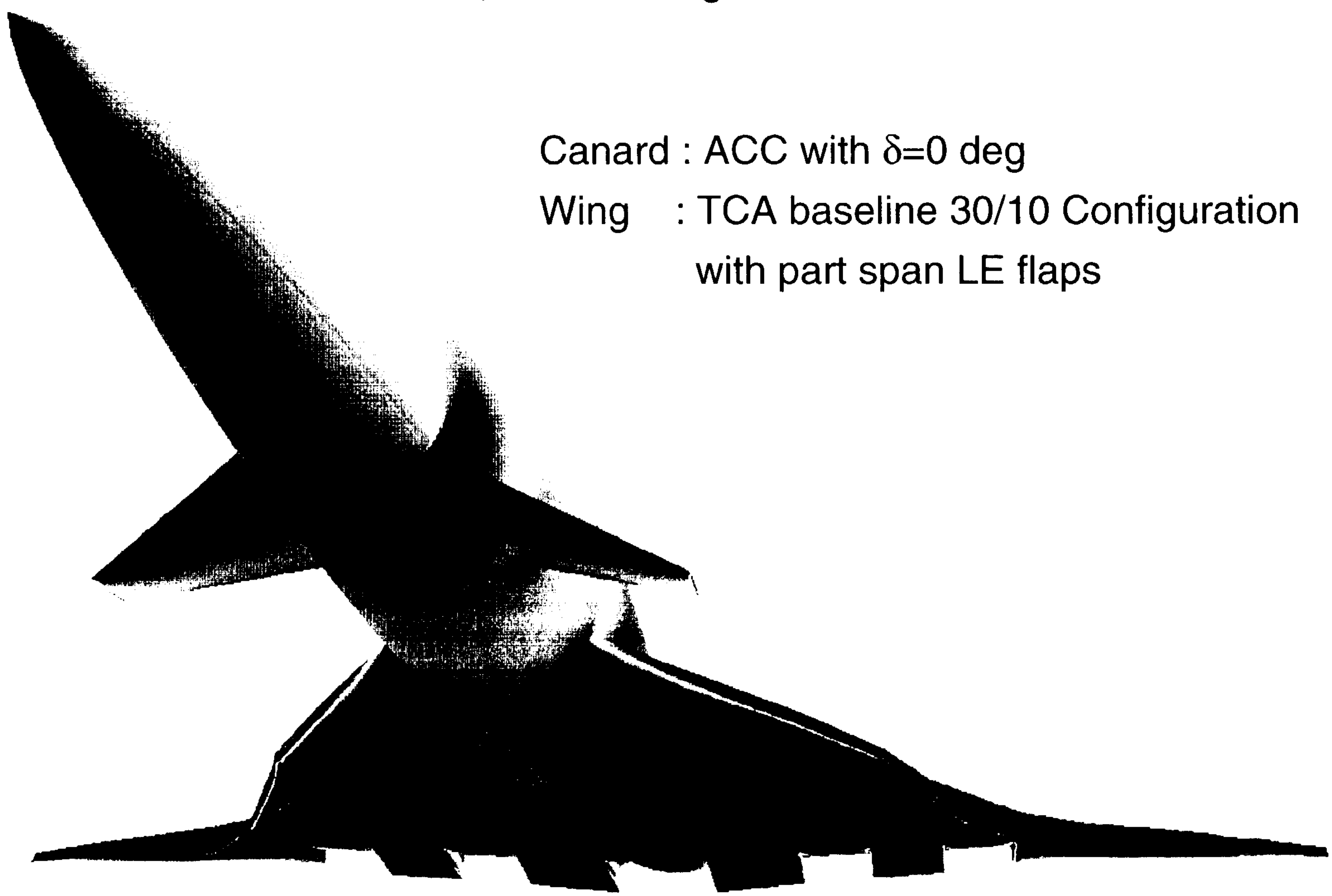

ACC Canard Upper Surface Flow Pattern

The ACC canard is a low-mount canard with an anhedral angle. The chord sections are described as bi-convex surfaces with a sharp leading-edge. This figure shows the flow solution on the canard upper surface with no canard deflection at 10 degrees angle of attack. Looking at the upper surface pressure and the limiting streamlines near the surface, it clearly shows that the canard is dominated with vortical flow where the LE vortex induced low pressure region and the typical spanwise flow phenomena are visible.

ACC Canard Upper Surface Flow Pattern

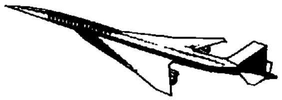

HSCT Aerodynamics, Long Beach

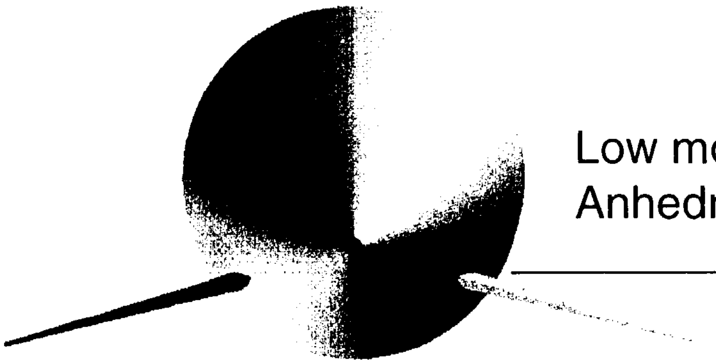

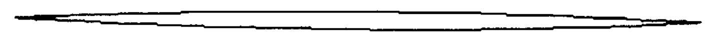

- M=0.3, δ=0 deg, α=10 deg, Re=8 million

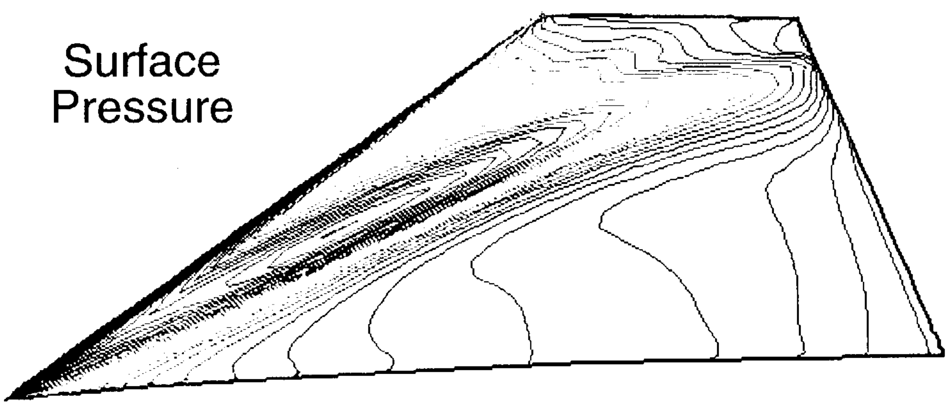

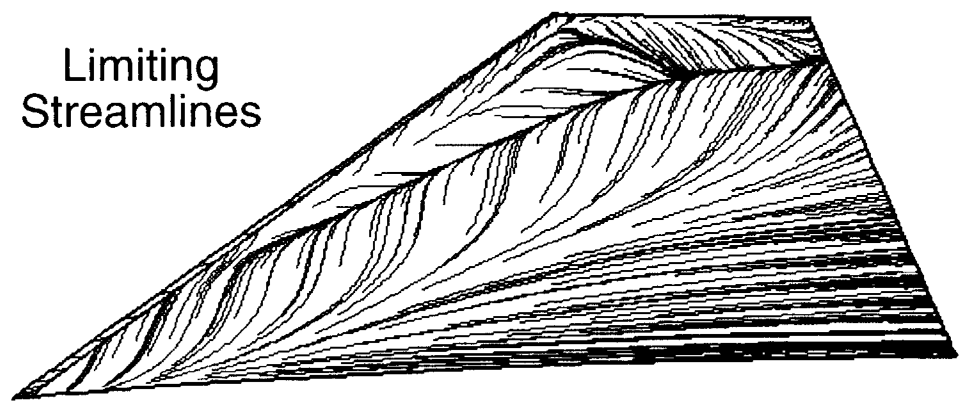

BOEING

Particle Traces Released from ACC Canard Edges

Free particle traces released along the leading edge and at the tip are shown in this figure. The blue traces are released near the LE while the red traces are originated from the canard tip region. It clearly shows the formation of the LE vortex and its interaction with the tip vortex. Behind the canard surface, the vortex is seen to convect approximately in the free stream direction.

Particle Traces Released from ACC Canard Edges

HSCT Aerodynamics, Long Beach

$M=0.3$,
$\delta=0$ deg,
$\alpha=10$ deg,
$Re=8$ million

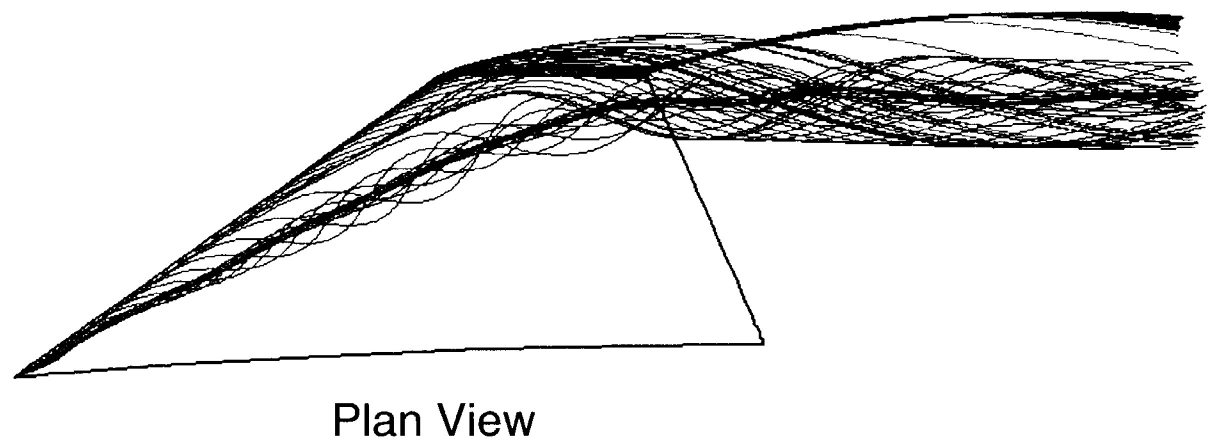

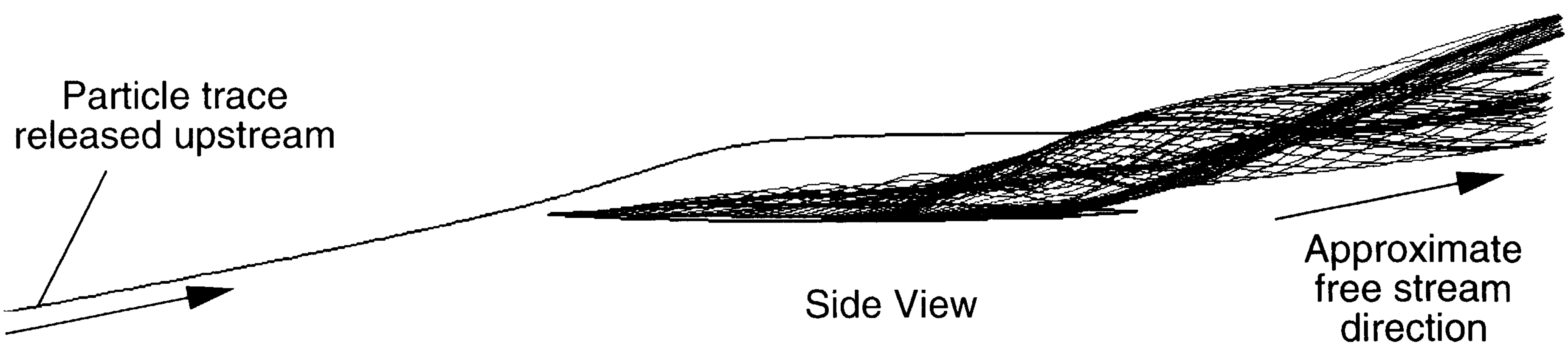

Cross-Flow solution for TCA W/B/C (30/10) Configuration

Total pressure contours are plotted at four selected fuselage stations to illustrate the formation and the convection of the canard vortex. At FS 900, the total pressure loss across the boundary layers and the shear layers around the canard vortex are clearly visible in the canard region. The canard vortex is shown to convect downstream above the wing upper surface. The formation of fuselage vortex as well as the wing LE vortex are also illustrated in the figure. The LE flap is seen to be under deflected at FS 2100 where the flow may be separated at the LE.

Cross–Flow Solution for TCA W/B/C (30/10) Configuration

HSCT Aerodynamics, Long Beach

M=0.3, AoA=10 deg, Re=8 million

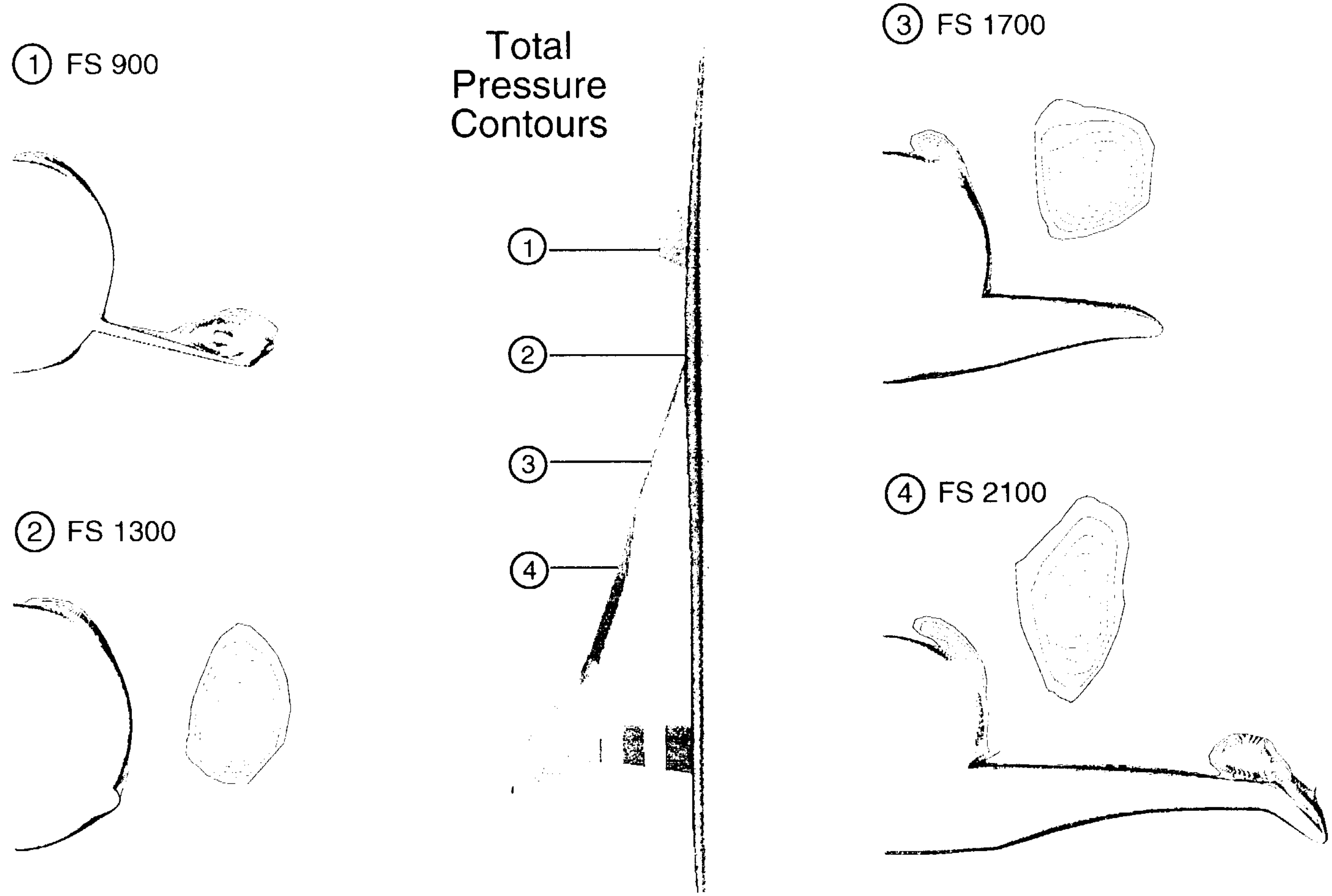

BOEING

Flow Solution for TCA W/B/C (30/10) Configuration

The flow solution for the TCA W/B/C 30/10 configuration is illustrated in this figure where it shows the total pressure contours at some cross flow plans accompanied by the particle traces released from the LE of the canard surface. This figure shows the canard vortex being convected above the wing. It also shows the formation of the wing LE vortex just inboard of the part span flap as well as the vortex interaction with the TE flap vortices in the wake region.

Flow Solution for TCA W/B/C (30/10) Configuration

HSCT Aerodynamics, Long Beach

M=0.3, AoA=10 deg, Re=8 million

Particle Traces & Total Pressure

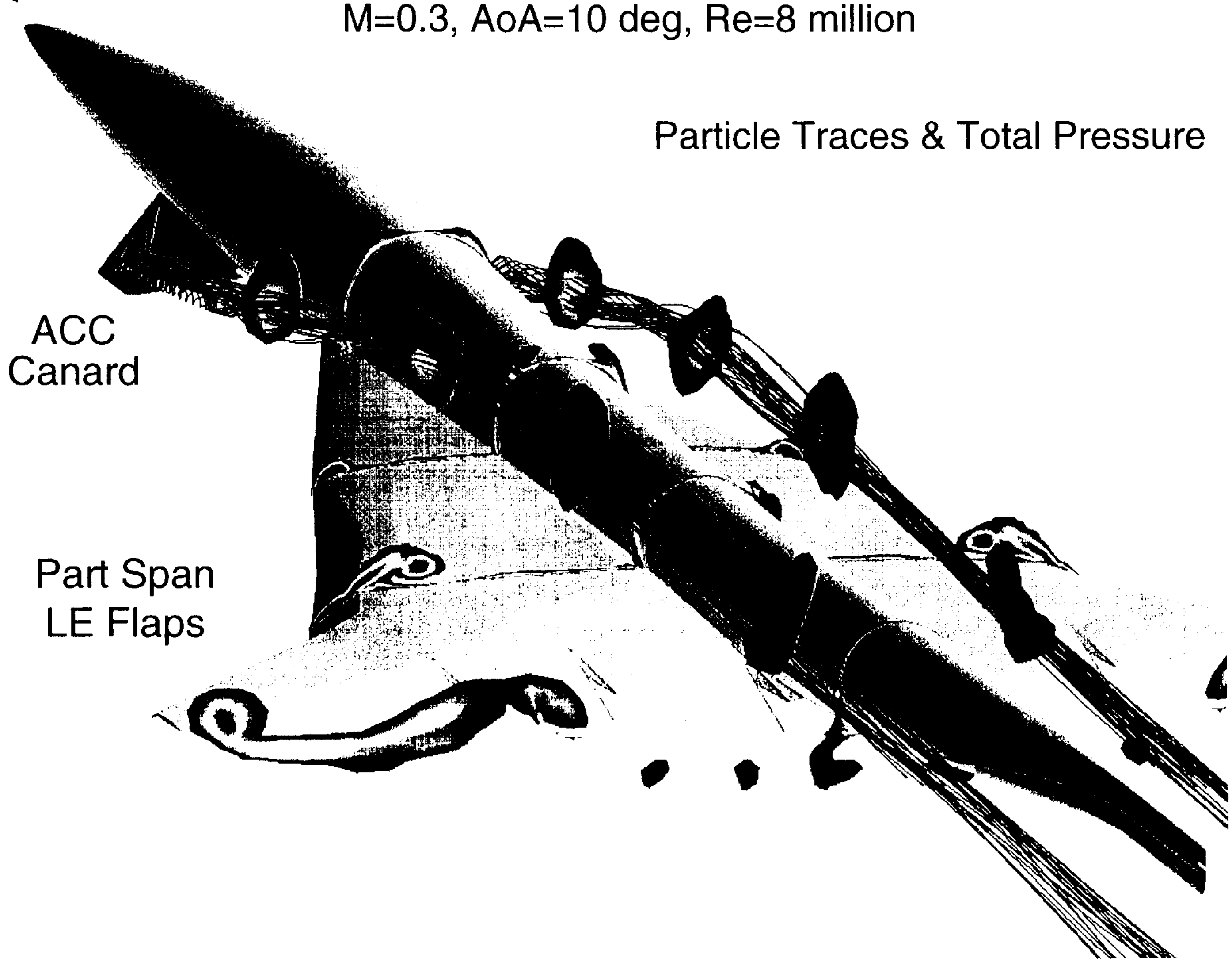

BOEING

3-View Canard Vortex Traces

To clearly visualize the footprint of the canard vortex, a 3-view plot of the canard vortex traces is illustrated in this figure. The canard vortex is shown to convect above the wing in a straight path initially. Once the influences of the wing and the LE vortices become large, the canard vortex is seen to move slightly inboard and parallel to the wing surface.

3–View Canard Vortex Traces

HSCT Aerodynamics, Long Beach

M=0.3, AoA=10 deg, Re=8 million

TCA 30/10

- Front View

- Top View

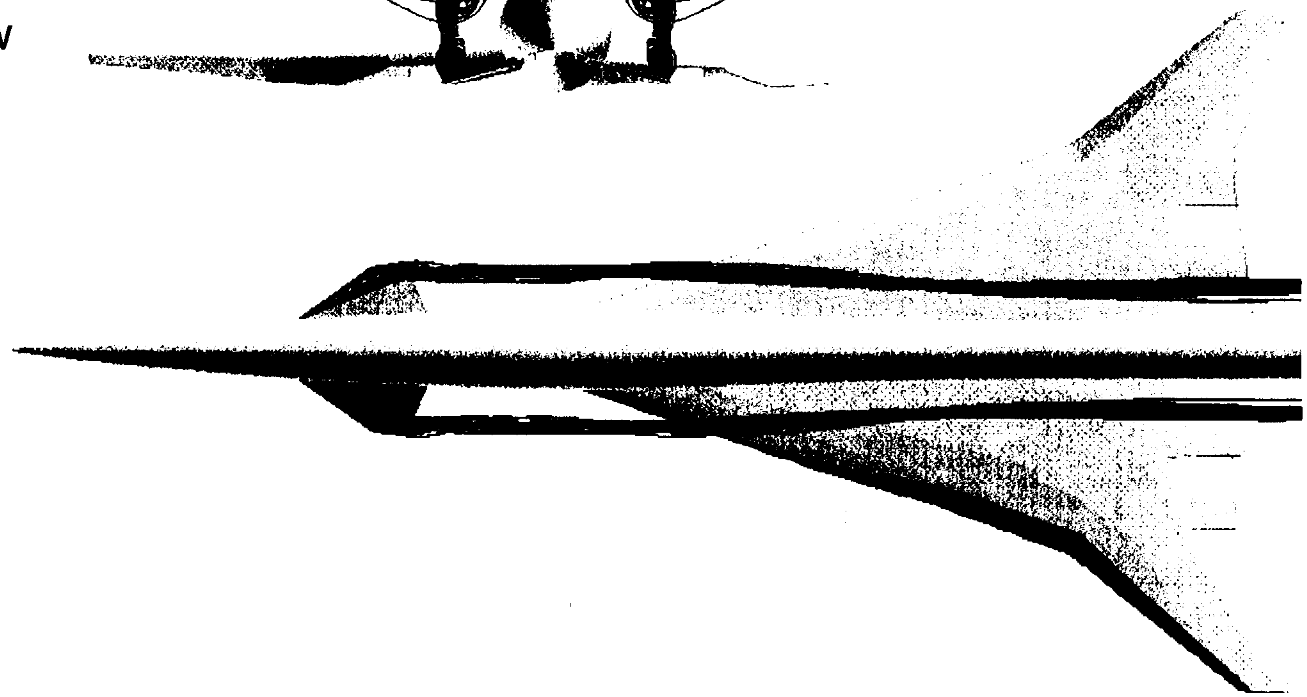

- Side View

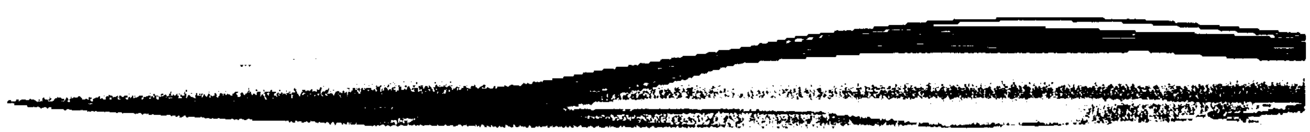

BOEING

Canard Influence on the Wing Upper Surface Pressure

The upper surface wing pressures for the cases with and without the canard surface are illustrated in the figure. Without the canard, the formation of a leading edge vortex is shown just inboard of the part span LE flap. The presence of the canard induces a higher pressure gradient outboard of canard vortex while it reduces the pressure gradient inboard of the canard vortex.

Canard Influence on the Wing Upper Surface Pressure

HSCT Aerodynamics, Long Beach

M=0.3, α=10 deg, Re=8 million

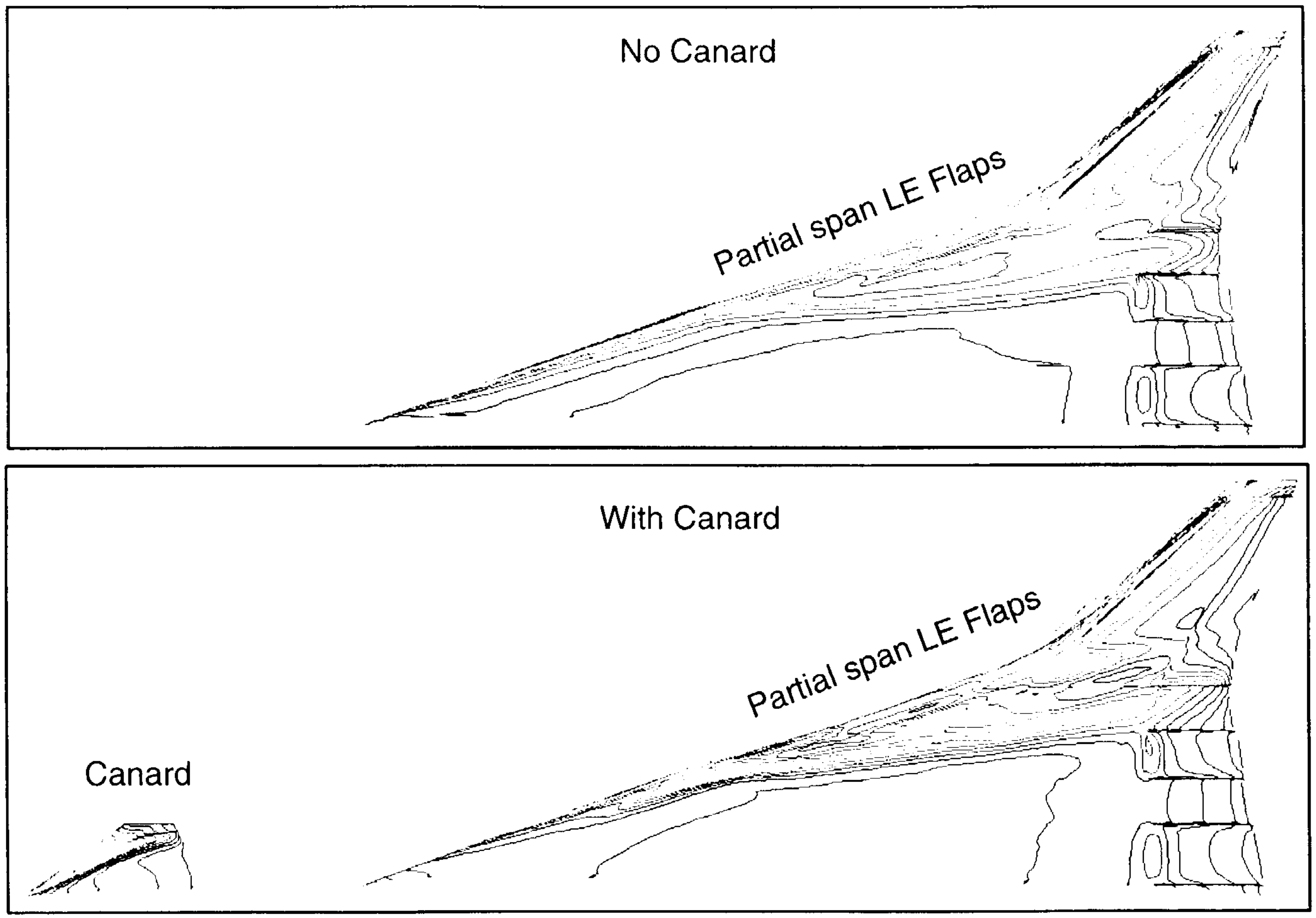

BOEING

Canard Influence on the Wing Limiting Streamlines

The influence of the canard vortex is seen to induce a more complicated vortical flow pattern on the wing just outboard of the canard buttline location, while creating a more favorable attached flow environment inboard of the canard vortex.

Canard Influence on the Wing Upper Surface Limiting Streamlines

HSCT Aerodynamics, Long Beach

M=0.3, α=10 deg, Re=8 million

TCA 30/10 Configuration

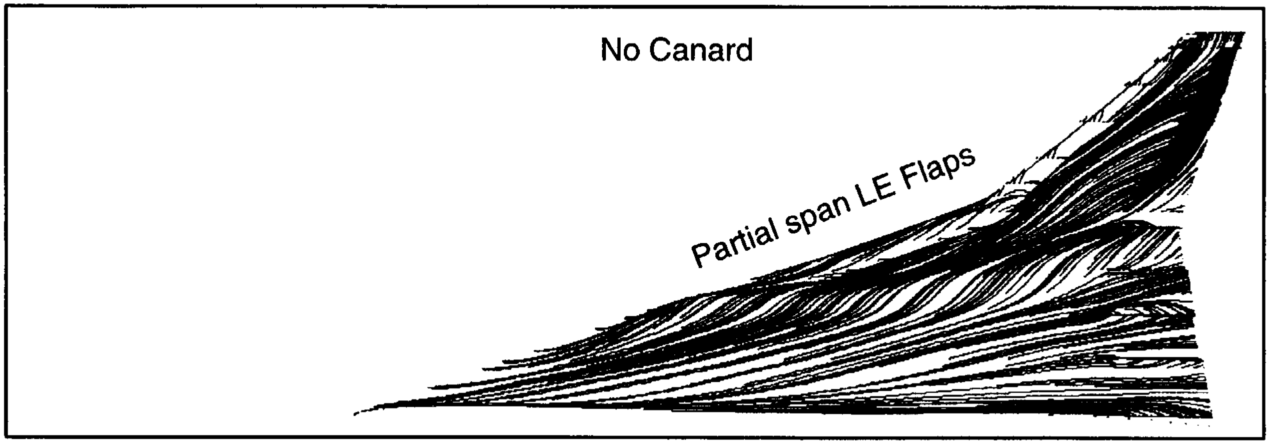

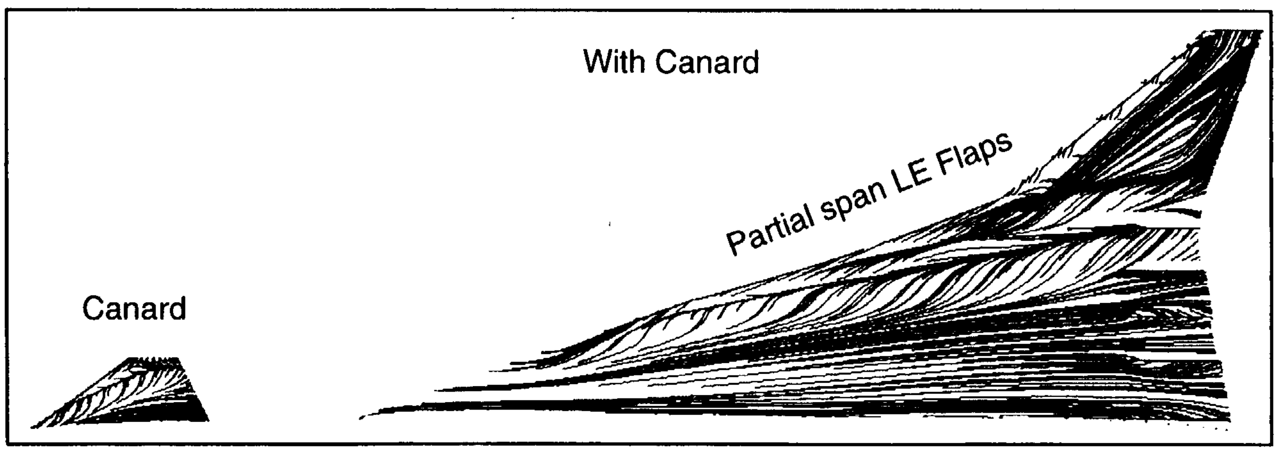

BOEING

Effect of Canard on Wing Surface Pressure

The effect of canard vortex on the wing spanwise surface is shown in this figure. A downwash effect is seen inboard of the canard vortex where the local angle of attack is lower resulting in a lower pressure on the wing lower surface while reduces the pressure difference between the upper and lower wing surfaces. On the other hand, an upwash is induced outboard of the canard vortex resulting in the formation of a leading edge vortex which induces a suction peak near the leading edge.

Effect of Canard on Wing Surface Pressure

HSCT Aerodynamics, Long Beach

M=0.3, α=10 deg, Re=8 million

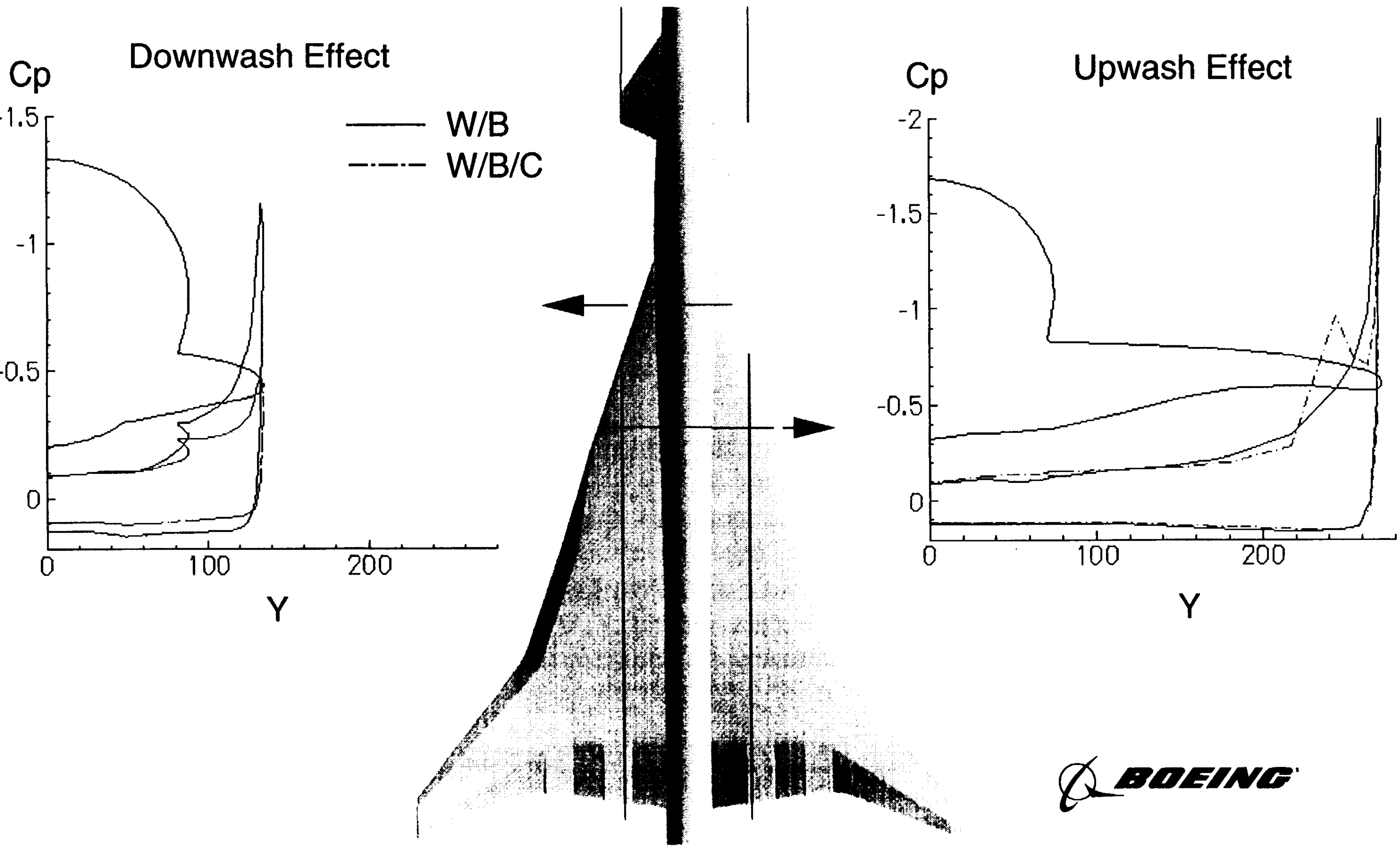

BOEING

Effect of Canard on TCA (30/10) Wing Separation

The effect of canard on the wing separation is illustrated by releasing the limiting particle traces near the wing leading-edge for the cases with and without the canard. The influence of the canard vortex is seen to create a more attached flow environment inboard of the canard vortex while enhances LE separation on the outboard of the canard vortex. The secondary flow separation pattern which appears on the tapered flap element seems to be stronger with the canard than without the canard surface. A stronger secondary separation usually is a viscous phenomena associated with a stronger vortex.

Effect of Canard on TCA (30/10) Wing Separation

HSCT Aerodynamics, Long Beach

M=0.3, AoA=10 deg, Re=8 million

Limiting Streamlines

Reference Location at Canard Tip

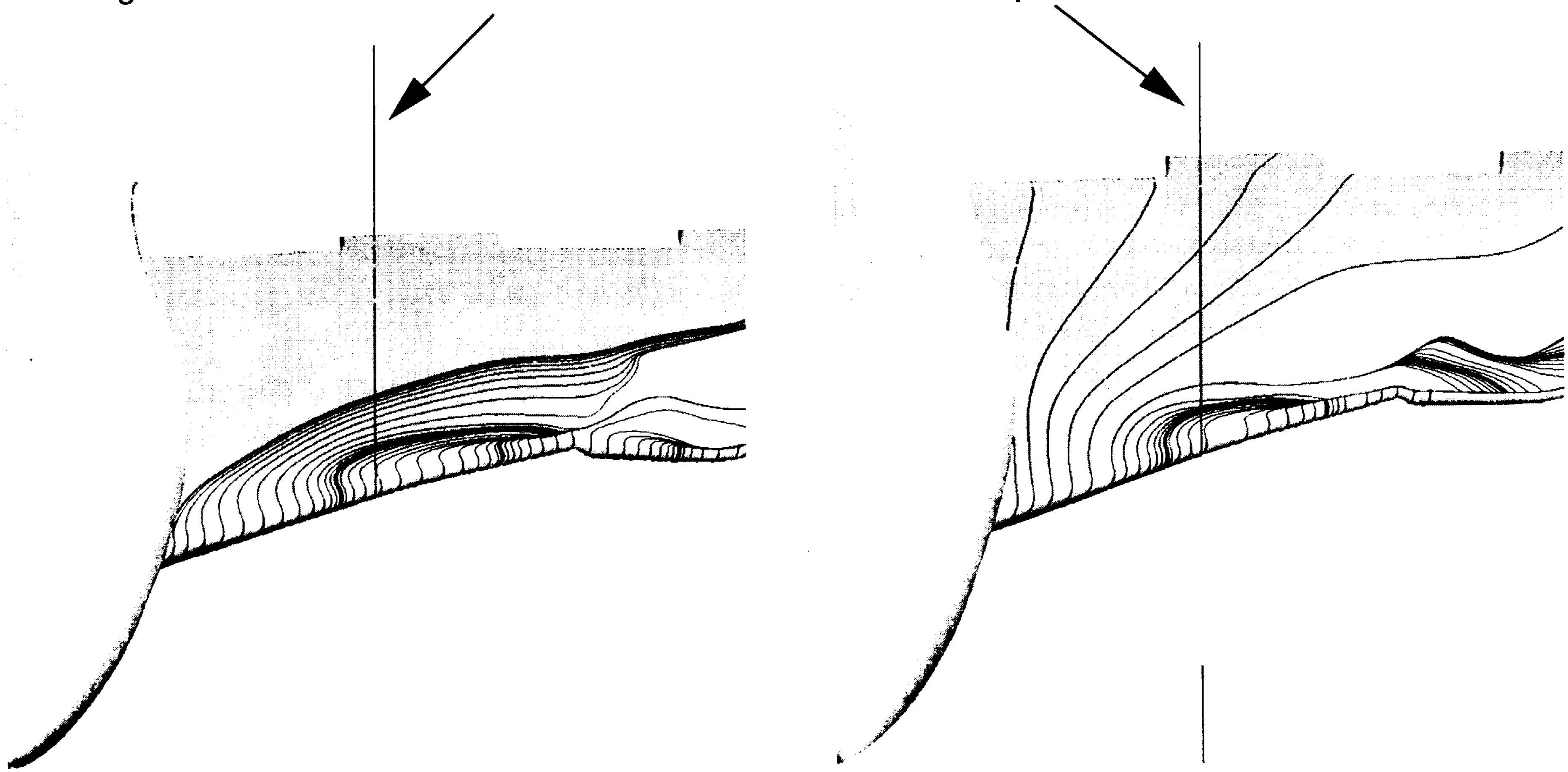

BOEING

Canard configuration for TCA-4 High Lift Test

This figure shows the geometric differences of the PTC canard which will be used for TCA-4 test and the currently analyzed ACC canard. The PTC canard has a smaller area which would have less loading (or a weak vortex) at the same flow conditions. The PTC canard is an mid-mount canard and positioned further upstream as compared to the ACC canard. Since the canard vortex has been shown to convect approximately in the direction of the free stream, the PTC canard vortex is expected to move further away from the wing surface than the ACC canard vortex. As a result, the PTC canard influence on the wing is expected to be less than the ACC canard.

The PTC canard has an aft-elevator which is geared to the canard deflection at high lift conditions. The sizable canard/fuselage gap created at large canard and the aft-elevator deflection needs to be modeled in order to properly resolve the actual flow phenomena in the test.

Canard Configuration for TCA–4 High–Lift Test

HSCT Aerodynamics, Long Beach

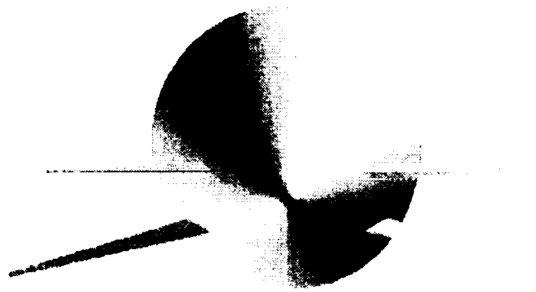

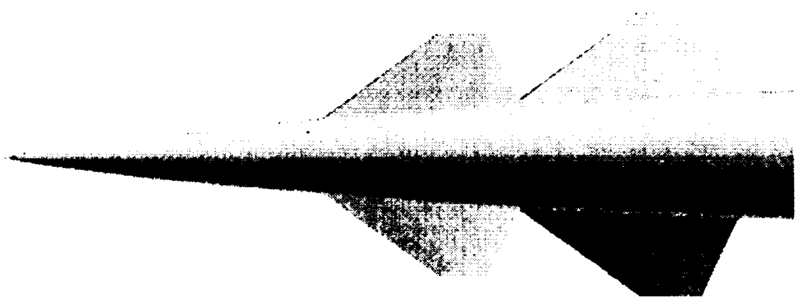

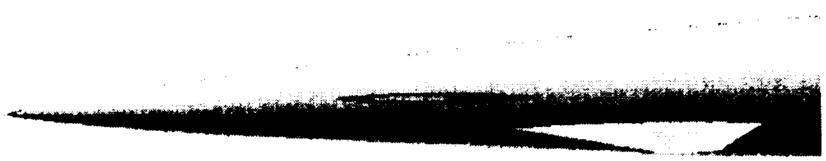

TCA–4 (PTC) canard vs. ACC canard

1. Smaller area
2. Further upstream
3. Mid–mount rather than low–mount
4. Movable canard with aft–elevator

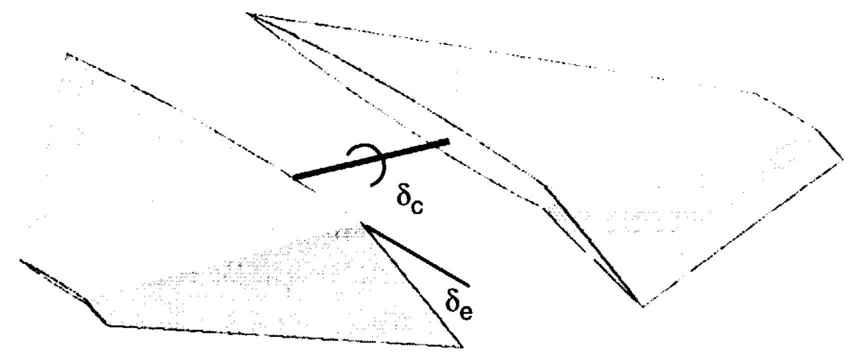

- Need to model canard/fuselage gap for large δ_c and δ_e under high lift conditions

BOEING

Summary

In summary, the numerical modeling of a canard and integration with a TCA high lift configuration has been accomplished and the numerical solution has been analyzed.

The numerical result has shown that the canard is dominated with vortical flow at high lift conditions. The canard vortex is shown to convect approximately in the free stream direction. The influence of the canard vortex is seen to create a lower local angel of attack inboard of the canard vortex which would create a more favorable attached flow environment. On the other hand, an upwash is induced outboard of the canard vortex which would promote LE separation resulting a stronger LE vortex. As a result, it may be desirable to extend the LE flap further inboard from the part span flap definition to account for the upwash created by the canard vortex. The influence of canard on the wing depends on the canard position and canard vortex strength which is a function of angle-of-attack, canard size, deflection and its position on the fuselage.

Based on the current numerical results and the geometric differences between the PTC and the ACC canard, it is expected that the influence of the PTC canard on the wing will be less than the currently analyzed result at a similar flow condition.

SUMMARY

- Automated canard integration procedure has been developed and demonstrated
- Numerical solution for an ACC canard on the TCA 30/10 configuration has been analyzed
- Numerical solution (at high lift condition) has shown:
  (1) Canard is dominated with vortical flow
  (2) Canard vortex is convected approximately in the free stream direction
  (3) Downwash created inboard of canard vortex – enhance attached flow
  (4) Upwash created outboard of canard vortex – promote LE separation
  (Full span LE flaps / Inboard camber may be desirable)
  (5) Canard influence on the wing : function(AoA, canard loading and position)
- Influence of PTC canard on the wing should be less than ACC canard due to its size and position

BOEING

High Lift CFD Activities for Canard Integration

The canard integration process will continue to model the PTC canard including the aft-elevator for pre-test analysis prior to the TCA-4 test. The canard/fuselage gap will be modeled to accurately resolve the actual flow phenomena in the tunnel. Additional numerical results will be generated and analyzed as needed for test planning, and code validation will be performed once the test data become available.

High Lift CFD Activities for Canard Integration

HSCT Aerodynamics, Long Beach

Current Activies:

* Conduct pre–test analysis for the TCA–4 test
* Enhance grid generation tools as needed
  - Aft–elevator modeling
  - Canard / fuselage gap
  - Wiping surface

Planned Activies:

* Continue wind–tunnel support for high lift configurations
* Perform code validation as test data becomes available
* Conduct parametric studies for performance optimization
  - Canard planform
  - Canard position

BOEING

This page is intentionally left blank.

Comparison of CFL3D Solutions Using Alternative Grid Interfacing Schemes

Xuetong Fan
Paul Hickey
ASE Technologies, Inc.

High Speed Research Program
Airframe Technical Review
Westin Hotel, Los Angeles Airport
February 9–13, 1998

This presentation documents the recent work at ASE Technologies, Inc. in applying the overset grid method to the CFD modeling of HSCT TCA Wing/Body/Nacelle High Lift configurations. The MAGGIE preprocessor in CFL3D is used in this work for the grid overlapping interpolations.

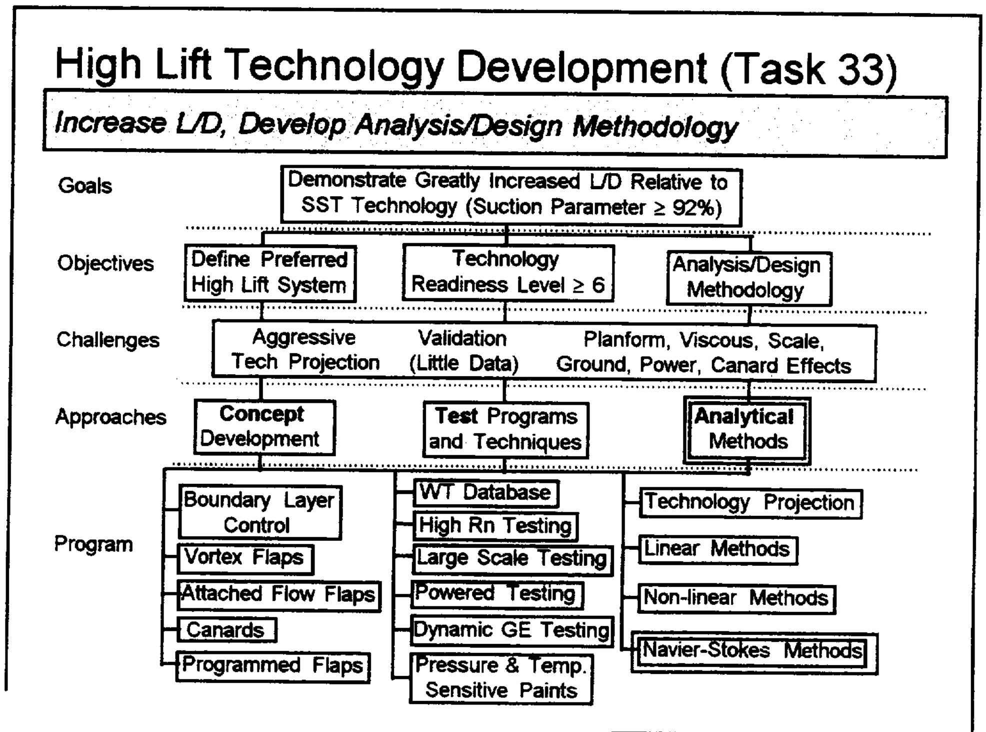

In the High Lift Technology Development program (Task 33), this work falls in the category of Navier-Stokes Methods under Analytical Methods. We hereby acknowledge the support and help from Roger Clark and David Yeh of Boeing Long Beach. We'd also like to thank Chung-Jin Woan of Boeing North American, Inc. for the fruitful discussions on the overset grid method.

Objectives

- Compare CFL3D solutions for TCA Wing/Body/Nacelle (WBN) high lift configurations using different grid interfacing schemes
  - Face–matched grid (RONNIE)
  - Overlapped grid (MAGGIE)
- Evaluate grid interfacing schemes for more efficient CFD modeling of TCA WBN configurations with and without deflected LE/TE flaps
  - Grid generation effort
  - Grid interface quality
  - Computer resources
  - Technical issues

The objectives of this work are twofold. The first objective is to compare and cross–examine the CFL3D solutions for the TCA W/B/N models using two different grid interfacing methods: face–matching (or patching) with RONNIE and overlapping with MAGGIE. The second objective is to evaluate these two methods and determine which one is better suited for the CFD modeling of the TCA W/B/N configurations. The grid interfacing method will be evaluated in terms of grid generation effort, block interface quality, and computer resources. Special attention is paid to the potential technical difficulities involved, especially in the case of deflected TE flaps for TCA high lift configurations.

Outline

- Background
- Overlapped grid model for TCA 0/0 WBN High Lift configuration
- CFL3D solution for TCA 0/0 WBN model with overlapped grid
  - Computer resources
  - Comparison with CFL3D solution using face–matched grid
- Comparison of the two schemes in TCA WBN applications
- Technical issues with overlapped grid
  - Interpolation near solid surfaces
  - Collar grid for adjoining solid surfaces
  - Special requirement in TCA 30/10 WBN case
- Summary

In this presentation, we will first put forth the background information for this work, including mostly our past experience in CFD modeling of the TCA W/B/N configurations using face–matched grid. Then we will describe the overlapped grid model for the TCA 0/0 WBN configuration and compare the CFL3D solution obtained from this model with the one from the previous face–match model. Based on the limited experience in using the two methods in the TCA WBN applications, a general comparison of the two methods is presented. Some of the technical issues involved with the overlapped grid method will be discussed. Finally, we will briefly summarize our effort and draw some preliminary conclusions.

Background

- Experience with CFL3D models using face–match grid for TCA WBN configurations with and without deflected LE/TE flaps
  - WBN grid is preferably based on WB grid
  - Grid generation is time consuming
  - Component grids are not portable
  - Grid quality is limited by the face–match requirement
  - Used wedges to model deflected TE flaps
- More efficient CFD modeling procedure is desired
- Alternative grid approach: Overlapped grid (MAGGIE)

Over the past two years, we have gained a lot of experience in the CFD modeling of HSCT W/B/N high lift configurations using face–matched grid. Though the face–matched models have performed well, the modeling procedure is less efficient primarily for the following reasons. (1) The W/B/N grid is based on the W/B grid for solution consistency. But for the N/D grid to face–match with the grid surfaces in the existing W/B model, it introduces constraints which make the grid generation process more time consuming. (2) The component grid for nacelles and diverters can not be easily used in other planforms. (3) Highly swept wing causes skewness in the grid. And interpolation across curved interfaces introduces numerical errors. (4) Wedges are necessary to model the deflected TE flaps in the W/B/N model, which cause local instability in the CFL3D solution.

The alternative approach to the CFD modeling of W/B/N configurations is the overlapped grid method. We need to determine if the overlapped grid will improve the CFD modeling procedure for TCA W/B/N configurations.

TCA 0/0 WBN Overlapped Model

- Comprised of the original W/B grid and the N/D grid from face–matched model
- Total 14 blocks and 4.4 million grid points
- Memory requirement: 180MW
- 1–1 point–matched and face–matched between N/D blocks
- N/D grid overlaps with W/B grid using MAGGIE preprocessor
- CPU usage for MAGGIE: 15 minutes on Cray C–90

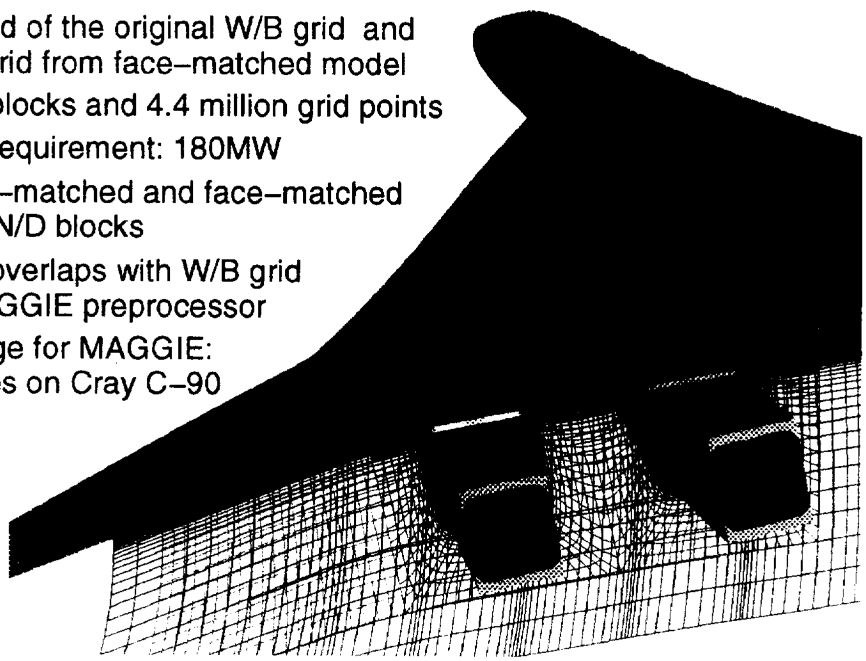

For the overset grid model for the TCA 0/0 W/B/N configuration, we simply used the N/D grid from the previously completed face–matched model and let them overlap with the original TCA 0/0 W/B grid. No additional grid generation was involved for this overset grid model. This model consists of 14 blocks with 4.4 million grid points. It requires 180 MW of memory on Cray C–90 to run the CFL3D solver for this model. The MAGGIE preprocessor in CFL3D was used to obtain the interpolation coefficients for grid overlapping between the N/D grid and the W/B grid. It used 15 minutes of CPU time on Cray C–90 for MAGGIE to complete the interpolations.

TCA 0/0 WBN Overlapped Model

Force integration on overlapped viscous surfaces

- Outer boundary of N/D grid on wing lower surface matches surface gridlines of the W/B grid
- Overlapped region from W/B grid on wing lower surface is not included for lift and drag force integration
- Black lines show the hole definition in W/B grid on wing lower surface

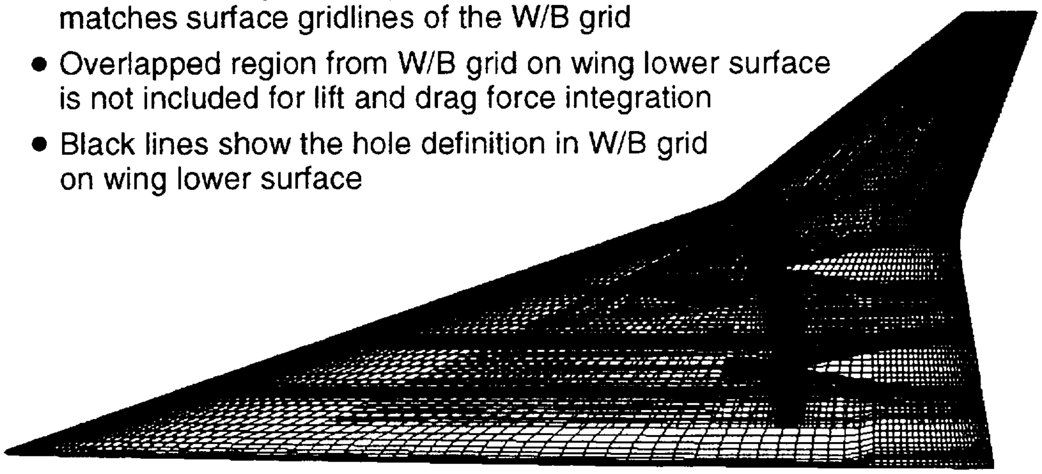

One of the technical issues involved in the overset grid approach is the force integration in the overlapped region on model solid surfaces. The general pratice is to go through additional post-processing steps to account for the right areas (See C.J. Woan's report for more information). In our overset grid model for the TCA 0/0 W/B/N configuration, since the N/D grid is directly from the face-matched model, the outer boundary of the N/D grid matches the surface grid lines of the W/B grid on wing lower surface. Therefore, by excluding the overlapped segment of the W/B grid on wing lower surface from force integration, the correct surface area is accounted for in the overall lift and drag calculations in the overset grid model.

CFL3D Convergence History

(TCA 0/0 WBN, Mach #=0.3, Re=8x10[6], AOA=10 degrees)

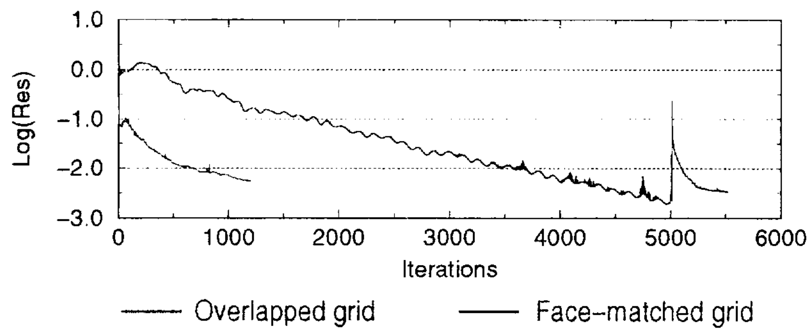

Overlapped model:

- No grid sequencing
- 3-level multi-grid
- 16 hours on Cray C-90

Face-matched model:

- 2-level grid sequencing
- 2-level multi-grid on fine level
- 18 hours on Cray C-90

The current version of CFL3D/MAGGIE allows multi-grid iterations but does not support grid sequencing for the overlapped grid model. The 1200 fine-level iterations completed for the TCA 0/0 W/B/N overset grid model used 16 CPU hours on Cray C-90. With the face-matched model for the TCA 0/0 W/B/N, the 5000 coarse level iterations and 500 fine level iterations used a total of 18 CPU hours on Cray C-90. Note that the original Baldwin-Lomax turbulence model with Degani-Schiff option was used in both models for the iterations cited in the above figure.

CFL3D Convergence History

(TCA 0/0 WBN, Mach #=0.3, Re=8x10^{6}, AOA=10 degrees)

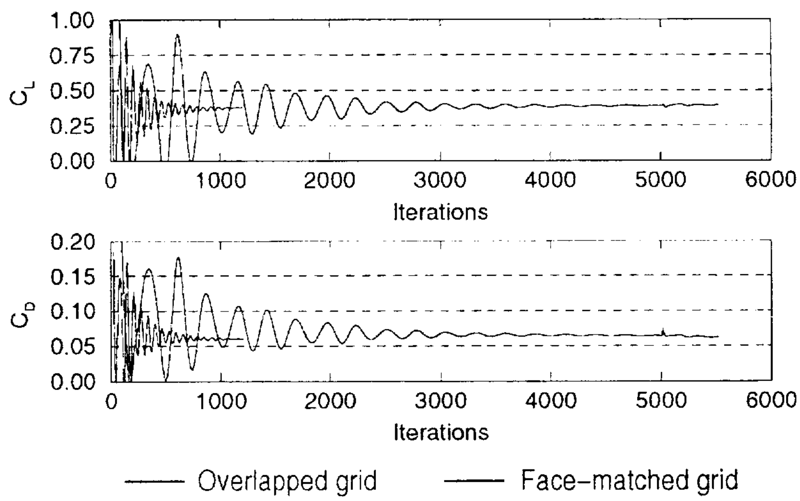

The convergence history for C_L and C_D from the two TCA 0/0 W/B/N models is shown here. For the last 200 iterations in both cases, the peak-to-valley variations in C_L and C_D are within 2% of their mean values.

TCA 0/0 WBN CFL3D Solutions:

(Mach #=0.3, Re=8x10^6, AOA=10 degrees)

Lift and Drag Coefficients

	Face–Matched Model	Overlapped Model	Difference
C_L	0.3958	0.3768	–0.0190
C_D	0.0627	0.0599	–0.0028

For comparison purposes, the original Baldwin–Lomax turbulence model with Degani–Schiff option was used for both models. The changes in the aerodynamic performance due to Yeh's modification to the turbulence model were +0.0158 in C_L and +0.0007 in C_D in the face–matched WBN CFD model.

For both the face–matched and the overlapped grid models, the mean values for C_L and C_D from the last 200 iterations are listed in the above table. Apparently there exist discrepancies between the two CFL3D solutions in terms of the integrated aerodynamic coefficients. Further investigation is necessary to determine the cause for the discrepancies.

TCA 0/0 WBN CFL3D Solutions

(Mach #=0.3, Re=8x10^6, AOA=10 degrees)
Cp on wing upper surfaces

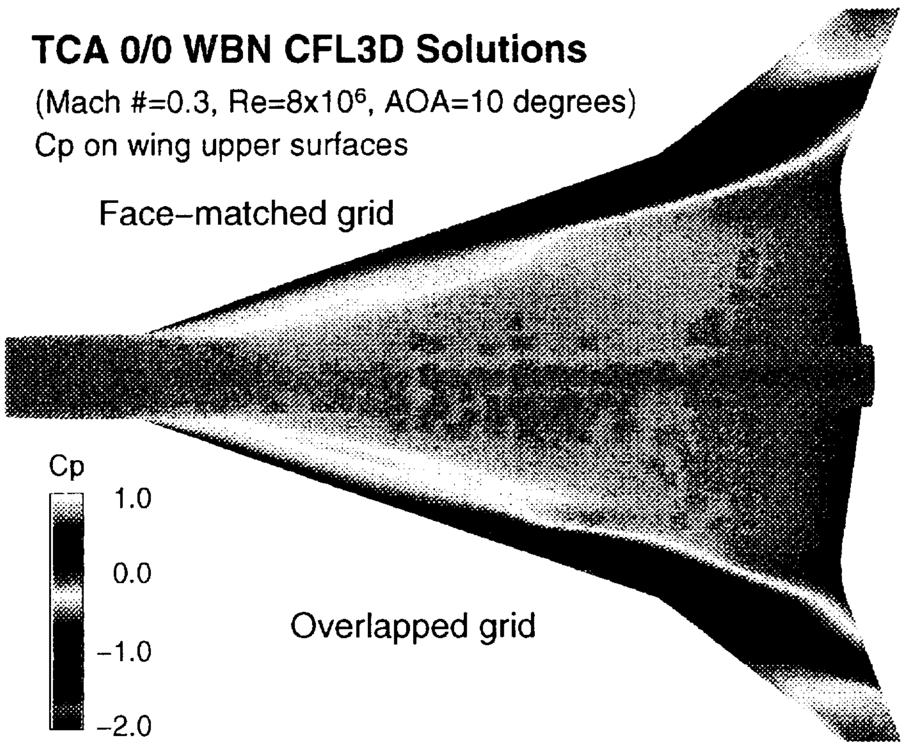

This figure shows the pressure distributions on the wing upper surface from the CFL3D solutions using the face-matched and the overlapped models. In general, the face-matched model and overlapped model captured very similar overall flow features for the TCA 0/0 W/B/N configuration.

TCA 0/0 WBN CFL3D Solutions

(Mach #=0.3, Re=8x10^6, AOA=10 degrees)
Cp on wing lower surfaces

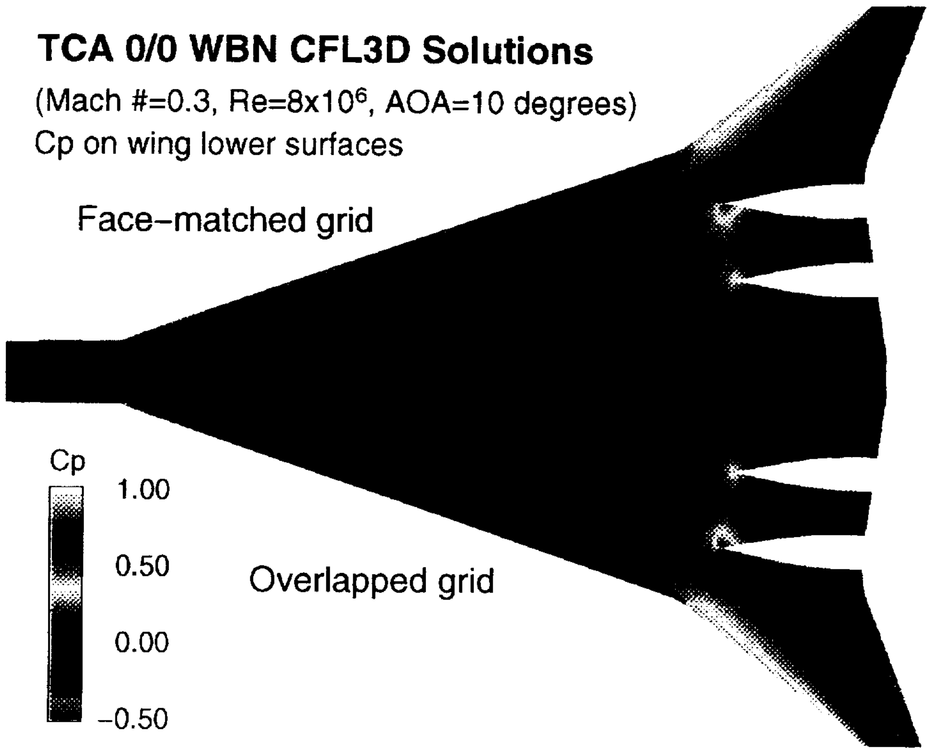

Similar resemblance in flow features captured by the two models can be seen in the pressure distribution on the wing lower surface shown above. More detailed contour plots for pressure coefficients on wing upper and lower surfaces may be necessary to explain the discrepancies in C_L values predicted by the two models.

Comparison of Face–Matched and Overlapped Grid Interfacing Schemes in TCA WBN Applications

	Face–Matching	Overlapping
Grid Generation	Additional constraints from surfaces of existing grid	Constrained by geometry only
Grid Portability	Less flexible	More flexible
Preprocessing	Less computer resource	More computer resource
Grid Interface	2–D	3–D
Model Size	Smaller	Larger
Grid Sequencing	Yes	No
Multi–Grid	Yes	Yes
Force Integration	Completed in CFL3D	Additional post–processing for overlapped solid surfaces

This table summarizes a general comparison of the face–matched method and the overlapped method based on our recent experience with modeling TCA WBN high lift configurations using CFL3D/RONNIE/MAGGIE. Overall, overset grid approach provides more potential in improving the CFD modeling procedure mainly because it is more flexible in generating the component grid as well as in using the component grid for different planforms. As for the pre–processing step, RONNIE can usually be completed in the debug queue on NAS supercomputers while MAGGIE has to be submitted to the batch queue. Also, since CFL3D/MAGGIE does not support grid sequencing, it will be more expensive and time consuming to debug an overlapped CFD model in the development stage.

Technical Issues with Overlapped Grid

MAGGIE Interpolation off Curved Solid Surfaces

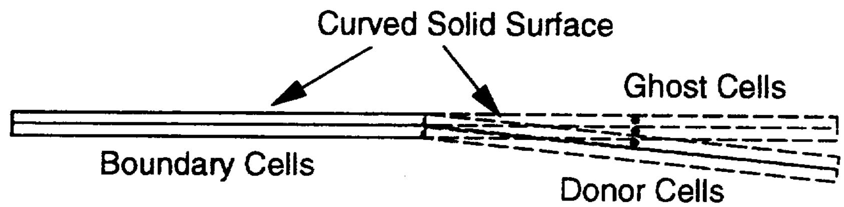

- Grid cells with high aspect ratio exist near solid surfaces in large scale model
- Ghost cells may exist out of bounds for even a slightly curved surface
- Several ghost cells may receive boundary condition data from the same donor cell in the overlapping grid through zeroth–order interpolation

One of the technical issues with the overset grid approach is associated with interpolation from donor cells to ghost cells at the outer boundary of the component grid. In large scale CFD models such as for the TCA W/B/N configurations, grid cells with very high aspect ratios exist near solid surfaces. When the solid surfaces are even slightly curved, the ghost cells can easily go out of bounds as shown in the above figure. In this case, several ghost cells may receive boundary condition data from the same donor cell through zeroth–order interpolation, which will lose the gradient information in the boundary layer profile and thus affect the numerical solution in the component grid as well as the overall solution.

Technical Issues with Overlapped Grid

Collar Grid for Adjoining Solid Surfaces

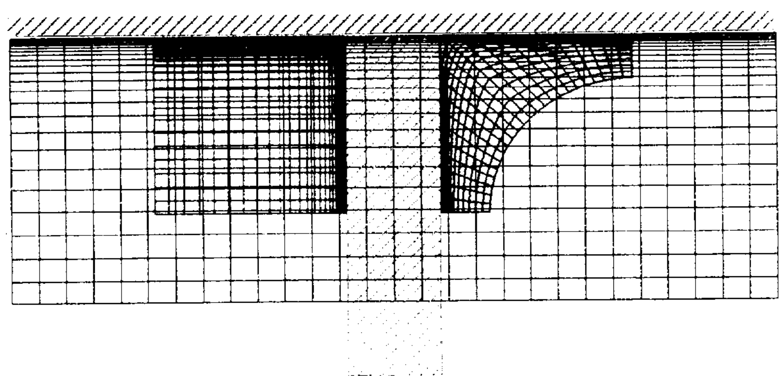

Method 1

- Two different grid faces for adjoining surfaces
- More flexible

Method 2

- One grid face for adjoining surfaces
- Less flexible

Another technical issue with the overset grid approach is the usage of collar grid for adjoining solid surfaces. In the literature, the collar grid described as method 2 in the above figure is often used and has been validated. However, sometimes it is difficult to fit this type of collar grid in the actual configuration, for example, in the leading edge region of nacelles and diverters adjoining wing lower surface. The collar grid described as method 1 in the above figure offers more flexibility but it needs to be validated.

Technical Challenge in Overlapped Grid for TCA 30/10 WBN Model

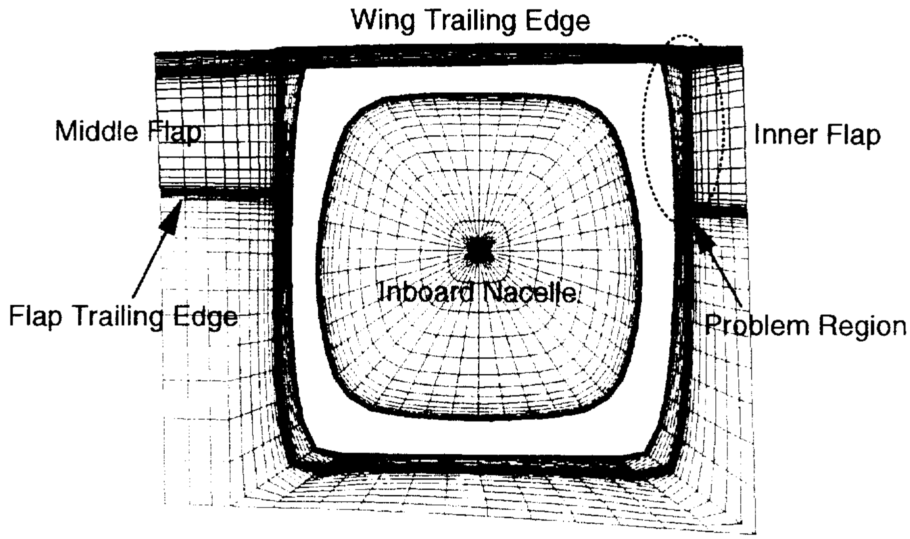

(Grid shown are from TCA 30/10 WBN face-matched grid)

Finally, the region between the nacelles/diverters and the deflected TE flaps still poses a technical challenge for overset grid approach due to the close proximity of the deflected TE flaps to the nacelles and diverters.

REPORT DOCUMENTATION PAGE	*Form Approved* *OMB No. 0704-0188*

1. AGENCY USE ONLY *(Leave blank)*	2. REPORT DATE	3. REPORT TYPE AND DATES COVERED
	December 1999	Conference Publication

4. TITLE AND SUBTITLE	5. FUNDING NUMBERS
1998 NASA High-Speed Research Program Aerodynamic Performance Workshop *Volume II—High Lift*	WU 537-07
6. AUTHOR(S)	
S. Naomi McMillin, Editor	

7. PERFORMING ORGANIZATION NAME(S) AND ADDRESS(ES)	8. PERFORMING ORGANIZATION REPORT NUMBER
NASA Langley Research Center Hampton, VA 23681-2199	L-17758C

9. SPONSORING/MONITORING AGENCY NAME(S) AND ADDRESS(ES)	10. SPONSORING/MONITORING AGENCY REPORT NUMBER
National Aeronautics and Space Administration Washington, DC 20546-0001	NASA/CP-1999-209692/VOL2

11. SUPPLEMENTARY NOTES

12a. DISTRIBUTION/AVAILABILITY STATEMENT	12b. DISTRIBUTION CODE
Unclassified–Unlimited Subject Category 02 Distribution: Nonstandard Availability: NASA CASI (301) 621-0390	

13. ABSTRACT *(Maximum 200 words)*

NASA's High-Speed Research Program sponsored the 1998 Aerodynamic Performance Technical Review on February 9–13, in Los Angeles, California. The review was designed to bring together NASA and industry High-Speed Civil Transport (HSCT) Aerodynamic Performance technology development participants in areas of Configuration Aerodynamics (transonic and supersonic cruise drag prediction and minimization), High-Lift, and Flight Controls. The review objectives were to (1) report the progress and status of HSCT aerodynamic performance technology development; (2) disseminate this technology within the appropriate technical communities; and (3) promote synergy among the scientists and engineers working HSCT aerodynamics. In particular, single- and multi-point optimized HSCT configurations, HSCT high-lift system performance predictions, and HSCT simulation results were presented along with executive summaries for all the Aerodynamic Performance technology areas. The HSR Aerodynamic Performance Technical Review was held simultaneously with the annual review of the following airframe technology areas: Materials and Structures, Environmental Impact, Flight Deck, and Technology Integration. Thus, a fourth objective of the Review was to promote synergy between the Aerodynamic Performance technology area and the other technology areas of the HSR Program.

14. SUBJECT TERMS	15. NUMBER OF PAGES
High-Speed Research; High-Speed Civil Transport	987
	16. PRICE CODE
	A99

17. SECURITY CLASSIFICATION OF REPORT	18. SECURITY CLASSIFICATION OF THIS PAGE	19. SECURITY CLASSIFICATION OF ABSTRACT	20. LIMITATION OF ABSTRACT
Unclassified	Unclassified	Unclassified	UL

Summary

- Developed an overlapped grid CFD model for TCA 0/0 Wing/Body/Nacelle high lift configuration.
- Obtained converged CFL3D solution using the overlapped grid for TCA 0/0 WBN at Mach No.=0.3, Re=$8x10^6$, AOA=10 degrees.
  - Face–matched and overlapped grids yield similar solutions.
  - Discrepancy exists between the integrated aerodynamic coefficients using different grid interfacing schemes. Further investigation is required.
- Evaluation of the alternative grid interfacing schemes reveals:
  - Overlapped grid method is more adaptable to configuration changes.
  - Less time–consuming grid generation with overlapped grid approach.
  - Technical challenges still exist for deflected TE flaps configurations.
  - Overlapped grid will be more efficient for TCA WBN configurations.

In summary, our recent work is directed towards the evaluation of overset grid method for the CFD modeling of TCA W/B/N high lift configurations. With the first overset grid model for the TCA 0/0 W/B/N configuration, we obtained a converged CFL3D solution which compares well with the CFL3D solution using the face–matched model in terms of overall flow features. Discrepancies exist between the integrated aerodynamic coefficients from the two CFL3D solutions and we will further investigate the reasons for the discrepancies. Based on our extensive experience with face–matched grid interfacing method and the limited experience with the overset grid interfacing method, we conclude that overset grid approach offers more potential in improving the CFD modeling procedure for the TCA W/B/N high lift configurations.